VITERBI DECODED LINEAR BLOCK CODES FOR NARROWBAND AND WIDEBAND WIRELESS COMMUNICATION OVER MOBILE FADING CHANNELS

By
Leonard Staphorst

Submitted in partial fulfilment of the requirements for the degree
Master of Engineering (Electronic)
in the
Department of Electrical, Electronic and Computer Engineering
of the
Faculty of Engineering, Built Environment and Information Technology
at the
UNIVERSITY OF PRETORIA

Promoter: Professor L.P. Linde

July 2005

SUMMARY

VITERBI DECODED LINEAR BLOCK CODES FOR NARROWBAND AND WIDEBAND WIRELESS COMMUNICATION OVER MOBILE FADING CHANNELS

by

Leonard Staphorst

Promoter: Professor L.P. Linde

Department of Electrical, Electronic and Computer Engineering

Master of Engineering (Electronic)

SINCE the frantic race towards the Shannon bound [1] commenced in the early 1950's, linear block codes have become integral components of most digital communication systems. Both binary and non-binary linear block codes have proven themselves as formidable adversaries against the impediments presented by wireless communication channels. However, prior to the landmark 1974 paper [2] by *Bahl et al.* on the optimal *Maximum a-Posteriori Probability* (MAP) trellis decoding of linear block codes, practical linear block code decoding schemes were not only based on suboptimal hard decision algorithms, but also code-specific in most instances. In 1978 *Wolf* expedited the work of *Bahl et al.* by demonstrating the applicability of a block-wise *Viterbi Algorithm* (VA) to *Bahl-Cocke-Jelinek-Raviv* (BCJR) trellis structures as a generic optimal soft decision *Maximum-Likelihood* (ML) trellis decoding solution for linear block codes [3].

This study, largely motivated by code implementers' ongoing search for generic linear block code decoding algorithms, builds on the foundations established by *Bahl*, *Wolf* and other contributing researchers by thoroughly evaluating the VA decoding of popular binary and non-binary linear block codes on realistic narrowband and wideband digital communication platforms in lifelike mobile environments. Ideally, generic linear block code decoding algorithms must not only be modest in terms of computational complexity, but they must also be channel aware. Such universal algorithms will undoubtedly be integrated into most channel coding subsystems that adapt to changing mobile channel conditions, such as the adaptive channel coding schemes of current *Enhanced Data Rates for GSM Evolution* (EDGE), 3^{rd} *Generation* (3G) and *Beyond 3G* (B3G) systems, as well as future 4^{th} *Generation* (4G) systems. In this study classic BCJR linear block code trellis construction is annotated and applied to contemporary binary and non-binary linear block codes. Since BCJR trellis structures are inherently sizable and intricate, rudimentary trellis complexity calculation and reduction algorithms are also presented and demonstrated. The block-wise VA for BCJR trellis structures, initially introduced by *Wolf* in [3], is revisited and improved to incorporate *Channel State Information* (CSI) during its ML decoding efforts.

In order to accurately appraise the *Bit-Error-Rate* (BER) performances of VA decoded linear block codes in authentic wireless communication environments, *Additive White Gaussian Noise* (AWGN), flat fading and multi-user multipath fading simulation platforms were constructed. Included in this task was the development of baseband complex flat and multipath fading channel simulator models, capable of reproducing the physical attributes of realistic mobile fading channels. Furthermore, a

complex *Quadrature Phase Shift Keying* (QPSK) system were employed as the narrowband communication link of choice for the AWGN and flat fading channel performance evaluation platforms. The versatile B3G multi-user multipath fading simulation platform, however, was constructed using a wideband RAKE receiver-based complex *Direct Sequence Spread Spectrum Multiple Access* (DS/SSMA) communication system that supports unfiltered and filtered *Complex Spreading Sequence*s (CSS). This wideband platform is not only capable of analysing the influence of frequency selective fading on the BER performances of VA decoded linear block codes, but also the influence of the *Multi-User Interference* (MUI) created by other users active in the *Code Division Multiple Access* (CDMA) system. CSS families considered during this study include *Zadoff-Chu* (ZC) [4, 5], *Quadriphase* (QPH) [6], *Double Sideband* (DSB) *Constant Envelope Linearly Interpolated Root-of-Unity* (CE-LI-RU) filtered *Generalised Chirp-like* (GCL) [4, 7–9] and *Analytical Bandlimited Complex* (ABC) [7, 10] sequences.

Numerous simulated BER performance curves, obtained using the AWGN, flat fading and multi-user multipath fading channel performance evaluation platforms, are presented in this study for various important binary and non-binary linear block code classes, all decoded using the VA. Binary linear block codes examined include Hamming and *Bose-Chaudhuri-Hocquenghem* (BCH) codes, whereas popular burst error correcting non-binary *Reed-Solomon* (RS) codes receive special attention. Furthermore, a simple cyclic binary linear block code is used to validate the viability of employing the reduced trellis structures produced by the proposed trellis complexity reduction algorithm. The simulated BER performance results shed light on the error correction capabilities of these VA decoded linear block codes when influenced by detrimental channel effects, including AWGN, Doppler spreading, diminished *Line-of-Sight* (LOS) signal strength, multipath propagation and MUI. It also investigates the impact of other pertinent communication system configuration alternatives, including channel interleaving, code puncturing, the quality of the CSI available during VA decoding, RAKE diversity combining approaches and CSS correlation characteristics. From these simulated results it can not only be gathered that the VA is an effective generic optimal soft input ML decoder for both binary and non-binary linear block codes, but also that the inclusion of CSI during VA metric calculations can fortify the BER performances of such codes beyond that attainable by classic ML decoding algorithms.

Keywords, phrases and acronyms: 3G, 4G, adaptive channel coding, AWGN, B3G, BCH code, BCJR trellis, BER, CDMA, code puncturing, CSI, CSS, DS/SSMA, EDGE, flat fading, Hamming code, hard decision decoding, channel interleaving, linear block code, MAP decoding, ML decoding, MUI, multipath fading, QPSK, RAKE, RS code, Shannon bound, soft decision decoding, VA

SAMEVATTING

VITERBI GEDEKODEERDE LINEÊRE BLOKKODES VIR NOUEBAND EN WYEBAND KOMMUNIKASIE OOR MOBIELE DEINENDE KANALE

deur
Leonard Staphorst
Promoter: Professor L.P. Linde
Departement Elektriese, Elektroniese en Rekenaar-Ingenieurswese
Meester in Ingenieurswese (Elektronies)

SEDERT die verwoede resies na die Shannon-grens [1] in die vroeë 1950's aanvang geneem het, het lineêre blokkodes integrale komponente van meeste digitale kommunikasiestelsels geword. Beide binêre en nie-binêre lineêre blokkodes het hulself bewys as gedugte teenstanders teen die belemmeringe wat draadlose kommunikasiekanale bied. Voor die mylpaal 1974 artikel [2] deur *Bahl et al.* oor die optimale *Maksimum a-Posteriori Waarskeinlikheid* (MAW) trellisdekodering van lineêre blokkodes, was praktiese lineêre blokkode dekoderingskemas egter nie net gebaseer op suboptimale harde beslissingsalgoritmes nie, maar ook kode-spesifiek in meeste gevalle. In 1978 het *Wolf* die werk van *Bahl et al.* aangehelp deur die toepasbaarheid van 'n bloktipe *Viterbi Algoritme* (VA) op *Bahl-Cocke-Jelinek-Raviv* (BCJR) trellisstrukture as 'n generiese optimale sagte beslissing *Maksimum Waarskeinlikheid* (MW) trellis dekoderingsoplossing vir lineêre blokkodes te demonstreer [3].

Hierdie studie, hoofsaaklik gemotiveer deur kode-implementeerders se voortdurende soeke na generiese lineêre blokkode dekoderingalgoritmes, bou op die fondasies wat deur *Bahl*, *Wolf* en ander bydraende navorsers gevestig is, deur die VA dekodering van gewilde binêre en nie-binêre lineêre blokkodes op realistiese noueband en wyeband digitale kommunikasieplatforms in lewenstroue mobiele omgewings deeglik te evalueer. Generiese lineêre blokkode dekoderingalgoritmes moet ideaal nie net beskeie wees in terme van bewerkingkompleksiteit nie, maar moet ook kanaal-bewus wees. Sulke universele algoritmes sal ongetwyfeld geïntegreer word in meeste kanaalkodering substelsels wat aanpas tot veranderende mobile kanaaltoestande, soos die aanpasbare kanaalkoderingskemas van huidige *Enhanced Data Rates for GSM Evolution* (EDGE), 3^{de} *Generasie* (3G) en *Bokant* 3^{de} *Generasie* (B3G) stelsels, asook toekomstige 4^{de} *Generasie* (4G) stelsels. In hierdie studie word klasieke BCJR trelliskonstruksie verduidelik en toegepas op hedendaagse binêre en nie-binêre lineêre blokkodes. Aangesien BCJR trellisstrukture inherent groot en ingewikkeld is, word elementêre trelliskompleksiteit berekening- en verminderingalgoritmes ook voorgestel en gedemonstreer. Die bloktipe VA vir BCJR trellisstrukture, oorspronklike voorgestel deur *Wolf* in [3], word heroorweeg en verbeter om *Kanaaltoestand Informasie* (KTI) te inkorporeer gedurende sy MW dekoderingspogings.

Om die *Bisfout Tempo* (BFT) werkverrigting van VA gedekodeerde lineêre blokkodes in outentieke draadloses kommunikasieomgewings akkuraat te waardeer, was *Sommeerbare Wit Gaussiese Ruis* (SWGR), plat deining en multi-gebruiker multipad deining simulasieplatforms geskep. Ingesluit in hierdie taak was die ontwikkeling van komplekse basisband plat en multipad deinende kanaal simulatormodelle, wat instaat is om die fisiese eienskappe van realistiese mobiele deinende kanale te

herproduseer. Verder was ’n komplekse *Kwadratuur Faseskuif Sleuteling* (KFSS) stelsel gebruik as die gekose nouband kommunikasieskakel vir die SWGR en plat deinende kanaal werkverrigting evaluasieplatforms. Die veelsydige B3G multi-gebruiker multipad deinende simulasieplatform was egter saamgestel deur gebruik te maak van ’n RAKE ontvanger gebaseerde komplekse wyeband *Direkte Sekwensie Spreispektrum Veelvuldige Toegang* (DS/SSVT) kommunikasiestelsel wat ongefilterde en gefilterde *Komplekse Spreisekwensie*s (KSS) ondersteun. Hierdie wyeband platform is nie net instaat om die invloed van frekwensie selektiewe deining op die BFT werkverrigting van VA gedekodeerde lineêre blokkodes te analiseer nie, maar so ook die invloed van die *Multi-gebruiker Steuring* (MGS) geskep deur die ander gebruikers wat aktief in die *Kode Divisie Veelvuldige Toegang* (KDVT) stelsel is. KSS families wat oorweeg is in hierdie studie sluit in *Zadoff-Chu* (ZC) [4, 5], *Kwadratuur Fasige* (KF) [6], *Dubbele Syband* (DSB) *Konstante Omhulling Lineêr Geïnterpoleerde Eenheidswortel* (KOLGI-EW) gefilterde *Algemene Tjirp-agtige* (ATA) [4, 7, 8] en *Analitiese Bandbeperkte Komplekse* (ABK) [7, 10] sekwensies.

Talryke gesimuleerde BFT werkverrigtingkurwes, verkry deur van die SWGR, plat deining en multigebruiker multipad deining werkverrigting evaluasieplatforms gebruik te maak, word in hierdie studie voorgelê vir verskeie belangrike binêre en nie-binêre lineêre blokkode klasse, almal gedekodeer deur van die VA gebruik te maak. Binêre lineêre blokkodes wat ondersoek is, sluit in Hamming en *Bose-Chaudhuri-Hocquenghem* (BCH) kodes, terwyl gewilde sarsiefout korrigerende nie-binêre *Reed-Solomon* (RS) kodes spesiale aandag ontvang. Verder word ’n eenvoudige sikliese binêre lineêre blokkode gebruik om die lewensvatbaarheid van die gebruik van die vereenvoudigde trellisstrukture, geproduseer deur die voorgestelde trellis kompleksiteit verminderingsalgoritme, te bekragtig. Die gesimuleerde BFT werkverrigtingresultate werp lig op die foutkorreksie vermoëns van hierdie VA gedekodeerde lineêre blokkodes wanneer hulle beïnvloed word deur nadelige kanaaleffekte, insluitend SWGR, Doppler spreiding, verminderde *Lyn-van-Sig* (LVS) seinsterkte, multipad voortplanting en MGS. Dit ondersoek ook die impak van ander toepaslike kommunikasiestelsel konfigurasiealternatiewe, insluitend kanaalintervlegging, kodeperforasie, die kwaliteit van die KTI beskikbaar gedurende VA dekodering, RAKE diversiteit samevoegingsbenaderings en KSS korrelasie karakteristieke. Vanuit hierdie gesimuleerde resultate kan dit nie net afgelei word dat die VA ’n effektiewe generiese optimale sagte inset MW dekodeerder is vir beide binêre en nie-binêre lineêre blokkodes nie, maar ook dat die insluiting van KTI gedurende VA metriekberekeninge die BFT werkverrigtinge van sulke kodes kan verbeter bo dit wat haalbaar is deur klassieke MW dekoderingsalgoritmes.

Sleutelwoorde, frases en akronieme: 3G, 4G, aanpasbare kanaalkodering, B3G, BCH kode, BCJR trellis, BFT, DS/SSVT, EDGE, Hamming kode, harde beslissingsdekodering, kanaalintervlegging, KDVT, KFSS, kodeperforasie, KTI, KSS, lineêre blokkode, MAW dekodering, MGS, multipad deining, MW dekodering, plat deining, RAKE, RS kode, sagte beslissingsdekodering, Shannon-grens, SWGR, VA

This dissertation is dedicated to:

God Almighty, for blessing me with many talents, and granting me countless opportunities to use them;
My loving family and friends, whose continuous support and encouragement carried me through the arduous times.

"The next best thing to a good education, is a pushy mother."

M.P. Staphorst

ACKNOWLEDGMENTS

I wish to extend my heartfelt gratitude to the following people and institutions who supported this study in one way or another:

First and foremost, my appreciation and thanks go to my parents, my aunt Joey and my sister Ronell. Their enduring love, support and encouragement were indispensable driving forces, especially during the gruelling times when completion of this study seemed like an unsurmountable task. A special mention goes to my mother for the time and effort she vested in proofreading this document.

I am especially grateful to my study leader and promotor, Prof. L.P. Linde, for his continued latitude, support and guidance during this study. To my informal signal processing and digital communication mentors, Jacques Cilliers and Danie van Wyk, I wish to extend this same gratitude.

My thanks goes to my fellow engineering friends Stefan Swanepoel, Jacques van Wyk, Ben Waldeck, Werner Büttner, Pieter de Villiers, Momin Jamil, Fernando Camisani-Calzolari, Pieter-Jan Vlok and Christian Bruwer, with whom I shared many insightful and intellectual discussions on our respective postgraduate projects. These discussions fuelled much of my motivation for this study.

Credit goes to the *University of Pretoria* and the *National Research Foundation* for the financial sponsorship of my Masters degree studies through personnel and prestigious postgraduate bursaries, respectively. Furthermore, I am indebted to *Intel* for their donation of the *I-percube* high performance computing cluster, as well as Paul Greeff, Jan Gütter and Simeon Miteff for their invaluable support in the usage thereof.

Last, but definitely not least, my thanks and gratitude go to my best friend and companion, Betsie van der Westhuizen. Her love, patience and fantastic cooking carried me during the last few difficult months leading to the conclusion of this study. I will always be indebted to her for not only sacrificing her time and social life to stand by my side, but also listening to countless, monotonous explanations on the work that I was doing.

TABLE OF CONTENTS

LIST OF FIGURES

LIST OF TABLES

LIST OF ABBREVIATIONS

2G	2^{nd} Generation
3G	3^{rd} Generation
4G	4^{th} Generation
ABC	Analytical Bandlimited Complex
AC	Alternating Current
ADC	Analogue-to-Digital Converter
ASIC	Application Specific Integrated Circuit
ATM	Asynchronous Transfer Mode
AWGN	Additive White Gaussian Noise
B3G	Beyond 3G
BCH	Bose-Chaudhuri-Hocquenghem
BCJR	Bahl-Cocke-Jelinek-Raviv
BEF	Bandwidth Expansion Factor
BER	Bit-Error-Rate
BPSK	Binary Phase Shift Keying
BSC	Binary Symmetric Channel
CC	Constituent Code
CD	Compact Disc
CD-ROM	Compact Disc Read Only Memory
CDMA	Code Division Multiple Access
CE-LI-RU	Constant Envelope Linearly Interpolated Root-of-Unity
CLT	Central Limit Theorem
CSI	Channel State Information
CSS	Complex Spreading Sequence
DPC	Differential Phase Combining
DPSK	Differential Phase Shift Keying
DS/SSMA	Direct Sequence Spread Spectrum Multiple Access
DSB	Double Sideband
DSP	Digital Signal Processor
DSSS	Direct Sequence Spread Spectrum
ECC	Error Control Coding
EDGE	Enhanced Data Rates for GSM Evolution
EGC	Equal Gain Combining
FDMA	Frequency Division Multiple Access
FEC	Forward Error Correction
FFCS	Flat Fading Channel Simulator
FHSS	Frequency Hopping Spread Spectrum
FIR	Finite Impulse Response
FPGA	Field Programmable Gate Array
GA	Gaussian Approximation

GCL	Generalised Chirp-like
GNU	GNU is Not Unix
GPRS	General Packet Radio Service
GSM	Global System for Mobile Communication
HCC	Hybrid Concatenated Code
HEC	Header Error Control
HPC	High Performance Computing
IID	Independent Identically Distributed
IIR	Infinite Impulse Response
IOWEF	Input-Output Weight Enumerating Function
JPL	Jet Propulsion Labs
LDPC	Low Density Parity-Check Code
LLR	Log-Likelihood Ratio
LOS	Line-of-Sight
MA	Multiple Access
MAP	Maximum a-Posteriori Probability
MC	Multi-Carrier
MFCS	Multipath Fading Channel Simulator
ML	Maximum-Likelihood
MLC	Multi-Level Code
MLSE	Maximum Likelihood Sequence Estimation
MRC	Maximal Ratio Combining
MUI	Multi-User Interference
NASA	National Aeronautical and Space Association
NLOS	Non-Line-of-Sight
NSC	Non-Systematic Convolutional
OFDM	Orthogonal Frequency Division Multiplexing
OOP	Object Orientated Programming
OS	Operating System
OSI	Open Standards Interface
PCC	Parallel Concatenated Code
PCCC	Parallel Concatenated Convolutional Code
PDF	Probability Density Function
PG	Processing Gain
PHY	Physical
PN	Pseudo-Noise
PSAM	Pilot Symbol Assisted Modulation
PSD	Power Spectral Density
QPH	Quadriphase
QPSK	Quadrature Phase Shift Keying
QoS	Quality of Service
RF	Radio Frequency
RMS	Root-Mean-Square
ROM	Read Only Memory
RS	Reed-Solomon
RSC	Recursive Systematic Convolutional
RU	Root-of-Unity
SCC	Serial Concatenated Code
SCCC	Serial Concatenated Convolutional Code

SDMA	Spatial Division Multiple Access
SF	Spreading Factor
SISO	Soft-Input Soft-Output
SMS	Short Message Service
SNR	Signal-to-Noise Ratio
SOVA	Soft Output Viterbi Algorithm
SOVE	Soft Output Viterbi Equaliser
SS	Spread Spectrum
SSB	Single Sideband
SSLD	Spreading Sequence Length Diversity
STC	Space Time Code
TC	Turbo Code
TCM	Trellis Coded Modulation
TCP	Transmission Control Protocol
TDMA	Time Division Multiple Access
UMTS	Universal Mobile Telephony System
VA	Viterbi Algorithm
VHF	Very High Frequency
WEF	Weight Enumerating Function
WLL	Wireless Local Loop
ZC	Zadoff-Chu

LIST OF IMPORTANT SYMBOLS

$\alpha_i(t)$	Instantaneous fading amplitude of the i^{th} multipath component
$\overline{\alpha}_m$	Vector of average fading amplitude values associated with $\overline{y}_m$
$\hat{\overline{\alpha}}_m$	Vector of estimates of the average fading amplitude values associated with $\overline{y}_m$
$AN(C)$	Number of active nodes in the expurgated trellis of linear block code C [nodes]
$A(W,Z)$	Input-Output weight enumerating function of a linear block code [code words]
$A_{w,h}$	Coefficients of a linear block code's input-output weight enumerating function [symbols]
B_C	Coherence bandwidth [Hz]
B_D	Maximum Doppler spread [Hz]
$\beta_i(t)$	Instantaneous amplitude of the i^{th} multipath component [V]
$\overline{\beta}_i$	Average amplitude of the i^{th} multipath component [V]
$b_i(t)$	i^{th} received multipath component [V]
$BM_{m,i,l}^{(j)}$	m^{th} decoded code word's branch metric associated with the j^{th} branch entering node (l,i) of a trellis
B_{sig}	Signal bandwidth [Hz]
CG_{BC}^{hard}	Asymptotic coding gain for a hard decision decoded linear block code [dB]
CG_{BC}^{soft}	Asymptotic coding gain for a soft decision decoded linear block code [dB]
CG_{CC}^{hard}	Asymptotic coding gain for a hard decision decoded convolutional code [dB]
CG_{CC}^{soft}	Asymptotic coding gain for a soft decision decoded convolutional code [dB]
$\overline{c}_m$	m^{th} vector of code word symbols [V]
$\hat{\overline{c}}_m$	Decoder estimate of the m^{th} vector of code word symbols [V]
$\overline{c}_m(D)$	m^{th} vector sequence of code bits generated by a binary convolutional code [V]
$c_m(p)$	m^{th} transmitted code word polynomial of a linear block code [V]
$CM_{m,i,l}$	m^{th} decoded code word's cumulative metric associated with the j^{th} branch leaving node (l,i) of a trellis
d_{free}	Minimum free distance of a convolutional code [bits]
$DF(z)$	Doppler spectral shaping infinite impulse response filter transfer function
$d_H\left(\overline{c}_m^1, \overline{c}_m^2\right)$	Hamming distance between vectors $\overline{c}_m^1$ and $\overline{c}_m^2$ [symbols]
$d_H\left(\overline{y}_{m,i}, \overline{u}_{i,l}^{(j)}\right)$	Hamming distance between vectors $\overline{y}_{m,i}$ and $\overline{u}_{i,l}^{(j)}$ [symbols]
$\overline{d}_m$	m^{th} vector of original message word symbols [V]
$\hat{\overline{d}}_m$	Decoder estimate of the m^{th} vector of original message word symbols [V]
$\overline{d}_m(D)$	m^{th} vector sequence of data bits entering a binary convolutional code [V]
d_{min}	Minimum Hamming distance of a linear block code [symbols]
$d_m(p)$	m^{th} message word polynomial of a linear block code [V]
E_b	Energy per uncoded data bit [J]
E_c	Energy per coded bit [J]
$e_m(p)$	m^{th} error word polynomial of a linear block code [V]
E_s	Energy per modulated symbol [J]

$\eta(t)$	Additive white Gaussian noise amplitude [V]
$\eth(\Pi)$	Interleaver fundamental permutation
$\eth\left(\Pi^{-1}\right)$	De-interleaver fundamental permutation
f	Frequency [Hz]
F	Interleaver width [symbols]
f_{bit}	Uncoded bit rate [b/s]
f_c	Carrier frequency [Hz]
f_{cut}	Filter cutoff frequency [Hz]
$f_{d,i}(t)$	Doppler frequency shift of the i^{th} multipath component [Hz]
f_{samp}	Sampling frequency [Hz]
$\gamma_{b,m,i}$	Signal to noise ratio per uncoded bit for the i^{th} bit of the m^{th} vector of bits
$\gamma_{c,m}$	Signal to noise ratio per code word for the m^{th} code word
$\Gamma_{m,i,a}$	Erasure value for the a^{th} bit in the i^{th} symbol of the m^{th} set of received code word symbols [V]
$\gamma_{s,m,i}$	Signal to noise ratio per modulated symbol for the i^{th} symbol of the m^{th} vector of channel symbols
G_{BC}	Generator matrix of a linear block code
$G_{CC}(D)$	Generator matrix of a binary convolutional code
$g_{BC}(p)$	Generator polynomial of a linear block code
$GF\left(2^{\xi}\right)$	Extended Galois field with 2^{ξ} elements
$g_{ip}(p)$	Irreducible polynomial
$G_{\pi}(D)$	Interleaver generator matrix
$G_{\pi^{-1}}(D)$	De-interleaver generator matrix
$h_{ave}(t)$	Fading amplitude averaging filter impulse response
H_{BC}	Linear block code parity check matrix
$h_b(\tau)$	Time-invariant baseband channel impulse response
$H_{CC}(D)$	Binary convolutional code's parity check matrix
$h_m^I(t)$	I-channel matched filter impulse response
$h_m^Q(t)$	Q-channel matched filter impulse response
$h_p^I(t)$	I-channel pulse shaping filter impulse response
$h_p^Q(t)$	Q-channel pulse shaping filter impulse response
$H_{Rx}(f)$	Receive filter frequency response
$h_{sqrt-Nyq}(t)$	Square-root Nyquist pulse shape
J	Interleaver depth [symbols]
k	Number of message word symbols processed per encoding instance [symbols]
k_{η}	Normal Gaussian distribution power scaling factor
K_i	Rician factor of the i^{th} multipath component
L	Number of discrete multipath components [paths]
λ	Wavelength [m]
$\Lambda(C)$	Dimension distribution of linear block code C
$\Lambda^{-1}(C)$	Inverse dimension distribution of linear block code C
$\ln\left(\text{Prob.}\left(\overline{y}_m\middle\|\hat{\overline{c}}_m\right)\right)$	Log-likelihood function of the conditional probability Prob. $\left(\overline{y}_m\middle\|\hat{\overline{c}}_m\right)$
$\max\{f_d(t)\}$	Maximum Doppler frequency [Hz]
M_{fam}	Spreading sequence family size [sequences]
M_{punct}	Puncturer period [bits]
M_{seq}	Spreading sequence length [chips]
M_{users}	Number of users in a CDMA system [users]
$\overline{\mu}^{in}(D)$	N-dimensional interleaver input vector sequence [V]
$\overline{\mu}_m^{in}$	m^{th} length-N interleaver input [V]

$\overline{\mu}^{out}(D)$	N-dimensional interleaver output vector sequence [V]
$\overline{\mu}_m^{out}$	m^{th} length-N interleaver output [V]
n	Number of code word symbols generated per encoding instance [symbols]
N	Interleaver length [symbols]
$NB(C)$	Number of branches in the expurgated trellis of linear block code C [branches]
N_0	Single-sided power spectral density of additive white Gaussian noise [W/Hz]
$\overline{o}_{i,l}^{(j)}$	Decoder output branch vector associated with the j^{th} branch entering node (l,i) of a trellis [V]
ω	Sliding window Viterbi algorithm window size [trellis sections]
$P_b(e)$	Bit error probability
P_{BSC}	Binary symmetric channel crossover probability
$\phi_i(t)$	Instantaneous phase of the i^{th} multipath component [rad]
PG	Processing gain [dB]
$\overline{\phi}_i$	Average phase of the i^{th} multipath component [rad]
$\Pi(i)$	Interleaver mapping function
$\Pi^{-1}(i)$	De-interleaver mapping function
$PM_{m,i,l}^{sur}$	m^{th} decoded code word's survivor path metric associated with the survivor path ending in node (l,i) of a trellis
$P_s(e)$	Symbol error rate
$P(\tau)$	Time-invariant power delay profile [W]
R_c	Code rate
$\rho(\eta(t))$	Additive white Gaussian noise amplitude probability density function
$\rho\left(\phi_i(t)\right)$	Probability density function of the phase of the i^{th} multipath component
$\rho\left(\varepsilon_i(t)\right)$	Probability density function of the envelope of the i^{th} multipath component
$r_m(t)$	m^{th} received signal [V]
R_p	Punctured code rate
$r_{m,filtered}^q(t)$	User-q's received signal after filtering [V]
$R_{S(t),S(t)}$	Periodic auto-correlation of the spreading sequence $S(t)$
$R_{S_1(t),S_2(t)}$	Periodic cross-correlation between spreading sequences $S_1(t)$ and $S_2(t)$
$SD_{b_i(t)}(f)$	Doppler spectrum of the i^{th} received multipath component [W/Hz]
$\sigma^2_{b_i^{LOS}(t)}$	Variance in the i^{th} multipath component's line-of-sight part [W]
$\sigma^2_{b_i^{NLOS}(t)}$	Variance in the i^{th} multipath component's non-line-of-sight part [W]
$\sigma^2_{\eta(t)}$	Additive white Gaussian noise variance [W]
σ^2_{MUI}	Variance of the multi-user interference [W]
$\sigma^2_{r(t)}$	Received signal variance [W]
$\sigma^2_{s(t)}$	Transmitted signal variance [W]
σ_τ	Root-mean-square delay spread [s]
$s_m(t)$	m^{th} transmitted signal [V]
SF	Spreading Factor
$S_{ASB}^q(t)$	User-q's ABC sequence [V]
$S_{DSB}^q(t)$	User-q's DSB-CE-LI-RU filtered GCL sequence [V]
$S_{ZC}^q(t)$	User-q's Zadoff-Chu sequence [V]
$S_I^q(t)$	User-q's I-channel spreading sequence [V]
$S_Q^q(t)$	User-q's Q-channel spreading sequence [V]
$S_{QPH}^q(t)$	User-q's Quadriphase sequence [V]
$SSC(C)$	State space complexity of linear block code C
$SSP(C)$	State space profile of linear block code C
t	Time [s]

τ	Time delay [s]
$\overline{\tau}$	Mean excess delay [s]
τ_i	Time delay of the i^{th} multipath component [s]
τ_{max}	Maximum excess delay [s]
T_b	Duration of an uncoded data bit [s]
$T_{C,i}$	Coherence time of the i^{th} multipath component [s]
$t_{correct}$	Number of correctable code word symbol errors [symbols]
t_{detect}	Number of detectable code word symbol errors [symbols]
$\theta_{A,i}(t)$	Angle of arrival of the i^{th} multipath component [rad]
T_p	Pre-pulse shaping symbol duration [s]
T_s	Duration of a modulator output symbol [s]
T_{samp}	Sampling period [s]
T_{sig}	Reciprocal signal bandwidth [s]
$\overline{u}_{i,l}^{(j)}$	Trellis branch weight vector for the j^{th} branch entering node (l,i) [V]
υ	Constraint length of a binary convolutional code encoder
Υ	Puncturing profile
$\varepsilon_i(t)$	Envelope of the i^{th} multipath component [V]
φ	Primitive element of $GF\left(2^{\xi}\right)$
$\overline{\varrho}^{in}(D)$	N-dimensional de-interleaver input vector sequence [V]
$\overline{\varrho}_m^{in}$	m^{th} length-N de-interleaver input [V]
$\overline{\varrho}^{out}(D)$	N-dimensional de-interleaver output vector sequence [V]
$\overline{\varrho}_m^{out}$	m^{th} length-N de-interleaver output [V]
ς	Square-root Nyquist pulse roll-off factor
$v_r(t)$	Relative velocity between the transmitter and receiver [m/s]
$w_H\left(\overline{c}_m\right)$	Hamming weight of the vector $\overline{c}_m$ [symbols]
$w_H\left(\overline{c}_m(D)\right)$	Hamming weight of the vector sequence $\overline{c}_m(D)$ [symbols]
$W(i)$	Hilbert transformer tap weights
$x^I(t)$	I-channel pulse shaping filter excitation signal
$x^Q(t)$	Q-channel pulse shaping filter excitation signal
$y_m(p)$	m^{th} demodulated code word polynomial of a linear block code [V]
$\overline{y}_m$	m^{th} vector of demodulated symbols [V]

CHAPTER ONE

INTRODUCTION

"...we are very close to practical achievement of the performance that Shannon promised nearly 50 *years ago. Is it therefore time to say 'Problem Solved' and move on to other things? I doubt it. Observe how much of this progress has been achieved only recently - e.g. in trellis codes, group codes, Turbo Codes, algebraic geometry codes and precoding. I doubt that it has been fully digested. In particular, we are still far from a fundamental understanding of the new code construction and decoding methods that seem to be embodied in Turbo Codes, nor have we fully exploited the promise of multilevel codes and multistage decoding. Moreover, every two years the boundary between 'feasible' and 'infeasible' advances by another factor of two. Indeed, I believe that in* 30 *years we will look back with nostalgia at the current era and say: 'That was a golden age.'"* [1]

G. David Forney, Jr.
Retired Vice President of Technical Staff, Motorola, Inc.

ALTHOUGH the debate on the existence of biological evolution rages on between the religious and scientific communities, one aspect of the human condition that has evolved at an exponential rate during the 30000 year age of modern man, is communication. In the early post-neanderthal days of homo sapiens, unintelligible grunts and mumbling soon gave way to verbalised speech, eventually progressing into current day's thousands of distinct languages and dialects. Simplistic cave drawings, telling the life and history of our pre-historic ancestors, grew into written language on stone tablets and papyrus. In the process, complex pictographic representations of spoken languages, such as Egyptian hieroglyphics and the Chinese alphabet, were developed. However, it was not until the invention of the printing press in 1450 by *Johann Gutenberg* that the true power of written language was revealed, inaugurating the dawn of modern literacy and education.

The notion of communication over long expanses has intrigued the human race for millennia. Written language carrier systems, such as message runners and carrier pigeons, evolved into today's modern postal services, the Internet, email systems and *Short Message Service*s (SMS). Moreover, the ever-present need for long distance transmission of verbal and unwritten information gave rise to the first terrestrial and wireless communication systems, such as the Navaho Indian's smoke signal system.

[1] *Source: Shannon Lecture on Code Performance and Complexity,* 1995

From such rudimentary long distance communication systems, modern day telegraphy and telephony were spawned. Undoubtedly, the fathers of modern day communication systems, such as *Alexander Graham Bell* and *Guglielmo Marconi*, could not have envisaged a global village, based on total wired and wireless connectivity, were information sources can be freely accessed and a long-distance verbal conversation initiated at the touch of a button.

Since the inception of the 7-layered *Open Standards Interface* (OSI) model for communication systems, research and development of wired and wireless communication systems have become a global effort, progressing at an astounding rate. Today, the first commercial *Global System for Mobile Communication* (GSM) systems are 10 years young, but already seem underpowered and antiquated when compared to the 3^{rd} *Generation* (3G) systems currently being rolled out worldwide. Nonetheless, it still remains to be seen whether communication systems will eventually develop up to the point that Captain James T. Kirk can flip open his shiny 23^{rd} century Star Fleet issue subspace communicator, which is capable of communicating across the expanses of the known universe, in order to command Scotty to get a battle-scared Enterprise space-worthy in a humanly impossible time-frame. There is, however, one unavoidable impediment plaguing the transmission quality and reliability of all past, present and future communication systems: Non-ideal transmission channels.

Intuitively, non-ideal communication channels will have a limited capacity to carry information. In the last century many researchers attempted to sufficiently describe this phenomenon, but it was not until *Shannon*'s groundbreaking 1948 paper [1], entitled *"A Mathematical Theory of Communications"*, that it was possible to calculate a quantitative measure for this capacity limit. In this paper, *Shannon* not only conceives the field of *Information Theory*, but also derives his famous channel capacity limit for *Additive White Gaussian Noise* (AWGN) channels. *Shannon* also shows that the channel capacity limit, which is a function of the transmission bandwidth and the *Signal-to-Noise Ratio* (SNR) of the AWGN channel being investigated, can be achieved by either increasing the number of transmission symbols in the signal space used during modulation, or by increasing the redundancy in the transmitted signals by incorporating channel coding into the communication system.

Unfortunately, *Shannon* could only postulate that good channel codes, which can achieve channel capacity, might exist. He was, however, unable to demonstrate how such codes were to be designed or selected. Hence, numerous communication engineers have devoted their research efforts to develop powerful channel codes during the span of the last 57 years. Their ongoing efforts have lead to four main categories within the channel coding field, namely block codes, convolutional codes, concatenated codes and coded modulation. Several important milestones that have been achieved during this time period include *Forney*'s 1966 proposal for classic concatenated codes [11], *Ungerboeck*'s 1982 introduction of *Trellis Coded Modulation* (TCM) [12] and the conception of *Turbo Code*s (TC) by *Thitimajshima et al.* in 1993 [13]. *Fig.* 1.1 shows a time line with these and other pivotal dates within the brief history of channel coding.

During the 1950's and 1960's channel coding subsystems were only incorporated into the communication systems designed by affluent government institutions, such as the *National Aeronautical and Space Association* (NASA). However, as the processing power and speed of digital circuitry, microprocessors and *Digital Signal Processor*s (DSP) increased, so also did the affordability of channel coding subsystems. For example, every *Compact Disc* (CD) *Read Only Memory* (ROM) drive currently manufactured employs non-binary *Reed-Solomon* (RS) block coding [14], which were thought to be extremely costly and complex to implement at the time of its inception in the early 1960's. Today, even the simplest digital communication systems contain some level of channel coding for error

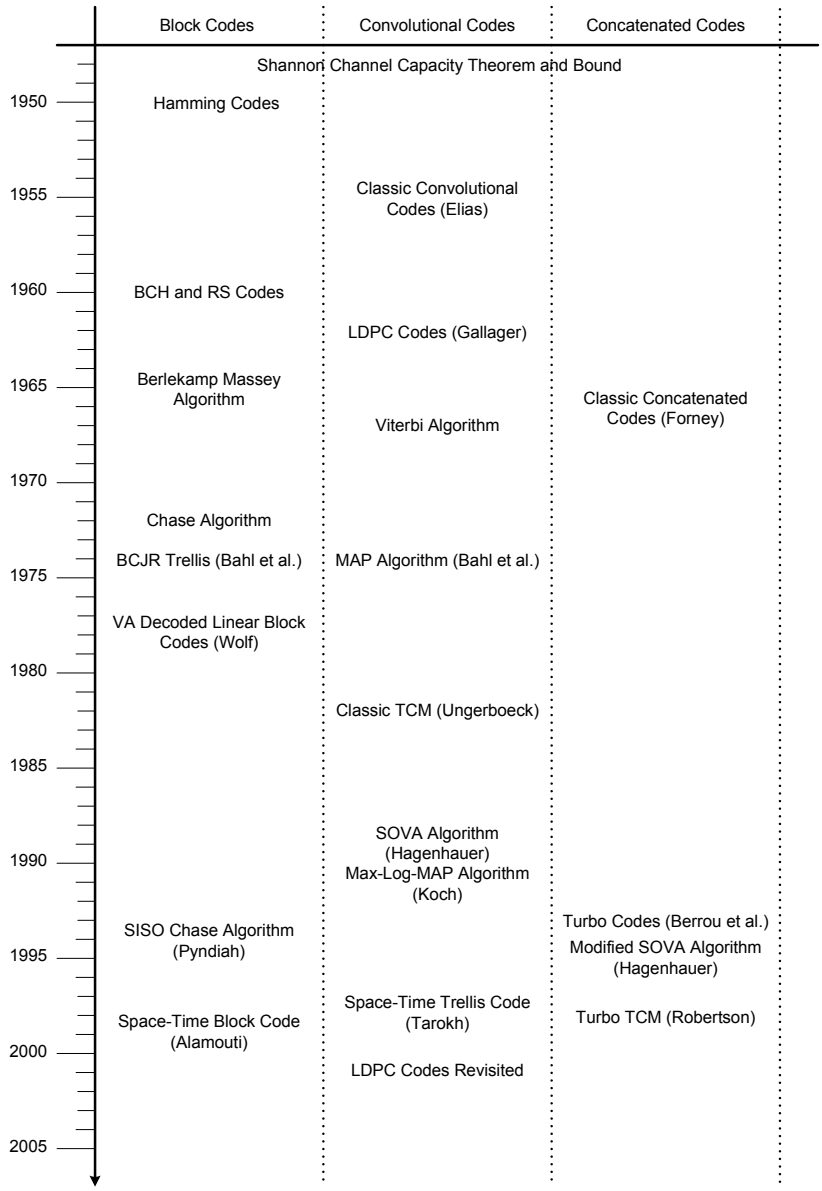

Figure 1.1: Time Line Showing Pivotal Events in Channel Coding History

detection and/or correction purposes. Current high-end communication systems, such as those used by *Jet Propulsion Labs*'s (JPL) deep space probes, make use of the latest generation iteratively decoded concatenated codes [15–33] and *Low Density Parity-Check Code*s (LDPC) [34] codes, which deliver *Bit-Error-Rate* (BER) performances close to the theoretical Shannon bound.

Recent years have seen several paradigm shifts with regards to the application of channel codes in communication systems. In the *Asynchronous Transfer Mode* (ATM) standard, for example, a linear block code is used to generate the *Header Error Control* (HEC) field of each 53-byte cell. The purpose of the HEC, however, is not just classic error detection and correction, but also cell delineation (i.e. frame synchronisation). Another paradigm shift of particular interest, is the move from classic *Forward Error Correction* (FEC) to *Error Control Coding* (ECC) approaches in modern channel coded communication systems: Classic FEC schemes attempt to correct all channel induced errors at the *Physical* (PHY) layer in the OSI model (i.e. layer 1) in a forward direction by performing

receiver-end intelligent decoding of transmitted data streams, which have been padded with redundant information using channel coding in the transmitter. Conversely, an ECC scheme not only performs FEC using one of several channel codes available in its adaptive coding scheme, but also requests alternative encoding and/or retransmissions of previously transmitted streams of channel coded information, if it discovers that the initial decoding effort yielded an unacceptable BER at the receiver. This process is usually accomplished using higher layer protocols in the OSI stack, for example the *Transmission Control Protocol* (TCP) at the Transport layer in the OSI model (i.e. layer 4). ECC schemes, such as the *incremental redundancy* scheme implemented in *Enhanced Data Rates for GSM Evolution* (EDGE), is therefore capable of providing the necessary *Quality of Service* (QoS) levels desired by today's communication market.

The efficiency of ECC schemes is grounded in their ability to adapt the parameters of communication systems' channel coding subsystems in response to varying channel conditions. As such, a wide variety of channel codes, interleaver mappings and puncturing profiles constitute essential components of any powerful ECC scheme. However, an unfortunate disadvantage of adaptive coding schemes, which seems simple in principle, is that switching between several different channel encoder and decoder modules as the communication environment, changes can be a complex and expensive implementation exercise. Current hardware and software constraints on communication transceiver DSPs hamper the multiple implementation of complex encoder and decoder algorithms for different types of channel codes with varying degrees of complexity. Fortunately, this problem mainly befalls block codes, whereas multiple convolutional coding and TCM schemes can easily be supported by a single DSP, since the decoding of these codes rely on simple generic trellis-based algorithms. Each type of block code, however, typically has its own associated optimal *Maximum-Likelihood* (ML) decoding algorithm. In addition, these code-specific decoding algorithms are usually not capable of supporting soft decision decoding or making use of *Channel State Information* (CSI). In this study this issue is addressed by investigating the applicability of the *Viterbi Algorithm* (VA) as an efficient generic ML trellis decoding algorithm for both binary and non-binary linear block codes, operating on narrowband and wideband wireless communication systems in realistic mobile fading channel conditions.

1.1 PERTINENT RESEARCH TOPICS AND RELATED LITERATURE

1.1.1 MOBILE COMMUNICATION CHANNEL CHARACTERISTICS, MODELLING AND REPRODUCTION

Accurate characterisation and modelling of mobile communication channels play a key role in the design of modulation and channel coding techniques for wireless communication systems. Furthermore, being able to reproduce the statistical behaviour of such channels enables the communications engineer to rigourously test future wireless communication systems in controlled environments. For these reasons, countless hours of research and numerous publications have been devoted to both the mathematical characterisation [35–38] and the development of relevant simulation models [39–41] for real-life mobile communication channels.

When studying the performances of mobile communication systems, a usual starting point is an understanding of classic AWGN, since it is an unavoidable limiting factor in the performance and capabilities of any communication system. The primary source of a communication system's performance degradation due to this type of channel is receiver generated thermal noise, which is characterised as having a flat broadband spectrum and a zero-mean Gaussian amplitude *Probability Density Function* (PDF).

In realistic mobile communication environments, however, transmitted signals are not only influenced by AWGN, but also experience reflection, scattering and diffraction, due to surrounding objects in the propagation environment. Moreover, this results a received signal that is composed of a number of scattered wavefronts. The combining of these wavefronts in a receiver antenna produces constructive and destructive interference, resulting the well-known fading phenomenon, where the envelope and phase of the received signal vary stochastically [37, 38]. Additionally, relative motion between the transmitter and the receiver produces the undesirable Doppler effect, where a fixed or varied disturbance in carrier frequency can be experienced, respectively referred to as Doppler shift and Doppler spread [37, 38].

During the simulation and performance evaluation of communication systems in controlled channel conditions, the ability to accurately describe and qualitatively classify the mobile fading environment is of cardinal importance. In general, the temporal and spectral disturbances experienced by a transmitted signal are the fundamental elements considered in the taxonomy of mobile fading channels:

1. **Temporal characteristics:** As the rate of relative motion between the transmitter and receiver structures of a mobile communication link increases, so also does the rate of signal fading, due to Doppler spreading. With respect to this fading rate, signal fading is categorised as either *slow fading* or *fast fading* [37, 38, 42]: When the Doppler spreading experienced by a transmitted signal is small compared to the actual information rate, the signal experiences slow fading. Moreover, in such a scenario a slow deep fade can potentially corrupt a large number of transmitted information symbols. Conversely, fast fading is earmarked by a high ratio of Doppler spreading to information rate, which produces shorter error burst at the receiver.

2. **Spectral characteristics:** Narrowband signals affected by realistic mobile fading channel conditions are distinguished, on a spectral level, by real-time uniform scaling of the *Power Spectral Density* (PSD) levels of the frequency components constituting the transmitted signal. This phenomenon, frequently observed when only a single propagation path exists, is known as *flat fading*. With wideband signals, however, it is not uncommon to observe several independently faded propagation paths from the transmitter to the receiver. Multipath propagation consequently produces non-uniform time-varying scaling of the PSD levels of the frequency components comprising the transmitted signal. In communications engineering nomenclature, this is known as *frequency selective fading* or *multipath fading* [37, 38, 42].

Through extensive simulations this study investigates the VA decoding of linear block codes on realistic communication links in lifelike mobile fading channel conditions. A classic narrowband *Quadrature Phase Shift Keying* (QPSK) communication system is used as simulation platform to evaluate such codes in pure AWGN channel conditions, typically encountered on stationary wireless links, such as *Wireless Local Loop*s (WLL). An identical QPSK communication system is used during the flat fading channel simulations in order to gauge the performance of VA decoded linear block codes on a typical narrowband mobile communication system. Slow and fast fading is considered in order to objectively analyse the influence of relative motion between the transmitter and receiver on the error correction capabilities of the VA decoded linear block codes. Since the needs for higher data rates and user capacity motivated the design of today's *Spread Spectrum* (SS)-based wideband 3G and *Beyond 3G* (B3G) systems, this study also considers the performance of the VA decoded linear block codes on a *Direct Sequence Spread Spectrum Multiple Access* (DS/SSMA) communication system in realistic multi-user multipath fading channel conditions.

1.1.2 SPREAD SPECTRUM WIDEBAND DIGITAL COMMUNICATION

While there does not appear to be a single *Multiple Access* (MA) technique in wireless communications that is superior, over the past two decades *Code Division Multiple Access* (CDMA) has

been shown to be a viable (and in many applications even favorable) alternative to both *Frequency Division Multiple Access* (FDMA) and *Time Division Multiple Access* (TDMA) [43]. The greatest advantage that CDMA poses over other MA schemes, is its high frequency re-use capacity in cellular systems [43, 44]. Unlike narrowband FDMA-based and TDMA-based systems, such as GSM, there is little need to use different carrier frequencies in neighbouring cells. Thus, as the digital communications industry expands with the daily addition of thousands of new cellular subscribers, increasing the load on the available radio spectrum at an unparalleled rate, CDMA has become an indispensable MA technique for current 3G, B3G and future 4^{th} *Generation* (4G) cellular systems [45].

With superior anti-jamming and anti-interception characteristics, as well as unparalleled MA capabilities, SS modulation, the quintessential underlying principle behind CDMA, have long since been of great interest to the military community [43, 44]. However, due to its ability to mitigate or alleviate illustrious communication problems, such as spectral overcrowding, user privacy and security, multipath fading channel effects and indoor propagation issues [43, 44], SS has since been employed in several commercial wireless communication standards, such as *Qualcomm*'s 2^{nd} *Generation* (2G) IS-95 [46] system, as well as 3G *Universal Mobile Telephony System* (UMTS) and cdma2000 systems.

In essence, all variants of SS can be classified into two main categories [43, 44, 47]: *Direct Sequence Spread Spectrum* (DSSS) and *Frequency Hopping Spread Spectrum* (FHSS). Classically, in the latter category, the carrier frequency onto which information is modulated is determined by a random sequence, unique to each user in a multi-user system [43, 44, 47]. Using dynamic frequency allocation, FHSS systems can be designed to avoid interference encountered within the allocated operational bandwidth by simply eluding interference occupied frequency slots. It is also a well known fact [43] that FHSS systems mitigate multipath effects, provided that the hopping rate is in access of the inverse of the differential delay between multipath components. The relatively infant wideband *Orthogonal Frequency Division Multiplexing* (OFDM) SS technique [43], which is integrated into the IEEE 802.11 standard, can also be considered to be a FHSS derivative. Here, however, information is modulated onto several orthogonal carriers in order to obtain diversity gains. In DSSS systems information symbols are directly modulated by user-specific random spreading sequences (also sometimes called signature sequences) [43, 44, 47]. The spreaded information symbols of each user are then modulated onto a carrier in order to obtain a wideband *Radio Frequency* (RF) signal. Given that the cross-correlation levels of the spreading sequences employed in the DSSS system are small (ideally zero), negligible *Multi-User Interference* (MUI) is generated, thereby making it theoretically possible to use a single carrier frequency for all of the users in the CDMA system.

Undoubtedly the user capacity and bandwidth requirements of B3G and future 4G wireless communication systems will far exceed that currently delivered by 2G and 3G systems [45]. Thus, one can speculate that these systems will incorporate combinations of MA schemes in order to ensure acceptable QoS levels for all mobile subscribers. Hence, TDMA and FDMA will still be used in order to fulfill user load requirements in densely populated areas where CDMA alone will not suffice. *Spatial Division Multiple Access* (SDMA) is another advanced MA technique that will find its way from theory to practise in these systems. Furthermore, much of the current SS research is focused on *Multi-Carrier* (MC) DS/SSMA modulation variants [43, 44, 47]. These modulation schemes are essentially mixtures of OFDM and DS/SSMA, which does not only deliver substantial user capacities through CDMA, but also superior suppression of interference and multipath fading channel effects through frequency diversity. It is likely that one or more MC DS/SSMA modulation schemes will be incorporated into future 4G wireless PHY layer definitions [45].

The application of binary spreading sequences, such as *Gold* and *Kasami* sequences [48], in

DS/SSMA systems has been exhaustively investigated since the introduction of SS. However, due to the availability of potentially sizable families of spreading sequences that exhibit acceptable auto-correlation and cross-correlation properties when compared to binary sequences, interest has started to shift towards the use of non-binary and *Complex Spreading Sequence*s (CSS) [6, 48–51]. There are numerous advantages of using CSSs in future B3G and 4G DS/SSMA systems, including the possibility to generate CE and *Single Sideband* (SSB) [4, 7, 10] transmitter output signals [4]. In this study, VA decoded linear blocks are tested on a CSS-based DS/SSMA platform in multi-user multipath fading channel conditions in order to evaluate the viability of such codes in the adaptive coding schemes of future wideband SS-based communication systems.

1.1.3 TRELLIS DECODING OF LINEAR BLOCK CODES

In 1974 *Bahl et al.* [2] described a novel technique whereby minimal trellis structures (in this study referred to as *Bahl-Cocke-Jelinek-Raviv* (BCJR) trellis structures) can be constructed for linear block codes. Consequently, block code decoding was no longer limited just to classic suboptimal algebraic techniques. Soft decision decoding of block codes using the BCJR algorithm [2], or variants thereof, were also made possible through these trellis structures. Soon after the landmark publication by *Bahl et al.*, *Wolf* [3] proposed that, as a less complex alternative to the BCJR algorithm, the VA can be applied to block code trellises as an efficient soft decision ML decoder. Since *Wolf* did not validate or investigate this claim through simulation studies or hardware implementations, recent years have seen the publication of numerous papers [52–55] by *Staphorst et al.*, specifically devoted to the performance evaluation of VA decoded binary and non-binary linear block codes in varying mobile communication channel environments.

Although several algebraic soft decision block code decoding algorithms which employ CSI have been proposed, such as the popular algorithms by *Chase* [56] and *Moorthy et al.* [57], their performances have been showed [2, 58, 59] to be suboptimal. In contrast, both the BCJR *Maximum a-Posteriori Probability* (MAP) and Viterbi ML trellis decoding algorithms are optimal soft decision trellis decoders. A further advantage of the Viterbi and BCJR trellis decoding algorithms is their capacity to utilise CSI during their decoding efforts, resulting in improved BER performances when employed in fading channel conditions [60].

Due to the inherently intricate nature of the BCJR trellis structures of linear block codes, one serious impediment to the use of trellis decoders for linear block codes with practical block lengths and dimensions, is decoding complexity. Ergo, the current cost effectiveness of using trellis-based decoders in commercial applications, especially for powerful non-binary block codes, such as RS (see *Section* 3.2.2.3.3) and *Bose-Chaudhuri-Hocquenghem* (BCH) (see *Section* 3.2.2.3.2) block codes, are questionable. However, the number of efficient soft output algebraic decoding algorithms for block codes are minuscule when compared to soft output trellis decoding algorithms, traditionally developed for convolutional codes. Hence, trellis-based soft output decoding algorithms, such as the *Soft Output Viterbi Algorithm* (SOVA) [61], will become invaluable components in future iteratively decoded concatenated coding schemes employing linear block codes as *Constituent Code*s (CC). Furthermore, the promise of having a single trellis decoder module that can decode not only classic convolutional codes, but also linear block codes, is an attractive notion for the developers of digital communication systems.

1.2 MOTIVATION FOR THIS STUDY

In essence, researchers actively participating in the field of channel coding can be categorised into two main groups, namely the *Decibel Chasers* and the *Code Realisers*. The *Decibel Chasers* are

researchers with the single-minded goal of creating new powerful channel coding schemes, capable of delivering BER performances that approach the Shannon bound [1, 13, 62]. Conversely, *Code Realisers* are more interested in translating the *Decibel Chasers*' theoretical and mathematical channel coding schemes into real-life hardware and/or software systems that can be integrated into commercial and military communication systems.

Since *Berrou, Glavieux* and *Thitimajshima*'s ground breaking paper [13] in 1993, which introduced the celebrated iteratively decoded TCs, the playing field for the *Decibel Chasers* have changed dramatically. Over the last decade, numerous new iteratively decoded *Parallel Concatenated Code*s (PCC) [15–26, 63–65], *Serial Concatenated Code*s (SCC) [27–31] and *Hybrid Concatenated Code*s (HCC) [30, 32, 33] have been proposed, capable of delivering BER performances within a fraction of a decibel from the Shannon bound [15, 21, 27, 32, 62–64, 66–69]. Gone are the days of code designers marvelling at substantial coding gains obtained from newly developed coding schemes. Presently, even a 0.01 dB improvement towards the theoretical Shannon bound, for example, is enough to create an uproar in the channel coding community.

Code Realisers have the difficult task of merging complex channel encoding and decoding algorithms with limited hardware and software platforms. This can be accomplished in two ways: Firstly, higher capacity and more scalable hardware and software platforms have to be developed, capable of supporting the requirements of new channel coding schemes. However, this is not the code designers responsibility, but rather that of DSP, *Field Programmable Gate Array* (FPGA) and *Application Specific Integrated Circuit* (ASIC) developers. Secondly, complex encoding and decoding algorithms, developed by the *Decibel Chasers*, have to be altered or condensed in order to conform with the available hardware and software platforms. Hence, the achievements of the *Code Realisers* always lag that of the *Decibel Chasers* and, to a fair extent, is paced at a rate of progression dictated by *Moore's Law* [70]. For example, in recent years JPL has devoted substantial funding and manpower on the research and development of iteratively decoded HCCs [30, 32, 33]. Since the encoding for HCCs is fairly straightforward, such encoder modules have already been implemented in the communication systems of NASA's newest generation deep space probes. However, the iterative decoding of HCCs is a mathematically complex and daunting exercise. As such, the *Code Realisers* at JPL are focused on the development of practical hardware and/or software iterative decoder modules for HCCs.

Optimal ML decoding of linear block codes through the application of the VA to their BCJR trellis structures [2], as proposed by *Wolf* in 1978 [3], is now a seasoned concept. Unfortunately, research in this field has remained fairly stagnant until the mid 1990's. This can be attributed mainly to the fact that the high complexities of BCJR trellises, even for rudimentary linear block codes, made hardware and/or software implementations of block code trellis decoders untenable. As new implementation platforms of higher speeds, capacities and scalability became available, renewed interest was sparked into the trellis decoding of linear block codes. Therefore, this study falls largely under the domain of the *Code Realisers*. From this perspective, the primary goals that motivated the research conducted during this study are the following:

1. Several advanced communication systems, such as EDGE, employ adaptive coding schemes, capable of dynamically switching between different block, convolutional and concatenated coding schemes in response to variations in the mobile channel environment and the users' QoS demands. Since the concept of *bandwidth-on-demand* is now well established and finding its way into the specifications of current communication systems, it is likely that adaptive coding will be an integral part of most future communication systems. In terms of implementation requirements, such adaptive coding schemes require extensive processing power and a multitude of decoding algorithms in

order to support an assortment of channel codes. Hence, having a single decoder algorithm, capable of decoding convolutional, block and concatenated codes, is an exiting proposition for *Code Realisers*. It is a well-known fact that the VA can be used as such a generic decoding algorithm. However, the application thereof to non-binary linear block codes, such as RS and BCH codes, have not been fully investigated in realistic mobile fading channels prior to this study. Also lacking prior attention, is the VA decoding of linear block codes in conjunction with code-augmentation techniques, such as interleaving and code puncturing.

2. Since the inception of the trellis decoding of linear block codes by *Bahl et al.* [2], *Code Realisers* have been faced with one unnerving implementation challenge: the storage and processing of the exceedingly complex BCJR trellis structures of linear block codes. This study attempts to address this problem by presenting and evaluating a promising BCJR trellis complexity reduction technique, applicable to both binary and non-binary linear block codes.

From a *Decibel Chaser*'s perspective, this study was motivated by the premise of obtaining improved BER performances for classic linear block codes in legacy digital communication systems by incorporating CSI into the VA's trellis decoding efforts. This is an attractive notion, especially since no additional hardware (except CSI estimators, which are usually already available) is required for potential coding gains in mobile fading channel conditions.

Secondary motivational factors that incited this study, rising from deficiencies identified within the general research field of channel coding, include the following:

1. The literature contains numerous simulation and performance evaluation studies of channel coding schemes in flat fading channel conditions. However, the greater majority of these studies are limited to pure Rayleigh flat fading channels. Furthermore, by typically assuming fading amplitudes which are *Independent Identically Distributed* (IID) for each code bit, channel code researchers neglect to investigate the effects of realistic Doppler effects. In *Section* 5.4.2 of this study presents a versatile flat fading performance evaluation platform, which addresses both of these deficiencies. Not only can this platform recreate realistic Rician fading amplitude distributions, but it also supports variable fading rates, ranging from slow to fast fading.

2. In general, most simulation studies presented in literature on the performance evaluation of channel coded DS/SSMA communication systems, operating in multi-user multipath fading channel conditions, also have much to be desired. Most of these studies assume non-realistic channel conditions and/or employ simplistic low-capacity spreading sequences, such as *Pseudo-Noise* (PN) codes. This study's wideband performance evaluation platform, presented in *Section* 5.4.3, recreates more realistic DS/SSMA communications in a multi-user multipath fading channel environment. The proposed simulation platform can be configured with realistic frequency selective fading channel conditions, unique to each user in the CDMA system. Furthermore, the DS/SSMA transmitter and RAKE receiver structures (presented in *Section* 5.3) support variable length binary or non-binary spreading sequence families. Hence, using this platform, channel coding schemes can be simulated on wideband wireless PHY layer configurations resembling the RF frontends of 3G, B3G and 4G systems.

3. Obtaining the simulated BER performance curve for an uncoded or coded communication system, without using theoretical upper or lower bounds, is an extremely lengthy and processor intensive task. The obstacle of excessive simulation execution time is addressed by this study on two fronts: Firstly, the AWGN, flat fading and multi-user multipath fading channel simulation platforms presented in this study were designed to operate purely in baseband, but recreate all channel phenomena experienced at any arbitrary carrier frequency. Secondly, the simulation software developed for this study distributes the computational load of the BER performance evaluation simulations over

the 16 processors constituting the *University of Pretoria*'s *I-percube High Performance Computing* (HPC) cluster, donated by *Intel*.

1.3 OBJECTIVES OF THIS STUDY

The primary goal of this study was the investigation and performance evaluation of VA decoded binary and non-binary linear block codes in AWGN, flat fading and multipath fading wireless channel environments. To that end, several secondary objectives had to be achieved. These are detailed below:

1. Thoroughly investigate the physical origins and accurately simulate the statistical behaviour of realistic mobile communication channel effects (see *Chapter* 2):
   (a) Scrutinise and reproduce classic AWGN channel effects.
   (b) Study the characterisation and mechanisms involved in flat fading. Topics of particular interest include Doppler spread effects and typical fading amplitude and phase distributions.
   (c) Research the elements partaking in frequency selective fading channels, including multipath propagation and time delay spread fading effects. Explore the characterisation and evaluation of these channels using concepts such as power delay profiles, time dispersion parameters and the concept of coherence bandwidth.
   (d) Design and implement a flexible flat fading channel simulator, capable of creating realistic Doppler spread effects, as well as Rayleigh and Rician fading amplitude distributions.
   (e) Develop and construct a versatile multipath fading channel simulator, composed of several flat fading channel simulators. This channel simulator must be capable of reproducing authentic multipath propagation and time delay spread fading effects.
   (f) Augment the proposed flat fading and multipath fading channel simulators in order to support full baseband simulation, thereby reducing processing power and execution time requirements.
2. Review the major building blocks that classic convolutional and linear block coding schemes are composed of (see *Chapter* 3):
   (a) Investigate the characteristics, encoder structures and trellis decoding of classic *Non-Systematic Convolutional* (NSC) and *Recursive Systematic Convolutional* (RSC) codes.
   (b) Mathematically describe the qualities, encoder structures and classic decoding techniques of the linear block codes of importance in this study, including binary Hamming, cyclic and BCH codes, as well as non-binary RS codes. A familiarisation with the Berlekamp-Massey syndrome decoding of non-binary RS codes forms an integral part of this investigation.
   (c) Inspect the concepts and mathematical portrayal of interleaving and de-interleaving, as well as puncturing and de-puncturing.
3. Explore the notion of linear block code trellis decoding via the application of the VA to BCJR trellises (see *Chapter* 4):
   (a) Study and implement the BCJR trellis construction method for linear block codes. Ascertain its usefulness with regards to non-binary linear blocks, such as RS codes.
   (b) Develop a simple trellis expurgation technique, applicable to both binary and non-binary linear block code BCJR trellis structures.
   (c) Define and determine the complexity of linear block code BCJR trellises.

(d) Devise and demonstrate an effective, yet elementary trellis complexity reduction technique for binary and non-binary block code BCJR trellises.

(e) Delve into the concepts and intricacies pertaining to the trellis decoding of binary and non-binary linear block codes via the application of the block-wise VA to BCJR trellises.

(f) Research both hard and soft decision metric calculation approaches during the block-wise VA decoding of linear block codes. An investigation into the inclusion of fading amplitude CSI in the VA metric calculations is of foremost importance.

4. Establish flexible AWGN, flat fading and multipath fading performance evaluation platforms with authentic channel configurations (see *Chapter* 5):

   (a) Design and implement novel narrowband complex QPSK communication system simulation models, capable of functioning completely in baseband.

   (b) Extend the narrowband complex QPSK transmitter and receiver structures into flexible RAKE receiver-based wideband complex DS/SSMA QPSK communication system models, intended exclusively for baseband simulations. The proposed wideband complex DS/SSMA QPSK communication system must support complex spreading using unfiltered and pre-filtered CSSs for multi-user CDMA purposes.

   (c) Construct a flexible baseband AWGN channel performance evaluation platform using the novel narrowband complex QPSK transmitter and receiver structures.

   (d) Incorporate the proposed complex flat fading channel simulator into the AWGN performance evaluation platform, thereby creating an adjustable baseband flat fading channel simulation environment, supporting variable Doppler spreads and fading distributions.

   (e) Assemble a baseband multi-user multipath fading performance evaluation platform, comprising of the complex RAKE receiver-based DS/SSMA QPSK and multipath fading channel simulator system models. The proposed simulation platform must be capable of supporting flexible power delay profiles with uniquely definable Doppler spreads and fading distributions for each propagation path of each user in the CDMA environment.

5. Implement the performance evaluation platforms and conduct an extensive simulation study (see *Chapter* 6):

   (a) Using an *Object Orientated Programming* (OOP) approach in C++, implement all the simulation building blocks required to construct the proposed AWGN, flat fading and multi-user multipath fading channel performance evaluation platforms. These building blocks include: Gaussian and uniform noise generators, *Infinite Impulse Response* (IIR) and *Finite Impulse Response* (FIR) filters, convolutional coders and sliding window VA decoders, block coders and ML (classic and VA) decoders, interleavers and de-interleavers, puncturers and de-puncturers, complex flat and multipath fading channel simulators, narrowband complex QPSK transmitters and receivers, as well as wideband complex DS/SSMA QPSK transmitters and RAKE receivers.

   (b) Define the necessary simulation building block configurations, such as filter coefficients and impulse responses, block code generator matrices, convolutional code shift register configurations, trellis definitions, realistic flat and multipath fading channel configurations, pulse shape definitions, transmitter and receiver configurations, interleaver mappings, puncturing profiles, CSSs' real and imaginary parts, etc.

   (c) Verify the functionality of the newly constructed simulation building blocks. Special attention must be given to the proposed novel channel simulators, as well as the narrowband and wideband complex transmitter and receiver structures.

(d) Using the simulation building blocks with their appropriate configurations, construct the AWGN, flat fading and multipath fading performance evaluation platforms in C++.

(e) Implement the performance evaluation platforms on the *University of Pretoria*'s *I-percube* HPC cluster, donated by *Intel*.

(f) Use the performance evaluation platforms to obtain simulated AWGN, flat fading and multi-user multipath fading BER performance results for narrowband and wideband systems employing classic convolutional codes, binary and non-binary linear block codes with VA decoding (using original and reduced complexity BCJR trellis structures), interleaved VA decoded convolutional and linear block codes, as well punctured VA decoded convolutional and linear block codes.

1.4 NOVEL CONTRIBUTIONS AND PUBLICATIONS EMANATING FROM THIS STUDY

1.4.1 NOVEL CONTRIBUTIONS

This study not only deliberated elements within the field of channel coding, but also investigated the characterisation and modelling of mobile communication channels, realistic narrowband and wideband communication systems, multi-user CDMA environments, and the creation of simulation platforms on multi-processor HPC clusters. As such, numerous contributions with varying degrees of importance and applicability were made in several research fields falling under the encompassing banner of digital communications. Excluding the introductory and final concluding chapters of this dissertation, each chapter ends with a short discussion on the innovative contributions it made. Below is a list with the most prolific contributions, compiled from these discussions:

1. Major contributions related to the research field of mobile communication channel modelling and reproduction:

   (a) A flexible complex flat fading channel simulator was developed, capable of producing Doppler spread effects and creating Rayleigh/Rician fading amplitude distributions (see *Section* 2.6.2.3). What sets this flat fading channel simulator apart from previous simulators, is the fact that it can realistically produce these channel effects in baseband, forfeiting the need for the communication system to operate at an actual RF.

   (b) Using multiple complex flat fading channel simulators, a generic complex multipath fading channel simulator structure was created (see *Section* 2.6.3.2). This frequency selective fading channel simulator can be configured to support any number of propagation paths (as defined by the required power delay profile), each with its own Doppler spread and fading distribution. As with the complex flat fading channel simulator, its novelty lays in the fact that it fully supports baseband simulations.

2. Major contributions related to the disciplines of information theory and channel coding:

   (a) A novel trellis expurgation (pruning) algorithm, applicable to both systematic binary and non-binary linear block codes' BCJR trellises, was derived (see *Section* 4.2.2).

   (b) Several existing BCJR trellis complexity calculation and reduction techniques, suitable only for binary linear block codes, were amalgamated and improved. The end result was a single BCJR trellis complexity calculation and reduction procedure, applicable to both binary and non-binary linear block codes (see *Section* 4.3).

   (c) *Wolf*'s original block-wise VA [3] for the ML decoding of linear block codes using their BCJR trellis structures, was upgraded to also incorporate fading amplitude CSI during its metric calculations (see *Section* 4.4).

3. Major contributions related to the modelling and simulation of communication systems:

   (a) Narrowband complex QPSK transmitter and receiver structures were fabricated (see *Section* 5.2). These building blocks' baseband functionality and the receiver's average fading amplitude CSI calculator (see *Section* 5.2.3) constitute novel contributions.

   (b) Wideband complex DS/SSMA QPSK transmitter and RAKE receiver structures, capable of employing unfiltered and filtered CSSs (see *Appendix D*), were created (see *Section* 5.3). The proposed DS/SSMA communication system employing these structures is unique for several reasons: Just as with the narrowband complex QPSK system, the wideband system operates entirely in baseband. It also employs its own novel average fading amplitude CSI calculator (see *Section* 5.3.3), based on the RAKE receiver's *Maximal Ratio Combining* (MRC) approach. Furthermore, this study also presents the first RAKE receiver-based implementation of DS/SSMA systems employing *Analytical Bandlimited Complex* (ABC) (see *Section* D.3.2.2) and *Double Sideband* (DSB) *Constant Envelope Linearly Interpolated Root-of-Unity* (CE-LI-RU) (see *Section* D.3.2.1) CSSs, whereas previously investigated systems [50, 51] only made use of simple correlator receivers.

   (c) A flexible AWGN performance evaluation platform, incorporating the novel narrowband complex QPSK transmitter and receiver structures, were developed (see *Section* 5.4.1). The evaluation of coded and uncoded narrowband QPSK systems in AWGN channel conditions was made possible by this platform.

   (d) Using the novel narrowband complex QPSK transmitter and receiver structures, as well as the unique complex flat fading channel simulator, a multifaceted flat fading performance evaluation platform was produced (see *Section* 5.4.2). This platform is capable of testing uncoded and coded narrowband QPSK communication systems in flat fading channel conditions with realistic Doppler spread effects and fading distributions.

   (e) A versatile multi-user multipath fading channel performance evaluation platform was produced (see *Section* 5.4.3) using the novel complex multipath fading channel simulator, as well as the wideband complex DS/SSMA QPSK transmitter and RAKE receiver simulation models. Using this platform, uncoded and coded wideband DS/SSMA QPSK communication systems can be evaluated in realistic frequency selective fading and/or multi-user CDMA environments.

   (f) The AWGN, flat fading and multi-user multipath fading simulation platforms created were fully implemented on the *University of Pretoria*'s *I-percube* HPC cluster, donated by *Intel*. All of *Chapter* 6's BER performance results were obtained using this HPC cluster.

4. Important and unique simulation results presented by this study, include:

   (a) various simulation results obtained using the novel complex flat fading and multipath fading channel simulators (see *Chapter* 6).

   (b) operational validation and simulated multi-user multipath fading BER performance results for uncoded and coded RAKE receiver-based wideband complex DS/SSMA QPSK communication systems employing CSSs (see *Chapter* 6).

   (c) simulation results investigating the influence of the CSS selection approach and sequence length on the BER performances of complex spreaded DS/SSMA systems, operating in multipath fading channel conditions.

   (d) simulated BER performance results for hard and soft decision VA decoded binary Hamming $(7, 4, 3)$ and non-binary RS $(7, 5, 3)$ linear block codes, obtained in AWGN, flat fading and multi-user multipath fading environments (see *Section* 6.5.3).

(e) simulated AWGN and flat fading BER performance results for hard and soft decision VA decoded binary cyclic $(5, 3, 2)$ linear block codes using original and reduced complexity BCJR trellis structures (see *Section* 6.5.4).

(f) simulated flat fading and multi-user multipath fading BER performance results for hard and soft decision VA decoded interleaved binary Hamming $(7, 4, 3)$ and non-binary RS $(7, 5, 3)$ linear block codes (see *Section* 6.5.5).

(g) simulated BER performance results for hard and soft decision VA decoded punctured binary BCH $(15, 7, 5)$ linear block codes in AWGN, flat fading and multi-user multipath fading channels (see *Section* 6.5.6.2).

(h) numerous simulation results investigating the BER performance improvements obtained by incorporating fading amplitude CSI into the soft decision VA decoding of linear block codes in fading environments (see *Chapter* 6).

1.4.2 PUBLICATIONS

During this study, the author researched and co-wrote three local conference papers, three international conference papers and a local journal article. Not only did these works lead to the development of a great number of the simulation building blocks crucial for this study, but also presented several relevant algorithms, concepts and simulation results. The following chronologically ordered list details the scope of these published papers, as well as their relevance to this study:

1. *"Trellis Decoding of Linear Block Codes"*, co-authored by *W.H. Büttner* and *Prof. L.P. Linde*, presented at IEEE COMSIG 1998 [52] at the *University of Cape Town, South Africa*, firstly describes the construction and expurgation of binary linear block code trellises, as suggested by *Bahl et al.* in [2]. In this paper the application of the VA as an efficient ML block code trellis decoder is investigated, followed by a complexity comparison between the VA trellis decoder and several classic algebraic decoding techniques, including classic ML and syndrome decoding. Simulated BER performance results for several VA trellis decoded binary linear block codes in AWGN channel conditions conclude the paper.

2. Obtaining the AWGN channel simulation results presented in the paper entitled *"Performance of a Synchronous Balanced QPSK CDMA System Using Complex Spreading Sequences in AWGN"* [50], co-authored by *M. Jamil* and *Prof. L.P. Linde*, required the development of flexible non-RAKE receiver-based DS/SSMA QPSK communication system building blocks. The transmitter and receiver building blocks of this paper, which was presented at IEEE AFRICON 1999 at the *Cape Town Technicon, South Africa*, are the forerunners of the DS/SSMA QPSK transmitter and RAKE receiver structures (see *Section* 5.3 of this dissertation) used in the simulation platform for the frequency selective fading channel simulations presented in *Chapter* 6. The paper also involved a thorough study of several classes of filtered and unfiltered CSSs. A lengthy *Gaussian Approximation* (GA)-based derivation of multi-user BER performance bounds for synchronous balanced QPSK CDMA communication systems employing such spreading sequences is also presented.

3. The development of a flexible multipath fading channel simulator (presented in *Section* 2.6 of this dissertation), used in the frequency selective fading channel simulations presented in *Chapter* 6 of this dissertation, was required to obtain the performance results given in the paper *"Performance Evaluation of a QPSK System Employing Complex Spreading Sequences in a Fading Environment"*, presented as a poster session at IEEE VTC-Fall 1999 in *Amsterdam, The Netherlands*. This paper [51], co-authored by *M. Jamil* and *Prof. L.P. Linde*, presents the AWGN and multipath fading channel BER performances of a synchronous non-RAKE receiver-based multi-user DS/SSMA system that employs CSSs with balanced QPSK modulation.

4. In the conference paper *"Performance Evaluation of Viterbi Decoded Reed-Solomon Block Codes in Additive White Gaussian Noise and Flat Fading Channel Conditions"* [55], written by *L. Staphorst* and *Prof. L.P. Linde*, presented at IEEE WCNC 2002 in *Orlando, Florida, USA*, simulated AWGN and flat fading channel BER performances for hard and soft decision VA trellis decoded non-binary RS $(7, 5, 3)$ codes, with code word symbols from Galois field $GF\left(2^3\right)$, are presented. The flat fading channel conditions considered included varying Rician factors (see *Section* 2.5.2.2 of this dissertation) and Doppler spreads (see *Section* 2.4.3.3 of this dissertation). In an attempt to improve on the classic hard and soft decision BER performance results, CSI (see *Section* 3.3.5 of this dissertation) is also included in the VA branch metric calculations (see *Section* 4.4.1 of this dissertation). The trellis expurgation technique presented in [52] for binary linear block codes is extended in this paper for non-binary linear block code trellises.

5. The simulated non-binary RS $(7, 5, 3)$ block code's flat fading channel BER results given [55] are repeated in *"Performance Evaluation of Viterbi Decoded Binary and Non-binary Linear Block Codes in Flat Fading Channels"* [53], presented at IEEE AFRICON 2002, *George, South Africa*. This paper, authored by *L. Staphorst* and *Prof. L.P. Linde*, also presented novel flat fading channel simulated BER performance results for hard and soft decision VA decoded binary Hamming codes. Again the effects on the BER performances using CSI in the VA are considered.

6. In the IEEE CCECE 2003 poster session paper *"Performance Evaluation of a Joint Source/Channel Coding Scheme for DS/SSMA Systems Utilising Complex Spreading Sequences in Multipath Fading Channel Conditions"* [71], presented by *L. Staphorst, J. Schoeman* and *Prof. L.P. Linde* in *Montreal, Quebec, Canada*, the simple DS/SSMA QPSK communication system of [50] is upgraded to include a flexible RAKE receiver. This realistic multi-user wideband communication system was used in conjunction with the multipath fading channel simulator presented in [51] to determine the BER performance of a CSS-based CDMA system employing Huffman source coding and classic convolutional coding with joint VA decoding.

7. The journal article entitled *"On the Viterbi Decoding of Linear Block Codes"* [54], authored by *L. Staphorst* and *Prof. L.P. Linde*, was published in the Transactions of the SAIEE in December 2003. This article restates all algorithms, as well as AWGN and flat fading channel simulation results presented in [52], [55] and [53]. Furthermore, the trellis complexity calculation and reduction algorithms presented in *Section* 4.3.1 and *Section* 4.3.2 of this dissertation, respectively, are explained in this paper. Simulated AWGN and flat fading channel BER performance results for a cyclic $(5, 3, 2)$ linear block code with VA decoding using original and reduced trellis structures are also presented. It is important to mention that this paper was reviewed and accepted without any changes by *Prof. J.K. Wolf*, who is seen as the father of the Viterbi decoding technique for linear block codes.

8. The following two paper series, authored by *L. Staphorst* and *Prof. L.P. Linde*, were published in the proceedings of the AFRICON 2004 conference and presented in September 2004 at *Gaborone, Botswana*:

   (a) *"Evaluating Viterbi Decoded Reed-Solomon Block Codes on a Complex Spreaded DS/SSMA CDMA System: Part I - Background and Communication System Models"* [72].

   (b) *"Evaluating Viterbi Decoded Reed-Solomon Block Codes on a Complex Spreaded DS/SSMA CDMA System: Part II - Channel Model, Evaluation Platform and Results"* [73].

   These two papers firstly present the complex multipath fading channel and RAKE receiver-based DS/SSMA QPSK communication system simulation models described in *Chapter* 5. This is followed by an overview of the simulation platform and configuration parameters used to obtain the wideband simulation results presented in *Chapter* 6. Lastly, simulated BER performance results

are presented for RS $(7, 5, 3)$ coded RAKE receiver-based DS/SSMA QPSK communication systems, employing the different CSS families presented in *Appendix D*, under realistic multi-user multipath channel fading effects.

1.5 ORGANISATION OF THE DISSERTATION

This dissertation consists of seven chapters. The contents of the chapters are as follows: *Chapter* 1 sets out by giving short introductions and historical overviews into wireless communication over mobile communication channels, the conception and evolution of channel coding, as well as the trellis decoding of linear block codes. This is then followed by the objectives that had to be met by this study, which collectively addressed the main problem statement of the performance evaluation of VA decoded binary and non-binary linear block codes, operating in mobile communication channel conditions. Next, the main contributions made by this study are summarised. Lastly, *Chapter* 1 lists a number of published conference and journal articles originating from the work presented in this dissertation.

The analyses and modelling of mobile fading channels are the focus areas of *Chapter* 2. Firstly, the mathematical description and statistical characteristics of AWGN, flat fading and frequency selective fading channels are considered. This is then followed by the development of the novel complex flat and frequency selective fading channel simulator models employed during the performance evaluation of the VA decoded linear block codes considered in this study.

Chapter 3 gives an overview of the main building blocks used in classic block and convolutional coding schemes. Encoder building blocks considered include: Convolutional coders, block coders, interleavers and code puncturers. Block and convolutional decoding algorithms, de-interleavers, code de-puncturers and CSI estimators are discussed under the topic of decoder building blocks.

The VA decoding of linear block codes is described in *Chapter* 4. This discussion includes the construction and reduction of linear block code trellis structures, as well as a thorough explanation of the block-wise VA applied to these trellis structures. Special attention is given to the inclusion of CSI in the VA's decoding efforts. Short theoretical derivations of the BER performances of VA decoded linear block codes in AWGN and flat fading channel conditions conclude this chapter.

The narrowband complex QPSK and wideband RAKE receiver-based DS/SSMA QPSK communication systems, employed in the simulations performed for this study, are described in *Chapter* 5. Following the descriptions and analyses of the proposed narrowband and wideband communication systems, is a discussion on the simulation platforms used in the AWGN and flat fading channel performance evaluation tests, built around the narrowband complex QPSK communication system. Finally, the simulation platform used for the multi-user multipath fading channel performance evaluation tests, assembled using the novel wideband complex RAKE receiver-based DS/SSMA QPSK communication system, is described.

Chapter 6 presents the simulation results obtained during this study. Firstly, simulation results that validate the operation of the novel complex flat fading and multipath fading channel simulator models are given. Next, simulation results to validate the functioning of the narrowband complex QPSK and wideband RAKE receiver-based complex DS/SSMA QPSK communication systems are presented. Lastly, a large number of simulated BER performance results are presented for the coding schemes considered in this study, evaluated on the narrowband and wideband communication platforms under AWGN, flat fading and frequency selective fading channel conditions. These coding schemes include

various VA decoded binary convolutional codes, as well as VA decoded binary and non-binary linear block codes. Employing original and reduced complexity BCJR trellis structures during the VA decoding of linear block codes are also scrutinised here, as well as the effects of performing puncturing and interleaving in conjunction with channel coding.

In *Chapter* 7 conclusions are drawn from the results obtained. During this study a number of areas have been identified for possible future research. These future research areas are also discussed in *Chapter* 7.

Five appendices, covering topics of importance to the understanding of the subject matter investigated in this study, follow the seven chapters outlined above: *Appendix A* lists the encoder parameters of different code rate optimal RSC codes, constructed by *Benedetto*, *Garello* and *Montorsi*. A simple example of the use of these parameters are also given. A conceptual description of the *Berlekamp-Massey* decoding algorithm [74, 75], frequently employed in the syndrome decoding of classic BCH and RS block codes, is presented in *Appendix B*. Although the algorithm is not described in detail, the major functions that it performs in its syndrome decoding efforts are described in this appendix. *Appendix C* considers a number of popular block interleaver structures, frequently encountered in iteratively and non-iteratively decoded concatenated coding schemes. These include deterministic and random interleaver structures. *Appendix D* summarises some of the important performances measures utilised in the analysis of CSSs. It also gives concise overviews of the filtered and unfiltered CSS families considered in this study. *Appendix E* supplies the reader with an extensive index of the simulation software developed for this study, including the Matlab functions and scripts, as well as C++ classes and compiled executables.

CHAPTER TWO

MOBILE FADING CHANNELS

2.1 CHAPTER OVERVIEW

THE first part of this chapter considers the characterisation of mobile communication channels, outlining the different mechanisms contributing to the detrimental effects induced by such channels. A concise overview of the root and nature of AWGN is followed by a thorough study of multipath fading channels, covering aspects such as multipath propagation and Doppler spread. Frequency and time domain characterisation of multipath fading channels are discussed, including multipath channel characterisation parameters, such as excess delay and power delay profiles. The part on mobile radio channel characterisation is concluded with an investigation into Rayleigh and Rician faded signals. It should be noted that *log-normal shadowing* and large-scale fading effects, such as *path-loss* are not addressed in this study. The interested reader is referred to [37] for more detail on the latter, and to [35] for an explanation of log-normal shadowing.

The simulation or reproduction of the statistical behaviour of mobile communication channels is among the most significant phases in the design, analysis and evaluation of wireless communication systems. As such, several statistical models that explain the nature of such channels have been proposed in recent years. The second part of this chapter not only addresses the issue of accurate AWGN generation, but also presents novel complex channel simulator models for frequency selective (multipath) and non-selective Rayleigh and Rician fading channels, based on *Clarke*'s flat fading channel model [76]. Several implementation issues concerning these models, such as Doppler spread spectral shaping filter design and the implementation of Hilbert transformers are also investigated. The discussion on the simulation of mobile fading channels is concluded with a short discussion on the exponential decay modelling of typical power delay profiles.

2.2 ADDITIVE WHITE GAUSSIAN NOISE CHANNELS

An unavoidable limiting factor in the performance and capabilities of communication systems is AWGN. Understanding the origins and nature of AWGN is therefore crucial if effective counter measures, such as channel coding, are to be investigated or designed.

Degradation of communication system performance in noisy channel conditions can be attributed

to a variety of noise sources, including galactic noise (for example radiation), terrestrial noise, amplifier noise, interference from other communication systems, and last but not least, thermal noise caused by the motion of electrons in conducting media. The primary statistical characteristic of the resultant noise, created by adding the effects of all of the aforementioned noise sources, is a Gaussian amplitude distribution, described by the following PDF:

$$\rho(\eta(t)) = \frac{1}{\sigma_{\eta(t)}\sqrt{2\pi}} \exp\left(-\frac{\eta^2(t)}{2\sigma^2_{\eta(t)}}\right) \tag{2.1}$$

where $\sigma^2_{\eta(t)}$ is the noise variance or power. The principle spectral characteristic of AWGN is its essentially flat two-sided PSD for frequencies up to approximately 10^{12} Hz. Thus, AWGN possess equal power per Hertz for all frequencies currently of interest in mobile radio communication.

2.3 MULTIPATH FADING CHANNEL OVERVIEW

In a realistic mobile radio environment a single received signal is composed of a number of scattered waves, caused by the reflection and diffraction of the original transmitted signal by objects in the surrounding geographical area. These multipath waves combine at the receiver antenna to give a resultant signal which can vary widely in amplitude and phase [37, 42, 44]. Physical factors influencing the characteristics of the fading experienced by the transmitted signal are [42, 44]:

1. **Multipath propagation:** A constantly changing environment is created by the presence of reflecting objects and scatterers in the propagation channel, thereby altering the signal energy in amplitude, phase and time. The result of these effects is the arrival of multiple versions of the transmitted signal, each arriving signal differing from the other with respect to time and spatial orientation. Signal fading and/or distortion is the result of the fluctuations in signal strength, caused by the random phases and amplitudes of the different multipath components.

2. **Relative motion between the receiver and transmitter:** Relative motion between a transmitter and receiver results in frequency modulation (shift in carrier frequency) of each of the multipath components, due to the Doppler effect. The Doppler shift in carrier frequency can be negative or positive, depending on the relative direction of movement between the transmitter and receiver. For example, consider a transmitter moving at a velocity of $v_r(t)$ [m/s] relative to the receiver, transmitting on a carrier with a wavelength of λ [m]. The time-variant Doppler frequency shift, denoted by $f_{d,i}(t)$ [Hz], experienced by the i^{th} multipath *Line-of-Sight* (LOS) signal component entering the receiver antenna, is given by:

$$f_{d,i}(t) = \frac{v_r(t)}{\lambda} \cos\left(\theta_{A,i}(t)\right) \tag{2.2}$$

   where $\theta_{A,i}(t)$ is the angle of arrival of this received signal component. In this study only time varying Doppler frequencies are considered, since this is a common characteristic exhibited by typical mobile fading environments which current 2G and 3G, as well as future 4G communication systems are subjected to. The resultant effect of a time-varying Doppler shift is a phenomenon known as *Doppler spread* (see *Section* 2.4.3.3). Fixed Doppler frequencies are commonly encountered in narrowband *Very High Frequency* (VHF) communication systems, operating in flat fading channels.

3. **Motion of the reflecting objects and scatterers:** A time varying Doppler shift is induced on each multipath component if the reflecting objects and scatterers in the propagation channel are in motion. If the speeds of the reflecting objects and scatterers are small compared to the speed of the mobile, the effect this has on the fading of the multipath components can be ignored.

4. **Transmission bandwidth of the signal:** The bandwidth of a multipath channel can be quantified by the so-called *coherence bandwidth* (See section *Section* 2.4.3.2). If the bandwidth of a transmitted signal exceeds the coherence bandwidth of the channel it has to traverse, the signal suffers severe distortions in time, but not in amplitude. In such a case the signal experiences frequency selective fading. Conversely, if the coherence bandwidth exceeds the signal bandwidth, the signal experiences flat fading, i.e. severe amplitude distortion, but minimal time distortion.

2.4 MULTIPATH PROPAGATION

2.4.1 MULTIPATH CHANNEL IMPULSE RESPONSE

Multipath fading radio channels can be modelled as linear filters with time varying impulse responses [40–42, 44]. This filter-like nature of multipath fading channels' transfer functions is caused by the summation of the amplitudes and the delays between multiple arriving waves at a given time instance. Time dependence of such transfer functions is a result of relative motion between the transmitters and the receivers. Assuming the passband input signal to a multipath fading channel is $s(t)$, ignoring the effects of AWGN, the passband output signal of the channel is given by [40, 42]:

$$r(t) = s(t) \otimes h(t, \tau) \tag{2.3}$$

where $\otimes$ represents continuous-time convolution and $h(t, \tau)$ the time varying passband multipath fading channel impulse response. The variable t represents the time dependance in the variations of the channel impulse response due to motion, whereas τ represents the channel multipath delay for a fixed value of t. The passband channel impulse response can also be written as [40, 42]:

$$h(t, \tau) = \mathrm{Re}\left\{h_b(t, \tau) \exp\left[j2\pi f_c t\right]\right\} \tag{2.4}$$

where $h_b(t, \tau)$ is the baseband equivalent of the channel impulse response and f_c the carrier frequency of the passband input signal. Assuming the existence of L discrete multipath components in the multipath fading channel, this baseband channel impulse response can be written as [42]:

$$h_b(t, \tau) = \sum_{i=1}^{L} \beta_i(t, \tau)\delta\left(\tau - \tau_i\left(t\right)\right) \exp\left[j\left(2\pi f_c \tau_i(t) + \theta_i(t, \tau)\right)\right] \tag{2.5}$$

where $\beta_i(t, \tau)$ and $\tau_i\left(t\right)$ are the delay dependent instantaneous amplitude and time delay associated with the i^{th} multipath component, respectively. The instantaneous phase shift encountered by the i^{th} multipath component, due to its delay, is represented by $2\pi f_c \tau_i(t)$, whereas any other possible phase alterations experienced by this multipath component is incorporated in $\theta_i(t, \tau)$. To simplify *Eq.* (2.5), these phase delays are lumped together and represented by $\phi_i(t, \tau)$, where:

$$\phi_i(t, \tau) = 2\pi f_c \tau_i(t) + \theta_i(t, \tau) \tag{2.6}$$

If it is assumed that the time delay associated with each of the multipath components remains constant, the instantaneous baseband channel impulse response reduces to:

$$h_b(t, \tau) = \sum_{i=1}^{L} \beta_i(t)\delta\left(\tau - \tau_i\right) \exp\left[j\phi_i(t)\right] \tag{2.7}$$

where $\beta_i(t)$ and $\phi_i(t)$, respectively, are the time varying amplitude and phase alterations, experienced by the i^{th} multipath component, which has a fixed delay of τ_i.

Assuming that the channel is time invariant, or at least wide sense stationary over a small time or distance interval, the fixed delay baseband channel impulse response can be further simplified to [42]:

$$h_b(\tau) = \sum_{i=1}^{L} \overline{\beta}_i \delta(\tau - \tau_i) \exp\left[j\overline{\phi}_i\right] \tag{2.8}$$

where $\overline{\beta}_i$ and $\overline{\phi}_i$ are the time averaged values of $\beta_i(t)$ and $\phi_i(t)$, respectively. The normalised instantaneous amplitude variation, called the *instantaneous fading amplitude*, experienced by the i^{th} multipath component, is now given by:

$$\alpha_i(t) = \frac{\beta_i(t)}{\overline{\beta}_i} \tag{2.9}$$

2.4.2 POWER DELAY PROFILES

The power delay profile of a time variant multipath fading channel is given by: [37, 40, 42, 44]:

$$P(t,\tau) = |h_b(t,\tau)|^2 \tag{2.10}$$

By averaging *Eq.* (2.10) over time, the following time-invariant power delay profile is obtained [37, 42, 44]:

$$P(\tau) = \overline{|h_b(t,\tau)|^2} = \sum_{i=1}^{L} P(\tau_i)\,\delta(\tau - \tau_i) \tag{2.11}$$

where $P(\tau_i)$ is the average power in the i^{th} multipath component, given by [37, 42, 44]:

$$P(\tau_i) = \overline{\beta}_i^2 \tag{2.12}$$

In order to facilitate the simulation of digital communication systems in multipath fading environments, power delay profiles models that closely resemble real measured profiles are often used. Common models used include exponential decay profiles (see *Section* 2.6.3.3), Gaussian profiles, equal-amplitude two path (double spike) profiles and *Rummler*'s two ray model [44].

2.4.3 MULTIPATH CHANNEL PARAMETERS

The accurate comparison of different multipath fading channels are often difficult, if not impossible. Therefore parameters which grossly quantify such channels have been defined. These parameters can also be useful during the design of future wireless systems that will operate in multipath fading channel conditions.

2.4.3.1 TIME DISPERSION PARAMETERS

The delay time between signal transmission and reception of the first multipath component (denoted by the variable τ_1) is sometimes referred to as the *first arrival delay* [44]. Using this definition, the *excess delay* [37, 42, 44] of the i^{th} multipath component is the time difference between the first arrival delay and the delay time between signal transmission and reception of this multipath component.

The time dispersive properties of wideband multipath fading channels are commonly quantified by means of the following three parameters:

1. **Mean Excess Delay:** The mean excess delay gives an estimate of the average time delay experienced by a signal propagating through a multipath fading channel. It is obtained by calculating the

first moment of the power delay profile [37, 42, 44]:

$$\overline{\tau} = \frac{\sum_{i=1}^{L} P(\tau_i)\,(\tau_i - \tau_1)}{\sum_{i=1}^{L} P(\tau_i)} = \frac{\sum_{i=1}^{L} \overline{\beta}_i^2\,(\tau_i - \tau_1)}{\sum_{i=1}^{L} \overline{\beta}_i^2} \tag{2.13}$$

2. Root-Mean-Square Delay Spread: The *Root-Mean-Square* (RMS) delay spread is given by [37, 42, 44]:

$$\sigma_\tau = \sqrt{\overline{\tau^2} - (\overline{\tau})^2} \tag{2.14}$$

where:

$$\overline{\tau^2} = \frac{\sum_{i=1}^{L} P(\tau_i)\,(\tau_i - \tau_1)^2}{\sum_{i=1}^{L} P(\tau_i)} = \frac{\sum_{i=1}^{L} \overline{\beta}_i^2\,(\tau_i - \tau_1)^2}{\sum_{i=1}^{L} \overline{\beta}_i^2} \tag{2.15}$$

3. Maximum Excess Delay: The maximum excess delay (denoted by τ_{max}) [37, 42, 44] of a multipath fading channel is the excess delay of the last (L^{th}) multipath component. If a multipath channel is quantified only by its maximum excess delay, the last multipath component in the power delay profile is assumed to have an average power level of P_{drop} [dB] relative to the maximum average power level multipath component (a typical value for P_{drop} is -30 dB). Thus, the maximum excess delay is defined as [37, 42, 44]:

$$\tau_{max} = \tau_a - \tau_1 \tag{2.16}$$

where τ_a is the maximum delay at which a multipath component is within P_{drop} [dB] of the strongest arriving multipath component. It is important to note that the strongest component need not be the first arrival component, as it can be preceded by a number of non-minimum phase precursor multipath components.

2.4.3.2 COHERENCE BANDWIDTH

The coherence bandwidth [37, 42, 44] is a commonly used statistical measure of the range of frequencies over which a multipath fading channel's frequency response can be considered to be flat (see *Section* 2.5.1.1). In other words, the coherence bandwidth is the maximum frequency separation between two frequency components propagating through the channel, which exhibits a preset amplitude correlation. The coherence bandwidth is defined as [37, 42, 44]:

$$B_C = \frac{1}{\psi.\sigma_\tau} \tag{2.17}$$

where σ_τ is the RMS delay spread (see *Section* 2.4.3.1) and ψ a constant, dependent on the strength of the correlation between the two frequency components. Typical values for ψ are 50 and 5 for correlation values of approximately 0.9 and 0.5, respectively [42].

2.4.3.3 DOPPLER SPREAD AND COHERENCE TIME

The measure of spectral broadening (smearing), caused by the rate of change of multipath components, due to relative motion between the transmitter and the receiver, is known as Doppler spread [37, 42, 44]. The Doppler spread associated with the i^{th} received multipath component, $b_i(t)$, is defined as the single sided spectral width of the smearing experienced by a single tone carrier input

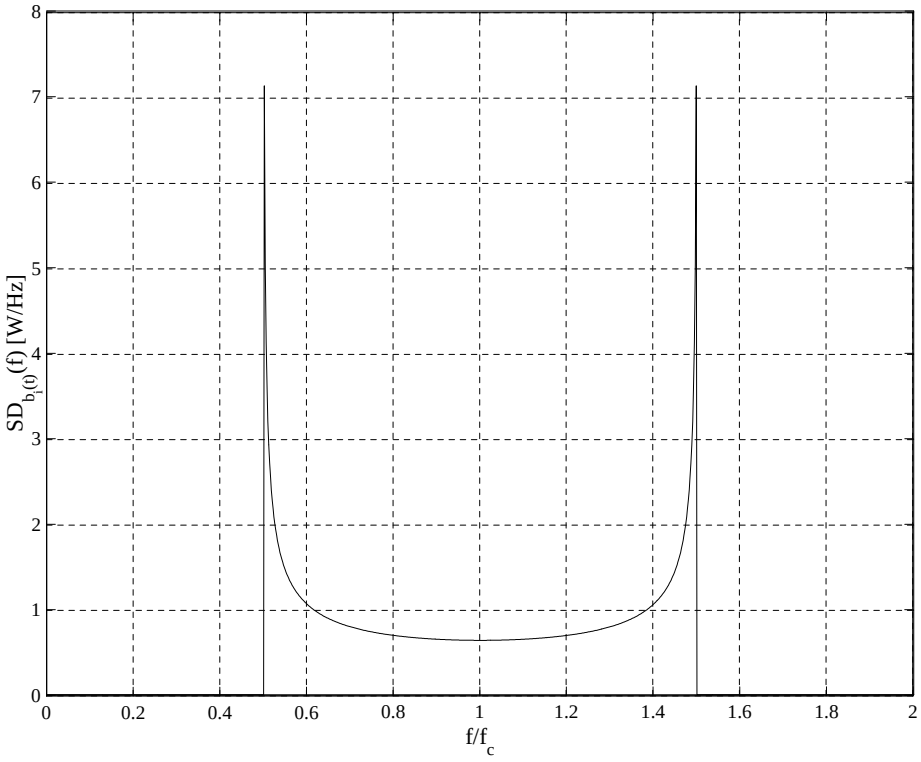

Figure 2.1: Classic Doppler Spectrum for $B_{D,i}/f_c = 0.5$ and $\sigma^2_{b_i(t)} = 1$

signal. Doppler spread is a function of the relative motion between the transmitter and receiver, as well as the angle of arrival of the scattered waves. For a sinusoidal channel input signal, experiencing a maximum Doppler shift of $\max\{f_{d,i}(t)\}$ (see *Eq.* (2.2)), it can be shown that the i^{th} multipath fading channel output signal's PSD approximates [37, 42, 44]:

$$SD_{b_i(t)}(f) = \begin{cases} \dfrac{\sigma^2_{b_i(t)}}{\pi\sqrt{\left(\max\{f_{d,i}(t)\}\right)^2-(f-f_c)^2}} & \text{if } |f-f_c| \leq \max\{f_{d,i}(t)\} \\ 0 & \text{if } |f-f_c| > \max\{f_{d,i}(t)\} \end{cases} \tag{2.18}$$

where f_c is the carrier frequency and $\sigma^2_{b_i(t)}$ is the average power of the transmitted signal. This PSD is usually referred to as a *classic Doppler spectrum* and is shown in *Fig.* 2.1 for $(\max\{f_{d,i}(t)\})/f_c = 0.5$ and $\sigma^2_{b_i(t)} = 1$. From *Eq.* (2.18) it is clear that the maximum Doppler spread is given by:

$$B_{D,i} = \max\{f_{d,i}(t)\} \tag{2.19}$$

The coherence time [42, 44] is a statistical measure of the time duration over which the flat fading channel impulse response is essentially time invariant. In other words, it is the maximum time interval between two received signals exhibiting a preset amplitude correlation. In general, it is given by [42, 44]:

$$T_{C,i} = \frac{\zeta}{B_{D,i}} \tag{2.20}$$

where ζ is a constant value dependent on the required amplitude correlation strength. Typical values for ζ are 1 and $9/(16\pi)$ for correlation values of 0.9 and 0.5, respectively [42].

2.5 SIGNAL FADING

2.5.1 TYPES OF SIGNAL FADING

The type of fading experienced by a signal propagating through a multipath fading channel is a function of both the nature of the transmitted signal and the characteristics of the channel. Different types of signals undergo different types of fading, depending on the signal parameters (bandwidth, etc.) and channel parameters (RMS delay spread, Doppler spread, etc.). Time and frequency dispersion mechanisms in multipath fading channels lead to four distinct types of signal fading, each of which is discussed in the following subsections.

2.5.1.1 MULTIPATH TIME DELAY SPREAD FADING EFFECTS

Signals propagating through a multipath fading channel undergo either frequency flat or frequency selective fading, due to time dispersion caused by multipath propagation [42]. These effects are discussed below:

1. **Flat Fading:** A signal propagating through a multipath fading channel that has a constant average gain and linear phase response over a larger bandwidth than the signal's bandwidth, experiences flat fading. The requirements for a signal to undergo flat fading are $B_{sig} << B_C$ and $T_{sig} >> \sigma_\tau$ [42], where B_{sig} and T_{sig} are the transmitted signal's bandwidth and reciprocal bandwidth, respectively. B_C and σ_τ are the channel's coherence bandwidth (see *Section* 2.4.3.2) and RMS delay spread (see *Section* 2.4.3.1), respectively.

   With this type of fading, the transmitted signal's spectral characteristics are preserved when it propagates through the channel. Only the received signal power fluctuates, due to the multipath effects. Since the reciprocal of the signal bandwidth is usually far greater than the RMS delay spread of the channel, modelling such channels as a single multipath component is a common approach [42].

2. **Frequency Selective Fading:** A signal propagating through a multipath fading channel that has a constant average gain and linear phase response over a smaller bandwidth than the signal's bandwidth, experiences frequency selective fading. This is due to the time dispersion experienced by the signals propagating through such a channel. The requirements for a signal to undergo frequency selective fading are $B_{sig} > B_C$ and $T_{sig} < \sigma_\tau$ [42], where B_{sig} and T_{sig} are the transmitted signal's bandwidth and reciprocal bandwidth, respectively. B_C and σ_τ are the channel's coherence bandwidth (see *Section* 2.4.3.2) and RMS delay spread (see *Section* 2.4.3.1), respectively.

   Under these conditions, the received channel output signal includes multiple versions of the transmitted signal, which are faded and delayed in time, resulting in ISI. Viewed in the frequency domain, certain frequency components of the received signal are faded differently from others.

2.5.1.2 DOPPLER SPREAD FADING EFFECTS

Signals propagating through a multipath fading channel undergo either fast or slow fading, due to the rate of change of the channel, caused by relative motion between the transmitter and the receiver. Signals propagating through the channel encounter either fast or slow fading effects [42], depending on the rate of change of the channel impulse response, as discussed below:

1. **Fast Fading:** If the channel impulse response changes rapidly within the symbol duration of the transmitted signal, the channel is called a *fast fading channel*. This implies that the coherence time (see *Section* 2.4.3.3) of the channel is smaller than the reciprocal bandwidth of the transmitted

signal. The requirements for a signal to undergo fast fading when propagating through a multipath fading channel are $T_{sig} > T_C$ and $B_{sig} < B_D$ [42], where B_{sig} and T_{sig} are the transmitted signal's bandwidth and reciprocal bandwidth, respectively. B_D and T_C are the channel's maximum Doppler spread and coherence time (see *Section* 2.4.3.3), respectively.

In the frequency domain, fast fading is characterised by frequency dispersion, due to Doppler spread. This frequency dispersion in turn causes time distortion on the transmitted signals.

2. **Slow Fading:** A *slow fading channel*'s impulse response varies at a rate much slower than the rate of change of the transmitted signal. Such a channel can be assumed to be static over a time period larger than the transmitted signal's reciprocal bandwidth interval. The requirements for a signal to undergo slow fading when propagating through a multipath fading channel are $T_{sig} << T_C$ and $B_{sig} >> B_D$ [42], where B_{sig} and T_{sig} are the transmitted signal's bandwidth and reciprocal bandwidth, respectively. B_D and T_C are the channel's maximum Doppler spread and coherence time (see *Section* 2.4.3.3), respectively.

2.5.2 FADING DISTRIBUTIONS

In the analysis of multipath fading channels, the phase and envelope distributions of the received multipath components of signals propagating through the channel are of great importance. Both the phase and envelope distributions are governed by the power of the unfaded or LOS signal component, relative to the faded or LOS signal component power in the total received multipath signal component. In the absence of a LOS signal component, the envelope distribution of a multipath component can be modelled as a Rayleigh PDF. Conversely, the presence of a LOS signal component dictates a signal envelope with a Rician PDF. The following subsections shed more light on the statistical nature of Rayleigh and Rician faded signals.

2.5.2.1 RAYLEIGH FADED SIGNALS

If the i^{th} received multipath component, denoted by $b_i(t)$, consists solely of a faded signal component, its enveloped, denoted by $\varepsilon_i(t)$, exhibits the Rayleigh distribution given by [37, 42, 44]:

$$\rho\left(\varepsilon_i(t)\right) = \begin{cases} \frac{\varepsilon_i(t)}{\sigma^2_{b_i(t)}} \exp\left(-\frac{\varepsilon_i^2(t)}{2\sigma^2_{b_i(t)}}\right) & \text{if } 0 \leq \varepsilon_i(t) < \infty \\ 0 & \text{if } \varepsilon_i(t) < 0 \end{cases} \tag{2.21}$$

where $\sigma_{b_i(t)}$ is the RMS value of $b_i(t)$ before enveloped detection. Since a Rayleigh distribution is obtained by setting $B_i = 0$ V in the expression for a Rician distribution (see *Eq.* (2.25) in *Section* 2.5.2.2), i.e. setting the LOS component in the signal $b_i(t)$ to zero, it follows that the curve shown in *Fig.* 2.2 for $K_i = -\infty$ dB depicts the Rayleigh PDF, described by *Eq.* (2.21). The mean value of the Rayleigh distribution is given by:

$$E\left[\varepsilon_i(t)\right] = \sigma_{b_i(t)} \cdot \sqrt{\frac{\pi}{2}} \tag{2.22}$$

where $E[\,\cdot\,]$ denotes expectancy. The variance (*Alternating Current* (AC) power in the envelope) of $\varepsilon_i(t)$ is given by:

$$\sigma_{\varepsilon_i^2(t)} = \sigma^2_{b_i(t)} \left(2 - \sqrt{\frac{\pi}{2}}\right) \tag{2.23}$$

Assuming a fixed phase channel input signal, it can be shown that the phase $\phi_i(t)$ of the i^{th} Rayleigh faded multipath signal component exhibits a uniform phase distribution, given by [37, 42, 44]:

$$\rho\left(\phi_i(t)\right) = \frac{1}{2\pi} \qquad \text{for } -\pi \leq \phi_i(t) \leq \pi \tag{2.24}$$

The curve for $K_i = -\infty$ dB in *Fig.* 2.3 depicts the phase distribution of a Rayleigh faded signal, as described by *Eq.* (2.24).

2.5.2.2 RICIAN FADED SIGNALS

When there are both LOS and *Non-Line-of-Sight* (NLOS) signal components, respectively denoted by $b_i^{LOS}(t)$ and $b_i^{NLOS}(t)$, present in the i^{th} received multipath component, the envelope of this multipath component, denoted by $\varepsilon_i(t)$, exhibits a Rician distribution, given by [42]:

$$\rho\left(\varepsilon_i(t)\right) = \begin{cases} \frac{\varepsilon_i(t)}{\sigma^2_{b_i^{NLOS}(t)}} \exp\left(-\frac{\varepsilon_i^2(t)+B_i^2}{2\sigma^2_{b_i^{NLOS}(t)}}\right) I_0\left(\frac{B_i.\varepsilon_i(t)}{\sigma^2_{b_i^{NLOS}(t)}}\right) & \text{if } B_i \geq 0 \text{ and } \varepsilon_i(t) \geq 0 \\ 0 & \text{if } \varepsilon_i(t) < 0 \end{cases} \tag{2.25}$$

where B_i is the maximum amplitude of $b_i^{LOS}(t)$, and $I_0\left(\cdot\right)$ is the modified Bessel function of the first kind and zero-th order. The parameters $\sigma^2_{b_i^{NLOS}(t)}$ and $\sigma^2_{b_i^{LOS}(t)}$ denote the time-average power in the NLOS and LOS signal components, respectively.

The nature of this distribution is governed by the power in the LOS signal component, relative to the power in the NLOS signal component. This ratio, usually given in [dB], is called the *Rician factor*. It is defined as follows:

$$K_i = 10\log_{10}\left(\frac{B_i^2}{2\sigma^2_{b_i^{NLOS}(t)}}\right) \tag{2.26}$$

As the LOS signal component's power tends to zero, and subsequently K_i tends to $-\infty$, the Rician PDF approaches a Rayleigh PDF. Considering the other extreme case where the LOS signal component becomes dominant, i.e. K_i tends to ∞, the Rician PDF approaches a Gaussian PDF. *Fig.* 2.2 shows Rician PDFs for $K_i = -\infty$ dB (Rayleigh), $K_i = 0$ dB (Rician) and $K_i = 6$ dB ($\approx$ Gaussian).

Assuming an input signal with a fixed phase θ_R, the phase distribution of a Rician faded multipath signal component is dependent on two factors: The NLOS signal component's phase distribution, given by *Eq.* (2.24), and the Rician factor (see *Eq.* (2.26)). For such a scenario, the PDF of the i^{th} Rician faded multipath component's phase $\phi_i(t)$, is given by [38, 77]:

$$\begin{aligned}\rho(\phi_i(t)) = &\frac{1}{2\pi}\exp\left(-\frac{B_i^2}{2\sigma^2_{b_i^{NLOS}(t)}}\right)\left\{1+\frac{B_i}{\sigma_{b_i^{NLOS}(t)}}\sqrt{\frac{\pi}{2}}\cos\left(\phi_i(t)-\theta_R\right)\cdot\right. \\ &\left.\exp\left(\frac{B_i^2\cos^2\left(\phi_i(t)-\theta_R\right)}{2\sigma^2_{b_i^{NLOS}(t)}}\right)\left[1+\operatorname{erf}\left(\frac{B_i\cos\left(\phi_i(t)-\theta_R\right)}{\sigma_{b_i^{NLOS}(t)}\sqrt{2}}\right)\right]\right\} \qquad \text{for } |\phi_i(t)| \leq \pi\end{aligned} \tag{2.27}$$

Fig. 2.3 shows the PDFs of the phases of Rician multipath signal components, calculated for the Rician factors $K_i = -\infty$ dB, $K_i = 0$ dB and $K_i = 6$ dB using *Eq.* (2.27).

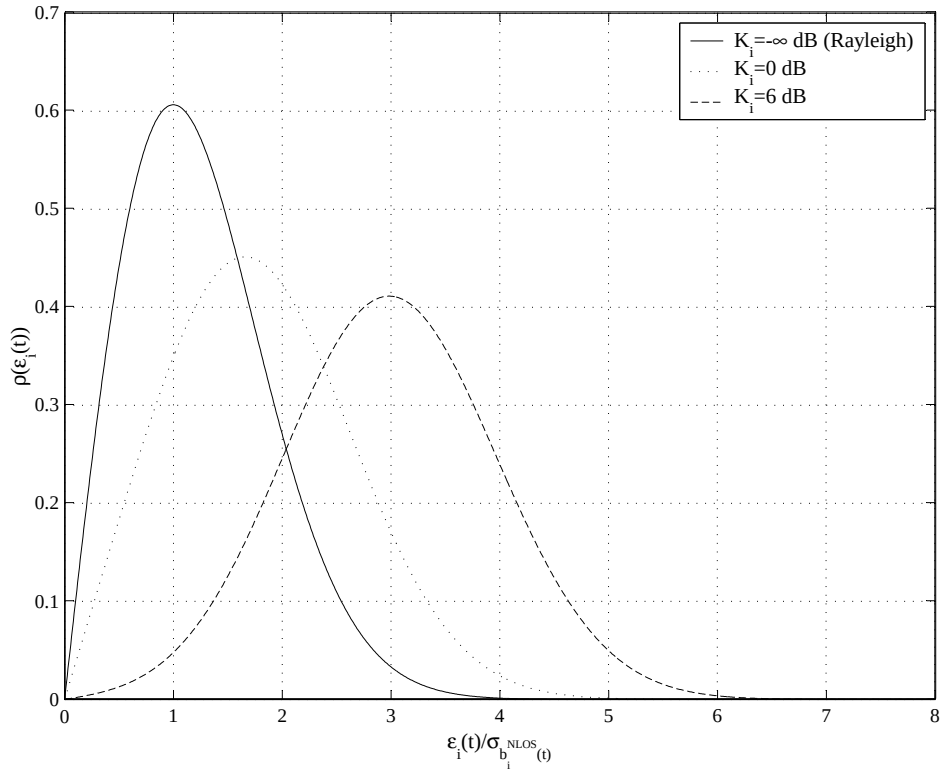

Figure 2.2: PDFs of the Envelopes of Rician Faded Multipath Signal Components for $K_i = -\infty$ dB (Rayleigh), $K_i = 0$ dB (Rician) and $K_i = 6$ dB ($\approx$ Gaussian)

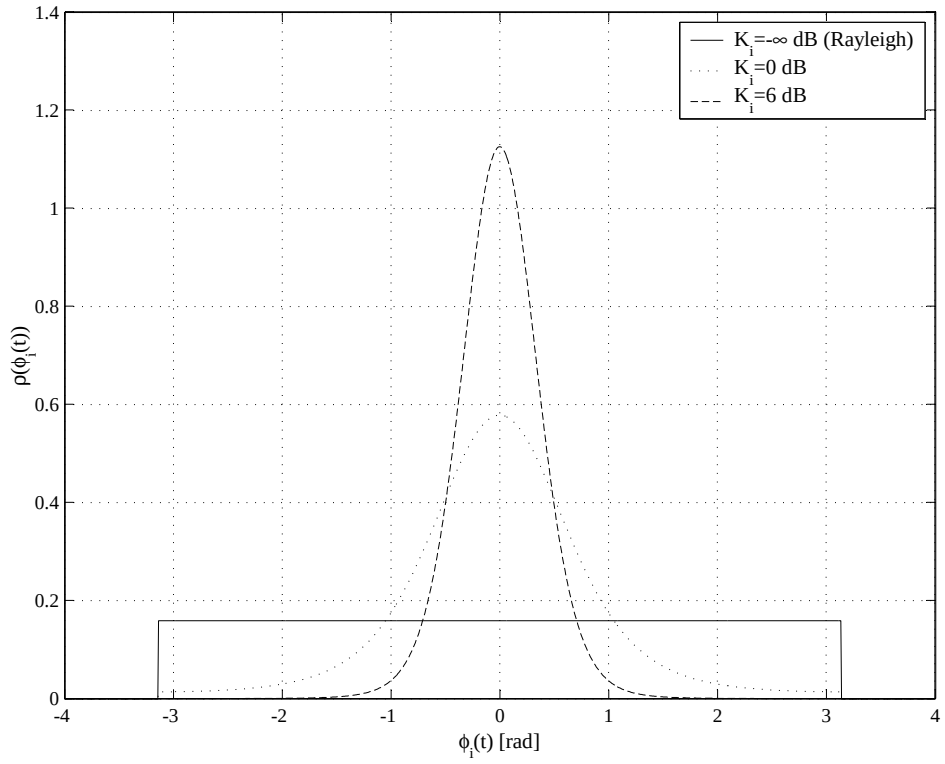

Figure 2.3: PDFs of the Phases of Rician Faded Multipath Signal Components for $K_i = -\infty$ dB, $K_i = 0$ dB and $K_i = 6$ dB with $\theta_R = 0$ rad

2.6 SIMULATING MOBILE RADIO CHANNELS

2.6.1 SIMULATING ADDITIVE WHITE GAUSSIAN NOISE CHANNELS

The next subsection gives a concise description of the accurate generation of AWGN. It is followed by a subsection that details the process whereby the variance of Gaussian noise samples can be scaled to obtain a specific E_b/N_0 value.

2.6.1.1 GENERATING GAUSSIAN DISTRIBUTED NOISE SAMPLES

When simulating mobile communication systems in AWGN channel conditions, transformation algorithms, such as the *Bray-Marsagalia* algorithm [78] and *Box-Muller* sine-cosine algorithm [79], are frequently utilised to generate samples that exhibit a Gaussian amplitude PDF with a zero mean and a variance of 1, using noise samples with uniformly distributed amplitude values ranging from 0 to 1 as inputs. Furthermore, the accurate simulation of AWGN channel conditions necessitates statistical independence between the uniformly distributed noise samples before being transformed to Gaussian distributed samples by the chosen transformation algorithm. Unfortunately, the uniform distribution random number generators implemented in programming languages such as C/C++, which are usually shift register-based PN generators, may not exhibit sufficient randomness. This is due to the fact that the sequence of samples that these generators produce for a given starting seed value, repeats too rapidly. In such cases it is good practise to rather use uniform distribution random number generator algorithms, such as the *Wichmann-Hill* algorithm [80]. Such random number generators exhibit lower statistical dependance between the uniformly distributed samples by increasing the sequence repetition length.

2.6.1.2 OBTAINING GAUSSIAN SAMPLES WITH THE REQUIRED NOISE VARIANCE AS DICTATED BY E_b/N_0

When investigating the performance of communication systems in typical mobile communication channel conditions, two quantities, namely the SNR and the E_b/N_0 [dB] value, are of importance. Although more commonly used in everyday jargon, the SNR, defined as the ratio of average transmitted signal power to noise power at the receiver output [81], is meaningless unless the noise equivalent bandwidth of the receiver is also specified. Consequently, the SNR is frequently normalised with respect to this bandwidth, resulting in the quantity E_b/N_0, which then becomes the independent variable in the performance measurements.

By stipulating the E_b/N_0 value for a specific performance measurement setup, it is possible to calculate the variance $\sigma^2_{\eta(t)}$ of the Gaussian noise samples required to realise the correct AWGN channel conditions. Assuming that the channel output signal enters the receiver through a noise limiting receive filter with the frequency response $H_{Rx}(f)$, the following relationship between the SNR and E_b/N_0 of coded binary communication systems holds:

$$SNR = \frac{\sigma^2_{s(t)}}{\sigma^2_{\eta(t)}} = \frac{E_b.f_{bit}}{N_0 \int_0^\infty |H_{Rx}(f)|^2 df} = \frac{E_c.(f_{bit}/R_c)}{N_0 \int_0^\infty |H_{Rx}(f)|^2 df} \tag{2.28}$$

where:
$\sigma^2_{s(t)}$ = Variance (power) of the transmitted signal.
$\sigma^2_{\eta(t)}$ = Variance (power) of the required Gaussian noise samples.
E_c = Energy in a transmitted coded bit.
R_c = Code rate.

E_b = Energy in an uncoded bit.
f_{bit} = Uncoded bit rate.
N_0 = Single-sided PSD level of AWGN.

Manipulating *Eq.* (2.28), an expression can be obtained for the required noise variance as a function of the specified E_b/N_0 [dB] ratio:

$$\sigma^2_{\eta(t)} = \frac{\sigma^2_{s(t)} \int_0^\infty |H_{Rx}(f)|^2 df}{10^{\left(\frac{1}{10}E_b/N_0\right)}.f_{bit}} \tag{2.29}$$

If Gaussian distributed noise samples are generated at a rate of f_{samp} [Hz] by a Gaussian transformation algorithm-based noise source, the effective noise bandwidth of the noise source is:

$$B_{ns} = \frac{f_{samp}}{2} \tag{2.30}$$

Furthermore, if the Gaussian PDF of the samples generated by the transformation algorithm has a variance of $\sigma^2_{ns(t)} = 1$, it follows that:

$$N_{ns}.B_{ns} = \sigma^2_{ns(t)} = 1 \tag{2.31}$$

where N_{ns} is the single-sided PSD level of the noise generated by the noise source. Using *Eq.* (2.30), it follows that this single-sided PSD level is given by:

$$N_{ns} = \frac{2}{f_{samp}} \tag{2.32}$$

Thus, the power of the noise generated by the transformation algorithm at the output of the receive filter is given by:

$$\sigma^2_{r(t)} = N_{ns} \int_0^\infty |H_{Rx}(f)|^2 df = \frac{2}{f_{samp}} \int_0^\infty |H_{Rx}(f)|^2 df \tag{2.33}$$

Since the required noise variance is given by *Eq.* (2.29), it follows that the factor k_η whereby the noise variance of the noise samples, generated by the transformation algorithm-based noise source, must be scaled, is given by:

$$k_\eta = \frac{\sigma^2_{\eta(t)}}{\sigma^2_{r(t)}} \tag{2.34}$$

Using *Eq.* (2.29), *Eq.* (2.33) and *Eq.* (2.34), the following expression for k_η is obtained:

$$k_\eta = \frac{\sigma^2_{s(t)}.f_{samp}}{10^{\left(\frac{1}{10}E_b/N_0\right)}.2.f_{bit}} \tag{2.35}$$

Since the scaling factor k_η is a power scaling factor, it follows that the noise samples generated by the transformation algorithm has to be scaled by $\sqrt{k_\eta}$ in order to produce Gaussian noise samples with a variance of $\sigma^2_{\eta(t)}$.

2.6.2 CLARKE'S FLAT FADING CHANNEL MODEL

Constructing an L-path statistical multipath fading channel simulator is accomplished by using L unique statistical flat fading channel simulators (see *Section* 2.6.3). Several statistical flat fading simulator models exist, among which the *Jakes* [82] and *Clarke* [76] models are the most popular.

This study makes use of the *Clarke* flat fading channel simulator model. Note that empirical multipath fading channel simulator models fall beyond the scope of this study.

2.6.2.1 BACKGROUND

Based on the statistical characteristics of the scattered electromagnetic fields constituting the signal entering a moving receiver, *Clarke* developed a model for flat fading channels [76]. The assumptions that he made in the development of this model are:

- The transmitter is fixed and employs an omnidirectional vertically polarised antenna.
- The field incident on the receiver consists of M_{apw} azimuthal plane waves.
- Each of the M_{apw} azimuthal plane waves have an arbitrary carrier phase. These phase angles are assumed to be uniformly distributed, as described by *Eq.* (2.24).
- Each of the M_{apw} azimuthal plane waves have an arbitrary angle of arrival.
- The M_{apw} azimuthal plane waves have equal average amplitudes, implying the absence of a LOS path.

Using *Rice*'s analysis [83, 84], which proved that an electromagnetic field can be expressed in an in-phase and quadrature form, *Clarke* showed [76] that the received signal's electromagnetic field is given by [42]:

$$E(t) = E_I(t)\cos(2\pi f_c t) - E_Q(t)\sin(2\pi f_c t) \tag{2.36}$$

with:

$$E_I(t) = E_o \sum_{j=1}^{M_{apw}} A_j(t)\cos(\phi_j(t)) \tag{2.37}$$

and:

$$E_Q(t) = E_o \sum_{j=1}^{M_{apw}} A_j(t)\sin(\phi_j(t)) \tag{2.38}$$

where E_o is the constant amplitude of the transmitted signal's electromagnetic field. The variables $A_j(t)$, and $\phi_j(t)$ are random variables representing the amplitude and phase of the j^{th} scattered electromagnetic field component arriving at the receiver, respectively. *Clarke* showed [76] that the variables $E_I(t)$ and $E_Q(t)$ are both Gaussian random processes. Therefore, the envelope of the received electromagnetic field, given by:

$$\varepsilon(t) = |E(t)| = \sqrt{(E_I(t))^2 + (E_Q(t))^2} \tag{2.39}$$

exhibits the Rayleigh distribution, given by *Eq.* (2.21).

2.6.2.2 CLASSIC IMPLEMENTATION OF CLARKE'S FLAT FADING CHANNEL MODEL

The classic flat fading channel simulator [39, 42, 44] for the i^{th} multipath component, based on *Clarke*'s model [76], is shown in *Fig.* 2.4. The simulator receives an input signal (denoted by $u_i(t)$) and creates in-phase (denoted by $u_i(t)$) and quadrature (denoted by $\hat{u}_i(t)$) versions of this signal using a *Hilbert transformer* (denoted by the block HT_i).

The quadrature signal $\hat{u}_i(t)$ is multiplied by $n_i^Q(t)$, which is a Doppler filtered version of zero-mean Gaussian noise, generated by noise generator $G_i^Q(t)$. The Doppler lowpass filter $DF_i^Q(f)$ is designed

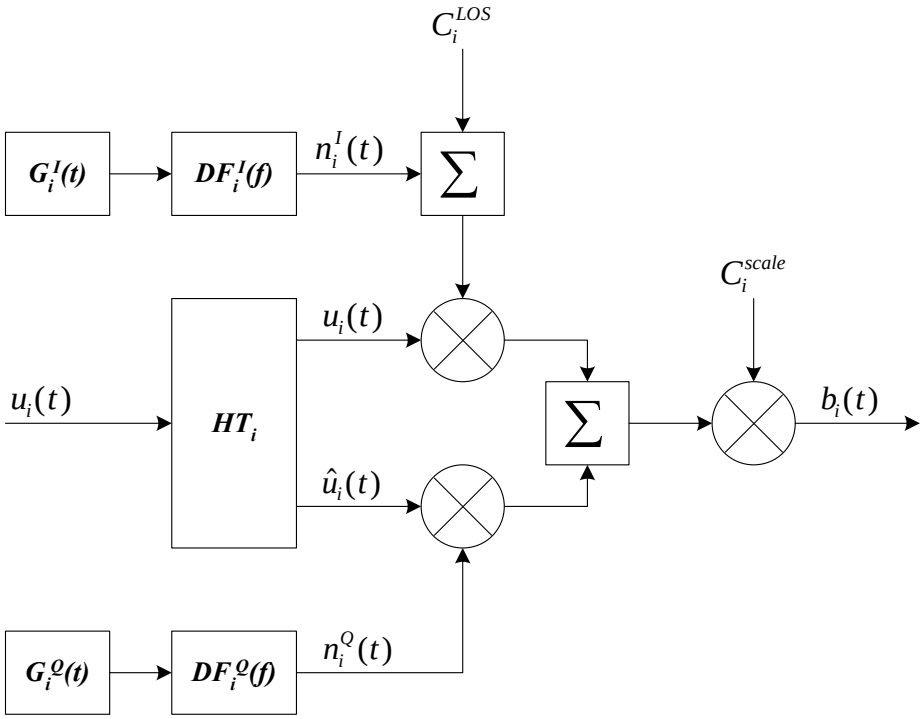

Figure 2.4: Classic Flat Fading Channel Simulator Based on *Clarke*'s Model

(see *Section* 2.6.2.4.2) to approximate a baseband equivalent of the output signal PSD shown in *Fig.* 2.1 [85]. The filter coefficients are also scaled to ensure that $n_i^Q(t)$ has unity power.

The in-phase signal $u_i(t)$ is multiplied by a linear combination of $n_i^I(t)$, which is a Doppler low-pass filtered version of the zero-mean Gaussian noise, generated by noise generator $G_i^I(t)$, and a constant value C_i^{LOS}, which facilitates a LOS signal component in the simulator output signal. The Doppler filter $DF_i^I(f)$ is identical to $DF_i^Q(f)$.

The output of the flat fading channel simulator, denoted by $b_i(t)$, is given by:

$$b_i(t) = C_i^{scale}\left[\left(n_i^I(t) + C_i^{LOS}\right)u_i(t) + n_i^Q(t).\hat{u}_i(t)\right] \tag{2.40}$$

where C_i^{scale} is a constant scale factor, which ensures that the power in the simulator input signal is equal to the power in the simulator output signal. The variable C_i^{scale} is calculated as follows: Assume the power in the input signal $u_i(t)$ is $P_{u_i(t)}$. Furthermore, let the power in the quadrature version of the input signal be $P_{\hat{u}_i(t)}$. The power in the output signal is now given by:

$$P_{b_i(t)} = \left(C_i^{scale}\right)^2\left[\left(1 + \left(C_i^{LOS}\right)^2\right)P_{u_i(t)} + P_{\hat{u}_i(t)}\right] \tag{2.41}$$

Since it is required that $P_{b_i(t)} = P_{u_i(t)} = P_{\hat{u}_i(t)}$, it can be shown that:

$$C_i^{scale} = \frac{1}{\sqrt{2 + \left(C_i^{LOS}\right)^2}} \tag{2.42}$$

As previously stated, the factor C_i^{LOS} is responsible for the presence a LOS signal component in the simulator output signal. The variable can be related to the Rician factor discussed in *Section* 2.5.2.2 as follows: Firstly, rewrite *Eq.* (2.40) so that the LOS and NLOS signal components, present in the simulator output, become clear:

$$b_i(t) = \underbrace{C_i^{scale}\left(n_i^I(t).u_i(t) + n_i^Q(t).\hat{u}_i(t)\right)}_{NLOS} + \underbrace{C_i^{scale}.C_i^{LOS}.u_i(t)}_{LOS} \tag{2.43}$$

It can be shown that the Rician factor, which is the ratio (in [dB]) of the average LOS signal component power to the average NLOS signal component power, simplifies to:

$$K_i = 20\log_{10}\left(\frac{C_i^{LOS}}{\sqrt{2}}\right) \tag{2.44}$$

2.6.2.3 COMPLEX IMPLEMENTATION OF CLARKE'S FLAT FADING CHANNEL MODEL

The use of the Hilbert transform in the classic *Clarke* flat fading channel simulator model of *Fig.* 2.4 can be eliminated by assuming that the i^{th} multipath signal component, transversing a multipath fading channel, has already been decomposed into real and imaginary parts, i.e.:

$$u_i(t) = \text{Re}\left\{u_i(t)\right\} + j.\,\text{Im}\left\{u_i(t)\right\} \tag{2.45}$$

Define a complex flat fading process, with an LOS component:

$$\varpi_i(t) = \alpha_i(t).\cos\left(\phi_i(t)\right) + C_i^{LOS} + j.\alpha_i(t).\sin\left(\phi_i(t)\right) \tag{2.46}$$

where $\alpha_i(t)$ and $\phi_i(t)$ are the instantaneous fading amplitude and phase of the i^{th} multipath signal component, respectively. It can easily be shown that the i^{th} complex multipath fading channel component is given by:

$$b_i(t) = \text{Re}\left\{b_i(t)\right\} + j.\,\text{Im}\left\{b_i(t)\right\} = \varpi_i(t).u_i(t) \tag{2.47}$$

Thus, the in-phase and quadrature outputs of the i^{th} flat fading channel, operating on a complex input signal, are given by:

$$\text{Re}\left\{b_i(t)\right\} = \text{Re}\left\{\varpi_i(t)\right\}.\text{Re}\left\{u_i(t)\right\} - \text{Im}\left\{\varpi_i(t)\right\}.\text{Im}\left\{u_i(t)\right\} \tag{2.48}$$

and:

$$\text{Im}\left\{b_i(t)\right\} = \text{Re}\left\{\varpi_i(t)\right\}.\text{Im}\left\{u_i(t)\right\} + \text{Im}\left\{\varpi_i(t)\right\}.\text{Re}\left\{u_i(t)\right\} \tag{2.49}$$

respectively. *Fig.* 2.5 shows a novel complex implementation of the *Clarke*'s flat fading channel that realises *Eq.* (2.48) and *Eq.* (2.49). From this figure it is clear that:

$$\text{Re}\left\{b_i(t)\right\} = C_i^{scale}\left[\left(n_i^I(t) + C_i^{LOS}\right).\text{Re}\left\{u_i(t)\right\} - n_i^Q(t).\text{Im}\left\{u_i(t)\right\}\right] \tag{2.50}$$

and:

$$\text{Im}\left\{b_i(t)\right\} = C_i^{scale}\left[\left(n_i^I(t) + C_i^{LOS}\right).\text{Im}\left\{u_i(t)\right\} + n_i^Q(t).\text{Re}\left\{u_i(t)\right\}\right] \tag{2.51}$$

Once again, the constant C_i^{scale} is chosen such that the channel simulator input signal power and output signal power have the same magnitude, resulting in an expression for C_i^{scale} which is identical to *Eq.* (2.42). Furthermore, following a similar approach as in *Section* 2.6.2.2, it can be shown that the Rician factor for the complex flat fading channel simulator is also given by *Eq.* (2.44).

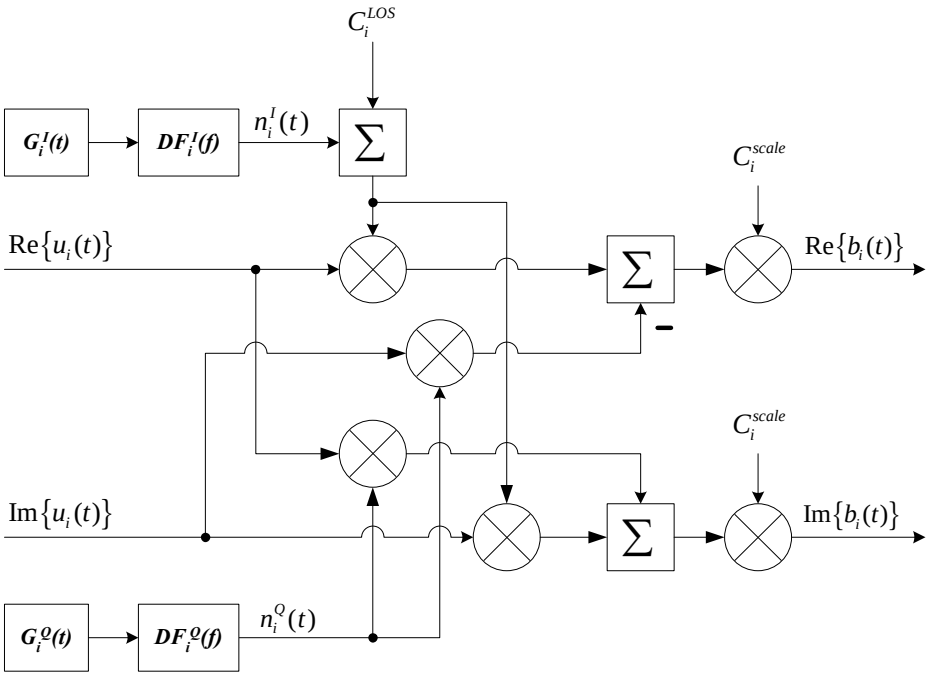

Figure 2.5: Complex Flat Fading Channel Simulator Based on *Clarke*'s Model

2.6.2.4 IMPLEMENTATION CONSIDERATIONS

2.6.2.4.1 Hilbert Transformer Realisation

Implementing the Hilbert transformer shown in *Fig.* 2.4 requires the use of a FIR filter and a delay line. The function of the FIR filter is to estimate the Hilbert transformation of the input signal in order to give the quadrature signal, whereas the delay line compensates for the FIR filter delay by the delaying the in-phase signal for a preset time period. The tap weights of a $(2F+1)$-tap Hilbert FIR filter are as follows [81]:

$$W(i) = \begin{cases} \frac{f_{samp}}{\pi . i} & \text{if } |i| \leq F, i \neq 0 \\ 0 & \text{if } i = 0 \text{ or } |i| > F \end{cases} \tag{2.52}$$

where f_{samp} is the sampling frequency used in the simulation. Note that the delay time induced by this FIR filter equals F sample periods.

2.6.2.4.2 Realisation of the Doppler Spread Spectral Shaping Filter

Assuming a maximum Doppler spread of $B_D = \max\{f_d(t)\}$ and a sampling period of T_{samp} [s], the Doppler filters used in the simulator of *Fig.* 2.4 can be approximated by using third order IIR filters with the following transfer function [38]:

$$DF(z) = C_{norm}\left[\frac{b_3 z^{-3} + b_2 z^{-2} + b_1 z^{-1} + b_0}{a_3 z^{-3} + a_2 z^{-2} + a_1 z^{-1} + a_0}\right] \tag{2.53}$$

where:

$$\begin{aligned}
b_0 &= b_3 = (2\pi B_D.T_{samp})^3 \\
b_1 &= b_2 = 3\,(2\pi B_D.T_{samp})^3 \\
a_0 &= 8 + 4A_{DF}.2\pi B_D.T_{samp} + 2B_{DF}\,(2\pi B_D.T_{samp})^2 + C_{DF}\,(2\pi B_D.T_{samp})^3 \\
a_1 &= -24 - 4A_{DF}.2\pi B_D.T_{samp} + 2B_{DF}\,(2\pi B_D.T_{samp})^2 + 3C_{DF}\,(2\pi B_D.T_{samp})^3 \\
a_2 &= 24 - 4A_{DF}.2\pi B_D.T_{samp} - 2B_{DF}\,(2\pi B_D.T_{samp})^2 + 3C_{DF}\,(2\pi B_D.T_{samp})^3 \\
a_3 &= -8 + 4A_{DF}.2\pi B_D.T_{samp} - 2B_{DF}\,(2\pi B_D.T_{samp})^2 + C_{DF}\,(2\pi B_D.T_{samp})^3
\end{aligned} \tag{2.54}$$

with:

$$\begin{aligned}
A_{DF} &= 1.55 \\
B_{DF} &= 1.090625 \\
C_{DF} &= 0.9953125
\end{aligned} \tag{2.55}$$

The variable C_{norm} is a constant scaling factor, dependent on the input signal's power, that ensures unity power in the filter output signal. *Fig.* 2.6 shows the frequency response of $DF(z)/C_{norm}$. Note that the frequency axis is normalised with respect to B_D.

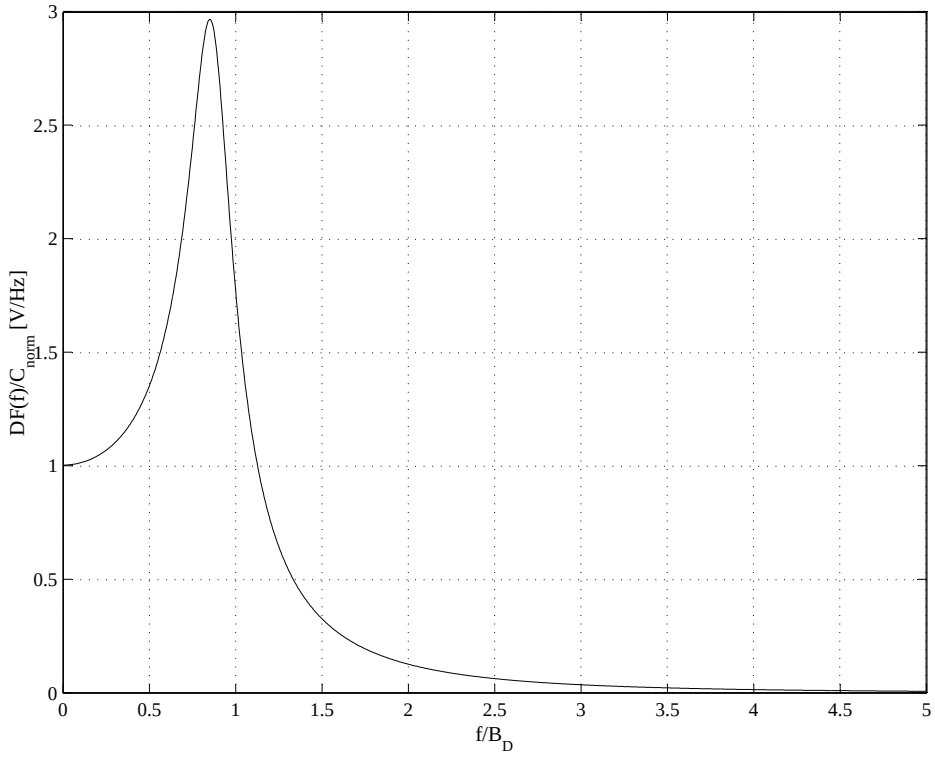

Figure 2.6: Frequency Response of the 3rd Order Doppler IIR Filter

Comparing the baseband frequency response of *Fig.* 2.6 with the required classic Doppler spectrum depicted in *Fig.* 2.1, it can be concluded that, due to the high spectral content in its tail end ($f > B_D$), the use of the proposed Doppler filter will result in more severe Doppler spread being produced by the simulator than by the mathematical model. Although higher order IIR Doppler filters will reduce this deviation from the mathematical model, the increased simulator complexity does not justify the improvement in the simulator's performance.

2.6.2.5 *OBTAINING CHANNEL STATE INFORMATION FROM THE CLARKE FLAT FADING CHANNEL SIMULATOR*

Perfect CSI, i.e. perfect fading amplitude and channel phase information, are easily obtainable from the *Flat Fading Channel Simulator*s (FFCS) shown in *Fig.* 2.4 and *Fig.* 2.5, respectively. The instantaneous fading amplitude of the i^{th} multipath component of a multipath fading channel employing such flat fading simulators, is calculated as follows:

$$\alpha_i(t) = \frac{\beta_i(t)}{\overline{\beta}_i} = \sqrt{\frac{\left(n_i^I(t) + C_i^{LOS}\right)^2 + n_i^Q(t)^2}{2 + \left(C_i^{LOS}\right)^2}} \tag{2.56}$$

where $\beta_i(t)$ and β_i are the instantaneous and average amplitude alterations experienced by the i^{th} multipath component, respectively. Calculation of the instantaneous phase change experienced by the i^{th} multipath component is accomplished as follows:

$$\phi_i(t) = -\arctan\left(\frac{n_i^Q(t)}{n_i^I(t) + C_i^{LOS}}\right) \tag{2.57}$$

Perfect, or near perfect knowledge of $\phi_i(t)$ is essential not only for coherent demodulation [86], but also for bit, frame and spreading sequence synchronisation. Estimation of the fading amplitude $\alpha_i(t)$ is required by channel coded systems employing CSI during decoder metric calculations. For example, the optimal operation of the iterative decoder structures associated with parallel, serial and hybrid concatenated codes [28, 30–33, 87], are dependent on accurate knowledge of $\alpha_i(t)$. Therefore, the use of CSI estimators in the receiver structures of modern communication systems, employing such concatenated codes, is indispensable. Refer to *Section* 3.3.5 for more information on practical CSI estimation techniques.

2.6.3 EMPLOYING CLARKE'S MODEL IN MULTIPATH FADING CHANNEL SIMULATORS

2.6.3.1 *CLASSIC MULTIPATH FADING CHANNEL SIMULATOR*

A frequency selective fading channel can be simulated using the general *Multipath Fading Channel Simulator* (MFCS) structure shown in *Fig.* 2.7 [39, 42, 44]. This simulator is capable of simulating a time-invariant multipath fading channel, consisting of L discrete and independently faded multipath components.

The simulator functions as follows: Firstly, an appropriate L-path power delay profile is chosen. L time-delayed versions of the transmitted signal are then created by using a L-tap delay line with delay times equal to that of the required power delay profile. Next, the time delayed signal $a_i(t)$, with $i = 1, 2, ..., L$, is scaled by the factor $\overline{\beta}_i$, which represents the average amplitude of the i^{th} multipath component, as specified by the power delay profile. These delayed and scaled signals are then processed by L unique FFCSs (denoted by blocks $Classic\,FFCS_1$ to $Classic\,FFCS_L$), such as the one shown in *Fig.* 2.4. Thus, it is possible to define a unique maximum Doppler frequency and Rician factor for each multipath component. The resultant outputs of the flat fading channel simulators, denoted by $b_i(t)$, with $i = 1, 2, 3, ..., L$, are then linearly combined to give the frequency selective fading channel's simulator output signal $r(t)$.

It is important to note that the power of the multi-path fading channel simulator's output signal $r(t)$ must equal the power of the transmitted signal $s(t)$. Since the L propagation paths undergo statisti-

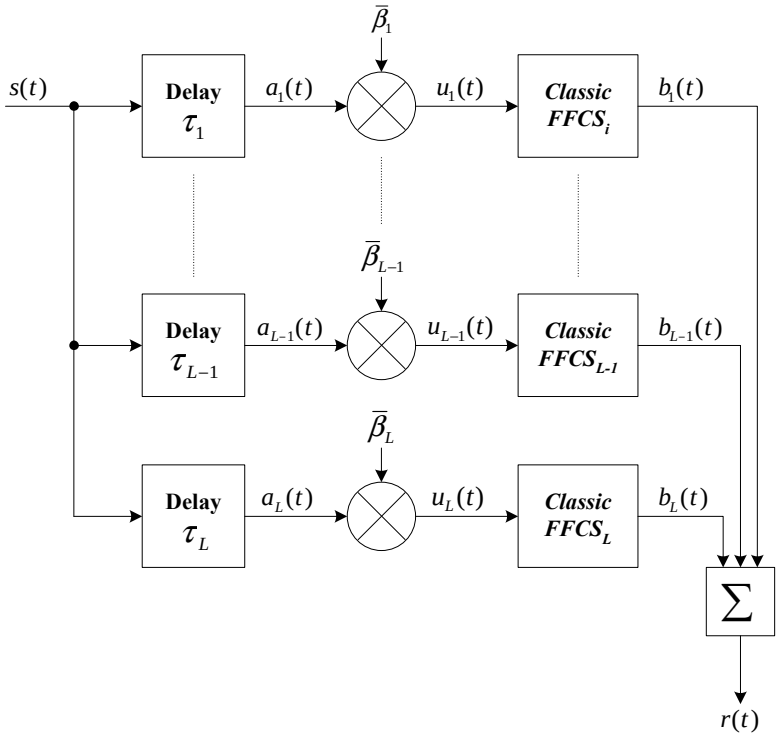

Figure 2.7: Classic Multipath Fading Channel Simulator

cally independent flat fading, it follows that the scaling factors $\overline{\beta}_i$, with $i = 1, 2, ..., L$, must conform to the following condition [86]:

$$\sum_{i=1}^{L} \left(\overline{\beta}_i\right)^2 = 1 \tag{2.58}$$

2.6.3.2 COMPLEX MULTIPATH FADING CHANNEL SIMULATOR

Fig. 2.8 shows an L-path complex multipath fading channel simulator, constructed using L distinct complex FFCSs (see *Section* 2.6.2.3), denoted by blocks $Complex\,FFCS_1$ to $Complex\,FFCS_L$. Aside from the fact that the complex multipath fading channel simulator processes complex input signals, it functions in a similar fashion as the classic implementation, described in *Section* 2.6.3.1. Furthermore, the average path gains $\overline{\beta}_i$, for $i = 1, 2, ..., L$, also need to comply with *Eq.* (2.58) in order to preserve equality between simulator input and output powers.

2.6.3.3 EXPONENTIAL DECAY MODELLING OF POWER DELAY PROFILES

Most measured outdoor power delay profiles appear to exhibit exponential decay profiles with superimposed spikes. As such, the use of exponential decay power delay profile models are used extensively when simulating the performance of digital communication systems in multipath fading channel conditions [42, 44]. An exponential decay power delay profile model is defined as follows:

$$P(\tau) = \frac{1}{P_{tot}} \exp\left(-\frac{\tau}{\tau_e}\right) \tag{2.59}$$

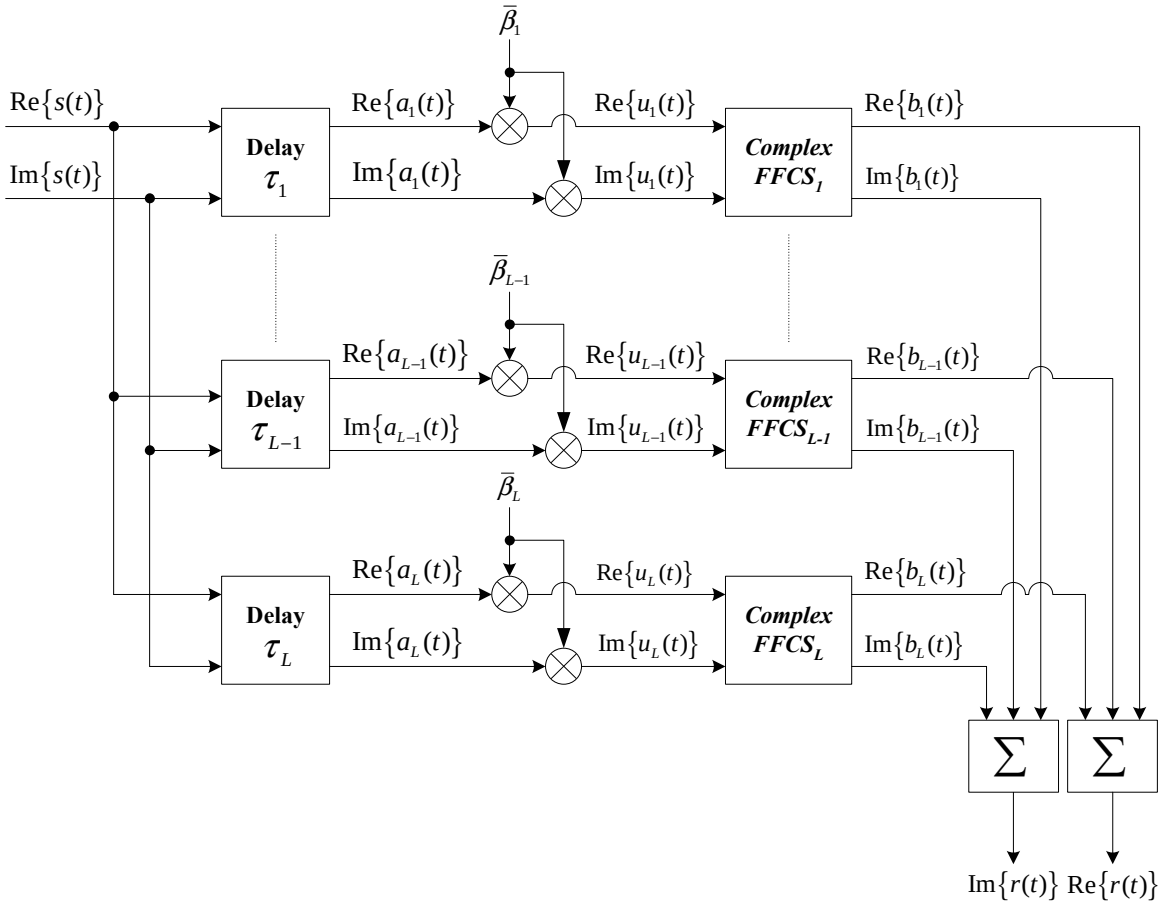

Figure 2.8: Complex Multipath Fading Channel Simulator

where P_{tot} is a normalisation factor and τ_e is the time constant of the profile. In order to comply with *Eq.* (2.58), the normalisation factor is calculated as follows:

$$P_{tot} = \sum_{i=1}^{L} P(\tau_i) = \sum_{i=1}^{L} \left(\overline{\beta}_i\right)^2 \tag{2.60}$$

Calculation of τ_e is dependent both on the maximum excess delay τ_{max} and the relative power drop between $P(\tau_{max})$ and $P(0)$, denoted by $P_{drop} = 10\log_{10}\left[P(\tau_{max})/P(0)\right]$ [dB]:

$$\tau_e = -\frac{\tau_{\max}}{\ln\left(10^{\frac{P_{drop}}{10}}\right)} \tag{2.61}$$

Recall from *Section* 2.4.3.1 that a typical value for P_{drop} is -30 dB.

2.7 CONCLUDING REMARKS

This chapter focused on the characterisation and statistical reproduction of realistic mobile communication channels, concentrating specifically on multipath fading channels. The chapter contains discussions on all aspects of AWGN, flat fading and frequency selective fading channel effects. Novel contributions made in this chapter are the following:

1. The erroneous Doppler spectral shaping IIR lowpass filter presented in [38] has been corrected. The improved filter is presented in *Section* 2.6.2.4.2.

2. A complex flat fading channel simulator model, extended from the classic *Clarke* model, is presented in *Section* 2.6.2.3. This model not only eliminates the use of Hilbert transformers, but also gives the communication engineer the capability to perform baseband flat fading channel simulations.

3. Extraction of CSI parameters from classic and complex flat fading channel simulators are addressed in *Section* 2.6.2.5.

4. An L-path complex multipath fading channel simulator, comprising of L unique complex flat fading channel simulators, is presented in *Section* 2.6.3.2. This model enables the communications engineer to conduct baseband frequency selective fading simulations.

5. A simple approach whereby realistic exponential decay power profiles can be created, is presented in *Section* 2.6.3.3.

CHAPTER THREE

BUILDING BLOCKS OF CLASSIC CODING SCHEMES

3.1 CHAPTER OVERVIEW

CLASSIC block and convolutional coding scheme encoder building blocks are the focus of the first part of this chapter. Topics covered include the mathematical descriptions and definitions of several important characterisation parameters for binary convolutional codes, binary and non-binary linear block codes, interleavers and code puncturers. Both FIR and IIR type binary convolutional codes are investigated. Classic binary linear block code families described in this chapter include Hamming and BCH linear block codes, whereas RS block codes are considered in the discussion on non-binary linear block codes.

The second part of this chapter revolves around the decoder building blocks encountered in classic block and convolutional coding schemes. Since the basic ML and MAP decoder structures and algorithms, associated with classic block and convolutional codes, are readily available in the literature, such algorithms are not described in detail in this study. However, attention is given to the construction of binary convolutional code trellises. The remainder of this part of the chapter details the inner workings of de-interleavers and code de-puncturers. The chapter is concluded with a short discussion on the concept of CSI estimation, as well as several valuable references to interesting CSI estimation techniques.

3.2 ENCODER BUILDING BLOCKS

3.2.1 BINARY CONVOLUTIONAL CODES

This subsection is concerned with the basic theory of binary convolutional codes. Following a concise mathematical description of convolutional codes, attention is given to the FIR NSC and IIR RSC classes of convolutional codes.

3.2.1.1 MATHEMATICAL DESCRIPTION OF BINARY CONVOLUTIONAL CODES

A rate $R_c = k/n$ binary convolutional code encoder is essentially a finite state linear device, consisting of k separate shift registers (one for each input bit), that accepts k-tupple binary inputs and

generates n-tupple binary outputs [87]. The linearity property of such an encoder refers to the fact that a linear combination, in Galois field $GF(2)$, of a set of binary data blocks, used as input, results in a linear combination, in $GF(2)$, of the binary output code blocks, generated for each of the input blocks [47].

When describing convolutional codes, it is convenient to relate the encoder output to the encoder input by means of a generator matrix $G_{CC}(D)$ [87]: Let the i^{th} length-k sequence contained within the m^{th} vector of input bits into the encoder, and the i^{th} length-n sequence contained within the m^{th} vector of output bits out of the encoder, be denoted by $\overline{d}_{m,i} = \{d_{m,i,0}, d_{m,i,1}, ..., d_{m,i,k-1}\}$ and $\overline{c}_{m,i} = \{c_{m,i,0}, c_{m,i,1}, ..., c_{m,i,n-1}\}$, respectively. Using the D-transform [87], the stream of encoder inputs can be represented by the k-dimensional vector sequence $\overline{d}_m(D)$, given by:

$$\overline{d}_m(D) = \sum_i \overline{d}_{m,i} D^i \tag{3.1}$$

where D represents a single delay period of T_b [s]. Likewise, the stream of encoder outputs can be represented by the n-dimensional vector sequence $\overline{c}_m(D)$, given by:

$$\overline{c}_m(D) = \sum_i \overline{c}_{m,i} D^i \tag{3.2}$$

The generator matrix $G_{CC}(D)$ of the encoder is then the $k \times n$ matrix that satisfies the following relationship [87]:

$$\overline{c}_m(D) = \overline{d}_m(D).G_{CC}(D) \tag{3.3}$$

where the multiplication is carried out over $GF(2)$. In general, the form of the generator matrix is as follows [87]:

$$G_{CC}(D) = \begin{bmatrix} g_{0,0}(D) & g_{0,1}(D) & \dots & g_{0,n-1}(D) \\ g_{1,0}(D) & g_{1,1}(D) & \dots & g_{1,n-1}(D) \\ \vdots & \vdots & \ddots & \vdots \\ g_{k-1,1}(D) & g_{k-1,1}(D) & \dots & g_{k-1,n-1}(D) \end{bmatrix} \tag{3.4}$$

where $g_{a,b}(D)$ is the generator polynomial describing the positions of the a^{th} input bit's shift register that must be linearly combined in $GF(2)$ to contribute to the b^{th} output bit.

Directly related to the generator matrix of a convolutional code, is its parity check matrix $H_{CC}(D)$. It is defined as an $(n-k) \times n$ matrix that, for an arbitrary code word vector sequence $\overline{c}_m(D)$, generated using the encoder's generator matrix $G_{CC}(D)$, satisfies the condition $\overline{c}_m(D).H_{CC}^T(D) = \overline{0}$ in $GF(2)$ [47], with $H_{CC}^T(D)$ the transpose of $H_{CC}(D)$.

Convolutional code encoders are classified as FIR or IIR type encoders [87]. The aforemention class of binary convolutional code encoders generate their outputs using only linear combinations of current and previous inputs. Thus, the generator polynomials of FIR type convolutional codes has the general form [87]:

$$g_{a,b}(D) = \sum_{j=0}^{\upsilon_a - 1} g_{a,b,j} D^j \tag{3.5}$$

where υ_a represents the total number of memory elements in the shift register used in conjunction with the a^{th} message word bit in $\overline{d}_{m,i}$. The variable $g_{a,b,j}$, which can take on values from the alphabet $\{0, 1\}$, indicates the presence or absence of a tap connecting the j^{th} memory element of the a^{th} shift register to the b^{th} output.

In the case of IIR type convolutional code encoders, not only is the current and previous inputs used to generate the current outputs, but also previous outputs. As such, the generator polynomials of IIR convolutional code encoders are rational functions in D [87].

3.2.1.2 IMPORTANT BINARY CONVOLUTIONAL CODE PARAMETERS AND DEFINITIONS

The following parameters and definitions are vital to the understanding of convolutional codes and their encoders:

1. **Hamming Distance:** The Hamming distance (see *Eq.* (4.29) in *Section* 4.4.2.1) between two separate encoder output vector sequences, $\overline{c}_m^1(D)$ and $\overline{c}_m^2(D)$, which is denoted by $d_H\left(\overline{c}_m^1(D), \overline{c}_m^2(D)\right)$, is defined as the number of bit positions in which they differ [47].

2. **Hamming Weight:** The Hamming weight $w_H\left(\overline{c}_m(D)\right)$ of an encoder vector output sequence $\overline{c}_m(D)$ is defined as the Hamming distance between $\overline{c}_m(D)$ and the all-zero vector sequence $\overline{0}$, i.e. $w_H\left(\overline{c}_m(D)\right) \triangleq d_H\left(\overline{c}_m(D), \overline{0}\right)$ [47].

3. **Constraint Length:** The constraint length of a rate $R_c = k/n$ convolutional code encoder is the number of delay elements used in its realisation. If the number of delay elements employed in the a^{th} input's shift register is denoted by υ_a, the constraint length of the encoder is given by [87]:

$$\upsilon = \sum_{a=0}^{k-1} \upsilon_a \tag{3.6}$$

   This parameter is the most important measure of the convolutional code's trellis complexity, since the number of states in the trellis of a binary convolutional code, with a constraint length of υ, is 2^{υ} (see *Section* 3.3.1.1).

4. **Minimal Encoders:** On closer inspection, it should be apparent that there might exist several encoder structures, each with its own memory (shift register) and tap configuration that might satisfy *Eq.* (3.3). However, it can be shown that there exists a subset of encoders, having identical state diagrams [47], which utilises a minimum number of memory elements to generate the convolutional code. Such encoders are called *minimal encoders* [87]. All the convolutional code encoders considered in this study are minimal encoders.

5. **Non-systematic Encoders:** At a certain encoding instance i of the m^{th} encoder input vector, the encoder input data stream of a non-systematic convolutional code do not form a substream of the encoder output data stream [87]. Thus, the encoder outputs bits consist solely of parity bits, i.e. $c_{m,i,a} = \text{v}_{m,i,a}$ for $a = 0, 1, ..., n-1$.

6. **Systematic Encoders:** A systematic convolutional code is one for which, at a certain encoding instance i of the m^{th} encoder input vector, the encoder input data stream forms a substream of the encoder output data stream [87]. The convention used throughout this study is that encoder output bits 0 to $k-1$ are the systematic bits, i.e. $c_{m,i,a} = d_{m,i,a}$ for $a = 0, 1, ..., k-1$, and outputs bits k to $n-1$ are the parity bits, i.e. $c_{m,i,a} = \text{v}_{m,i,a}$ for $a = k, k+1, ..., n-1$.

7. **Minimum Free Distance:** The minimum free distance d_{free} of a binary convolutional code is defined as [47]:

$$d_{free} \triangleq \min_{d_m^1(D) \neq d_m^2(D)} d_H\left(\overline{c}_m^1(D), \overline{c}_m^2(D)\right) \tag{3.7}$$

   where $\overline{c}_m^1(D) = \overline{d}_m^1(D).G_{CC}(D)$ and $\overline{c}_m^2(D) = \overline{d}_m^2(D).G_{CC}(D)$ in $GF(2)$. Essentially, d_{free} is a measure of how good a convolutional code is: The larger d_{free}, the better a code's performance,

i.e. more code bits must be in error in order for one code word to be mistaken for another by the decoder. Determining the structure of an optimal convolutional code encoder with a preset code rate and number of states in its trellis, involves an exhaustive search through all possible minimal encoders capable of generating the code, finally selecting the code with the largest d_{free}. Although not of crucial importance to this study, it is worth mentioning that d_{free} can be determined effortlessly from the code's *transfer function*, which in turn is determined from the encoder's *state diagram* [47].

8. **Asymptotic Coding Gain in AWGN Channel Conditions:** The asymptotic coding gain for binary convolutional codes, operating in AWGN channel conditions, decoded using soft decision ML decoding and employing QPSK modulation with coherent demodulation, is upper bounded as follows [47]:

$$CG_{CC}^{soft} \leq 10\log_{10}(R_c.d_{free}) \qquad \text{[dB]} \tag{3.8}$$

If hard decision decoding is employed, a 2 dB degradation in BER performance can be expected when compared to soft decision decoding, resulting in the following upper bound [47]:

$$CG_{CC}^{hard} \leq 10\log_{10}(R_c.d_{free}) - 2 \qquad \text{[dB]} \tag{3.9}$$

3.2.1.3 TYPES OF BINARY CONVOLUTIONAL CODES

Discussed in the following subsections are the two main types of binary convolutional codes, namely NSC and RSC codes. Although only NSC codes are used in classic coding schemes employing convolutional codes (due to the fact that RSC codes exhibit inferior BER performances at low values of E_b/N_0 when compared to NSC codes), both classes have found application as CCs in recently proposed iteratively decoded concatenated coding schemes.

3.2.1.3.1 Finite Impulse Response Non-Systematic Convolutional Codes

Although both IIR and FIR NSC codes can be constructed, FIR type NSC codes have proven to be a more attractive solution in classic convolutional coded systems, as well as recent *Serial Concatenated Convolutional Code* (SCCC) schemes [27,29]. As such, this study only concerns itself with FIR NSC codes.

Tables with the generator polynomials of the most optimal binary convolutional code encoders, along with their associated d_{free} values, have been extensively documented in the literature. As an example, *Fig.* 3.1 shows the encoder structure of a minimal 8-state, rate $R_c = 1/2$, $\upsilon = 3$, FIR NSC code, taken from [47]. Using the generator matrix encoder description method detailed in *Section* 3.2.1.1, the generator matrix defining this encoder is:

$$G_{CC}(D) = \begin{bmatrix} 1 + D + D^3 & 1 + D + D^2 + D^3 \end{bmatrix} \tag{3.10}$$

It has been shown [47] that the NSC code generated by this generator matrix has a free distance of $d_{free} = 6$. This specific NSC code is used extensively in the simulations detailed in *Chapter* 6.

3.2.1.3.2 Recursive Systematic Convolutional Codes

The importance for the constituent encoders of *Parallel Concatenated Convolutional Code* (PCCC) encoding schemes to be both systematic for decoding simplicity, and recursive in order to maximise the *interleaver gain*, is now well recognised in the literature [19, 88]. As such, a class of systematic IIR codes have been proposed [89] for the building blocks of PCCC encoders. These codes are com-

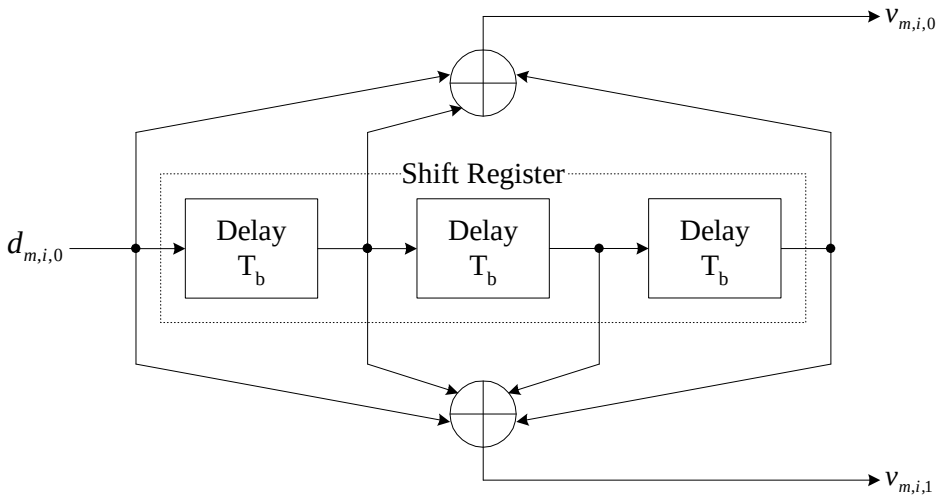

Figure 3.1: Optimal 8-State, Rate $R_c = 1/2$ NSC Code Encoder

monly referred to as RSC codes.

The RSC CC encoders used in a PCCC coding scheme need not be identical with regard to their constraint lengths or rates. When designing a PCCC encoder, the goal is to choose the best component codes by maximising the effective free distance [90] of the PCCC. At large values of E_b/N_0, this is tantamount to maximising the minimum weight code word [91, 92]. However, at low values of E_b/N_0 (the region of greatest interest) optimising the weight distribution of the code words is more important than maximising the minimum weight [91].

Listed in *Appendix A* are the encoder parameters of one of the most extensive sets of optimal RSC encoders, as determined by *Benedetto*, *Garello* and *Montorsi* through exhaustive searches [88]. Also specified for each of the encoders listed, is the minimum free distance d_{free}. The construction of the optimal 8-state, $\upsilon = 3$, rate $R_c = 2/3$ RSC encoder (see *Fig.* A.2) in *Section* A.3 illustrates how the listed encoder parameters are interpreted. The generator matrix of this encoder, which is employed in several of the simulations discussed in *Chapter* 6, is given by:

$$G_{CC}(D) = \begin{bmatrix} 1 & 0 & \frac{1+D^2+D^3}{1+D+D^3} \\ 0 & 1 & \frac{1+D+D^2}{1+D+D^3} \end{bmatrix} \tag{3.11}$$

According to *Table* A.5, the minimum free distance of this code is $d_{free} = 4$.

Another example of an RSC code encoder is shown in *Fig.* 3.2. In this figure, the encoder structure for an optimal 8-state, $\upsilon = 3$, rate $R_c = 1/2$ RSC code is depicted. From *Table* A.3 in *Appendix A* it follows that this code has a minimum free distance of $d_{free} = 6$ and is defined by the following generator matrix:

$$G_{CC}(D) = \begin{bmatrix} 1 & \frac{1+D+D^2+D^3}{1+D^2+D^3} \end{bmatrix} \tag{3.12}$$

3.2.2 LINEAR BLOCK CODES

The focus of this subsection falls on linear block codes. Following a concise mathematical description of general linear block codes, a number of important linear block code definitions and parameters are explained. A short description of the characteristics of binary Hamming, binary BCH and non-binary

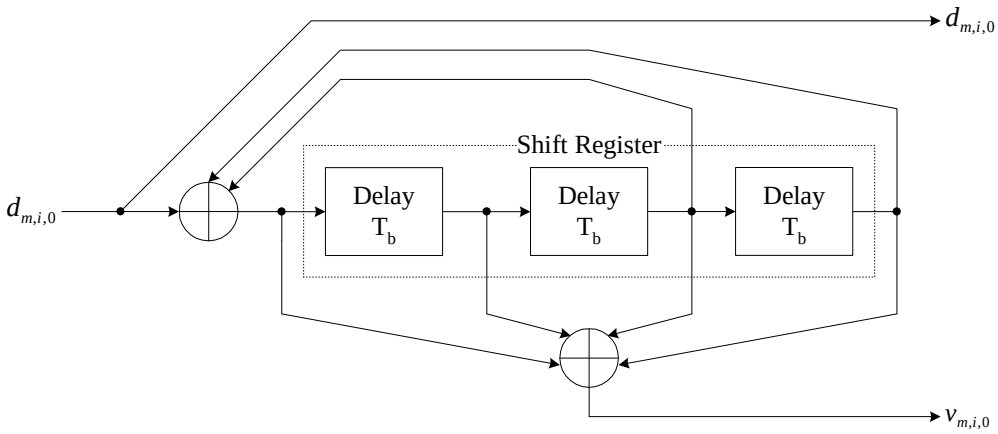

Figure 3.2: Optimal 8-State, Rate $R_c = 1/2$ RSC Code Encoder

RS block codes conclude the subsection.

3.2.2.1 MATHEMATICAL DESCRIPTION OF LINEAR BLOCK CODES

Consider an (n, k, d_{min}) linear block code with message and code word symbols from $GF\left(2^{\xi}\right)$. This code has $2^{\xi.k}$ unique n-symbol code words and a minimum Hamming distance (see *Section* 3.2.2.2) of d_{min} [symbols]. Suppose, at encoding instance m, the n-symbol code word vector $\overline{c}_m = \{c_{m,0}, c_{m,1}, c_{m,2}, ..., c_{m,n-1}\}$ is the output produced by the linear block code encoder, given the k-symbol input message word $\overline{d}_m = \{d_{m,0}, d_{m,1}, d_{m,2}, ..., d_{m,k-1}\}$. The encoding process performed by the linear block code encoder can be described by means of a set of n linear equations [47, 93, 94]:

$$c_{m,j} = d_{m,0}.g^e_{0,j} + d_{m,1}.g^e_{1,j} + ... + d_{m,k-1}.g^e_{k-1,j} \qquad \text{for } j = 0, 1, ..., n-1 \tag{3.13}$$

where the variables $g^e_{i,j}$, with $i = 0, 1, ..., k-1$ and $j = 0, 1, ..., n-1$, dictate the one-to-one relationship, specific to the type of linear block code and the code constraints, between $\overline{c}_m$ and $\overline{d}_m$. These variables can only take on values from $GF\left(2^{\xi}\right)$. Furthermore, the multiplication and addition operations of *Eq.* (3.13) and all subsequent equations are also performed in $GF\left(2^{\xi}\right)$. A more convenient method that can used to describe the encoding process, is as follows [47, 93, 94]:

$$\overline{c}_m = \overline{x}_m.G_{BC} \tag{3.14}$$

where G_{BC}, commonly referred to as the generator matrix of the block code, is a rank k size $k \times n$ matrix, given by:

$$G_{BC} = \begin{bmatrix} g^e_{0,0} & g^e_{0,1} & \cdots & g^e_{0,n-1} \\ g^e_{1,0} & g^e_{1,1} & \cdots & g^e_{1,n-1} \\ \vdots & \vdots & \ddots & \vdots \\ g^e_{k-1,0} & g^e_{k-1,1} & \cdots & g^e_{k-1,n-1} \end{bmatrix} \tag{3.15}$$

The linearity characteristic of a linear block code refers to the fact that the $GF\left(2^{\xi}\right)$ linear combination of two distinct code words $\overline{c}^1_m$ and $\overline{c}^2_m$, generated by G_{BC} for the respective message words $\overline{d}^1_m$ and $\overline{d}^2_m$, is equal to the encoder output code word $\overline{c}^3_m$ for the input message word $\overline{d}^3_m = \overline{d}^1_m + \overline{d}^2_m$. Thus, any of the $2^{\xi.k}$ code words in the linear block code can be constructed by linearly combining several of the other code words in $GF\left(2^{\xi}\right)$ [47, 93, 94].

Closely related to the generator matrix G_{BC}, is a linear block code's $(n-k) \times n$ parity check matrix H_{BC}, defined by the following relationship [47, 93, 94]:

$$G_{BC}.H_{BC}^{T} = \overline{0} \tag{3.16}$$

where $\overline{0}$ denotes an all-zero $k \times (n-k)$ matrix and H_{BC}^{T} is the transpose of H_{BC}. With the linearity property in mind, it can be shown that all of the $2^{\xi \cdot k}$ code words in the linear block code is orthogonal to every row of the parity check matrix H_{BC}. As such, the parity check matrix is used extensively in algebraic linear block code decoding techniques [47, 93, 94], such as syndrome decoding, in order to isolate and possibly correct errors in corrupted code words.

3.2.2.2 IMPORTANT LINEAR BLOCK CODE PARAMETERS AND DEFINITIONS

Several parameters and definitions that are crucial for the understanding and characterisation of linear block codes are listed below. Since these parameters and definitions are valid for both binary and non-binary linear codes, all addition and multiplication operations present in this discussion are carried out in the Galois field over which the linear block code is defined.

1. **Hamming Distance:** Identical to the definition given for binary convolutional codes in *Section* 3.2.1.2, the Hamming distance between two block code encoder output code words $\overline{c}_m^1$ and $\overline{c}_m^2$, denoted by $d_H\left(\overline{c}_m^1, \overline{c}_m^2\right)$, is defined as the number of code word symbol positions in which they differ [47, 93, 94].

2. **Minimum Hamming Distance:** Analogous to the d_{free} of a binary convolutional code (see *Section* 3.2.1.2), the minimum Hamming distance of a linear block code, denoted by d_{min}, is the most salient measure of the error detection and correction capabilities of the code. Its mathematical definition is as follows [47, 93, 94]:

$$d_{min} \triangleq \min_{d_m^1 \neq d_m^2} d_H\left(\overline{c}_m^1, \overline{c}_m^2\right) \tag{3.17}$$

   where $\overline{c}_m^1 = \overline{d}_m^1.G$ and $\overline{c}_m^2 = \overline{d}_m^2.G$. If the minimum Hamming distance of a linear block code is known, it can be shown [47, 93, 94] that the number of code word symbol errors that is detectable by the code for a single code word, is $t_{detect} = d_{min} - 1$, whereas the number of correctable code word symbol errors is $t_{correct} = \left\lfloor \frac{1}{2}\left(d_{min} - 1\right) \right\rfloor$.

3. **Hamming Weight:** The Hamming weight $w_H\left(\overline{c}_m\right)$ of a linear block code's output code word $\overline{c}_m$ is defined as the Hamming distance between $\overline{c}_m$ and the all-zero code word $\overline{0}$, i.e. $w_H\left(\overline{c}_m\right) \triangleq d_H\left(\overline{c}_m, \overline{0}\right)$ [47, 93, 94].

4. **Non-systematic Linear Block Codes:** Identical to the definition for binary non-systematic convolutional codes, the message word $\overline{d}_m$ used as input into a non-systematic linear block code encoder at timing instance m, does not form a substream of the encoder output code word $\overline{c}_m$. Thus, the encoder output code word symbols consist solely of parity symbols, i.e. $c_{m,i} = \mathrm{v}_{m,i}$ for $i = 0, 1, 2, ..., n-1$.

5. **Systematic Linear Block Codes:** An (n, k, d_{min}) linear block code is said to be systematic if the length-n encoder output code word $\overline{c}_m$, generated at encoding instance m, contains a length-k substring that is an exact replica of the k-symbol encoder input message word $\overline{d}_m$. The convention adopted throughout this study for such linear block codes, is that the first k code word symbols of $\overline{c}_m$ are the systematic symbols, i.e. $c_{m,i} = d_{m,i}$ for $i = 0, 1, 2, ..., k-1$, and the last $n-k$ code word symbols are the parity symbols added by the encoder, i.e. $c_{m,i} = \mathrm{v}_{m,i}$ for $i = k, k+1, ..., n-1$.

Hence, the generator matrix of such a systematic linear block code has the following general form [47, 93, 94]:

$$G_{BC} = [I_k|P] = \left[\begin{array}{cccc|cccc} 1 & 0 & \dots & 0 & P^s_{0,0} & P^s_{0,1} & \dots & P^s_{0,n-k-1} \\ 0 & 1 & \dots & 0 & P^s_{1,0} & P^s_{1,1} & \dots & P^s_{1,n-k-1} \\ \vdots & \vdots & \ddots & \vdots & \vdots & \vdots & \ddots & \vdots \\ 0 & 0 & \dots & 1 & P^s_{k-1,0} & P^s_{k-1,1} & \dots & P^s_{k-1,n-k-1} \end{array}\right] \tag{3.18}$$

where I_k is the $k \times k$ identity matrix and P^s is a $k \times (n-k)$ matrix that determines the $n-k$ parity symbols added to each code word during encoding. An important characteristic of linear block codes, is that any non-systematic generator matrix, given by *Eq.* (3.15), can be reduced to the systematic form of *Eq.* (3.18) by means of a number of row operations and column permutations [47] (using Gaussian elimination is a popular approach).

Recalling that addition and subtraction are equivalent in $GF(2)$, it can be shown that the parity check matrix of a binary linear systematic block code is easily determined as follows [47, 93, 94]:

$$H_{BC} = \left[(P^s)^T | I_{n-k}\right] \tag{3.19}$$

where $(P^s)^T$ represents the transpose of P^s and I_{n-k} the $(n-k) \times (n-k)$ identity matrix.

6. **Weight Enumerating Function:** The *Weight Enumerating Function* (WEF) of an (n, k, d_{min}) linear block code is a compact method to describe its weight distribution. It is defined as follows [47, 93, 94]:

$$A(Z) = \sum_{w=0}^{n} A_w Z^w \tag{3.20}$$

where A_w is the number of code words in the block code that has a Hamming weight of w. The WEF can be used to compute the exact expression of the probability of undetected errors, as well as upper bounds on the word error probability.

7. **Input-Output Weight Enumerating Function:** The *Input-Output Weight Enumerating Function* (IOWEF) of an (n, k, d_{min}) linear block code, also sometimes referred to as the input-redundancy weight enumerating function, splits each term in the WEF into the separate contributions of the parity and message word symbols to the total Hamming weight of each code word. It is defined as follows [27, 63, 66, 87]:

$$A(W, Z) = \sum_{w=0}^{k} \sum_{h=0}^{n} A_{w,h} W^w Z^h \tag{3.21}$$

where $A_{w,h}$ is the number of code words in the block code that has a Hamming weight of h, generated by message words with a Hamming weight of w.

8. **Cyclic Linear Block Codes and Their Generator Polynomials:** Cyclic linear block codes have the property that all possible cyclic shifts of the elements of one code word results in another valid code word [47, 93, 94]. When describing these block codes, it is convenient to express a message word $\overline{d}_m = \{d_{m,0}, d_{m,1}, ..., d_{m,k-1}\}$ and its associate code word $\overline{c}_m = \{c_{m,0}, c_{m,1}, ..., c_{m,n-1}\}$ in terms of a degree $k-1$ message polynomial $d_m(p) = d_{m,k-1}.p^{k-1} + d_{m,k-2}.p^{k-2} + ... + d_{m,0}$ and a degree $n-1$ code word polynomial $c_m(p) = c_{m,n-1}.p^{n-1} + c_{m,n-2}.p^{n-2} + ... + c_{m,0}$, respectively. Using this notation, the cyclic nature of the code can be easily verified: If $\overline{c}^1_m$ is a code word from the cyclic linear block code, $\overline{c}^2_m$ will also be a valid code word, given that the

following condition is satisfied [47, 93, 94]:

$$\overline{c}_m^2 = p^i.\overline{c}_m^1 \mod (p^n + 1) \tag{3.22}$$

where i can take on any integer value.

Generation of the code word polynomial $c_m(p)$, given the message polynomial $d_m(p)$, can be described using a degree $n-k$ generator polynomial $g_{BC}(p) = g_{n-k}^c.p^{n-k} + g_{n-k-1}^c.p^{n-k-1} + ... + g_0^c$. The encoding process is as follows:

1. *Non-systematic Encoding* - If a cyclic linear block code has to generate non-systematic code words, the encoding process of message polynomial $d_m(p)$ to code word polynomial $c_m(p)$ is as follows [47]:
$$c_m(p) = d_m(p).g_{BC}(p) \tag{3.23}$$
2. *Systematic Encoding* - The systematic encoding of a message polynomial $d_m(p)$ by a cyclic linear block code encoder to give the code word polynomial $c_m(p)$, entails the following [47]:
   (a) Multiply the message polynomial $d_m(p)$ by p^{n-k}.
   (b) Obtain the remainder polynomial $r_m(p)$ from the division of $p^{n-k}.x_m(p)$ by $g_{BC}(p)$.
   (c) Construct the systematic code word polynomial as follows:
$$c_m(p) = p^{n-k}.d_m(p) + r_m(p) \tag{3.24}$$

The construction of a non-systematic generator matrix G_{BC} (see *Section* 3.2.2.1) for a cyclic linear block code from its generator polynomial, is easily accomplished by firstly setting $g_{i,(n-k-j+i)}^e = g_j^c$ for $i = 0, 1, ..., k-1$ and $j = 0, 1, 2, ..., n-k$. All the remaining elements of G_{BC} are then set to zero [47].

9. **Coding Gain in AWGN Channel Conditions:** The coding gain of an (n, k, d_{min}) linear block code, operating in AWGN channel conditions, decoded using soft decision ML decoding and employing QPSK modulation with coherent demodulation, is upper bounded as follows [47]:
$$CG_{BC}^{soft} \leq 10\log_{10}\left(R_c.d_{min} - k.\frac{N_0}{E_b}.\ln(2)\right) \quad \text{[dB]} \tag{3.25}$$
Typically a 2 dB degradation in BER performance can be expected if hard decision decoding is employed. Hence, the following upper bound can be calculated for the hard decision decoding approach [47]:
$$CG_{BC}^{hard} \leq 10\log_{10}\left(R_c.d_{min} - k.\frac{N_0}{E_b}.\ln(2)\right) - 2 \quad \text{[dB]} \tag{3.26}$$

3.2.2.3 LINEAR BLOCK CODES OF IMPORTANCE FOR THIS STUDY

The next two subsections describe the main characteristics of binary Hamming and BCH block codes, respectively. This is then followed by a subsection that gives a brief description of non-binary RS block codes.

3.2.2.3.1 Binary Hamming Block Codes

R. W. Hamming first presented the well-known class of linear Hamming block codes in 1950 [95]. Since then, it has been shown that these single error correcting systematic or non-systematic block

codes can be classified as cyclic linear block codes (see *Section* 3.2.2.2). Although both binary and non-binary Hamming block codes can be constructed, this study is limited to the binary class of Hamming block codes, characterised by the following properties [47]:

$$(n, k, d_{min}) = (2^a - 1, 2^a - 1 - a, 3) \tag{3.27}$$

where a is a positive integer.

Another property of an $(n, k, 3)$ binary Hamming block code, frequently used in its construction, is that the n columns of its parity check matrix H_{BC} consists of all possible binary vectors with $n - k = a$ elements, except the all-zero vector.

3.2.2.3.2 Binary Bose-Chaudhuri-Hocquenghem Block Codes

BCH block codes, discovered independently by *Hocquenghem* in 1959 [96], and *Bose* and *Ray-Chaudhuri* in 1960 [97, 98], comprise of a large class of cyclic linear block codes defined over binary and non-binary symbol alphabets. Although this subsection only covers binary BCH block codes, the popular class of RS block codes, which is a subclass of non-binary BCH block codes, is briefly described in *Section* 3.2.2.3.3.

Binary BCH codes are constructed in compliance with the following code parameter restrictions: The number of code word bits per code word is given by [47]:

$$n = 2^a - 1 \tag{3.28}$$

where $a \geq 3$ is an integer value. If the number of correctable bit errors per code word is $t_{correct}$, the number of parity bits added to each message word during encoding is bounded as follows [47]:

$$n - k =\leq a.t_{correct} \tag{3.29}$$

resulting in the following minimum Hamming distance [47]:

$$d_{min} = 2.t_{correct} + 1 \tag{3.30}$$

The generator polynomial $g_{BC}(p)$ for such a binary BCH code can be constructed from the factors of $p^{2^a-1} + 1$. An extensive list of binary BCH block code generator polynomials for $2 \leq a \leq 34$ is presented in [99].

3.2.2.3.3 Non-binary Reed-Solomon Block Codes

The subclass of maximum distance non-binary BCH block codes, commonly known as RS block codes [14], is the focus of this subsection. The subsection starts by outlining a number of basic RS block code parameters and characteristics. This is then followed by a section that presents a short discussion on classic cyclic encoding.

3.2.2.3.3.1 Parameters and Characteristics of Reed-Solomon Block Codes

Consider an (n, k, d_{min}) RS block code with message and code word symbols from the extended binary Galois field $GF\left(2^{\xi}\right)$, where $\xi > 1$. Assuming that the RS block code has to correct $t_{correct}$ symbol errors, it can be characterised by the following set of parameters: The number of code word

and parity symbols per code word are given by [14, 93]:

$$n = 2^{\xi} - 1 \tag{3.31}$$

and

$$n - k = 2.t_{correct} \tag{3.32}$$

respectively. Measured in $GF\left(2^{\xi}\right)$ symbols, the minimum Hamming distance of the RS block code is [14]:

$$d_{min} = 2.t_{correct} + 1 \tag{3.33}$$

An important characteristic of RS block codes is that these codes are maximum distance codes, i.e. for a given n and k, there is no other linear block code that has a larger d_{min} than an RS code [14, 47, 93].

Since encoding takes place in $GF\left(2^{\xi}\right)$, message and code word symbols will consist of length-ξ binary streams, uniquely defined for each of the 2^{ξ} symbols in $GF\left(2^{\xi}\right)$. Thus, the total number of bits used per message and code word are $n_{bits} = n.\xi$ and $k_{bits} = k.\xi$, respectively.

3.2.2.3.3.2 Classic Encoding of Reed-Solomon Block Codes

Recall from *Section* 3.2.2.3.2 that BCH block codes are cyclic linear block codes. Consequently, an (n, k, d_{min}) RS block code, with message and code word symbols from $GF\left(2^{\xi}\right)$, is also a cyclic linear block code, which can be described by means of a degree-$(n-k)$ generator polynomial with generator coefficients from $GF\left(2^{\xi}\right)$ [93]. Assuming the RS block code can correct $t_{correct}$ symbol errors, the general form of this generator polynomial is as follows [14]:

$$g_{BC}\left(p\right) = \prod_{i=1}^{2.t_{correct}} \left(p + \varphi^{i}\right) \tag{3.34}$$

where φ is the primitive element of $GF\left(2^{\xi}\right)$. Note that this element satisfies the condition $g\left(\varphi^{i}\right) = 0$ for any integer i. For example, consider the $t_{correct} = 1$ symbol correcting RS $(7, 5, 3)$ code, operating in $GF\left(2^{3}\right)$. Since $GF\left(2^{3}\right)$ is defined by the irreducible (primitive) polynomial $g_{ip}(p) = 1 + p + p^{3}$, it follows from *Eq.* (3.34) that the generator polynomial of the RS $(7, 5, 3)$ code is the following:

$$g_{BC}\left(p\right) = \prod_{i=1}^{2} \left(p + \varphi^{i}\right) = (p + \varphi)(p + \varphi^{2}) = \varphi^{3} + \varphi^{4}p + p^{2} \tag{3.35}$$

The generator polynomial can now be used to generate either systematic or non-systematic code words, as described in *Section* 3.2.2.2.

3.2.3 INTERLEAVERS

An interleaver can be described as a simple single input, single output device that takes symbols from a fixed alphabet as input and produces an identical set of symbols at the output in an altered temporal order [87]. Thus, the basic function of an interleaver is to effectively shuffle the order of a sequence of symbols. In traditional applications, interleaving was used to ”randomise” the locations of errors caused by bursty (correlative) channels, which in turn improves the performance of classic block and convolutional coding schemes designed and optimised for non-correlative channels, such as the AWGN channel (see *Section* 2.2). With iteratively decoded concatenated coding schemes, however, interleavers are used mainly to decrease the correlation between the information encoded by the different CCs, thereby improving the distance properties of the resultant concatenated code.

3.2.3.1 MATHEMATICAL DESCRIPTION OF INTERLEAVERS

Let the m^{th} length-N sequence of symbols used as input to an interleaver π be denoted by $\overline{\mu}_m^{in} = \{\mu_{m,0}^{in}, \mu_{m,1}^{in}, ..., \mu_{m,(N-2)}^{in}, \mu_{m,(N-1)}^{in}\}$. The interleaving of $\overline{\mu}_m^{in}$ by π can be described as follows:

$$\pi\left(\overline{\mu}_m^{in}\right) = \overline{\mu}_m^{out} = \{\mu_{m,0}^{out}, \mu_{m,1}^{out}, ..., \mu_{m,(N-2)}^{out}, \mu_{m,(N-1)}^{out}\} \tag{3.36}$$

where $\overline{\mu}_m^{out}$ represents the N-symbol/sample output of the interleaver π. This output can also be written as:

$$\overline{\mu}_m^{out} = \{\mu_{m,0}^{out}, \mu_{m,1}^{out}, ..., \mu_{m,(N-2)}^{out}, \mu_{m,(N-1)}^{out}\} = \{\mu_{m,\Pi(0)}^{out}, \mu_{m,\Pi(1)}^{out}, ..., \mu_{m,\Pi(N-2)}^{out}, \mu_{m,\Pi(N-1)}^{out}\} \tag{3.37}$$

where $\Pi(i)$, with i any integer value, is a function that describes the mapping of the interleaver output time indices to interleaver input time indices. Since interleaving can be considered as a periodic re-ordering of blocks of N symbols, the function $\Pi(i)$ describes a one-to-one mapping over the integers i modulo the period N. Thus, it follows that:

$$\Pi(i) - N = \pi(i - N) \qquad \text{for all } i \tag{3.38}$$

For example, the simple $N = 3$ interleaver described in [87] is defined by the following mapping function:

$$\Pi(i) = \begin{cases} i & \text{if } i \bmod 3 = 0 \\ i - 3 & \text{if } i \bmod 3 = 1 \\ i - 6 & \text{if } i \bmod 3 = 2 \end{cases} \tag{3.39}$$

The interleaver mapping function can also be described in terms of a *fundamental permutation*, defined as follows:

$$\eth\left(\Pi\right) = \begin{pmatrix} 0 & 1 & \cdots & N-1 \\ \Pi(0) & \Pi(1) & \cdots & \Pi(N-1) \end{pmatrix} \tag{3.40}$$

For example, the fundamental permutation of the interleaver, defined by the mapping function of *Eq.* (3.39), is given by

$$\eth\left(\Pi\right) = \begin{pmatrix} 0 & 1 & 2 \\ 0 & -2 & -4 \end{pmatrix} \tag{3.41}$$

The remaining values of the interleaver mapping function, spanning all integer values of i, are obtained by combining the fundamental permutation, given by *Eq.* (3.40), and the periodicity condition, given by *Eq.* (3.38). Shown in *Table* 3.1 is the interleaver mapping function for the example interleaver of *Eq.* (3.39), calculated for $i = -1, 0, ..., 5$. To further the understanding of interleaving,

Table 3.1: Mapping of the Simple $N = 3$ Interleaver, Described by *Eq.* (3.39)

i	-1	0	1	2	3	4	5
$\Pi(i)$	-7	0	-2	-4	3	1	-1

the stream of interleaver input sequences can be represented by the N-dimensional D-transform [87] vector sequence $\overline{\mu}^{in}(D)$, given by:

$$\overline{\mu}^{in}(D) = \sum_m \overline{\mu}_m^{in} D^m \tag{3.42}$$

where D represents one interleaver delay period of N symbols. Using this representation for the interleaver input stream, the interleaver output stream can be described as follows:

$$\overline{\mu}^{out}(D) = \overline{\mu}^{in}(D) \cdot G_{\pi}(D) \tag{3.43}$$

where $G_{\pi}(D)$, referred to as the *generator matrix* of the interleaver, is an $N \times N$ non-singular matrix with the following restrictions:

1. Only one entry in each row/column can be non-zero to ensure a one-to-one mapping.
2. Non-zero entries are of the form D^i, where i is an integer.

For example, the generator matrix associated with the interleaver mapping, given by *Eq.* (3.39) and illustrated in *Table* 3.1, is as follows:

$$G_{\pi}(D) = \begin{bmatrix} 1 & 0 & 0 \\ 0 & D^1 & 0 \\ 0 & 0 & D^2 \end{bmatrix} \tag{3.44}$$

From this generator matrix it is clear that the implementation of the interleaver requires the use of delay elements. In general, such interleavers are called *convolutional interleavers*, since they are constructed using shift registers, not unlike convolutional code encoders (see *Section* 3.2.1.1). More information concerning the structure and characteristics of these interleavers can be found in [87]. Interleavers that do not require the use of delay elements are referred to as *block interleavers*. This type of interleaver is discussed in more detail in *Section* 3.2.3.3.

3.2.3.2 INTERLEAVER PARAMETERS

The following parameters are often encountered in the study and characterisation of interleavers and de-interleavers:

1. **Interleaver Delay:** The delay of an interleaver is defined as the total delay introduced into a system by first interleaving and then de-interleaving a block of N symbols [87].
2. **Interleaver Causality:** A causal interleaver has the property that all elements in $G_{\pi}(D)$ are of the form D^i, with $i \geq 0$ for elements on, or under the diagonal of $G_{\pi}(D)$, and $i \geq 1$ for elements above the diagonal [87]. Therefore, the interleaver defined by *Eq.* (3.39) is causal.
3. **Interleaver Memory:** The memory of an interleaver is defined as the minimum number of memory elements required to implement a causal version thereof [87]. It is easily calculated by summing the absolute values of the exponents of the D elements in $G_{\pi}(D)$.
4. **Interleaver Spreading Factor:** If an interleaver has the spreading factor (M_{spread}, t_{burst}), it indicates that the individual symbols in a burst of a length smaller than t_{burst} symbols at the input of the interleaver are separated into distinct blocks of a length greater than or equal to M_{spread} at the output [87].
5. **Interleaver Dispersion:** The dispersion of an interleaver can be used to study its "randomness" [87]. It is calculated by determining the number of unique *displacement vectors* of the interleaver, normalised with respect to $N \cdot (N-1)/2$. The interested reader is referred to [87] for a discussion on the calculation of interleaver displacement vectors.

3.2.3.3 BLOCK INTERLEAVER STRUCTURES

It has been shown [87] that block interleavers, i.e. interleavers with generator matrices $G_\pi(D)$ having elements with only exponents of zero, are better suited than convolutional interleavers for both classic block and iteratively decoded concatenated coding techniques. Therefore, only block interleavers are of importance for this study.

Several types of block interleaver structures are available to the communications engineer. *Appendix C* considers several popular deterministic and random block interleavers that have attracted the attention of classic block and concatenated code designers over recent years. The deterministic interleaver structures discussed comprise of classic block interleavers, *Berrou-Glavieux* interleavers and JPL interleavers, whereas the random interleavers of interest are PN generator interleavers, random number generator interleavers and s-random interleavers. A description of the *uniform interleaver* [100, 101], a probabilistic device frequently encounter in the mathematical derivation of BER performance bounds for concatenated codes, concludes the appendix.

3.2.4 CODE PUNCTURERS

The price of the performance gains obtained by employing low rate codes in communication systems, is increased transmission bandwidths and/or lower data rates. Fortunately, by using a process called *code puncturing* [102–105], it is possible to maintain most of a code's error correcting capabilities, but increase the code rate, thereby decreasing the required transmission bandwidth. Consequently, this technique allows for the use of a single code over a wide variety of code rates with negligible performance losses. As such, it has become an indispensable component in the channel coding subsystems of numerous prevalent wireless communication standards. For example, it is used extensively in the voice, data and signalling channel coding schemes employed by GSM, as well as the 4 coding schemes (denoted CS-1 through CS-4) of *General Packet Radio Service* (GPRS).

Code puncturing is accomplished by deleting selected encoder output bits according to a chosen perforation pattern, also known as a *puncturing profile*. In general, the period-M_{punct} puncturing profile used to increase the code rate of a binary rate $R_c = k/n$ code, can be expressed by the following matrix:

$$\Upsilon = \begin{bmatrix} \Upsilon_{0,0} & \Upsilon_{0,1} & \cdots & \Upsilon_{0,M_{punct}-1} \\ \Upsilon_{1,0} & \Upsilon_{1,1} & \cdots & \Upsilon_{0,M_{punct}-1} \\ \vdots & \vdots & \ddots & \vdots \\ \Upsilon_{n-1,0} & \Upsilon_{n-1,0} & \cdots & \Upsilon_{n-1,M_{punct}-1} \end{bmatrix} \tag{3.45}$$

where the elements of Υ can only take on the values 0 and 1. The puncturing profile specifies that the j^{th} code bit of the i^{th} n-bit encoder output is deleted from the stream of coded bits to be transmitted, if $\Upsilon_{j,a} = 0$, where $a = i \bmod M_{punct}$. Alternatively, if $\Upsilon_{j,a} = 1$, the specific code bit is preserved. The code rate achieved after puncturing is easily calculated as follows:

$$R_p = \frac{k.M_{punct}}{\sum_{j=0}^{n-1} \sum_{a=0}^{M_{punct}-1} \Upsilon_{j,a}} \tag{3.46}$$

For example, assume a single rate $R_c = 1/3$ RSC code (see *Section* 3.2.1.3.2) has to be used in a communication system, but the required code rate is $1/2$. A further requirement is that the systematic output bits generated by the encoder may not be punctured. One possible period-1 puncturing approach is to permanently delete one of the two parity bits generate by the encoder for every input bit. However, this might lead to an unacceptable degradation in the code's performance. A more

attractive solution is to alternate the puncturing between the two parity bits. The following period-2 puncturing profile is one of two possible profiles that will implement the aforementioned puncturing requirements:

$$\Upsilon = \begin{bmatrix} 1 & 1 \\ 1 & 0 \\ 0 & 1 \end{bmatrix} \tag{3.47}$$

3.3 DECODER BUILDING BLOCKS

3.3.1 BINARY CONVOLUTIONAL CODE DECODERS

Since classic ML decoding techniques [106] have become cornerstone algorithms in convolutional code decoding, they are not repeated here. The unenlightened reader is referred to [106] for comprehensive explanations and examples of the application of the VA in the decoding of convolutional codes, and [107] for a discussion on the non-optimal *Fano* sequential decoding technique.

Most ML convolutional code decoding algorithms (such as the *sliding window* VA) and MAP convolutional code decoding algorithms (such as the BCJR algorithm [2]) make use of convolutional code *trellises*. The trellis of a rate $R_c = k/n$ binary convolutional code is essentially a time-indexed state diagram for the underlying binary circuit defined by the generator matrix $G_{CC}(D)$ [47]. As such, it contains all relevant information crucial for ML and MAP decoding algorithms. The following subsection describes the construction of binary block code trellises.

3.3.1.1 CONSTRUCTING THE TRELLIS OF A BINARY CONVOLUTIONAL CODE

Given that the constraint length of the convolutional code encoder is υ, the trellis of the code has 2^{υ} states, with trellis state l being defined as the decimal equivalent of the υ-bit binary number created by concatenating the encoder's memory elements' outputs at a certain encoding instance. The number of branches leaving or entering a state (node) in a binary convolutional code's trellis, is either 0 (in the fan-out section of the trellis) or 2^k [47].

An important characteristic of a depth-$M_{sections}$ convolutional code trellis, distinguishing it from a linear block code trellis (see *Section* 4.2), is that it can be constructed by concatenating $M_{section}$ identical trellis sections, where a trellis section is defined as a single depth trellis showing all possible state transitions of the convolutional code encoder under investigation [47]. Consequently, a convolutional code's trellis can be described as being "time-invariant", whereas a linear block code's trellis is "time-variant", since each trellis section is unique.

Construction of a single convolutional code trellis section involves determining the destination state and associated n-bit encoder output, given that the i^{th}, for $i = 1, 2, ..., 2^k$, possible k-bit encoder input is used with the encoder in an origin state l, for $l = 0, 1, ..., 2^{\upsilon} - 1$. The transition from an initial (origin) state to a destination state is indicated by the presence of a branch. Each branch has an associated n-bit branch weight or decoder input branch vector, as well as a k-bit decoder output branch vector. The decoder input and output branch vectors of the j^{th} branch leaving the l^{th} state at a trellis depth of i are denoted by $\overline{u}_{i,l}^{(j)}$ and $\overline{o}_{i,l}^{(j)}$, respectively.

In the graphical representation of a single trellis section, the decoder input and output sequences, associated with each branch, are usually indicated by means of a *"Decoder Output Sequence / Decoder Input Sequence"* (or equivalent *"Encoder Input Sequence / Encoder Output Sequence"*) label. *Fig.* 3.3 shows such a trellis section, obtained by following the foregoing procedure for the optimal

8-state, $\upsilon = 3$, rate $R_c = 1/2$ RSC code, defined by *Eq.* (3.12).

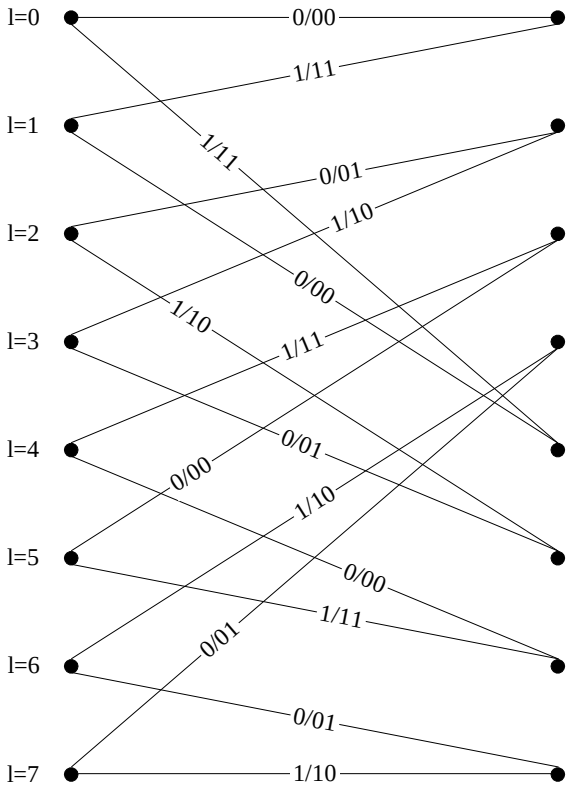

Figure 3.3: Trellis Section of the Optimal 8-State, Rate $R_c = 1/2$ RSC Code, Defined by *Eq.* (3.12)

3.3.2 LINEAR BLOCK CODE DECODERS

Since the classic algebraic algorithms employed in the decoding of linear block codes are well known, these algorithms are not repeated in this dissertation. However, the interested reader is referred [47,93,94] for descriptions of the classic syndrome and ML decoding techniques used for most classes of binary linear block codes. The *Berlekamp-Massey* syndrome decoding algorithm [74, 75], which is the classic hard decision decoding algorithm, employed for both BCH and RS block codes, is addressed in *Appendix B*. Since it falls beyond the scope of this study, the classic *Berlekamp-Massey* algorithm is not described in much detail. However, several valuable references that focus on variations of this decoding algorithm are cited for the interested reader.

Chapter 4 focusses on the trellis decoding of linear block codes by means of a fixed window (or block-wise) VA. This chapter not only describes this decoding algorithm in detail, but also investigates the construction of BCJR block code trellises.

3.3.3 DE-INTERLEAVERS

De-interleavers are in actual fact also interleavers. Their function, however, is to undo the temporal ordering of the symbols, created by the associated interleaver. The following subsection presents a short mathematical description of de-interleavers, building on *Section* 3.2.3.1's discussion of interleavers.

3.3.3.1 MATHEMATICAL DESCRIPTION OF DE-INTERLEAVERS

If the m^{th} length-N sequence of interleaved symbols used as input to a de-interleaver, π^{-1}, associated with an interleaver π, is denoted by $\overline{\varrho}_m^{in} = \{\varrho_{m,0}^{in}, \varrho_{m,1}^{in}, ..., \varrho_{m,(N-2)}^{in}, \varrho_{m,(N-1)}^{in}\}$, the de-interleaving of $\overline{\varrho}_m^{in}$ by π^{-1} can be described as follows [87]:

$$\pi^{-1}\left(\overline{\varrho}_m^{in}\right) = \overline{\varrho}_m^{out} = \{\varrho_{m,0}^{out}, \varrho_{m,1}^{out}, ..., \varrho_{m,(N-2)}^{out}, \varrho_{m,(N-1)}^{out}\} \tag{3.48}$$

where $\overline{\varrho}_m^{out}$ represents the N-symbol/sample output of the de-interleaver. The de-interleaver output can also be written as [87]:

$$\begin{aligned}\overline{\varrho}_m^{out} &= \{\varrho_{m,0}^{out}, \varrho_{m,1}^{out}, ..., \varrho_{m,(N-2)}^{out}, \varrho_{m,(N-1)}^{out}\} \\ &= \{\varrho_{m,\Pi^{-1}(0)}^{in}, \varrho_{m,\Pi^{-1}(1)}^{in}, ..., \varrho_{m,\Pi^{-1}(N-2)}^{in}, \varrho_{m,\Pi^{-1}(N-1)}^{in}\}\end{aligned} \tag{3.49}$$

where $\Pi^{-1}(i)$, with i any integer value, is the de-interleaver mapping function that describes the mapping of the de-interleaver output time indices to de-interleaver input time indices. The mapping function, $\Pi^{-1}(i)$, is defined such that it will undo the temporal shuffling caused by the mapping function $\Pi(i)$ of the interleaver π. For example, the mapping function for the de-interleaver associated with the example period $N = 3$ convolutional interleaver, defined by the mapping function of *Eq.* (3.39), is as follows:

$$\Pi^{-1}(i) = \begin{cases} i & \text{if } i \bmod 3 = 0 \\ i+3 & \text{if } i \bmod 3 = 1 \\ i+6 & \text{if } i \bmod 3 = 2 \end{cases} \tag{3.50}$$

From this mapping function, the de-interleaver's fundamental permutation follows readily:

$$\eth\left(\Pi^{-1}\right) = \begin{pmatrix} 0 & 1 & 2 \\ 0 & 4 & 8 \end{pmatrix} \tag{3.51}$$

Following a similar approach as with interleavers, the stream of de-interleaver input sequences can be presented by the N-dimensional vector sequence $\overline{\varrho}(D)$, given by:

$$\overline{\varrho}^{in}(D) = \sum_m \overline{\varrho}_m^{in} D^m \tag{3.52}$$

where D represents one de-interleaver delay period of N symbols. Defining the generator matrix of the de-interleaver $G_{\pi^{-1}}(D)$, the de-interleaver output stream can be described as follows:

$$\overline{\varrho}^{out}(D) = \overline{\varrho}^{in}(D) \cdot G_{\pi^{-1}}(D) \tag{3.53}$$

Obviously the de-interleaver generator matrix is an $N \times N$ non-singular matrix with the same restrictions as $G_\pi(D)$. Assuming perfect channel conditions, employing interleaver π's output (see *Eq.* (3.43)) as input for the de-interleaver π^{-1}, *Eq.* (3.53) can be rewritten as follows:

$$\overline{\varrho}^{out}(D) = \overline{\varrho}^{in}(D) \cdot G_{\pi^{-1}}(D) = \left(\overline{\mu}^{in}(D) \cdot G_\pi(D)\right) \cdot G_{\pi^{-1}}(D) \tag{3.54}$$

Since the de-interleaver π^{-1} has to undo the shuffling of the interleaver π, i.e. $\overline{\varrho}^{out}(D) = \overline{\mu}^{in}(D)$, the de-interleaver's generator matrix can be determined as follows [87]:

$$G_{\pi^{-1}}(D) = G_\pi^{-1}(D) \tag{3.55}$$

For example, the generator matrix associated with the de-interleaver mapping given by *Eq.* (3.50) must be the inverse of the matrix given by *Eq.* (3.44):

$$G_{\pi^{-1}}(D) = G_{\pi}^{-1}(D) = \begin{bmatrix} 1 & 0 & 0 \\ 0 & D^{-1} & 0 \\ 0 & 0 & D^{-2} \end{bmatrix} \tag{3.56}$$

From this generator matrix it is clear that the example de-interleaver is non-causal, as will always be the case for de-interleavers associated with causal interleavers [87].

3.3.4 CODE DE-PUNCTURERS

Code de-puncturing, also known as *insertion*, is the process whereby the bits punctured from a stream of encoded bits prior to modulation, are reinserted into the received and demodulated stream before being decoded. Since de-puncturing fills all the "holes" in the stream of encoded bits used as input by the decoder, decoding can be accomplished by the standard decoding structure associated with the transmitter's encoder, eliminating the need for an altered decoder, which has been adapted to accommodate a punctured stream of bits as input [105].

An important question now arises: Were the punctured code bits ones or zeros? Since the receiver has no way of knowing the answer to this question, the best solution is to declare *erasures* in the deleted bit positions. Erasures can be though of as "I am not sure" values, the size of which depends on the code bit alphabet employed by the encoder/modulator and demodulator/decoder, as well as the a-priori probabilities for the code bit ones and zeros. The erasure value $\Gamma_{m,i,a}$ for the a^{th} delete code bit in the i^{th} symbol of the m^{th} n-symbol $GF\left(2^{\xi}\right)$ channel coder output can be calculated as follows for slow Rayleigh flat fading channel conditions with AWGN noise effects: Assuming the receiver has perfect knowledge of the instantaneous channel phase and no puncturing was performed, coherent demodulation renders the following demodulator output for the a^{th} bit in the i^{th} symbol of the m^{th} set of received code word symbols:

$$y_{m,i,a} = \overline{\alpha}_{m,i,a}.c_{m,i,a} + \eta_{m,i,a} \tag{3.57}$$

where $\overline{\alpha}_{m,i,a}$ and $\eta_{m,i,a}$ represents the average fading amplitude (see *Section* 5.2.3 and *Section* 5.3.3) and AWGN demodulator output components for this code bit, respectively. With the demodulator output defined by *Eq.* (3.57), it can be shown that the conditional PDF $\rho\left(y_{m,i,a}|c_{m,i,a}\right)$ is given by [60]:

$$\rho\left(y_{m,a,i}|c_{m,a,i}\right) = \frac{1}{\sqrt{2\pi}\sigma_{\eta_{m,i,a}}} \exp\left[-\frac{\left(y_{m,i,a} - \overline{\alpha}_{m,i,a}.c_{m,a,i}\right)^2}{2\sigma_{\eta_{m,i,a}}^2}\right] \tag{3.58}$$

where $\sigma_{\eta_{m,i,a}}^2$ is the variance in the AWGN component. Furthermore, assume the code bit can take on values from the amplitude alphabet $\{C_{zero}, C_{one}\}$. Calculation of the appropriate erasure value $\Gamma_{m,i,a}$ involves finding the intersection between the PDFs for the demodulator output, given $c_{m,a,i} = C_{zero}$ or $c_{m,a,i} = C_{one}$ was transmitted [81]:

$$\begin{aligned} &\text{Prob.}\left(c_{m,a,i} = C_{zero}\right).\rho\left(y_{m,a,i}|c_{m,a,i} = C_{zero}\right)\big|_{y_{m,a,i}=\Gamma_{m,i,a}} = \\ &\text{Prob.}\left(c_{m,a,i} = C_{one}\right).\rho\left(y_{m,a,i}|c_{m,a,i} = C_{one}\right)\big|_{y_{m,a,i}=\Gamma_{m,i,a}} \end{aligned} \tag{3.59}$$

where $\text{Prob.}\left(c_{m,a,i} = C_{one}\right)$ and $\text{Prob.}\left(c_{m,a,i} = C_{zero}\right)$ represent the a-priori probabilities of transmitting ones and zeros, respectively. Solving *Eq.* (3.59) yields the following expression for the

optimal erasure value:

$$\Gamma_{m,i,a} = \frac{\log\left(\frac{\text{Prob.}(c_{m,i,a}=C_{one})}{\text{Prob.}(c_{m,i,a}=C_{zero})}\right).2\pi\sigma^2_{\eta_{m,i,a}} - (\overline{\alpha}_{m,i,a}.C_{one})^2 + (\overline{\alpha}_{m,i,a}.C_{zero})^2}{(2.\overline{\alpha}_{m,i,a}.C_{zero} - 2.\overline{\alpha}_{m,i,a}.C_{one})} \tag{3.60}$$

For example, assuming an antipodal code bit representation from the alphabet $\{-1, 1\}$ for equiprobable code bits, the de-puncturer will replace the deleted code bits with $\Gamma_{m,i,a} = 0$.

Although de-puncturing has a definite influence on the performance of ML and MAP decoders, the gains obtained by employing punctured low rate codes surpass the gains of higher rate codes with equivalent overall code rates [105]. Furthermore, the combination of code puncturing and de-puncturing allows the use of a single code over a wide variate of transmission rates, without requiring alteration of the encoder or decoder structures. As such, code puncturing is frequently encountered in coded communication systems that support rate adaptation.

3.3.5 CHANNEL STATE INFORMATION ESTIMATORS

Although the accurate estimation of mobile communication channel parameters has always been an area of particular appeal to communication engineers, classic channel code designers refrained from using CSI in their decoder algorithms. This was due to the fact that the performance improvements obtained using side information in classic ML decoding did not necessarily justify the required increased system complexity [56]. However, the introduction of TCs in 1993 sparked a renewed interest into this research field, since these codes, like most modern concatenated channel codes, require the use of reliable CSI during iterative decoding [87, 108].

Explained in terms of *Chapter* 2's mathematical framework for mobile communication channels, CSI estimator structures, integrated into current and future wireless communication systems, must accomplish one or more of the following tasks:

1. Estimate the AWGN present at the output of the receiver/demodulator in order to predict the current operational E_b/N_0. Accurate knowledge of the SNR per bit [47] is crucial during the iterative decoding of PCCs, SCCs, HCCs, product codes and LDPCs. This parameter forms an integral part of the *Log-Likelihood Ratio* (LLR) calculations performed by each of the *Soft-Input Soft-Output* (SISO) decoding modules (for example, MAP and SOVA decoders) incorporated into these codes' iterative decoder structures [28, 30–33, 87, 108].

2. Determine the power delay profiles (or impulse responses) of multipath fading channels [109]. For an L-path channel, this entails estimating the average path powers $\overline{\beta}_i$ and path delays τ_i, for $i = 1, 2, ..., L$. For wideband DS/SSMA communication systems, full exploitation of the potential diversity gains achievable by using MRC during RAKE reception, is only possible if these parameters are perfectly known at all time instances [110]. Power control algorithms in DS/SSMA systems also require such knowledge in order to avoid near-far problems in CDMA environments [111].

3. Approximate the fading amplitude and phase for each propagation path in an L-path multipath fading channel, i.e. find $\alpha_i(t)$ and $\phi_i(t)$, for $i = 1, 2, ..., L$. Tracking of the phase changes introduced by the channel (as well as other system components, such as filters), are essential not only for coherent demodulation [86], but also for bit, frame and sequence (in DS/SSMA systems) synchronisation. On the other hand, obtaining real-time estimates of the fading amplitudes are not crucial to the signal detection process. However, these estimates are an integral part of the metric calculations of any channel coded system employing CSI-enhanced decoding. Although perfect tracking of these parameters for each path in a multipath fading channel is desired, implementation

thereof might require excessive system complexity. Therefore, most hardware implementations of RAKE receivers (see *Section* 5.3.2) usually only attempt to track the fading amplitudes and phases of the dominant propagation path, partially forfeiting information carried by the precursor and post-cursor [47, 112] paths.

4. Efficient multi-user detection in CDMA systems is a crucial component of most multi-user cancellation techniques, which are geared at minimising the effects of the MUI present in the channel [43, 44, 113].

Over the last few decades, numerous channel parameter tracking methods and algorithms have been proposed. However, this field is still in its infancy. A universal channel estimation technique, capable of handling all modulation schemes and mobile channel characteristics, still eludes the communication engineering society. Current schemes are mostly application specific, integrated into the modulation technique, MA scheme, channel equalisation subsystem or channel coding/decoding algorithms employed by modern communication systems. That being said, it is still possible to organise the myriad of proposed schemes into two main categories:

1. **Blind Channel Estimation:** With this approach, no additional information, which might assist with CSI estimation, is embedded into data transmissions. At the receiving end, channel parameters must be extracted directly from the modulated information signals. Obviously, schemes falling in this category are highly complex, but also much sought after, since no transmission bandwidth is relinquished for CSI estimation purposes. Many classic carrier, sequence, bit and frame synchronisation loops fall in this category, for example *Costas* loops [47], decision directed early-late code locked loops [43, 47], etc. Multipath fading channel impulse response (power delay profile) and AWGN power level estimations via first, second and higher order statistics (calculation of mean values, variances, auto-correlations, cross-correlations, etc.) can also be grouped into this category. One might also consider free-running equalisers (after successfully training) to be blind channel estimators. Unfortunately, very few fading amplitude estimation schemes exist that can be considered to be purely blind. However, for constant envelope transmitter output signals, blind estimation of the fading amplitude is easily accomplished.

2. **Pilot Assisted Channel Estimation:** This approach relies on the use of dedicated pilot information (such as pilot tones, pilot symbols, etc.) from which channel parameters can effortlessly be determined. This category can be further subdivided into:

    1. In-band pilot signalling, where pilot signalling occupies the same bandwidth as the information being transmitted. For example, with *Pilot Symbol Assisted Modulation* (PSAM), non-information carrying symbols are injected directly into the transmitted data stream, effectively sacrificing a percentage of the transmission bandwidth. At the receiving end, *Kalman* filters [114, 115] can be used to interpolate between the amplitude changes observed in consecutive pilot symbols, thereby estimating the fading amplitude of the mobile channel. Another example of in-band signalling is the use of equaliser training sequences, present in every normal burst of GSM.
    2. Out-of-band pilot signalling, where dedicated bandwidth is assigned for pilot signalling purposes. A system that uses a pilot channel to carry a pilot tone for carrier synchronisation purposes, is a good example of out-of-band pilot signalling.

Although an in depth investigation into channel estimation schemes falls outside the scope of this study, the list of journal articles and conference papers below attempts to spark the curiosity of the interest reader:

- PSAM techniques for the estimation of flat fading channel parameters and statistics are discussed and analysed in [116–118].

- *Maximum Likelihood Sequence Estimation* (MLSE) algorithms (such as the VA) and per-survivor processing for channel estimation purposes are covered in [119–123].
- In [109, 124–126] the estimation of multipath fading channel power delay profiles (impulse responses), as well as other channel statistics are addressed.
- Several joint data detection and channel estimation approaches are considered in [122, 123, 125] for flat and frequency selective fading channels.
- Blind equalisation and channel estimation techniques, including second order cyclostationary statistical methods, the use of chaotic coded signals, least-squares approaches, linear prediction methods, periodic modulation precoders, *Soft Output Viterbi Equaliser* (SOVE) algorithms and tricepstrum-based algorithms are presented in [127–136].
- Various multipath fading channel estimation techniques, targeted at DS/SSMA systems, are given in [111, 137, 138]. In [139] the influence of channel state estimation on the performance of a coherent DS/SSMA system is investigated.
- A technique for multi-user detection through adaptive channel estimation is described in [140].

Chapter 6 presents a great number of simulated BER performance curves for convolutional and linear block codes, employing soft decision VA decoding with perfect fading amplitude CSI. This information was directly extracted (see *Section* 2.6.2.5) from the novel complex flat fading and multipath fading channel simulator structures, presented in *Section* 2.6.2.3 and *Section* 2.6.3.2, respectively.

3.4 CONCLUDING REMARKS

The encoder and decoder building blocks encountered in classic block and convolutional coding schemes were considered in this chapter. This included discussions on binary convolutional codes, binary and non-binary linear block codes, interleaver and de-interleaver structures, the concept of code puncturers and de-puncturers, and last, but not least, CSI estimators. The following unique, albeit insignificant contributions were made in this chapter:

1. A unified generator matrix approach is employed to describe convolutional codes, linear block codes, interleavers and de-interleavers. Although this is commonplace for linear block codes, the same can not be said for binary convolutional codes, interleavers or de-interleavers.
2. In *Section* 3.3.4, which focuses on the issue of code de-puncturing, a simple formula is presented that calculates an optimal erasure value for non-equiprobable code bits, transmitted through a slow Rayleigh flat fading channel with AWGN effects.

CHAPTER FOUR

VITERBI DECODING OF LINEAR BLOCK CODES

4.1 CHAPTER OVERVIEW

THIS chapter sets out by describing the BCJR linear block code trellis construction method [2] for (n, k, d_{min}) linear block codes, where k is the message length, n is the code word length, and d_{min} is the minimum Hamming distance property (see *Section* 3.2.2.2) of the code. For illustrative purposes, it is used to created the trellis of a shortened binary Hamming $(5, 2, 3)$ block code (see *Section* 3.2.2.3.1). The next part of the chapter is concerned with the quantification of the complexity of a linear block code's trellis: Using a binary Hamming $(7, 4, 3)$ block code (see *Section* 3.2.2.3.1) as example, it firstly describes a simple, but tedious method whereby the state space profile and complexity [141–143] of a block code's trellis can be determined. Secondly, it discusses a trellis reduction method and illustrates the use thereof for a binary cyclic $(5, 3, 2)$ block code. In the final part of this chapter, the application of a block-wise VA [3] as an optimal ML trellis decoder for BCJR block code trellises is considered. Both hard and soft decision VA metric calculation approaches are addressed.

Although the block codes used as examples in this chapter are all binary linear block codes, the algorithms presented are readily applicable to non-binary codes, such as RS (see *Section* 3.2.2.3.3) and BCH (see *Section* 3.2.2.3.2) block codes. Unfortunately, due to the size and complexity of such codes' trellises, they do not lend themselves to be good examples whereby the algorithms presented here can be effectively demonstrated.

4.2 LINEAR BLOCK CODE TRELLIS CONSTRUCTION

In principle, every linear block code has a unique trellis description: By creating a set of parallel trellis paths, one for each code word, a simple albeit inefficient trellis is generated. In [2] *Bahl et al.* presents a more elegant approach to derive an efficient trellis structure from the linear block code's parity check matrix (see *Section* 3.2.2.1). The following two subsections are devoted to a description of this trellis construction technique.

4.2.1 CONSTRUCTING AN UNEXPURGATED LINEAR BLOCK CODE TRELLIS

As previously stated, the BCJR trellis construction method for a (n, k, d_{min}) linear block code with code word symbols from Galois field $GF\left(2^{\xi}\right)$, requires the code's parity check matrix, given by:

$$H_{BC} = [\overline{h}_0\ \overline{h}_1\ ...\ \overline{h}_{n-1}] \tag{4.1}$$

In *Eq.* (4.1) $\overline{h}_i$, with $i = 1, 2, ..., n$, is the i^{th} column of the parity check matrix, containing $(n-k)$ elements from the Galois field $GF\left(2^{\xi}\right)$. The trellis construction technique is based on the fact that the i^{th} $(n-k)$-tuple syndrome vector $\overline{\$}_m^i$ [47] for the m^{th} n-tuple valid code word vector $\overline{c}_m = \{c_{m,0}, c_{m,1}, ..., c_{m,n-1}\}$ can be calculated using the following recursion formula [2, 87]:

$$\overline{\$}_m^i = \overline{\$}_m^{i-1} + c_{m,i-1}.\overline{h}_{i-1} \tag{4.2}$$

where $c_{m,i}$ is the i^{th} code word symbol contained in the vector $\overline{c}_m$. The initial condition is $\overline{\$}_m^0 = \overline{0}$. Note that addition and multiplication are carried out symbol-wise in $GF\left(2^{\xi}\right)$. The block code trellis, which is a compact method to represent all $2^{k.\xi}$ code words in the code, consists of $(n+1)$ sets of nodes (states), each set containing $2^{\xi.(n-k)}$ nodes. By interconnecting the nodes with branches in a topology uniquely defined by H_{BC}, the trellis is constructed. For the purpose of this discussion, the sets of nodes are indexed by a parameter i, with $i = 0, 1, 2, ..., n$. Nodes in set i are indexed by a parameter l, with $l = 0, 1, 2, ..., 2^{\xi.(n-k)} - 1$. Therefore, the l^{th} node in the i^{th} set has an index (l, i). The branches emanating from the nodes in the trellis are indexed by the parameter j. Each branch in the trellis has an associate branch weight or decoder input branch vector, as well as a decoder output branch vector. For example, the branch weight vector and decoder output branch vector of the j^{th} branch leaving node (l, i) are $\overline{u}_{i,l}^{(j)}$ and $\overline{o}_{i,l}^{(j)}$, respectively. The trellis construction procedure is described below:

1. Set $i = 0$, where i is the trellis depth counter.

2. At a depth of $i = 0$, only node $(0, 0)$ has 2^{ξ} emanating branches. From any node (l, i), with $i > 0$, that has incoming branches, 2^{ξ} branches flow forth. The destination nodes in set $i+1$ of the branches leaving any node (l, i) are determined as follows:

   (a) Determine a length-$(n-k)$ vector $\overline{\epsilon}_i$, which contains the l^{th} possible combination of $(n-k)$ elements from $GF\left(2^{\xi}\right)$.

   (b) Let the $GF\left(2^{\xi}\right)$ symbol associated with the j^{th} branch be denoted by b_j. With $j = 0, 1, 2, ..., 2^{\xi} - 1$, proceed as follows:

      i. Compute the $(n-k)$-tuple $GF\left(2^{\xi}\right)$ vector $\overline{q}_{i,j} = (\overline{h}_i^T.b_j) + \overline{\epsilon}_i$, where addition and multiplication are carried out symbol-wise in $GF\left(2^{\xi}\right)$. The vector $\overline{h}_i^T$ represents the transpose of $\overline{h}_i$.

      ii. The destination node in set $i+1$ is node $(z_{i,j}, i+1)$, where the vector $\overline{q}_{i,j}$ contains the $z_{i,j}^{\text{th}}$ possible combination of $(n-k)$ elements from $GF\left(2^{\xi}\right)$.

      iii. If bit-wise comparison has to be used in the metric calculations of the trellis decoder, as is always the case with binary block codes, the branch weight vector assigned to the j^{th} branch is given by value $\overline{u}_{i,l}^{(j)} = \overline{w}_j$, where $\overline{w}_j$ is the sequence of binary bits representing the $GF\left(2^{\xi}\right)$ symbol b_j. When, for non-binary block codes such as RS and BCH block codes, the code word symbols are used directly in the decoding process, i.e. symbol-wise comparison during the branch metric calculations, the branch weight vector consists of a single element, namely $\overline{w}_j = b_j$.

iv. The decoder output branch vector of the j^{th} branch is equal to the branch weight vector, i.e. $\overline{o}_{i,l}^{(j)} = \overline{u}_{i,l}^{(j)}$.

(c) Repeat steps (a) and (b) for every l, where node (l, i) has one or more incoming branches.

3. Repeat step 2 for $i = 1, 2, .., n-1$.

Following the procedure outlined above, a trellis with more paths than code words in the code is created. Such a trellis is called an *unexpurgated* [3] or *unconstrained* [87] block code trellis. Shown in *Fig.* 4.1 is the unexpurgated trellis, obtained using the BCJR trellis construction method, for a binary Hamming $(5, 2, 3)$ block code (see *Section* 3.2.2.3.1) (constructed by shortening the Hamming $(7, 4, 3)$ block code, defined by the generator matrix of *Eq.* (4.4)) with the following parity check matrix:

$$H_{BC} = \begin{bmatrix} 1 & 0 & 1 & 0 & 0 \\ 1 & 1 & 0 & 1 & 0 \\ 0 & 1 & 0 & 0 & 1 \end{bmatrix} \tag{4.3}$$

In this figure, the VA decoder (see *Section* 4.4) output and input sequences associated with each branch of the trellis are indicated by the *Decoder Output Sequence* $\overline{o}_{i,l}^{(j)}$ / *Decoder Input Sequence* $\overline{u}_{i,l}^{(j)}$ labels.

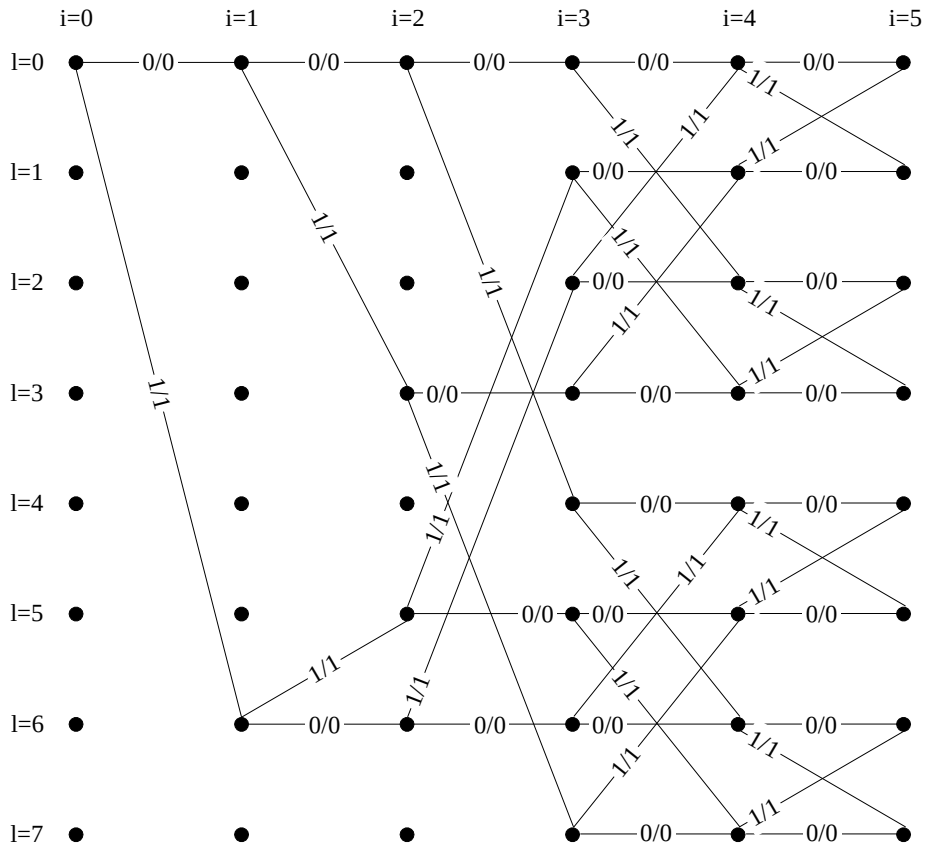

Figure 4.1: Unexpurgated Trellis of the Shortened Binary Hamming $(5, 2, 3)$ Code

4.2.2 EXPURGATING A BLOCK CODE TRELLIS

Removal of all non-code word representing paths in the unexpurgated trellis of a block code, with code word symbols from $GF\left(2^{\xi}\right)$, a process referred to as *trellis expurgation* [3], involves discard-

ing all paths that do not end in node $(0, n)$. The resultant trellis is called an *expurgated* or *constrained* block code trellis. In this trellis, only $2^{\xi.k}$ unique paths, representing the valid code words in the block code, are retained.

Although the expurgation process seems simple, it usually involves tedious back-tracing through the trellis. A simple technique, applicable to the BCJR trellis structures of unextend systematic linear block codes, presented by *Staphorst*, *Büttner* and *Linde* in [52] for binary block codes and in [55] for non-binary block codes, involves removing all branches from nodes in set $i-1$ entering the node (l, i) for $i = k+1, k+2, k+3, .., n$ and $l = 2^{\xi.(n-i)}, 2^{\xi.(n-i)}+1, .., 2^{\xi.(n-k)}-1$. *Fig.* 4.2 shows the expurgated trellis obtained for the binary Hamming $(5, 2, 3)$ code, defined by *Eq.* (4.3), after this path removal algorithm has been applied to the unexpurgated trellis of *Fig.* 4.1.

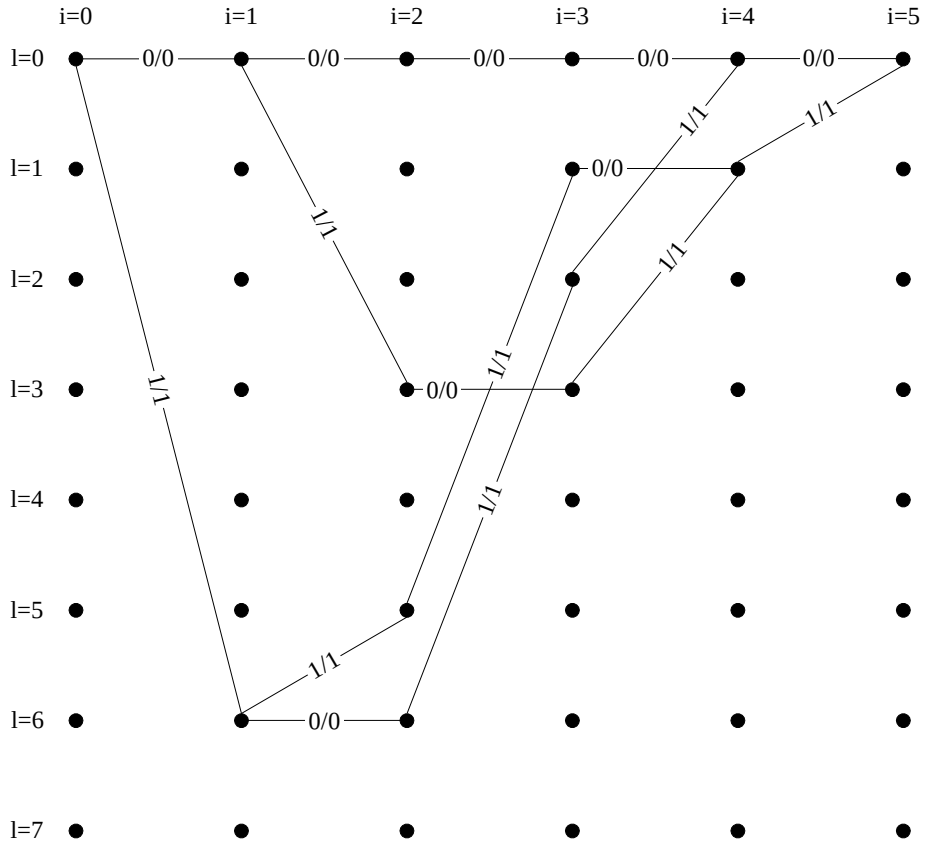

Figure 4.2: Expurgated Trellis of the Shortened Binary Hamming $(5, 2, 3)$ Code

It should be noted that the VA can be just as successfully applied to an unexpurgated trellis, as long as it is configured to only select paths starting in state $(0, 0)$ and ending in state $(0, n)$ (see *Section* 4.4). Moreover, identical BER performances are obtained by applying the VA to unexpurgated or expurgated BCJR trellis structures, irrespective of the channel conditions. However, this will result in unnecessary computations, larger decoder memory requirements and overall increased system complexity. For example, a VA applied to the unexpurgated trellis of *Fig.* 4.1 must perform 46 branch metric calculations for the branches connecting its $AN(C) = 31$ active nodes, whereas a VA running on the expurgated trellis of *Fig.* 4.2 only needs to calculate 16 branch metrics for the branches connecting its $AN(C) = 14$ active nodes.

4.3 COMPLEXITY OF LINEAR BLOCK CODE TRELLISES

For most block codes of practical interest, such as the extended binary BCH $(32, 21, 6)$ block code, used extensively in several paging protocols, the code rate $R_c = k/n$ is greater than or equal to 0.5, while the number of parity symbols $(n-k)$ is at least 10. Given the extensive use of such block codes in wireless communication systems, these codes lend themselves to be prime candidates for trellis decoding. Unfortunately, the complexity of an (n, k, d_{min}) block code's trellis grows exponentially with $\min\{k, (n-k)\}$ [3]. For example, the expurgated trellis of the previously mentioned $(32, 21, 6)$ extended BCH block code has a staggering 14972 branches [144]. Thus, the cost effectiveness of block code trellis decoders for such codes is questionable. The following subsections firstly illustrates a procedure whereby the complexity of a block code's trellis can be calculated, followed by a simple block code trellis reduction method.

4.3.1 TRELLIS COMPLEXITY CALCULATION

A simple state space complexity calculation method [141–143, 145, 146] for an (n, k, d_{min}) block code with code and message word symbols from $GF\left(2^{\xi}\right)$, defined by generator matrix G_{BC} (see *Section* 3.2.2.1), is detailed in this subsection. As is shown in this subsection, the state space complexity of a block code gives a good indication of the complexity of the block code's trellis. The state space complexity calculation procedure is illustrated for a binary Hamming $(7, 4, 3)$ block code (see *Section* 3.2.2.3.1) with the following generator matrix:

$$G_{BC} = \begin{bmatrix} 1 & 0 & 0 & 0 & 1 & 0 & 1 \\ 0 & 1 & 0 & 0 & 1 & 1 & 1 \\ 0 & 0 & 1 & 0 & 1 & 1 & 0 \\ 0 & 0 & 0 & 1 & 0 & 1 & 1 \end{bmatrix} \tag{4.4}$$

Due to the considerable number of lengthy intermediate results obtained during the calculation of a block code's state space complexity, some of these results are omitted in the following discussion for the Hamming $(7, 4, 3)$ block code.

The first step in the estimation of the block code's state space complexity is to determine all possible code words obtainable from G_{BC}. In general, the number of unique code words that can be generated by an (n, k, d_{min}) block code's generator matrix G_{BC} is $2^{\xi \cdot k}$. For the Hamming $(7, 4, 3)$ block code, $2^4 = 16$ unique code words exist. Let C denote this set of code words, with $\overline{c}_m = \{c_{m,0}, c_{m,1}, ..., c_{m,(n-1)}\}$ the m^{th} code word in the set.

Next, the block code's dimension and inverse dimension distributions [145, 146], denoted by $\Lambda(C) = \{\Lambda_0, \Lambda_1, \Lambda_2, ..., \Lambda_n\}$ and $\Lambda^{-1}(C) = \{\Lambda_0^{-1}, \Lambda_1^{-1}, \Lambda_2^{-1}, ..., \Lambda_n^{-1}\}$, respectively, are determined. The procedure is as follows [145, 146]:

1. Define a master indexing set $\Omega(C) = \{0, 1, 2, ..., n-1\}$. The master indexing set for the Hamming $(7, 4, 3)$ block code is $\Omega(C) = \{0, 1, 2, 3, 4, 5, 6\}$.

2. Let i denote the dimension distribution element index. With $i = 0, 1, 2, ..., n$, proceed as follows:

   (a) For $j = 0, 1, 2, ..., \binom{n}{i}$, complete the following steps:

      i. Select an indexing set $\Phi^j(C) = \{\Phi_1^j, \Phi_2^j, ..., \Phi_i^j\}$, such that it is a subset from $\Omega(C)$, containing i elements that have not been selected for any previous value of j. The size of $\Phi^j(C)$ is therefore $|\Phi^j(C)| = i$. For example, if $i = 3$, one possible j^{th} indexing set

for the Hamming $(7, 4, 3)$ block code is:

$$\Phi^j(C) = \{1, 3, 6\} \tag{4.5}$$

ii. Next, a subset of code words is created from C by manipulating the symbols of each code word, pointed to by the indexing elements in $\Phi^j(C)$: For each code word in C, the code word symbols at positions $\Phi_1^j, \Phi_2^j, ..., \Phi_i^j$ are replaced with zeros, resulting in $2^{\xi.k}$ new, but necessarily unique, code words. By only keeping the unique code words, a new set of code words, denoted by $\vartheta\left(\Phi^j(C)\right)$, is created. For example, as specified by the chosen indexing subset given in *Eq.* (4.5), set $c_{m,1} = c_{m,3} = c_{m,6} = 0$ for $m = 1, 2, ..., 16$. This results in 16 new, but not necessarily unique code words. From these 16 it can be shown that there are only 8 distinct code words in this new set, given by:

$$\vartheta\left(\Phi^j(C)\right) = \begin{bmatrix} \{0,0,0,0,0,0,0\} \\ \{1,0,0,0,1,0,0\} \\ \{1,0,1,0,0,0,0\} \\ \{1,0,1,0,1,1,0\} \\ \{0,0,1,0,1,0,0\} \\ \{1,0,0,0,0,1,0\} \\ \{0,0,1,0,0,1,0\} \\ \{0,0,0,0,1,1,0\} \end{bmatrix} \tag{4.6}$$

iii. Determine $k[\vartheta\left(\Phi^j(C)\right)]$, a parameter which can be interpreted as the effective number of message symbols that is required to generate the number of code words contained in $\vartheta\left(\Phi^j(C)\right)$ [145, 146]:

$$k[\vartheta\left(\Phi^j(C)\right)] = \log_{2^\xi}\left\{\text{Number of code words in } \vartheta\left(\Phi^j(C)\right)\right\} \tag{4.7}$$

From *Eq.* (4.6) it is clear that $k[\vartheta\left(\Phi^j(C)\right)] = 3$ for the indexing subset defined in *Eq.* (4.5) for the Hamming $(7, 4, 3)$ block code.

iv. The next step is to define an inverse indexing subset $\Psi^j(C) = \{\Psi_1^j, \Psi_2^j, ..., \Psi_{n-i}^j\}$ which contains all the elements from $\Omega(C)$, except those already in $\Phi^j(C)$. The inverse indexing subset associated with the indexing subset given in *Eq.* (4.5), is given by:

$$\Psi^j(C) = \{0, 2, 4, 5\} \tag{4.8}$$

v. The inverse indexing subset is now used to create a new set of code words $\vartheta\left(\Psi^j(C)\right)$, containing all the code words from C that have zero code word symbols at the positions indicated by the indexing elements in $\Psi^j(C)$. Using the selected inverse indexing set given in *Eq.* (4.8) produces the following set of new unique code words:

$$\vartheta\left(\Psi^j(C)\right) = \begin{bmatrix} \{0,0,0,0,0,0,0\} \\ \{0,1,0,1,0,0,1\} \end{bmatrix} \tag{4.9}$$

vi. From the new set of code words $\vartheta\left(\Psi^j(C)\right)$, determine $k[\vartheta\left(\Psi^j(C)\right)]$, defined as:

$$k[\vartheta\left(\Psi^j(C)\right)] = \log_{2^\xi}\left\{\text{Number of code words in } \vartheta\left(\Psi^j(C)\right)\right\} \tag{4.10}$$

From *Eq.* (4.9) it follows that $k[\vartheta\left(\Psi^j(C)\right)] = 1$ for the Hamming $(7, 4, 3)$ block code.

(b) The i^{th} elements of the code's dimension and inverse dimension distributions are given by $\Lambda_i = \max\{k[\vartheta\left(\Phi^j(C)\right)]\}$ and $\Lambda_i^{-1} = \max\{k[\vartheta\left(\Psi^j(C)\right)]\}$ for $j = 0, 1, 2, ..., \binom{n}{i}$, respectively.

If the procedure outlined above is completed for the Hamming $(7, 4, 3)$ block code, the dimension and inverse dimension distributions obtained will be:

$$\Lambda(C) = \{0, 1, 2, 3, 4, 4, 4, 4\} \tag{4.11}$$

and:

$$\Lambda^{-1}(C) = \{0, 0, 0, 0, 1, 2, 3, 4\} \tag{4.12}$$

respectively. With an (n, k, d_{min}) linear block code's dimension and inverse dimension distributions known, its state space profile is determined as follows [145, 146]:

$$\begin{aligned} SSP(C) &= \{S_0, S_1, ..., S_n\} \\ &= \{(\Lambda_0 - \Lambda_0^{-1}), (\Lambda_1 - \Lambda_1^{-1}), ..., (\Lambda_n - \Lambda_n^{-1})\} \end{aligned} \tag{4.13}$$

Using *Eq.* (4.11) and *Eq.* (4.12), the state space profile for the Hamming $(7, 4, 3)$ block code under investigation follows readily:

$$SSP(C) = \{0, 1, 2, 3, 3, 2, 1, 0\} \tag{4.14}$$

At a depth of i into the code's expurgated trellis, the number of active nodes (states), i.e nodes having incoming and/or outgoing branches, is $2^{\xi.S_i}$. Thus, the total number of active nodes in the block code's expurgated trellis is [59, 145, 146]:

$$AN(C) = \sum_{i=0}^{n} 2^{\xi.S_i} \tag{4.15}$$

The final important parameter to calculate is the state space complexity of the linear block code [145, 146]:

$$SSC(C) = \max\{S_i\} \qquad \text{for } i = 0, 1, 2, ..., n \tag{4.16}$$

From the Hamming $(7, 4, 3)$ block code's state space profile, given in *Eq.* (4.14), it follows that the number of active nodes and the state space complexity of the code are $AN(C) = 30$ and $SSC(C) = 3$, respectively.

With the number of active states in the trellis known, the next step is to determine an upper bound on the number of branches $NB(C)$ present in the trellis: For a trellis depth of $i < n$ into the unexpurgated BCJR trellis of an (n, k, d_{min}) linear block code with code and message word symbols from $GF\left(2^{\xi}\right)$, the number of branches exiting an active node is 2^{ξ}. Since all paths end in node $(0, n)$, it follows that $AN(C) - 1$ nodes in an expurgated trellis have departing branches. Hence, the number of branches present in an expurgated trellis is upper bounded as follows:

$$NB(C) \leq (AN(C) - 1).2^{\xi} \tag{4.17}$$

The state space complexity is a key measure [59, 141, 142, 147] of the trellis complexity, and thus also the decoding complexity of a specific linear block code. A lower value of the state space complexity results in a less complex trellis structure, leading to faster decoding and less complex trellis decoder structures.

4.3.2 REDUCING TRELLIS COMPLEXITY

It is a known fact [93, 148] that the swapping of columns of a generator matrix of an (n, k, d_{min}) block code, with code word symbols from $GF(2^{\xi})$, results in an equivalent block code. Although

the resultant block code has different code words, it has the same error correcting capabilities as the original code, since the minimum Hamming distance d_{min} (see *Section* 3.2.2.2) remains unchanged. However, it can be shown [149, 150] that the state space dimension of the new code differs from that of the original code. Therefore, swapping columns in a code's generator matrix influences the complexity of the resultant block code's trellis. As will be illustrated by the following trellis reduction example, it is possible to obtain an equivalent code with a lower complexity trellis [149, 150].

The binary cyclic $(5, 3, 2)$ block code (see *Section* 3.2.2.2) to be used as an example in this section, is defined by the following generator matrix:

$$G_{BC} = \begin{bmatrix} 1 & 0 & 0 & 1 & 1 \\ 0 & 1 & 0 & 1 & 0 \\ 0 & 0 & 1 & 0 & 1 \end{bmatrix} \tag{4.18}$$

From this generator matrix, the following parity check matrix can be determined:

$$H_{BC} = \begin{bmatrix} 1 & 1 & 0 & 1 & 0 \\ 1 & 0 & 1 & 0 & 1 \end{bmatrix} \tag{4.19}$$

Fig. 4.3 depicts the expurgated trellis obtained for this parity check matrix using the algorithms

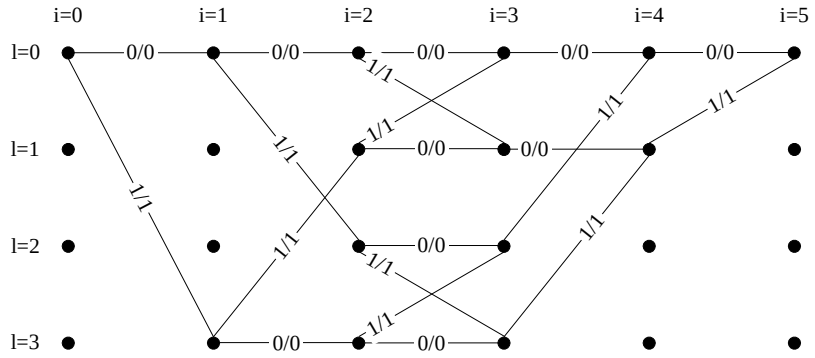

Figure 4.3: Expurgated Trellis of the Original Binary Cyclic $(5, 3, 2)$ Code

presented in *Section* 4.2.1 and *Section* 4.2.2. Following the procedures described in *Section* 4.3.1, it can be shown that the state space profile of the binary cyclic $(5, 3, 2)$ block code is given by:

$$SSP(C) = \left\{ \begin{array}{cccccc} 0 & 1 & 2 & 2 & 1 & 0 \end{array} \right\} \tag{4.20}$$

The number of active nodes in the binary cyclic $(5, 3, 2)$ block code's expurgated trellis is:

$$AN(C) = \sum_{i=0}^{5} 2^{\xi.S_i} = 1 + 2 + 4 + 4 + 2 + 1 = 14 \tag{4.21}$$

Comparing these results with *Fig.* 4.3, it is clear that the calculated and actual number of active nodes in the expurgated trellis correspond. Furthermore, according to *Eq.* (4.17) the number of branches in the expurgated trellis is upper bounded by $NB(C) \leq (14 - 1).2 = 26$. To be precise, $NB(C) = 20$.

In order to find an equivalent code with the least complex trellis, the state space complexity of every possible swapped column permutation of the generator matrix has to be considered [143, 149, 150]. Thus, the state space profile has to be calculated for $n! = 5! = 120$ different permutations of the

code's generator matrix. The following data was obtained from this analysis:

- There exists 8 generator matrices with $AN(C) = 10$ and $SSC(C) = 1$.
- There exists 32 generator matrices with $AN(C) = 12$ and $SSC(C) = 2$.
- There exists 80 generator matrices with $AN(C) = 14$ and $SSC(C) = 2$.

From these results it is apparent that by selecting one of the 8 generator matrices which has 10 active nodes, a minimally complex trellis is obtained. For example, one of these 8 minimal trellis generator matrices is given by:

$$G_{BC} = \begin{bmatrix} 1 & 0 & 1 & 0 & 1 \\ 1 & 1 & 0 & 0 & 0 \\ 0 & 0 & 0 & 1 & 1 \end{bmatrix} \tag{4.22}$$

with the following associated parity check matrix:

$$H_{BC} = \begin{bmatrix} 1 & 1 & 1 & 0 & 0 \\ 0 & 0 & 1 & 1 & 1 \end{bmatrix} \tag{4.23}$$

The state space profile for this equivalent code is given by:

$$SSP(C) = \begin{Bmatrix} 0 & 1 & 1 & 1 & 1 & 0 \end{Bmatrix} \tag{4.24}$$

Fig. 4.4 shows the expurgated trellis of this equivalent code. Comparing *Fig.* 4.3 and *Fig.* 4.4, the

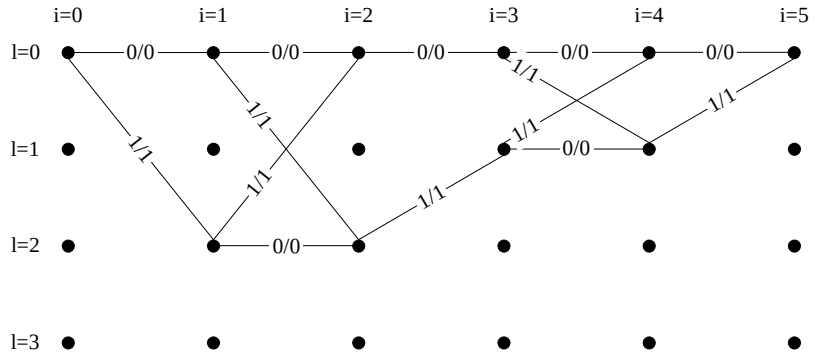

Figure 4.4: Optimally Reduced Expurgated Trellis of the Equivalent Binary Cyclic $(5, 3, 2)$ Code

reduction in trellis complexity is clearly visible. By applying the VA to the reduced trellis, decoding time as well as decoder complexity will be noticeably reduced.

4.4 TRELLIS DECODING OF LINEAR BLOCK CODES USING THE VITERBI ALGORITHM

Algebraic ML decoding of an (n, k, d_{min}) linear block code, with code word symbols from $GF\left(2^{\xi}\right)$, involves the comparison of the received code word with each of the $2^{\xi.k}$ valid code words, selecting the one which proves to be the closest as the most likely transmitted one. This process can be time consuming and complex, especially for codes where both n and k are large.

Conversely, the application of the VA as ML block code decoder results in the most likely path in the code's trellis, describing the received code word, to be chosen, discarding several unlikely code words along the way before even comparing them with the received one. Depending on the parameters n and k, this decoding approach may greatly reduce decoding time and complexity.

4.4.1 THE BLOCK-WISE VITERBI ALGORITHM FOR LINEAR BLOCK CODE TRELLISES

Let $\overline{c}_m$ and $\overline{y}_m$ denote the m^{th} transmitted and the received code words, respectively, associated with the message word $\overline{d}_m$. ML decoding entails obtaining the best estimate of $\overline{c}_m$, denoted by $\hat{\overline{c}}_m$, by comparing the received code word $\overline{y}_m$ with all valid code words. Since there exists a one-to-one mapping between $\overline{d}_m$ and $\overline{c}_m$, the data vector associated with $\hat{\overline{c}}_m$, denoted by $\hat{\overline{d}}_m$, shall be identical to $\overline{d}_m$, if and only if $\hat{\overline{c}}_m = \overline{c}_m$. If $\hat{\overline{c}}_m \neq \overline{c}_m$, a decoding error is incurred. Thus, the decoding rule whereby an ML decoder chooses the optimal estimate $\hat{\overline{c}}_m$, given $\overline{y}_m$, is by minimising the probability of a decoding error. Assuming equiprobable message words, the probability of decoding error is minimised if the overall *log-likelihood function* $\ln\left(\text{Prob.}\left(\overline{y}_m|\hat{\overline{c}}_m\right)\right)$ is maximised, where Prob. $\left(\overline{y}_m|\hat{\overline{c}}_m\right)$ represents the conditional probability of receiving the code word $\overline{y}_m$, given that $\hat{\overline{c}}_m$ was the transmitted code word. The VA accomplishes this by, moving from trellis depth 0 to n, systematically discarding paths that do not maximise the overall log-likelihood function, $\ln\left[\text{Prob.}\left(\overline{y}_m|\hat{\overline{c}}_m\right)\right]$.

Since every branch in an expurgated trellis represents a symbol in a valid code word, finding the most likely path involves comparing each incoming symbol (hard decision) or sample (soft decision) of the received vector to the corresponding branch symbols. For non-binary codes, this can be done on a symbol level or on a bit level, depending on the application. For example, when an RS block code's code word symbols are transmitted as equivalent bit streams, bit level comparison will be used by the VA trellis decoder. In this dissertation only bit level comparison is considered.

Before describing the VA, as applied to block code trellises, the concept of a *metric* is introduced: In the broad sense, a metric is a measure of similarity between two entities. True to this general definition, VA decoding entails the calculation of branch and path metrics (based on the computation of log-likelihood values) in order to indicate the degree of similarity between the received bits/samples of the m^{th} transmitted code word and the valid code word paths in the code's trellis. Assuming that the $n.\xi$ received bits/samples representing the n transmitted $GF\left(2^{\xi}\right)$ code word symbols are statistically independent, the mathematical definition of the branch metric, indicating the similarity between m^{th} received code word's i^{th} set of ξ received and demodulated bits/samples (denoted by $\overline{y}_{m,i}$) and the branch weight vector of the j^{th} branch leaving node l at a trellis depth of i (denoted by $\overline{u}_{i,l}^{(j)}$) is given by:

$$\begin{aligned} BM_{m,i,l}^{(j)} &= \ln\left[\text{Prob.}\left(\overline{y}_{m,i}|\overline{u}_{i,l}^{(j)}\right)\right] \\ &= \ln\left[\prod_{a=0}^{\xi-1}\text{Prob.}\left(y_{m,i,a}|u_{i,l,a}^{(j)}\right)\right] \\ &= \sum_{a=0}^{\xi-1}\ln\left[\text{Prob.}\left(y_{m,i,a}|u_{i,l,a}^{(j)}\right)\right] \end{aligned} \tag{4.25}$$

where $y_{m,i,a}$ denotes the a^{th} element of the i^{th} ξ-tuple vector $\overline{y}_{m,i}$ of demodulated bits/samples, and $u_{i,l,a}^{(j)}$ the a^{th} branch weight vector element of the j^{th} branch leaving node (l,i). Several hard and soft decision methods whereby $BM_{m,i,l}^{(j)}$ can be calculated are discussed in *Section* 4.4.2.

As input samples (soft decision decoding) or bits (hard decision decoding) are received, path metrics are computed, indicating the probability that a certain path through the trellis, starting at node $(0,0)$ and ending in node $(0,n)$, represents the transmitted code word. The VA for linear block codes therefore operates in a block-wise fashion, whereas a more traditional sliding window approach is used for convolutional code decoding [106].

Since there are $2^{\xi.(n-k)}$ states in the trellis, there will be $2^{\xi.(n-k)}$ path metrics. At a decoding depth of i into the trellis for the m^{th} received code word, the path metric of the survivor path ending in node (l, i), is denoted by $PM^{sur}_{m,i,l}$. The cumulative metric [47] of the j^{th} branch leaving node l at a trellis depth of i, is given by:

$$CM^{(j)}_{m,i,l} = PM^{sur}_{m,i,l} + BM^{(j)}_{m,i,l} \tag{4.26}$$

It should be noted that, although according to the general modus operandi of ML decoders, as described at the beginning of this subsection, the probability of a decoding error is minimised if the largest path metric is chosen as the most optimal at each trellis depth, there exists certain conditions for which *Eq.* (4.25) can be simplified to such an extent that the *smallest* path metric dictates a minimum probability of decoding error. More attention is given to such scenarios in the following two subsections.

With the aforementioned definitions in mind, the forward tracing procedure performed by the VA in order to determine the survivor path metrics for the active nodes in the trellis, is as follows:

1. Set the survivor path metric $PM^{sur}_{m,0,0}$, representing the non-existent survivor path ending in node $(0, 0)$, to $PM^{sur}_{m,0,0} = 0$.

2. Set the survivor path metrics $PM^{sur}_{m,0,l}$, with $l = 1, 2, .., 2^{\xi.(n-k)} - 1$, of the non-existent survivor paths entering the other nodes at this depth to either $-\infty$ (if an increase in path metric dictates a decrease in the probability of decoding error), or ∞ (if a decrease in path metric dictates a decrease in the probability of decoding error).

3. At decoding time instance m, $n.\xi$ bits or samples are received, which are contained within the vector $\overline{y}_m$. Using this vector, the forward tracing procedure that determines the survivor path metrics associated with the $2^{\xi.(n-k)}$ paths through the trellis are as follows:

   (a) Begin decoding at a trellis depth of $i = 0$.

   (b) For every node (l, i) at a trellis depth of i that has exiting branches, proceed as follows:

      i. Calculate the cumulative metric $CM^{(j)}_{m,i,l}$ for the j^{th} branch leaving node (l, i) using *Eq.* (4.26).

      ii. For every node $(b, i + 1)$ at a trellis depth of $i + 1$ that has incoming branches, set the survivor path metric $PM^{sur}_{m,i+1,b}$ equal to the most optimal cumulative metric calculated for these incoming branches. Discard all the branches entering node $(b, i + 1)$, except the branch associated with the most optimal cumulative metric.

   (c) Repeat step (b) for $i = 1, 2, .., n - 1$.

When the procedure as outlined above is followed, only one complete path, starting at node $(0, 0)$ and ending in node $(0, n)$, will survive. Hence, the m^{th} most likely transmitted code word can be found by noting the entries in the output branch vectors of the branches in this surviving path.

After acquiring the most likely transmitted code word using the VA, a conventional algebraic decoding method can be employed to obtain the associated k-symbol message word. In the case of a systematic block code, the associated message word is simply the k systematic symbols of the VA decoded n-symbol code word.

4.4.2 HARD VERSUS SOFT DECISION DECODING

If demodulated data samples are processed by the VA immediately after demodulation, without any previous decisions having been made, the decoding process is called *soft decision decoding*. Alter-

natively, if the demodulated samples are classified as 1s and 0s prior to VA decoding, it is referred to as *hard decision decoding*. It has been shown [47] that soft decision decoding shows an asymptotic BER performance gain of approximately 2.1 dB over hard decision decoding for binary transmitted data in AWGN channel (see *Section* 2.2) conditions. This can be attributed to the fact that the entropy of an analogue information source, such as the output of a demodulator, is decreased by hard decision processing, i.e. 1-bit analogue to digital conversion [47]. Thus, less information is utilised during hard decision metric calculations than with soft decision metric calculations, resulting in poorer BER performances. Unfortunately, soft decision decoding's gain comes at the price of higher implementation hardware complexity, i.e. the need for high precision *Analogue-to-Digital Converter*s (ADC) and DSPs. The following subsections briefly outline branch metric calculation methods for both hard and soft decision decoding.

4.4.2.1 HARD DECISION DECODING

Two hard decision decoding branch metric calculation methods are described in this subsection. The first, which employs the *Binary Symmetric Channel* (BSC) [47] crossover probability P_{BSC}, calculates the branch metric as follows:

$$BM_{m,i,l}^{(j)} = \sum_{a=0}^{\xi-1} \begin{cases} \ln(1-P_{BSC}) & \text{if } y_{m,i,a} = u_{i,l,a}^{(j)} \\ \ln(P_{BSC}) & \text{if } y_{m,i,a} \neq u_{i,l,a}^{(j)} \end{cases} \tag{4.27}$$

The second method, which is simpler to implement in hardware, uses the Hamming distance (see *Section* 3.2.2.2) between the input bit sequence and branch weight vector to calculate the branch metric:

$$BM_{m,i,l}^{(j)} = d_H\left(\overline{y}_{m,i}, \overline{u}_{i,l}^{(j)}\right) \tag{4.28}$$

where the Hamming distance is defined as the number of bits that $\overline{y}_{m,i}$ and $\overline{u}_{i,l}^{(j)}$ differ, i.e.:

$$d_H\left(\overline{y}_{m,i}, \overline{u}_{i,l}^{(j)}\right) = \sum_{a=0}^{\xi-1} \begin{cases} 0 & \text{if } y_{m,i,a} = u_{i,l,a}^{(j)} \\ 1 & \text{if } y_{m,i,a} \neq u_{i,l,a}^{(j)} \end{cases} \tag{4.29}$$

It should be apparent that the size of a path metric and the probability of decoding error are directly proportional for the latter calculation method, whereas an indirect proportionality exists for the branch metric calculation method of *Eq.* (4.27).

4.4.2.2 SOFT DECISION DECODING

Assume that the linear block code encoder output bits of the m^{th} transmitted code were modulated and transmitted over a mobile radio channel exhibiting both slow flat (see *Section* 2.5.1.1) fading (see *Section* 2.5.1.1) and AWGN channel (see *Section* 2.2) effects. The demodulator output is described by *Eq.* (3.57), having the PDF given in *Eq.* (3.58). Using *Eq.* (3.58), the probability Prob. $\left(y_{m,i,a}|u_{i,l,a}^{(j)}\right)$ can easily be calculated [47], an exercise which is not repeated here. Employing this probability in *Eq.* (4.25), removing all factors and terms that are common to all cumulative metrics calculated at a trellis depth of i, it follows that the general expression for the VA branch metric calculation for soft decision decoding with fading amplitude CSI, is given by [60]:

$$BM_{m,i,l}^{(j)} = \sum_{a=0}^{\xi-1} \left(y_{m,i,a} - \hat{\overline{\alpha}}_{m,i,a}.u_{i,l,a}^{(j)}\right)^2 \tag{4.30}$$

where $\hat{\bar{\alpha}}_{m,i,a}$ is an estimate of the average fading amplitude associated with $y_{m,i,a}$. Once again the size of a branch metric is directly proportional to the probability of decoding error. This metric calculation method can also be readily applied to hard decision decoding. Completing the square and further removing common factors and terms, *Eq.* (4.30) simplifies to:

$$BM_{m,i,l}^{(j)} = \sum_{a=0}^{\xi-1} \left(2.y_{m,i,a}.\hat{\bar{\alpha}}_{m,i,a}.u_{i,l,a}^{(j)} - \left(\hat{\bar{\alpha}}_{m,i,a}.u_{i,l,a}^{(j)} \right)^2 \right) \tag{4.31}$$

Yet another simplification can be performed if antipodal code bit representation is used, i.e. the branch weight vectors have elements from the alphabet $\{-1, 1\}$, since $\left(u_{i,l,a}^{(j)} \right)^2 = 1$ for all branches at a trellis depth of i, resulting in:

$$BM_{m,i,l}^{(j)} = \sum_{a=0}^{\xi-1} y_{m,i,a}.\hat{\bar{\alpha}}_{m,i,a}.u_{i,l,a}^{(j)} \tag{4.32}$$

It should be noted that *Eq.* (4.32) now describes a branch metric calculation method where an increase in the path metric dictates a decrease in the probability of decoding error.

In the event that the receiver achieves perfect coherent demodulation, but no fading amplitude information is available (or only AWGN channel effects are present), the VA employs any of the above soft decision branch metric calculation methods with $\hat{\bar{\alpha}}_{m,i,a} = 1$.

4.5 ANALYTICAL BIT-ERROR-RATE PERFORMANCE EVALUATION OF VITERBI DECODED LINEAR BLOCK CODES

The following subsections briefly presents BER performance upper bounds for VA or classic ML decoded binary linear block codes in AWGN (see *Section* 2.2) and flat (see *Section* 2.5.1.1) Rayleigh (see *Section* 2.5.2.1) fading channel conditions, assuming they are employed in narrowband QPSK systems (see *Section* 5.2).

4.5.1 AWGN CHANNEL BIT-ERROR-RATE PERFORMANCE UPPER BOUND

Assuming coherent demodulation and ML decoding, the BER performance for a narrowband QPSK system employing an (n, k, d_{min}) binary linear block code, operating in AWGN channel conditions (see *Section* 2.2), is upper bounded as follows [63, 100, 151]::

$$P_b(e) \leq \sum_{h=d_{\min}}^{n} \left[\left(\sum_{w=1}^{k} \frac{w}{k} A_{w,h} \right) Q\left(\sqrt{2.h.R_c \frac{E_b}{N_0}} \right) \right] \tag{4.33}$$

where $R_c = k/n$, E_b is the energy per message word bit, N_0 is the single sided PSD of the AWGN, $Q(\cdot)$ represents the Q-function, and $\{A_{w,h}\}$ are the coefficients of the block code's IOWEF, as defined by *Eq.* (3.21) in *Section* 3.2.2.2. Defining the following constant:

$$B_h = \sum_{w=1}^{k} \frac{w}{k} A_{w,h} \tag{4.34}$$

the upper bound of *Eq.* (4.33) can be further simplified:

$$P_b(e) \leq \sum_{h=d_{\min}}^{n} B_h.Q\left(\sqrt{2.h.R_c\frac{E_b}{N_0}}\right) \tag{4.35}$$

Note that $k.B_h$ represents the total Hamming weight of all message words that yield code words of Hamming weight h. *Eq.* (4.35) suggests that there are two possible methods to decrease the BER of the block coded QPSK system:

- The BER of the system can be reduced by increasing d_{min}. This is the classic approach taken by block code designers. In addition, a well designed block code keeps the number of minimum distance code words as small as possible.
- By reducing B_h of the most significant terms in *Eq.* (4.35), which corresponds to the lowest weight code words, the BER can be reduced. This is the technique employed by PCC coding schemes [66].

4.5.2 SLOW RAYLEIGH FLAT FADING CHANNEL BIT-ERROR-RATE PERFORMANCE UPPER BOUND

Let the code word bits generated by an (n, k, d_{min}) binary linear block code be modulated by a QPSK transmitter and transmitted over flat Rayleigh fading channel (see *Section* 2.5.1.1 and *Section* 2.5.2.1). For simplicity, it is assumed that each transmitted code word bit experiences independent Rayleigh fading. This assumption is valid for a fully interleaved (see *Section* 3.2.3) flat Rayleigh fading channel where the fading amplitudes of the respective transmitted code word bits are IID stochastic variables. If the QPSK receiver achieves perfect coherent demodulation, ML decoding results in the following BER bound, conditioned on $\gamma_{c,m}^h$, the SNR per code word for the m^{th} code word of Hamming weight h [151]:

$$P_b\left(e|\gamma_{c,m}^h\right) \leq \sum_{h=d_{\min}}^{n}\left[\left(\sum_{w}^{k}\frac{w}{k}A_{w,h}\right)Q\left(\sqrt{2.R_c.\gamma_{c,m}^h}\right)\right] \tag{4.36}$$

where $R_c = k/n$, $Q(\cdot)$ represents the Q-function, and $\{A_{w,h}\}$ are the coefficients of the linear block code's IOWEF (see *Section* 3.2.2.2). The SNR per code word in this equation, is given by [151]:

$$\gamma_{c,m}^h = \sum_{i=0}^{h-1}\frac{E_b}{N_0}\overline{\alpha}_{m,i}^2 = \sum_{i=0}^{h-1}\gamma_{b,m,i} \tag{4.37}$$

where $\overline{\alpha}_{m,i}$ is the average fading amplitude experienced by the i^{th} received code word bit in the m^{th} code word. Furthermore, it is assumed that the fading amplitude is approximately constant over a code word symbol period under slow fading conditions. Since $\overline{\alpha}_{m,i}$ is a stochastic variable with a Rayleigh PDF, it follows that $\gamma_{b,m,i} = E_b/N_0.\overline{\alpha}_{m,i}^2$ has a chi-squared PDF with two degrees of freedom, given by *Eq.* (5.22) in *Section* 5.2.4.2 [47, 152]. Thus, it can be shown that the PDF of $\gamma_{c,m}^h$, denoted by $\rho\left(\gamma_{c,m}^h\right)$, resembles *Eq.* (5.45) in *Section* 5.3.4. Finally, obtaining an averaged BER performance upper bound necessitates averaging $P_b\left(e|\gamma_{c,m}^h\right)$ over the PDF of $\gamma_{c,m}^h$ [151, 152]:

$$\begin{aligned} P_b(e) &\leq \int_0^{\infty} P_b\left(e|\gamma_{c,m}^h\right)\rho\left(\gamma_{c,m}^h\right)d\gamma_{c,m}^h \\ &= \frac{1}{2}\sum_{h=d_{min}}^{n}\left(\sum_{w=1}^{k}\frac{w}{h}A_{w,h}\right)\left[\frac{1}{1+R_c.\overline{E}_b/N_0}\right]^h = \frac{1}{2}\sum_{h=d_{min}}^{n}B_h\left[\frac{1}{1+R_c.\overline{E}_b/N_0}\right]^h \end{aligned} \tag{4.38}$$

where the constant of *Eq.* (4.34) has been employed and $\overline{E}_b$ represents the average energy per message word bit. By assuming a fully interleaved channel, this bound will be loose when used to study block coded QPSK systems functioning in Rayleigh fading channels exhibiting a high level of correlation, i.e. slow fading (see *Section* 2.5.1.2) and no channel interleaving. A tighter upper bound, which takes the Doppler spread (see *Section* 2.4.3.3) of the slow fading channel into account, is presented in [69, 153]. However, this bound is more cumbersome to calculate than *Eq.* (4.38).

4.6 CONCLUDING REMARKS

This chapter considered the VA decoding of binary and non-binary linear block codes. Firstly, a detailed description was given of the BCJR trellis construction technique for linear block codes, followed by novel trellis complexity calculation and reduction techniques. Next followed an in-depth discussion on the block-wise VA as applied to BCJR trellises. Several hard and soft decision branch metric calculation methods, employing CSI, were considered. Lastly, BER bounds were presented for AWGN and slow Rayleigh flat fading channels. The main contributions of this chapter are the following:

1. *Section* 4.2.1 presents "The Complete Idiots Guide to..." for the construction of unexpurgated BCJR linear block code trellises. The simple step-by-step algorithm presented is applicable to both binary and non-binary linear block codes.

2. A novel BCJR trellis expurgation scheme is presented in *Section* 4.2.2. This algorithm can be used to prune both binary and non-binary BCJR linear block code trellises to contain only paths representing valid code words.

3. *Section* 4.3.1 describes a method whereby the trellis complexity of BCJR trellises for binary and non-binary linear block codes can be calculated (or at least closely estimated). This is then followed in *Section* 4.3.2 by a rudimentary technique that can be used to reduce the complexity of the BCJR trellis structures for binary linear block codes.

4. In *Section* 4.4.1 the classic block-wise VA, applicable to BCJR linear block code trellises, is presented. *Section* 4.4.2.2 gives attention to the inclusion of fading amplitude CSI into the branch metric calculations used during soft decision decoding.

CHAPTER FIVE

PERFORMANCE EVALUATION PLATFORMS

5.1 CHAPTER OVERVIEW

THE first part of this chapter details the operation of the general baseband complex QPSK transmitter and receiver structures [81] employed in the AWGN and flat fading channel simulations of *Chapter* 6. Also briefly described is the estimation of the average fading amplitude associated with each of the individual demodulated QPSK receiver output data bit estimates. Analytical BER performances for uncoded coherently demodulated QPSK communication systems, functioning in a variety of mobile radio channel conditions, is the final topic discussed in this part of the chapter.

The baseband complex DS/SSMA QPSK transmitter and RAKE receiver structures [47] employed in the frequency selective fading channel simulations of *Chapter* 6 are the first topics discussed in the second part of this chapter. This is followed by a discussion on the estimation of the average fading amplitude associated with each of the RAKE receiver output data bit estimates. A concise derivation of an approximate BER curve for the wideband transmitter and RAKE receiver structures concludes this part of the chapter.

Considered in the third and final part of this chapter is the general simulation platforms employed in *Chapter* 6. This includes the transmitter and receiver setups for both the narrowband QPSK and wideband DS/SSMA QPSK communication systems employed, as well as a comprehensive overview of the wide variety of AWGN, flat fading and multipath fading channel configurations considered.

5.2 NARROWBAND COMPLEX QPSK COMMUNICATION SYSTEMS

The following subsections describe the general transmitter and receiver structures, as well as the analytic BER performances, of the complex QPSK communication system employed in the AWGN and flat fading channel simulations of *Chapter* 6. These baseband models were designed to be used in conjunction with the complex flat fading channel simulator shown in *Fig.* 2.5, negating the need for unnecessary carriers and subsequent high sampling frequencies during the simulations.

5.2.1 COMPLEX QPSK TRANSMITTER STRUCTURE AND OPERATION

Shown in *Fig.* 5.1 is the general structure of a baseband complex QPSK transmitter [47]. Let the m^{th} set of W antipodal coded or uncoded data bits that are to be transmitted by the complex

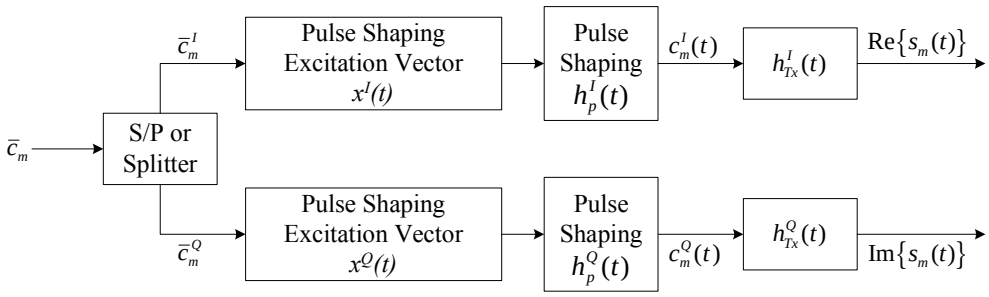

Figure 5.1: Complex QPSK Transmitter Structure

QPSK transmitter, having values from the antipodal alphabet $\{1, -1\}$, be contained in the vector $\bar{c}_m = \{c_{m,0}, c_{m,1}, ..., c_{m,W-1}\}$.

The first action taken by the transmitter is to subdivide this input data stream vector into I-channel and Q-channel symbol stream vectors according to one of two possible methods: The classic method, commonly referred to as unbalanced or dual-channel modulation, entails subdividing $\bar{c}_m$ into distinct length-$W/2$ I-channel and Q-channel symbol streams using a *serial-to-parallel* converter (denoted by the block S/P in *Fig.* 5.1). These I-channel and Q-channel symbol streams are given by:

$$\bar{c}_m^I = \{c_{m,0}^I, c_{m,1}^I, ..., c_{m,W/2-1}^I\} = \{c_{m,0}, c_{m,2}, c_{m,4}, ..., c_{m,W-2}\} \tag{5.1}$$

and:

$$\bar{c}_m^Q = \{c_{m,0}^Q, c_{m,1}^Q, ..., c_{m,W/2-1}^Q\} = \{c_{m,1}, c_{m,3}, c_{m,5}, ..., c_{m,W-1}\} \tag{5.2}$$

respectively. Note that the duration of a QPSK symbol is twice that of an uncoded data bit, i.e. $T_s = 2.T_b$.

Alternatively, the same data bits from $\bar{c}_m$ can be used on both the I-channel and the Q-channel, resulting in a *balanced* narrowband complex QPSK transmitter structure. With this transmitter configuration, the respective length-W I-channel and Q-channel symbol stream vectors are given by:

$$\bar{c}_m^I = \{c_{m,0}^I, c_{m,1}^I, ..., c_{m,W-1}^I\} = \{c_{m,0}, c_{m,1}, ..., c_{m,W-1}\} \tag{5.3}$$

and:

$$\bar{c}_m^Q = \{c_{m,0}^Q, c_{m,1}^Q, ..., c_{m,W-1}^Q\} = \{c_{m,0}, c_{m,1}, ..., c_{m,W-1}\} \tag{5.4}$$

Thus, a balanced complex QPSK transmitter is in essence a complex *Binary Phase Shift Keying* (BPSK) transmitter. The QPSK symbol rate is now the same as the bit rate, i.e. $T_s = T_b$.

Next, the antipodal I-channel and Q-channel symbols contained in these stream vectors are pulse shaped in order to minimise the transmission bandwidth and the ISI at the receiver. The first step in the pulse shaping process is to multiply the antipodal values with appropriate excitation signals for the pulse shaping filters. Since this study's narrowband complex QPSK simulations make use of square-root Nyquist pulse shaping filters (see *Section* 5.4.1), designed for impulse transmission [154], the following I-channel and Q-channel excitation signals are employed:

$$x^I(t) = x^Q(t) = \begin{cases} 1 & \text{if } t \bmod (T_p) = 0 \\ 0 & \text{Otherwise} \end{cases} \tag{5.5}$$

where $T_p = T_s$ is the duration of a QPSK symbol. Let the I-channel and Q-channel pulse shaping filters' impulse responses be denoted by $h_p^I(t)$ and $h_p^Q(t)$ (see *Section* 5.4.1), respectively. The m^{th} I-channel and Q-channel pulse shaping filter outputs are now:

$$c_m^I(t) = \left(\sum_{i=0}^{Y} c_{m,i}^I . x^I \left(t - i.T_s \right) \right) \otimes h_p^I(t) \tag{5.6}$$

and:

$$c_m^Q(t) = \left(\sum_{i=0}^{Y} c_{m,i}^Q . x^Q \left(t - i.T_s \right) \right) \otimes h_p^Q(t) \tag{5.7}$$

respectively, where $Y = W/2 - 1$ for dual-channel modulation, or $Y = W - 1$ for balanced modulation.

Further bandlimiting of the pulse shaped symbols are accomplished by the I-channel and Q-channel transmit filters, characterised by the respective impulse responses $h_{Tx}^I(t)$ and $h_{Tx}^Q(t)$. The outputs of these filters form the respective real and imaginary parts of the m^{th} output signal $s_m(t)$ of the complex QPSK transmitter:

$$s_m(t) = \text{Re}\left\{ s_m(t) \right\} + j.\,\text{Im}\left\{ s_m(t) \right\} = c_m^I(t) \otimes h_{Tx}^I(t) + j.c_m^Q(t) \otimes h_{Tx}^Q(t) \tag{5.8}$$

5.2.2 COMPLEX QPSK RECEIVER STRUCTURE AND OPERATION

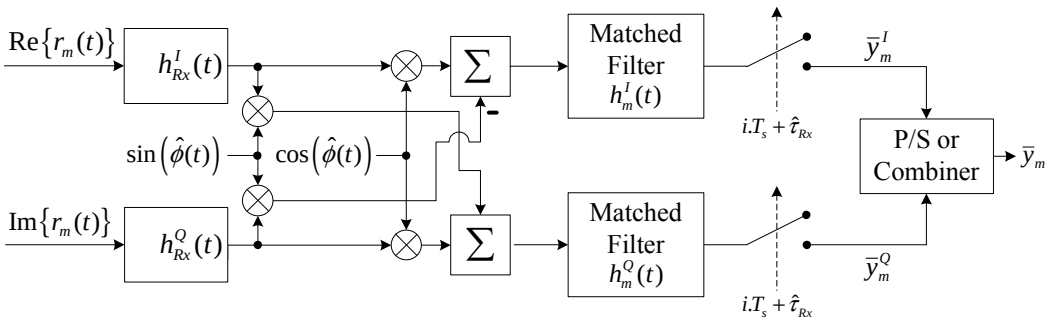

Figure 5.2: Complex QPSK Receiver Structure

The complex QPSK receiver structure [47] associated with the transmitter structure discussed in *Section* 5.2.1, is shown in *Fig.* 5.2. Assume that the m^{th} complex QPSK output signal $s_m(t)$ has been adversely effected by AWGN and flat fading channel effects, yielding the complex receiver input signal $r_m(t)$:

$$r_m(t) = \text{Re}\left\{ r_m(t) \right\} + j.\,\text{Im}\left\{ r_m(t) \right\} = \left(\text{Re}\left\{ s_m(t) \right\} + j.\,\text{Im}\left\{ s_m(t) \right\} \right) . \varpi(t) + \eta(t) \tag{5.9}$$

where $\varpi(t)$ is a complex flat fading process, defined by *Eq.* (2.46). The AWGN $\eta(t)$ is also a complex process:

$$\eta(t) = \text{Re}\left\{ \eta(t) \right\} + j.\,\text{Im}\left\{ \eta(t) \right\} \tag{5.10}$$

The complex QPSK receiver functions as follows: Firstly, the real and imaginary parts of the complex receiver input signal $r_m(t)$ are filtered by the lowpass receive filters $h_{Rx}^I(t)$ and $h_{Rx}^Q(t)$, respectively, in order to bandlimit the AWGN entering the receiver. The outputs of the receive filters are phase corrected to create the in-phase and quadrature coherent inputs for the in-phase matched filter $h_m^I(t)$ and quadrature matched filter $h_m^Q(t)$, respectively. The outputs of the in-phase and quadrature matched

filters are sampled at time instance $i.T_s + \hat{\tau}_{Rx}$ to give:

$$y^I_{m,i} = \Big[\Big(\big[h^I_{Rx}(t) \otimes \mathrm{Re}\{r_m(t)\}\big] \cos\Big(\hat{\phi}(t)\Big) - \Big[h^Q_{Rx}(t) \otimes \mathrm{Im}\{r_m(t)\}\Big] \sin\Big(\hat{\phi}(t)\Big)\Big) \otimes h^I_m(t)\Big]_{t=i.T_s+\hat{\tau}_{Rx}} \tag{5.11}$$

and:

$$y^Q_{m,i} = \Big[\Big(\Big[h^Q_{Rx}(t) \otimes \mathrm{Im}\{r_m(t)\}\Big] \sin\Big(\hat{\phi}(t)\Big) + \big[h^I_{Rx}(t) \otimes \mathrm{Re}\{r_m(t)\}\big] \cos\Big(\hat{\phi}(t)\Big)\Big) \otimes h^Q_m(t)\Big]_{t=i.T_s+\hat{\tau}_{Rx}} \tag{5.12}$$

respectively, where $\hat{\phi}(t)$ is the sum of an estimate of the channel phase alteration experienced by the transmitted signal (see *Section* 3.3.5) and the phase distortion introduced by the receive filters. The parameter $\hat{\tau}_{Rx}$ is an estimate of the time delay a complex QPSK symbol experiences due to the receive filters. These sampled matched filter outputs are then stored in the vectors $\overline{y}^I_m = \{y^I_{m,0}, y^I_{m,1}, ..., y^I_{m,W/2-1}\}$ and $\overline{y}^Q_m = \{y^Q_{m,0}, y^Q_{m,1}, ..., y^Q_{m,W/2-1}\}$, respectively.

The final action taken by the complex QPSK receiver is to create the resultant receiver output vector $\overline{y}_m$, which is an estimate of the original data bit vector $\overline{c}_m$ used by the transmitter as input (see *Section* 5.2.1): For dual-channel modulation, $\overline{y}_m$ is constructed by interweaving the m^{th} I-channel and Q-channel estimate vectors using a *parallel-to-serial* converter (denoted by the block P/S in *Fig.* 5.2), whereas with balanced modulation, $\overline{y}^I_m$ and $\overline{y}^Q_m$ are linearly combined to form $\overline{y}_m$.

5.2.3 AVERAGE FADING AMPLITUDE CALCULATION FOR COMPLEX QPSK SYSTEMS

Calculation of the average fading amplitude, associated with each output estimate contained in the vector $\overline{y}_m$, is accomplished by filtering an estimate of the instantaneous fading amplitude using an averaging filter $h_{ave}(t)$ which has an impulse response identical to the matched filters used in *Fig.* 5.2. Extraction of the average fading amplitude from this filter differs for balanced and unbalanced transmitter configurations: With balanced modulation the i^{th} symbols transmitted on the I-channel and Q-channel are identical. Hence, an estimate of the average fading amplitude associated with the i^{th} element in $\overline{y}_m$ is determined as follows:

$$\hat{\overline{\alpha}}_{m,i} = [\hat{\alpha}(t) \otimes h_{ave}(t)]_{t=i.T_s+\hat{\tau}_{Rx}} \tag{5.13}$$

where $\hat{\alpha}(t)$ represents an estimate of the instantaneous fading amplitude, as described by *Eq.* (2.9) for the trivial case of a single path multipath channel. Considering dual-channel modulation, recall from *Section* 5.2.1 that the i^{th} I-channel and Q-channel symbols are transmitted simultaneously. Therefore, it is apparent that they will experience the same instantaneous amplitude fading (see *Section* 2.4.1). Hence, an estimate of the average fading amplitudes associated with the $(2.i)^{\text{th}}$ and $(2.i+1)^{\text{th}}$ elements in the output vector $\overline{y}_m$ is obtained as follows:

$$\hat{\overline{\alpha}}_{m,(2.i)} = \hat{\overline{\alpha}}_{m,(2.i+1)} = [\hat{\alpha}(t) \otimes h_{ave}(t)]_{t=(2.i).T_s+\hat{\tau}_{Rx}} \tag{5.14}$$

5.2.4 ANALYTICAL BIT ERROR PROBABILITIES OF UNCODED NARROWBAND COMPLEX QPSK COMMUNICATION SYSTEMS

5.2.4.1 AWGN CHANNEL CONDITIONS

Assuming coherent demodulation, it can be shown that the symbol error probability for a dual-channel QPSK system functioning in AWGN channel (see *Section* 2.2) conditions is given by [81]:

$$P_s\left(e\right) = 2Q\left(\sqrt{\gamma_{s,m,i}}\right) - \frac{1}{2}\left[Q\left(\sqrt{\gamma_{s,m,i}}\right)\right]^2 \tag{5.15}$$

where $Q(\,.\,)$ denotes the Q-function [47]. The SNR per QPSK symbol for the i^{th} symbol in the m^{th} set of symbols, denoted by $\gamma_{s,m,i}$, is defined as follows:

$$\gamma_{s,m,i} = \frac{E_s}{N_0} \tag{5.16}$$

where E_s is the energy per transmitted symbol and N_0 is the single sided PSD of the AWGN. Note that the squared term in *Eq.* (5.15) becomes negligible if $\gamma_{s,m,i}/2 >> 1$ [81]. Thus, it is commonplace to approximate *Eq.* (5.15) with:

$$P_s\left(e\right) \simeq 2Q\left(\sqrt{\gamma_{s,m,i}}\right) \tag{5.17}$$

Recall that two data bits are transmitted per symbol in an uncoded dual-channel narrowband QPSK system. Hence, the energy per bit is simply $E_b = E_s/2$ [J]. Thus, employing Gray mapping of bits to QPSK symbols, the bit error probability of such a system can be approximated by [81]:

$$P_b\left(e\right) = \left.\frac{P_s\left(\gamma_{s,m,i}\right)}{2}\right|_{\gamma_{s,m,i}=2.\gamma_{b,m,i}} \simeq Q\left(\sqrt{2.\gamma_{b,m,i}}\right) \tag{5.18}$$

where $\gamma_{b,m,i}$ is the SNR per bit for the i^{th} bit in the m^{th} vector of data bits, given by:

$$\gamma_{b,m,i} = \frac{E_b}{N_0} \tag{5.19}$$

In *Section* 5.2.1 it is stated that a QPSK transmitter configured for balanced modulation is essentially a BPSK transmitter. Thus, the bit error probability for a balanced QPSK communication system in AWGN channel conditions will be given by [81]:

$$P_b\left(e\right) = Q\left(\sqrt{2.\gamma_{b,m,i}}\right) = Q\left(\sqrt{\frac{2E_b}{N_0}}\right) \tag{5.20}$$

where *Eq.* (5.19) remains valid. Thus, the BER for balanced and unbalanced narrowband QPSK systems are essentially the same.

5.2.4.2 SLOW RAYLEIGH FLAT FADING CHANNEL CONDITIONS

Assume a narrowband QPSK signal (balanced or unbalanced) is transmitted through a slow (see *Section* 2.5.1.2) Rayleigh (see *Section* 2.5.2.1) flat fading (see *Section* 2.5.1.1) channel. If the multiplicative fading process is slow enough that the Rayleigh distributed fading amplitude may be regarded as a constant during at least one symbol interval, i.e. $\alpha_{m,i}(t) = \overline{\alpha}_{m,i}$ for the i^{th} bit in the m^{th} message bit vector, the system's SNR per bit is given by [47, 152]:

$$\gamma_{b,m,i} = \overline{\alpha}_{m,i}^2 \frac{E_b}{N_0} \tag{5.21}$$

The $\overline{\alpha}_{m,i}^2$ is time-invariant with a *chi-squared* PDF with two degrees of freedom. Hence, $\gamma_{b,m,i}$ is a stochastic variable, which also has a chi-squared PDF with two degrees of freedom, given by [47,152]:

$$\rho\left(\gamma_{b,m,i}\right) = \frac{1}{\overline{\gamma}_{b,m,i}} \exp\left(-\frac{\gamma_{b,m,i}}{\overline{\gamma}_{b,m,i}}\right) \qquad \text{for } \gamma_{b,m,i} \geqslant 0 \tag{5.22}$$

where $\overline{\gamma}_{b,m,i}$ is the average SNR per bit, given by [47, 152]:

$$\overline{\gamma}_{b,m,i} = E\left[\overline{\alpha}_{m,i}^2\right] \frac{E_b}{N_0} = \frac{\overline{E}_b}{N_0} \tag{5.23}$$

In this equation $\overline{E}_b$ is the average energy per bit and $E[\,.\,]$ denotes expectation. Since the derivation of the bit error probabilities of *Eq.* (5.18) and *Eq.* (5.20) were done for non-faded channel conditions, i.e. $\overline{\alpha}_{m,i} = 1$, these equations can be viewed as conditional error probabilities, with the condition that $\overline{\alpha}_{m,i}$ remains fixed. Therefore, obtaining the average bit error probability for balanced and unbalanced narrowband QPSK systems when $\overline{\alpha}_{m,i}$ is random, necessitates averaging $P_b\left(e|\gamma_{b,m,i}\right)$ over the PDF of $\gamma_{b,m,i}$ [47, 152]:

$$\begin{aligned} P_b\left(e\right) &= \int_0^\infty P_b\left(e|\gamma_{b,m,i}\right) \rho\left(\gamma_{b,m,i}\right) d\gamma_{b,m,i} \\ &= \frac{1}{2}\left(1 - \sqrt{\frac{\overline{\gamma}_{b,m,i}}{1+\overline{\gamma}_{b,m,i}}}\right) \\ &= \frac{1}{2}\left(1 - \sqrt{\frac{\frac{\overline{E}_b}{N_0}}{1+\frac{\overline{E}_b}{N_0}}}\right) \end{aligned} \tag{5.24}$$

5.3 RAKE RECEIVER-BASED COMPLEX DS/SSMA QPSK COMMUNICATION SYSTEMS

In the following subsections the RAKE receiver-based complex DS/SSMA QPSK communication system, employed in the multipath fading channel simulations of *Chapter* 6, is presented. Thorough descriptions of the transmitter and receiver structures are followed by a theoretical BER performance analysis of the system. The complex transmitter and receiver models presented here were designed to be used in conjunction with the complex multipath fading channel simulator shown in *Fig.* 2.8, once again negating the need for unnecessary carriers and subsequent high simulation sampling frequencies.

5.3.1 COMPLEX DS/SSMA QPSK TRANSMITTER STRUCTURE AND OPERATION

Fig. 5.3 depicts the generic structure of the baseband complex DS/SSMA QPSK transmitter of user-q in a multi-user CDMA system [43, 47]. Assume that the m^{th} input to this transmitter is $\overline{c}_m^q = \{c_{m,0}^q, c_{m,1}^q, ..., c_{m,W-1}^q\}$, which is a vector containing W antipodal bits with values from the alphabet $\{1, -1\}$. As shown in *Fig.* 5.3, two options are available for the initial processing of this vector of data bits: The first option is to subdivide it using a serial-to-parallel converter (denoted by the block S/P in *Fig.* 5.3) into distinct I-channel and Q-channel symbol stream vectors, given by:

$$\overline{c}_m^{I,q} = \{c_{m,0}^{I,q}, c_{m,1}^{I,q}, ..., c_{m,W/2-1}^{I,q}\} = \{c_{m,0}^q, c_{m,2}^q, c_{m,4}^q, ..., c_{m,W-2}^q\} \tag{5.25}$$

and

$$\overline{c}_m^{Q,q} = \{c_{m,0}^{Q,q}, c_{m,1}^{Q,q}, ..., c_{m,W/2-1}^{Q,q}\} = \{c_{m,1}^q, c_{m,3}^q, c_{m,5}^q, ..., c_{m,W-1}^q\} \tag{5.26}$$

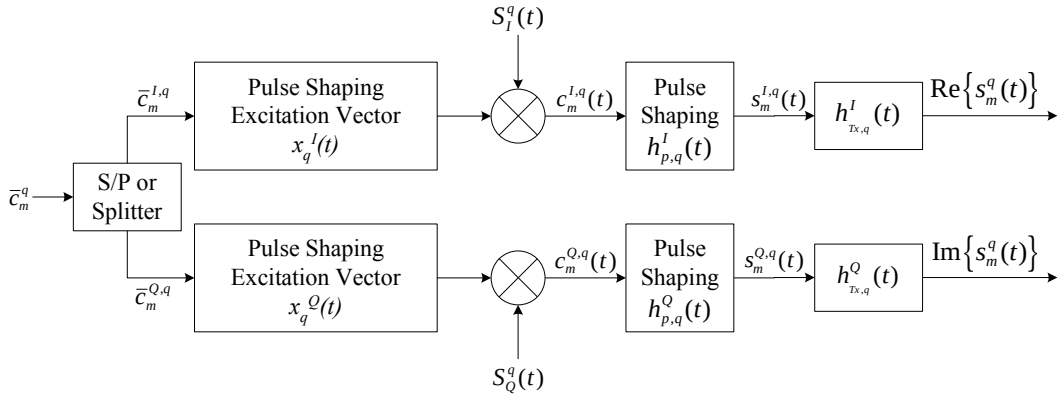

Figure 5.3: Complex DS/SSMA QPSK Transmitter Structure

respectively. This approach is frequently used when binary spreading sequences are employed in the DS/SSMA QPSK system. The symbol rate of the transmitter is half the uncoded bit rate, i.e. $T_s = 2.T_b$.

The second option is to use the same data bits on both the I-channel and Q-channel, creating a *balanced* complex DS/SSMA QPSK transmitter structure [43, 46, 50, 51] with length-W I-channel and Q-channel symbols stream vectors, given by:

$$\bar{c}_m^{I,q} = \{c_{m,0}^{I,q}, c_{m,1}^{I,q}, ..., c_{m,W-1}^{I,q}\} = \{c_{m,0}^{q}, c_{m,1}^{q}, ..., c_{m,W-1}^{q}\} \tag{5.27}$$

and

$$\bar{c}_m^{Q,q} = \{c_{m,0}^{Q,q}, c_{m,1}^{Q,q}, ..., c_{m,W-1}^{Q,q}\} = \{c_{m,0}^{q}, c_{m,1}^{q}, ..., c_{m,W-1}^{q}\} \tag{5.28}$$

respectively. This transmitter configuration, where the symbol and bit rates are equivalent, is frequently used in DS/SSMA QPSK systems employing pre-filtered CSSs (see *Section* D.3.2) in order to take full advantage of the spectral characteristics of the CSSs (see *Section* 6.4.3). For example, in [7, 10] such a balanced transmitter structure is employed in conjunction with ABC sequences (see *Section* D.3.2.2) to deliver SSB transmitter output signals.

The antipodal values contained in the I-channel and Q-channel symbol stream vectors are now pulse shaped. This is accomplished by first multiplying these symbols with appropriate pulse shaping excitation signals. Excitation vectors similar to those given in *Eq.* (5.5) are used, with $T_p = T_{chip}$ (the duration of a CSS chip). Square-root Nyquist pulse shaping filters (see *Section* 5.4.1), designed for impulse transmission, are used in *Chapter* 6's DS/SSMA simulations that employ unfiltered CSSs (see *Section* D.3.1). Alternatively, the simulations presented in this study that make use of filtered CSSs (see *Section* D.3.2) employ no additional pulse shaping, hence the following I-channel and Q-channel chip-level pulse shaping filter impulse responses are used in user-q's transmitter:

$$h_{p,q}^I(t) = h_{p,q}^Q(t) = \begin{cases} 1 & \text{for } 0 < t \leq T_{chip} \\ 0 & \text{Otherwise} \end{cases} \tag{5.29}$$

After multiplication with the excitation signals, the I-channel and Q-channel are spreaded with user-q's I-channel and Q-channel spreading sequences, denoted by $S_I^q(t)$ and $S_Q^q(t)$, respectively. These spreading sequences are unique to user-q. When CSSs are employed in the CDMA system, $S_I^q(t)$ and $S_Q^q(t)$ can be the real and imaginary parts of user-q's unique CSS (see *Section* D.3.1), respectively [50, 51]. Another possibility is that $S_I^q(t)$ and $S_Q^q(t)$ may be linear combinations of the real and

imaginary parts of the CSS [155]. In this study the former approach was employed, i.e. $S_I^q(t) = \mathrm{Re}\{S^q(t)\}$ and $S_Q^q(t) = \mathrm{Im}\{S^q(t)\}$. The resultant spreaded I-channel and Q-channel streams are given by:

$$c_m^{I,q}(t) = \sum_{j=0}^{Y} c_{m,j}^{I,q}.x_q^I(t - j.T_s).S_I^q(t) \tag{5.30}$$

and:

$$c_m^{Q,q}(t) = \sum_{j=0}^{Y} c_{m,j}^{Q,q}.x_q^Q(t - j.T_s).S_Q^q(t) \tag{5.31}$$

respectively, where $Y = W - 1$ or $Y = W/2 - 1$ for balanced or unbalanced (dual-channel) transmitter structures, respectively. In *Eq.* (5.30) and *Eq.* (5.31), T_s [s] is the symbol duration. The actual pulse shaping of the spreaded I-channel and Q-channel information are now accomplished using user-q's in-phase and quadrature pulse shaping filters, characterised by the impulse responses $h_{p,q}^I(t)$ and $h_{p,q}^Q(t)$, respectively. The resultant I-channel and Q-channel spreaded pulse shaped symbols are given by:

$$s_m^{I,q}(t) = c_m^{I,q}(t) \otimes h_{p,q}^I(t) \tag{5.32}$$

and:

$$s_m^{Q,q}(t) = c_m^{Q,q}(t) \otimes h_{p,q}^Q(t) \tag{5.33}$$

respectively, where $\otimes$ denotes convolution.

Lastly, the in-phase and quadrature pulse shaped symbol streams are bandlimited by the transmit filters $h_{Tx,q}^I(t)$ and $h_{Tx,q}^Q(t)$, respectively, to give user-q's complex DS/SSMA QPSK transmitter output signal:

$$\begin{aligned} s_m^q(t) &= \mathrm{Re}\{s_m^q(t)\} + j.\,\mathrm{Im}\{s_m^q(t)\} \\ &= s_m^{I,q}(t) \otimes h_{Tx,q}^I(t) + j.s_m^{Q,q}(t) \otimes h_{Tx,q}^Q(t) \end{aligned} \tag{5.34}$$

5.3.2 COMPLEX DS/SSMA QPSK RAKE RECEIVER STRUCTURE AND OPERATION

Assume that user-q's m^{th} complex DS/SSMA QPSK transmitter output signal traverses a time-invariant discrete multipath fading channel (see *Section* 2.4.1), consisting of L^q statistically independent flat fading (see *Section* 2.5.1.1) paths [156]. The average path gain and delay associated with this multipath channel's i^{th} path, for $i = 1, 2, ..., L^q$, are $\overline{\beta}_i^q$ and τ_i^q, respectively. Note that the complex input to user-q's receiver, denoted by $r_m^q(t)$, will consist not only of a distorted version of the signal generated by user-q's transmitter, but also distorted signals originating from the transmitters of the other users in the CDMA system.

Since a multipath fading channel exhibits a tapped delay line nature, it is apparent that the receiver is provided with L^q scaled replicas of the same transmitted signal, each replica experiencing flat fading, which is hopefully statistically independent from that experienced by the other replicas [47, 110]. Hence, a receiver that is capable of optimally processing the received signal, collecting the signal energy contained within each of the received multipath components, will achieve the performance of an equivalent L^q-th order diversity communication system. In 1958 *Price* and *Green* [157] proposed such a receiver structure for which the name "RAKE receiver" has been coined, since its energy accumulation action is somewhat analogous to an ordinary garden rake. *Fig.* 5.4 depicts the RAKE receiver structure [43, 47], capable of optimally processing user-q's complex received signal [158].

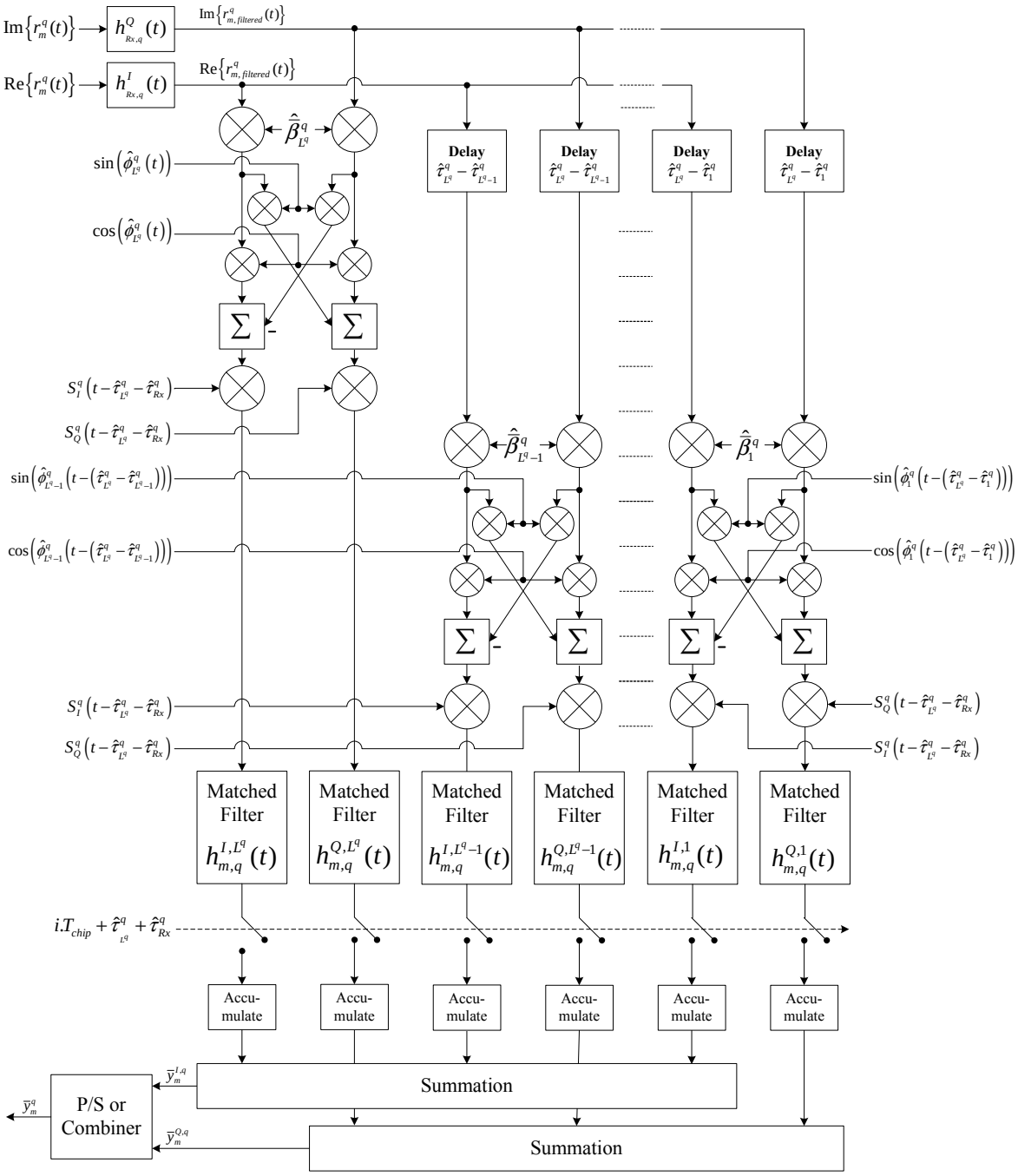

Figure 5.4: Complex DS/SSMA QPSK RAKE Receiver Structure

The first step in the demodulation process is to bandlimit the AWGN present in the complex received signal $r_m^q(t)$ using the I-channel lowpass receive filter $h_{Rx,q}^I(t)$ and Q-channel lowpass receive filter $h_{Rx,q}^Q(t)$. The resultant filtered complex received signal is given by:

$$\begin{aligned} r_{m,filtered}^q(t) &= \mathrm{Re}\left\{r_{m,filtered}^q(t)\right\} + j.\,\mathrm{Im}\left\{r_{m,filtered}^q(t)\right\} \\ &= \mathrm{Re}\left\{r_m^q(t)\right\} \otimes h_{Rx,q}^I(t) + j.\,\mathrm{Im}\left\{r_m^q(t)\right\} \otimes h_{Rx,q}^Q(t) \end{aligned} \tag{5.35}$$

Next, the noisy flat faded L^q received delayed versions of user-q's m^{th} original complex transmitted signal are realigned with the last received multipath component. This is accomplished by creating L^q delayed versions of the signal $r_{m,filtered}^q(t)$, namely $r_{m,filtered}^q\left(t-\left(\hat{\tau}_{L^q}^q-\hat{\tau}_i^q\right)\right)$, with $i=1,2,...,L^q$. The term $\hat{\tau}_i^q$ is an estimate of the path delay of the i^{th} multipath component. In order for the RAKE receiver to function optimally, it requires perfect knowledge of the path delay of each of the multipath components, i.e. $\hat{\tau}_i^q=\tau_i^q$ for $i=1,2,...,L^q$ (see *Section* 3.3.5).

Since the multipath components arriving at the receiver have experienced statistically independent flat fading and attenuation, as dictated by the power delay profile of user-q's multipath fading channel (see *Section* 2.4.2), each received component's contribution to the total realigned m^{th} complex received signal varies. In order to increase the influence of strong multipath components and decrease the influence of weak multipath components, each of the delayed complex received signal versions is scaled, prior to demodulation, with an estimate (see *Section* 3.3.5) of its average envelope amplitude (see *Section* 2.4.1). For example, the delayed filtered complex received signal $r_{m,filtered}^q\left(t-\left(\hat{\tau}_{L^q}^q-\hat{\tau}_i^q\right)\right)$ is scaled by the average envelope amplitude estimate $\hat{\overline{\beta}}_i^q$. The use of this scaling technique is commonly referred to as MRC [43, 47, 152]. Other popular RAKE combining techniques are *Equal Gain Combining* (EGC) and *Differential Phase Combining* (DPC) [158]. Optimal MRC processing of the complex received signal only occurs if the receiver has perfect knowledge of the average envelope amplitude of each of the multipath components, i.e. $\hat{\overline{\beta}}_i^q=\overline{\beta}_i^q$ for $i=1,2,...,L^q$.

Next, the receiver phase corrects each of the scaled and delayed versions of the m^{th} filtered complex received signal. For the i^{th} delayed, scaled and filtered complex received signal component $\hat{\overline{\beta}}_i^q.r_{m,filtered}^q\left(t-\left(\hat{\tau}_{L^q}^q-\hat{\tau}_i^q\right)\right)$, this is accomplished by mixing it with the complex exponent $\exp\left(-j.\hat{\phi}_i^q\left(t-\left(\hat{\tau}_{L^q}-\hat{\tau}_i^q\right)\right)\right)$. The instantaneous phase $\hat{\phi}_i^q\left(t-\left(\hat{\tau}_{L^q}-\hat{\tau}_i^q\right)\right)$ is an estimate (see *Section* 3.3.5) of the channel phase changes experienced by the i^{th} complex received multipath component at the time of its reception, as well as phase distortion added by the I-channel and Q-channel receive filters. Coherent demodulation takes place in the event that the receiver has perfect knowledge of the path delays, I-channel and Q-channel receive filter phase distortions and each of the multipath component's channel phase [86], i.e. $\hat{\phi}_i^q\left(t-\left(\hat{\tau}_{L^q}-\hat{\tau}_i^q\right)\right)=\phi_i^q\left(t-\left(\tau_{L^q}-\tau_i^q\right)\right)$ for $i=1,2,...,L^q$.

In order to despread user-q's m^{th} complex received signal, each of the L^q phase corrected I-channel and Q-channel signals are respreaded with delayed versions of user-q's I-channel and Q-channel spreading sequences, $S_I^q\left(t-\hat{\tau}_{L^q}^q-\hat{\tau}_{Rx}^q\right)$ and $S_Q^q\left(t-\hat{\tau}_{L^q}^q-\hat{\tau}_{Rx}^q\right)$, respectively. The time delays $\hat{\tau}_{L^q}^q$ and $\hat{\tau}_{Rx}^q$ introduced into the spreading sequences are estimates of the total delay experienced by the realigned set of complex received signals and the time delay introduced by the receive filters, respectively. Despreading is completely successful only if the receiver has perfect knowledge of these time delays.

Continuing the demodulation procedure, the I-channel and Q-channel despreaded signals of the i^{th} RAKE receiver tap are now processed by the respective matched filters, $h_{m,q}^{I,i}(t)$ and $h_{m,q}^{Q,i}(t)$. These

filters are matched to the chip-level pulse shaping filters employed in the DS/SSMA QPSK transmitter. The outputs of the L^q I-channel and Q-channel matched filters are sampled at time instances $t = a.T_{chip} + \hat{\tau}^q_{L^q} + \hat{\tau}^q_{Rx}$, with T_{chip} the duration of a spreading sequence chip. Each of the I-channel and Q-channel matched filter outputs are accumulated for a duration of T_s [s], whereafter the accumulated values are normalised with respect to T_s/T_{chip}. The L^q I-channel accumulated values are then linearly combined to give an estimate of the j^{th} symbol in the original transmitted I-channel symbol vector $\overline{c}^{I,q}_m$, created by the DS/SSMA QPSK transmitter:

$$\begin{aligned} y^{I,q}_{m,j} = & \frac{T_{chip}}{T_s} \sum_{i=1}^{L^q} \sum_{a=1}^{T_s/T_{chip}} \left[\left(\hat{\overline{\beta}}^q_i \left[\text{Re} \left\{ r^q_{m,filtered} \left(t - \left(\hat{\tau}^q_{L^q} - \hat{\tau}^q_i \right) \right) \right\} . \cos \left(\hat{\phi}^q_i \left(t - \left(\hat{\tau}_{L^q} - \hat{\tau}^q_i \right) \right) \right) - \right. \right. \right. \\ & \left. \left. \left. \text{Im} \left\{ r^q_{m,filtered} \left(t - \left(\hat{\tau}^q_{L^q} - \hat{\tau}^q_i \right) \right) \right\} . \sin \left(\hat{\phi}^q_i \left(t - \left(\hat{\tau}_{L^q} - \hat{\tau}^q_i \right) \right) \right) \right] \times \right. \\ & \left. S^q_I \left(t - \hat{\tau}^q_{L^q} - \hat{\tau}^q_{Rx} \right) \right) \otimes h^{I,i}_{m,q}(t) \Big]_{t = j.T_s + a.T_{chip} + \hat{\tau}^q_{L^q} + \hat{\tau}^q_{Rx}} \end{aligned} \tag{5.36}$$

Linearly combining the normalised L^q Q-channel accumulated values results in an estimate of the j^{th} symbol of the original transmitted Q-channel symbol vector $\overline{c}^{Q,q}_m$:

$$\begin{aligned} y^{Q,q}_{m,j} = & \frac{T_{chip}}{T_s} \sum_{i=1}^{L^q} \sum_{a=1}^{T_s/T_{chip}} \left[\left(\hat{\overline{\beta}}^q_i \left[\text{Im} \left\{ r^q_{m,filtered} \left(t - \left(\hat{\tau}^q_{L^q} - \hat{\tau}^q_i \right) \right) \right\} . \sin \left(\hat{\phi}^q_i \left(t - \left(\hat{\tau}_{L^q} - \hat{\tau}^q_i \right) \right) \right) + \right. \right. \right. \\ & \left. \left. \left. \text{Re} \left\{ r^q_{m,filtered} \left(t - \left(\hat{\tau}^q_{L^q} - \hat{\tau}^q_i \right) \right) \right\} . \cos \left(\hat{\phi}^q_i \left(t - \left(\hat{\tau}_{L^q} - \hat{\tau}^q_i \right) \right) \right) \right] \times \right. \\ & \left. S^q_Q \left(t - \hat{\tau}^q_{L^q} - \hat{\tau}^q_{Rx} \right) \right) \otimes h^{Q,i}_{m,q}(t) \Big]_{t = j.T_s + a.T_{chip} + \hat{\tau}^q_{L^q} + \hat{\tau}^q_{Rx}} \end{aligned} \tag{5.37}$$

Finalising the demodulation process, user-q's DS/SSMA QPSK RAKE receiver creates the output vector $\overline{y}^q_m$, which is an estimate of the original DS/SSMA QPSK transmitter input vector $\overline{c}^q_m$. This is accomplished by one of two possible methods: If the transmitter structure is configured for balanced modulation, $\overline{y}^q_m$ is constructed by linearly combining the elements from $\overline{y}^{I,q}_m$ and $\overline{y}^{Q,q}_m$. Alternatively, a *parallel-to-serial* converter (denoted by the block P/S in *Fig.* 5.4) creates $\overline{y}^q_m$ by interlacing the elements of $\overline{y}^{I,q}_m$ and $\overline{y}^{Q,q}_m$.

5.3.3 AVERAGE OUTPUT FADING AMPLITUDE CALCULATION FOR COMPLEX DS/SSMA QPSK SYSTEMS WITH RAKE RECEIVERS

The first step in the calculation of user-q's average fading amplitude for the i^{th} multipath fading channel component is to delay an estimate of its instantaneous fading amplitude $\hat{\alpha}^q_i(t)$ by $\left(\hat{\tau}^q_{L^q} - \hat{\tau}^q_i \right)$. Next, this delayed estimate of the i^{th} channel component's instantaneous fading amplitude is filtered using an averaging filter $h^i_{ave,q}(t)$, which has an impulse response identical to the matched filters used in *Fig.* 5.4. Recall that the delayed complex received signal $r^q_{m,filtered} \left(t - \left(\hat{\tau}^q_{L^q} - \hat{\tau}^q_i \right) \right)$, with $i = 1, 2, ..., L^q$, is scaled by the average envelope amplitude estimate $\hat{\overline{\beta}}^q_i$ during MRC. Hence, the average fading amplitudes associated with the elements in the receiver output vector $\overline{y}^q_m$ are normalised averages of the linear combination of the delayed average fading amplitudes experienced by each of the multipath components. However, the calculation thereof differs for the balanced and unbalanced DS/SSMA QPSK communication system configurations in *Fig.* 5.3 and *Fig.* 5.4: For the balanced modulation scenario, the same data bits are transmitted on the I-channel and Q-channel. Hence, calculation of an estimate of the average fading amplitude associated with the j^{th} element of user-q's

receiver output vector $\overline{y}_m^q$, is accomplished as follows:

$$\hat{\overline{\alpha}}_{m,j}^q = \frac{T_{chip}}{T_s} \sum_{i=1}^{L^q} \sum_{a=1}^{T_s/T_{chip}} \hat{\overline{\beta}}_i^q \left[\hat{\alpha}_i^q \left(t - \left(\hat{\tau}_{L^q}^q - \hat{\tau}_i^q \right) \right) \otimes h_{ave,q}^i(t) \right]_{t=j.T_s+a.T_{chip}+\hat{\tau}_{L^q}^q+\hat{\tau}_{Rx}^q} \tag{5.38}$$

where $\hat{\overline{\beta}}_i^q$ and $\hat{\tau}_i^q$ are estimates of the i^{th} multipath component's average envelope amplitude (see *Section* 2.4.1) and delay, respectively. In the case of dual-channel modulation, the j^{th} set of symbols that are transmitted on the I-channel and Q-channel are two consecutive data bits from the transmitter input vector $\overline{c}_m^q$, defined in *Section* 5.3.1. Consequently, an estimate of the average fading amplitude associated with the $(2.j)^{\text{th}}$ and $(2.j+1)^{\text{th}}$ elements of user-q's receiver output vector $\overline{y}_m^q$, can be calculated as follows:

$$\begin{aligned} \hat{\overline{\alpha}}_{m,(2.j)}^q &= \hat{\overline{\alpha}}_{m,(2.j+1)}^q \\ &= \frac{T_{chip}}{T_s} \sum_{i=1}^{L^q} \sum_{a=1}^{T_s/T_{chip}} \hat{\overline{\beta}}_i^q \left[\hat{\alpha}_i^q \left(t - \left(\hat{\tau}_{L^q}^q - \hat{\tau}_i^q \right) \right) \otimes h_{ave,q}^i(t) \right]_{t=(2.j).T_s+a.T_{chip}+\hat{\tau}_{L^q}^q+\hat{\tau}_{Rx}^q} \end{aligned} \tag{5.39}$$

5.3.4 ANALYTICAL BIT ERROR PROBABILITY FOR SINGLE USER DS/SSMA QPSK SYSTEMS WITH RAKE RECEIVERS

In [47] an approximate bit error probability is derived for the RAKE receiver-based DS/SSMA QPSK system discussed in the previous subsections. The derivation is made under the following assumptions:

- User-q is the only user present in the CDMA system. Consequently, MUI is absent from the communication system.
- The periodic auto-correlation (see *Section* D.2.2) of user-q's I-channel and Q-channel spreading sequences is perfect, i.e.:

$$R_{S_I^q(t),S_I^q(t)}(\tau) = R_{S_Q^q(t),S_Q^q(t)}(\tau) = \delta(\tau) \tag{5.40}$$

- The periodic cross-correlation (see *Section* D.2.3) between user-q's I-channel and Q-channel spreading sequences is perfect, i.e.:

$$R_{S_I^q(t),S_Q^q(t)}(\tau) = 0 \qquad \forall \tau \tag{5.41}$$

- Slow Rayleigh (see *Section* 2.5.2.1) flat fading (see *Section* 2.5.1.1) is experienced by each of the L^q statistically independent paths of user-q's multipath fading channel.
- User-q's DS/SSMA QPSK RAKE receiver has perfect knowledge of the instantaneous phase, delay and envelope amplitude CSI parameters of each of the L^q paths in the multipath fading channel.

Derivation of the bit error probability, valid for both balanced and unbalanced modulation, is accomplished by first recognising that the conditional probability of error for user-q's RAKE receiver-based DS/SSMA QPSK system is given by [47]:

$$P_b^q\left(e|\gamma_{b,m,j}^q\right) = Q\left(\sqrt{2.\gamma_{b,m,j}^q}\right) \tag{5.42}$$

where $\gamma^q_{b,m,j}$ is user-q's total received SNR per bit for the j^{th} bit in the m^{th} vector of data bits. Thus, user-q's bit error probability $P^q_b(e)$ can obtained by averaging $P^q_b\left(e|\gamma^q_{b,m,j}\right)$ over the PDF of the total SNR per bit, denoted by $\rho\left(\gamma^q_{b,m,j}\right)$: If the flat fading experienced by each of the L^q paths is slow enough that the Rayleigh distributed fading amplitude may be regarded as a constant (during at least one symbol interval), i.e. $\beta^q_i(t) = \overline{\beta}^q_i$ for $i = 1, 2, ..., L^q$, it can be shown that the SNR per bit for the j^{th} bit in the m^{th} vector of data bits of user-q's i^{th} received multipath component is given by:

$$\gamma^{q,i}_{b,m,j} = \left(\overline{\beta}^q_i\right)^2 \frac{\overline{E}^q_b}{N_0} \tag{5.43}$$

where $\overline{E}^q_b$ is user-q's average transmitted energy per bit. It is worthwhile to note that the energy per bit for balanced and unbalanced modulation is identical for the transmitter structure shown in *Fig.* 5.3 [50]. Thus, user-q's total received SNR per bit for the j^{th} bit in the m^{th} message word can be calculated as follows:

$$\gamma^q_{b,m,j} = \sum_{i=1}^{L^q} \gamma^{q,i}_{b,m,j} = \frac{\overline{E}^q_b}{N_0} \sum_{i=1}^{L^q} \left(\overline{\beta}^q_i\right)^2 \tag{5.44}$$

Since $\gamma^{q,i}_{b,m,j}$, with $i = 1, 2, ..., L^q$, are random variables with chi-squared distributions (with two degrees of freedom), it can be shown that the PDF of the total SNR per bit is given by [47, 152]:

$$\rho\left(\gamma^q_{b,m,j}\right) = \sum_{i=1}^{L^q} \left[\frac{1}{\overline{\gamma}^{q,i}_{b,m,j}} \left(\prod_{a=1, a\neq i}^{L^q} \frac{\overline{\gamma}^{q,i}_{b,m,j}}{\overline{\gamma}^{q,i}_{b,m,j} - \overline{\gamma}^{q,a}_{b,m,j}} \right) \exp\left(-\frac{\gamma^q_{b,m,j}}{\overline{\gamma}^{q,i}_{b,m,j}} \right) \right] \qquad \text{for } \gamma^q_{b,m,j} \geq 0 \tag{5.45}$$

where $\overline{\gamma}^{q,i}_{bm,j}$ is the average SNR per bit for the j^{th} bit in the m^{th} message word vector on the i^{th} path, defined as:

$$\overline{\gamma}^{q,i}_{b,m,j} = E\left[\left(\overline{\beta}^q_i\right)^2\right] \frac{E^q_b}{N_0} \tag{5.46}$$

with $E[\ .\ ]$ denoting expectancy. Thus, with $\rho\left(\gamma^q_{b,m,j}\right)$ as defined by *Eq.* (5.45), the bit error probability for user-q can be determined as follows [47, 152]:

$$\begin{aligned} P^q_b(e) &= \int_0^\infty P^q_b\left(e|\gamma^q_{b,m,j}\right) \rho\left(\gamma^q_{b,m,j}\right) d\gamma^q_{b,m,j} \\ &= \frac{1}{2} \sum_{i=1}^{L^q} \left[\left(\prod_{a=1, a\neq i}^{L^q} \frac{\overline{\gamma}^{q,i}_{b,m,j}}{\overline{\gamma}^{q,i}_{b,m,j} - \overline{\gamma}^{q,a}_{b,m,j}} \right) \left(1 - \sqrt{\frac{\overline{\gamma}^{q,i}_{b,m,j}}{1 + \overline{\gamma}^{q,i}_{b,m,j}}} \right) \right] \end{aligned} \tag{5.47}$$

According to the *Central Limit Theorem* (CLT), MUI can be incorporated into *Eq.* (5.47) by means of a GA [49, 50], or improved GA, at high user loads. This entails modelling the MUI as a zero mean Gaussian process with a variance of σ^2_{MUI}, and then adding this variance to the AWGN (see *Section* 2.2) variance present in *Eq.* (5.47) [50]. The variance σ^2_{MUI} will be a function of the type and the length of the spreading sequences used in the CDMA system, the received signal power of each CDMA user's signal at user-q's receiver, and most importantly, the number of users present in the CDMA system [50]. Although better approaches than the GA and improved GA are available to described MUI in DS/SSMA systems [113], these usually requiring more complex, higher order statistical analyses of the spreading sequences employed.

The complexity and scope this study's multi-user multipath fading performance evaluation platform, discussed in *Section* 5.4.3, far exceeds the mobile environment assumed during the derivation of the

theoretical BER performance curve of *Eq.* (5.47). Furthermore, *Eq.* (5.47)'s theoretical curve has several deficiencies, as discussed above. As such, this theoretical curve was not used for reference purposes during the examination of the simulated multi-user multipath fading channel BER performance results, presented in *Section* 6.5. Instead, Monte Carlo simulation results, presented by *Povey et al.* in [158] for a 32-tap RAKE receiver-based DS/SSMA system, are used for baseline reference purposes.

5.4 GENERAL SIMULATION CONFIGURATIONS

The following three subsections detail the general experimental setups for the AWGN, flat fading and multipath fading channel simulations of *Chapter* 6. This includes the transmitter, receiver and channel configurations employed in the simulation study.

5.4.1 SIMULATIONS IN AWGN CHANNEL CONDITIONS

Shown in *Fig.* 5.5 is the general narrowband complex QPSK communication system employed in the AWGN channel simulations of *Chapter* 6. For a specific E_b/N_0 ratio, this simulation platform

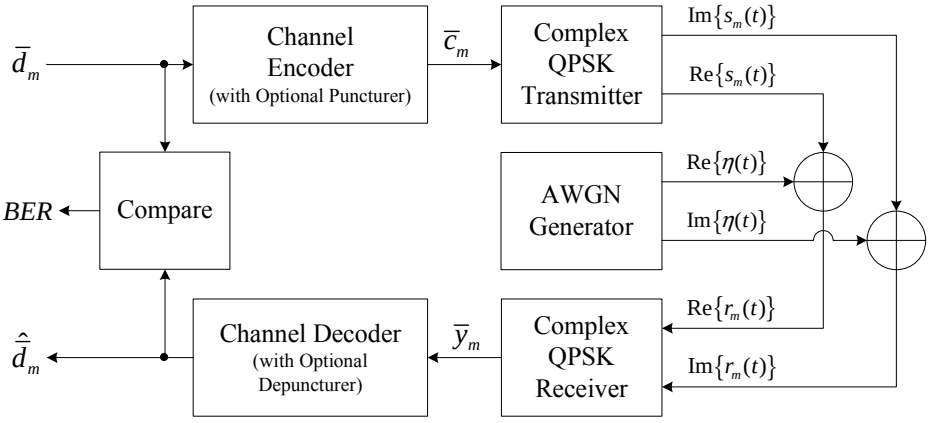

Figure 5.5: General AWGN Channel Simulation Platform

operates as follows: Firstly, the m^{th} data vector $\overline{d}_m$ is encoded by the channel encoder under investigation. If so required, the resultant set of code bits are then punctured (see *Section* 3.2.4), giving $\overline{c}_m$. Next, the transmitter creates the m^{th} set of complex QPSK symbols $\overline{s}_m(t)$ by modulating the code bits in $\overline{c}_m$. *Table* 5.1 details the general configuration of the transmitter structure. Most of these

Table 5.1: Narrowband Complex QPSK Transmitter Configuration

Configuration Option/Parameter	**Setting**
Symbol Rate [symbols/s]	1000
Effective RF Carrier [MHz]	900
Simulation RF Carrier [MHz]	0
Transmit Filters	None
Pulse Shaping Filters	Shaping: Square-Root Nyquist Roll-off Factor: $\varsigma = 0.5$
Modulation Approach	Balanced

parameters were arbitrarily chosen. For example, the QPSK symbol rate was conveniently chosen as 1000 symbols/s, since it has no bearing on the BER performance of such a system at a specific E_b/N_0 value in AWGN channel conditions. Although the simulations were performed completely in baseband, i.e. at a carrier frequency of 0 MHz, an effective RF frequency of 900 MHz was assumed, since this a common RF carrier frequency used in commercial wireless communication systems, such as GSM. The effective RF carrier has no real influence on the BER performance results obtained under AWGN channel conditions, but plays an important role in flat fading and frequency selective fading simulations.

As indicated by *Table* 5.2, square-root Nyquist pulse shaping [44, 154, 159, 160] was employed. A square-root Nyquist pulse is defined as follows:

$$h_{sqrt-Nyq}(t) = \left(\frac{1}{1-\left(\frac{4\varsigma t}{T_p}\right)^2}\right)\left[\left(\frac{1-\varsigma}{\sqrt{T_p}}\right)\left(\frac{\sin\left(\frac{\pi(1-\varsigma)t}{T_p}\right)}{\left(\frac{\pi(1-\varsigma)t}{T_p}\right)}\right)+\frac{4\varsigma}{\pi\sqrt{T_p}}\left(\cos\left(\frac{\pi\left(1+\varsigma\right)t}{T_p}\right)\right)\right] \tag{5.48}$$

where ς is the roll-off factor [44, 159, 160] of the pulse. In this study a roll-off factor of $\varsigma = 0.5$ was used. The parameter T_p represents the pre-pulse shaping symbol duration, which was set to $T_p = T_s$ for the narrowband simulations in AWGN and flat fading channel conditions. *Fig.* 5.6 depicts a normalised square-root Nyquist pulse for $\varsigma = 0.5$ and arbitrary T_p. Thus, for the transmitter of *Fig.* 5.1, $h_p^I(t) = h_p^Q(t) = h_{sqrt-Nyq}(t)$ with $T_p = T_s$. An estimate of the baseband transmitted signal's bandwidth is easily calculated as follows [47]:

$$B_{sig} = \frac{1}{2.T_s}(1+\varsigma) = 750 \text{ Hz} \tag{5.49}$$

Next, the QPSK modulated symbols experience the adverse effects of AWGN, presenting the nar-

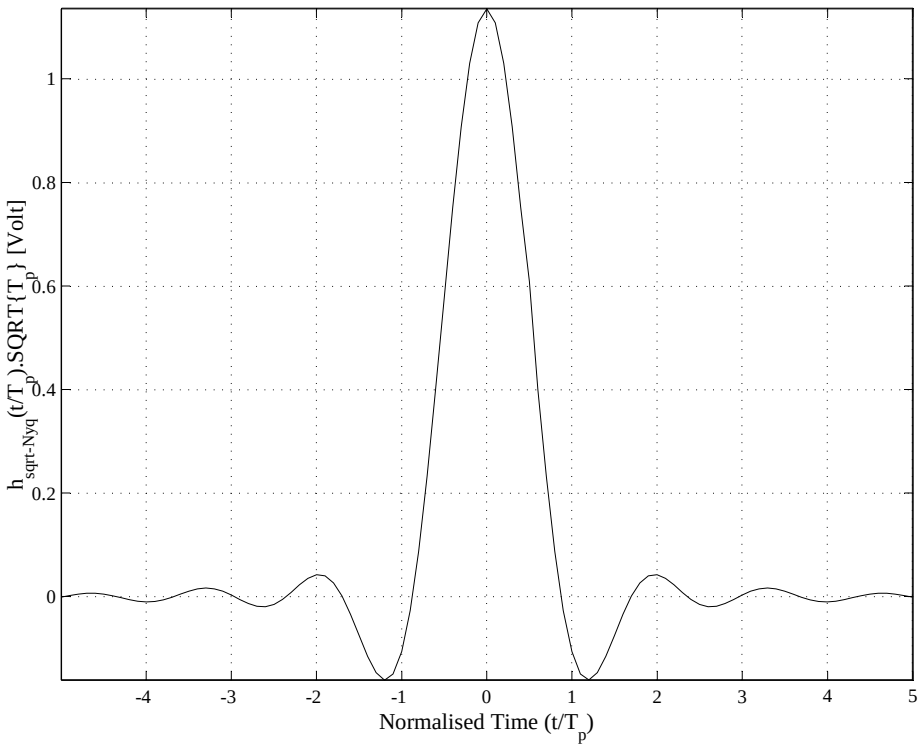

Figure 5.6: Normalised Square-Root Nyquist Pulse Shape for $\varsigma = 0.5$

rowband complex QPSK receiver, configured according to *Table* 5.2, with the m^{th} noisy input $\overline{r}_m(t)$. *Table* 5.2 states that the baseband receiver employs 6^{th} order lowpass elliptic receive filters [44, 114, 161] on the I-channel and Q-channel branches, which minimise the AWGN entering the receiver. Shown in *Fig.* 5.7 are the amplitude and phase responses of these filters, normalised with respect to the cutoff frequency f_{cut}. This type of lowpass filter was used, since it exhibits linear phase characteristics (see the bottom figure shown in *Fig.* 5.7). Note that $f_{cut} = 1000$ Hz, which was chosen somewhat larger than B_{sig} to ensure minimal phase distortion throughout the frequency band $0 \leq f \leq B_{sig}$. Furthermore, *Table* 5.2 states that square-root Nyquist matched filters are employed on the I-channel and Q-channel of the narrowband complex QPSK receiver. Thus, it follows that $h_m^I(t) = h_m^Q(t) = h_{sqrt-Nyq}(t)$ with $T_p = T_s$.

Table 5.2: Narrowband Complex QPSK Receiver Configuration

Configuration Option/Parameter	**Setting**
Symbol Rate [symbols/s]	1000
Effective RF Carrier [MHz]	900
Simulation RF Carrier	Baseband Simulation
Symbol Synchronisation	Perfect
Carrier Synchronisation	Perfect
Receive Filters	Type: Elliptic Order: 6 Cutoff Frequency [Hz]: $f_{cut} = 1/T_s = 1000$ Passband Ripple [dB]: 0.1 Stopband Attenuation [dB]: 40
Demodulation Approach	Balanced Matched Filtering
Matched Filters	Shaping: Square-Root Nyquist Roll-off Factor: $\varsigma = 0.5$

After demodulation, the channel decoder is presented with $\overline{y}_m$, a noisy estimate of the original code bits modulated by the narrowband complex QPSK transmitter. Before it attempts to decode $\overline{y}_m$, the channel decoder first restores possible punctured code bits by declaring the necessary erasures (see *Section* 3.3.4). Thereafter its decoding efforts produce $\hat{\overline{d}}_m$, which is an estimate of the original data bit vector $\overline{d}_m$. By comparing $\hat{\overline{d}}_m$ and $\overline{d}_m$, the number of errors incurred by the coded narrowband complex QPSK system for the m^{th} vector of data bits at the current E_b/N_0 is determined. Repeating the above process numerous times a statistically acceptable BER can be determined.

5.4.2 SIMULATIONS IN FLAT FADING CHANNEL CONDITIONS

Fig. 5.8 depicts the general simulation platform employed in the flat fading simulations of *Chapter* 6. Except for the addition of a complex flat fading channel simulator, this simulation platform is essentially identical to the AWGN channel simulation platform detailed in *Section* 5.4.1. As such, the narrowband complex QPSK transmitter and receiver, shown in *Fig.* 5.8, are also configured according to *Table* 5.1 and *Table* 5.2, respectively.

Table 5.3 details the complex flat fading channel configurations considered in *Chapter* 6. Recall

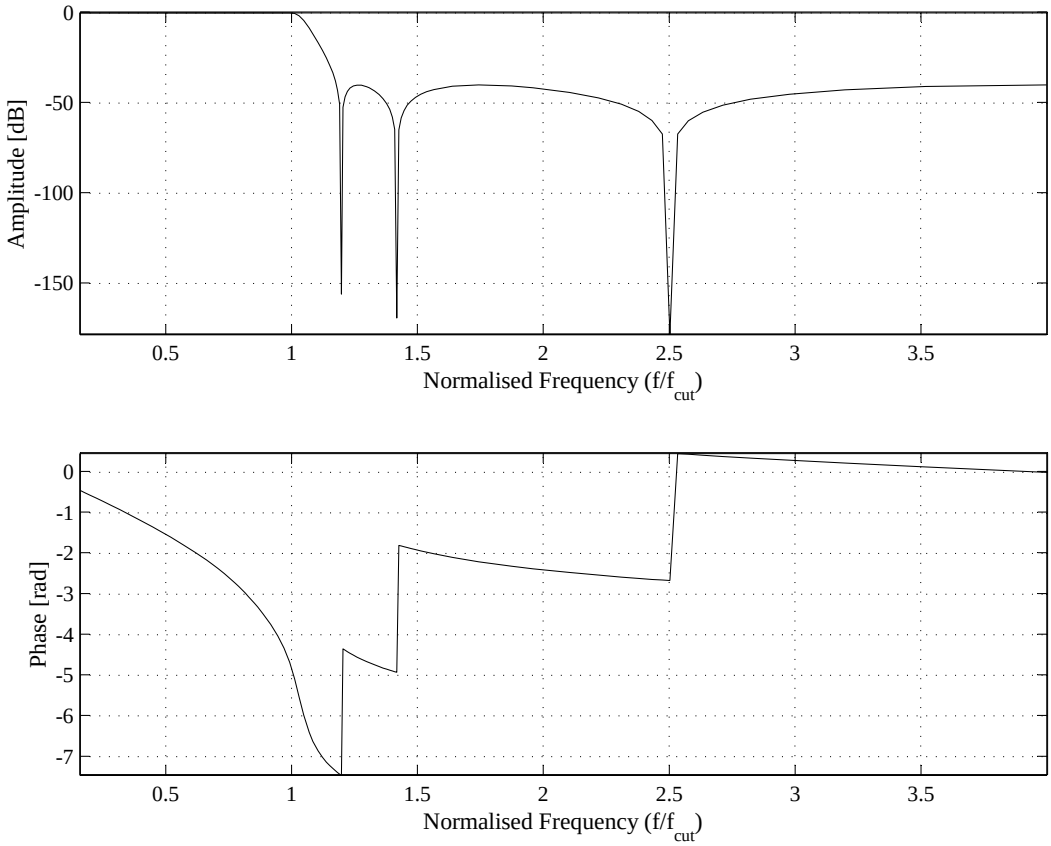

Figure 5.7: Amplitude and Phase Responses of the 6^{th} Order Lowpass Elliptic Receive Filters

Table 5.3: Possible Flat Fading Channel Simulator Configurations

Configuration Option/Parameter	**Settings Supported**
Rician Factors [dB]	$9, 6, 0, -100$
Doppler Spread [Hz]	100 (Velocity of 120 km/h, RF Carrier @ 900 MHz)
	67 (Velocity of 80 km/h, RF Carrier @ 900 MHz)
	33 (Velocity of 40 km/h, RF Carrier @ 900 MHz)

from *Table* 5.1 and *Table* 5.2 that an effective RF carrier frequency of 900 MHz is used. Thus, using *Eq.* (2.2) with an angle of arrival of $\theta_A(t) = 0$ rad, the supported Doppler spread frequencies of 33 Hz, 67 Hz and 100 Hz relate to relative transmitter-to-receiver velocities of 40 km/h, 80 km/h and 120 km/h, respectively. Recall from *Section* 5.4.1 that the QPSK transmitter's output signal has a bandwidth of approximately $B_{sig} = 750$ Hz. Since $B_D < B_{sig}$, it follows that the system experiences relatively slow flat fading. However, the ratio of signal bandwidth to Doppler spread is not large enough to assume a fading amplitude that remains essentially constant during one QPSK symbol period.

This simulation platform operates in a similar fashion as the AWGN channel simulation platform discussed in *Section* 5.4.1, with the exception of the following:

- Prior to the modulation of the channel coded bits by the narrowband complex QPSK transmitter, optional interleaving (see *Section* 3.2.3) is now also supported. At the receiver de-interleaving (see

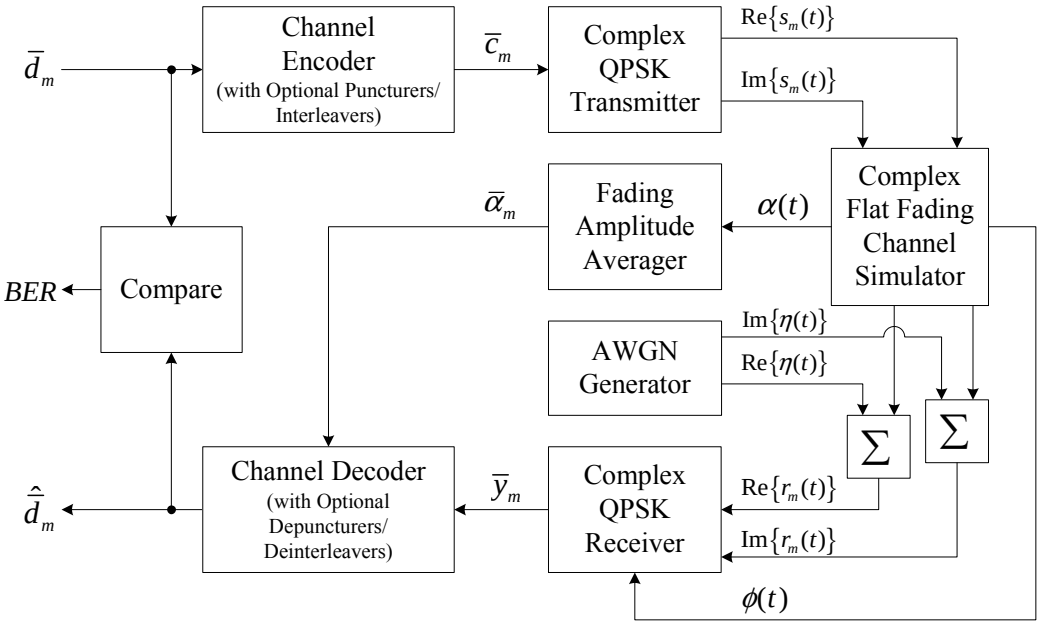

Figure 5.8: General Flat Fading Channel Simulation Platform

Section 3.3.3) can be performed to undo any interleaving introduced at the transmitter.

- The complex QPSK channel symbols experience not only the adverse effects of AWGN, but also that of flat fading, created by the complex flat fading channel simulator.
- The channel decoder is capable of using CSI, obtained directly from the complex flat fading channel simulator (see *Section* 2.6.2.5), in its decoding efforts.

5.4.3 SIMULATIONS IN FREQUENCY SELECTIVE FADING CHANNEL CONDITIONS

Fig. 5.9 depicts the frequency selective fading channel simulation platform used in this study [156]. This platform is built around the RAKE receiver-based complex DS/SSMA QPSK communication system discussed in *Section* 5.3. *Table* 5.4 summarises the general wideband transmitter configuration supported by each of the users in the CDMA environment. As stated in this table, this dissertation investigated the BER performances of coded wideband systems employing either unfiltered (see *Section* D.3.1), or filtered (see *Section* D.3.2) CSS families: With unfiltered CSS families, such as the *Zadoff-Chu* (ZC) and *Quadriphase* (QPH) families considered in this study, there is no bandlimiting built into the CSSs. Thus, additional pulse shaping is required to ensure effective spectrum utilisation. Similar to the narrowband simulation platforms discussed in the previous sections, square-root Nyquist pulse shaping is employed. However, pulse shaping is performed at CSS chip-level, i.e. the pulse shape $h_{sqrt-Nyq}(t)$ shown in *Fig.* 5.6 is employed with $T_p = T_{chip}$. Thus, for the pulse shaped CSS scenarios, the bandwidth of the baseband transmitter output signal can be approximated as follows:

$$B_{sig} = \frac{1}{2.T_{chip}}(1+\varsigma) = 47250 \text{ Hz} \tag{5.50}$$

In the case of the pre-filtered ABC and DSB CE-LI-RU filtered *Generalised Chirp-like* (GCL) CSSs, no additional bandlimiting is required, i.e. simple rectangular pulse shaping can be used. It has been shown that, when the spreading sequence length M_{seq} is sufficiently large, the *linearly interpolating root-of-unity* filtering technique [7, 8] employed in the generation of a DSB CE-LI-RU filtered GCL CSSs produces a signal bandwidth equivalent to that generated by Nyquist filtering with a roll-off

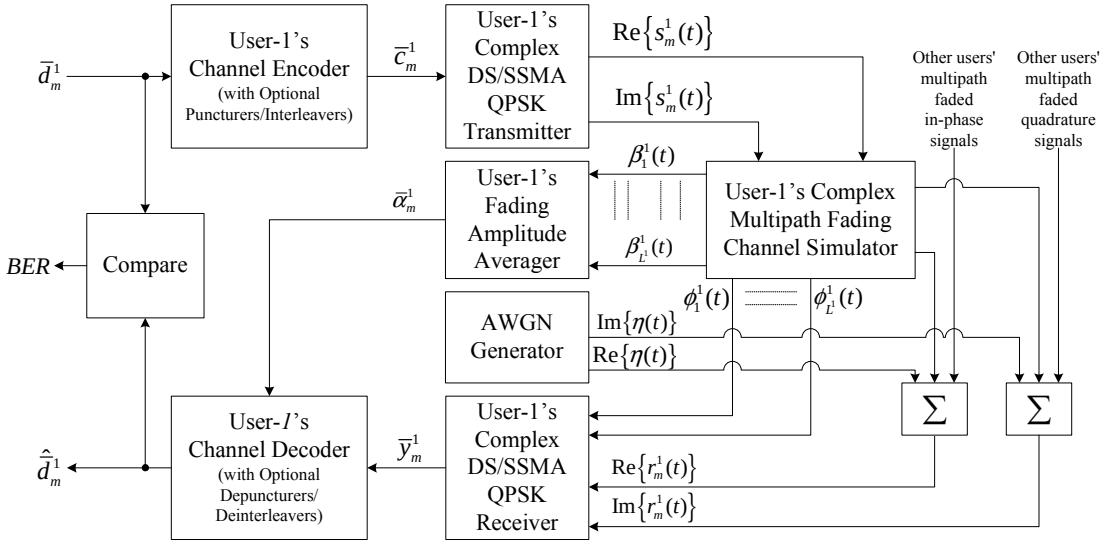

Figure 5.9: General Multipath Fading Channel Simulation Platform

factor approaching $\varsigma = 0$. Thus, the signal bandwidth of a baseband complex DS/SSMA QPSK communication system, configured to employ DSB CE-LI-RU filtered GCL CSSs, can be calculated as follows:

$$B_{sig} = \frac{1}{2.T_{chip}} = 31500 \text{ Hz} \tag{5.51}$$

In the case of the ABC sequences, balanced quadrature modulation will result in only the lower or upper sideband being transmitted, subsequently halving the required signal bandwidth:

$$B_{sig} = \frac{1}{4.T_{chip}} = 15750 \text{ Hz} \tag{5.52}$$

Up to 10 distinct CDMA users are supported by the simulation platform depicted in *Fig.* 5.9. However, only a single baseband complex RAKE receiver (user-1's receiver was used in this study) is present in the simulation platform, since only a single user's corrupted signal is demodulated and processed to determine the coded CDMA system's BER performance. Other users' signals present at this receiver's input create the MUI in the CDMA system. The BER performance of the RAKE receiver-based complex DS/SSMA QPSK communication systems in the presence of MUI is not only a function of the length of the CSSs employed (denoted by M_{seq}), but also the selection of good CSSs from a complete CSS family. This was found to be true for all of the CSS families considered, but especially for ABC sequences. In *Section* 6.5.1.3.2 and *Section* 6.5.1.3.3 in-depth studies are undertaken into the influence of these two factors on the BER performance of uncoded DS/SSMA QPSK communication systems employing ABC sequences.

For each of the 10 possible users in the CDMA system a unique complex multipath fading channel simulator (see *Section* 2.6.3.2) configuration was chosen, since the movement of the users' wideband complex transmitters relative to the single complex RAKE receiver is stochastic. However, perfect power control is assumed, i.e. the average powers of all the users' corrupted signals entering user-1's RAKE receiver are equal. Listed in *Table* 5.5 and *Table* 5.6 are the complex multipath fading channel simulator configurations for the 10 possible users. Each user's multipath fading channel simulator was configured to have 3 statistically independent paths, a choice frequently encountered in literature related to simulation studies on wideband CDMA systems. The Rician factor and Doppler spread for

Table 5.4: Wideband Complex DS/SSMA QPSK Transmitter Configuration

Configuration Option/Parameter	**Setting**
CSS Families Supported	ABC, DSB CE-LI-RU Filtered GCL, Unfiltered ZC, Unfiltered QPH
Unspreaded Symbol Rates [symbols/s]	1032.786 (Length-61 ABC Sequences) 984.375 (Length-64 ABC Sequences) 496.063 (Length-127 ABC Sequences) 1000 (All Length-63 Sequences)
Spreading Sequence Lengths [chips]	61 (Only ABC Sequences) 63 (All CSS Families) 64 (Only ABC Sequences) 127 (Only ABC Sequences)
Spreading Sequence Rate [chips/s]	63000
Effective RF Carrier [MHz]	900
Simulation RF Carrier [MHz]	0
Transmit Filters	None
Pulse Shaping Filters: Unfiltered Complex Spreading Sequences	Shaping: Square-Root Nyquist Roll-off Factor: $\varsigma = 0.5$
Pulse Shaping Filters: Filtered Complex Spreading Sequences	Shaping: Rectangular Roll-off Factor: N/A
Modulation Approach	Balanced
Power Control	Perfect

the i^{th} path of each user's channel simulator, respectively denoted by K_i and $B_{D,i}$, were randomly chosen from the options supported by the complex flat fading channel simulator, given in *Table* 5.3. Recalling the possible transmitter signal bandwidths for the different classes of CSSs, given by *Eq.* (5.50), *Eq.* (5.51) and *Eq.* (5.52), the different signal duration possibilities can be estimated as $T_{sig} = 1/B_{sig}$. With these signal bandwidths and durations known, each user's path powers and relative path delays, respectively denoted by τ_i and P_i, with $i = 1, 2, 3$, were chosen according to exponential decay power delay profiles (see *Section* 2.6.3.3) that conform to the requirements for frequency selective fading, i.e. $B_{sig} > B_C$ and $T_{sig} < \sigma_\tau$ (see *Section* 2.5.1.1). Note that the maximum excess delay (see *Section* 2.4.3.1) of user-1 is $\tau_{max} = 200$ μs, which is 12.6 CSS chips, or one fifth of a length-63 CSS in duration.

Table 5.7 details the complex DS/SSMA QPSK RAKE receiver's general configuration. Note that the lowpass elliptic receive filters employed in the RAKE receiver were identical to those used in the narrowband receivers, with the exception of the cutoff frequency, $f_{cut} = 1/T_{chip} = 63000$ Hz. Thus, *Fig.* 5.7, with $f_{cut} = 1/T_{chip}$, also depicts the frequency response of the wideband system's receive filters. Furthermore, the single RAKE receiver present in the CDMA system was configured to be perfectly synchronised with the received signal initially generated by user-1's wideband complex transmitter, i.e. perfect carrier, chip and symbol synchronisation were assumed on each of the RAKE taps.

Table 5.5: Complex Multipath Fading Channel Simulator Configurations for Users 1 to 5

		User Number				
		1	2	3	4	5
Path 1 **Setup**	P_1 [dB]	-0.1394	-0.3866	-0.2820	-0.5303	-1.0279
	$K_1[dB]$	9	9	9	9	9
	$B_{D,1}$ [Hz]	100	33	67	33	100
	τ_1 [μs]	0	20	30	10	40
Path 2 **Setup**	P_2 [dB]	-15.1394	-10.8866	-12.2820	-9.5303	-7.0279
	K_2 [dB]	0	0	0	0	0
	$B_{D,2}$ [Hz]	67	100	33	67	33
	τ_2 [μs]	100	90	110	70	80
Path 3 **Setup**	P_3 [dB]	-30.1394	-24.3866	-24.2820	-24.5303	-19.0279
	K_3 [dB]	-100	-100	-100	-100	-100
	$B_{D,3}$ [Hz]	33	67	100	100	67
	τ_3 [μs]	200	180	190	170	160
RMS Delay Spread σ_τ [μs]		18.286	21.288	21.108	20.947	20.208
Coherence Bandwidth B_C [Hz]		10937	9395	9475	9548	9897

Table 5.6: Complex Multipath Fading Channel Simulator Configurations for Users 6 to 10

		User Number				
		6	7	8	9	10
Path 1 **Setup**	P_1 [dB]	-0.3820	-0.2131	-0.3764	-0.2063	-0.5303
	$K_1[dB]$	9	9	9	9	9
	$B_{D,1}$ [Hz]	67	100	67	33	33
	τ_1 [μs]	20	30	10	0	30
Path 2 **Setup**	P_2 [dB]	-10.8820	-13.7131	-10.8764	-13.7063	-9.5303
	K_2 [dB]	0	0	0	0	0
	$B_{D,2}$ [Hz]	100	100	67	33	67
	τ_2 [μs]	90	120	80	90	90
Path 3 **Setup**	P_3 [dB]	-25.8820	-22.7131	-28.8764	-24.2063	-24.5303
	K_3 [dB]	-100	-100	-100	-100	-100
	$B_{D,3}$ [Hz]	33	67	33	67	33
	τ_3 [μs]	190	180	200	160	190
RMS Delay Spread σ_τ [μs]		20.897	21.060	20.288	20.555	20.947
Coherence Bandwidth B_C [Hz]		9571	9497	9858	9730	9548

Table 5.7: Wideband Complex DS/SSMA QPSK RAKE Receiver Configuration

Configuration Option/Parameter	**Setting**
CSS Families Supported	ABC, DSB CE-LI-RU Filtered GCL, Unfiltered ZC, Unfiltered QPH
Unspreaded Symbol Rates [symbols/s]	1032.786 (Length-61 ABC Sequences) 984.375 (Length-64 ABC Sequences) 496.063 (Length-127 ABC Sequences) 1000 (All Length-63 Sequences)
Spreading Sequence Lengths [chips]	61 (Only ABC Sequences) 63 (All CSS Families) 64 (Only ABC Sequences) 127 (Only ABC Sequences)
Spreading Sequence Rate [chips/s]	63000
Effective RF Carrier [MHz]	900
Simulation RF Carrier [MHz]	0
Receive Filters	Type: Elliptic Order: 6 Cutoff Frequency [Hz]: $f_{cut} = 63000$ Passband Ripple [dB]: 0.1 Stopband Attenuation [dB]: 40
Matched Filters: Unfiltered Complex Spreading Sequences	Shaping: Square-Root Nyquist Roll-off Factor: $\varsigma = 0.5$
Matched Filters: Filtered Complex Spreading Sequences	Shaping: Rectangular Roll-off Factor: N/A
Demodulation Approach	Balanced Matched Filtering
RAKE Receiver Configuration	MRC, Perfect Knowledge of Path Delays and Instantaneous Fading Amplitudes
Symbol Synchronisation	Perfect for Each RAKE Receiver Tap
Carrier Synchronisation	Perfect for Each RAKE Receiver Tap
Code Lock	Perfect for Each RAKE Receiver Tap

The frequency selective fading channel simulation platform shown in *Fig.* 5.9 operates as follows: Firstly, user-1's m^{th} data bit vector $\overline{d}_m^1$ is encoded by the channel coder under investigation. If so required, the channel coded bits are interleaved and/or punctured to give $\overline{c}_m^1$. The vector $\overline{c}_m^1$ is modulated by user-1's baseband complex DS/SSMA QPSK transmitter to give $\overline{s}_m^1(t)$. The output $\overline{s}_m^1(t)$ is now processed by user-1's complex multipath fading channel simulator. Similar processing is done by the other users' multipath fading channel simulators on their respective modulated symbols. Next, the channel simulator outputs are summed, followed by the addition of AWGN. The result is user-1's complex RAKE receiver input $\overline{r}_m^1(t)$. This input is demodulated by the complex RAKE receiver, giving $\overline{y}_m^1$, which is a soft estimate of $\overline{c}_m^1$. Following possible de-puncturing and/or de-interleaving of $\overline{y}_m^1$, the channel decoder creates an estimate of $\overline{d}_m^1$, denoted by $\hat{\overline{d}}_m^1$. Repeating the process described above numerous times, comparing $\overline{d}_m^1$ and $\hat{\overline{d}}_m^1$ for each encoding instance, the BER performance of the coded RAKE receiver-based complex DS/SSMA QPSK communication system can be estimated for the current channel conditions.

5.5 CONCLUDING REMARKS

This chapter set out to describe the performance evaluation platforms implemented in the simulation study of this dissertation. Firstly, the operation, average fading amplitude calculation and theoretical BER performances of the narrowband complex QPSK communication system employed in the AWGN and flat fading channel simulations of *Chapter* 6 were considered. This was followed by a similar discussion on the wideband RAKE receiver-based complex DS/SSMA QPSK communication system, employed in *Chapter* 6's frequency selective fading channel simulations. Lastly, *Chapter* 6's AWGN, flat fading and frequency selective fading channel simulation platforms, constructed using the above mentioned narrowband and wideband communication systems, were described in detail. Listed below are the unique contributions that were made in this chapter:

1. *Section* 5.2 describes the operation and theoretical BER performances of a novel baseband complex QPSK communication system. This model is ideal for simulation purposes, since it negates the use of high sampling frequencies. A novel average fading amplitude CSI calculation technique is presented in *Section* 5.2.3.

2. A unique baseband RAKE receiver-based complex DS/SSMA QPSK communication system is presented in *Section* 5.3. The general operation of the baseband complex DS/SSMA QPSK transmitter and RAKE receiver structures are detailed in this subsection. *Section* 5.3.3 describes a simple, but innovative method whereby average fading amplitude CSI can be calculated for each of the output demodulated code bits after the RAKE receiver's MRC demodulation efforts. Lastly, a simplified theoretical derivation of the wideband system's multipath fading channel BER performance, in the absence of MUI, is considered.

3. A flexible baseband simulation platform, suitable for AWGN channel performance testing of channel coding schemes, is presented in *Section* 5.4.1. This platform employs the narrowband complex QPSK transmitter and receiver structures of *Section* 5.2. Furthermore, this platform includes realistic pulse shaping and receiver filters in order to ensure the authenticity of the simulation results presented in *Chapter* 6.

4. Also built around the baseband complex QPSK transmitter and receiver structures described in *Section* 5.2, is the baseband flat fading channel simulation platform described in *Section* 5.4.2. This platform employs the novel complex implementation of *Clarke*'s flat fading channel simulator model, presented in *Section* 2.6.2.3. A number of frequently encountered Doppler spread frequencies and Rician factors are supported by this simulation platform, making it possible to

determine the BER performances for channel coding schemes in a multitude of realistic flat fading channel conditions.

5. *Section* 5.4.3 presents one of the major contributions of this dissertation, namely a baseband multi-user multipath fading channel simulation platform, employing RAKE receiver-based complex DS/SSMA QPSK communication systems (see *Section* 5.4.3). Not only is this simulation platform a useful tool with which the communications engineer can determine the effects of multipath fading on different channel coding schemes, but it also supports multi-user CDMA experiments. Since each user's wideband transmitter output signal is processed by an individual complex multipath fading channel simulator, realistic wideband multi-user mobile communication environments can be recreated.

CHAPTER SIX

SIMULATION RESULTS

6.1 CHAPTER OVERVIEW

THIS chapter commences with extensive investigations into the operation of the complex flat and multipath fading channel simulator structures, proposed in *Section* 2.6.2.3 and *Section* 2.6.3.2, respectively. Numerous simulation results verify accurate functioning of the complex channel simulators. Included are detailed time and frequency domain analyses of the output signals generated by these complex channel simulators. Studies into the statistical behaviours of the proposed simulators are also given.

Next, *Chapter* 6 focusses on the narrowband complex QPSK and wideband complex DSSS/MA QPSK communication systems, presented in *Section* 5.2 and *Section* 5.3, respectively. The functioning of these narrowband and wideband communication systems are scrutinised in perfect and fading channel conditions. A multitude of time signals, measured at crucial system interfaces, are presented and extensively analysed. The frequency characteristics of the output signals generated by the narrowband and wideband communication systems' transmitter structures are also investigated.

Chapter 5 presented multi-functional AWGN (see *Section* 5.4.1), flat fading (see *Section* 5.4.2) and multipath fading (see *Section* 5.4.3) simulation platforms, built around the narrowband complex QPSK and wideband complex DSSS/MA QPSK communication systems (described in *Section* 5.2 and *Section* 5.3, respectively), as well as the novel complex flat and multipath fading channel simulators (proposed in *Section* 2.6.2.3 and *Section* 2.6.3.2, respectively). These simulation platforms were used to obtain the large number of simulated AWGN, flat fading and multipath fading channel BER performance results, presented in the remainder of *Chapter* 6. Simulated BER performance results are given for uncoded narrowband and wideband systems, as well as communication systems employing various VA decoded convolutional and linear block coding schemes. Convolutional codes considered include binary 4-state, rate $R_c = 1/2$ NSC codes (see *Section* 3.2.1.3.1), binary 8-state, rate $R_c = 2/3$ RSC codes (see *Section* 3.2.1.3.2) and punctured (see *Section* 3.2.4) binary 4-state, rate $R_c = 1/2$ RSC codes. VA decoded binary linear block codes (see *Chapter* 4) investigated include Hamming $(7, 4, 3)$ codes (see *Section* 3.2.2.3.1), cyclic $(5, 3, 2)$ linear block codes (see *Section* 3.2.2.2), interleaved (see *Section* 3.2.3) Hamming $(7, 4, 3)$ codes and punctured BCH $(15, 7, 5)$ codes (see *Section* 3.2.2.3.2). In the case of the binary cyclic $(5, 3, 2)$ block code, VA decoding using original and reduced BCJR trellis structures are compared. The only VA decoded non-binary linear block

code considered in this study, with and without interleaving, is the RS $(7, 5, 3)$ code (see *Section* 3.2.2.3.3). BER performance improvements observed due to the inclusion of fading amplitude CSI during the VA decoding of the convolutional and linear block codes investigated in this study, receive special attention.

The simulation platforms of *Chapter* 5, as well as the VA decoded convolutional and block coding schemes considered in this study, were developed in a C++ environment using an OOP approach. A large number of Matlab scripts and functions, primarily responsible for the creation and evaluation of filters, pulse shapes, power delay profiles, interleavers and block code generator matrices, were also developed. The BER performance results presented in this chapter were obtained through command-line driven executable applications, compiled using *Intel*'s *ICC* and *GNU is Not Unix*'s (GNU) *G++* compilers for *Linux* platforms. In order to minimise simulation execution times, theses applications' computational load were distributed over multiple workstations in the *University of Pretoria*'s *I-percube*, donated by *Intel*. The *I-percube* is an HPC cluster, which consists of seventeen 2.4 GHz *Pentium* 4 stations, each station running a *Mandrake Linux Operating System* (OS). *Fast Ethernet* connections are used to interconnect the seventeen drone stations in the HPC cluster. *Open Mosix* for *Linux* is responsible for transparent process migration and message handling between the stations. *Appendix E* supplies an index of the simulation software scripts, function, classes and compiled applications developed during this study. Upon request, a *Compact Disc Read Only Memory* (CD-ROM) containing the simulation software modules listed in *Appendix E* can be obtained from the author.

6.2 VALIDATION OF THE COMPLEX MOBILE CHANNEL SIMULATOR MODELS

The following subsections present simulation results obtained during the testing and validation of the novel complex flat and multipath fading channel simulators, presented in *Section* 2.6.2.3 and *Section* 2.6.3.2, respectively.

6.2.1 COMPLEX FLAT FADING CHANNEL SIMULATOR

In order to verify the correctness of its operation, three simulation tests were performed on the complex implementation of *Clarke*'s flat fading channel simulator, shown in *Fig.* 2.5. These tests include the measurement of output signals' envelope PDFs, phase PDFs and Doppler spectra for the different channel configurations, stated in *Table* 5.3. All simulation results were obtained using the complex exponential simulator input signal $u_i(t) = \exp(j.2\pi.f_c.t)$, with the carrier frequency chosen as $f_c = 2$ kHz.

6.2.1.1 MEASURED ENVELOPE PROBABILITY DENSITY FUNCTION RESULTS

Fig. 6.1 shows measured envelope PDFs, obtained using the complex flat fading channel simulator, configured for Rician factors of $K_i = -100$ dB, $K_i = 0$ dB and $K_i = 6$ dB. These simulation results were acquired by calculating the PDFs of the fading amplitude experienced by the simulator output signal $b_i(t)$, for each of the different Rician factor scenarios. The fading amplitude information was extracted directly from the complex flat fading channel simulator using *Eq.* (2.56). Although it is of no real consequence, it can be noted that the channel simulator was configured for a maximum Doppler spread of $B_{D,i} = 100$ Hz during the execution of these tests.

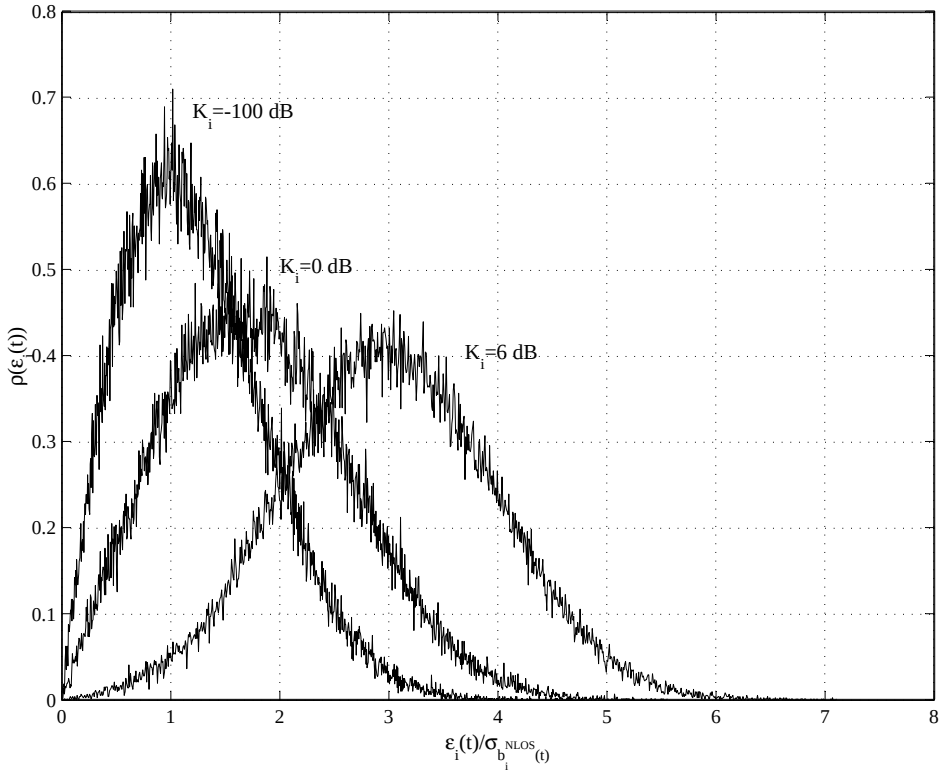

Figure 6.1: Measured Complex Flat Fading Channel Simulator Output Signal Envelope PDF Results for Rician Factors of $K_i = -100$ dB, $K_i = 0$ dB and $K_i = 6$ dB

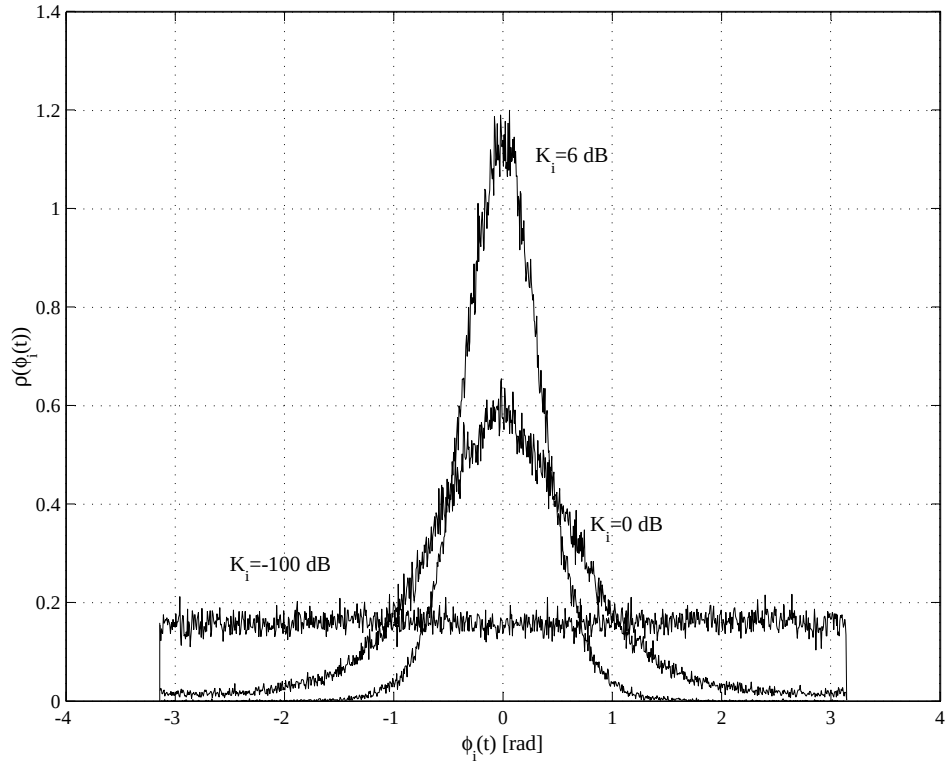

Figure 6.2: Measured Complex Flat Fading Channel Simulator Output Signal Phase PDF Results for Rician Factors of $K_i = -\infty$ dB (Rayleigh), $K_i = 0$ dB (Rician) and $K_i = 6$ dB ($\approx$ Gaussian)

6.2.1.2 MEASURED PHASE PROBABILITY DENSITY FUNCTION RESULTS

With the complex flat fading channel simulator once again configured for a maximum Doppler spread of $B_{D,i} = 100$ Hz and Rician factors of $K_i = -100$ dB, $K_i = 0$ dB and $K_i = 6$ dB, the measured phase PDFs shown in *Fig.* 6.2 were obtained as follows: Firstly, the instantaneous phase variation $\phi_i(t)$ experienced by the simulator output signal $b_i(t)$ was extracted directly from the complex flat fading channel simulator, using *Eq.* (2.57). The results shown in *Fig.* 6.2 were then obtained by calculating the PDF of the output signal's phase variations for the different Rician factors.

6.2.1.3 MEASURED DOPPLER SPECTRA RESULTS

In order to determine whether the novel complex flat fading channel simulator produces valid Doppler spectral characteristics, the simulator output signal's PSD was measured for $B_{D,i} = 33$ Hz, $B_{D,i} = 67$ Hz and $B_{D,i} = 100$ Hz. During these simulation tests, a Rician factor of $K_i = -100$ dB was chosen, i.e. almost no LOS signal component was present in the simulator output signal $b_i(t)$. *Fig.* 6.3 shows the measured output signal PSD results obtained for the above mentioned channel configuration parameters.

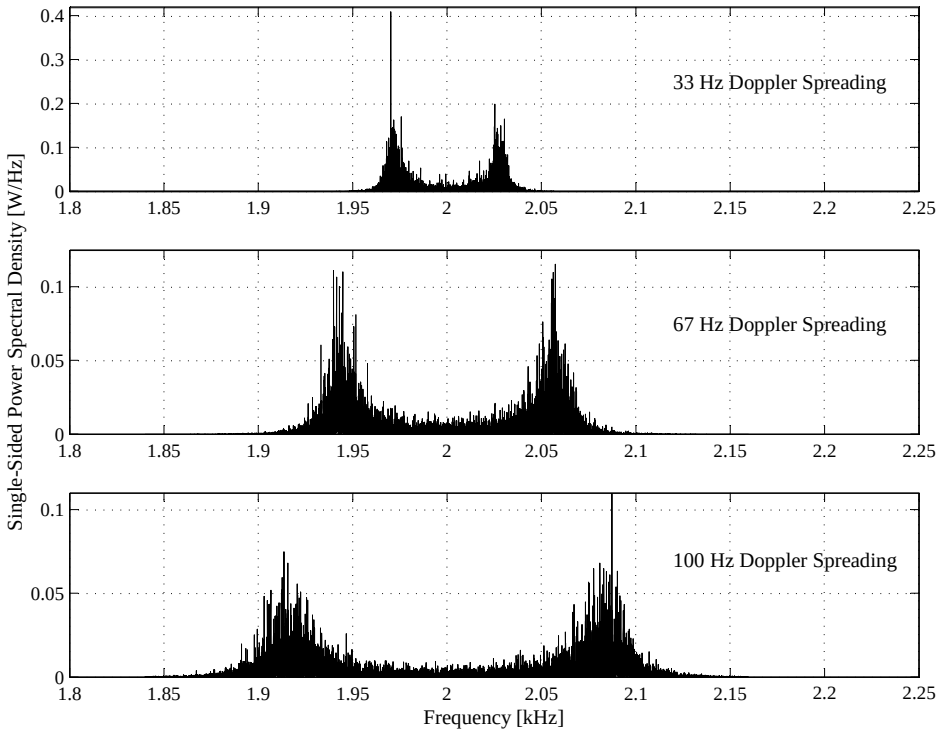

Figure 6.3: Measured Complex Flat Fading Channel Simulator Output Signal PSD Results for Maximum Doppler Spreads of $B_{D,i} = 33$ Hz, $B_{D,i} = 67$ Hz and $B_{D,i} = 100$ Hz

6.2.1.4 DISCUSSION OF THE SIMULATION RESULTS

From the measured complex flat fading channel simulator results presented in the preceding three subsections, the following conclusions can be made:

- By comparing *Fig.* 2.2 and *Fig.* 6.1, it is clear that the novel complex flat fading channel simulator is capable of producing Rayleigh and Rician fading envelope PDFs that closely match the mathematical models, discussed in *Section* 2.5.2.

- The theoretical flat fading channel phase distributions shown in *Fig.* 2.3 and the measured complex flat fading channel simulator output signal phase PDFs shown in *Fig.* 6.2 are comparable. Thus, the simulator is also capable of creating realistic flat fading channel phase distortions.
- Although the Doppler spectra presented in *Fig.* 6.3 do not match the theoretical PSD shown in *Fig.* 2.1 to a tee, it is close enough to ensure that the simulator output signal's fading envelope and phase exhibit acceptable temporal characteristics. Using higher order IIR Doppler filters will deliver improved results, but at the cost of higher channel simulator complexity.

6.2.2 COMPLEX MULTIPATH FADING CHANNEL SIMULATOR

Temporal and spectral simulation results, substantiating the satisfactory operation of the novel complex multipath fading channel simulator, presented in *Fig.* 2.8 of *Section* 2.6.3.2, is presented in the following subsection. These results were obtained using a complex exponential simulator input signal $s(t) = \exp(j.2\pi.f_c.t)$, with a carrier frequency of $f_c = 126$ kHz. Furthermore, the simulation tests were performed on a complex multipath fading channel simulator configured according to user-1's channel parameters, as given by *Table* 5.5.

6.2.2.1 MEASURED PATH DELAYS AND POWER SPECTRAL DENSITIES

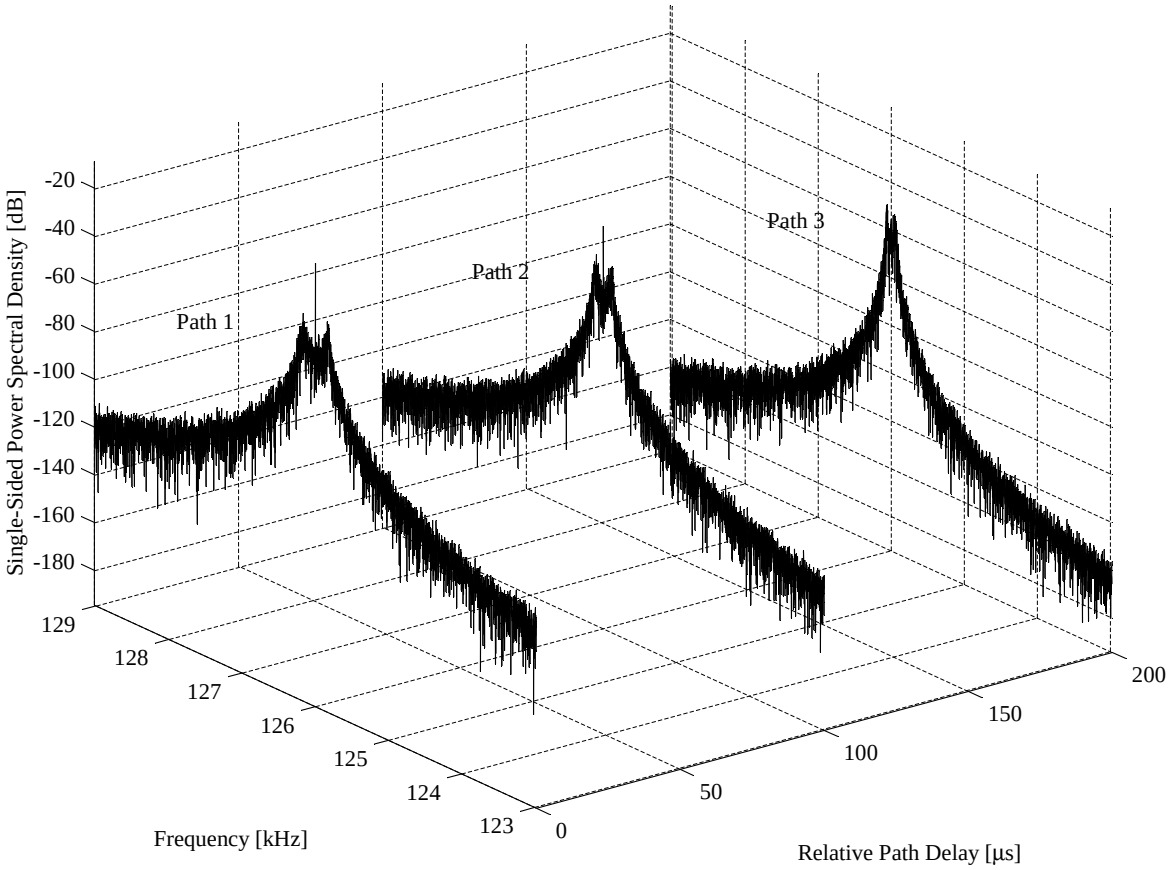

Figure 6.4: Measured Path Delays and PSDs Created by User-1's Complex Multipath Fading Channel Simulator

Each of the three flat faded paths, created by the complex multipath fading channel simulator for the complex input signal $s(t)$, were observed for a large number of samples. From the time signals

obtained for each path, relative path delays and PSDs were determined. *Fig.* 6.4 summarises these findings.

6.2.2.2 DISCUSSION OF THE SIMULATION RESULTS

From *Fig.* 6.4 it is clear that the first, second and third paths exhibit maximum Doppler spreads of 100 Hz, 67 Hz and 33 Hz, respectively. The PSDs of the first and second paths also show different, but noticeable LOS signal components, i.e. carrier components at 126 kHz. Thus, these paths are predominantly Rician distributed. The third path, however, experiences Rayleigh flat fading, since no LOS component is present. In summary, the following conclusions can be drawn from *Fig.* 6.4:

- The novel complex multipath fading channel simulator is capable of generating a variable number of statistically independent flat faded paths. Each path can be configured with its own maximum Doppler spread and Rician factor.
- The relative path delays and average path powers can be configured to exhibit realistic power delay profiles. In this study, exponential decay power delay profiles (see *Section* 2.6.3.3) were employed.
- Only fixed relative path delays are supported by the complex multipath fading channel simulator. Thus, the channel simulator can only mimic time invariant, or wide sense stationary multipath channels (see *Section* 2.4.1).

6.3 EVALUATION OF THE NARROWBAND COMPLEX QPSK COMMUNICATION SYSTEM

The general operation of the narrowband complex QPSK communication system (described in *Section* 5.2), used during the BER performance evaluation tests performed in AWGN and flat fading channel conditions, is evaluated in the following subsections. The complex QPSK transmitter and receiver structures were configured according to *Table* 5.1 and *Table* 5.2, respectively. Furthermore, no AWGN was included during the tests presented in the following subsections.

6.3.1 MEASURED TIME SIGNALS

Several I-channel and Q-channel narrowband complex QPSK receiver (see *Section* 5.2.2) time signals, including the matched filter and averaged fading amplitude outputs, were measured in noiseless, flat fading channel conditions in order to ensure the receiver's error-free operation. A complex flat fading channel simulator (see *Section* 2.6.2.3) configuration, consisting of a 9 dB Rician factor and 33 Hz Doppler spread, were chosen for these tests. Time signals measured in the receiver, together with the transmitter's original I-channel and Q-channel input symbol streams (prior to square-root Nyquist pulse shaping), are shown in *Fig.* 6.5. Note that the same symbols are present on the I-channel and Q-channel, since the system was configured for balanced operation.

From this figure, it is clear that there is a time lag of approximately 10 symbols between the transmitter's symbol streams (prior to pulse shaping) and the receiver's demodulated streams. This is the result of the time delays induced by the pulse shaping filters, elliptic receive filters (see *Fig.* 5.7) and matched filters. Note that this delay can be reduced by employing asymmetrically matched square-root Nyquist pulse shaping filtered in the transmitter and receiver [44]. Even with this time delay, which is compensated for during the BER performance measurements, the receiver functions satisfactorily (i.e. without any bit errors). Furthermore, it is clear that the average fading amplitude calculation, accomplished by implementing *Eq.* (5.13) in the receiver, was also successful, since it tracks the average changes in the symbol amplitudes perfectly.

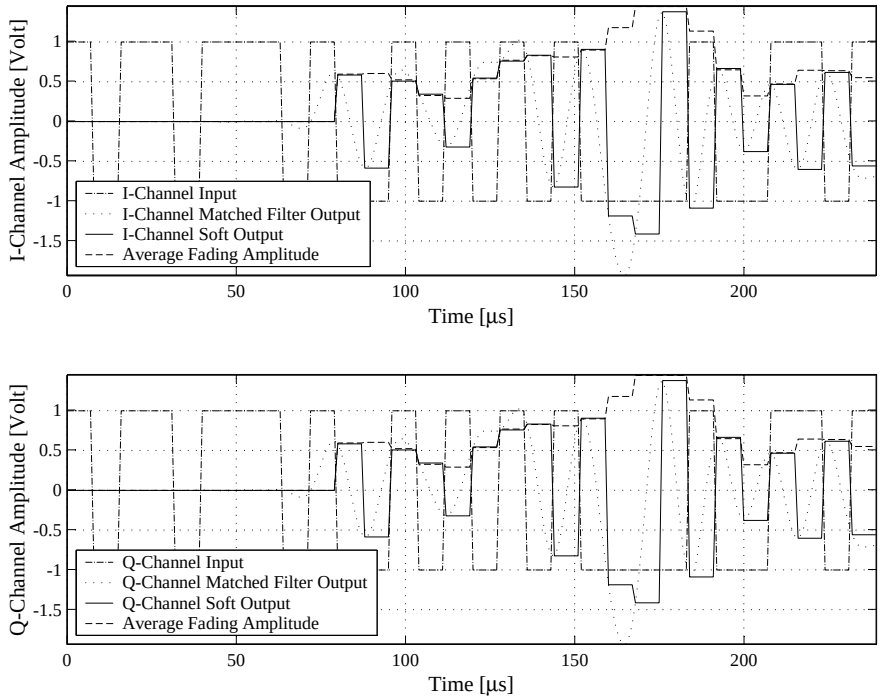

Figure 6.5: Measured Narrowband Complex QPSK Receiver's I-Channel and Q-Channel Time Signals

6.3.2 MEASURED EYE DIAGRAMS

Ensuring the correct operation of the I-channel and Q-channel square-root Nyquist pulse shaping filters (see *Eq.* (5.48)), employed in the narrowband complex QPSK transmitter (see *Section* 5.2.1), entailed obtaining the eye diagrams of their outputs. *Fig.* 6.6 shows that the eyes created by the transmitter's pulse shaping filters are not open, which was to be expected for square-root Nyquist pulse shaping.

Similar eye diagram results were obtained for the I-channel and Q-channel matched filter outputs in the narrowband complex QPSK receiver, which are shown in *Fig.* 6.7. From inspection it is clear that the receiver's eye diagrams are completely open at the appropriate sampling instances. This was to be expected, since the square-root Nyquist pulse shaping in the transmitter and matched filtering in the receiver combine to give overall Nyquist filtering with open eye diagrams [44]. Note that a noiseless channel, without any fading effects, were used to obtain these results.

6.3.3 MEASURED POWER SPECTRAL DENSITIES

PSDs were calculated for several of the critical time signals present in the narrowband complex QPSK communication system. These included PSDs for the transmitter's I-channel and Q-channel symbol streams, before and after square-root Nyquist pulse shaping, as well as PSDs for the outputs of the I-channel and Q-channel AWGN limiting elliptic receive filters. A perfect channel, without any AWGN or flat fading effects, was used to obtain these PSDs. From these results, depicted in *Fig.* 6.8, it is clear the square-root Nyquist pulse shaping limited the transmitter's effective output signal bandwidth from 1000 Hz to 750 Hz, as predicted by *Eq.* (5.49). Furthermore, the PSDs for the outputs of the I-channel and Q-channel elliptic receive filters show significant reductions in the frequency components above 750 Hz, without causing major distortions in the amplitude spectra of the information carrying frequency band from 0 Hz to 750 Hz.

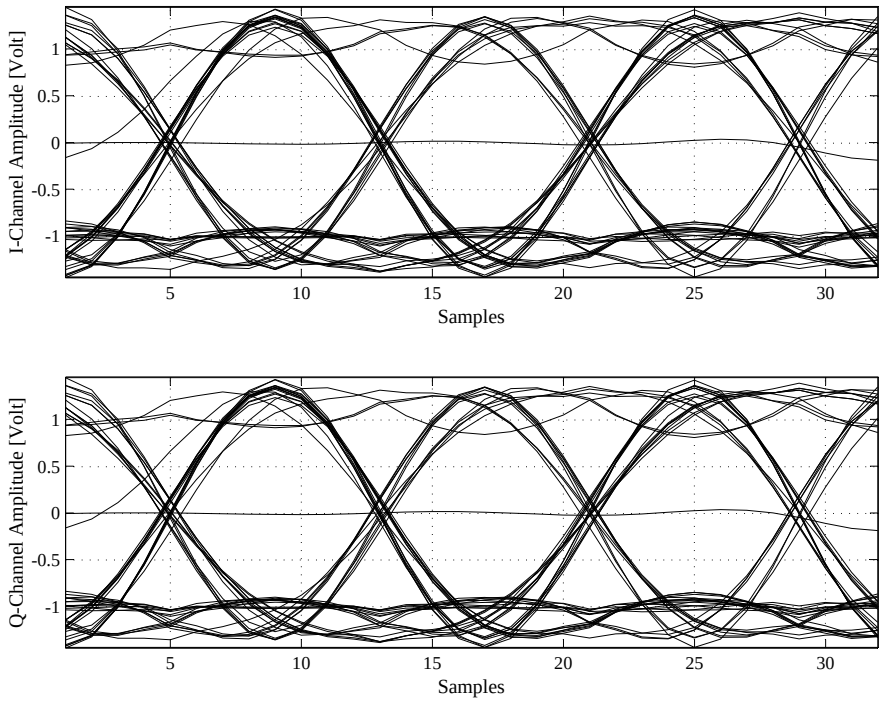

Figure 6.6: Measured Eye Diagrams of the Narrowband Complex QPSK Transmitter's I-Channel and Q-Channel Pulse Shaping Filter Outputs

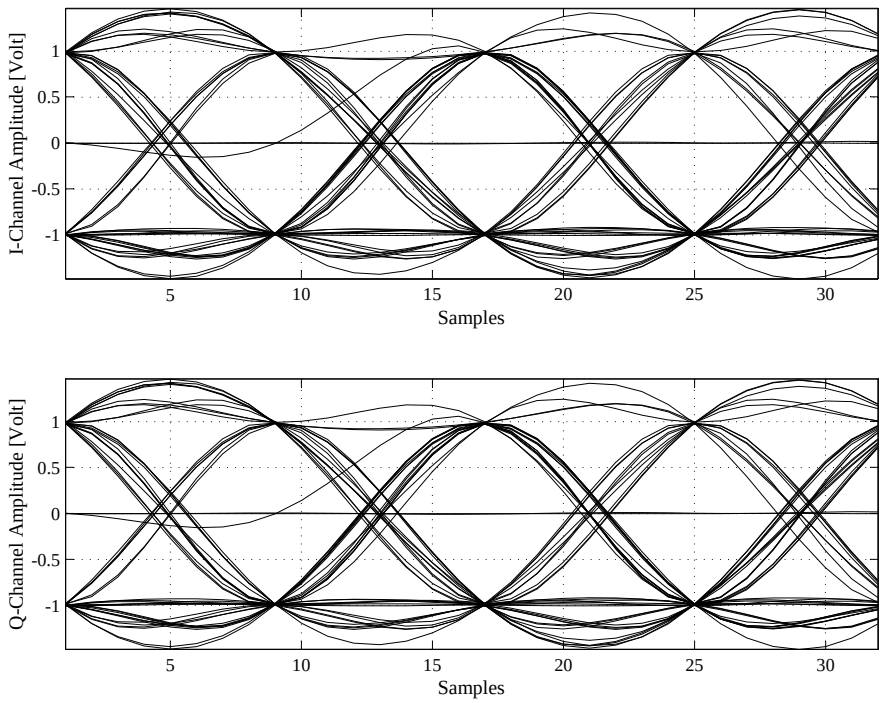

Figure 6.7: Measured Eye Diagrams of the Narrowband Complex QPSK Receiver's I-Channel and Q-Channel Matched Filter Outputs

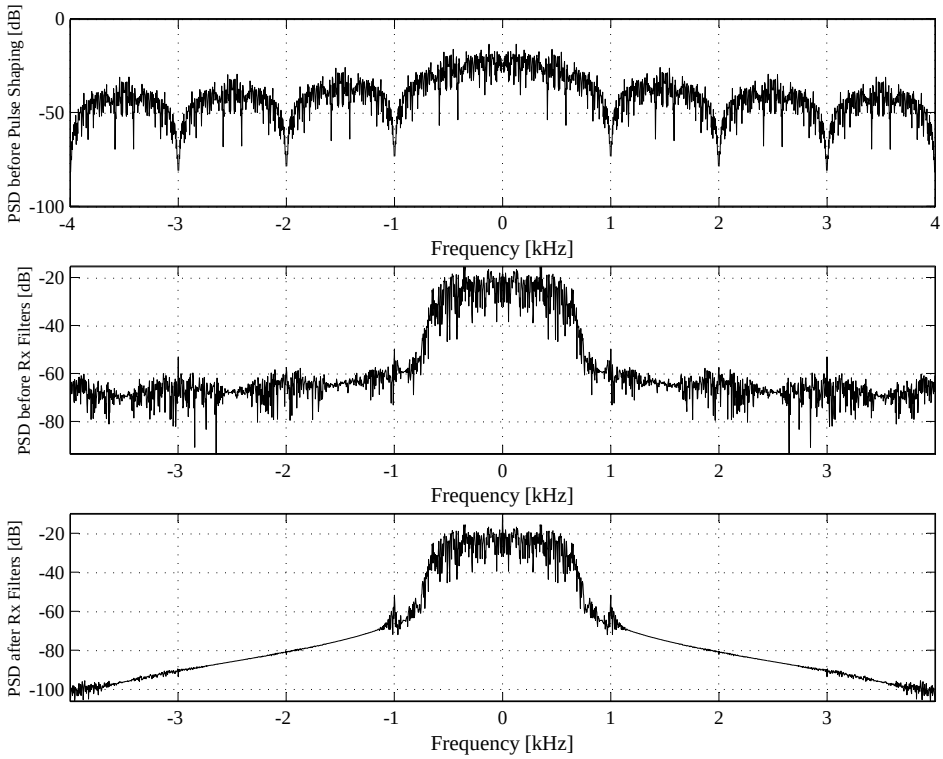

Figure 6.8: Measured PSDs of the Narrowband Complex QPSK Communication System

6.3.4 DISCUSSION OF THE SIMULATION RESULTS

From the eye diagram, time signal and PSD simulation results presented in the preceding subsections, the following observations can be made:

- The square-root Nyquist pulse shaping employed in the narrowband complex QPSK transmitter, effectively reduces the required transmission bandwidth by 25%.
- Applying square-root Nyquist matched filtering in the narrowband complex QPSK receiver, results in open eye diagrams under perfect channel conditions, i.e. no ISI is present in the demodulated signals.
- Initial limiting of the AWGN entering the narrowband complex QPSK receiver is successfully accomplished by the 6^{th} order elliptic lowpass receive filters, present on the I-channel and Q-channel branches (see *Fig.* 5.2). By splitting the Nyquist filtering function between the transmitter and receiver, additional AWGN suppression is achieved.
- The average fading amplitude calculation method proposed in *Section* 5.2.3 proved to be successful. Thus, perfect fading amplitude CSI information can be extracted from the complex flat fading channel simulator for use in the VA (see *Section* 4.4.2.2).

6.4 EVALUATION OF THE RAKE RECEIVER-BASED COMPLEX DS/SSMA QPSK COMMUNICATION SYSTEM

In the following subsections the general operation of the complex RAKE receiver-based DS/SSMA QPSK communication system, described in *Section* 5.3, is evaluated. Recall from *Section* 5.4.3 that

this communication system forms the basis of the simulation platform employed during the BER performance evaluation tests performed in multipath fading channel conditions. The results presented in the following subsections were obtained in noiseless channel conditions, with a single wideband transmitter (see *Fig.* 5.3.1), configured according to *Table* 5.4, and RAKE receiver (see *Fig.* 5.3.2), configured according to *Table* 5.7. Furthermore, the results presented here were obtained using length-63 CSSs.

6.4.1 MEASURED TIME SIGNALS

Time signals were measured at critical points in the complex DS/SSMA QPSK communication system, functioning in noiseless multipath fading channel conditions. This was done to ensure the overall error-free operation of the complex RAKE receiver-based DS/SSMA QPSK system's modulator, demodulator and average fading amplitude estimator (see *Section* 5.3.3). ABC sequences (see *Section* D.3.2.2) and ZC CSSs (see *Section* D.3.1.1) were adequate selections to prove the operation of these building blocks for filtered and unfiltered CSS families, respectively. The complex multipath fading channel simulator (see *Fig.* 2.8 in *Section* 2.6.3.2) employed, were configured according to user-1's channel parameters in *Table* 5.5. *Fig.* 6.9 depicts the measured time signals obtained for the complex

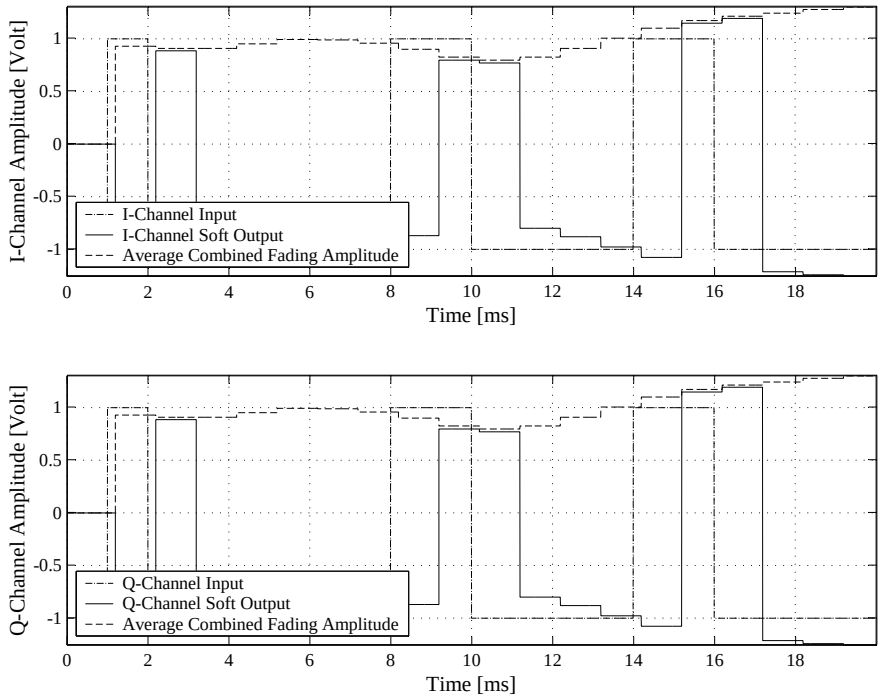

Figure 6.9: Measured I-Channel and Q-Channel Time Signals for a Wideband Complex DS/SSMA QPSK Communication System Employing ABC Sequences (with Rectangular Pulse Shaping) in Noiseless Multipath Fading Channel Conditions

DS/SSMA QPSK communication system using ABC sequences, without any additional chip-level pulse shaping, other than the default rectangular pulse shaping. Similar results are shown in *Fig.* 6.10 for a system employing ZC CSSs with square-root Nyquist pulse shaping (see *Eq.* (5.48)) in the transmitter and matched filtering in the RAKE receiver.

From *Fig.* 6.9 and *Fig.* 6.10 the following observations can be made: Firstly, the same symbols are transmitted on the I-channel and Q-channel, since the system is configured for balanced operation. Secondly, note the minor time delays between the transmitted symbols and demodulated symbols.

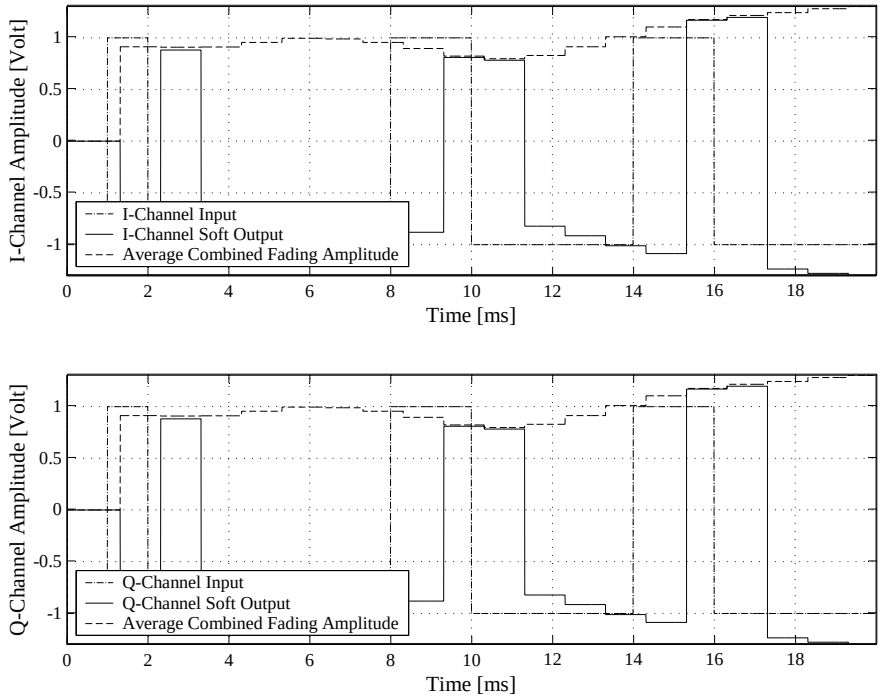

Figure 6.10: Measured I-Channel and Q-Channel Time Signals for a Wideband Complex DS/SSMA QPSK Communication System Employing ZC CSSs (with Square-Root Nyquist Pulse Shaping) in Noiseless Multipath Fading Channel Conditions

This delay is approximately 216 μs ($\tau_{max} = 200\mu$s maximum excess delay (see *Eq.* (2.13)), plus 16 μs rectangular pulse shaping and matched filtering delay) for the system employing ABC sequences and 320 μs ($\tau_{max} = 200\mu$s maximum excess delay, plus 120 μs square-root Nyquist pulse shaping and matched filtering delay) for the system employing ZC CSSs.

6.4.2 MEASURED EYE DIAGRAMS

Shown in *Fig.* 6.11 are the measured eye diagrams of the I-channel and Q-channel pulse shaping filter outputs of a complex DS/SSMA QPSK transmitter, employing QPH CSSs with chip-level square-root Nyquist pulse shaping. The motivation behind using QPH CSSs during the validation of the operation of the wideband complex transmitter's square-root Nyquist pulse shaping filters, are two-fold: Firstly, recall from *Table* 5.4 that no additional pulse shaping is employed for the ABC sequences and DSB CE-LI-RU filtered GCL CSSs (see *Section* D.3.2.1). Secondly, QPH CSSs are chosen over ZC CSSs, due to the fact that these CSSs' chips take on only bipolar amplitude levels on the I-channel and Q-channel branches prior to square-root Nyquist pulse shaping. Conversely, ZC CSSs exhibit a multitude of chip amplitudes (see *Section* D.3.1 in *Appendix D*), resulting in intricate eye diagrams.

As was to be expected, the eyes in *Fig.* 6.11 are not completely open. However, applying square-root Nyquist matched filtering on the I-channel and Q-channel branches in the complex DS/SSMA QPSK RAKE receiver, not only limits the AWGN and MUI entering the receiver, but also thoroughly opens the eyes. *Fig.* 6.12 shows such I-channel and Q-channel matched filter output eye diagrams for a complex RAKE receiver-based DS/SSMA QPSK system employing QPH CSSs (see *Section* D.3.1.2). Note that these eye diagram results were obtained in perfect noiseless channel conditions with no multipath fading effects.

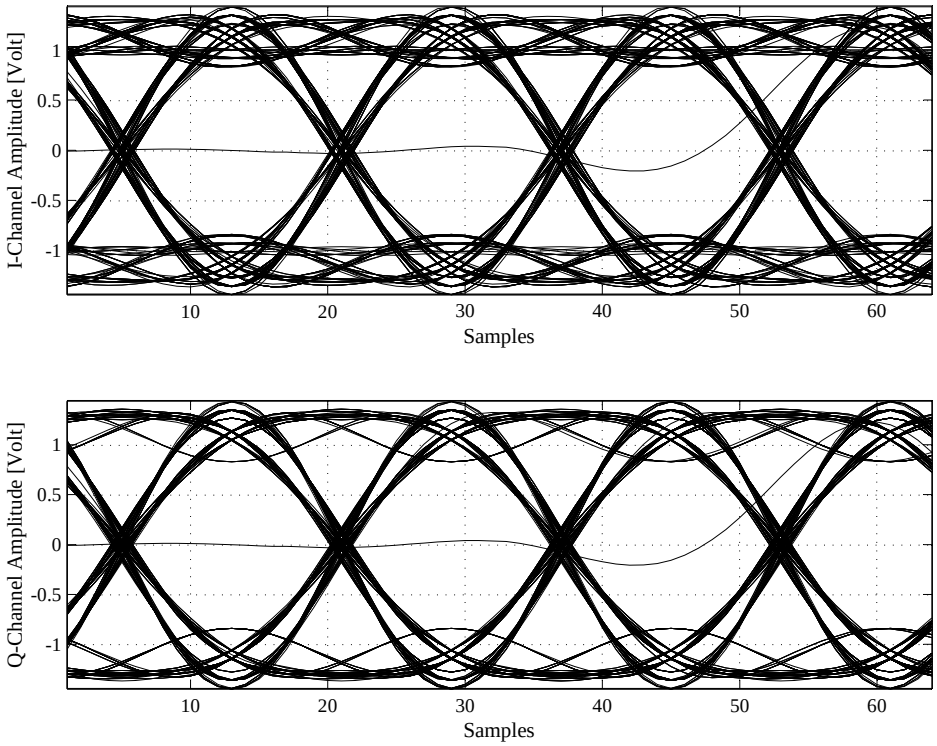

Figure 6.11: Measured Eye Diagrams of the QPH CSS-Based Wideband Complex DS/SSMA QPSK Transmitter's I-Channel and Q-Channel Pulse Shaping Filter Outputs

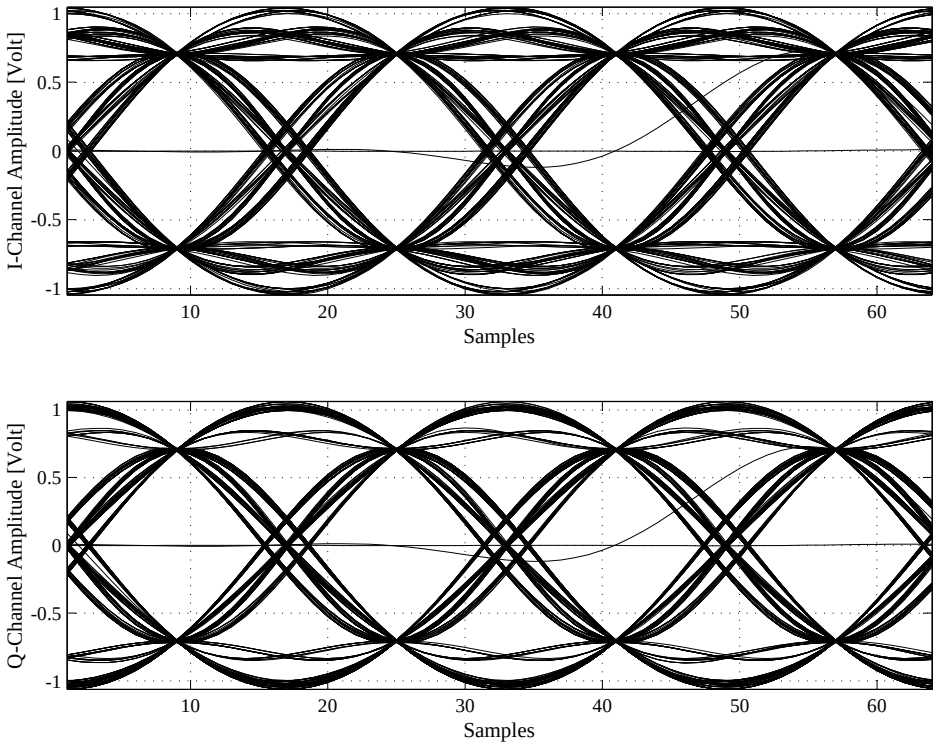

Figure 6.12: Measured Eye Diagrams of the QPH CSS-Based Wideband Complex DS/SSMA QPSK RAKE Receiver's I-Channel and Q-Channel Matched Filter Outputs

6.4.3 MEASURED POWER SPECTRAL DENSITIES

A multitude of PSDs were calculated for RAKE receiver-based complex DS/SSMA QPSK communication systems, employing the filtered and unfiltered CSS families presented in *Appendix D*. The PSDs were computed for transmitter output signals (before and after pulse shaping), as well as elliptic receive filter output signals. Perfect noiseless channel conditions, with no multipath fading effects, were used to obtain the PSD results presented here for DS/SSMA systems using length $M_{seq} = 63$ CSSs.

Fig. 6.13 shows the PSD results obtained for a system employing unfiltered ZC CSSs. Note that the first zero in the spectrum occurs at 63000 kHz, as was to be expected. After square-root Nyquist filtering, the transmission bandwidth required is reduced to approximately $B_{sig} = 47250$ kHz, as was predicted by *Eq.* (5.50). Lastly, the PSD of the output of the 6^{th} order elliptic receive filter (bottom PSD in *Fig.* 6.13) clearly shows a considerable suppression of out-of-band signal components.

Results similar to that of *Fig.* 6.13 are shown in *Fig.* 6.14 for a system employing QPH CSSs. Once again, square-root Nyquist pulse shaping has limited the required transmission bandwidth to approximately $B_{sig} = 47250$ kHz. Furthermore, 6^{th} order elliptic receive filtering suppressed unwanted signal components entering the RAKE receiver outside this band.

The measured PSDs of the first filtered CSS family considered, showed in *Fig.* 6.15, are those of DSB CE-LI-RU filtered GCL sequences. Recall that no additional pulse shaping is employed for these sequences, since built-in filtering occurs during their generation (see *Section* D.3.2.1). Furthermore, from *Fig.* 6.15 it is clear that, when this filtered CSS family is employed in a complex DS/SSMA QPSK system (configured for balanced operation), transmitter output PSD characteristics consistent with Nyquist's minimum (roll-off factor $\varsigma = 0$) bandwidth criteria, as was claimed in *Section* D.3.2.1, are obtained. Thus, the required transmission bandwidth is approximately $B_{sig} = 31500$ Hz, as was predicted by *Eq.* (5.51). According to the bottom figure in *Fig.* 6.15, the elliptic receive filters once again limited the out-of-band noise entering the RAKE receiver.

Finally, the PSDs of a complex DS/SSMA QPSK system, employing ABC sequences in a balanced configuration, fall under the spotlight in *Fig.* 6.16. Note that the application of this CSS family in such a transmitter configuration, results in SSB transmitter output PSDs. For the wideband system presented in this study, upper sideband SSB transmitter output signals are generated. Furthermore, the upper sideband appears in correspondence with Nyquist's minimum (roll-off factor $\varsigma = 0$) bandwidth criteria. Thus, as predicted by *Eq.* (5.52), the required transmission bandwidth is approximately $B_{sig} = 15750$ Hz. Wideband noise (AWGN or MUI) entering the RAKE receiver will be sufficiently bandlimited by the elliptic receive filters, as can be seen from the bottom PSD in *Fig.* 6.16.

6.4.4 DISCUSSION OF THE SIMULATION RESULTS

Some insights into the operation of the complex RAKE receiver-based DS/SSMA QPSK communication system presented in this study, gained from the eye diagram, time signal and PSD simulation results discussed in the preceding subsections, are as follows:

- The transmission bandwidth of complex DS/SSMA QPSK transmitters, employing unfiltered ZC and QPH CSSs, were reduced by 25% by employing square-root Nyquist pulse shaping. Furthermore, the square-root Nyquist matched filtering, applied in the complex DS/SSMA RAKE receivers for these CSS families, delivered open eye diagrams under perfect channel conditions.

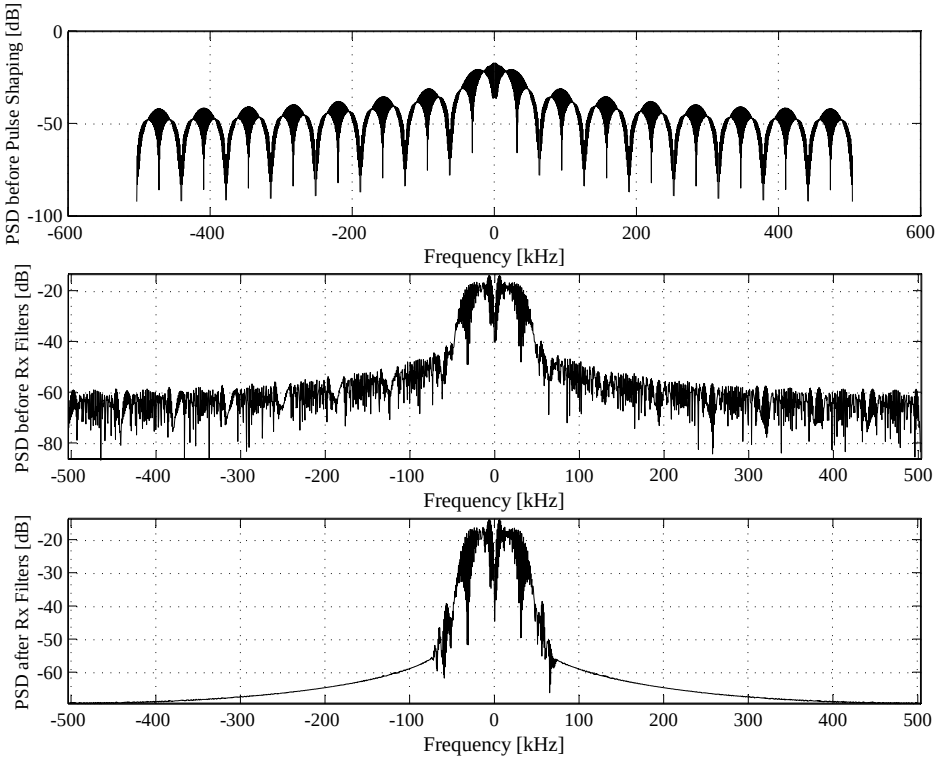

Figure 6.13: Measured PSDs of a Wideband Complex DS/SSMA QPSK Communication System Employing Length-63 ZC CSSs

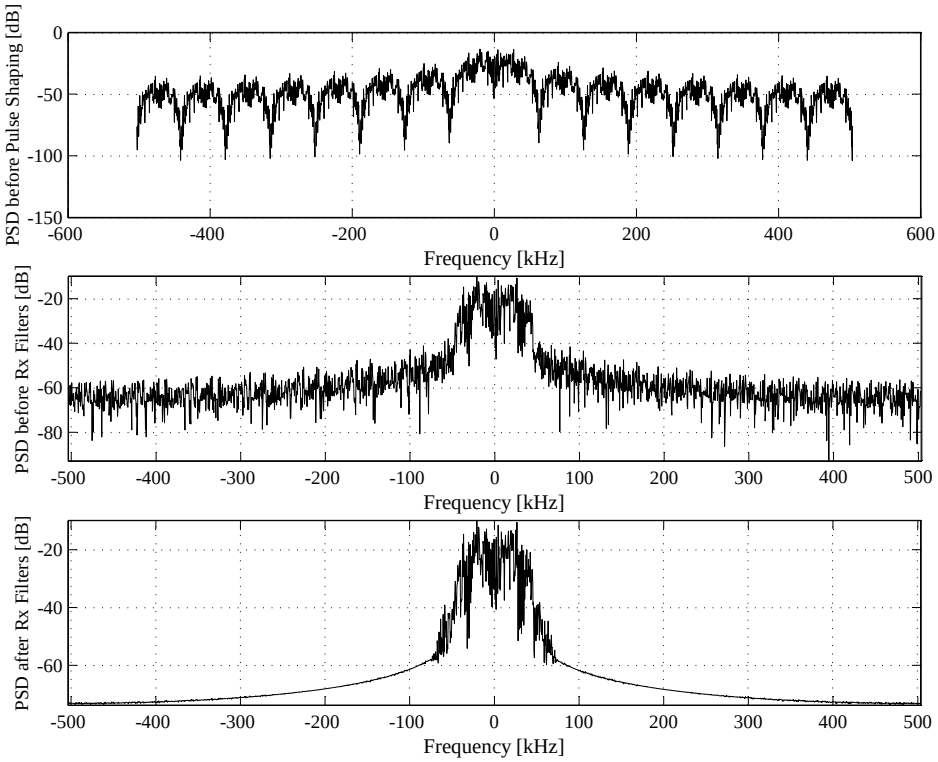

Figure 6.14: Measured PSDs of a Wideband Complex DS/SSMA QPSK Communication System Employing Length-63 QPH CSSs

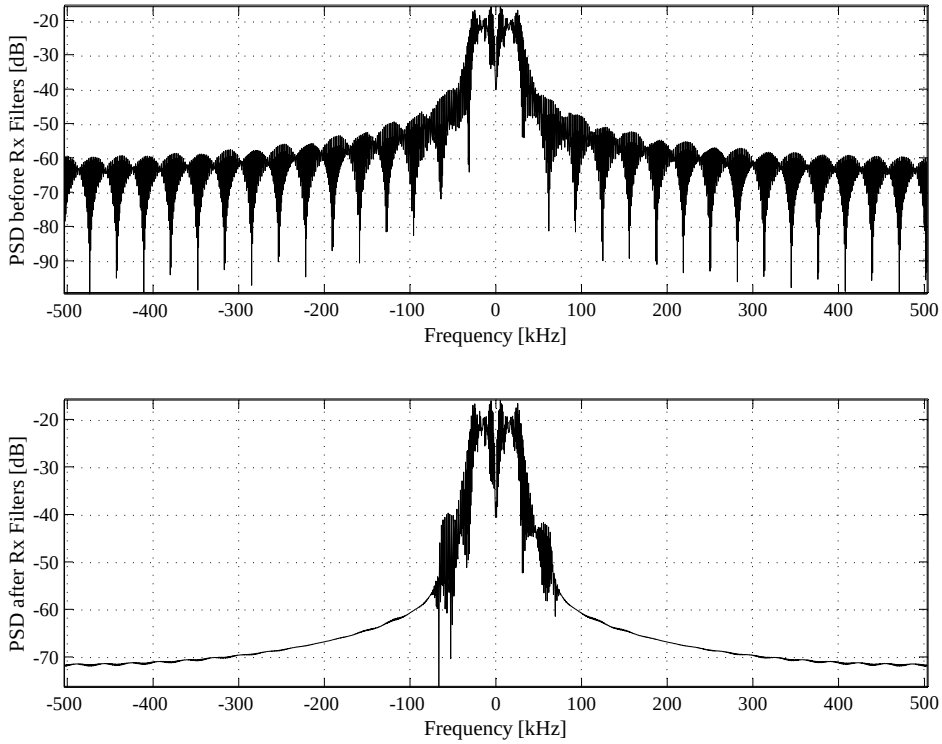

Figure 6.15: Measured PSDs of a Wideband Complex DS/SSMA QPSK Communication System Employing Length-63 DSB CE-LI-RU filtered GCL CSSs

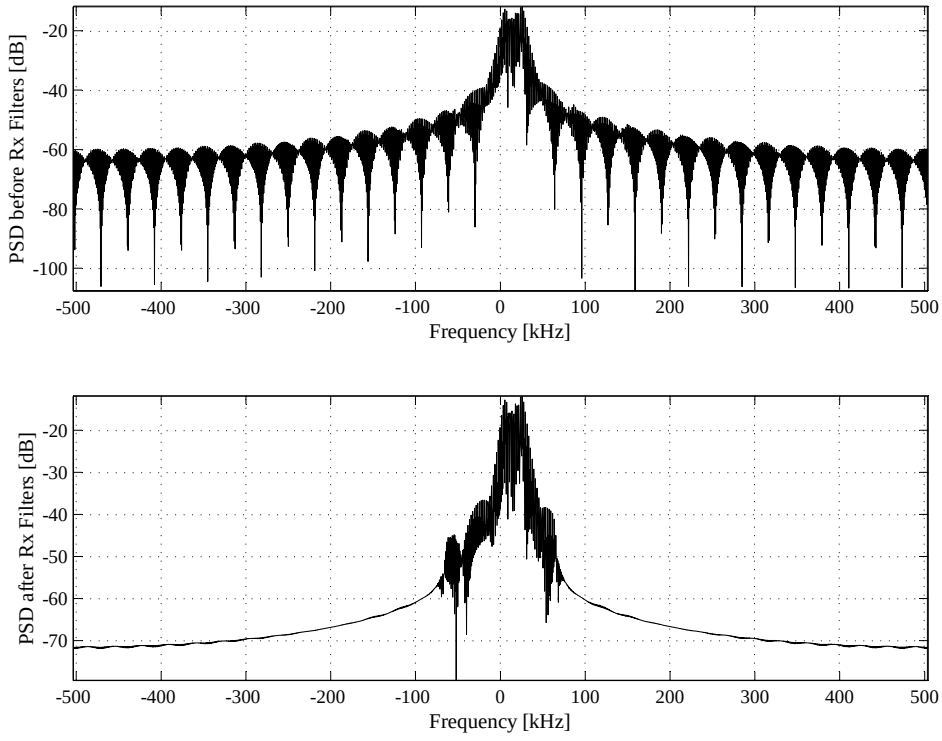

Figure 6.16: Measured PSDs of a Wideband Complex DS/SSMA QPSK Communication System Employing Length-63 ABC Sequences

- By employing filtered CSSs, even greater improvements were made on the required transmission bandwidth: DSB CE-LI-RU filtered GCL sequences require 66.67% of the transmission bandwidth that the unfiltered CSSs (with chip-level square-root Nyquist pulse shaping) require. Moreover, by generating SSB wideband transmitter output signals, ABC sequences further reduce this bandwidth requirement to only 33.33%.

- Primary limiting of AWGN and MUI entering the wideband complex DS/SSMA QPSK RAKE receiver is effectively accomplished by the 6^{th} order elliptic lowpass filters, present on both the I-channel and Q-channel branches (see *Fig.* 5.4). Further noise and interference suppression is performed by the matched filtering, which attempts to maximise the SNR.

- From *Fig.* 6.9 and *Fig.* 6.10 it is clear that the average fading amplitude calculation scheme for complex DS/SSMA QPSK RAKE receivers, proposed in *Section* 5.3.3, is successful for systems employing filtered or unfiltered CSSs. Thus, perfect fading amplitude CSI information can be extracted, from a complex multipath fading channel simulator, for use in the VA (see *Section* 4.4.2.2).

- The PSDs of the QPH CSSs, shown in *Fig.* 6.13, exhibit classic *sinc*-like profiles, since these sequences are generated using multiple, unique binary sequences (see *Section* D.3.1.2). However, the GCL CSSs [9] considered, i.e. ZC, ABC and DSB CE-LI-RU filtered GCL CSSs, appear to possess relatively flat PSDs in their respective transmission bandwidths. This can be attributed to their chirp-like natures (see *Section* D.3).

- Recall from *Table* 5.4 that the symbol rate of the complex DS/SSMA QPSK transmitters, employing length $M_{seq} = 63$ CSSs, are 1000 Hz prior to spreading. Hence, using *Eq.* (D.4) and *Eq.* (D.5) from *Section* D.2.4, it follows that $SF = 63$ and $PG = 17.99$ dB for all of the CSS families considered. Thus, in the presence of narrowband interferers or jamming signals, length-63 CSSs will be able to improve the SNR (or signal-to-inference ratio, to be precise) of the wideband communication system by at least 17.99 dB. Since ABC sequences only occupy half of the transmission bandwidth required by the other CSSs considered, it can be argued that DS/SSMA communication systems employing these sequences will only be affected by jamming signals, attacking half of the effective transmission bandwidth required by the non-SSB CSSs. Hence, it can be postulated that ABC sequences will exhibit superior narrowband interference suppression, when compared to the other CSSs families. In this study, however, SS was investigated purely as a MA mechanism, and not as a narrowband interference suppression approach. As such, in this study the *Processing Gain* (PG) is not of such great importance, but rather the periodic auto-correlation (see *Section* D.2.2) and cross-correlation (see *Section* D.2.3) characteristics of the CSSs employed, since these characteristics govern the BER performance of a DS/SSMA system due to the presence of MUI.

- An inspection of the PSDs presented in *Fig.* 6.13 to *Fig.* 6.16 reveals that, when compared to DS/SSMA systems using binary spreading sequences or unfiltered CSSs, wideband systems employing either square-root Nyquist chip-level pulse shaping or the filtered CSS families described in *Appendix D*, require less transmission bandwidth. This is most apparent for the ABC and DSB CE-LI-RU filtered GCL CSSs. Thus, for a fixed data rate, using square-root Nyquist pulse shaping, or CE-LI-RU filtering, in conjunction with CSSs, it is possible to employ longer sequences without conceding PG or exceeding the transmission bandwidth requirements of an equivalent DS/SSMA system using, for example, unfiltered binary Gold spreading sequences. This sequence length increase (and resultant user capacity increase) can be modelled as an equivalent *Spreading Sequence Length Diversity* (SSLD), a novel concept which is introduced in *Section* D.2.6. Using the calculated bandwidth results, given by *Eq.* (5.50) to *Eq.* (5.52), for an unspreaded bit rate of 1000 b/s and CSS length of $M_{seq} = 63$, the *Bandwidth Expansion Factor*s (BEF) (see *Section* D.2.5) and SSLDs given in *Table* 6.1 were calculated for wideband complex DS/SSMA systems employing the CSS families presented in *Appendix D*. Also given in this table, are the BEFs and SSLDs for

DS/SSMA systems employing unfiltered binary Gold sequences, unfiltered ZC CSSs and unfiltered QPH CSSs. According to *Table* 6.1, in order to occupy a 126 kHz transmission bandwidth, it is

Table 6.1: Comparison of the BEFs and SSLDs for Different Filtered and Unfiltered Spreading Sequence Families with $f_{bit} = 1000$ b/s, $M_{seq} = 63$ chips and $f_{chip} = 63000$ Hz.

Spreading Sequence Family	BEF	SSLD
Unfiltered Binary Gold Sequences	63	1
Unfiltered ZC CSSs	63	1
Unfiltered QPH CSSs	63	1
Square-Root Nyquist (Roll-off Factor $\varsigma = 0.5$) Filtered ZC CSSs	47.25	1.333
Square-Root Nyquist (Roll-off Factor $\varsigma = 0.5$) Filtered QPH CSSs	47.25	1.333
DSB CE-LI-RU filtered GCL CSSs	31.5	2
ABC Sequences	15.75	4

possible to use ABC sequences with four times the length (for example length $M_{seq} = 251$) of unfiltered binary Gold sequences, thereby producing a 6 dB improvement in PG, better periodic correlation characteristics (i.e. lowered RAKE self-noise and MUI levels), but most importantly, a higher CDMA user capacity. To illustrate this statement, consider an arbitrary size-$M_{fam}^{filtered}$ family of filtered length-$M_{seq}^{filtered}$ GCL-like CSSs (such as ABC or DSB CE-LI-RU filtered GCL CSSs). If $M_{seq}^{filtered}$ is a prime number, $M_{fam}^{filtered}$ is calculated as follows (derived from *Eq.* (D.9)):

$$\begin{aligned} M_{fam}^{filtered} &= M_{seq}^{filtered} - 1 \\ &\approx SSLD.M_{seq}^{unfiltered} - 1 \\ &\approx SSLD.\left(M_{fam}^{unfiltered} + 1\right) - 1 \end{aligned} \tag{6.1}$$

In this equation $M_{seq}^{unfiltered}$ and $M_{fam}^{unfiltered}$ respectively denote the CSS length (also a prime number) and family size of an unfiltered CSS family, requiring the same transmission bandwidth as the filtered CSS family. For example, a DS/SSMA system using unfiltered length $M_{seq} = 61$ ZC CSSs will require approximately the same transmission bandwidth as a system using length $M_{seq} = 241$ ABC sequences. However, the ZC sequence-based system supports only 60 users, whereas the ABC sequence-based system supports approximately $243 = 4.(60 + 1) - 1$ users (to be precise, it supports up to 240 users). Although the remainder of this study presents BER performances for coded wideband RAKE receiver-based complex DS/SSMA systems using only length $M_{seq} = 63$ CSSs, the influence of sequence length on MUI in uncoded wideband complex DS/SSMA systems, employing ABC sequences, is briefly investigated in *Section* 6.5.1.3.3.

6.5 BIT-ERROR-RATE PERFORMANCE EVALUATION RESULTS

The following subsections present the BER performances results obtained for several different coding schemes under AWGN, flat fading and multipath fading channel conditions. These coding schemes include uncoded systems, NSC codes (see *Section* 3.2.1.3.1), RSC codes (see *Section* 3.2.1.3.2), binary cyclic block codes (VA decoded using original and reduced trellis structures (see *Section* 4.3.2)), binary Hamming block codes (see *Section* 3.2.2.3.1) (with classic ML and VA decoding), binary BCH block codes (see *Section* 3.2.2.3.2) with VA decoding, as well as non-binary RS block codes (see *Section* 3.2.2.3.3) with *Berlekamp-Massey* (see *Appendix B*) and VA decoding. The influence of

puncturing (see *Section* 3.2.4) and interleaving (see *Section* 3.2.3) are also investigated for several of these coding schemes.

Simple narrowband complex QPSK (see *Section* 5.2) transmitters (configured according to *Table* 5.1) and receivers (configured according to *Table* 5.2) were employed in the AWGN and flat fading BER performance evaluation platforms, shown in *Fig.* 5.5 (see *Section* 5.4.1) and *Fig.* 5.8 (see *Section* 5.4.2), respectively. *Table* 5.3 summarises the different channel configurations considered during the flat fading channel BER performance tests.

Multipath fading BER performance test results were obtained using the simulation platform portrayed in *Fig.* 5.9 (see *Section* 5.4.3). *Table* 5.4 and *Table* 5.7 detail the respective complex DS/SSMA QPSK transmitter (see *Section* 5.3.1) and RAKE receiver (see *Section* 5.3.2) configurations employed by each of the users in the CDMA system. Up to 10 users were supported in these performance evaluation tests in order to investigate the effects of MUI. *Table* 5.5 and *Table* 5.6 contain the individual complex multipath fading channel simulator (see *Section* 2.6.3.2) configurations, associated with each of the 10 possible CDMA users. Results presented here not only contrast the BER performances obtained using different CSS families, but also the influence of CSS length and sequence selection approach for ABC sequence-based CDMA system.

6.5.1 UNCODED COMMUNICATION SYSTEMS

In the following two subsections simulated and theoretical BER performance results are presented for uncoded narrowband complex QPSK communication systems (see *Section* 5.2), functioning in AWGN (see *Section* 2.2) and flat fading (see *Section* 2.5.1.1) channel conditions. Thereafter, simulated BER performance results are presented for uncoded wideband complex DS/SSMA QPSK systems (see *Section* 5.3), employing the filtered and unfiltered CSSs of *Appendix D*, in multi-user frequency selective fading (see *Section* 2.5.1.1) channel conditions. The results given here will be used as baseline references for the simulated BER performance results of the coded systems, presented in the remainder of this chapter.

6.5.1.1 AWGN CHANNEL RESULTS

Fig. 6.17 shows the simulated BER performance of an uncoded complex QPSK communication system (see *Section* 5.2) in an AWGN environment (see *Section* 2.2). The theoretical curve, defined by *Eq.* (5.20), is also present on this figure.

6.5.1.2 FLAT FADING CHANNEL RESULTS

The simulated BER performance results for uncoded complex QPSK systems (see *Section* 5.2), operating in flat fading channel conditions with maximum Doppler spreads (see *Section* 2.4.3.3) of $B_{D,i} = 33$ Hz and $B_{D,i} = 100$ Hz, are shown in *Fig.* 6.18 and *Fig.* 6.19, respectively. The simulated results shown here include BER curves for Rician factors (see *Section* 2.5.2.2) of $K_i = -100$ dB (i.e. fading amplitudes with near-Rayleigh PDFs), $K_i = 0$ dB and $K_i = 9$ dB. Also depicted on these figures are the uncoded system's AWGN BER performance curve, as well as the theoretical BER performance curve for slow Rayleigh flat fading channel conditions, given by *Eq.* (5.24).

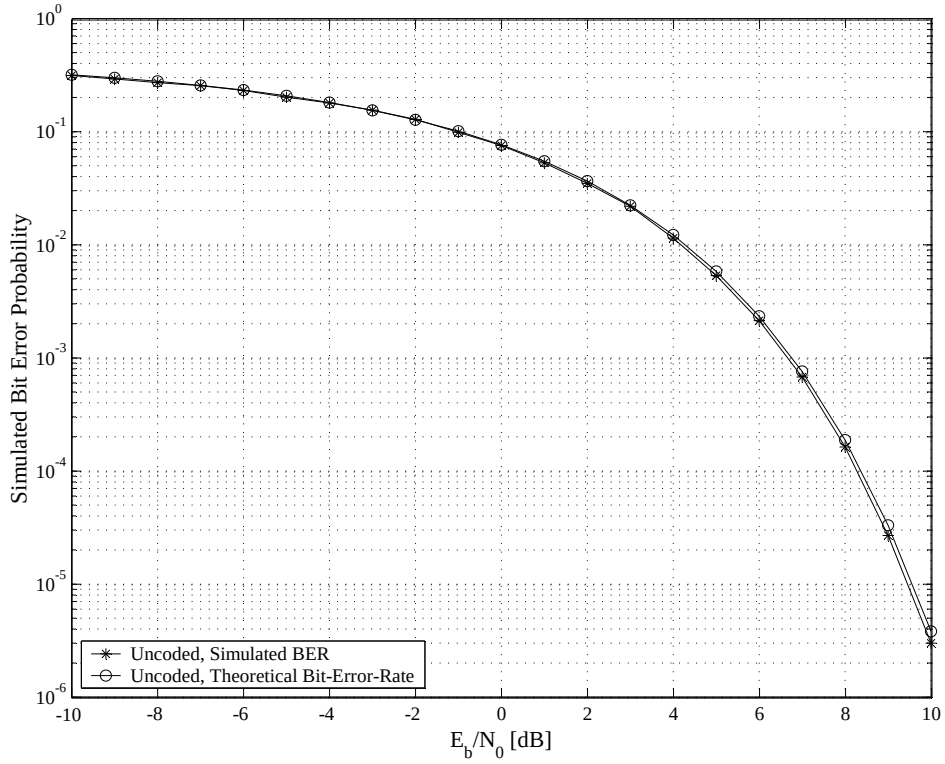

Figure 6.17: BER Performances of an Uncoded Narrowband Complex QPSK Communication System in AWGN Channel Conditions

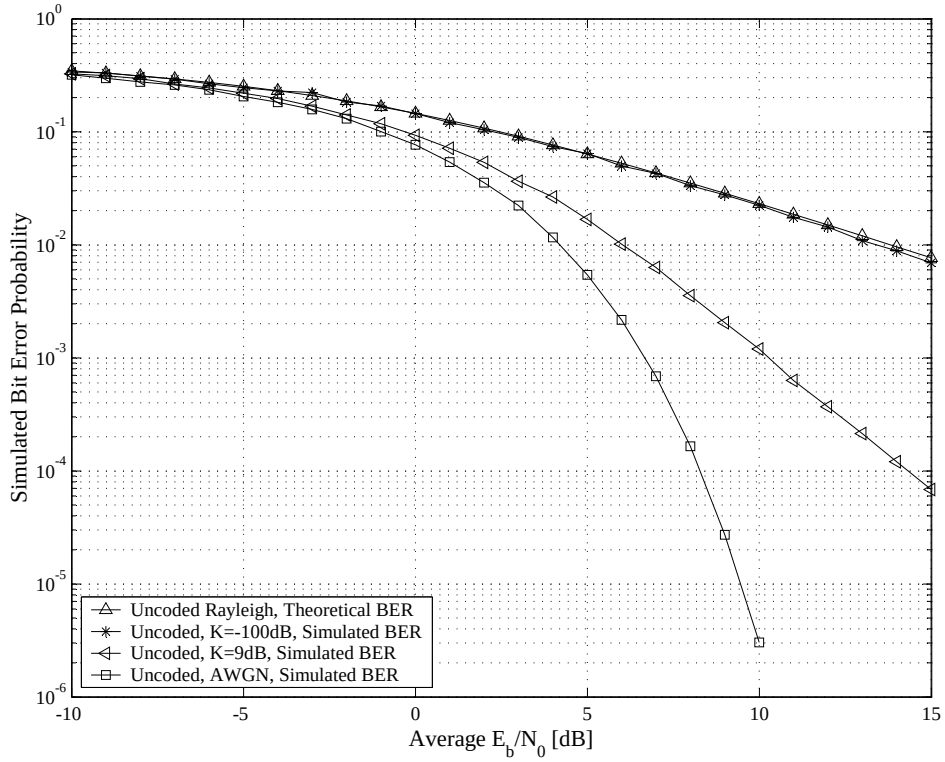

Figure 6.18: BER Performances of an Uncoded Narrowband Complex QPSK Communication System in Flat Fading Channel Conditions, $B_{D,i} = 33$ Hz

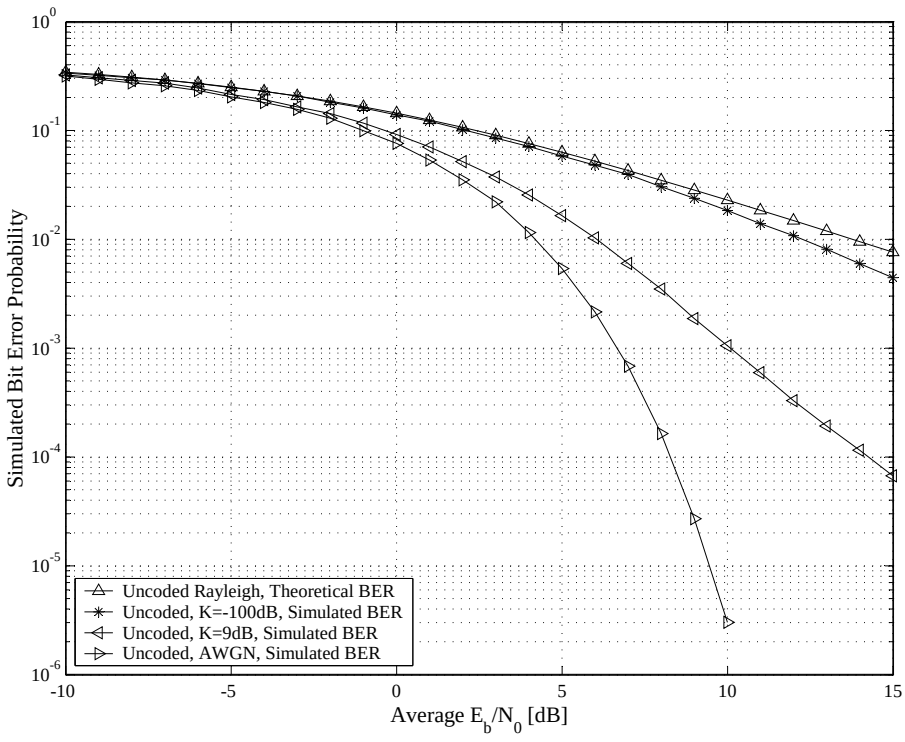

Figure 6.19: BER Performances of an Uncoded Narrowband Complex QPSK Communication System in Flat Fading Channel Conditions, $B_{D,i} = 100$ Hz

6.5.1.3 MULTIPATH FADING CHANNEL RESULTS

6.5.1.3.1 BER Performance Results for the Different CSS Families

The simulated BER performance curves for uncoded RAKE receiver-based complex DS/SSMA QPSK communication systems, employing length $M_{seq} = 63$ ABC (see *Section* D.3.2.2), DSB CE-LI-RU filtered GCL (see *Section* D.3.2.1), ZC (see *Section* D.3.1.1) and QPH (see *Section* D.3.1.2) CSSs in multipath fading channel conditions, are shown in *Fig.* 6.20, *Fig.* 6.21, *Fig.* 6.22 and *Fig.* 6.23, respectively. Note that sequences were optimally selected (see *Section* 6.5.1.3.2) for the ABC sequences scenario, whereas arbitrarily selected sequences were used during the experiments with DSB CE-LI-RU filtered GCL, ZC and QPH CSSs. The reasoning behind this sequence selection approach is motivated in *Section* 6.5.1.3.2.

In *Fig.* 6.20 to *Fig.* 6.23 simulated BER performance curves are shown for complex DS/SSMA QPSK communication systems employing two different types of receiver structures: Firstly, the BER performance curves for systems employing classic non-RAKE receiver structure (i.e. single tap RAKE receivers) are shown. Secondly, simulated BER performance results for systems using the complex DS/SSMA QPSK RAKE receiver structure of *Fig.* 5.4, are depicted. In the case of the RAKE receiver-based simulations, user-1's receiver was configured according to *Table* 5.7, with the RAKE receiver's tap delays and weights configured for perfect MRC (see *Section* 5.3.2) by matching them to user-1's unique multipath fading channel parameters. Due to their obvious superior performances, only RAKE receiver structures were used to obtain the multipath fading channel simulation results presented in the remainder of this chapter. For reference purposes, the BER performance of an uncoded DS/SSMA QPSK communication system (without a RAKE receiver), operating in a single path, non-fading AWGN channel, is also present on these figures.

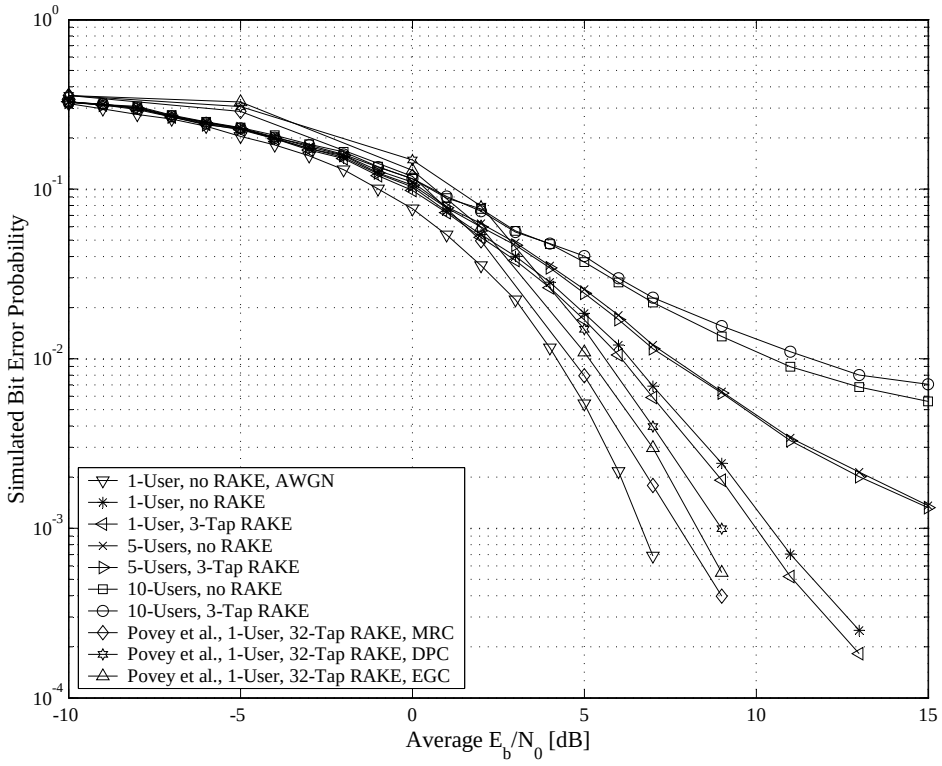

Figure 6.20: BER Performances of Uncoded Wideband Complex QPSK Communication Systems Employing ABC Sequences in Multi-User Multipath Fading Channel Conditions, $M_{seq} = 63$

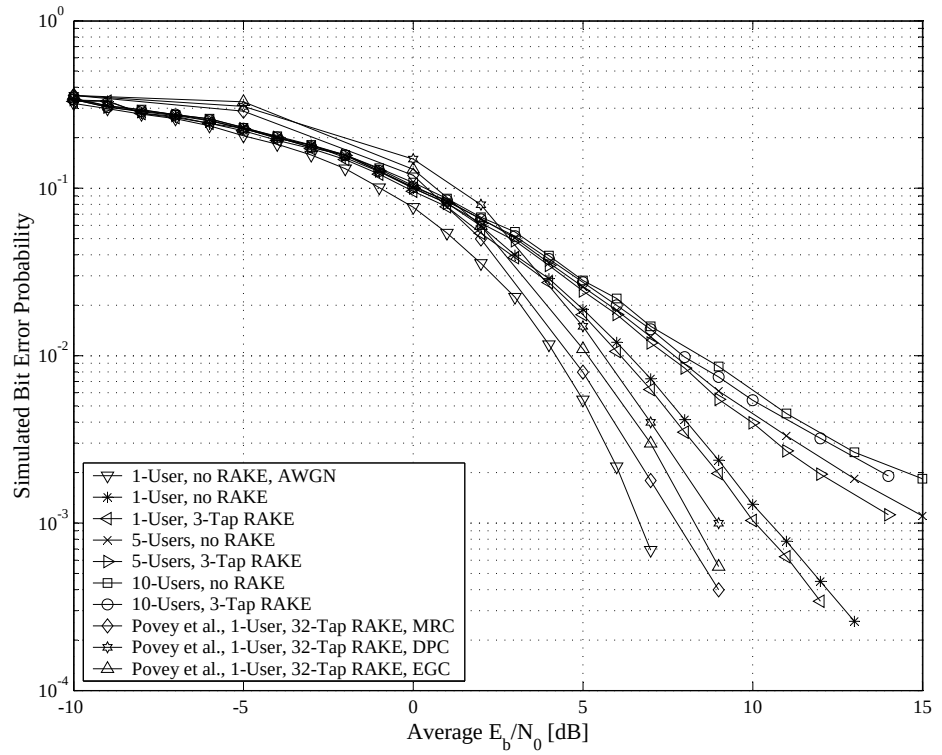

Figure 6.21: BER Performances of Uncoded Wideband Complex QPSK Communication Systems Employing DSB CE-LI-RU Filtered GCL CSSs in Multi-User Multipath Fading Channel Conditions, $M_{seq} = 63$

The simulated BER performance results, presented by *Povey et al.* in [158] for a DS/SSMA system a employing 32-tap RAKE receiver structure, are also included in *Fig.* 6.20, *Fig.* 6.21, *Fig.* 6.22 and *Fig.* 6.23. In [158], *Povey et al.* considered a DS/SSMA *Differential Phase Shift Keying* (DPSK) system, configured for a bit rate of 4.8 kb/s and a PN spreading sequence of length $M_{seq} = 1024$ chips. The multipath fading channel model *Povey et al.* employed during their Monte Carlo simulations, consisted of $L = 32$ resolvable paths, each path configured to generate a Rayleigh fading distribution (see *Section* 2.5.2.1) and maximum Doppler spread of $B_{D,i} = 100$ Hz (see *Section* 2.4.3.3). Furthermore, this multipath fading channel implements an exponential decay power delay profile (see *Section* 2.6.3.3) and a maximum excess delay of $\tau_{max} = 6.5$ μs (see *Section* 2.4.3.1), with the 32 paths evenly spread over this time frame. In their study, *Povey et al.* considered MRC, DPC and EGC RAKE combining techniques.

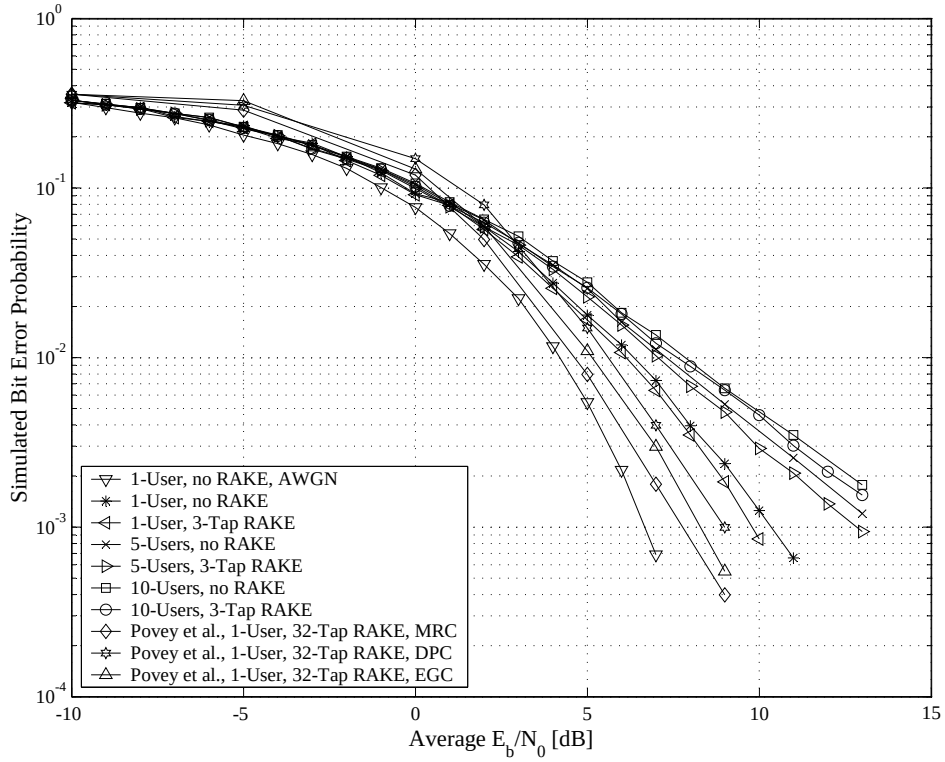

Figure 6.22: BER Performances of Uncoded Wideband Complex QPSK Communication Systems Employing ZC CSSs in Multi-User Multipath Fading Channel Conditions, $M_{seq} = 63$

6.5.1.3.2 The Influence of CSS Selection - An ABC Sequences Case Study

Not only is it intuitively understandable, but also a known fact that the spreading sequence length M_{seq} is the predominant factor dictating the sequence family size M_{fam}. For example, for the GCL sequences [9] considered in this study (ABC, DSB CE-LI-RU filtered GCL and ZC CSSs), the family size can be determined using *Eq.* (D.9). From this equation it is apparent that the largest sequence families are obtained using prime sequence lengths. This notwithstanding, generation of GCL CSSs [9] require the selection of sequence numbers that are relatively prime to M_{seq}. As such, in order to obtain a valid length-63 ABC sequence, the sequence number a must be selected such that $a \in SN_v$,

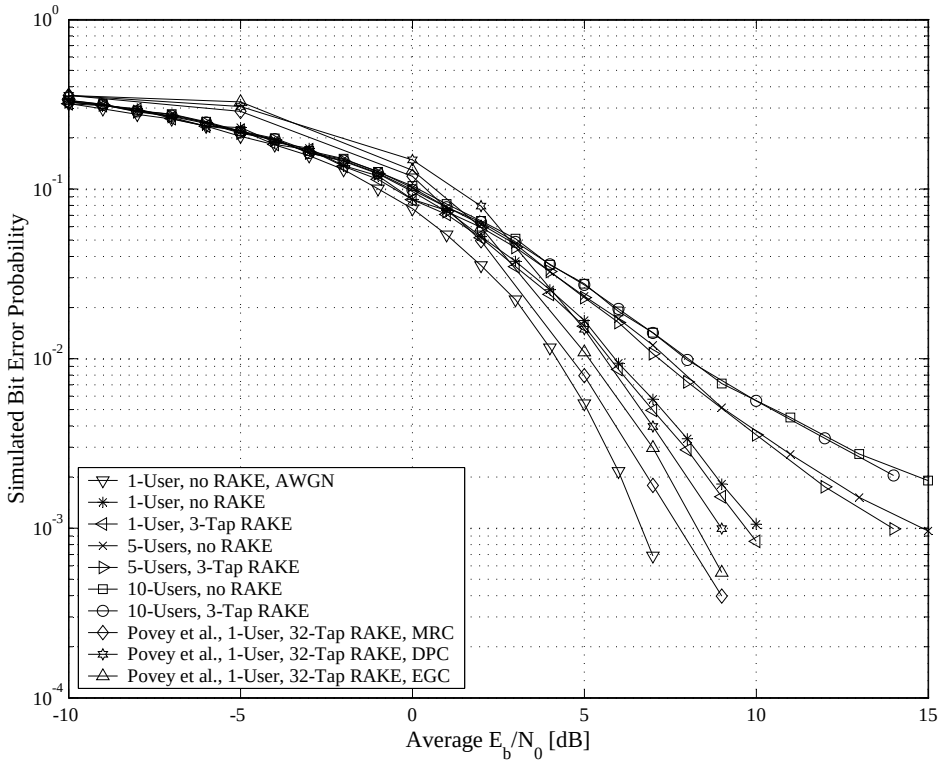

Figure 6.23: BER Performances of Uncoded Wideband Complex QPSK Communication Systems Employing QPH CSSs in Multi-User Multipath Fading Channel Conditions, $M_{seq} = 63$

with SN_v the valid sequence number set, given by:

$$\begin{aligned} SN_v &= \left\{ SN_v^1, SN_v^2, ..., SN_v^{M_{fam}} \right\} \\ &= \{1, 2, 4, 5, 8, 10, 11, 13, 16, 17, 19, 20, 22, 23, 25, 26, 29, 31, 32, \\ &\quad 34, 37, 38, 40, 41, 43, 44, 46, 47, 50, 52, 53, 55, 58, 59, 61, 62\} \end{aligned} \tag{6.2}$$

Although all of these sequence numbers represent unique CSSs that can be assigned to M_{user} unique CDMA users, care must be taken during this assignment process in order to maximising the BER performance of the DS/SSMA system with regards to MUI, especially when $M_{fam} > M_{user}$. Optimal sequence selection for a M_{user}-user CDMA system involves finding the M_{user} CSSs which exhibit the best periodic auto-correlation and cross-correlation properties (see *Section* D.2) for all possible pair-wise comparisons of sequences in the family. This exhaustive search selection process can be extremely tedious to perform manually, as well as fairly complex to automate, especially for long CSSs that exhibit intricate periodic correlation functions [48]. Hence, spreading sequence designers are always interested in finding simple rule-of-thumb sequence selection algorithms for popular spreading sequence families. One such a rule-of-thumb selection method for GCL CSSs has been proposed by *Staphorst* and *Linde* in [162]. The proposed optimal GCL CSS selection method generates the subset of optimal valid sequence numbers $SN_o \subseteq SN_v$, with $SN_o = \left\{ SN_o^1, ..., SN_o^{M_{optimal}} \right\}$. This is accomplished by firstly setting $SN_o^1 = 1$, followed by exhaustively extracting all $SN_o^i \in SB_v$, with $i = 2, ..., M_{optimal}$, for which $SN_o^i \bmod \left(SN_v^j \right) \neq 0$, with $j = 2, ..., M_{fam}$ and $j \neq i$. Thus, according to the proposed selection algorithm, the optimal values of the sequence number a must not only be limited to integer values relatively prime to M_{seq}, but also all possible pair-wise combinations of the elements in SN_o, except for pairings with $SN_o^1 = 1$, must be relatively prime. Executing this

selection procedure for the valid sequence number set given by *Eq.* (6.2) for length $M_{seq} = 63$ ABC sequences, the following optimal valid sequence number subset is obtained:

$$SN_o = \{1, 2, 5, 11, 13, 17, 19, 23, 29, 31\} \tag{6.3}$$

Fig. 6.24 presents the simulated multi-user multipath fading BER performance curves obtained for uncoded complex DS/SSMA QPSK systems, employing length-63 ABC sequences arbitrarily selected from *Eq.* (6.2)'s valid sequence number set and sequentially selected from *Eq.* (6.3)'s optimal sequence number set. Both non-RAKE and RAKE complex receiver structures are considered.

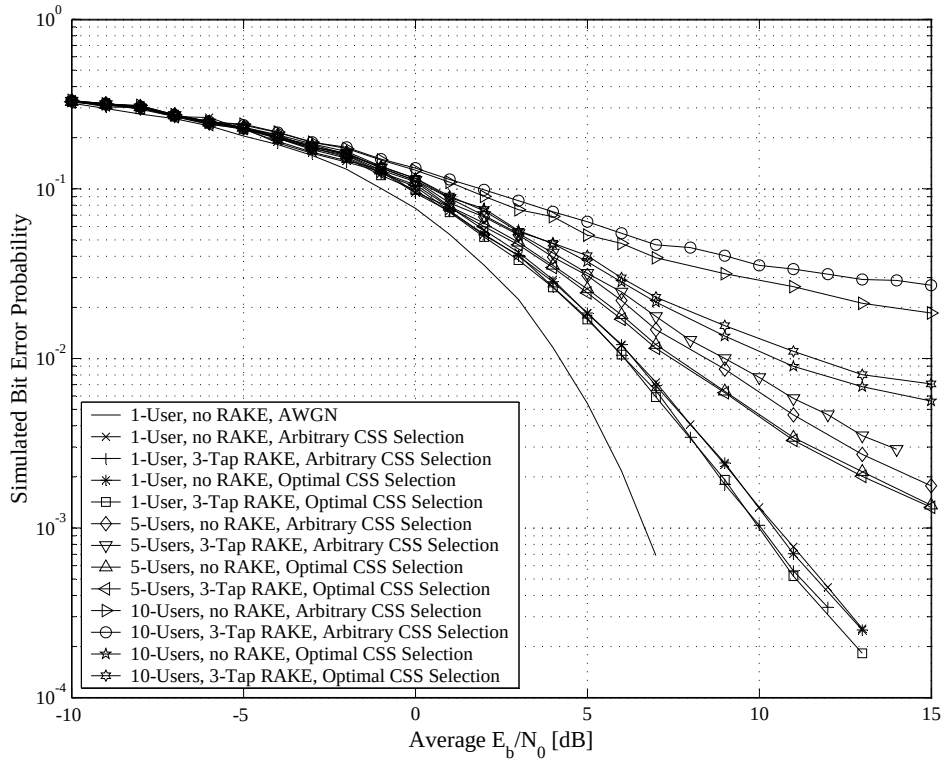

Figure 6.24: BER Performances of Uncoded Wideband Complex QPSK Communication Systems Employing Arbitrarily and Optimally Selected ABC Sequences in Multi-User Multipath Fading Channel Conditions, $M_{seq} = 63$

Similar experiments were performed with complex DS/SSMA systems employing DSB CE-LI-RU filtered GCL and ZC CSSs, but no major BER performance improvements were obtained. Thus, the success of the proposed sequence selection technique is limited to ABC sequences. As such, the multi-user multipath fading results presented in the remainder of this chapter were obtained with optimally selected ABC sequences and arbitrarily selected DSB CE-LI-RU filtered GCL, ZC and QPH CSSs.

6.5.1.3.3 The Influence of CSS Length - An ABC Sequences Case Study

According to the discussion in *Section* 6.4.4 on the comparison of the spectral characteristics of the different CSS families considered in this study, it is possible to increase the length of filtered CSSs by a factor of SSLD in order to produce a BEF equivalent to that obtained when direct spreading is performed with unfiltered CSSs or binary sequences. Longer sequence lengths provide larger se-

quence family sizes, which in turn allows for increased user capacity in the DS/SSMA system without increasing transmission bandwidth or relinquishing PG. Moreover, at a fixed user load, longer CSSs produce better BER performances than shorter CSSs, due to their improved periodic correlation characteristics [48]. *Fig.* 6.25 depicts the multi-user multipath fading channel BER performances obtained using length 61, 64, 63, and 127 ABC sequences in a complex RAKE receiver-based DS/SSMA system. Length-127 ABC sequences are of particular interest, since these sequences produce a BEF nearly identical to that of length-63 DSB CE-LI-RU filtered GCL CSSs, which is used extensively during the remainder of this chapter's multi-user multipath fading channel simulations. Simulated curves are included on *Fig.* 6.25 for length-61 and length-64 ABC sequences in order to investigate the validity of widespread beliefs that prime length and even length ABC sequences produce superior and inferior MUI BER performances, respectively. Note that, for all of the sequence lengths considered, the ABC sequences assigned to CDMA users were optimally selected from the respective sequence families, as described in *Section* 6.5.1.3.2.

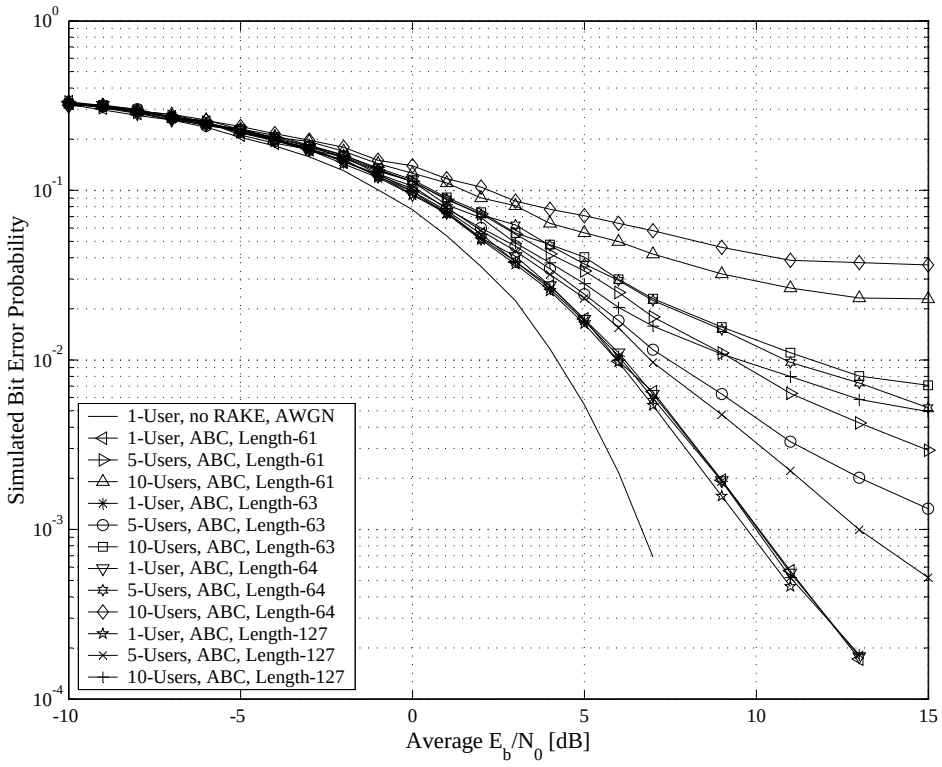

Figure 6.25: BER Performances of Uncoded Wideband Complex QPSK Communication Systems Employing ABC Sequences of Different Lengths in Multi-User Multipath Fading Channel Conditions

6.5.1.4 DISCUSSION OF THE SIMULATION RESULTS

The following important observations can be made from the uncoded narrowband and wideband communication systems' AWGN, flat fading and multipath fading channel BER performance results, presented in the preceding three subsections:

1. Conclusions and observations from the AWGN channel results:

   - The simulated and theoretical BER performance curves for narrowband complex QPSK communication systems, operating in AWGN channel conditions, shown in *Fig.* 6.17, are almost

identical, as was to be expected. The slight deviation between these two curves can be attributed to the AWGN-limiting operation of the elliptic receive filters (see *Section* 5.4.1).

2. Conclusions and observations from the flat fading channel results:

   - The BER performance curve shown in *Fig.* 6.18 for flat fading channel conditions with a Rician factor of $K_i = -100$ dB (i.e. Rayleigh fading amplitude PDF) and a maximum Doppler spread of $B_{D,i} = 33$ Hz, closely resembles the theoretical curve, defined by *Eq.* (5.24). However, the same can not be said for the $B_{D,i} = 100$ Hz maximum Doppler spread scenario (shown in *Fig.* 6.19), especially at high $\overline{E}_b/N_0$ values. The difference in the degree of similarity between the theoretical and simulated curves for different maximum Doppler spread scenarios can easily be explained: Recall from *Section* 5.2.4.2 that a slow flat fading channel, where the fading amplitude stays essentially constant during each symbol interval, was assumed in the derivation of *Eq.* (5.24). As such, for the symbol rate of 1000 Hz (see *Table* 5.1), a maximum Doppler spread of $B_{D,i} = 33$ Hz results in a slow flat fading channel scenario, which is similar to the theoretical channel conditions assumed in *Section* 5.2.4.2.

3. Conclusions and observations from the multi-user multipath fading channel results:

   (a) Comparison of complex DS/SSMA systems employing length-63 CSSs from the different families considered in this study:

   - From the multipath fading channel results shown in *Fig.* 6.20 to *Fig.* 6.23, it is clear that, for a single user scenario, the 3-tap RAKE receivers perform better than the non-RAKE receivers for all families of CSSs considered in this study. This is also true for the 5-user and 10-user CDMA systems employing DSB CE-LI-RU filtered GCL, ZC and QPH CSSs. In the case of ABC sequences, the RAKE receiver structure produces results that are inferior to regular single branch DSSS/MA QPSK receivers. This can be attributed to the weak periodic auto-correlation and cross-correlation properties [48] (see *Section* D.2.3) of ABC sequences, which result in the generation of excessive self-noise and MUI on each of the respective taps of the complex DS/SSMA QPSK RAKE receiver (see *Fig.* 5.4). DSB CE-LI-RU filtered GCL CSSs also suffer from poor periodic correlation characteristics [48], which are arguably the major contributing factors for the RAKE receiver's less than impressive BER performance results (if weighed against the BER performances of the non-RAKE receiver), when compared to that of the ZC and QPH CSS-based systems.
   - The DSB CE-LI-RU filtered GCL and ABC sequences tend to exhibit inferior periodic cross-correlation properties [48]. As a result, these CSSs generate more MUI than the ZC and QPH CSSs, which yields poor BER performances at high user loads. For example, from *Fig.* 6.21, a 10-user complex RAKE receiver-based DS/SSMA QPSK system, employing DSB CE-LI-RU filtered GCL CSSs, operating at $\overline{E}_b/N_0 = 13$ dB, has a BER of $P_b(e) \approx 1/430$, whereas system employing ABC sequences performs even worse with an error floor of $P_b(e) \approx 1/140$. In contrast, of all the CSS families considered, a 10-user CDMA system employing ZC CSSs delivers the best performance at $\overline{E}_b/N_0 = 13$ dB, with a BER of $P_b(e) \approx 1/650$.
   - In general, the use of RAKE receivers did not results in large BER performance improvements over that of the non-RAKE receivers. This can be attribute to the fact that the first propagation path in each CDMA user's exponential decay power delay profile (see *Section* 2.6.3.3) carries the majority of the transmitted output power. From *Table* 5.5 it follows that, if user-1 transmits at 1 W output power, 0.9684 W, 0.0306 W and 0.00096841 W of the transmitted power will be carried by paths 1, 2 and 3, respectively. As such, a non-RAKE receiver effectively processes 0.9684 W of the total

received power. Thus, by using RAKE receiver structures, a tentative improvement of at least $10.\log_{10}\left(\frac{1}{0.9684}\right) = 0.1394$ dB in average E_b/N_0 was to be expected. The fact that gains higher than this are achieved, especially at low user loads, is the nett result of the diversity obtained through the RAKE receiver's MRC operation.

- From *Fig.* 6.20, *Fig.* 6.21, *Fig.* 6.22 and *Fig.* 6.23 it is abundantly clear that, irrespective of the CSS family employed, the 32-tap RAKE receiver system, presented by *Povey et al.* in [158], outperforms the 3-tap RAKE receiver system presented in this study, even though the multipath fading channel environment they considered was far more severe ($L = 32$ independent paths with no LOS signal component present on any of the paths). However, their RAKE receiver linearly processes 32 distinct copies of the transmitted signal, thereby achieving extremely high diversity gains. According to the CLT [47], by combining such a high number of statistically independent Rayleigh paths, more ideal, Gaussian-like channel conditions are produced. Furthermore, the length $M_{seq} = 1024$ PN sequence considered in their study has near-perfect periodic auto-correlation properties (see *Section* D.2.2). Hence, no detrimental self-noise is generated inside the RAKE receiver structure. However, the same can not be said of RAKE receiver structures employing the CSSs presented in *Appendix D*.
- The BER performance results obtained by *Povey et al.* [158], presented in *Fig.* 6.20, *Fig.* 6.21, *Fig.* 6.22 and *Fig.* 6.23, indicate that MRC is a more powerful RAKE combining technique than EGC or DPC [158]. As such, it justifies this study's use of MRC in the RAKE receiver structures of the wideband complex DS/SSMA QPSK systems used throughout the multi-user multipath fading channel simulations.

(b) Investigation into the influence of the sequence selection approach on the BER performance of a ABC sequence-based DS/SSMA system:

- *Fig.* 6.24 is evidence that a complex DS/SSMA system employing length-63 ABC sequences, chosen according to *Staphorst* and *Linde*'s proposed optimal GCL sequence selection method [162] (detailed in *Section* 6.5.1.3.2), has a BER performance superior to that of a system employing arbitrarily selected sequences. This is especially true for high user loads. For example, when employed in a 10-user RAKE receiver-based complex DS/SSMA system at a BER of $P_b(e) = 3/100$, optimally selected ABC sequences show a gain of 6 dB over arbitrarily selected ABC sequences. These remarkable gains, however, are only obtainable for ABC sequences, since using the proposed optimal sequence selection method in conjunction with DSB CE-LI-RU filtered GCL and ZC CSSs, deliver mediocre BER performance improvements.
- By allowing only the CSSs with the best periodic cross-correlation characteristics (see *Section* D.2.3) to be assigned to CDMA users, the proposed optimal sequence selection method of [162] (see *Section* 6.5.1.3.2) not only improves the overall BER performance of a complex DS/SSMA system employing ABC sequences, but also improves the BER performances of RAKE receivers relatively to non-RAKE receivers for non-unity user loads. From *Fig.* 6.20 and *Fig.* 6.24 it is apparent that MRC RAKE reception is outperformed by non-RAKE reception for 5-user and 10-user complex DS/SSMA systems employing arbitrarily selected ABC sequences. Optimally selecting CSSs, however, improves the 5-user RAKE receiver-based system to a comparable level as the non-RAKE receiver-based system. Unfortunately, at high user loads, such as the 10-user scenario, the optimal sequence selection method of *Section* 6.5.1.3.2 is incapable of avoiding the poor periodic cross-correlation characteristics of ABC sequences [48]. Hence, for this user load the self-noise generated by the RAKE receiver structure still outweighs the diversity gains it achieves through MRC.

(c) Investigation into the influence of sequence length on the BER performance of ABC sequence-based DS/SSMA systems:

- As was to be expected, the complex RAKE receiver-based DS/SSMA system employing length-127 ABC sequences outperforms all of the other complex DS/SSMA systems employing shorter ABC sequences. This can be attributed to the improvement of the CSSs' periodic correlation characteristics as the sequence length increases [48]. Unfortunately, for a 10-user CDMA environment, the BER performance of the RAKE receiver-based complex DS/SSMA system employing length-127 ABC sequences is only marginally better than that of a system using length-63 DSB CE-LI-RU filtered GCL CSSs (see *Fig.* 6.21). Note that both these systems have similar BEFs. However, by arbitrarily selecting CSSs, the length-127 ABC sequence-based system supports a maximum of 126 CDMA users, whereas the length-63 DSB CE-LI-RU filtered GCL CSS-based system supports only 36 users (see *Eq.* (6.2)). Hence, it can be concluded that, using ABC sequences instead of binary or unfiltered CSSs, increases the PG and user capacity (directly related to the SSLD, introduced in *Section* D.2.6) of DS/SSMA systems, without unduly increasing their BEFs. The increased user capacity does, however, come at the expense of inferior BER performances, making this CSS family a poor choice for CDMA purposes.
- Comparing *Fig.* 6.21's BER performance results for the RAKE receiver-based complex DS/SSMA systems employing length-61 and length-63 ABC sequences (these systems have comparable PGs and BEFs), it is apparent that the popular belief [48] that GCL CSSs with prime numbered sequence lengths exhibit superior periodic cross-correlation properties (see *Section* D.2.3), resulting in lower MUI levels, is fallacious. However, using prime numbered sequence lengths do increase the user capacity of the system dramatically, as shown by *Eq.* (D.9) in *Section* D.3.1.1.
- From *Fig.* 6.21 it is clear that the RAKE receiver-based complex DS/SSMA system employing length-64 ABC sequences exhibits the weakest BER performance results, due to the high levels of MUI present in the CDMA system. Hence, even numbered sequence lengths must be avoided for GCL CSSs, not only because of the limited family sizes that can be generated (see *Eq.* (D.9)), but also because of these sequences' poor periodic cross-correlation characteristics (see *Section* D.2.3).

6.5.2 BINARY CONVOLUTIONAL CODED COMMUNICATION SYSTEMS

The following subsections present simulated BER performance results for classic binary 4-state, rate $R_c = 1/2$ NSC (see *Section* 3.2.1.3.1) and 8-state, rate $R_c = 2/3$ RSC (see *Section* 3.2.1.3.2) coded narrowband complex QPSK systems (see *Section* 5.2) in AWGN and flat fading channel conditions, as well as wideband complex DS/SSMA QPSK communication systems (see *Section* 5.3) in multi-user multipath fading channel conditions. Note that length $M_{seq} = 63$ CSSs were employed in the RAKE receiver-based complex DS/SSMA communication systems during the multi-user multipath fading channel simulations. The ABC sequences used were selected for optimum periodic cross-correlation (see *Section* 6.5.1.3.2), whereas the CSSs used from the other families were arbitrarily selected. The BER performance results discussed here serve as baseline references during the examination of the simulation results for the VA decoded linear block codes, presented later in this chapter.

6.5.2.1 4-STATE, RATE $R_C = 1/2$ NSC CODED COMMUNICATION SYSTEMS

In the following subsections the BER performance results of the 4-state, rate $R_c = 1/2$ NSC code, defined by the following generator matrix (see *Section* 3.2.1.1):

$$G_{CC}(D) = \left[\begin{array}{cc} 1 + D^2 & 1 + D + D^2 \end{array} \right] \tag{6.4}$$

are presented and examined. From [47] the minimum free distance (see *Section* 3.2.1.2) of this binary NSC code is $d_{free} = 5$. Furthermore, according to *Section* 3.2.1.2, this NSC code has a minimal encoder structure with a constraint length of $v = 2$. As such, a simple sliding window VA decoder (see *Section* 3.3.1) with a window size [47] of $\omega = 5.v = 10$ trellis sections (see *Section* 3.3.1.1) was employed as ML decoder. Both hard and soft decision (see *Section* 4.4.2.2) decoding approaches were considered. In the case of soft decision decoding, the effects of using perfect fading amplitude CSI (see *Section* 3.3.5) in the VA metric calculations on the BER performance results, were also investigated.

6.5.2.1.1 AWGN Channel Results

Fig. 6.26 shows several simulated BER performance curves for 4-state, rate $R_c = 1/2$ NSC coded (see *Section* 3.2.1.3.1) narrowband complex QPSK communication systems (see *Section* 5.2), operating in AWGN channel conditions (see *Section* 2.2). Hard and soft decision (without using fading amplitude CSI in the VA branch metric calculations) decoding BER performance results are present on *Fig.* 6.26. Also depicted on this figure is the BER performance curve of an uncoded narrowband QPSK system in AWGN, theoretically defined by *Eq.* (5.20).

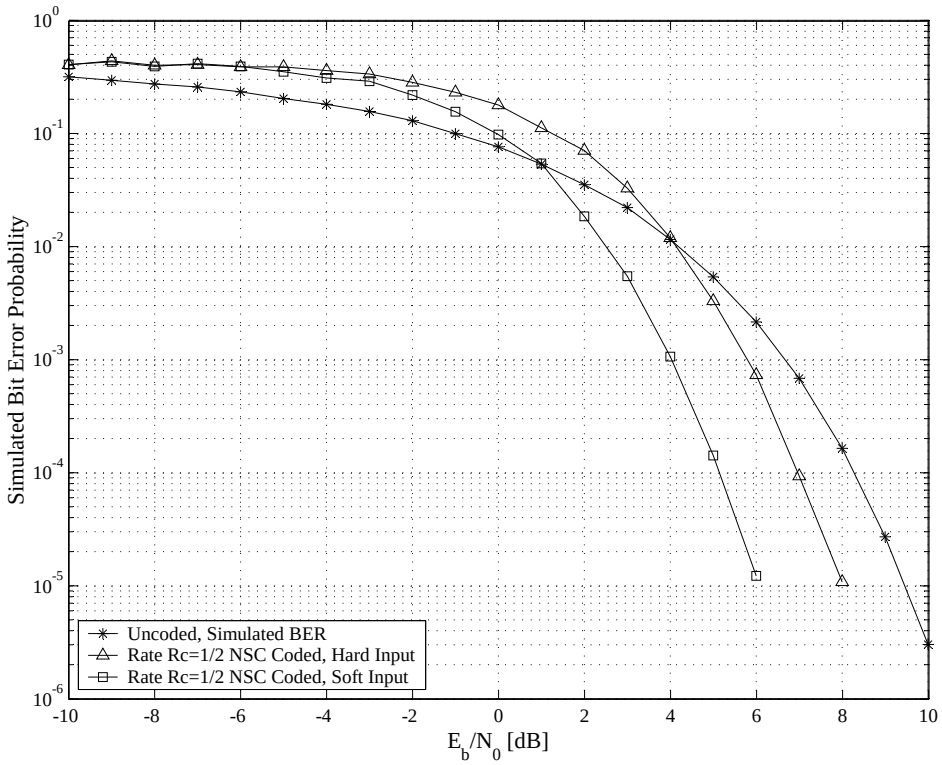

Figure 6.26: BER Performances of 4-State, Rate $R_c = 1/2$ NSC Coded Narrowband Complex QPSK Communication Systems in AWGN Channel Conditions

6.5.2.1.2 Flat Fading Channel Results

Simulated flat fading channel (see *Section* 2.5.1.1) BER performance results of 4-state, rate $R_c = 1/2$ NSC (see *Section* 3.2.1.3.1) coded narrowband complex QPSK communication systems (see *Section* 5.2) for maximum Doppler spreads (see *Section* 2.4.3.3) of $B_{D,i} = 33$ Hz and $B_{D,i} = 100$ Hz, are shown in *Fig.* 6.27 and *Fig.* 6.28, respectively. These figures depict simulated BER performance

results for Rician factors (see *Section* 2.5.2.2) of $K_i = -100$ dB, $K_i = 0$ dB and $K_i = 9$ dB. Furthermore, two soft decision decoding approaches were investigated, namely soft decision decoding without any fading amplitude CSI and soft decision decoding with perfect fading amplitude CSI (see *Section* 3.3.5 and *Section* 5.2.3). Also depicted on these figures are simulated BER performance curves for uncoded QPSK systems in AWGN, as well as *Eq.* (5.24)'s theoretical BER performance curve for uncoded narrowband QPSK systems in slow Rayleigh flat fading channel conditions.

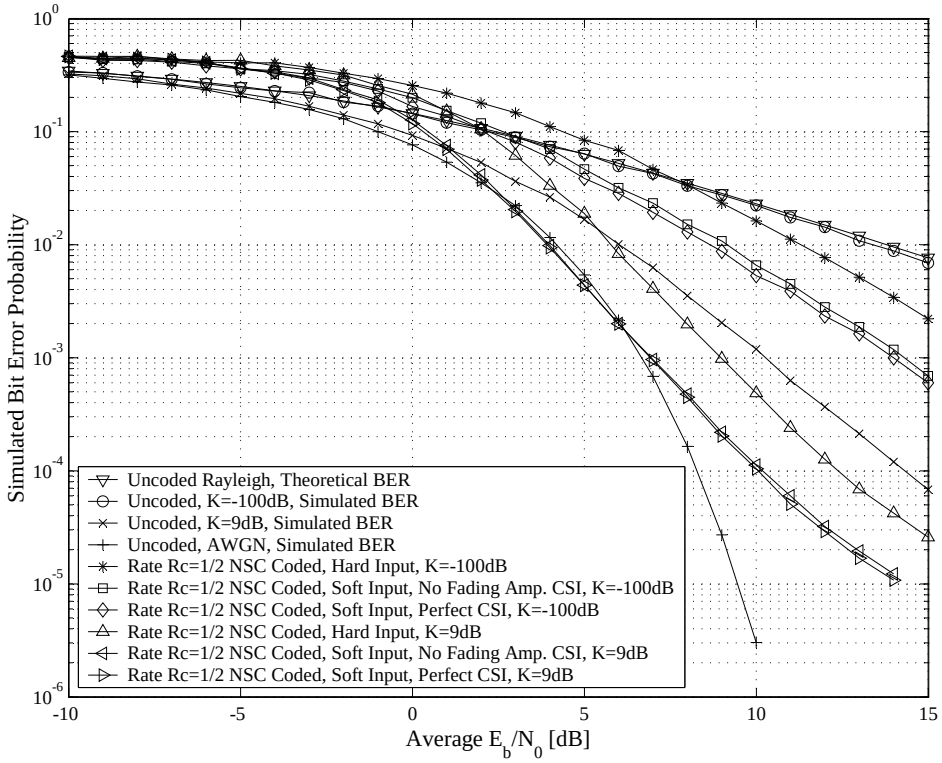

Figure 6.27: BER Performances of 4-State, Rate $R_c = 1/2$ NSC Coded Narrowband Complex QPSK Communication Systems in Flat Fading Channel Conditions, $B_{D,i} = 33$ Hz

6.5.2.1.3 Multipath Fading Channel Results

Fig. 6.29, *Fig.* 6.30, *Fig.* 6.31 and *Fig.* 6.32 present the simulated multi-user multipath fading channel BER performance results obtained for 4-state, rate $R_c = 1/2$ NSC coded RAKE receiver-based wideband complex DS/SSMA QPSK systems (see *Section* 5.3), employing length $M_{seq} = 63$ ABC (see *Section* D.3.2.2), DSB CE-LI-RU filtered GCL (see *Section* D.3.2.1), ZC (see *Section* D.3.1.1) and QPH (see *Section* D.3.1.2) CSSs, respectively. Results are shown for sliding window VA decoding using hard decisions, soft decisions without any fading amplitude CSI and soft decisions with perfect fading amplitude CSI (see *Section* 3.3.5 and *Section* 5.3.3). For comparative purposes, the simulated BER performances for the uncoded RAKE receiver-based wideband complex DS/SSMA QPSK systems, presented in *Section* 6.5.1.3.1, are also present on these figures. Also shown is the BER performance of an uncoded DS/SSMA QPSK communication system (without a RAKE receiver), operating in a non-fading AWGN environment.

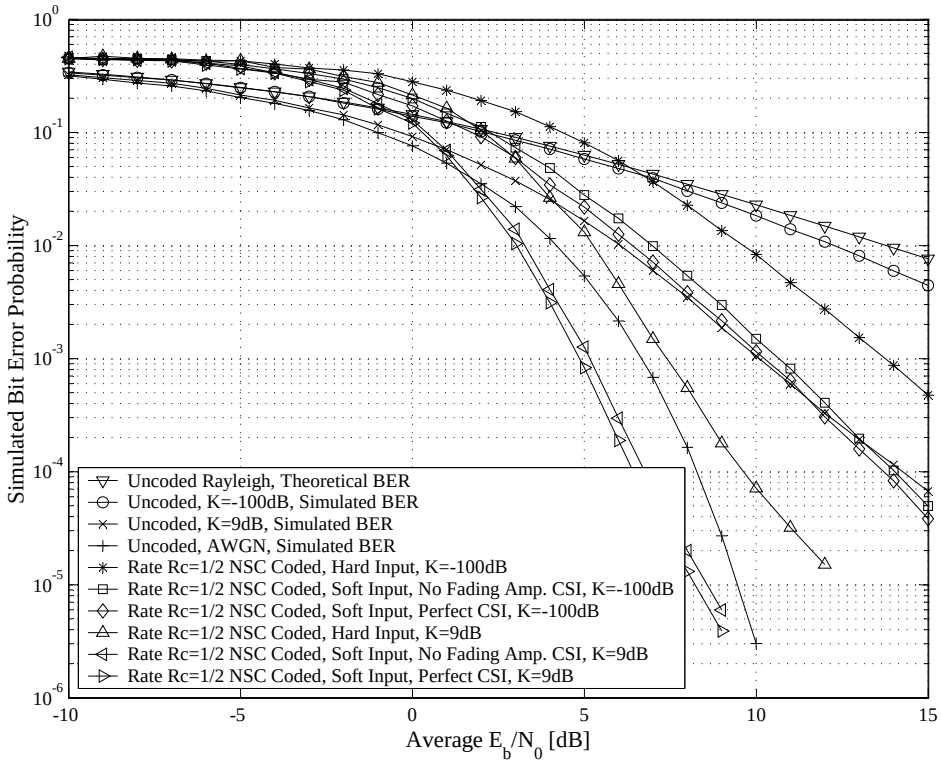

Figure 6.28: BER Performances of 4-State, Rate $R_c = 1/2$ NSC Coded Narrowband Complex QPSK Communication Systems in Flat Fading Channel Conditions, $B_{D,i} = 100$ Hz

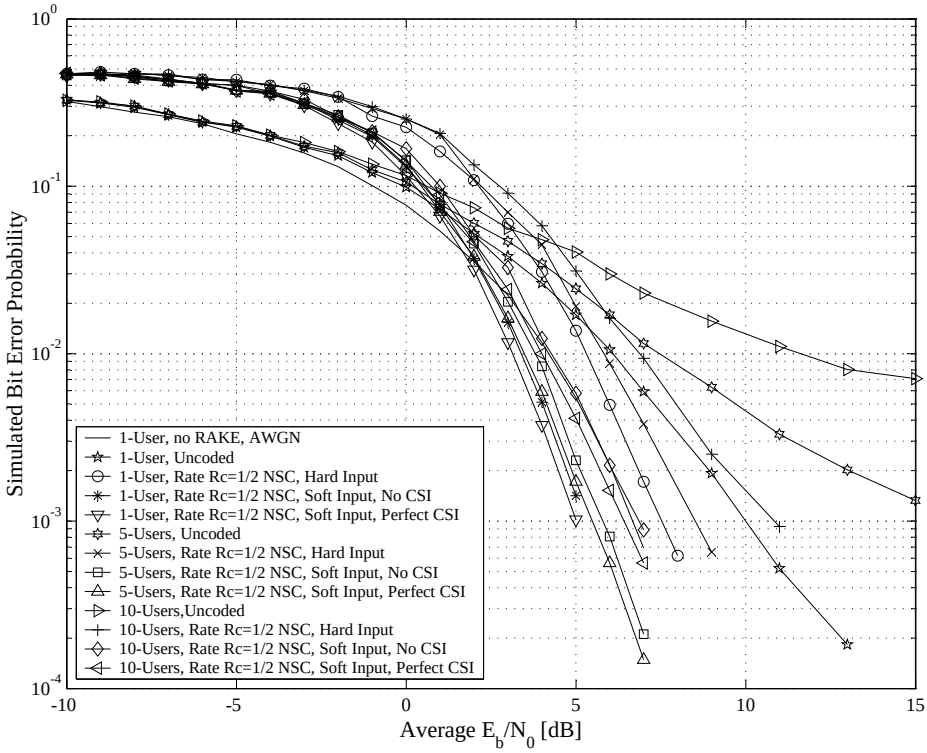

Figure 6.29: BER Performances of 4-State, Rate $R_c = 1/2$ NSC Coded Wideband Complex QPSK Communication Systems Employing ABC Sequences in Multi-User Multipath Fading Channel Conditions, $M_{seq} = 63$

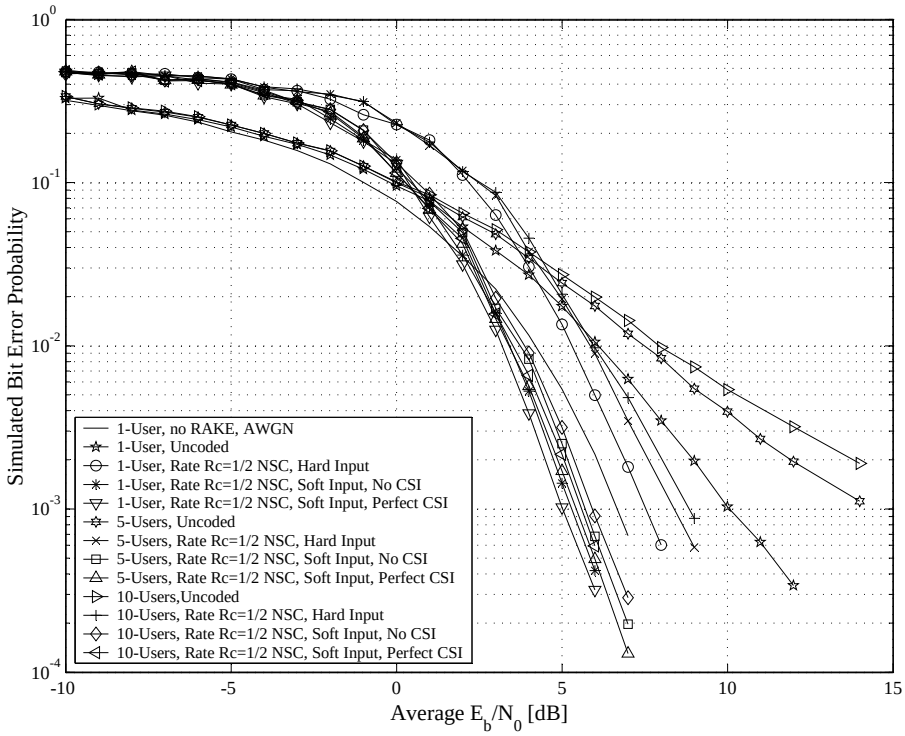

Figure 6.30: BER Performances of 4-State, Rate $R_c = 1/2$ NSC Coded Wideband Complex QPSK Communication Systems Employing DSB CE-LI-RU Filtered GCL CSSs in Multi-User Multipath Fading Channel Conditions, $M_{seq} = 63$

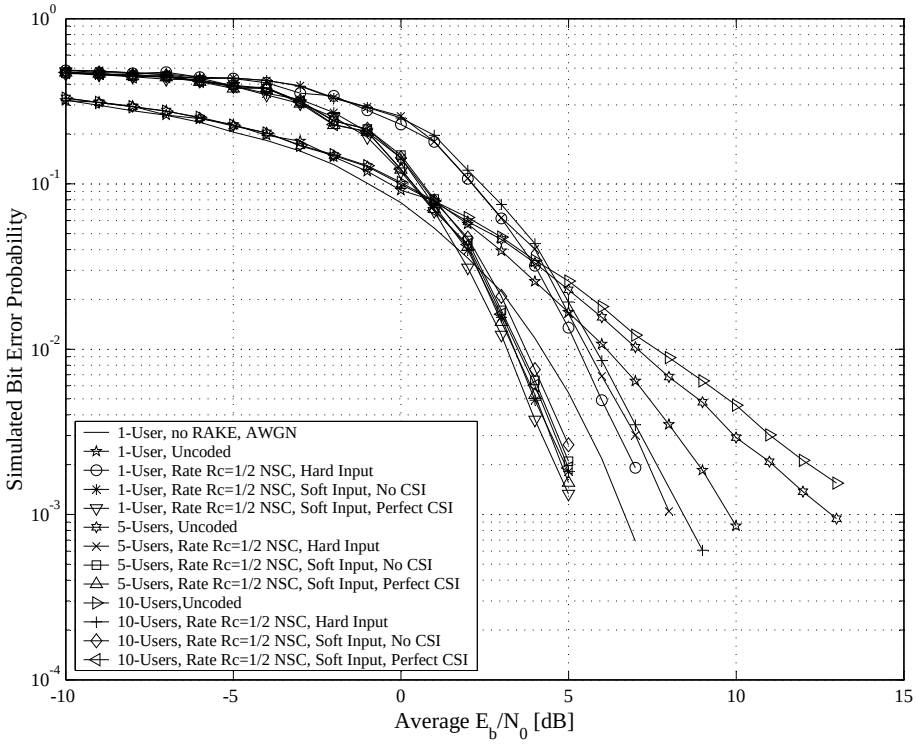

Figure 6.31: BER Performances of 4-State, Rate $R_c = 1/2$ NSC Coded Wideband Complex QPSK Communication Systems Employing ZC CSSs in Multi-User Multipath Fading Channel Conditions, $M_{seq} = 63$

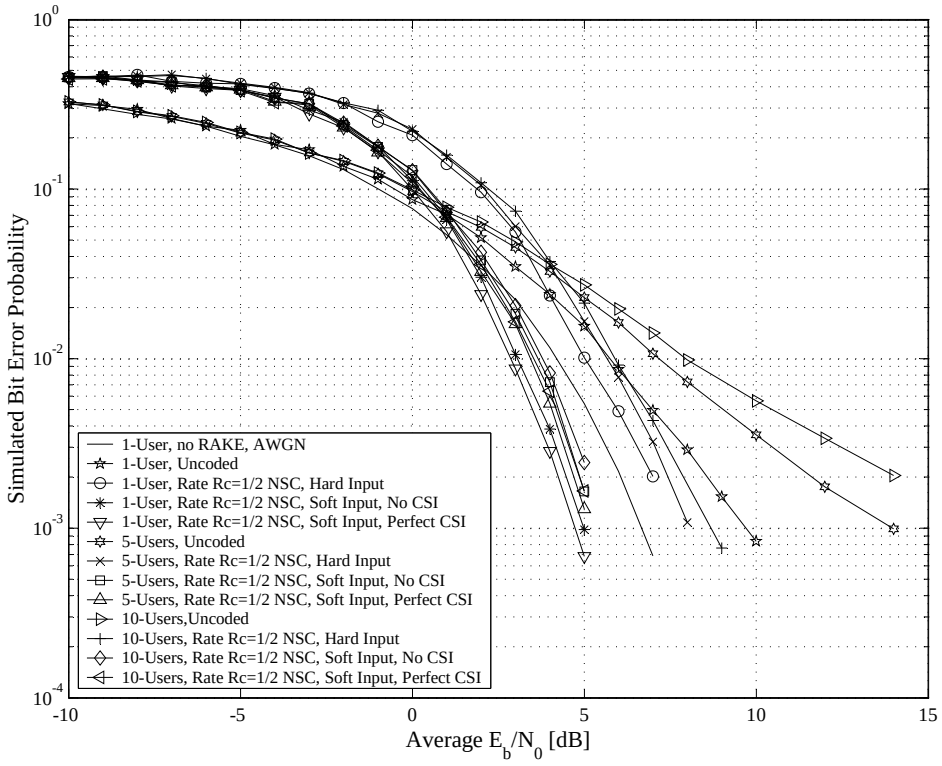

Figure 6.32: BER Performances of 4-State, Rate $R_c = 1/2$ NSC Coded Wideband Complex QPSK Communication Systems Employing QPH CSSs in Multi-User Multipath Fading Channel Conditions, $M_{seq} = 63$

6.5.2.1.4 Discussion of the Simulation Results

From the simulated AWGN, flat fading and multi-user multipath fading channel BER performance results for the 4-state, rate $R_c = 1/2$ NSC coded narrowband and wideband communication systems, presented in the preceding subsections, the following conclusions can be drawn:

1. Conclusions and observations from the AWGN channel results:

   - From the simulated AWGN channel BER performances for 4-state, rate $R_c = 1/2$ NSC coded narrowband complex QPSK communication systems, shown in *Fig.* 6.26, it is clear that the system employing soft decision VA decoding of the convolutional code exhibits a measured asymptotic gain of approximately 3.6 dB over the uncoded system. This measured coding gain corresponds with *Eq.* (3.8)'s calculated maximum asymptotic gain of $CG_{CC}^{soft} = 3.98$ dB.
   - Comparing *Fig.* 6.26's soft decision VA decoding BER performance results with that of the hard decision decoding approach, a 2 dB asymptotic gain is evident, as was to be expected [47] (see *Section* 3.2.1.2).
   - At low E_b/N_0 values, hard and soft decision VA decoding of the rate $R_c = 1/2$ NSC code in AWGN channel conditions result in poorer BER performances than the uncoded system. To be precise, soft decision VA decoding starts to show gains for $E_b/N_0 > 1$ dB, whereas hard decision VA decoding is only useful for $E_b/N_0 > 4.2$ dB. The E_b/N_0 points at which coded systems start to show gains over the uncoded system are commonly referred to as the *BER cross-over points* [47].

2. Conclusions and observations from the flat fading channel results:

   - On closer investigation of the flat fading channel simulation results (presented in *Fig.* 6.27 and *Fig.* 6.28), it is evident that the BER performances of hard and soft decision VA decoded rate $R_c = 1/2$ NSC codes improve as the Rician factor K_i (see *Section* 2.5.2.2) increases. Since binary NSC codes were initially intended for FEC purposes in AWGN channel conditions, this BER performance improvement can be attributed to the increase in the channel's LOS component, resulting in the fading amplitude PDF changing from a Rayleigh-like distribution to a Gaussian-like distribution (see *Section* 2.5.2.2).
   - A comparison of *Fig.* 6.27 and *Fig.* 6.28 shows that the hard and soft decision VA decoded rate $R_c = 1/2$ NSC codes' BER performances deteriorate as the maximum Doppler spread frequency decreases. At fixed symbol rate of 1000 symbols/s (see *Section* 5.4.2), a maximum Doppler spread of $B_{D,i} = 33$ Hz will result in more information bits being corrupted during a slow deep fade, than during a faster $B_{D,i} = 100$ Hz deep fade. Thus, for a maximum Doppler spread of $B_{D,i} = 100$ Hz, bit error occurrences incurred by the channel will appear less bursty in nature. Since binary NSC codes are not intended to combat bursty errors, they are better suited for fast flat fading channels than for slow flat fading channels.
   - From *Fig.* 6.27 and *Fig.* 6.28 it is apparent that hard decision VA decoding lags soft decision decoding (without any fading amplitude CSI) by approximately 2 dB. Soft decision VA decoding, with fading amplitude CSI, in turn performs better that soft decision decoding without fading amplitude CSI. However, this performance improvement is minuscule. For the $B_{D,i} = 33$ Hz scenario, an improvement of approximately 0.15 dB was obtained for all Rician factors, whereas an average improvement of 0.25 dB can be observed for $B_{D,i} = 100$ Hz.
   - The simple binary rate $R_c = 1/2$ NSC code shows impressive coding gains over uncoded systems. For example, for $B_{D,i} = 100$ Hz and $K_i = 9$ dB, soft decision VA decoding (without fading amplitude CSI) shows a gain of 5 dB at a BER of $P_b(e) = 10^{-3}$. Furthermore, comparing the results of *Fig.* 6.27 and *Fig.* 6.28 for a fixed K_i, it is clear that the rate $R_c = 1/2$ NSC code exhibits larger coding gains for $B_{D,i} = 100$ Hz than for $B_{D,i} = 33$ Hz.

3. Conclusions and observations from the multi-user multipath fading channel results:

   - From the multi-user multipath fading channel results shown in *Fig.* 6.29, *Fig.* 6.30, *Fig.* 6.31 and *Fig.* 6.32, it is apparent that the increased MUI, created by additional CDMA users sharing the mobile communication environment, has a definite negative impact on the BER performance of the rate $R_c = 1/2$ NSC code. However, even for ABC sequences, no error floors are apparent at high $\overline{E}_b/N_0$. Thus, for the unfiltered and filtered CSS families considered, this binary NSC code effectively combats MUI through code diversity. In fact, for the 1-user and 5-user scenarios, better BER performances were obtained through soft decision VA decoding than that achievable by a single user uncoded system, operating purely in AWGN.
   - From a comparison of the results given in *Fig.* 6.29, *Fig.* 6.30, *Fig.* 6.31 and *Fig.* 6.32 it is evident that rate $R_c = 1/2$ NSC coded complex DS/SSMA systems employing the unfiltered CSS families perform superior to those using the pre-filtered CSS families. Specifically, pre-filtered ABC sequences exhibited the weakest BER performances, whereas QPH CSSs showed the best performances, marginally outperforming ZC CSSs. For example, for a 10-user CDMA environment, ZC CSSs performed no worse than 0.25 dB below QPH CSSs for hard decision VA decoding.
   - For 1-user and 5-user CDMA environments, it is barely possible to distinguish between the BER performance results of the rate $R_c = 1/2$ NSC coded complex DS/SSMA systems

employing the unfiltered ZC and QPH CSS families, both for the hard and soft decision VA decoding scenarios. These exceptional BER performances, even at high user loads, can be attributed to the unfiltered CSS families' superior periodic cross-correlation properties, as was also observed for the uncoded systems in *Section* 6.5.1.3.1. For a 10-user system, however, there is a marked decrease in BER performance, even for the unfiltered CSS families.

- A comparison of hard decision and soft decision VA decoding of the rate $R_c = 1/2$ NSC code in multi-user multipath fading channel conditions, indicates that, at low user loads, hard decision decoding asymptotically lags soft decision decoding (without fading amplitude CSI) by the characteristic 2 dB margin, irrespective of the CSS family used by the wideband complex DS/SSMA communication systems. This observation also remains true at high user loads, except for ABC sequences, where the asymptotic gain of soft decision (without fading amplitude CSI) over hard decision VA decoding expands to approximately 2.5 dB. Furthermore, inclusion of perfect fading amplitude CSI during soft decision decoding results in a further 0.25 dB improvement, regardless of the user load or the CSS family employed in the CDMA system.

6.5.2.2 8-STATE, RATE $R_C = 2/3$ RSC CODED COMMUNICATION SYSTEMS

The binary IIR RSC code (see *Section* 3.2.1.3.2) considered here is depicted in *Fig.* A.2 of *Appendix A* and is defined by the generator matrix given in *Eq.* (3.11). According to *Table* A.5, the minimum free distance (see *Section* 3.2.1.2) of this code is $d_{free} = 4$. Furthermore, the RSC code considered here has a constraint length (see *Section* 3.2.1.2) of $v = 3$. As such, a simple sliding window VA, with a window size of $\omega = 5.v = 15$ trellis sections, was employed as ML decoder. Both hard and soft decision decoding (with and without perfect fading amplitude CSI (see *Section* 3.3.5)) approaches are considered. Due to time constraints, this code's BER performances were determined, through extensive simulations, for only AWGN and flat fading channel conditions.

6.5.2.2.1 AWGN Channel Results

Several simulated BER performance curves for 8-state, rate $R_c = 2/3$ RSC coded (see *Section* 3.2.1.3.2) narrowband complex QPSK communication systems (see *Section* 5.2), functioning in AWGN channel conditions (see *Section* 2.2), are shown in *Fig.* 6.33. Note from this figure that VA decoding using both hard and soft decision metric calculations were considered. Obviously, in the case of soft decision decoding no fading amplitude CSI was used. The BER performance curve of an uncoded narrowband QPSK system in AWGN channel conditions, theoretically defined by *Eq.* (5.20), is also depicted in this figure.

6.5.2.2.2 Flat Fading Channel Results

Fig. 6.34 and *Fig.* 6.35 show simulated flat fading channel (see *Section* 2.5.1.1) BER performance results of 8-state, rate $R_c = 2/3$ RSC (see *Section* 3.2.1.3.2) coded narrowband complex QPSK communication systems (see *Section* 5.2) for maximum Doppler spreads (see *Section* 2.4.3.3) of $B_{D,i} = 33$ Hz and $B_{D,i} = 100$ Hz, respectively. Simulated BER performance results for Rician factors (see *Section* 2.5.2.2) of $K_i = -100$ dB, $K_i = 0$ dB and $K_i = 9$ dB are present on these figures. Hard and soft decision VA decoding of the 8-state, rate $R_c = 2/3$ RSC codes were considered. Note that two soft decision decoding approaches were investigated, namely soft decision decoding without any fading amplitude CSI and soft decision decoding with perfect fading amplitude CSI (see *Section* 3.3.5 and *Section* 5.2.3). These figures also include simulated BER performance curves for uncoded QPSK systems in AWGN, as well as theoretical BER performance curves for uncoded QPSK systems in slow Rayleigh flat fading channel conditions, defined by *Eq.* (5.24).

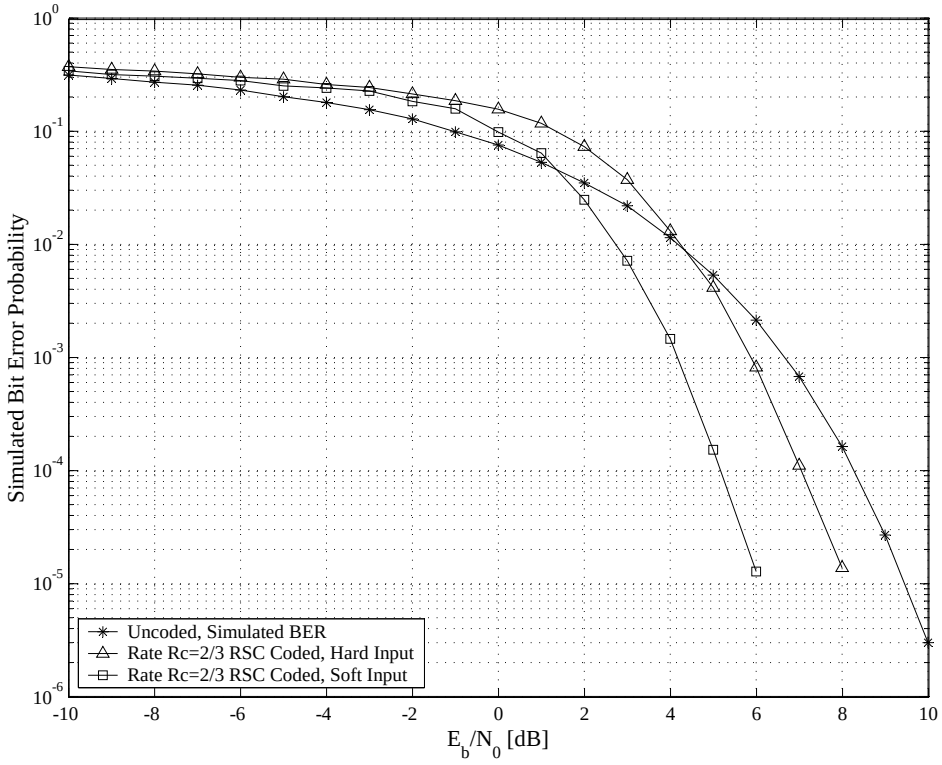

Figure 6.33: BER Performances of 8-State, Rate $R_c = 2/3$ RSC Coded Narrowband Complex QPSK Communication Systems in AWGN Channel Conditions

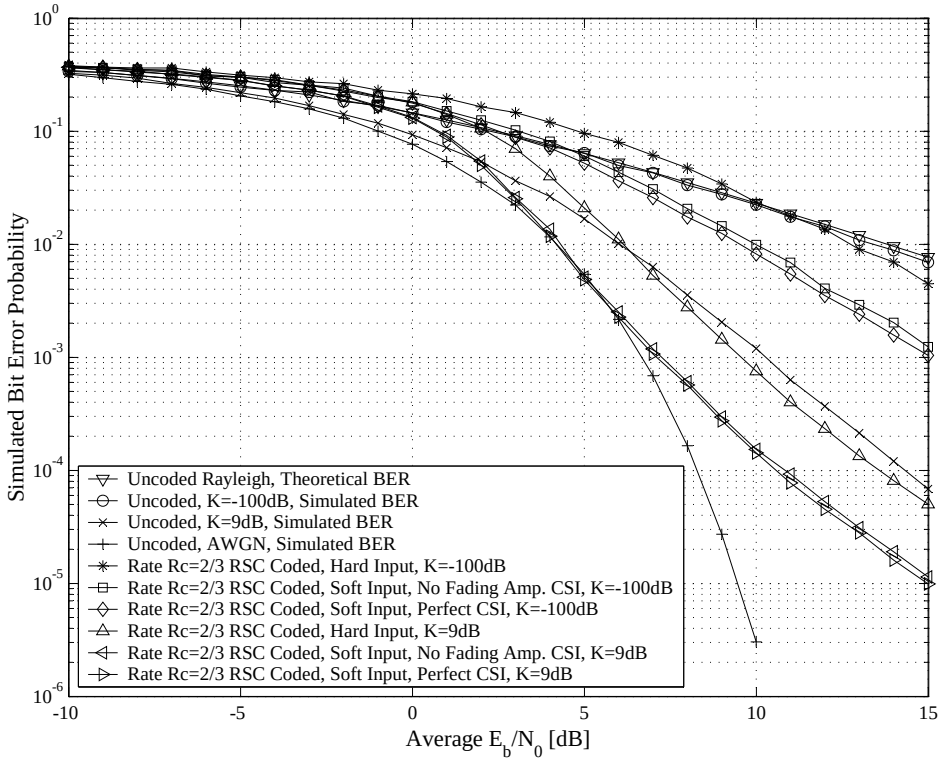

Figure 6.34: BER Performances of 8-State, Rate $R_c = 2/3$ RSC Coded Narrowband Complex QPSK Communication Systems in Flat Fading Channel Conditions, $B_{D,i} = 33$ Hz

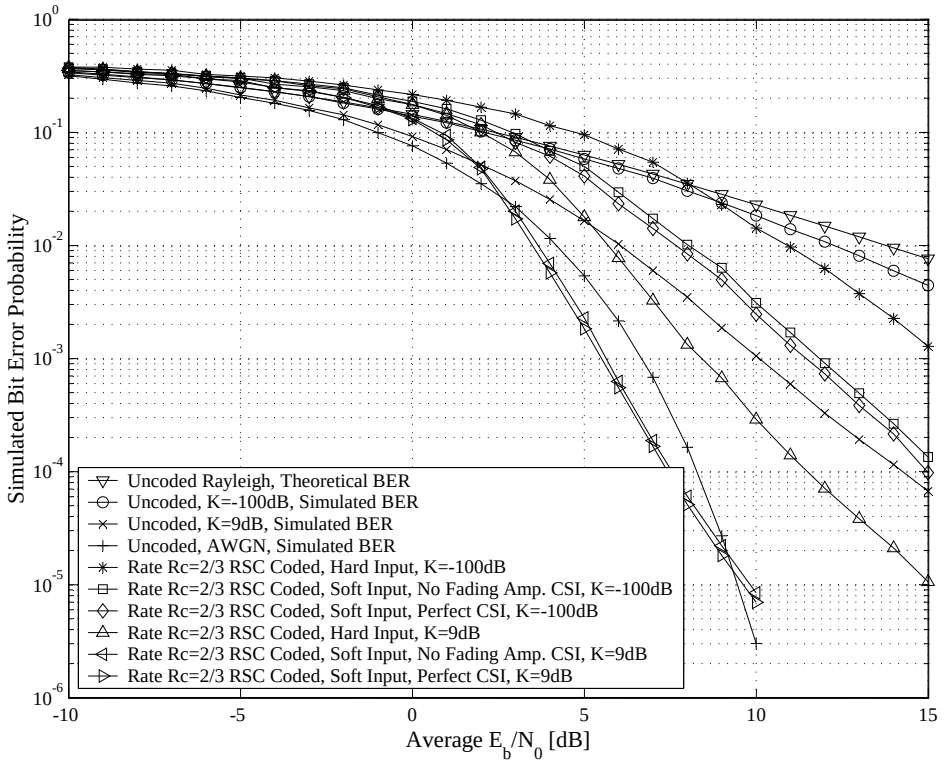

Figure 6.35: BER Performances of 8-State, Rate $R_c = 2/3$ RSC Coded Narrowband Complex QPSK Communication Systems in Flat Fading Channel Conditions, $B_{D,i} = 100$ Hz

6.5.2.2.3 Discussion of the Simulation Results

Listed below are several conclusions, drawn from the simulated AWGN and flat fading channel BER performance results for the 8-state, rate $R_c = 2/3$ RSC coded narrowband complex QPSK communication systems, presented in the preceding subsections:

1. Conclusions and observations from the AWGN channel results:

   - With a measured AWGN channel asymptotic coding gain of 3.8 dB over an uncoded narrowband complex QPSK communication system, *Fig.* 6.33 corroborates *Eq.* (3.8)'s theoretical maximum coding gain of $CG_{CC}^{soft} = 4.23$ dB for the soft decision VA decoded 8-state, rate $R_c = 2/3$ RSC code. Note that this code's coding gain is not only superior to that of the 4-state, rate $R_c = 1/2$ NSC code, considered in *Section* 6.5.2.1, but it also requires a lower bandwidth sacrifice. However, decoding complexity for the RSC code exceeds that of the NSC code, since the RSC code's VA functions on a 8-state trellis (see *Section* 3.3.1.1), whereas the NSC code's VA employs a 4-state trellis.
   - A comparison of *Fig.* 6.33's hard and soft decision VA decoding results in AWGN, reveals an expected asymptotic coding gain of 2.1 dB for soft decision decoding over the hard decision decoding.
   - The cross-over points for hard and soft decision VA decoding in AWGN channel conditions are 1.7 dB and 4.3 dB, respectively. Although the RSC code considered here is more powerful than *Section* 6.5.2.1's NSC code in terms of coding gain, its error correcting capabilities only become useable at higher E_b/N_0 values. This undesirable characteristic, inherent in all RSC codes, is the major reason why NSC codes have attracted more attention since the inception

of convolutional coding in the 1960's. However, the introduction of TCs has sparked a new and vigourous interest in RSC codes, due to their inherent recursive structures [88].

2. Conclusions and observations from the flat fading channel results:

   - *Fig.* 6.34 and *Fig.* 6.35 confirm that an increase in the flat fading channel's Rician factor K_i (see *Section* 2.5.2.2), results in improved BER performances for both hard and soft decision VA decoded rate $R_c = 2/3$ RSC codes.
   - From the flat fading channel simulation results (presented in *Fig.* 6.34 and *Fig.* 6.35), it is clear that the binary RSC code investigated here is better suited for non-bursty type errors, since its BER performances for $B_{D,i} = 100$ Hz exceed that of $B_{D,i} = 33$ Hz.
   - As was the case with the AWGN channel conditions, hard decision VA decoding of the rate $R_c = 2/3$ RSC code in a flat fading environment produced BER performance results inferior to that obtained through soft decision decoding. Specifically, soft decision VA decoding (without fading amplitude CSI), shows a familiar 2 dB asymptotic gain over hard decision decoding for all K_i and $B_{D,i} = 100$ Hz. However, for $B_{D,i} = 33$ Hz, this soft decision over hard decision gain is less, measuring approximately 1.7 dB for both $K_i = -100$ dB and $K_i = 9$ dB.
   - The inclusion of perfect fading amplitude CSI during soft decision VA decoding produced gains of 0.2 dB and 0.1 dB over standard soft decision decoding (i.e. without fading amplitude CSI) in flat fading channel conditions with $B_{D,i} = 100$ Hz and $B_{D,i} = 33$ Hz, respectively.
   - The coding gains observed for the rate $R_c = 2/3$ RSC in flat fading conditions are far less impressive than those obtained for the rate $R_c = 1/2$ NSC code, considered in *Section* 6.5.2.1. This can be largely attributed to the fact that the d_{free} of the RSC code is smaller than that of the NSC code. It is also interesting to note that, just as was the case with the binary NSC code of *Section* 6.5.2.1, better BER performances are obtained at higher maximum Doppler spreads.

6.5.3 COMMUNICATION SYSTEMS EMPLOYING VITERBI DECODED LINEAR BLOCK CODES

The following subsections present simulated BER performances of Viterbi decoded binary Hamming $(7, 4, 3)$ and non-binary RS $(7, 5, 3)$ coded communication systems under varying channel conditions. These codes were tested in AWGN and flat fading channel conditions, using narrowband complex QPSK communication systems (presented in *Section* 5.2), as well as multi-user multipath fading channel conditions, using wideband complex DS/SSMA communication systems (presented in *Section* 5.3). The RAKE receiver-based complex DS/SSMA communication systems employed length $M_{seq} = 63$ CSSs. For all of the CSS families considered, except ABC sequences, CSSs were arbitrarily selected from their respective sequence families. With the ABC sequences, CSSs were optimally selected, as discussed in *Section* 6.5.1.3.2.

6.5.3.1 BINARY HAMMING $(7, 4, 3)$ CODED COMMUNICATION SYSTEMS

Simulated AWGN, flat fading and multi-user multipath fading BER performance results for the classic binary Hamming $(7, 4, 3)$ code (see *Section* 3.2.2.3.1), described by the generator matrix defined in *Eq.* (4.4), are presented and examined in this subsection. Note that the binary Hamming code considered here is systematic and, like all other Hamming codes, has a minimum Hamming distance (see *Section* 3.2.2.2) of $d_{min} = 3$ bits. Furthermore, its BCJR trellis (see *Section* 4.2), which is not shown here due to its fairly complex structure, has a depth of 8 layers of nodes, each layer consisting of 8 nodes with 2 branches emanating from each active node. Both classic ML (brute force code book

searches) and VA (see *Section* 4.4) decoding approaches were considered using hard and soft (with and without perfect fading amplitude CSI) decision (see *Section* 4.4.2) strategies.

6.5.3.1.1 AWGN Channel Results

In *Fig.* 6.36 simulated AWGN channel (see *Section* 2.2) BER performances are shown for binary Hamming $(7, 4, 3)$ coded (see *Section* 3.2.2.3.1) narrowband complex QPSK communication systems (see *Section* 5.2). Both hard decision and soft decision (without using any fading amplitude CSI) classic ML [47] and VA decoding (see *Section* 4.4) results are present on this figure. Furthermore, the BER performance curve of an uncoded narrowband QPSK system in AWGN channel conditions, theoretically defined by *Eq.* (5.20), is also given in this figure as baseline reference.

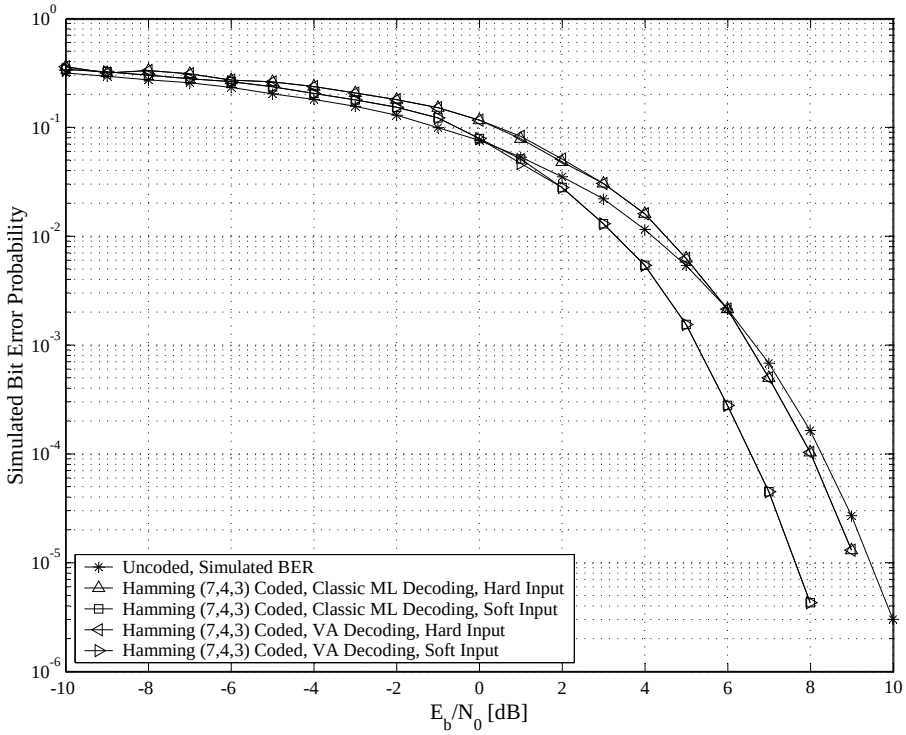

Figure 6.36: BER Performances of Binary Hamming $(7, 4, 3)$ Coded Narrowband Complex QPSK Communication Systems in AWGN Channel Conditions

6.5.3.1.2 Flat Fading Channel Results

Simulated BER performance results are shown in *Fig.* 6.37 and *Fig.* 6.38 for classic ML decoded binary Hamming $(7, 4, 3)$ coded narrowband complex QPSK communication systems (see *Section* 5.2) in flat fading channel conditions (see *Section* 2.5.1.1) with maximum Doppler spreads (see *Section* 2.4.3.3) of $B_{D,i} = 33$ Hz and $B_{D,i} = 100$ Hz, respectively. Similar results are shown respectively in *Fig.* 6.39 and *Fig.* 6.40 for VA decoding. Hard and soft (with and without perfect fading amplitude CSI) decision decoding were considered for both the classic ML and the VA decoding approaches. Furthermore, for both $B_{D,i} = 33$ Hz and $B_{D,i} = 100$ Hz, results include simulated BER curves for Rician factors (see *Section* 2.5.2.2) of $K_i = -100$ dB, $K_i = 0$ dB and $K_i = 9$ dB. The theoretical BER performance curves for uncoded QPSK systems in slow Rayleigh flat fading channel conditions, defined by *Eq.* (5.24), as well as simulated BER performance curves for uncoded QPSK systems in AWGN channel conditions are present on all four figures.

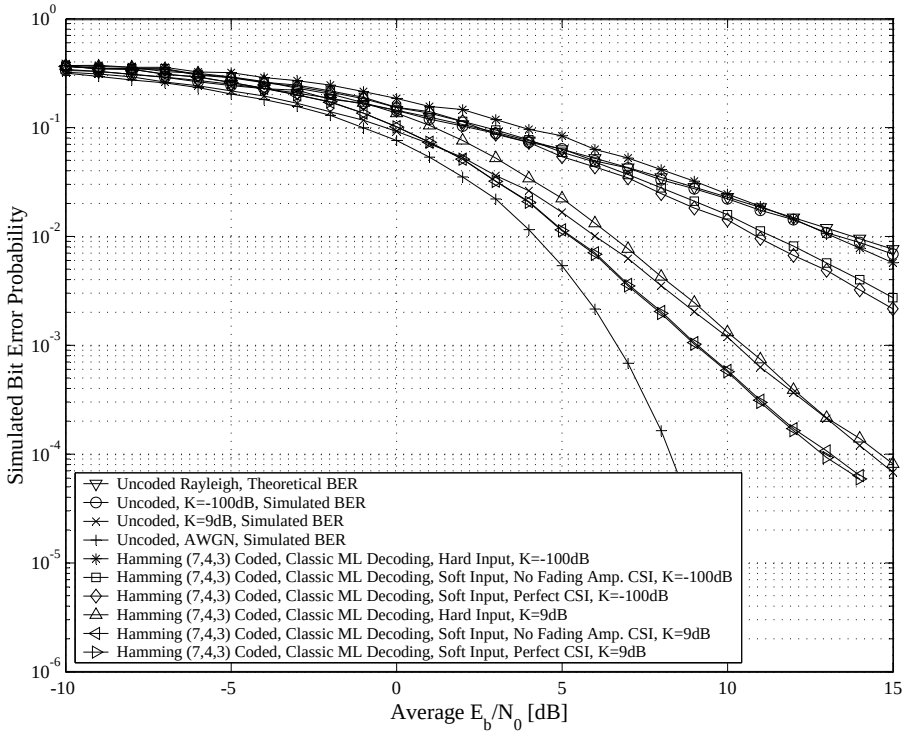

Figure 6.37: BER Performances of Binary Hamming $(7, 4, 3)$ Block Coded Narrowband Complex QPSK Communication Systems in Flat Fading Channel Conditions, $B_{D,i} = 33$ Hz, Classic ML Decoding

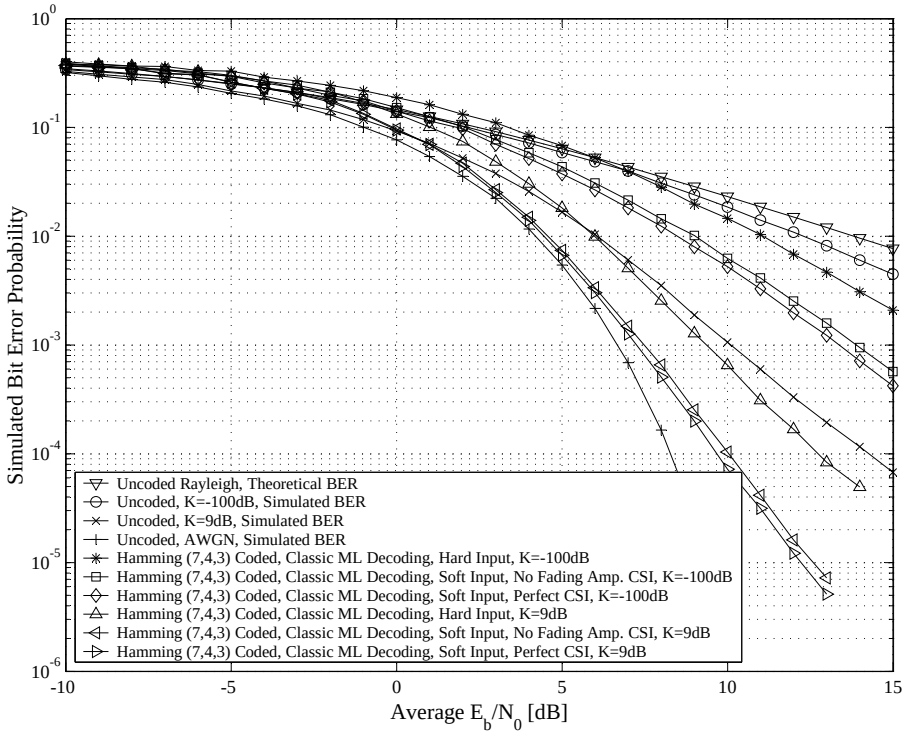

Figure 6.38: BER Performances of Binary Hamming $(7, 4, 3)$ Block Coded Narrowband Complex QPSK Communication Systems in Flat Fading Channel Conditions, $B_{D,i} = 100$ Hz, Classic ML Decoding

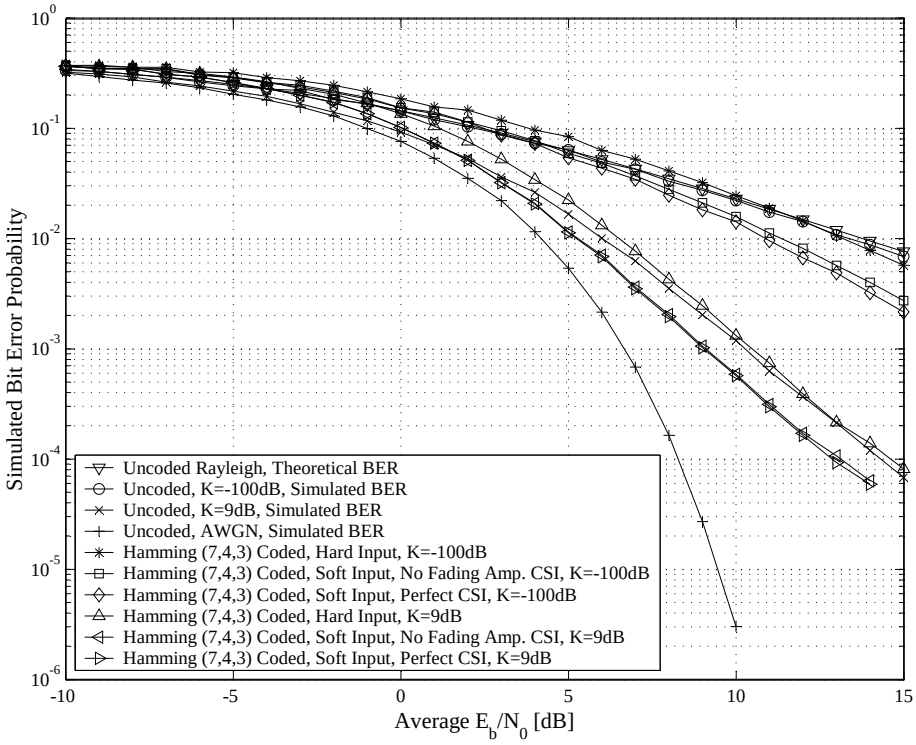

Figure 6.39: BER Performances of Binary Hamming $(7, 4, 3)$ Block Coded Narrowband Complex QPSK Communication Systems in Flat Fading Channel Conditions, $B_{D,i} = 33$ Hz, VA Decoding

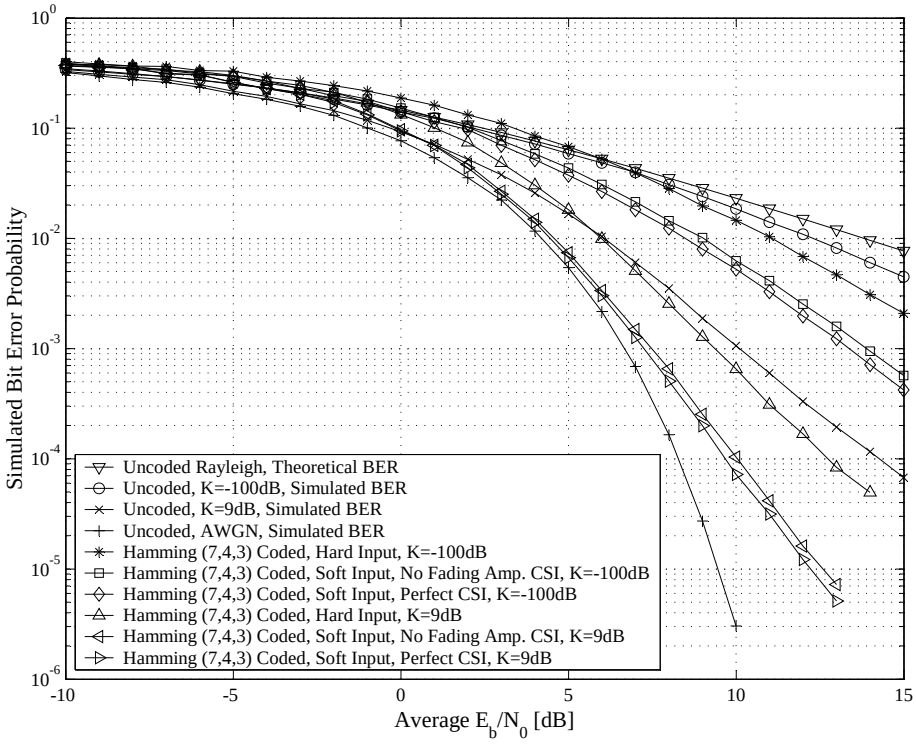

Figure 6.40: BER Performances of Binary Hamming $(7, 4, 3)$ Block Coded Narrowband Complex QPSK Communication Systems in Flat Fading Channel Conditions, $B_{D,i} = 100$ Hz, VA Decoding

6.5.3.1.3 Multipath Fading Channel Results

Simulated multi-user multipath fading channel BER performance results for binary Hamming $(7, 4, 3)$ coded RAKE receiver-based wideband complex DS/SSMA QPSK systems (see *Section* 5.3) with VA decoding, employing length $M_{seq} = 63$ ABC (see *Section* D.3.2.2), DSB CE-LI-RU filtered GCL (see *Section* D.3.2.1), ZC (see *Section* D.3.1.1) and QPH (see *Section* D.3.1.2) CSSs, are shown in *Fig.* 6.41, *Fig.* 6.42, *Fig.* 6.43 and *Fig.* 6.44, respectively. Hard and soft decision (with and without fading amplitude CSI (see *Section* 3.3.5 and *Section* 5.3.3)) VA decoding (see *Section* 4.4) were considered during these simulations. Also depicted on these figures are the simulated BER performances for uncoded RAKE receiver-based wideband complex DS/SSMA QPSK systems (presented in *Section* 6.5.1.3.1), as well as the BER performance of an uncoded system, without a RAKE receiver, operating in a purely AWGN environment.

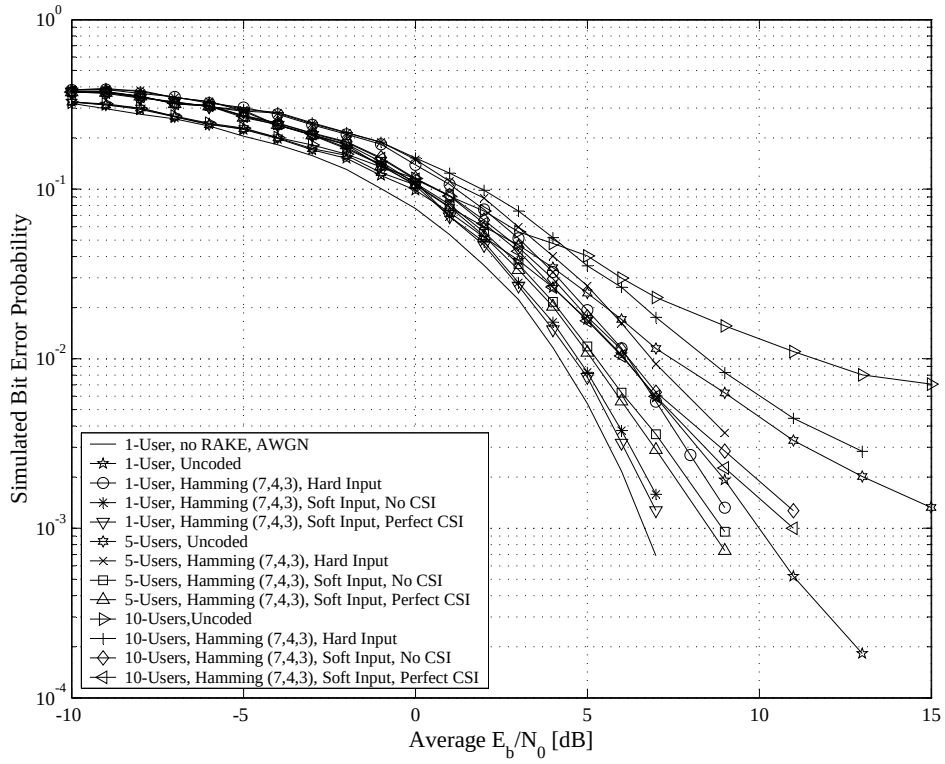

Figure 6.41: BER Performances of Binary Hamming $(7, 4, 3)$ Coded Wideband Complex QPSK Communication Systems Employing ABC Sequences in Multi-User Multipath Fading Channel Conditions, $M_{seq} = 63$

6.5.3.1.4 Discussion of the Simulation Results

The preceding subsections' simulated AWGN, flat fading and multi-user multipath fading channel BER performance results for VA decoded binary Hamming $(7, 4, 3)$ codes, running on narrowband complex QPSK communication systems and RAKE receiver-based wideband complex DS/SSMA QPSK systems, were thoroughly examined. The list below summarises the conclusions drawn from these results:

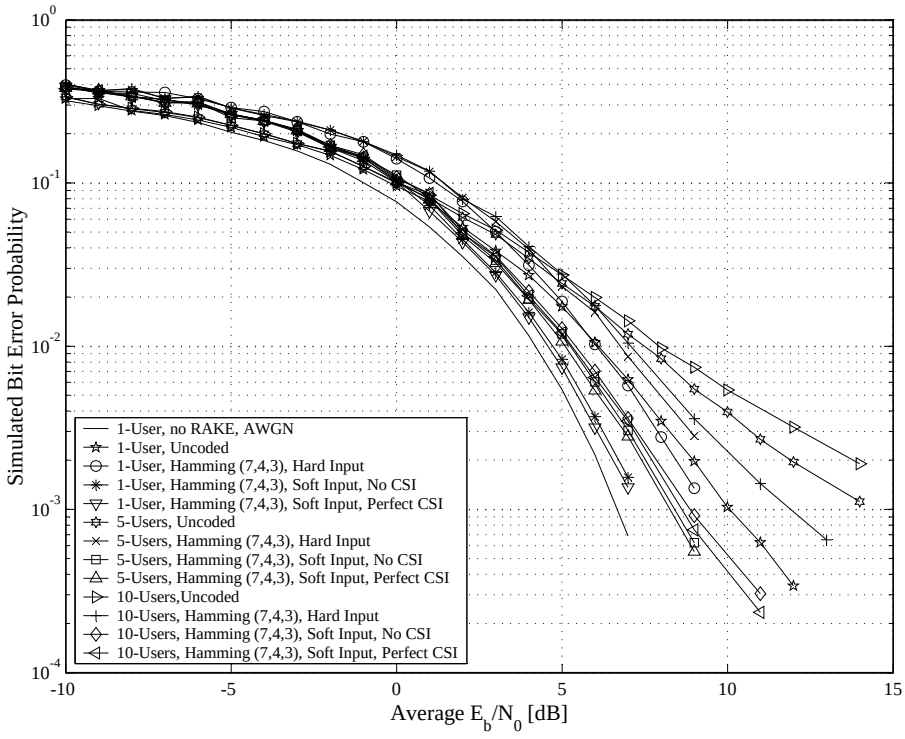

Figure 6.42: BER Performances of Binary Hamming $(7, 4, 3)$ Coded Wideband Complex QPSK Communication Systems Employing DSB CE-LI-RU Filtered GCL CSSs in Multi-User Multipath Fading Channel Conditions, $M_{seq} = 63$

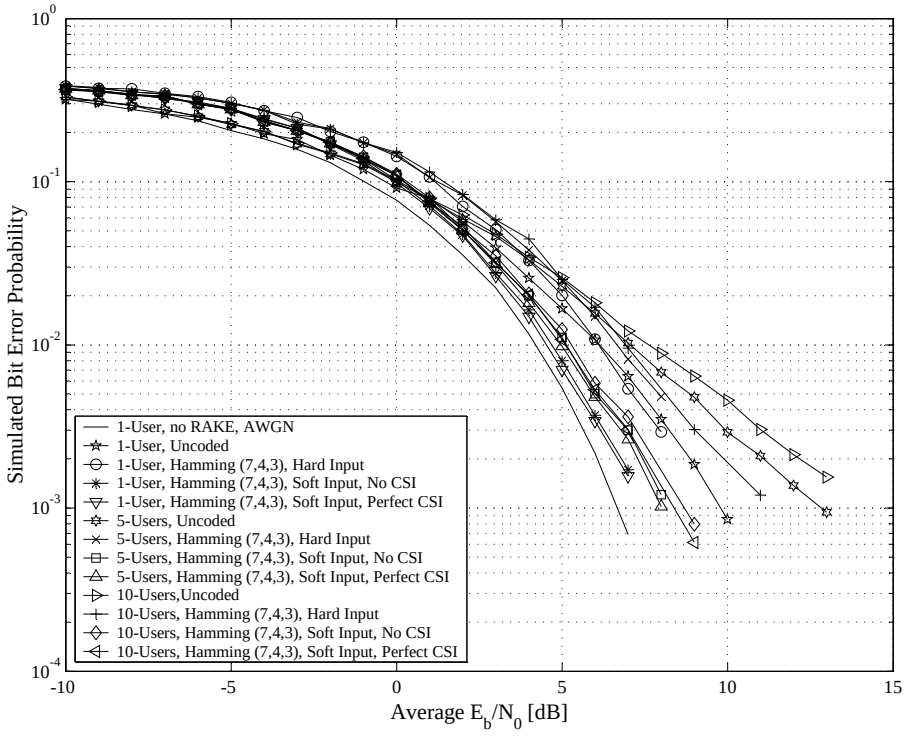

Figure 6.43: BER Performances of Binary Hamming $(7, 4, 3)$ Coded Wideband Complex QPSK Communication Systems Employing ZC CSSs in Multi-User Multipath Fading Channel Conditions, $M_{seq} = 63$

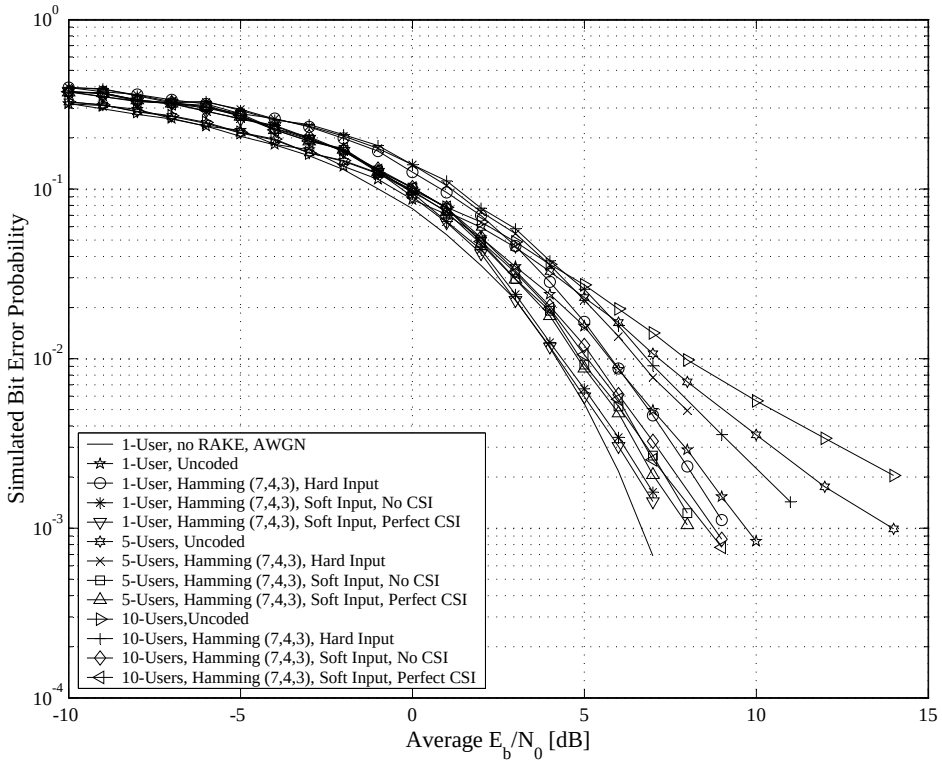

Figure 6.44: BER Performances of Binary Hamming $(7, 4, 3)$ Coded Wideband Complex QPSK Communication Systems Employing QPH CSSs in Multi-User Multipath Fading Channel Conditions, $M_{seq} = 63$

1. Conclusions and observations from the AWGN channel results:

   - According to *Eq.* (3.25), a soft decision ML decoded binary Hamming $(7, 4, 3)$ code, implemented on narrowband complex QPSK communication system in an AWGN environment, delivers a theoretical maximum asymptotic coding gain of $CG_{BC}^{soft} = 2.11$ dB at $E_b/N_0 = 15$ dB. *Fig.* 6.36 shows this theoretical coding gain to be adequately accurate for both classic ML and VA decoding with soft decisions, since a measured asymptotic coding gain of 1.9 dB can be observed for both decoding strategies.
   - From *Fig.* 6.36 it is apparent that hard and soft decision VA decoding of binary Hamming $(7, 4, 3)$ codes, employed on narrowband complex QPSK systems in AWGN channel conditions, deliver BER performances virtually identical to classic hard and soft decision ML decoding (brute force code book searches [47]).
   - Soft decision ML decoding's distinctive 2 dB gain over hard decision ML decoding in AWGN [47] is unmistakeably noticeable from *Fig.* 6.36. Furthermore, note that the system complexity associated with a hard decision ML decoded binary Hamming $(7, 4, 3)$ code barely justifies the resultant improvement in BER performance. However, for soft decision ML decoding a cross-over point (see *Section* 6.5.2.1.4) of approximately 0.5 dB can be observed. As such, it can be argued that the use of simple binary Hamming $(7, 4, 3)$ codes (with soft decision VA decoding) in high SNR applications warrants the increased system complexity.

2. Conclusions and observations from the flat fading channel results:

- Comparisons of *Fig.* 6.37 with *Fig.* 6.39, and *Fig.* 6.38 with *Fig.* 6.40 verify that, for both hard and soft decision metric calculations, classic ML decoding and VA trellis decoding of the binary Hamming $(7, 4, 3)$ code achieve equivalent BER performances in varying flat fading channel conditions.
- From the myriad of flat fading simulation results presented in *Section* 6.5.3.1.2, it is abundantly clear that the BER performance of VA and classic ML decoded binary Hamming $(7, 4, 3)$ codes, employed in narrowband QPSK systems, improve as the channel's LOS signal component increases with respect to the NLOS signal component. On average, however, the increased BER performance obtained by increasing K_i, is most evident at $B_{D,i} = 100$ Hz. This was to be expected, since the binary Hamming $(7, 4, 3)$ code is not designed to mitigate the detrimental effects of error bursts, which manifested itself with increased durations as the fading rate becomes slower.
- A comparison of hard decision decoding with soft decision decoding (without fading amplitude CSI) in a flat fading environment reveals soft decision decoding's renowned 2 dB gain over hard decision decoding. Inclusion of perfect fading amplitude CSI during soft decision decoding resulted in a marginal improvement in the measured performances. This improvement, which is most noticeable at $K_i = -100$ dB, was approximately 0.25 dB for $B_{D,i} = 100$ Hz, whereas as an average gain of 0.4 dB is discernible for $B_{D,i} = 33$ Hz.

3. Conclusions and observations from the multi-user multipath fading channel results:

- Substantiating the AWGN and flat fading channel observations, the results presented in *Fig.* 6.41, *Fig.* 6.42, *Fig.* 6.43 and *Fig.* 6.44 for VA decoded binary Hamming $(7, 4, 3)$ block codes in multi-user multipath fading channel conditions indicate that this linear block code is not particularly effective for FEC purposes. For the single user scenario, hard decision VA decoded Hamming $(7, 4, 3)$ codes, implemented on RAKE receiver-based wideband complex DS/SSMA QPSK communication systems, only starts to show gains for $\overline{E}_b/N_0 > 6$ dB, irrespective of the CSS family employed. Strangely enough, as the user load increases, hard decision VA decoding makes headway over uncoded systems at lower average E_b/N_0 values. The conclusion that can be formulated from this is that the binary Hamming $(7, 4, 3)$ code does have some potency against the effects of MUI, even though it was not designed for that purpose. When soft decision VA decoding (without fading amplitude CSI) is employed in a single user CDMA system, asymptotic gains of up to 2.5 dB and 2.2 dB are achieved by the filtered and unfiltered CSS families, respectively. This correlates well with the expected AWGN coding gain of $CG_{BC}^{soft} = 2.11$ dB, predicted by *Eq.* (3.25).
- As was to be expected, the pre-filtered CSSs were once again outperformed by the unfiltered CSS families. According to *Fig.* 6.41, *Fig.* 6.42, *Fig.* 6.43 and *Fig.* 6.44, VA decoded binary Hamming $(7, 4, 3)$ linear block codes, running on RAKE receiver-based complex DS/SSMA QPSK systems employing ABC sequences deliver the poorest BER performance results, whereas QPH CSSs has the best BER performance results at high user loads, closely followed by ZC CSSs. In fact, the performance difference between ZC and QPH CSSs never exceeds 0.25 dB. In third place is DSB CE-LI-RU filtered GCL CSSs, which outperform ABC sequences for all decoder approaches and user load scenarios. Also worth mentioning is that this filtered CSS family performs comparable with the unfiltered families considered, even for a 10-user load.
- Once again the unfiltered CSS families' superior periodic cross-correlation properties are evident. For both hard and soft decision VA decoding, the 1-user and 5-user BER performance results for binary Hamming $(7, 4, 3)$ coded complex DS/SSMA systems employing the unfiltered ZC and QPH CSS families are nearly the same. However, for a 10-user CDMA system, there is a marked decrease in BER performance, even for the unfiltered CSS families.

- At low user loads soft decision (without fading amplitude CSI) VA decoding of the binary Hamming $(7, 4, 3)$ linear block code in multi-user multipath fading channel conditions performs approximately 2 dB better than hard decision VA decoding, regardless of the CSS family used. At higher user loads, this asymptotic gain decreases. For example, at a BER of $P_b(e) = 2/100$ for a 10-user QPH CSS-based CDMA system, soft decision decoding (without fading amplitude CSI) exhibits a gain of only 1.8 dB over hard decision decoding. This performance decrease at high user loads is most severe for the filtered CSS families. Furthermore, an additional average improvement of 0.2 dB is attained by including perfect fading amplitude CSI during soft decision VA decoding, irrespective of the user load or the CSS family employed in the CDMA system.

6.5.3.2 NON-BINARY REED-SOLOMON $(7, 5, 3)$ CODED COMMUNICATION SYSTEMS

Gauging the BER performances of Viterbi decoded non-binary RS block codes (see *Section* 3.2.2.3.3) in AWGN, flat fading and multi-user multipath fading channel conditions is the focus of the following subsections. Due to the complexity of the BCJR trellis structures (see *Section* 4.3) of non-binary linear block codes, the applicability of the block-wise VA as efficient ML trellis decoder was evaluated only on the simple RS $(7, 5, 3)$ code, operating in $GF\left(2^3\right)$, defined by the generator polynomial of *Eq.* (3.35). Since this RS code is cyclic (see *Section* 3.2.2.2), its non-systematic generator matrix can be constructed using the procedure outlined in *Section* 3.2.2.2. This non-systematic generator matrix can be reworked into a systematic form (see *Section* 3.2.2.2) by performing a number of row and column permutations (using, for example, Gaussian elimination) in $GF\left(2^3\right)$, resulting in the following systematic generator matrix:

$$G_{BC} = \begin{bmatrix} 1 & 0 & 0 & 0 & 0 & \varphi^4 & \varphi \\ 0 & 1 & 0 & 0 & 0 & \varphi^5 & \varphi \\ 0 & 0 & 1 & 0 & 0 & \varphi^5 & \varphi^3 \\ 0 & 0 & 0 & 1 & 0 & 1 & 1 \\ 0 & 0 & 0 & 0 & 1 & \varphi^4 & \varphi^3 \end{bmatrix} \tag{6.5}$$

where φ is a primitive element of $GF\left(2^3\right)$. This code has a minimum Hamming distance of $d_{min} = 3$ $GF\left(2^3\right)$ symbols and its BCJR trellis (see *Section* 4.2), which is not shown here due to its extremely complex structure, has a depth of 8 layers of nodes, each layer consisting of 64 nodes with 8 branches emanating from each active node.

Also included in the simulation results presented in the following subsections, are the BER performance curves obtained using Berlekamp-Massey syndrome decoding (see *Appendix B*). These results act as baseline references for the hard decision VA decoding (see *Section* 4.4) results. Soft decision VA decoding (see *Section* 4.4.2.2) with no fading amplitude CSI is compared to soft decision VA decoding with perfect fading amplitude CSI (see *Section* 3.3.5).

6.5.3.2.1 AWGN Channel Results

Fig. 6.45 depicts simulated AWGN channel BER performances for narrowband complex QPSK communication systems (see *Section* 5.2) employing non-binary RS $(7, 5, 3)$ codes (see *Section* 3.2.2.3.3), with message and code word symbols from $GF\left(2^3\right)$. Not only are hard decision and soft decision (without using any fading amplitude CSI) VA decoding (see *Section* 4.4) results present on this figure, but also hard decision results obtained through classic Berlekamp-Massey syndrome decoding (see *Appendix B*). As baseline reference, the theoretical BER performance curve of an uncoded narrowband QPSK system in AWGN channel conditions, defined by *Eq.* (5.20), is also present on this figure.

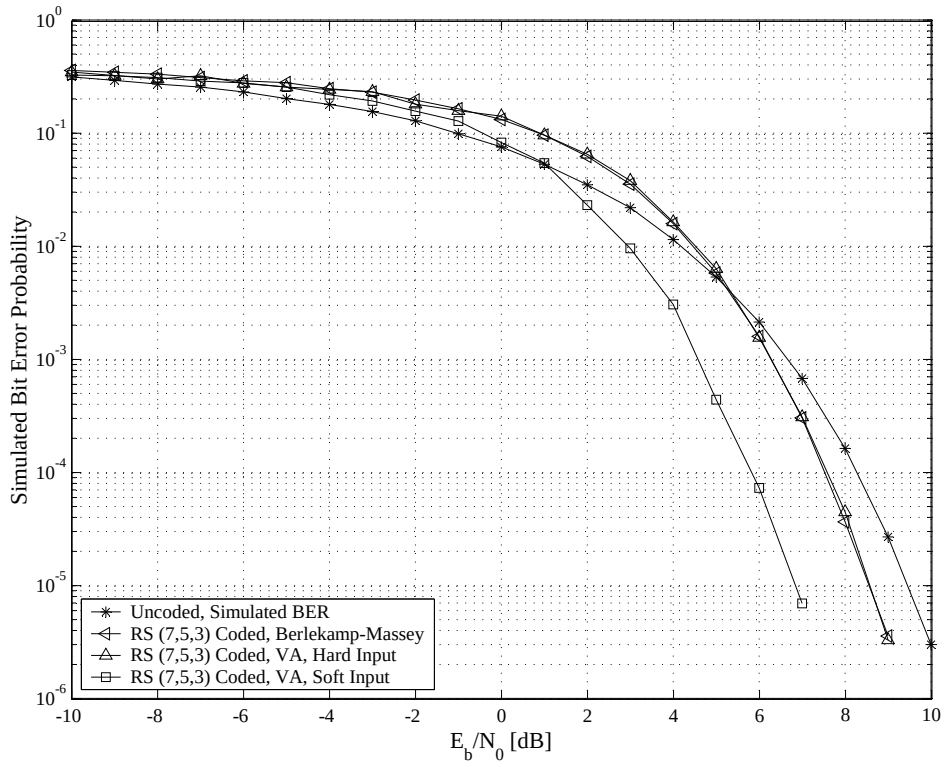

Figure 6.45: BER Performances of Non-Binary RS $(7, 5, 3)$ Coded Narrowband Complex QPSK Communication Systems in AWGN Channel Conditions

6.5.3.2.2 Flat Fading Channel Results

Fig. 6.46 and *Fig.* 6.47 depict BER performance results (obtained through simulations) for non-binary RS $(7, 5, 3)$ (see *Section* 3.2.2.3.3) coded narrowband complex QPSK communication systems (see *Section* 5.2) operating in flat fading channel (see *Section* 2.5.1.1) conditions with maximum Doppler spreads (see *Section* 2.4.3.3) of $B_{D,i} = 33$ Hz and $B_{D,i} = 100$ Hz, respectively. As shown on these figures, Rician factors (see *Section* 2.5.2.2) of $K_i = -100$ dB, $K_i = 0$ dB and $K_i = 9$ dB were considered. Furthermore, note that both hard and soft decision VA decoding (see *Section* 4.4) of the RS $(7, 5, 3)$ codes were evaluated, with fading amplitude CSI (see *Section* 3.3.5 and *Section* 5.2.3) of varying degrees of accuracy being employed during the soft decision decoding simulation experiments. Also included on both figures are the simulated BER performance curves of uncoded QPSK systems in AWGN channel conditions, as well as *Eq.* (5.24)'s theoretical BER performance curve for uncoded QPSK systems in slow Rayleigh flat fading channel conditions.

6.5.3.2.3 Multipath Fading Channel Results

Fig. 6.48, *Fig.* 6.49, *Fig.* 6.50 and *Fig.* 6.51 depict simulated multi-user multipath fading channel BER performance results for non-binary RS $(7, 5, 3)$ coded (see *Section* 3.2.2.3.3) RAKE receiver-based wideband complex DS/SSMA QPSK systems (see *Section* 5.3), which make use of length $M_{seq} = 63$ ABC (see *Section* D.3.2.2), DSB CE-LI-RU filtered GCL (see *Section* D.3.2.1), ZC (see *Section* D.3.1.1) and QPH (see *Section* D.3.1.2) CSSs, respectively. VA decoding (see *Section* 4.4) was employed, with both hard and soft decision (with and without fading amplitude CSI (see

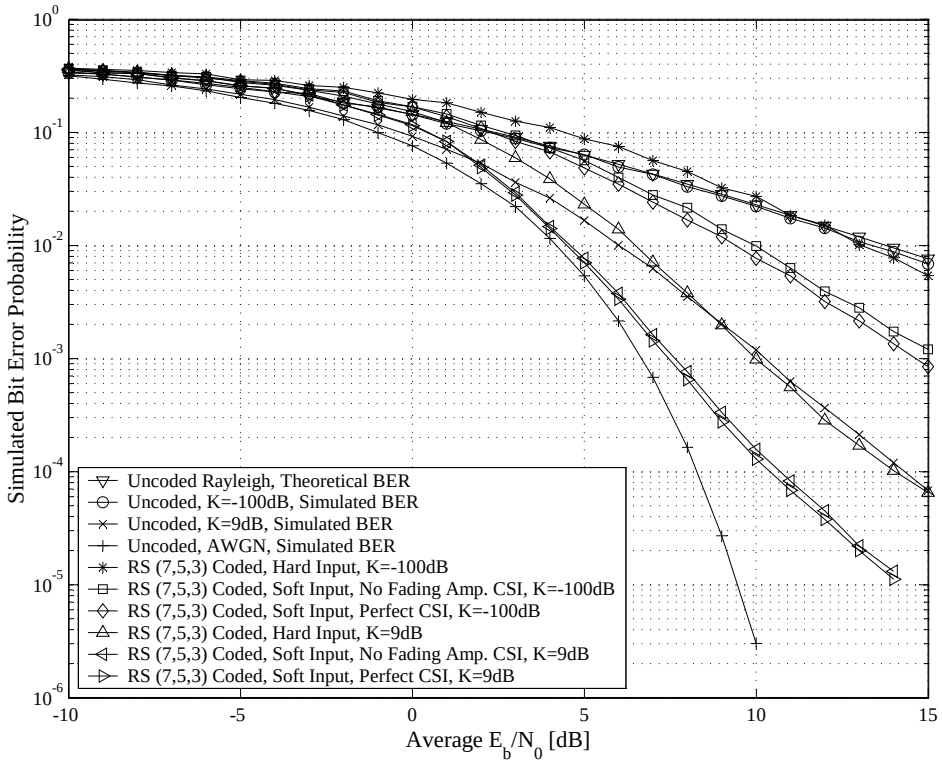

Figure 6.46: BER Performances of Non-binary RS $(7, 5, 3)$ Coded Narrowband Complex QPSK Communication Systems in Flat Fading Channel Conditions, $B_{D,i} = 33$ Hz

Section 3.3.5 and *Section* 5.3.3)) BER performance results shown on these figures for each of the CSS families. Furthermore, *Section* 6.5.1.3.1's uncoded RAKE receiver-based wideband complex DS/SSMA QPSK systems' simulated BER performances, as well as the BER performance of an uncoded system (without a RAKE receiver), operating in a purely AWGN environment, are also shown for baseline reference purposes.

6.5.3.2.4 Discussion of the Simulation Results

Numerous simulated AWGN, flat fading and multi-user multipath fading channel BER performance results are presented in the preceding subsections for non-binary RS $(7, 5, 3)$ coded narrowband complex QPSK communication systems and RAKE receiver-based wideband complex DS/SSMA QPSK systems. Classic Berlekamp-Massey and block-wise VA decoding approaches were considered. From these results the following interesting observations and valuable conclusions can be made:

1. Conclusions and observations from the AWGN channel results:

   - *Fig.* 6.45's simulated AWGN channel BER performance results undeniably affirms the applicability of the hard decision VA as a viable ML decoder replacement for the classic Berlekamp-Massey syndrome decoding algorithm (see *Appendix B*).
   - The simulated AWGN channel soft decision VA decoding results for a non-binary RS $(7, 5, 3)$ coded narrowband complex QPSK system, presented in *Fig.* 6.45, not only exhibit the expected 2 dB improvement over hard decision decoding, but also an asymptotic coding gain of 2.8 dB over an uncoded system. This measurement correlates well with *Eq.* (3.25)'s theoretical maximum coding gain of $CG_{BC}^{soft} = 3.1$ dB at $E_b/N_0 = 15$ dB.

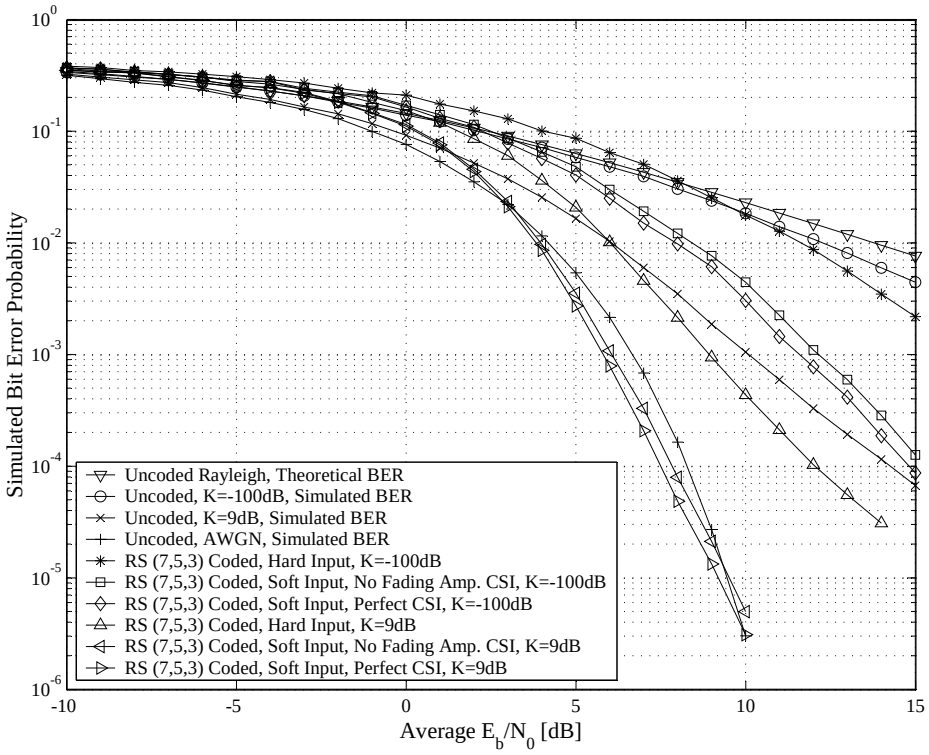

Figure 6.47: BER Performances of Non-binary RS $(7, 5, 3)$ Coded Narrowband Complex QPSK Communication Systems in Flat Fading Channel Conditions, $B_{D,i} = 100$ Hz

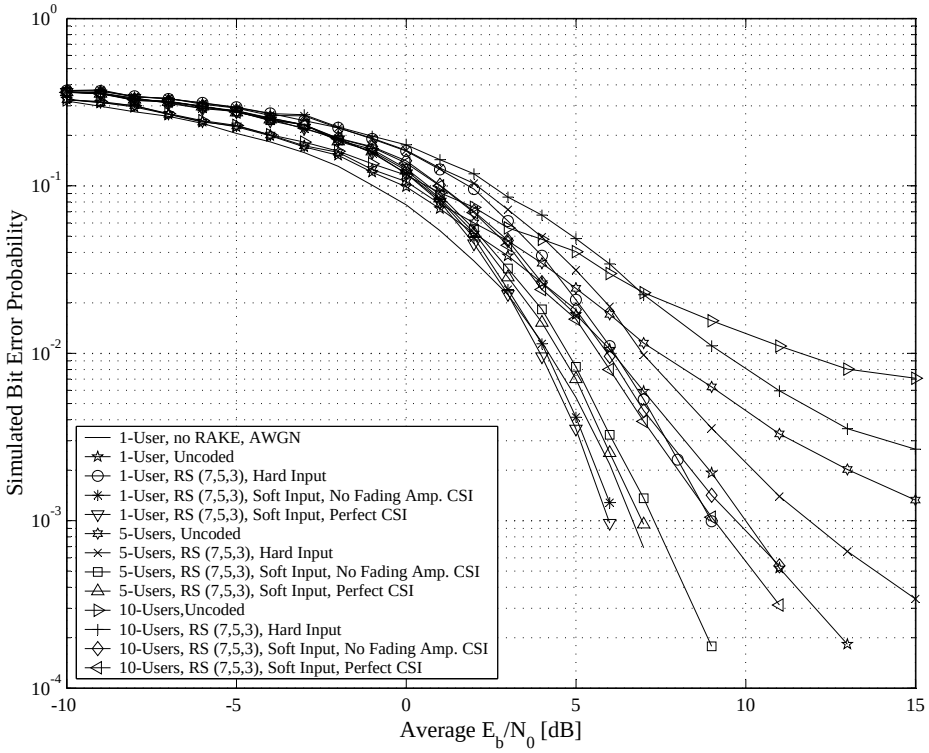

Figure 6.48: BER Performances of Non-Binary RS $(7, 5, 3)$ Coded Wideband Complex QPSK Communication Systems Employing ABC Sequences in Multi-User Multipath Fading Channel Conditions, $M_{seq} = 63$

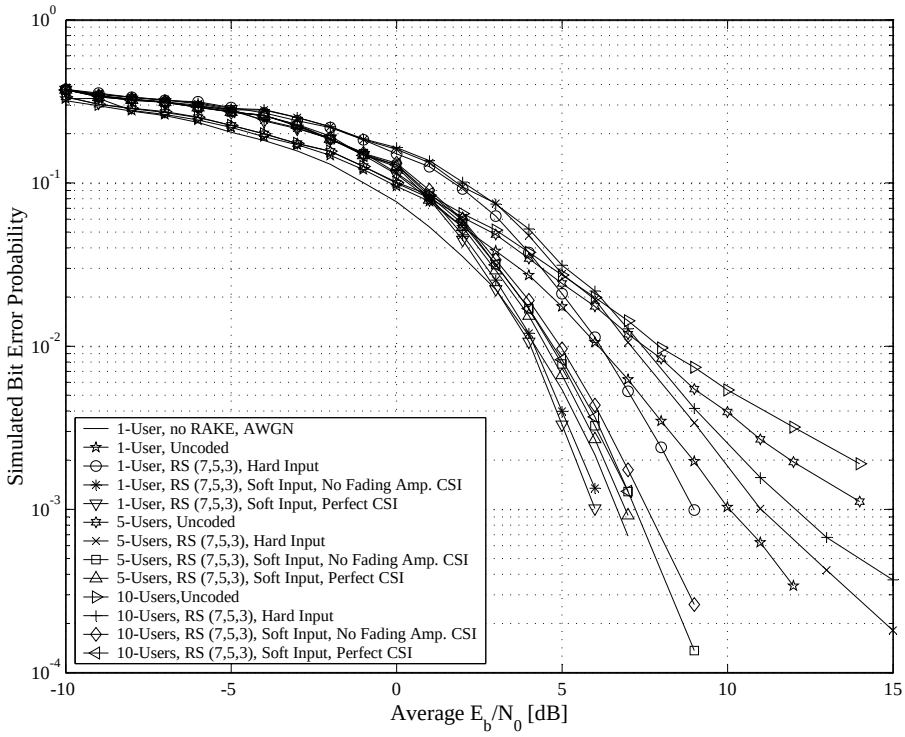

Figure 6.49: BER Performances of Non-Binary RS $(7, 5, 3)$ Coded Wideband Complex QPSK Communication Systems Employing DSB CE-LI-RU Filtered GCL CSSs in Multi-User Multipath Fading Channel Conditions, $M_{seq} = 63$

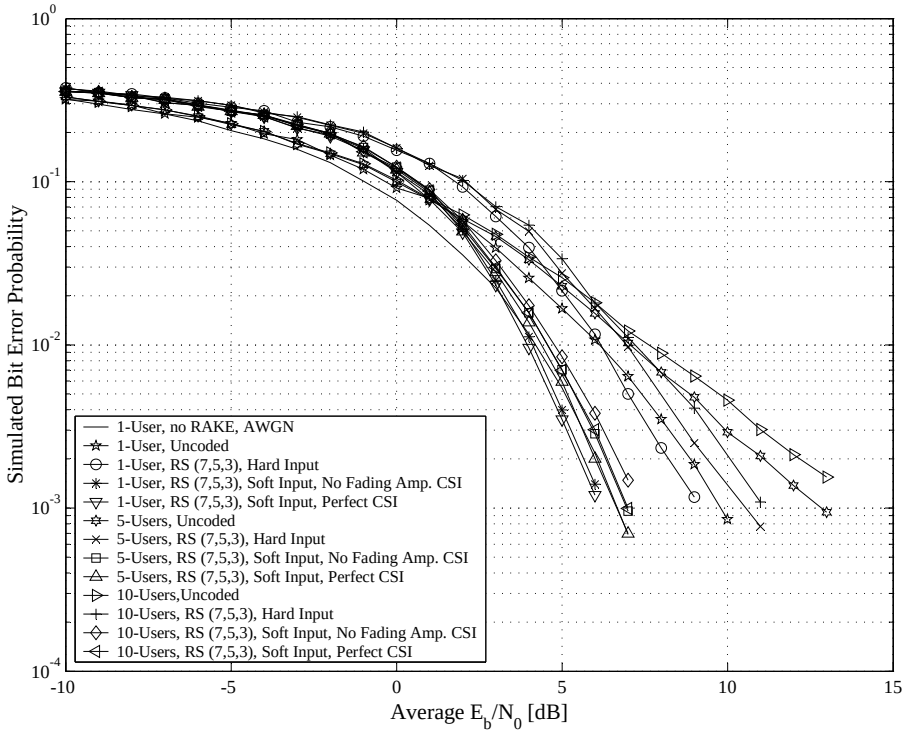

Figure 6.50: BER Performances of Non-Binary RS $(7, 5, 3)$ Coded Wideband Complex QPSK Communication Systems Employing ZC CSSs in Multi-User Multipath Fading Channel Conditions, $M_{seq} = 63$

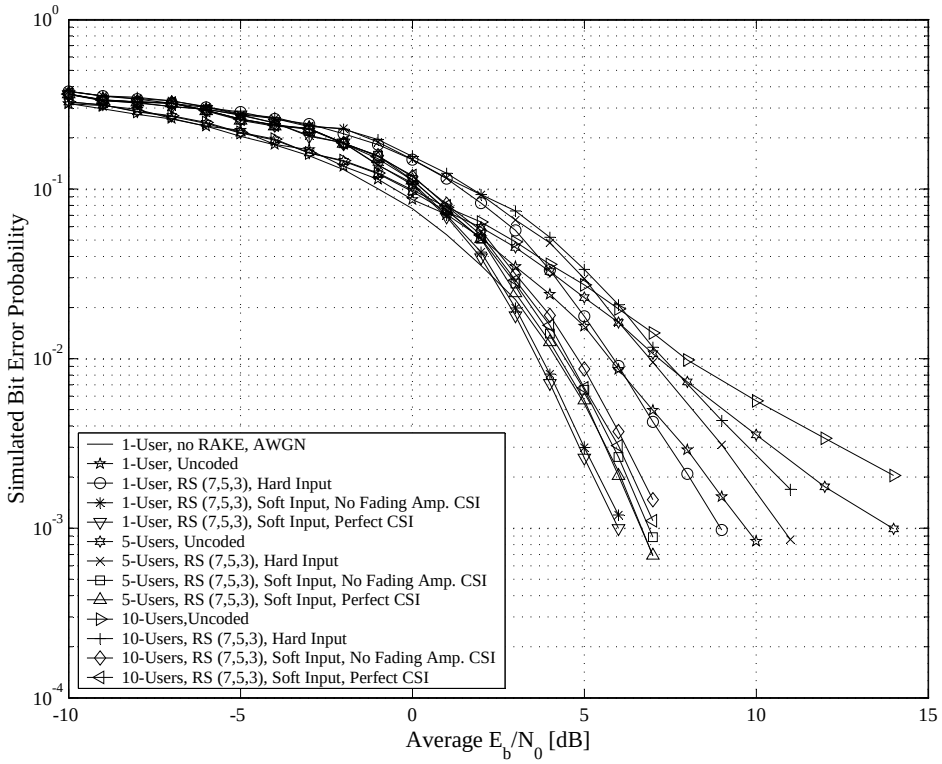

Figure 6.51: BER Performances of Non-Binary RS $(7, 5, 3)$ Coded Wideband Complex QPSK Communication Systems Employing QPH CSSs in Multi-User Multipath Fading Channel Conditions, $M_{seq} = 63$

- The respective cross-over points (see *Section* 6.5.2.1.4) for hard and soft decision VA decoded non-binary RS $(7, 5, 3)$ codes on narrowband complex QPSK systems are 5 dB and 1 dB. Strangely enough, these cross-over points are akin to those of the binary Hamming $(7, 4, 3)$ code (considered in *Section* 6.5.3.1), which is a substantially less powerful linear block code.

2. Conclusions and observations from the flat fading channel results:

- As indicated by *Fig.* 6.46 and *Fig.* 6.47, VA decoded non-binary RS $(7, 5, 3)$ linear block codes show marked BER performance improvements in flat fading channel conditions as the channels' Rician factors K_i (see *Section* 2.5.2.2) increase. This was to be expected, since an increase in a flat fading channel's Rician factor tends to make it appear more Gaussian-like in nature, which is necessary requirement by all linear block codes, including RS codes, for optimal BER performances.
- Inspection of *Fig.* 6.46 and *Fig.* 6.47 not only shows that VA decoded non-binary RS codes, implemented on a narrowband complex QPSK communication system, perform better at higher maximum Doppler spreads, but also that the gain of soft decision decoding, with perfect fading amplitude CSI, over that of soft decision decoding, without fading amplitude CSI, increases as the maximum Doppler spread increases. For a Rician factor of $K_i = 9$ dB, this gain is approximately 0.26 dB and 0.4 dB for $B_{D,i} = 33$ Hz and $B_{D,i} = 100$ Hz, respectively.
- As stated previously, the RS code performs better at $B_{D,i} = 100$ Hz than at $B_{D,i} = 33$ Hz. However, the performance improvement is less dramatic than that observed for the foregoing binary convolutional and linear block codes. This can be attributed to the fact that RS codes are burst error correcting codes, capable of correcting groups of errors. Recall that the RS

$(7, 5, 3)$ code considered here has a $d_{min} = 3$ $GF\left(2^3\right)$ symbols. Hence, each code word is capable of correcting a single error burst, consisting of 3 well-organised (i.e. adjacent) bit errors.

- In flat fading channel conditions, hard decision VA decoding lags soft decision VA decoding by almost 3 dB. For $B_{D,i} = 100$ Hz and $K_i = 9$ dB, this gain is not asymptotic, since it increases non-linearly as the average E_b/N_0 increases.

3. Conclusions and observations from the multi-user multipath fading channel results:

- Investigation of the multi-user multipath fading channel results given in *Fig.* 6.48, *Fig.* 6.49, *Fig.* 6.50 and *Fig.* 6.51 confirms that the VA decoding of non-binary RS $(7, 5, 3)$ linear block codes, implemented on RAKE receiver-based wideband complex DS/SSMA QPSK systems, delivers marked BER performance improvements for all CSS families considered. Although the non-binary RS code effectively combats the bursty errors induced by the multipath fading channel, it is not as efficient at mitigating the effects of MUI as the binary rate $R_c = 1/2$ NSC code, considered in *Section* 6.5.2.1. This is most noticeable for ABC sequences, where hard decision VA decoding in a 10-user system exhibits a cross-over point only at 7 dB. For the other CSS families, this crossover-point is substantially lower, especially for the unfiltered families.
- When soft decision (without fading amplitude CSI) VA decoding is employed in a single user environment, the RS $(7, 5, 3)$ code performs better at high $\overline{E}_b/N_0$ values than an uncoded DS/SSMA system operating in purely AWGN channel conditions. Furthermore, for the single user scenario, soft decision (without fading amplitude CSI) VA decoding of RS code exhibits increasing coding gains over the uncoded system as the average E_b/N_0 increases. For example, at $P_b(e) = 10^{-3}$ a coding gain of $CG_{BC}^{soft} = 3.4$ dB is observed, irrespective of the CSS family used.
- In terms of overall performance, the unfiltered CSSs exhibited the best performances, with QPH CSSs outperforming ZC CSSs by no more than 0.3 dB at high user loads. As was to be expected, ABC sequences demonstrated the poorest BER performances, which is evident from a comparison of the results shown in *Fig.* 6.48, *Fig.* 6.49, *Fig.* 6.50 and *Fig.* 6.51. DSB CE-LI-RU filtered GCL CSSs again delivered BER performances far superior to ABC sequences, coming close to that of the unfiltered CSS families.
- Soft decision (without fading amplitude CSI) VA decoding of the non-binary RS $(7, 5, 3)$ linear block code at low user loads performs approximately 2.7 dB better than hard decision VA decoding, regardless of the CSS family used. This asymptotic gain decreases as the user load increases. For example, for ZC CSSs soft decision decoding (without fading amplitude CSI) exhibits a gain of only 2.5 dB over hard decision decoding at a BER of $P_b(e) = 2/1000$ in a 10-user system. Furthermore, by including perfect fading amplitude CSI during soft decision VA decoding, an additional average improvement of 0.2 dB is attained, regardless of the user load or the CSS family employed in the CDMA system.

6.5.4 REDUCING THE COMPLEXITY OF A BCJR TRELLIS - THE BINARY CYCLIC $(5, 3, 2)$ LINEAR BLOCK CODE

The VA decoding of linear block codes employing reduced trellis structures, obtained using the approach outlined in *Section* 4.3.2, falls under the spotlight in the following subsections. Recall from *Section* 4.3.2 that finding a minimal trellis structure for a (n, k, d_{min}) block code is a tedious process. As such, only the simple binary cyclic $(5, 3, 2)$ block code (see *Section* 3.2.2.2), used as an example to illustrate the trellis reduction technique of *Section* 4.3.2, is used here. This code's original systematic generator matrix is given by *Eq.* (4.22), with its corresponding unreduced BCJR trellis structure

shown in *Fig.* 4.3. After executing the trellis reduction procedure, an equivalent binary cyclic $(5, 3, 2)$ block code with the minimal trellis structure shown in *Fig.* 4.4 was obtained. Note that this equivalent code, defined by *Eq.* (4.22), is non-systematic. Thus, obtaining the simulation results presented in the following subsections required not only VA decoding, but also a mapping of decoded code words to decoded message words. In contrast, obtaining decoded message words for the systematic block codes, presented in the preceding subsections, simply involved stripping the parity symbols from the decoded code words.

Due to time constraints, only AWGN and flat fading channel BER performance simulation tests were performed, using narrowband complex QPSK systems (see *Section* 5.2), on VA decoded (see *Section* 4.4) binary cyclic $(5, 3, 2)$ block codes with reduced complexity trellises. Both hard and soft decision VA decoding approaches were considered. The influence of using perfect fading amplitude CSI (see *Section* 3.3.5 and *Section* 5.2.3) during soft decision decoding (see *Section* 4.4.2.2) was also investigated.

6.5.4.1 AWGN CHANNEL RESULTS

Simulated AWGN channel BER performance results for VA decoded binary cyclic $(5, 3, 2)$ linear block codes, running on narrowband complex QPSK communication systems (see *Section* 5.2), are given in *Fig.* 6.52. Present on this figure are results obtained by performing hard and soft decision VA decoding (see *Section* 4.4) on the original and reduced complexity trellises, shown in *Fig.* 4.3 and *Fig.* 4.4, respectively. Note that the soft decision decoding results were obtained without the use of fading amplitude CSI in the VA metric calculations. For comparative purposes, the theoretical BER performance curve of an uncoded narrowband QPSK system in AWGN channel conditions, defined by *Eq.* (5.20), is also present on this figure.

6.5.4.2 FLAT FADING CHANNEL RESULTS

This subsection is concerned with the simulated BER performance results obtained for binary cyclic $(5, 3, 2)$ codes with VA decoding using original and reduced complexity trellises, tested on narrowband complex QPSK communication systems, operating in flat fading channel conditions. The first set of figures (*Fig.* 6.53 and *Fig.* 6.54) show the simulated BER performance results obtained through hard and soft decision (with and without perfect fading amplitude CSI) VA decoding (see *Section* 4.4) using the original unreduced trellis structure of *Fig.* 4.3 for maximum Doppler spreads (see *Section* 2.4.3.3) of $B_{D,i} = 33$ Hz and $B_{D,i} = 100$ Hz, respectively. Comparable results are respectively contained in *Fig.* 6.55 and *Fig.* 6.56 for VA decoding using the reduced trellis structure of *Fig.* 4.4. For both sets of figures, Rician factors (see *Section* 2.5.2.2) of $K_i = -100$ dB, $K_i = 0$ dB and $K_i = 9$ dB were considered. Also provided on all four figures presented in this subsection, are the theoretical BER performance curve for uncoded QPSK systems in slow Rayleigh flat fading channel conditions (defined by *Eq.* (5.24)), as well as simulated BER performance curves for uncoded QPSK systems in AWGN channel conditions.

6.5.4.3 DISCUSSION OF THE SIMULATION RESULTS

The effects of using reduced trellis structures during the VA decoding of binary cyclic $(5, 3, 2)$ block coded narrowband complex QPSK communication systems, operating in AWGN and flat fading channel conditions, was the focus of the preceding subsections. From the simulated BER performance results obtained, the following conclusions can be drawn:

1. Conclusions and observations for the AWGN channel results:

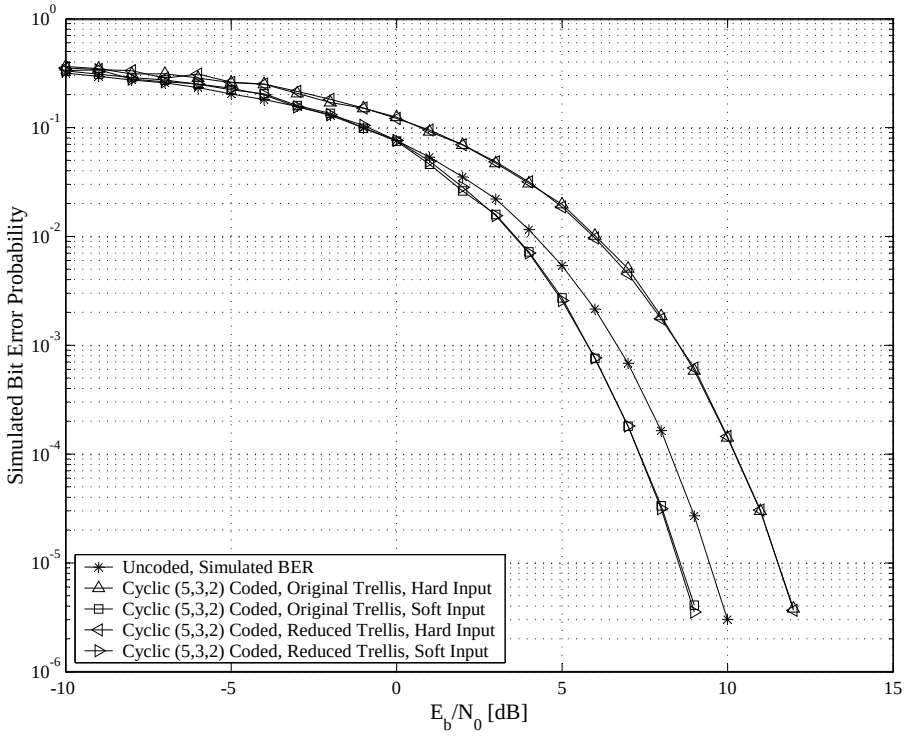

Figure 6.52: AWGN Channel BER Performance Results for Narrowband Complex QPSK Communication Systems Employing Binary Cyclic $(5, 3, 2)$ Linear Block Codes with VA Decoding Using Original and Reduced Trellis Structures

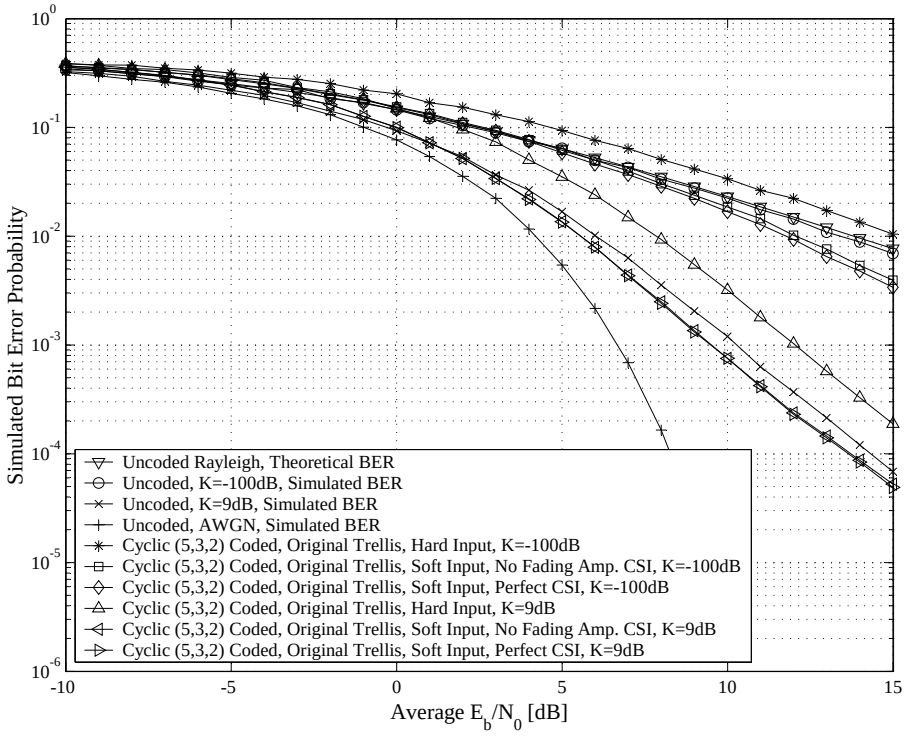

Figure 6.53: BER Performances of Binary Cyclic $(5, 3, 2)$ Block Coded Narrowband Complex QPSK Communication Systems in Flat Fading Channel Conditions ($B_{D,i} = 33$ Hz), VA Decoding Using the Original Trellis Structure of *Fig.* 4.3

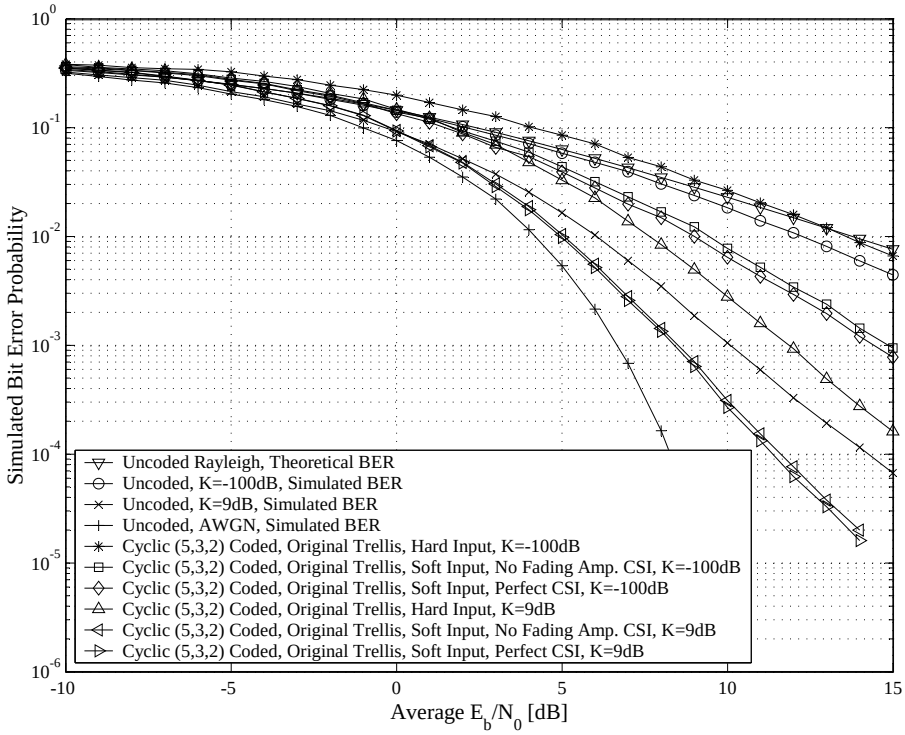

Figure 6.54: BER Performances of Binary Cyclic $(5, 3, 2)$ Block Coded Narrowband Complex QPSK Communication Systems in Flat Fading Channel Conditions ($B_{D,i} = 100$ Hz), VA Decoding Using the Original Trellis Structure of *Fig.* 4.3

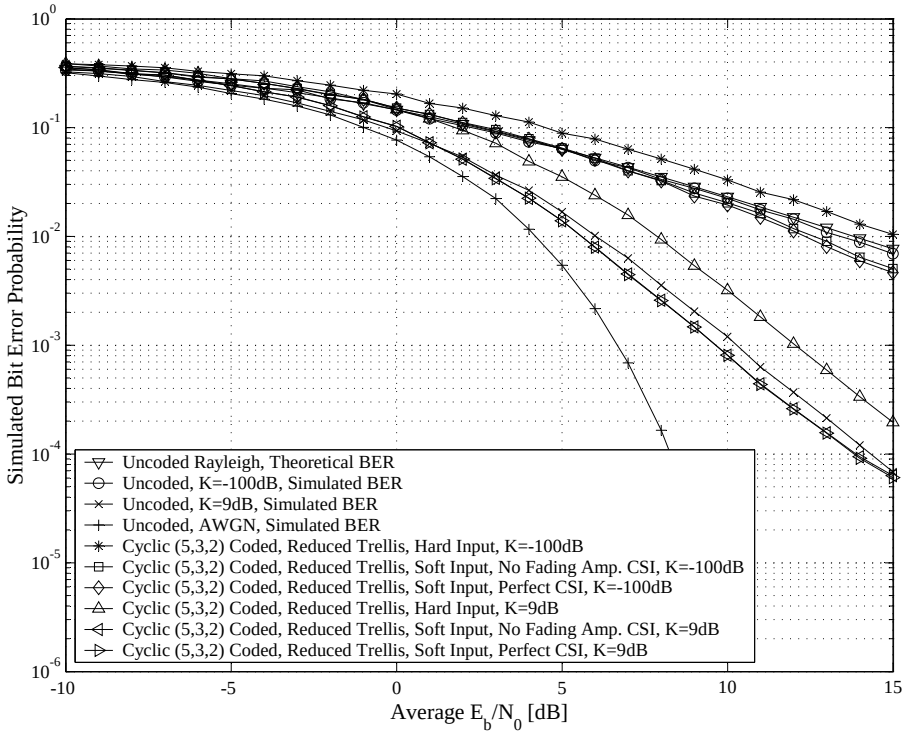

Figure 6.55: BER Performances of Binary Cyclic $(5, 3, 2)$ Block Coded Narrowband Complex QPSK Communication Systems in Flat Fading Channel Conditions ($B_{D,i} = 33$ Hz), VA Decoding Using the Reduced Trellis Structure of *Fig.* 4.4

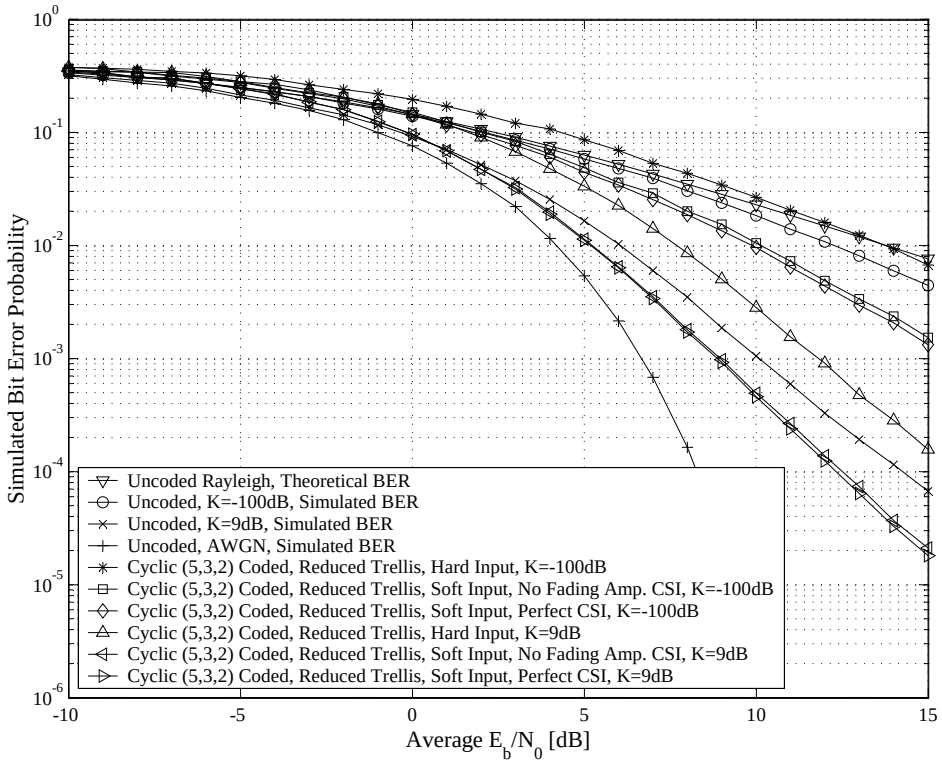

Figure 6.56: BER Performances of Binary Cyclic $(5, 3, 2)$ Block Coded Narrowband Complex QPSK Communication Systems in Flat Fading Channel Conditions ($B_{D,i} = 100$ Hz), VA Decoding Using the Reduced Trellis Structure of *Fig.* 4.4

- From *Fig.* 6.52 it is clear that, in AWGN channel conditions, VA decoding of a simple binary cyclic $(5, 3, 2)$ linear block code using original (see *Section* 4.2) and reduced complexity (see *Section* 4.3.2) BCJR trellis structures deliver almost identical BER performances. This was to be expected, since the reduced complexity trellis was obtained using *Eq.* (4.22)'s generator matrix, which is a non-systematic equivalent of the original generator matrix, given by *Eq.* (4.18).
- In terms of coding gain, soft decision VA decoded binary cyclic $(5, 3, 2)$ linear block codes deliver mediocre BER performances in AWGN channel conditions. Soft decision VA decoding shows a simulated asymptotic coding gain of 0.7 dB over an uncoded narrowband complex QPSK system (comparable with *Eq.* (3.25)'s theoretical gain of $CG_{BC}^{soft} = 0.79$ dB), as well as a cross-over point (see *Section* 6.5.2.1.4) of 1 dB. Since hard decision VA decoding asymptotically lags soft decision decoding by 3 dB (unexpectedly higher than the classic 2 dB) in terms of BER performance, the uncoded system will outperform hard decision VA decoding at any SNR.

2. Conclusions and observations from the flat fading channel results:

- A comparison of *Fig.* 6.53 with *Fig.* 6.54, and *Fig.* 6.55 with *Fig.* 6.56, confirms the following expected observations: For both the $B_{D_i} = 33$ Hz and $B_{D_i} = 100$ Hz flat fading channel scenarios, VA decoding of the binary cyclic $(5, 3, 2)$ linear block code (using the original and reduced complexity trellis structures) delivers increasingly improved BER performances as the channels' Rician factors increase. Furthermore, soft decision VA decoding, with perfect fading amplitude CSI, shows gains of 0.25 dB at $B_{D_i} = 100$ Hz and 0.1 dB at $B_{D_i} = 33$ Hz

over soft decision VA decoding without any fading amplitude CSI. Lastly, on average the VA decoded binary cyclic $(5, 3, 2)$ block code performs better at a faster fading rate, since it is not intended to correct large error bursts.

- Inexplicably, in flat fading channel conditions, the VA decoding of the binary cyclic $(5, 3, 2)$ code, using the reduced complexity trellis structure, performs weaker than when the original trellis is used. For example, with $B_{D,i} = 100$ Hz and $K_i = 9$ dB, VA decoding using the reduced trellis structure lags by 0.75 dB in performance. This difference in BER performance for the different trellis structures is less severe for the slower $B_{D,i} = 33$ Hz channel configuration, measuring only 0.3 dB for $K_i = 9$ dB. Although the author of this dissertation is unable to deliver a bona fide explanation for this phenomenon, it can be conjectured that these inferior performances, obtained using the reduced complexity trellis structure, might be attributed to error propagation: Recall that the equivalent binary cyclic $(5, 3, 2)$ code obtained after executing the trellis reduction procedure described in *Section* 4.3.2, is non-systematic. As such, VA decoding alone will not produce an estimate of the original data input vector $\overline{d}_m$. A second stage ML mapping from decoded code word estimate $\hat{\overline{c}}_m$ to decoded message word estimate $\hat{\overline{d}}_m$ is required. Thus, any errors present in $\hat{\overline{c}}_m$ after VA decoding will not only propagate, but possibly increase in quantity by performing the second stage ML mapping. The end result is reduced BER performances. In [163] *Fossorier et al.* made similar observations when linear block codes with identical dimensions and d_{min}, but with different generator matrices G_{BC} were compared. *Fossorier et al.* went on to show that the systematic encoding of linear block codes not only simplifies decoding, but also minimises the probability of a bit error.

6.5.5 COMMUNICATION SYSTEMS EMPLOYING INTERLEAVED VITERBI DECODED LINEAR BLOCK CODES

The nett result of flat and frequency selective fading on wirelessly transported data streams is the phenomenon of error bursts [60]. Certain types of codes, such as non-binary RS block codes (see *Section* 3.2.2.3.3), are inherently designed to mitigate the detrimental effects of such error bursts [164]. However, using interleaving and de-interleaving (see *Section* 3.2.3) in conjunction with channel coding yields remarkable BER performance improvements for communication systems operating in fading channel conditions, even when burst error correcting codes are already employed [60]. The following subsections investigate the BER performance improvements gained by using interleaved VA decoded (see *Section* 4.4) binary Hamming $(7, 4, 3)$ and non-binary RS $(7, 5, 3)$ linear block codes in narrowband complex QPSK (see *Section* 5.2) and wideband complex DS/SSMA QPSK (see *Section* 5.3) communication systems, operating in flat and multi-user multipath fading channel conditions, respectively. Similar to *Section* 6.5.3, the RAKE receiver-based complex DS/SSMA communication systems employed length $M_{seq} = 63$ CSSs. Again, for all of the CSS families considered, except ABC sequences, sequences were arbitrarily selected from their respective sequence families. For the ABC sequences case, sequences were optimally selected (see *Section* 6.5.1.3.2).

A simple random number generator interleaver (see *Section* C.3.2) of length $N = 105$ bits was employed for both the binary Hamming (7,4,3) (see *Section* 3.2.2.3.1) and non-binary RS $(7, 5, 3)$ (see *Section* 3.2.2.3.3) linear block coded systems. The choice for the length of the interleaver is justified as follows: From the chosen flat fading channel parameters (shown in *Table* 5.1) and multipath fading channel parameters (shown in *Table* 5.5 and *Table* 5.6), the minimum Doppler spread (see *Section* 2.4.3.3) considered in this study is $\min\{B_{D,i}\} = 33$ Hz. Furthermore, both the narrowband complex QPSK and wideband complex DS/SSMA QPSK transmitters are configured for balanced modulation with coded, unspreaded symbol rates of 1000 b/s (see *Table* 5.1 and *Table* 5.4). As such,

a quick rule-of-thumb calculation shows that a slow deep fade can corrupt a maximum of approximately $1000/33 \approx 30$ coded bits. Thus, an interleaver length of $N = 105$ is more than adequate to spread the effects of such a worst case scenario error burst over multiple code words.

6.5.5.1 INTERLEAVED BINARY HAMMING $(7, 4, 3)$ CODED COMMUNICATION SYSTEMS

The binary Hamming $(7, 4, 3)$ code (see *Section* 3.2.2.3.1) considered in *Section* 6.5.3.1 is revisited here again. Since each code word consists of 7 bits, interleaving using the length $N = 105$ random number generator interleaver results in the shuffling of 15 complete code words' code bits. VA decoded interleaved Hamming $(7, 4, 3)$ coded narrowband complex QPSK and wideband complex DS/SSMA systems' simulated BER performances are presented and discussed in the following subsections for flat fading and multi-user multipath fading channel conditions, respectively. Again, hard and soft decision VA decoding (see *Section* 4.4.2) are considered, with varying degrees of fading amplitude CSI (see *Section* 3.3.5) employed during soft decision decoding.

6.5.5.1.1 Flat Fading Channel Results

Fig. 6.57 and *Fig.* 6.58 present the simulation results, obtained during the BER performance tests performed for interleaved binary Hamming $(7, 4, 3)$ coded (see *Section* 3.2.2.3.1) narrowband complex QPSK communication systems (see *Section* 5.2) in flat fading (see *Section* 2.5.1.1) channel conditions, with maximum Doppler spreads (see *Section* 2.4.3.3) of $B_{D,i} = 33$ Hz and $B_{D,i} = 100$ Hz, respectively. Hard and soft decision VA decoding (see *Section* 4.4), following the de-interleaving process, were considered for Rician factors (see *Section* 2.5.2.2) of $K_i = -100$ dB, $K_i = 0$ dB and $K_i = 9$ dB. Results are shown for soft decision decoding without any fading amplitude CSI and soft decision decoding with perfect fading amplitude CSI (see *Section* 3.3.5 and *Section* 5.2.3). Also depicted on these figures are *Eq.* (5.24)'s theoretical BER performance curve for an uncoded QPSK system in slow Rayleigh flat fading channel conditions, as well as simulated BER performance curves for uncoded QPSK systems in the presence of only AWGN.

6.5.5.1.2 Multipath Fading Channel Results

Simulated multi-user multipath fading channel BER performance results for block-wise VA decoded (see *Section* 4.4) interleaved binary Hamming $(7, 4, 3)$ codes (see *Section* 3.2.2.3.1), running on RAKE receiver-based wideband complex DS/SSMA QPSK systems (see *Section* 5.3), are shown in *Fig.* 6.59, *Fig.* 6.60, *Fig.* 6.61 and *Fig.* 6.62 for length $M_{seq} = 63$ ABC (see *Section* D.3.2.2), DSB CE-LI-RU filtered GCL (see *Section* D.3.2.1), ZC (see *Section* D.3.1.1) and QPH (see *Section* D.3.1.2) CSSs, respectively. Both hard and soft decision (with and without fading amplitude CSI (see *Section* 3.3.5 and *Section* 5.3.3)) block-wise VA decoding of the interleaved binary Hamming $(7, 4, 3)$ codes were considered. The simulated uncoded RAKE receiver-based wideband complex DS/SSMA QPSK systems' multi-user multipath fading channel BER performance results, presented in *Section* 6.5.1.3.1, are also present on these figures for comparative purposes, as is the BER performance of an uncoded non-RAKE DS/SSMA system, operating solely in AWGN.

6.5.5.1.3 Discussion of the Simulation Results

The preceding two subsections presented flat and multipath fading BER performance results for interleaved binary Hamming $(7, 4, 3)$ coded narrowband complex QPSK and wideband complex DSSS/MA QPSK systems (with de-interleaving and VA decoding employed in the RAKE receiver), respectively. Listed below are several noteworthy observations and important conclusions drawn from these results:

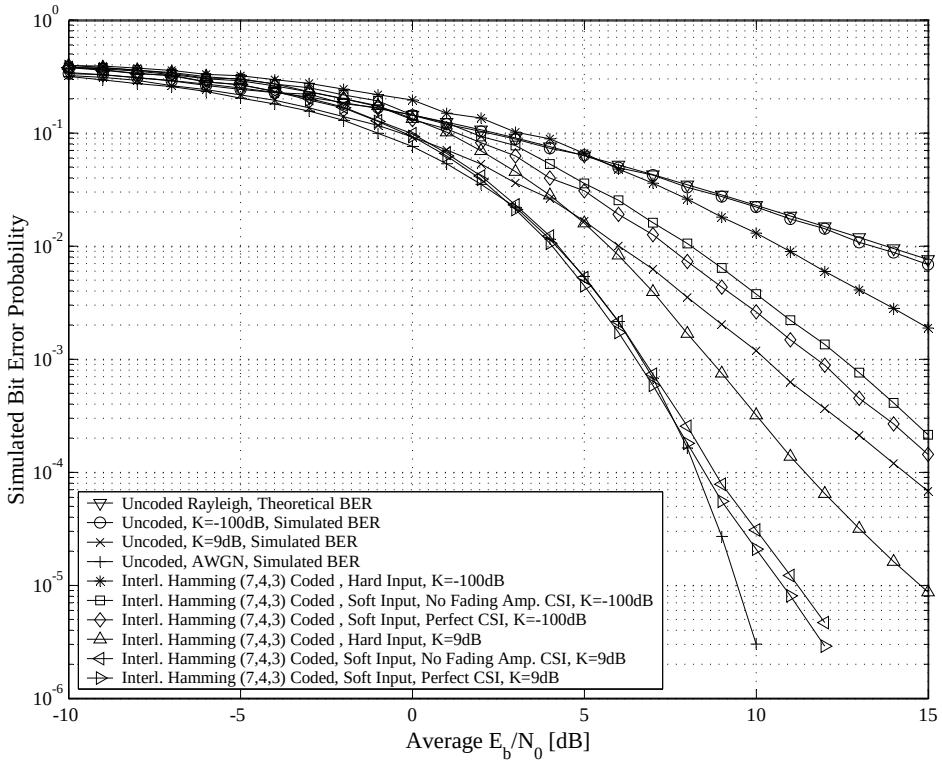

Figure 6.57: BER Performances of Interleaved Binary Hamming $(7, 4, 3)$ Coded Narrowband Complex QPSK Communication Systems in Flat Fading Channel Conditions, $B_{D,i} = 33$ Hz

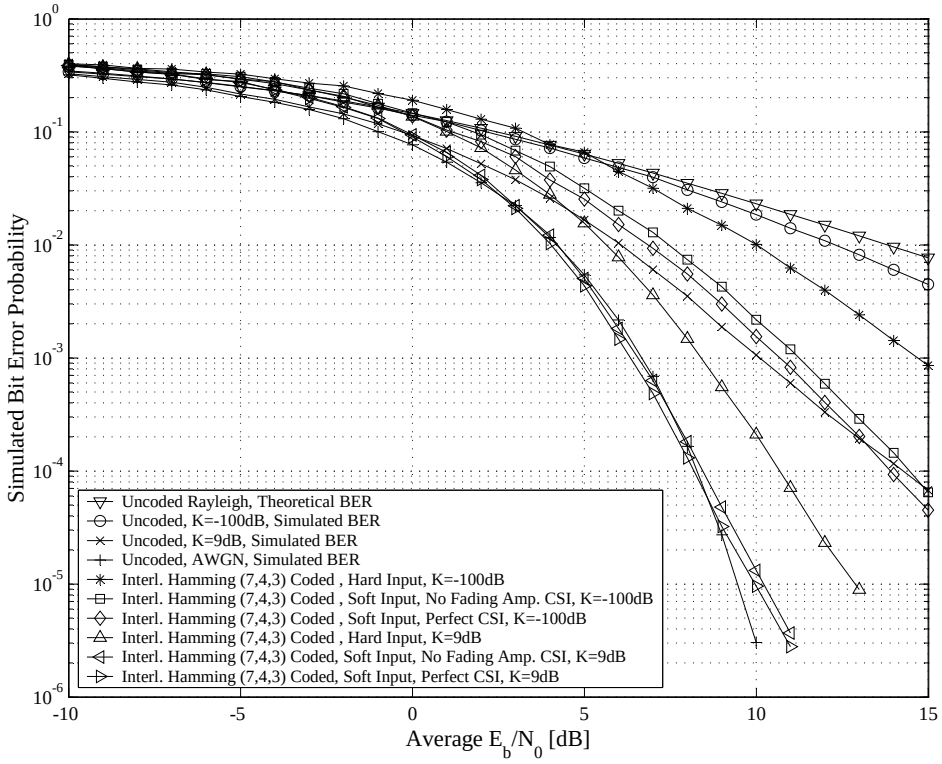

Figure 6.58: BER Performances of Interleaved Binary Hamming $(7, 4, 3)$ Coded Narrowband Complex QPSK Communication Systems in Flat Fading Channel Conditions, $B_{D,i} = 100$ Hz

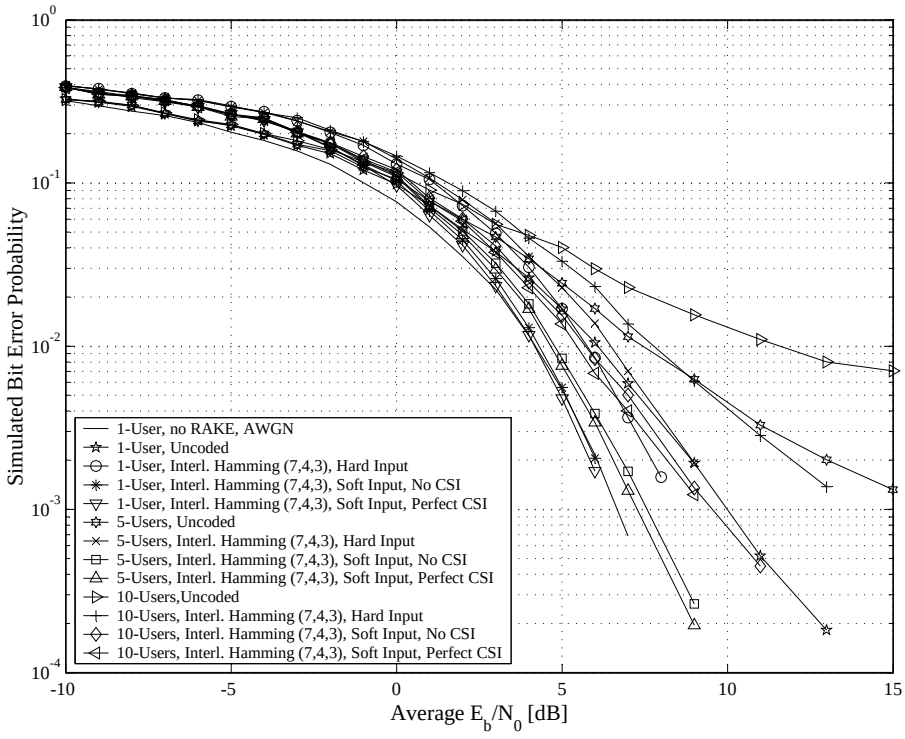

Figure 6.59: BER Performances of Interleaved Binary Hamming $(7, 4, 3)$ Coded Wideband Complex QPSK Communication Systems Employing ABC Sequences in Multi-User Multipath Fading Channel Conditions, $M_{seq} = 63$

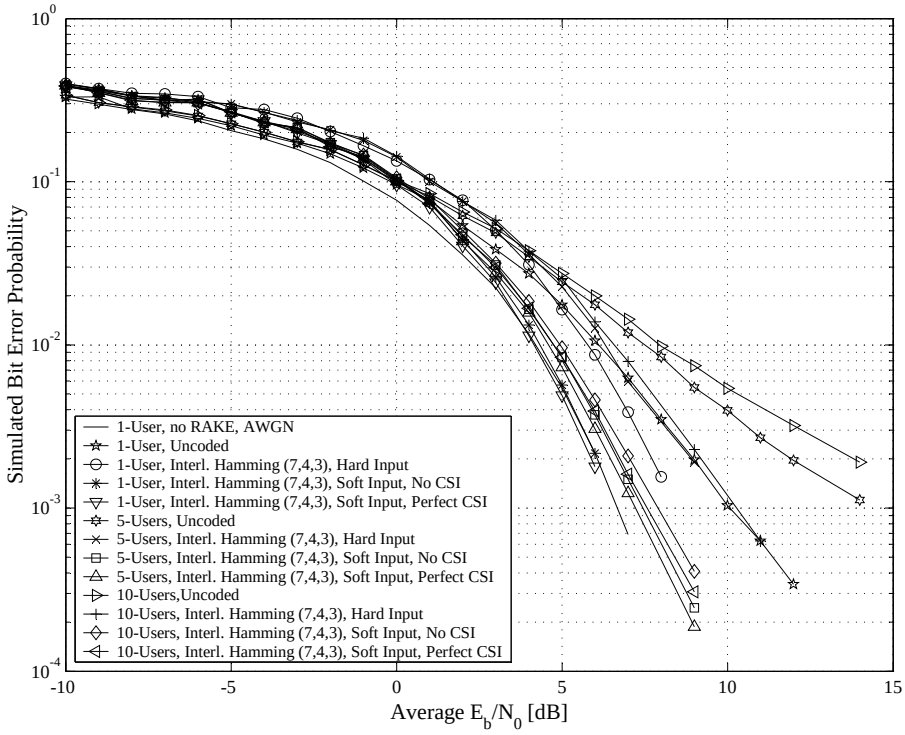

Figure 6.60: BER Performances of Interleaved Binary Hamming $(7, 4, 3)$ Coded Wideband Complex QPSK Communication Systems Employing DSB CE-LI-RU Filtered GCL CSSs in Multi-User Multipath Fading Channel Conditions, $M_{seq} = 63$

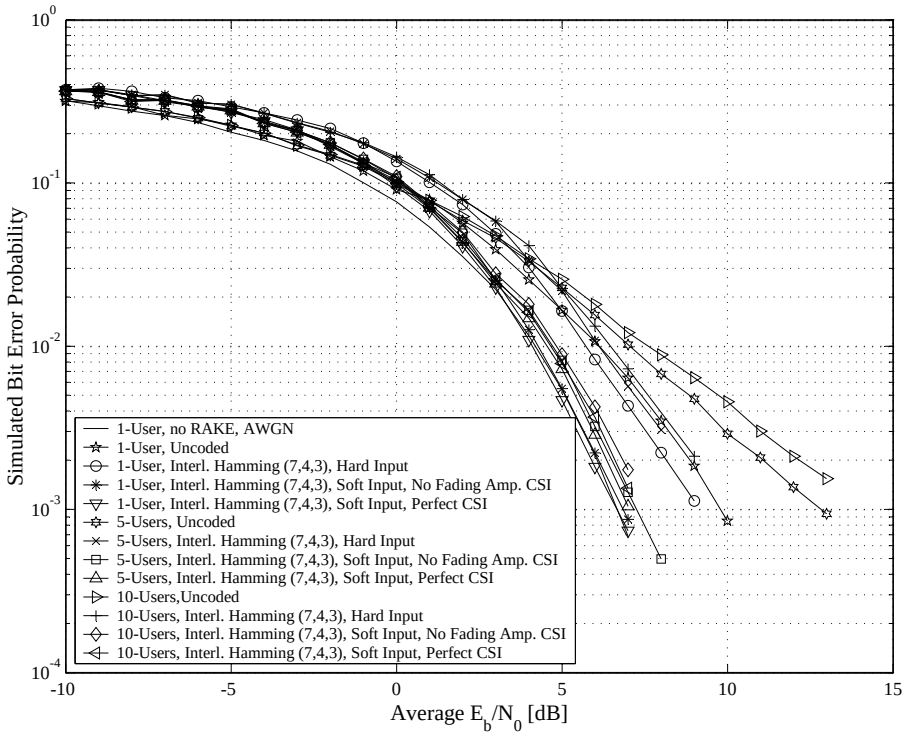

Figure 6.61: BER Performances of Interleaved Binary Hamming $(7, 4, 3)$ Coded Wideband Complex QPSK Communication Systems Employing ZC CSSs in Multi-User Multipath Fading Channel Conditions, $M_{seq} = 63$

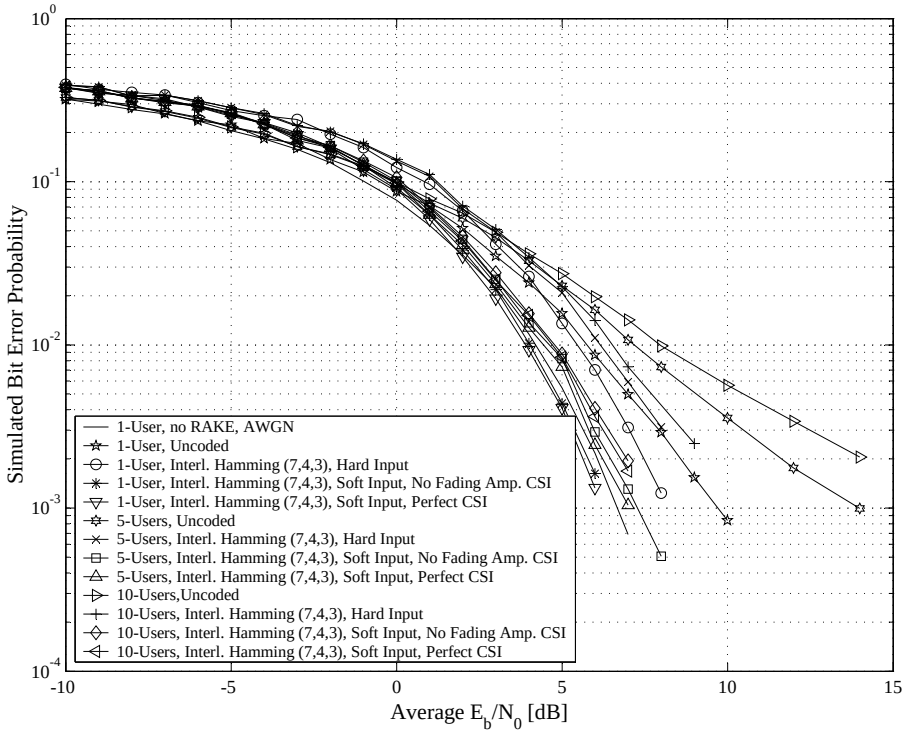

Figure 6.62: BER Performances of Interleaved Binary Hamming $(7, 4, 3)$ Coded Wideband Complex QPSK Communication Systems Employing QPH CSSs in Multi-User Multipath Fading Channel Conditions, $M_{seq} = 63$

1. Conclusions and observations from the flat fading channel results:

   - Contrasting *Fig.* 6.57 with *Fig.* 6.39, and *Fig.* 6.58 with *Fig.* 6.40 reveal that the interleaving process substantially improved the BER performance of hard and soft decision VA decoded binary Hamming $(7, 4, 3)$ codes in flat fading channel conditions (especially for the $B_{D,i} = 33$ Hz case). For example, with $B_{D,i} = 100$ Hz and $K_i = 9$ dB at $P_b(e) = 10^{-4}$, interleaving improved soft decision VA decoding (without any fading amplitude CSI) by approximately 1.75 dB. However, as the Rician factor K_i decreases, the gains obtained using interleaving reduce. Thus, it can be argued that the fading channel's tendency to move from a Gaussian-like to a Rician-like statistical demeanour, starts to overtake the temporal characteristics as the dominating channel effect.
   - A comparison of *Fig.* 6.57 with *Fig.* 6.58 shows that, even after interleaving, VA decoded binary Hamming $(7, 4, 3)$ block codes in flat fading channel conditions with $B_{D,i} = 33$ Hz show inferior BER performances to that obtained for $B_{D,i} = 100$ Hz. However, the performance difference is far less extreme than was the case with the non-interleaved VA decoded binary Hamming $(7, 4, 3)$ block codes (see *Section* 6.5.3.1.2). Thus, it can be concluded that a length $N = 105$ interleaver was not sufficiently capable of decomposing error bursts to obtain IID fading distributions on the received code bits.
   - By incorporating interleaving into the binary Hamming $(7, 4, 3)$ coded narrowband complex QPSK system (operating in flat fading channel conditions), the resultant improvement obtained by employing perfect fading amplitude CSI during soft decision VA decoding, increased. This is particularly evident at $B_{D,i} = 33$ Hz. For example, at $P_b(e) = 10^{-4}$ with $K_i = 9$ dB, fading amplitude CSI improved soft decision VA decoding by approximately 0.25 dB when using interleaving, whereas the non-interleaved scenario showed an almost negligible gain of 0.05 dB.

2. Conclusions and observations from the multi-user multipath fading channel results:

   - Comparing the multi-user multipath fading results presented in *Section* 6.5.3.1.3 and *Section* 6.5.5.1.2 for VA decoded non-interleaved and interleaved binary Hamming $(7, 4, 3)$ linear block codes, respectively, indicates that the use of interleaving improved the BER performance positively. The largest performance improvements were observed at low user loads with hard decision VA decoding. For example, by using interleaving together with hard decision VA decoding, a 1-user system with a BER of $P_b(e) = 2/1000$ obtained a gain of almost 1 dB, irrespective of the CSS family. By employing soft decision decoding (without fading amplitude CSI), this gain diminished to 0.8 dB. However, it was still adequate enough to boost the single user's multipath fading performance results over that of the uncoded DS/SSMA system (without RAKE reception) in AWGN channel conditions for $\overline{E}_b/N_0 > 4$ dB.
   - From *Section* 6.5.5.1.2's BER performance results for the different filtered and unfiltered CSS families considered in this study, it is apparent that, after interleaving, ABC sequences still exhibit the poorest MUI performance, distantly followed by DSB CE-LI-RU filtered GCL CSSs. However, by incorporating interleaving into VA decoded binary Hamming $(7, 4, 3)$ codes, these two pre-filtered CSS families showed the largest BER performance improvements for the 10-user scenario. Thus, it can be speculated that interleaving actually alleviates the detrimental correlative and temporal effects of the MUI caused by the CSSs' poor periodic cross-correlation properties, thereby creating less bursty errors. The unfiltered QPH and ZC CSS families, which performed almost identically, surpassed ABC and DSB CE-LI-RU filtered GCL CSSs for all VA decoder approaches and user load options.
   - Differing from the observations made from *Section* 6.5.5.1.1's flat fading channel results, it was discovered that, in multi-user multipath fading channel conditions, interleaving has no

influence on the performance improvement obtained by incorporating fading amplitude CSI into soft decision VA decoding. The same can also be said of the asymptotic gain of soft decision (without fading amplitude CSI) over hard decision VA decoding, since it remains constant at 2 dB, regardless of the user load or CSS family used.

6.5.5.2 *INTERLEAVED NON-BINARY REED-SOLOMON* $(7, 5, 3)$ *CODED COMMUNICATION SYSTEMS*

Simulated BER performance curves are introduced in the following subsections for interleaved RS $(7, 5, 3)$ block coded (see *Section* 3.2.2.3.3) narrowband complex QPSK (see *Section* 5.2) and wideband complex DS/SSMA QPSK (see *Section* 5.3) communication systems, operating in flat fading and multi-user multipath fading channels, respectively. The non-binary RS (7,5,3) code used throughout these simulations, functions in $GF\left(2^3\right)$ and is defined by *Eq.* (6.5) in *Section* 6.5.3.2. Since each RS code word consists of seven $GF\left(2^3\right)$ code word symbols, with each $GF\left(2^3\right)$ symbol in turn consisting of three bits, it follows that the length $N = 105$ random number generator interleaver shuffles the information of 5 consecutive code words prior to transmission. The following subsections present simulated BER performance results obtained through hard and soft decision (with and without perfect fading amplitude CSI) VA decoding.

6.5.5.2.1 Flat Fading Channel Results

Simulated flat fading channel (see *Section* 2.5.1.1) BER performance results are shown in *Fig.* 6.63 (maximum Doppler spread of $B_{D,i} = 33$ Hz) and *Fig.* 6.64 (maximum Doppler spread of $B_{D,i} = 100$ Hz) for VA decoded (see *Section* 4.4) interleaved non-binary RS $(7, 5, 3)$ coded (see *Section* 3.2.2.3.3) narrowband complex QPSK communication systems (see *Section* 5.2). These figures contain simulation results obtained using flat fading channels configured for Rician factors (see *Section* 2.5.2.2) of $K_i = -100$ dB, $K_i = 0$ dB and $K_i = 9$ dB. Hard and soft decision (with and without perfect fading amplitude CSI (see *Section* 3.3.5 and *Section* 5.2.3)) branch metric calculation approaches were considered for the VA decoding following the de-interleaving process in the receiver. Furthermore, simulated BER performance curves for uncoded QPSK systems in AWGN conditions, as well as *Eq.* (5.24)'s theoretical BER performance curve for an uncoded QPSK system in slow Rayleigh flat fading channel conditions, are also included on *Fig.* 6.63 and *Fig.* 6.64.

6.5.5.2.2 Multipath Fading Channel Results

Simulated multi-user multipath fading channel BER performance results for length $M_{seq} = 63$ ABC (see *Section* D.3.2.2), DSB CE-LI-RU filtered GCL (see *Section* D.3.2.1), ZC (see *Section* D.3.1.1) and QPH (see *Section* D.3.1.2) CSS-based interleaved non-binary RS $(7, 5, 3)$ coded (see *Section* 3.2.2.3.3) wideband complex DS/SSMA QPSK systems (see *Section* 5.3), with VA decoding (see *Section* 4.4) using BCJR trellises, are shown in *Fig.* 6.65, *Fig.* 6.66, *Fig.* 6.67 and *Fig.* 6.68, respectively. Block-wise VA decoding approaches considered include hard and soft decision (with and without fading amplitude CSI (see *Section* 3.3.5 and *Section* 5.3.3)) decoding. Also present on these figures are the simulated uncoded RAKE receiver-based wideband complex DS/SSMA QPSK systems' multi-user multipath fading channel BER performance results, previously presented in *Section* 6.5.1.3.1.

6.5.5.2.3 Discussion of the Simulation Results

Continuing *Section* 6.5.5's investigation into the effects of interleaving on block coded narrowband complex QPSK and wideband complex DSSS/MA QPSK systems (with VA decoding) in flat fading

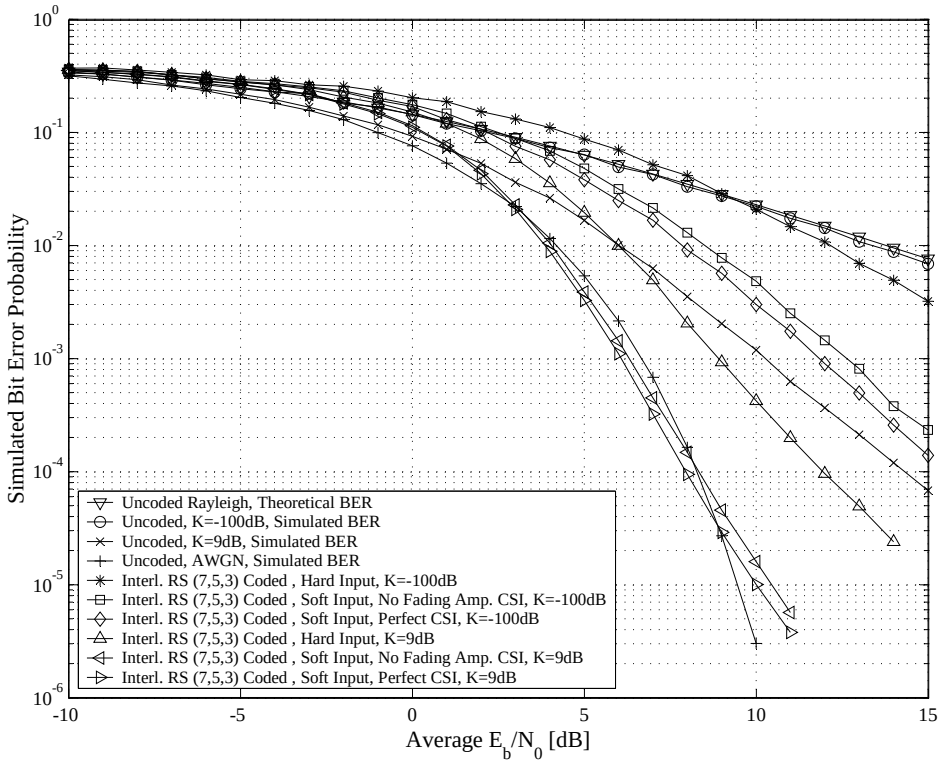

Figure 6.63: BER Performances of Interleaved Non-Binary RS $(7, 5, 3)$ Coded Narrowband Complex QPSK Communication Systems in Flat Fading Channel Conditions, $B_{D,i} = 33$ Hz

and multi-user multipath fading channel conditions, respectively, *Section* 6.5.5.2 brought interleaved non-binary RS $(7, 5, 3)$ codes under the spotlight. Important conclusions and observations from these results are listed below:

1. Conclusions and observations from the flat fading channel results:

   - Coinciding with the findings of *Section* 6.5.5.1, the incorporation of interleaving into non-binary RS $(7, 5, 3)$ coded complex QPSK systems, employing VA decoding, improved the overall BER performances in flat fading channel conditions. However, this improvement is less dramatic for the non-binary RS $(7, 5, 3)$ code than for the binary Hamming $(7, 4, 3)$ code. For example, a comparison between *Fig.* 6.46 and *Fig.* 6.63 indicates that interleaving delivers an additional gain of only 0.2 dB for soft decision decoding (without fading amplitude CSI) at $P_b(e) = 10^{-4}$ with $B_{D,i} = 100$ Hz and $K_i = 9$ dB. This modest gain can be attributed to the fact that RS codes have the inherent capacity to correct bursty errors. It is interesting to note, however, that the gains obtained for both $B_{D,i} = 33$ Hz and $B_{D,i} = 100$ Hz by including interleaving, increase as the Rician factor K_i decreases.
   - Contrasting the flat fading channel results presented in *Section* 6.5.3.2.2 with that given in *Section* 6.5.5.2.1 confirms the observations made in *Section* 6.5.5.1: In general, applying interleaving results in more impressive BER performances at lower maximum Doppler spreads. For the VA decoded non-binary RS $(7, 5, 3)$ code considered here, the resultant improvements obtained through interleaving yield more comparable BER performances between $B_{D,i} = 33$ Hz and $B_{D,i} = 100$ Hz than was the case for the interleaved binary Hamming $(7, 4, 3)$ codes. This can once again be attributed to the RS code's inherent ability to correct any small error bursts still present at the output of the random interleaver.

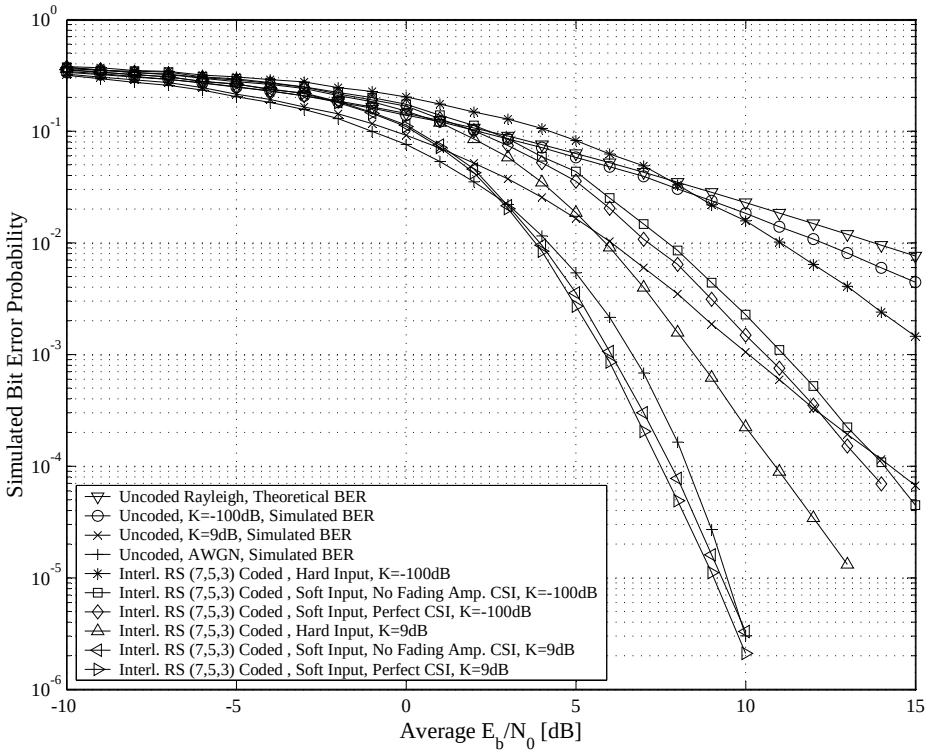

Figure 6.64: BER Performances of Interleaved Non-Binary RS $(7, 5, 3)$ Coded Narrowband Complex QPSK Communication Systems in Flat Fading Channel Conditions, $B_{D,i} = 100$ Hz

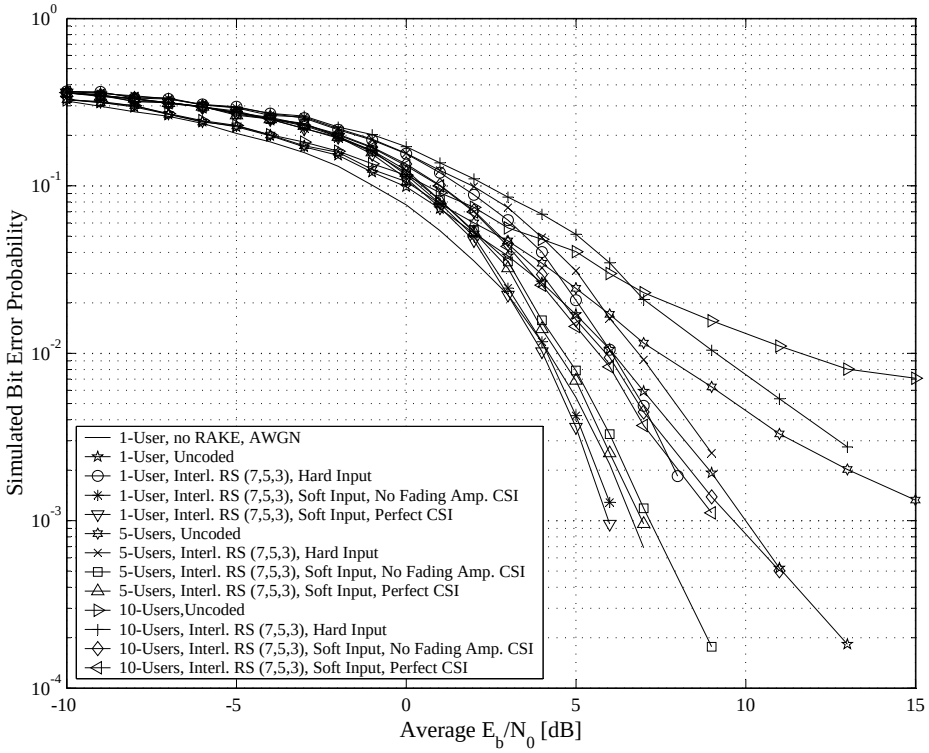

Figure 6.65: BER Performances of Interleaved Non-binary RS $(7, 5, 3)$ Coded Wideband Complex QPSK Communication Systems Employing ABC Sequences in Multi-User Multipath Fading Channel Conditions, $M_{seq} = 63$

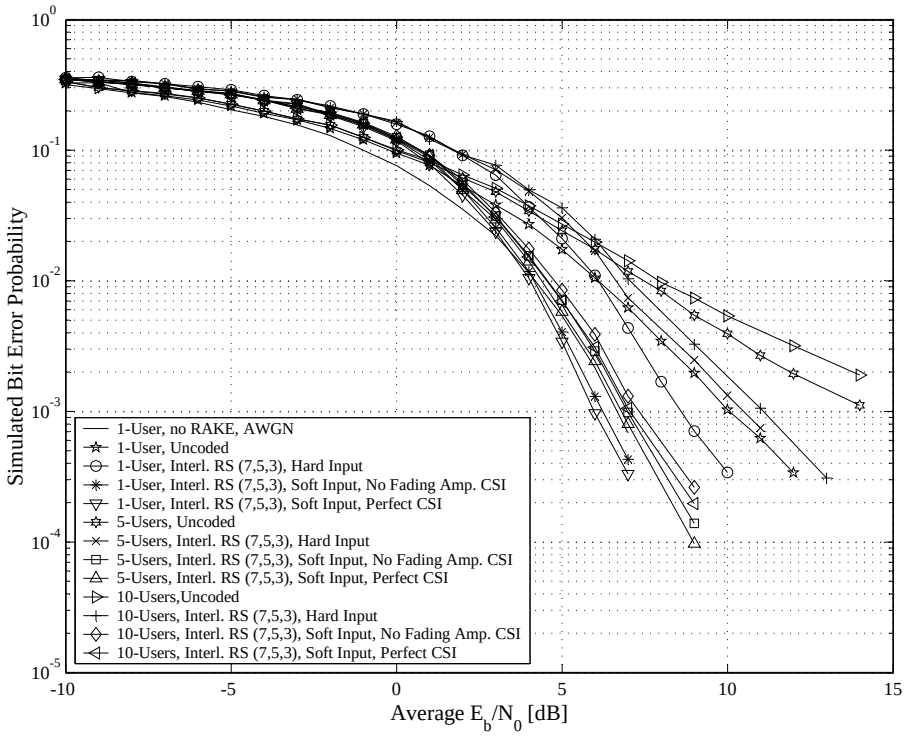

Figure 6.66: BER Performances of Interleaved Non-binary RS $(7, 5, 3)$ Coded Wideband Complex QPSK Communication Systems Employing DSB CE-LI-RU Filtered GCL CSSs in Multi-User Multipath Fading Channel Conditions, $M_{seq} = 63$

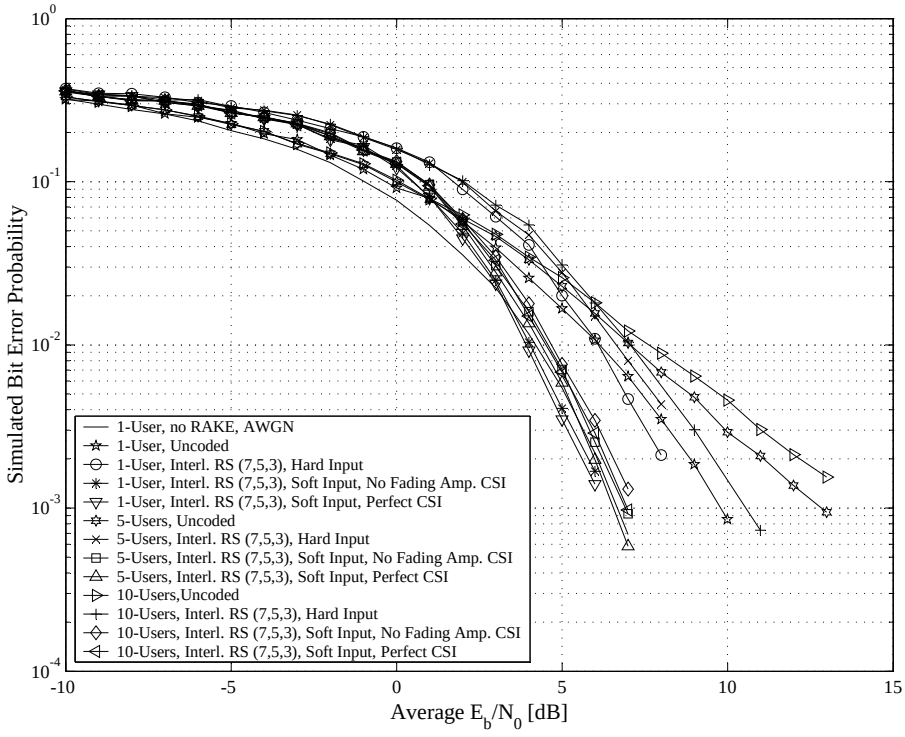

Figure 6.67: BER Performances of Interleaved Non-binary RS $(7, 5, 3)$ Coded Wideband Complex QPSK Communication Systems Employing ZC CSSs in Multi-User Multipath Fading Channel Conditions, $M_{seq} = 63$

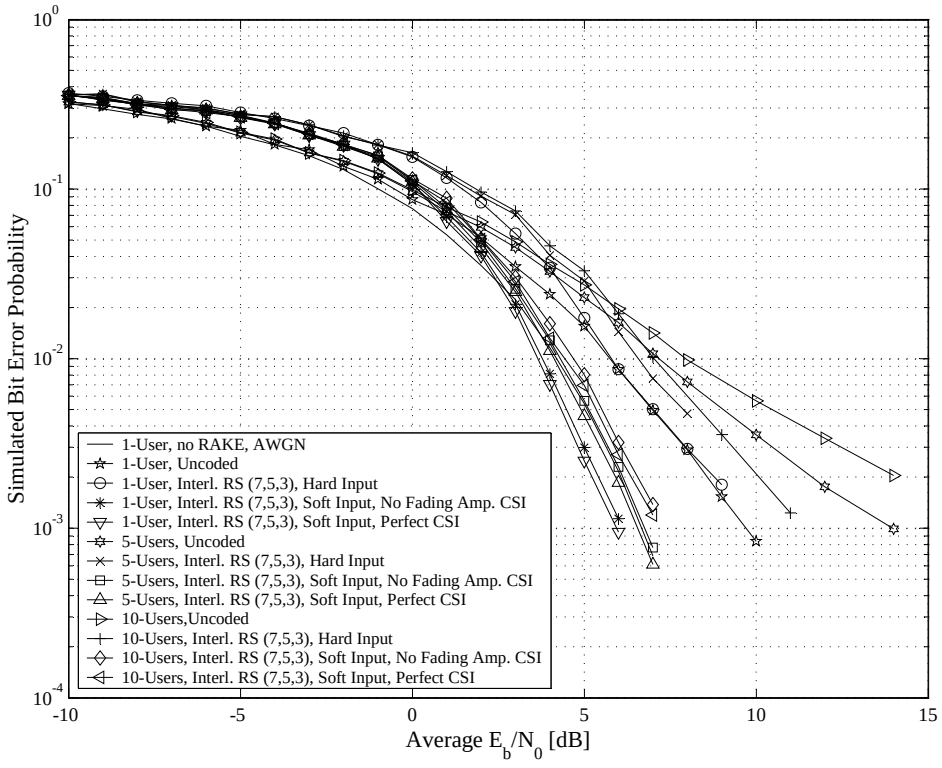

Figure 6.68: BER Performances of Interleaved Non-binary RS $(7, 5, 3)$ Coded Wideband Complex QPSK Communication Systems Employing QPH CSSs in Multi-User Multipath Fading Channel Conditions, $M_{seq} = 63$

- Comparing *Fig.* 6.63 and *Fig.* 6.64 with the results given in *Section* 6.5.3.2.2, it is apparent that, in terms of the BER performance improvement obtained by including perfect fading amplitude CSI into the soft decision VA metric calculations, interleaving proved to be beneficial only for low maximum Doppler spreads. By incorporating interleaving this gain increased from 0.2 dB to 0.4 dB for $B_{D,i} = 33$ Hz, whereas no change was observed for $B_{D,i} = 100$ Hz.

2. Conclusions and observations from the multi-user multipath fading channel results:

- Comparing the results given in *Section* 6.5.3.2.3 and *Section* 6.5.5.2.2, it is apparent that interleaving has little influence on the BER performance of VA decoded non-binary RS $(7, 5, 3)$ block codes in multi-user multipath fading channel conditions. Only the RS $(7, 5, 3)$ coded complex DS/SSMA QPSK systems employing the ABC and DSB CE-LI-RU filtered GCL CSSs showed notable improvements. For example, for $P_b(e) = 3/1000$, the 10-user ABC sequence-based system showed an improvement of 0.2 dB after interleaving. Thus, it can be concluded that the RS code was sufficiently capable of handling the bursty errors created by the multipath fading and MUI, without having to resort to interleaving.
- For all of the CSS families considered, soft decision VA decoding of the interleaved RS $(7, 5, 3)$ block code in a single user CDMA system delivered better performances than an uncoded non-RAKE DS/SSMA QPSK system in AWGN conditions with $\overline{E}_b/N_0 > 4$ dB.
- As was to be expected, ABC sequences exhibited the poorest BER performances, especially at high user loads. QPH and ZC CSSs delivered nearly identical BER performance results, with DSB CE-LI-RU filtered GCL CSSs trailing by no more than 1 dB for the 10-user worst case scenario.

- Coinciding with the observations made from the soft decision VA decoded interleaved binary Hamming $(7, 4, 3)$ block code's multi-user multipath fading BER performance results, it seems that interleaving has no significant influence on the performance improvements obtained by incorporating fading amplitude CSI into the metric calculations.

6.5.6 COMMUNICATION SYSTEMS EMPLOYING VITERBI DECODED PUNCTURED CONVOLUTIONAL AND LINEAR BLOCK CODES

Rate adaptation through code puncturing (see *Section* 3.2.4) has become a standard feature in the channel coding schemes employed by most commercial mobile communication systems (e.g. GSM, GPRS and EDGE). The advantages of using puncturing are twofold: Firstly, puncturing allows for flexible data rates using a single coding scheme, a crucial feature in any communication system that is intended to supply *bandwidth-on-demand*. Secondly, puncturing enables the telecommunications engineer to harness the error correction capabilities of powerful low rate codes, without having to concede considerable transmission bandwidth [102–104].

The following subsections investigate the influence of puncturing on the BER performances of VA decoded RSC codes (see *Section* 3.2.1.3.2) and binary BCH linear block codes (see *Section* 3.2.2.3.2). BER performance results were obtained for these punctured codes on narrowband complex QPSK communication systems (see *Section* 5.2), operating in AWGN and flat fading channel conditions. Multi-user multipath fading simulation results are also presented for the binary BCH $(15, 7, 5)$ code. The RAKE receiver-based complex DS/SSMA communication systems (see *Section* 5.3) employed during these simulations, were configured for length $M_{seq} = 63$ CSSs. The ABC sequences used were optimally selected, as described in *Section* 6.5.1.3.2. CSSs were arbitrarily selected for the other CSS families considered.

6.5.6.1 PUNCTURED BINARY 4-STATE, RATE $R_C = 1/2$ RSC CODED COMMUNICATION SYSTEMS

In the following subsections a punctured [102–104] binary 4-state, rate $R_c = 1/2$ RSC code's BER performances are investigated in AWGN and flat fading channel conditions (multipath fading channel conditions were omitted due to time constraints). From *Table* A.3 the original 4-state, rate $R_c = 1/2$ RSC code is defined by the following generator matrix (see *Section* 3.2.1.3.2):

$$G_{CC}(D) = \left[\begin{array}{cc} 1 & \frac{1+D^2}{1+D+D^2} \end{array} \right] \tag{6.6}$$

As indicated in *Table* A.3, this code has a minimum free distance of $d_{free} = 5$. Code words generated by the encoder structure, defined by *Eq.* (6.6), is punctured according to the following puncturing profile (see *Section* 3.2.4):

$$\Upsilon = \left[\begin{array}{cc} 1 & 1 \\ 1 & 0 \end{array} \right] \tag{6.7}$$

Using *Eq.* (3.46), it readily follows that the resultant punctured code has a rate of $R_p = 2/3$, making it comparable with the RSC code investigated in *Section* 6.5.2.2. Furthermore, note that the systematic information (see *Section* 3.2.1.2) remains intact after puncturing. Hence, this punctured code can still be classified as a binary IIR RSC code (see *Section* 3.2.1.3.2). Furthermore, a equiprobable symbol-generating information source was employed in the transmitter structures used during this subsection's simulations. As such, the receiver-end de-puncturers declare erasure values (see *Eq.* (3.60)) of $\Gamma_{m,i,a} = 0$ in the punctured bit positions, prior to sliding window VA decoding.

6.5.6.1.1 AWGN Channel Results

Fig. 6.69 shows the simulated AWGN channel BER performance results, obtained for narrowband complex QPSK communication systems, employing the punctured 4-state, rate $R_c = 1/2$ RSC code, described in *Section* 6.5.6.1. For comparative purposes the results presented in *Section* 6.5.2.2 for the 8-state, rate $R_c = 2/3$ RSC code are repeated in *Fig.* 6.69. VA decoding using hard and soft decision (without fading amplitude CSI) metric calculations were considered for both the unpunctured rate $R_c = 2/3$ and punctured rate $R_c = 1/2$ RSC codes. *Eq.* (5.20), which defines the theoretical BER performance curve of an uncoded narrowband QPSK system in AWGN channel conditions, is also included in *Fig.* 6.69.

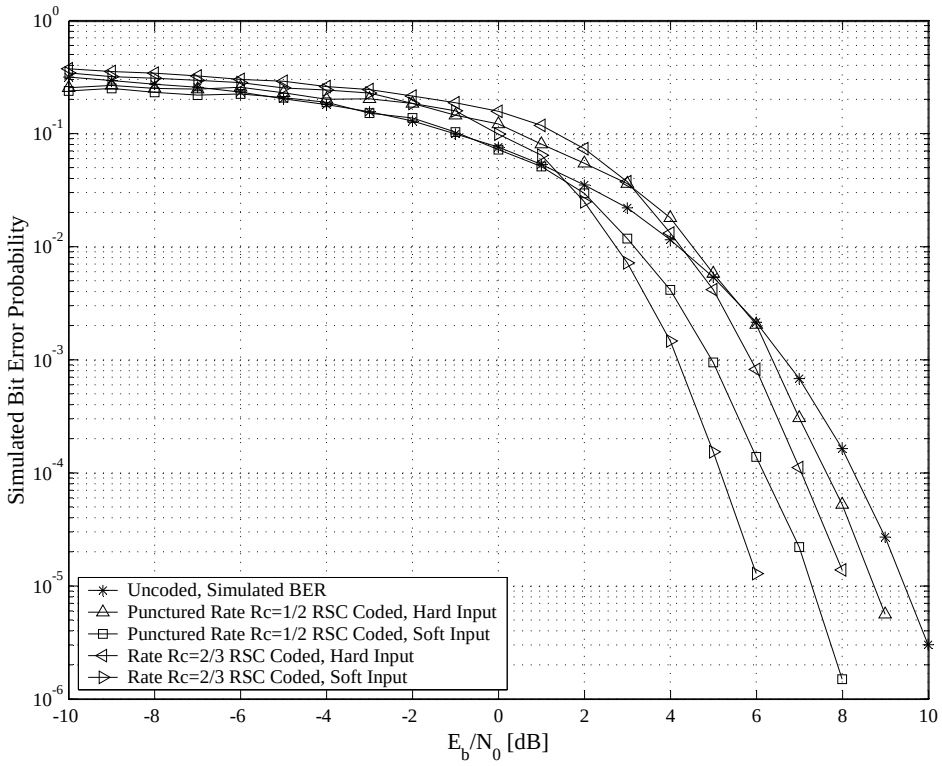

Figure 6.69: BER Performances of Punctured 4-State, Rate $R_c = 1/2$ RSC Coded Narrowband Complex QPSK Communication Systems in AWGN Channel Conditions

6.5.6.1.2 Flat Fading Channel Results

Fig. 6.70 and *Fig.* 6.71 show simulated BER performance results for punctured 4-state, rate $R_c = 1/2$ RSC (see *Section* 3.2.1.3.2) coded narrowband complex QPSK communication systems (see *Section* 5.2) in flat fading channel conditions (see *Section* 2.5.1.1) with maximum Doppler spreads of $B_{D,i} = 33$ Hz and $B_{D,i} = 100$ Hz, respectively. During these simulations the flat fading channel configurations considered included Rician factors (see *Section* 2.5.2.2) of $K_i = -100$ dB, $K_i = 0$ dB and $K_i = 9$ dB. After de-puncturing in the receiver, sliding window VA decoding of the 4-state, rate $R_c = 1/2$ RSC codes were performed. Both hard and soft decision decoding were considered, with either perfect or no fading amplitude CSI (see *Section* 3.3.5 and *Section* 5.2.3) used during soft decision decoding. Simulated BER performance curves for uncoded QPSK systems in AWGN, as well as theoretical BER performance curves for uncoded QPSK systems in slow Rayleigh flat fading channel conditions (defined by *Eq.* (5.24)) are present on *Fig.* 6.70 and *Fig.* 6.71.

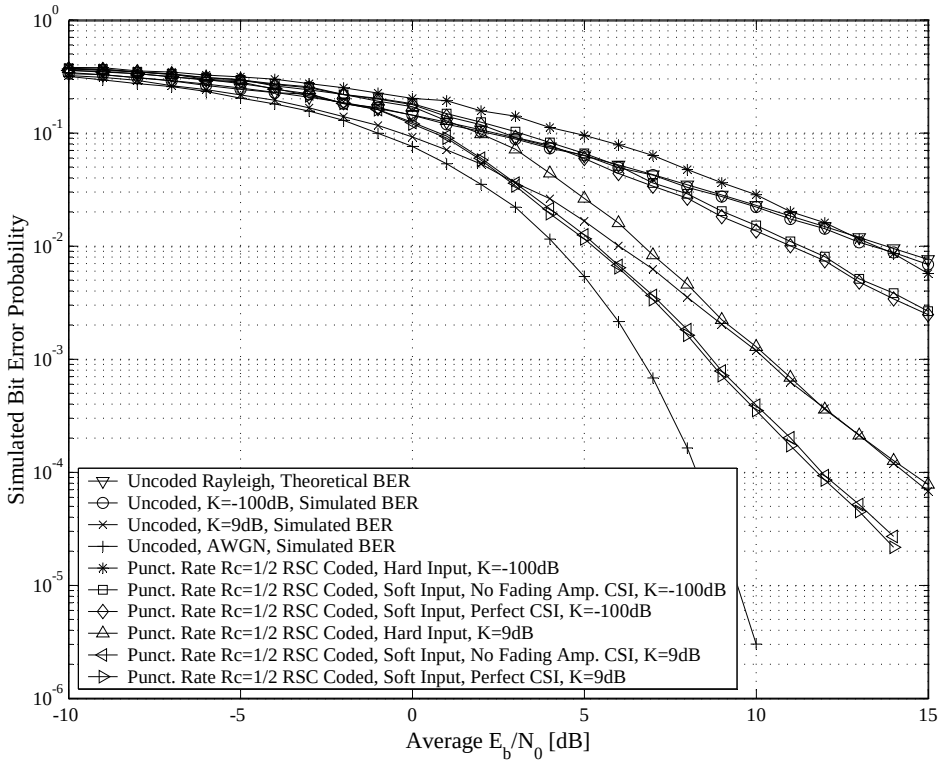

Figure 6.70: BER Performances of Punctured 4-State, Rate $R_c = 1/2$ RSC Coded Narrowband Complex QPSK Communication Systems in Flat Fading Channel Conditions, $B_{D,i} = 33$ Hz

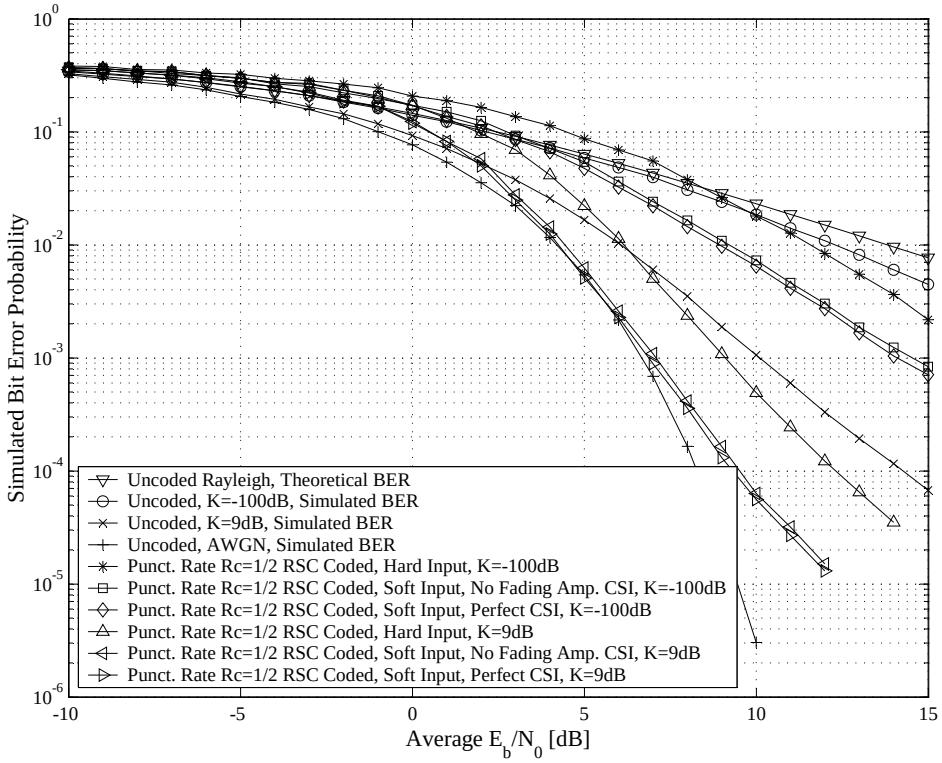

Figure 6.71: BER Performances of Punctured 4-State, Rate $R_c = 1/2$ RSC Coded Narrowband Complex QPSK Communication Systems in Flat Fading Channel Conditions, $B_{D,i} = 100$ Hz

6.5.6.1.3 Discussion of the Simulation Results

Punctured binary 4-state, rate $R_c = 1/2$ RSC coded narrowband complex QPSK systems were evaluated in *Section* 6.5.6.1.1 and *Section* 6.5.6.1.2. The narrowband systems were tested in AWGN and flat fading channel conditions. From the simulated BER performance results presented in the two preceding subsections, the following is evident:

1. Conclusions and observations from the AWGN channel results:

   - The simulated AWGN channel results of *Fig.* 6.69 show that the punctured 4-state, rate $R_c = 1/2$ RSC code does not perform as well as the unpunctured 8-state, rate $R_c = 2/3$ RSC code of *Section* 6.5.2.2, even though both codes have the same minimum free distance. This can be attributed to the fact puncturing decreased the effective minimum free distance of the rate $R_c = 1/2$ RSC code. Exact calculation of the punctured code's overall minimum free distance is a cumbersome process. However, reverse engineering *Eq.* (3.8), using a measured asymptotic coding gain of $GC_{CC}^{soft} = 2.2$ dB for soft decision VA decoding over an uncoded system, the effective minimum free distance for the punctured RSC code can be estimated as $d_{free} = 3$.
   - It is interesting to note from *Fig.* 6.69's AWGN channel results that, although the cross-over point (see *Section* 6.5.2.1.4) for hard decision VA decoding of the punctured rate $R_c = 1/2$ RSC code is higher than that of the unpunctured rate $R_c = 2/3$ RSC code, these two codes have similar cross-over points for soft decision VA decoding.
   - In AWGN channel conditions (see *Fig.* 6.69), soft decision VA decoding of the punctured rate $R_c = 1/2$ RSC code shows an improvement of 1.7 dB, which is less than the expected 2 dB.

2. Conclusions and observations from the flat fading channel results:

   - *Fig.* 6.70 and *Fig.* 6.71 not only show that the punctured rate $R_c = 1/2$ RSC code's performance in flat fading channel conditions improve as the Rician factor K_i increases, but also that the punctured RSC code is presented with more adverse temporal distortions to overcome when $B_{D,i} = 33$ Hz. In general, the BER performances of hard and soft decision VA decoded punctured rate $R_c = 1/2$ RSC codes deteriorate as the maximum Doppler spread decreases, regardless of the Rician factor K_i.
   - From the $B_{D,i} = 33$ Hz and $B_{D,i} = 100$ Hz flat fading channel results, shown in *Fig.* 6.70 and *Fig.* 6.71, respectively, it is clear that the use of perfect fading amplitude CSI during soft decision VA decoding resulted in minor BER performance improvements. For the $B_{D,i} = 100$ Hz the improvement was most noticeable, measuring approximately 0.25 dB for $K_i = 9$ dB. Furthermore, it is interesting to note that the asymptotic gain of soft decision decoding (without any fading amplitude CSI) over hard decision decoding is an impressive 2.5 dB for the $B_{D,i} = 100$ Hz scenario, but only 2 dB for $B_{D,i} = 33$ Hz.
   - The flat fading channel BER performance results, given in *Section* 6.5.2.2.2, for the unpunctured 8-state, rate $R_c = 2/3$ RSC code, are superior to the results obtained here for the punctured rate $R_c = 1/2$ RSC code. Although practical implementation of both codes result in identical bandwidth enlargements, the punctured RSC code has a smaller number of states in its trellis (see *Section* 3.3.1.1), resulting in an inferior minimum free Hamming property (see *Section* 3.2.1.2). This, in turn, produces weaker BER performances.

6.5.6.2 *PUNCTURED BINARY BCH* $(15, 7, 5)$ *CODED COMMUNICATION SYSTEMS*

The effects of puncturing on the BER performances of a VA decoded binary BCH $(15, 7, 5)$ code (see *Section* 3.2.2.3.2), operating in varying channel conditions, are considered in the following subsections. The code under investigation is defined by the following generator polynomial [47]:

$$g_{BC}(p) = p^8 + p^7 + p^6 + p^4 + 1 \tag{6.8}$$

which can be used to construct the following equivalent systematic generator matrix (see *Section* 3.2.2.2):

$$G_{BC} = \begin{bmatrix} 1 & 0 & 0 & 0 & 0 & 0 & 0 & 1 & 1 & 1 & 0 & 1 & 0 & 0 & 0 \\ 0 & 1 & 0 & 0 & 0 & 0 & 0 & 0 & 1 & 1 & 1 & 0 & 1 & 0 & 0 \\ 0 & 0 & 1 & 0 & 0 & 0 & 0 & 0 & 0 & 1 & 1 & 1 & 0 & 1 & 0 \\ 0 & 0 & 0 & 1 & 0 & 0 & 0 & 0 & 0 & 0 & 1 & 1 & 1 & 0 & 1 \\ 0 & 0 & 0 & 0 & 1 & 0 & 0 & 1 & 1 & 1 & 0 & 0 & 1 & 1 & 0 \\ 0 & 0 & 0 & 0 & 0 & 1 & 0 & 0 & 1 & 1 & 1 & 0 & 0 & 1 & 1 \\ 0 & 0 & 0 & 0 & 0 & 0 & 1 & 1 & 1 & 0 & 1 & 0 & 0 & 0 & 1 \end{bmatrix} \tag{6.9}$$

From [47] this BCH code has a minimum Hamming distance (see *Section* 3.2.2.2) of $d_{min} = 5$ bits. Furthermore, since it has a code rate of $R_c = 7/15$, incorporating it into a communication system will come at the expense of a 114.29% inflation in transmission bandwidth. This bandwidth expansion can be alleviated by incorporating the following puncturing profile (see *Section* 3.2.4) into the communication system's channel coding subsystem:

$$\Upsilon = \begin{bmatrix} 0 & 1 & 1 & 1 \\ 1 & 0 & 1 & 1 \\ 1 & 1 & 0 & 1 \\ 1 & 1 & 1 & 1 \\ 1 & 1 & 1 & 0 \\ 1 & 1 & 1 & 1 \\ 0 & 1 & 1 & 1 \\ 1 & 0 & 1 & 1 \\ 1 & 1 & 0 & 1 \\ 1 & 1 & 1 & 1 \\ 1 & 1 & 1 & 0 \\ 1 & 1 & 1 & 1 \\ 0 & 1 & 1 & 1 \\ 1 & 0 & 1 & 1 \\ 1 & 1 & 0 & 1 \end{bmatrix} \tag{6.10}$$

From *Eq.* (3.46) it follows that, when using this puncturing profile in conjunction with the binary BCH $(15, 7, 5)$ block code, a punctured code rate of $R_p = 4/7$ is obtained. Thus, the resultant punctured binary BCH code is comparable with the binary Hamming $(7, 4, 3)$ code, examined in *Section* 6.5.3.1 and *Section* 6.5.5.1. Although this puncturing profile was arbitrarily chosen to deliver an overall code rate of $R_c = 4/7$, the author did attempt to uniformly distribute the deletion of code bits from consecutive BCH code words. However, at no point can it be claimed that the puncturing profile of *Eq.* (6.10) is in any sense optimal.

The following subsections present AWGN and flat fading channel BER performance results, obtained using narrowband complex QPSK communication systems (see *Section* 5.2) employing the punctured binary BCH $(15, 7, 5)$ block code. Also given here are multi-user multipath fading channel BER performance results for punctured binary BCH $(15, 7, 5)$ block codes, running on wideband

complex DS/SSMA QPSK communication systems (see *Section* 5.3). Hard decision VA decoding, as well soft decision VA decoding, with varying degrees of fading amplitude CSI (see *Section* 3.3.5), are considered. The punctured binary BCH $(15, 7, 5)$ code BER performance results are compared with that obtained for the binary Hamming $(7, 4, 3)$ code.

6.5.6.2.1 AWGN Channel Results

Simulated AWGN channel BER performance results are depicted in *Fig.* 6.72 for narrowband complex QPSK communication systems, employing the punctured binary BCH $(15, 7, 5)$ block code detailed in *Section* 6.5.6.2. As is clear from this figure, hard and soft decision (without fading amplitude CSI) VA decoding results were obtained. Since the punctured binary BCH $(15, 7, 5)$ code is comparable with the binary Hamming $(7, 4, 3)$ block code of *Section* 6.5.3.1, the hard and soft decision VA decoding AWGN channel results provided in *Fig.* 6.36 are included in *Fig.* 6.72. Also depicted on this figure is the BER performance curve of an uncoded narrowband QPSK system in AWGN, theoretically defined by *Eq.* (5.20).

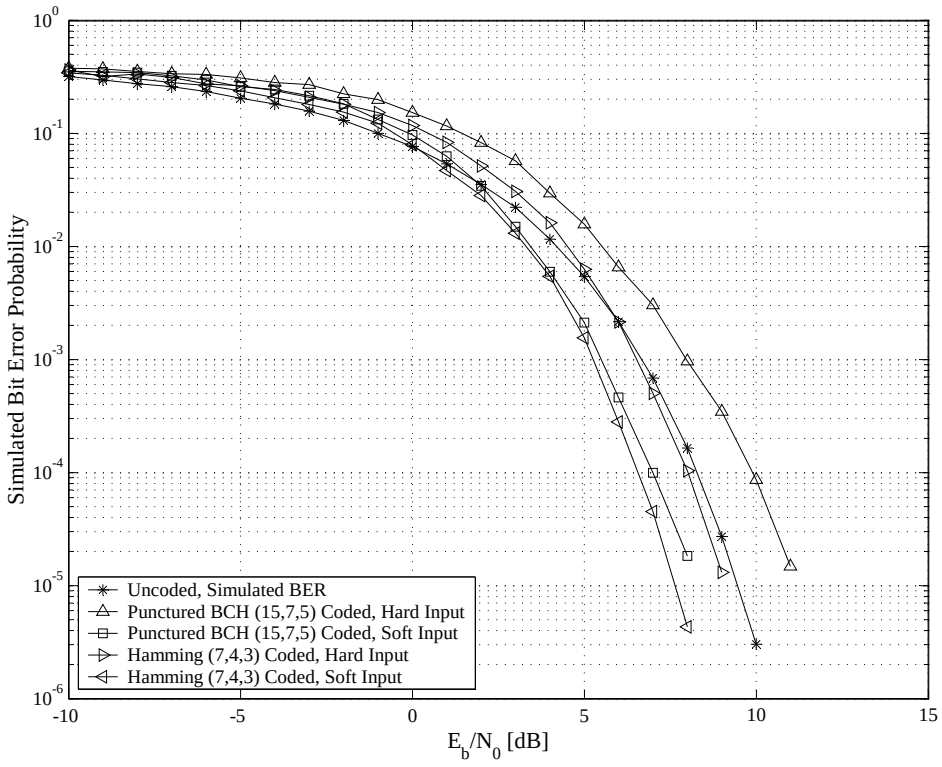

Figure 6.72: BER Performances of Punctured Binary BCH $(15, 7, 5)$ Coded Narrowband Complex QPSK Communication Systems in AWGN Channel Conditions

6.5.6.2.2 Flat Fading Channel Results

Flat fading channel (see *Section* 2.5.1.1) simulated BER performance results are depicted in *Fig.* 6.63 (maximum Doppler spread of $B_{D,i} = 33$ Hz) and *Fig.* 6.64 (maximum Doppler spread of $B_{D,i} = 100$ Hz) for VA decoded (see *Section* 4.4) punctured binary BCH $(15, 7, 5)$ coded (see *Section* 3.2.2.3.2) narrowband complex QPSK communication systems (see *Section* 5.2). Simulation results are included for flat fading channels configured with Rician factors (see *Section* 2.5.2.2) of $K_i = -100$ dB, $K_i = 0$ dB and $K_i = 9$ dB. After de-puncturing in the narrowband complex QPSK

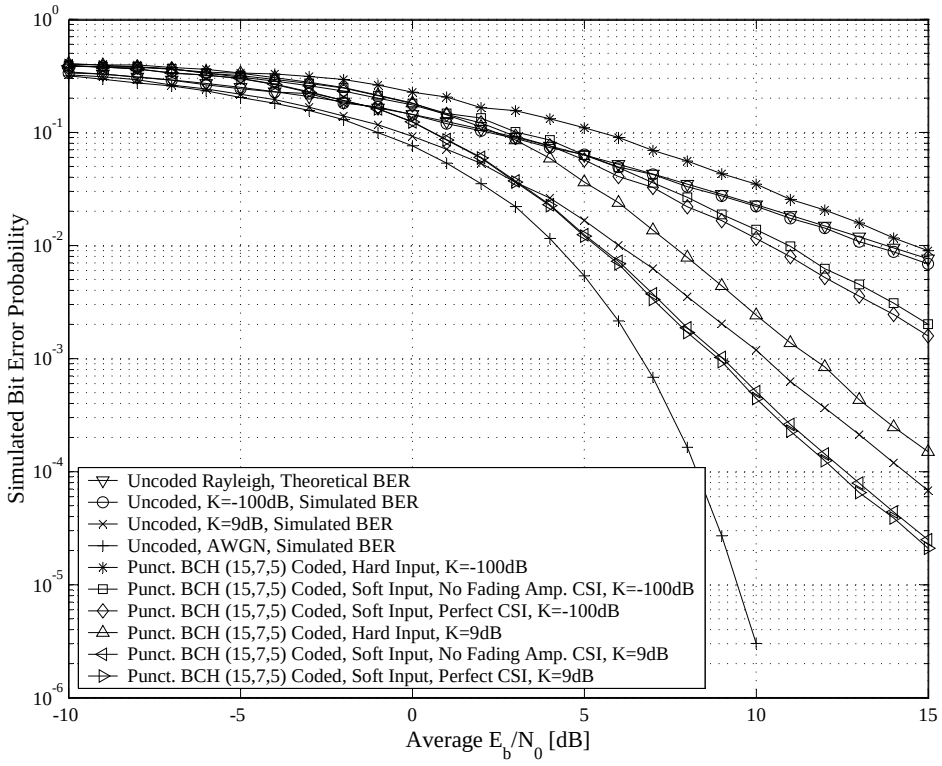

Figure 6.73: BER Performances of Punctured Binary BCH $(15, 7, 5)$ Coded Narrowband Complex QPSK Communication Systems in Flat Fading Channel Conditions, $B_{D,i} = 33$ Hz

receiver, VA decoding using either hard or soft decisions (with and without perfect fading amplitude CSI (see *Section* 3.3.5 and *Section* 5.2.3)) were performed. For comparative purposes, simulated BER performance curves for uncoded QPSK systems in AWGN, as well as the theoretical BER performance curve for uncoded QPSK systems in slow Rayleigh flat fading channel conditions (given in *Eq.* (5.24)), are also included on *Fig.* 6.73 and *Fig.* 6.74.

6.5.6.2.3 Multipath Fading Channel Results

Fig. 6.75, *Fig.* 6.76, *Fig.* 6.77 and *Fig.* 6.78 respectively show simulated multi-user multipath fading channel BER performance results for length-63 ABC (see *Section* D.3.2.2), DSB CE-LI-RU filtered GCL (see *Section* D.3.2.1), ZC (see *Section* D.3.1.1) and QPH (see *Section* D.3.1.2) CSS-based punctured binary BCH $(15, 7, 5)$ coded (see *Section* 3.2.2.3.2) wideband complex DS/SSMA QPSK systems (see *Section* 5.3). Following the de-puncturing process (see *Section* 3.3.4) at the RAKE receiver, block-wise VA decoding, using the binary BCH $(15, 7, 5)$ code's BCJR trellis, which consists of 16 layers with 64 nodes each, was employed. Simulation results are given for hard and soft decision (with and without fading amplitude CSI (see *Section* 3.3.5 and *Section* 5.3.3)) VA decoding approaches. The multi-user multipath fading and AWGN channel BER performance results for uncoded RAKE receiver-based and non-RAKE receiver-based wideband complex DS/SSMA QPSK systems, respectively, are also included on these four figures.

6.5.6.2.4 Discussion of the Simulation Results

The focus of the preceding three subsections were the effects of using puncturing in conjunction with VA decoded binary BCH $(15, 7, 5)$ codes. Simulated BER performance results were presented for

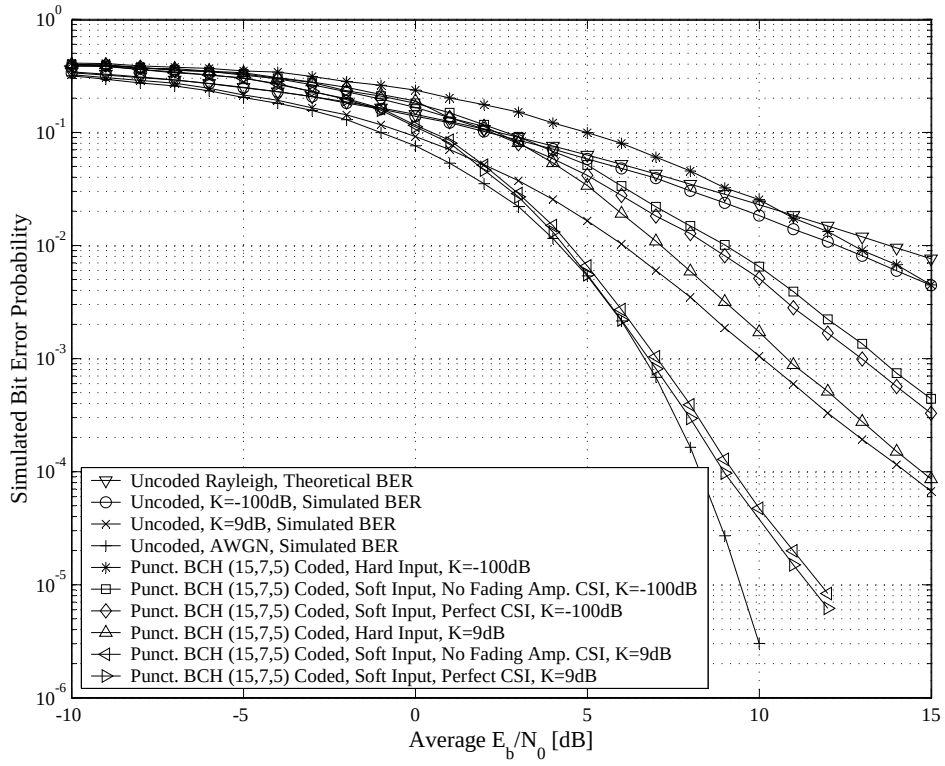

Figure 6.74: BER Performances of Punctured Binary BCH $(15, 7, 5)$ Coded Narrowband Complex QPSK Communication Systems in Flat Fading Channel Conditions, $B_{D,i} = 100$ Hz

punctured binary BCH $(15, 7, 5)$ coded narrowband complex QPSK communication systems (operating in AWGN and flat fading channel conditions) and multi-user wideband complex DSSS/MA QPSK systems (operating in multipath fading channel conditions). The following observations were made from these results:

1. Conclusions and observations from the AWGN channel results:

   - Investigation of the AWGN channel BER performance results for the VA decoded punctured binary BCH $(15, 7, 5)$ codes, implemented on narrowband complex QPSK systems (see *Fig.* 6.72), indicates that the puncturing process not only decreased the strain on the transmission bandwidth, but also decreased the binary BCH $(15, 7, 5)$ code's error correcting capabilities. For soft decision VA decoding of the punctured binary BCH $(15, 7, 5)$ code a mundane asymptotic coding gain of 1.8 dB is achieved, whereas hard decision decoding shows a coding loss of 1.9 dB. Thus, reverse engineering *Eq.* (3.25) shows that puncturing (using the profile given by *Eq.* (6.10)) has effectively decreased the BCH code's minimum Hamming distance (see *Section* 3.2.2.2) from $d_{min} = 5$ to approximately $d_{min} = 3$.
   - Comparing the AWGN channel BER performance results for VA decoded binary Hamming $(7, 4, 3)$ and punctured binary BCH $(15, 7, 5)$ codes on narrowband complex QPSK systems (shown in *Fig.* 6.36 and *Fig.* 6.72, respectively), establishes that the soft decision decoding (with or without fading amplitude CSI) of both codes deliver comparable results. However, hard decision VA decoding of the binary BCH $(15, 7, 5)$ code failed to perform at the same level as hard decision VA decoded binary Hamming $(7, 4, 3)$ codes. Specifically, for high average E_b/N_0 values, hard decision VA decoded BCH $(15, 7, 5)$ codes showed an asymptotic performance loss of 2 dB when compared to the hard decision VA decoded binary Hamming $(7, 4, 3)$ code.

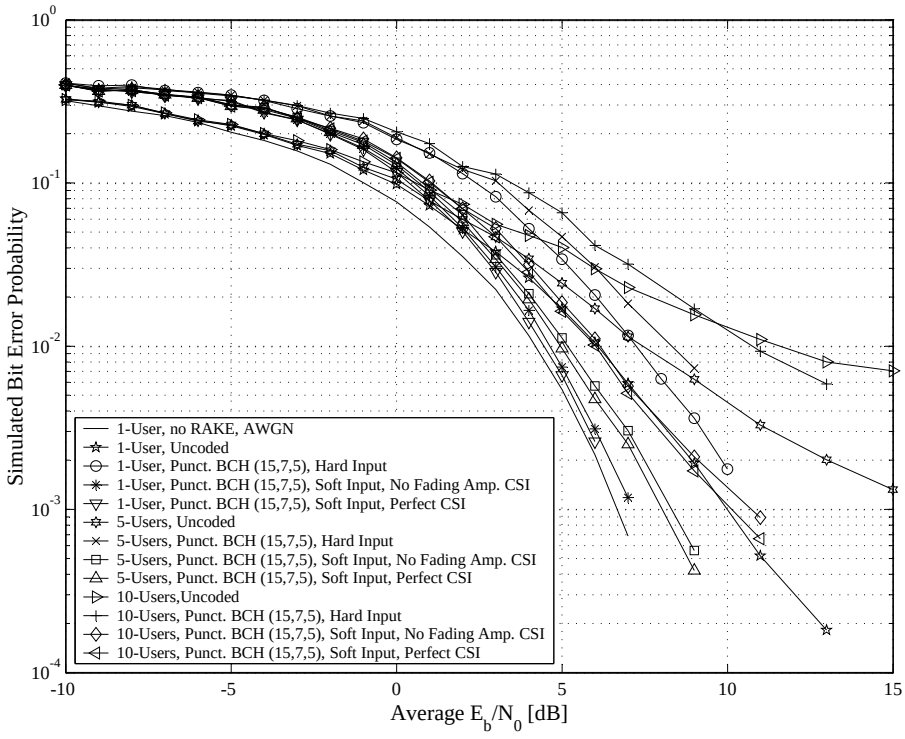

Figure 6.75: BER Performances of Punctured Binary BCH $(15, 7, 5)$ Coded Wideband Complex QPSK Communication Systems Employing ABC Sequences in Multi-User Multipath Fading Channel Conditions, $M_{seq} = 63$

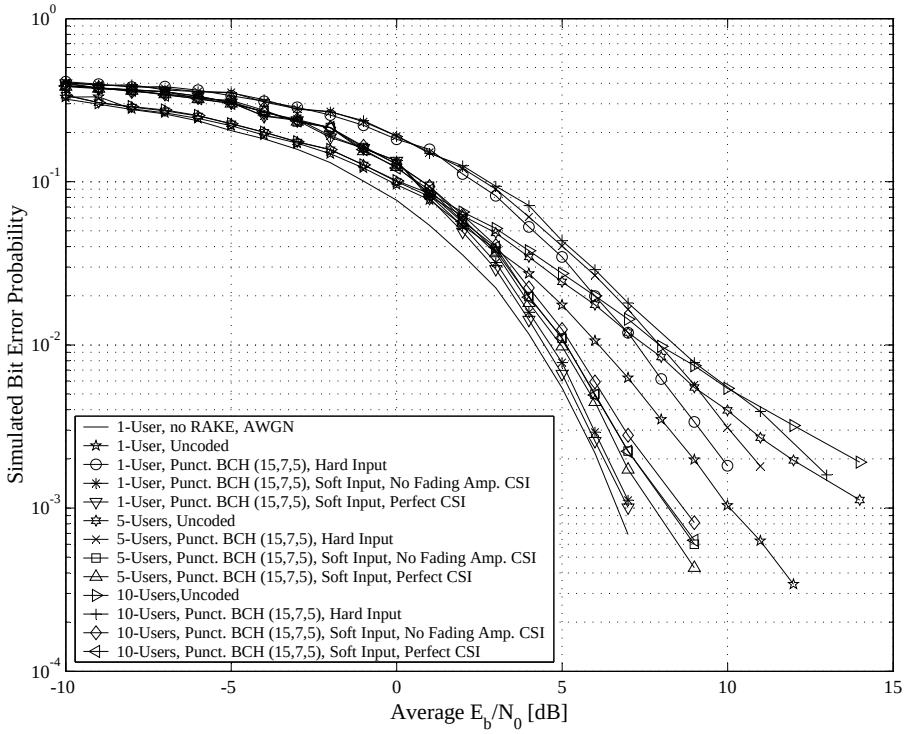

Figure 6.76: BER Performances of Punctured Binary BCH $(15, 7, 5)$ Coded Wideband Complex QPSK Communication Systems Employing DSB CE-LI-RU Filtered GCL CSSs in Multi-User Multipath Fading Channel Conditions, $M_{seq} = 63$

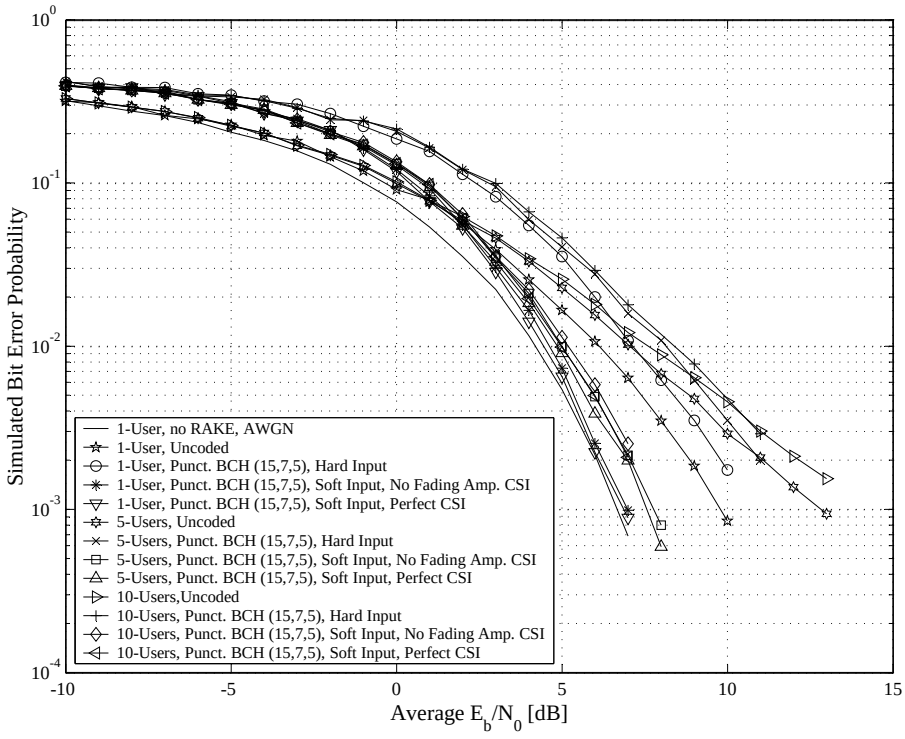

Figure 6.77: BER Performances of Punctured Binary BCH $(15, 7, 5)$ Coded Wideband Complex QPSK Communication Systems Employing ZC CSSs in Multi-User Multipath Fading Channel Conditions, $M_{seq} = 63$

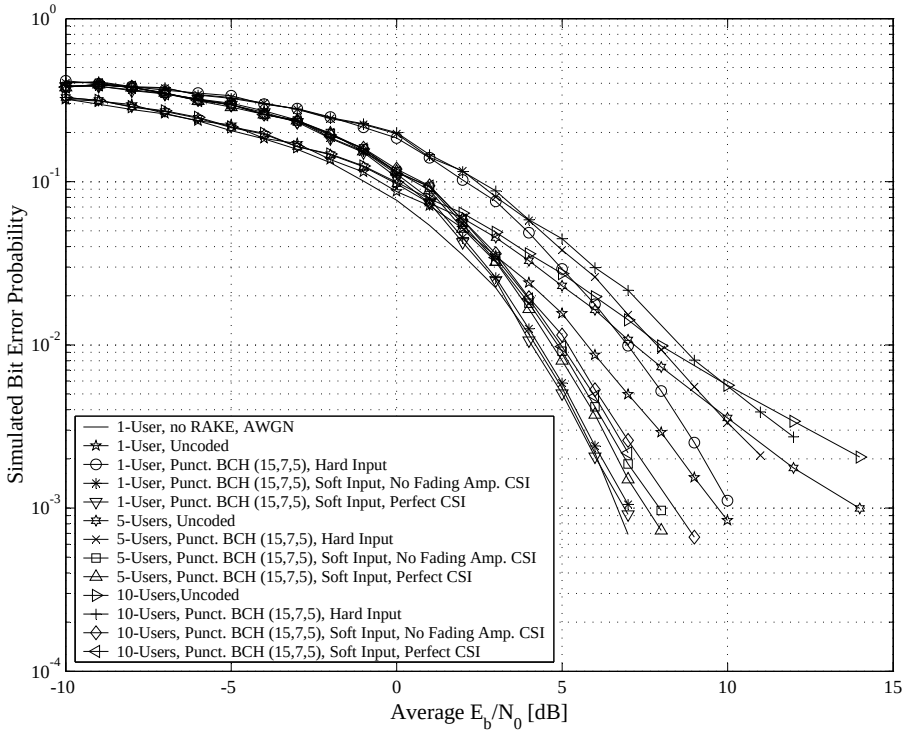

Figure 6.78: BER Performances of Punctured Binary BCH $(15, 7, 5)$ Coded Wideband Complex QPSK Communication Systems Employing QPH CSSs in Multi-User Multipath Fading Channel Conditions, $M_{seq} = 63$

- *Fig.* 6.72 demonstrates that soft decision VA decoding of the punctured binary BCH $(15, 7, 5)$ code outperforms hard decision decoding with approximately 3 dB. This result far exceeds the characteristic 2 dB gain for hard over soft decision ML decoding, characteristic with non-punctured linear block codes [47].

2. Conclusions and observations from the flat fading channel results:

   - The punctured binary BCH $(15, 7, 5)$ code exhibits an increase in flat fading channel BER performance as the Rician factor K_i increases (refer to *Fig.* 6.73 and *Fig.* 6.74). This is true for both $B_{D,i} = 33$ Hz and $B_{D,i} = 100$ Hz. On average, the punctured code performs best at the maximum Doppler spread, i.e. $B_{D,i} = 100$ Hz. Since the flat fading channel creates shorter error bursts at higher maximum Doppler spreads, the VA decoding of the punctured binary BCH $(15, 7, 5)$ code (which is not intended for burst error correction) produces better BER performance results, irrespective of the channel's Rician factor K_i.
   - Referring to *Fig.* 6.73 and *Fig.* 6.74 it is clear that the use of perfect fading amplitude CSI during the soft decision VA decoding of the punctured BCH $(15, 7, 5)$ codes resulted in relatively small gains over soft decision decoding (without any fading amplitude CSI). For both $B_{D,i} = 33$ Hz and $B_{D,i} = 100$ Hz this gain was approximately 0.15 dB when $K_i = 9$ dB. Moreover, hard decision VA decoding asymptotically lags soft decision decoding (without any fading amplitude CSI) by 1.75 dB for $B_{D,i} = 33$ Hz, and 2.25 dB for $B_{D,i} = 100$ Hz.
   - Recall from *Section* 6.5.6.2 that the puncturing profile defined by *Eq.* (6.10) was designed with the singular intention to reduce the binary BCH $(15, 7, 5)$ code's rate to that of the binary Hamming $(7, 4, 3)$ code, but still preserve its superior error correction capabilities. As was observed from the AWGN channel results, puncturing unfortunately reduced the code's effectively minimum Hamming distance, resulting in poorer BER performances. Corresponding to the observations made for AWGN channel conditions, a comparison of the simulated results presented in *Section* 6.5.3.1.2 and *Section* 6.5.6.2.2 shows that, in flat fading channel conditions, soft decision VA decoding of the two codes performed similarly. With hard decision VA decoding, however, the binary BCH $(15, 7, 5)$ codes proved to be inferior to the binary Hamming $(7, 4, 3)$ codes.

3. Conclusions and observations from the multi-user multipath fading channel results:

   - Matching *Section* 6.5.6.2.3's multi-user multipath fading BER results with that presented in *Section* 6.5.3.1.3 for VA decoded binary Hamming $(7, 4, 3)$ codes, it is clear that soft decision decoding of the binary Hamming $(7, 4, 3)$ code and the punctured binary BCH $(15, 7, 5)$ code deliver nearly the same performances, irrespective of the quality of the fading amplitude CSI employed in the metric calculations. Unfortunately, the BER performances obtained using hard decision VA decoding of the punctured binary BCH $(15, 7, 5)$ code follows the pattern observed for the AWGN and flat fading channels. At a BER of $P_b(e) = 2/1000$, for example, hard decision decoding of the punctured binary BCH $(15, 7, 5)$ code exhibits a loss of 1.5 dB in a single user CDMA system, employing DSB CE-LI-RU filtered GCL CSSs. This poor BER performance trend, observed for the hard decision VA decoding of the punctured binary BCH $(15, 7, 5)$ code, increases in severity as the user load increases, regardless of the CSS family employed.
   - On the whole, VA decoded punctured binary BCH $(15, 7, 5)$ codes, implemented on RAKE receiver-based DS/SSMA QPSK systems using ABC sequences, delivered the poorest BER performances at high user loads. QPH CSSs produced the best results, with ZC CSSs a close second. Furthermore, for the single user scenario at high $\overline{E}_b/N_0$ values, only the unfiltered

CSS families were capable of performing better or equivalent to the single user uncoded non-RAKE receiver-based DS/SSMA QPSK system, operating purely in AWGN. However, the unfiltered CSS families did come close to this AWGN curve, lagging by no more than 0.2 dB behind the unfiltered CSS families.

- Contrasting the hard and soft decision VA decoding results of *Fig.* 6.75, *Fig.* 6.76, *Fig.* 6.77 and *Fig.* 6.78, soft decision decoding (without fading amplitude CSI) gains, ranging between approximately 2.4 dB and 2.8 dB, can be observed for user loads ranging from low to high, irrespective of the CSS family. Furthermore, the inclusion of perfect fading amplitude CSI during soft decision VA decoding produces an average gain of 0.2 dB for all user loads and CSS families.

6.6 CONCLUDING REMARKS

Chapter 6 presented a culmination of simulation results that investigated, evaluated and verified the theories, algorithms, communication system building blocks, simulation platforms and VA decoded coding schemes covered in the previous chapters. Firstly, it examined the operation of the novel complex flat fading and multipath fading channel simulators, presented in *Section* 2.6.2.3 and *Section* 2.6.3.2, respectively. Next, attention shifted to the verification of the narrowband complex QPSK (see *Section* 5.2) and wideband complex DSSS/MA QPSK communication systems (see *Section* 5.3). Lastly, numerous simulated AWGN, flat fading and multi-user multipath fading channel BER performance results, obtained using *Section* 5.4's comprehensive simulation platforms, were presented and assessed for uncoded, as well as VA decoded convolutional and linear block coded narrowband and wideband communication systems. This chapter not only documents several interesting and important findings from the simulation results presented here, but it also makes a number of unique contributions. Important results presented and novel contributions made by this chapter, are listed below:

1. Measured phase and fading amplitude PDFs, as well as measured Doppler spectra, are presented in *Section* 6.2.1 for the novel complex fading channel simulator, featured in *Section* 2.6.2.3. These simulation results not only certifies the accuracy of the proposed complex flat fading channel simulator's operation, but also serves as proof of its flexibility in terms of supported fading distributions and fading rates.

2. The functioning and configurability of the unique complex multipath fading channel simulator, proposed in *Section* 2.6.3.2, are authenticated in *Section* 6.2.2 via simulated power delay profile and Doppler spread PSD measurements.

3. Simulated time signals, PSDs and eye diagrams are given in *Section* 6.3 for the unique complex QPSK transmitter and receiver models, presented in *Section* 5.2. The PSD and eye diagram results were obtained in perfect, noiseless channel conditions, whereas the simulated time signals were measured in noiseless, flat fading channel conditions. These results not only prove the optimal operation of the proposed complex QPSK system, but also validates the average fading amplitude calculation method, detailed in *Section* 5.2.3.

4. The functioning of the proposed RAKE receiver-based wideband complex DS/SSMA QPSK system, described in *Section* 5.3, is scrutinised in *Section* 6.4. Simulated PSDs for the ABC, DSB CE-LI-RU filtered GCL, ZC and QPH CSS families considered in this study (see *Appendix D*), were obtained in perfect noiseless channel conditions. These PSDs illustrate the perfect single sideband and Nyquist bandwidth-like spectral characteristics of the ABC and DSB CE-LI-RU filtered GCL CSSs, respectively. Eye diagram results (also obtained in perfect noiseless channel

conditions) for the complex DS/SSMA QPSK system, employing QPH CSSs, verify the acceptable operation of the square-root Nyquist chip-level pulse shaping filters, used at the wideband transmitter and RAKE receiver for the unfiltered CSS families. Time signal measurements, procured in noiseless multipath fading channel conditions, certify the usefulness of the average fading amplitude calculation method, proposed in *Section* 5.3.3.

5. *Chapter* 6 presented numerous simulated AWGN, flat fading and multi-user multipath fading channel BER performance results for binary NSC (see *Section* 3.2.1.3.1) and RSC (see *Section* 3.2.1.3.2) codes. These results acted mostly as baseline references for the VA decoded binary and non-binary linear block codes considered in this study. However, a number of unique contributions were made to the discipline of convolutional coding, including an investigation into the effects of perfect fading amplitude CSI on the soft decision VA decoding of convolutional codes, as well as the influence of puncturing on binary RSC codes' BER performances. The most significant contribution, however, is the BER performance results obtained for VA decoded binary convolutional codes, implemented on RAKE receiver-based wideband complex DS/SSMA systems. These results substantiate convolutional codes' effectiveness in combatting the effects of MUI and multipath fading.

6. Simulated AWGN and flat fading channel BER performance results, acquired for narrowband complex QPSK systems employing VA decoded binary Hamming $(7, 4, 3)$ and non-binary RS $(7, 5, 3)$ linear block codes (see *Section* 6.5.3.1 and *Section* 6.5.3.2, respectively), are some of the major contributions of this chapter. Even more pivotal are the simulated BER performance results obtained for these VA decoded linear block codes, running on RAKE receiver-based wideband complex DS/SSMA QPSK systems (employing the unfiltered and filtered CSS families presented in *Appendix D*) in multi-user multipath fading channel conditions. From the results obtained for the various mobile communication channel environments considered, it is evident that the application of the VA to the BCJR trellis structures of linear block codes deliver optimal ML decoding BER performances.

7. Novel simulated AWGN and flat fading channel BER performance results are presented in *Section* 6.5.4 for binary cyclic $(5, 3, 2)$ linear block codes, VA decoded using original and reduced complexity trellis structures. These results show that BCJR trellis complexity has no influence on the BER performance results obtained in AWGN conditions. However, for flat fading channel conditions, usage of the reduced complexity BCJR trellis delivered slightly weaker BER performances.

8. *Section* 6.5.5's investigation into the BER performance improvements obtained by interleaving the VA decoded binary Hamming $(7, 4, 3)$ and non-binary RS $(7, 5, 3)$ linear block codes in flat fading and multi-user multipath fading channel conditions, produced unique and valuable simulation results. From these results it can be surmised that interleaving improves the BER performances of both the binary Hamming $(7, 4, 3)$ and non-binary RS $(7, 5, 3)$ linear block codes. However, the improvements observed for the non-binary RS $(7, 5, 3)$ linear block codes were less impressive, due their inherent ability to mitigate the bursty errors typically created by fading effects in mobile communication channels.

9. *Section* 6.5.6.2 focused on the VA decoding of punctured binary BCH $(15, 7, 5)$ linear block codes in AWGN, flat fading and multi-user multipath fading channel conditions. Soft decision VA decoding of this punctured code delivered novel BER performance results comparable to the binary Hamming $(7, 4, 3)$ code (which also has a code rate of $R_c = 4/7$), irrespective of the quality of the fading amplitude CSI used during the metric calculations. Hard decision VA decoding of the punctured binary BCH $(15, 7, 5)$ code, however, did not only performed inferior to soft decision decoding, but also to hard decision VA decoding of the binary Hamming $(7, 4, 3)$ code.

10. This chapter's simulated BER performance results for binary convolutional codes, as well as binary and non-binary linear block codes, tested on narrowband and wideband communication systems in flat fading and multi-user multipath fading channel conditions, respectively, are instrumental in the determination of the influence of fading amplitude CSI during VA decoding. Of particular interest in this study, were the underlying effects of code complexity, fading rates, Rician factors, interleaving, puncturing, CDMA user loads and CSS families on the performance gains achieved through soft decision VA decoding with fading amplitude CSI.

11. Although this chapter's major contribution is undoubtable the simulated BER performances of VA decoded binary and non-binary linear block codes, operating in a wide variety of mobile channel conditions, the respective investigations of *Section* 6.5.1.3.2 and *Section* 6.5.1.3.3 into the influence of CSS selection and length on the multi-user multipath fading channel BER performances of uncoded complex DS/SSMA QPSK systems, are also pivotal. Not only was the concept of SSLD introduced (mathematically defined in *Section* D.2.6), but also a simple GCL CSS selection scheme, proposed by *Staphorst* and*Linde* in [162]. From the simulation results it is apparent that, when used in RAKE receiver-based DS/SSMA systems, ABC sequences deliver mediocre BER performances. However, for a fixed BEF (see *Section* D.2.5), ABC sequences support much higher user loads than the other CSS families considered in this study. Furthermore, it was shown that care must be taken in the selection of sequences from a ABC sequence family, since the assignment of CSSs to CDMA users has a definite impact of the overall BER performance of the system due to MUI.

CHAPTER SEVEN

CONCLUSIONS AND FUTURE RESEARCH

7.1 CHAPTER OVERVIEW

THE most significant conclusions forthcoming from the body of work presented in this study are detailed in the first section of this final chapter. This is then followed by a number of possible related research areas, identified during the run of the study.

7.2 CONCLUSIONS

This study thoroughly examined the viability of the VA as an efficient ML trellis decoder for linear block codes in future wireless communication systems. Several VA decoded binary and non-binary linear block codes were extensively evaluated on narrowband QPSK and wideband DS/SSMA QPSK communication systems, operating in realistic mobile communication channel conditions, ranging from pure AWGN to multi-user multipath fading. Not only was the influence of different mobile channel effects on the BER performances of VA decoded binary and non-binary linear block codes considered, but also that of interleaving, puncturing, MUI and improved VA metric calculations that make use of fading amplitude CSI. From the body of work presented in this study, a large number of conclusions can be drawn. The most significant findings are listed below:

1. Conclusions pertaining to the operation and statistical behaviour of the novel complex flat fading and multipath fading channel simulator structures, presented in *Section* 2.6.2.3 and *Section* 2.6.3.2, respectively:

   (a) From *Section* 6.2.1's measured Doppler spectra, as well as fading amplitude and phase PDF's, it is apparent that the novel *Clarke*-based complex flat fading channel simulator, presented in *Section* 2.6.2.3, is capable of recreating flat fading channel conditions with realistic Doppler spreading and fading distribution characteristics. Most importantly, the proposed flat fading channel simulator structure is capable of doing so completely in baseband, eliminating the need for undesirable carrier frequencies during simulation studies.

   (b) Using *Section* 2.6.3.3's proposed exponential decay power delay profile creation method, the novel complex multipath fading channel simulator, presented in *Section* 2.6.3.2, can be configured to recreate realistic outdoor frequency selective channel conditions, ideal for the testing of wideband communication systems. The results shown in *Fig.* 6.2.2.1 not only prove that the proposed complex multipath fading channel simulator is capable of creating different fading distributions on each of the propagation paths, but also distinct Doppler spreads.

(c) *Eq.* (2.56) and *Eq.* (2.57) enables the communication engineer to extract perfect fading amplitude and phase CSI, respectively, for each flat fading propagation path in the complex multipath fading channel simulator of *Fig.* 2.8. The extracted CSI can then be processed in the receiver of the communication system under investigation for the purposes of carrier tracking, code locking, improved decoder metric calculations, etc.

2. Conclusions relating to the theoretical analysis and functioning of the novel narrowband complex QPSK and wideband RAKE receiver-based complex DS/SSMA QPSK communication system models, introduced in *Section* 5.2 and *Section* 5.3, respectively:

   (a) The narrowband complex QPSK transmitter and receiver simulation models, presented in *Section* 5.2, can be used to create baseband AWGN and flat fading channel performance evaluation platforms for narrowband communication systems that support realistic carrier tracking, transmit and receive filtering, pulse shaping and matched filtering. In the complex QPSK receiver, *Eq.* (5.2.3) can be used to obtain accurate average fading amplitude estimates, which is required by most CSI-enabled channel decoder structures.

   (b) *Section* 5.3 introduced novel wideband complex DS/SSMA QPSK transmitter and RAKE receiver simulation models, capable of supporting the unfiltered and filtered CSS families presented in *Appendix D*. These simulation models can be used to construct baseband performance evaluation platforms that represent realistic CDMA systems in frequency selective fading environments. Furthermore, not only can the communications engineer use the baseband equivalent models to investigate the performance of channel coding schemes, but also carrier tracking loops, power control schemes, code locked loops, pulse shaping filters, RAKE combining techniques, the MUI characteristics of different CSS families, etc. Furthermore, average fading amplitude calculation through *Eq.* (5.3.3) can be used to determine CSI for SISO-type channel decoder structures.

3. Conclusions regarding the configurability, general operation and relevance of the flexible AWGN (see *Section* 5.4.1), flat fading (see *Section* 5.4.2) and multi-user multipath fading channel (see *Section* 5.4.3) performance evaluation platforms constructed for this study:

   (a) The performance evaluation platform shown in *Fig.* 5.5 can be used to investigate the performance of different channel coding schemes when implemented in a typical narrowband digital communication system, operating in realistic AWGN channel conditions. Thus, uncoded and coded narrowband QPSK communication systems, operating in channel conditions without any fading effects (i.e. when there is no relative movement between the transmitter and receiver structures), can be recreated using this simulation platform.

   (b) Coded and uncoded narrowband QPSK communication systems, operating in a wide variety of flat fading channel conditions, can be investigated using the performance evaluation platform of *Fig.* 5.8 in *Section* 5.4.2. This flat fading channel performance evaluation platform can not only be configured to recreate Rayleigh or Rician fading distribution, but also realistic Doppler spreads. Hence, the performance of different channel coding schemes, implemented in narrowband QPSK communication systems, can be experimentally determined for slow or fast flat fading channel conditions with varying degrees of LOS signal strength.

   (c) The influence of realistic multipath fading channel effects on uncoded and coded wideband DS/SSMA systems can be experimentally investigated by means of the multi-user performance platform, shown in *Fig.* 5.9. Each CDMA user active in the simulation platform, can be assigned its own unique power delay profile in order to recreate realistic movement of mobile users in a cellular environment. Furthermore, the influence of MUI, the near-far effect and the accuracy of the RAKE receiver's MRC efforts on the user capacity and BER performance of the DS/SSMA system, can also be explored using this platform.

(d) The AWGN, flat fading and multi-user multipath performance evaluation platforms, detailed in *Chapter* 5, were successfully implemented in C++ on the *University of Pretoria*'s *I-percube* HPC cluster, donated by *Intel*. Using this HPC cluster, numerous simulated BER performance results were efficiently and swiftly obtained for a wide variety of uncoded and coded narrowband and wideband communication systems in varying mobile channel conditions (see *Chapter* 6).

4. Conclusions from the extensive investigation into the construction, complexity calculation and complexity reduction of linear block code BCJR trellises, as well as the application of the block-wise VA to these trellis structures for optimal ML decoding (see *Chapter* 4):

   (a) Unlike convolutional codes, linear block codes are not state machines. Hence, the orthodox approach whereby a convolutional code's trellis diagram is constructed by creating a time-indexed version of its state diagram, is not applicable to linear block codes. However, following the BCJR syndrome-based trellis construction procedure, described in *Section* 4.2, an irregular trellis-like structure, containing paths representing only valid code words, can be created for any binary or non-binary linear block code.

   (b) BCJR trellis structures of linear block codes always start and end in state 0. Hence, in contrast to convolutional codes, no termination or tail biting overhead bits are required by a linear block coder in order to supply the associated trellis decoder with known starting and ending states. Thus, the trellis decoding of a linear block code is by default a block-wise operation, eliminating the need for sliding window decoders, or intricate interleaver designs when such codes are used as CCs in iteratively decoded PCCs.

   (c) The complexity (i.e. number of active nodes and branches) of a linear block code's BCJR trellis can be obtained from its state space profile, as described in *Section* 4.3.1. In general, for the (n, k, d_{min}) linear block code C, having code and message word symbols from $GF\left(2^{\xi}\right)$, the number of active nodes $AN(C)$ is upper bounded by the dimensions of its BCJR trellis. Since a BCJR trellis consist of $n+1$ sets of nodes, each set of nodes consisting of $2^{\xi(n-k)}$ unique states, it follows that $AN(C) < 2^{\xi(n-k)}(n+1)$. Furthermore, with $AN(C)$ known, the number of branches in an expurgated trellis is upper bounded by $NB(C) \leq 2^{\xi}(AN(C) - 1)$ (see *Section* 4.3.1).

   (d) Unfortunately, the BCJR trellis structures required for the effective trellis decoding of powerful linear block codes (i.e. low rate codes with high $(n-k)$), are exceeding large. This is especially true for non-binary codes, such as RS block codes, operating in $GF\left(2^{\xi}\right)$ with $\xi > 1$. By comparing the complexity of the BCJR trellis of a binary (n, k, d_{min}) linear block code with that of a non-binary (n, k, d_{min}) linear block code, operating in $GF\left(2^{\xi}\right)$, it is apparent that the number of branches emanating from an active node in an BCJR trellis does not only increase exponentially with ξ, but so also does the number of unique states.

   (e) The trellis reduction method presented in *Section* 4.3.2 was shown to be successful in obtaining equivalent linear block code generator matrices that exhibit lower complexity BCJR trellis structures. Unfortunately, the proposed trellis complexity reduction scheme requires an exhaustive search through all equivalent generator matrices in order to find those demonstrating the lowest state space complexities. This becomes an arduous task for linear block codes with large dimensions. Luckily, the search process only has to be conducted once during code design, prior to the hardware and/or software implementation of an appropriate trellis decoder.

   (f) In contrast to classic sub-optimal soft input linear block code decoding algorithms, such as the algorithms proposed by *Chase* [56] and *Moorthy et al.* [57], the block-wise VA algorithm can efficiently accomplish optimal soft input ML decoding for any type of binary or non-binary linear block code.

(g) It is safe to assume that most future mobile communication systems will support adaptive channel coding schemes, capable of dynamically adjusting the level of error protection provided as a function of the channel characteristics and the end-users' required QoS profiles. The concept of *incremental redundancy*, introduced in EDGE, is an excellent example of current commercial systems that already incorporate adaptive channel coding. Furthermore, with the processing power of DSPs and ASICs rapidly increasing, the incorporation of iteratively decoded concatenated codes (such as TCs) in the suite of codes supported by future commercial communication systems' adaptive channel coding schemes, is becoming a reality. Since most SISO-based iterative decoding algorithms require accurate CSI parameters, CSI estimators (see *Section* 3.3.5) will become indispensable peripheral hardware/software in future adaptive channel coding subsystems. This study showed that, using the fading amplitude CSI obtained by such estimators, fading channel BER performances of classic linear block codes, possibly incorporated in the suites of supported channel codes of future adaptive channel coding schemes, can be improved by as much as 0.5 dB.

5. General conclusions from the simulated BER performance results for uncoded and coded narrowband complex QPSK communication systems, operating in AWGN channel conditions (see *Section* 6.5):

   (a) The AWGN channel BER performance results, presented in *Chapter* 6, is evidence that the performance evaluation platform presented in *Section* 5.4.1 is capable of precisely reproducing the operations of uncoded and coded narrowband QPSK communication systems in fade-free, pure AWGN channel conditions.

   (b) Inspection of the simulated AWGN BER performances obtained for the binary and non-binary linear block codes investigated in this study, establishes that the VA decoding approach produces BER performance results equivalent to that obtained through classic optimal ML exhaustive code book searches. This is not only true for hard and soft decision trellis decoding using the original BCJR trellis structures, but also when reduced complexity BCJR trellis structures are used.

   (c) Typical asymptotic gains, ranging from 1.9 dB (VA decoded binary Hamming $(7, 4, 3)$ code) to 3 dB (VA decoded punctured binary BCH $(15, 7, 5)$ code), were observed for hard decision over soft decision VA decoding. Thus, the soft input VA decoding of linear block codes produces better AWGN BER performances than those obtained through classic hard decision decoding algorithms, such as the Berlekamp-Massey algorithm for non-binary RS block codes.

6. General conclusions from the simulated BER performance results for uncoded and coded narrowband complex QPSK communication systems, operating in flat fading channel conditions (see *Section* 6.5):

   (a) The ability of the flat fading channel performance evaluation platform, presented in *Section* 5.4.2, to accurately reproduce the operation of uncoded and coded narrowband QPSK communication systems in flat fading channel conditions with varying Rician factors and Doppler spreads, is reflected by the myriad of flat fading channel BER performance results presented in *Chapter* 6.

   (b) The PDF of the fading amplitude created by a flat fading channel ranges from pure Rayleigh to pure Gaussian as the ratio of LOS to NLOS signal components vary from $-\infty$ dB to ∞ dB. Furthermore, the convolutional and linear block codes investigated in this study are best suited for mobile communication channels generating Gaussian-like signal amplitude PDFs. Hence, the general tendency of coded narrowband complex QPSK communication systems

to exhibit increased BER performances in flat fading channel conditions as the Rician factor increases, can be observed from the simulated BER performance results of *Chapter* 6.

(c) As the ratio of maximum Doppler spread to transmitted symbol rate of a narrowband digital communication system, which utilises a flat fading channel as transmission medium, increases, one intuitively expects the number of symbols lost due to deep fades to decrease. For example, for the $B_D = 100$ Hz fast flat fading channel scenario considered in this study, this ratio calculates to 10% for the selected transmitted symbol rate of 1000 symbols/s. Thus, using a simple rule-of-thumb calculation, it is safe to assume that on average 10 coded symbols will be lost per deep fade in such flat fading channel conditions. Similarly, for the $B_D = 33$ Hz slow flat fading scenario investigated in this study, the ratio of maximum Doppler spread to transmitted symbol rate calculates to 3.3%, which in turn translates to an average loss of 30 bits per deep fade. Hence, assuming a fixed transmitted symbol rate, the average size of an error burst, induced by flat fading channel conditions, increases as the maximum Doppler spread decreases. Moreover, all channel coding schemes have limited burst error correction capabilities, depending on the complexity of the Galois field used for message and code word symbol representation. Hence, the decrease in BER performance as the maximum Doppler spread decreases relatively to the fixed transmitted symbol rate of 1000 symbols/s, observed for all of *Chapter* 6's coded narrowband complex QPSK systems in flat fading channel conditions, was to be expected.

(d) Closer inspection of the simulated BER performance results of *Section* 6.5.1.2 shows that an uncoded narrowband complex QPSK communication system, operating in a Rayleigh flat fading channel with a maximum Doppler spread of $B_D = 33$ Hz, performs close to the theoretical bound of *Eq.* (5.24), whereas the results obtained for $B_D = 100$ Hz deviates significantly from the theoretical curve at high E_b/N_0 levels. This is easily explained: The theoretical curve of *Eq.* (5.24) was derived under the assumptions of slow IID Rayleigh flat fading. Although these assumptions are idealistic, it does resemble the characteristics of realistic flat fading channels with low maximum Doppler spreads, i.e. slow flat fading channels where the fading amplitude does not vary significantly during a single transmitter symbol period.

(e) *Chapter* 6's simulated BER performance results for VA decoded binary convolutional and linear block codes, implemented on narrowband QPSK communication systems in flat fading channel conditions, demonstrate that maximum asymptotic gains in the region of 2 dB can be obtained using hard decision over soft decision (without fading amplitude CSI) ML decoding. In the case of the non-binary RS $(7, 5, 3)$, however, this gain was close to 3 dB for fast fading and high LOS channel conditions. Thus, the standard assumption that hard decision ML decoding usually lags soft decision ML decoding by 2 dB does not hold for all types of channel codes and for all flat fading channel conditions.

(f) The inclusion of perfect fading amplitude CSI in the metric calculations of the VA during soft decision decoding proved to fortify the BER performances of both binary and non-binary linear block codes and convolutional codes in flat fading channel conditions. This was most notable for the non-binary RS $(7, 5, 3)$ linear block code, where a gain of 0.4 dB was obtained by soft decision VA decoding with perfect fading amplitude CSI for a maximum Doppler spread of $B_D = 100$ Hz and Rician factor of $K_i = 9$ dB. In general, one can conclude that the improvements delivered by incorporating fading amplitude CSI during the soft decision VA decoding of convolutional and linear block codes decrease as the maximum Doppler spread (i.e. fading rate) and Rician factor (i.e. LOS signal strength) of the flat fading channel decrease.

7. General conclusions from the simulated BER performance results for uncoded and coded wide-

band complex DS/SSMA QPSK communication systems, operating in multi-user multipath fading channel conditions (see *Section* 6.5):

(a) From *Chapter* 6's host of multi-user multipath fading channel BER performance results, it can be concluded that the performance evaluation platform presented in *Section* 5.4.3 enables the communications engineer to investigate not only different coding schemes for wideband DS/SSMA systems in frequency selective fading channel conditions, but also the MUI resilience of different spreading sequence families and the effectiveness of RAKE combining techniques. As such, it is an essential simulation tool for research into future B3G and 4G PHY layer architectures.

(b) For 1-user and 5-user scenarios, CSS-based DS/SSMA communication systems employing RAKE reception and any of the four CSS families described in *Appendix D*, perform superior to non-RAKE receiver-based systems. In fact, for the single user case, the MRC diversity action of the RAKE receiver in multipath fading proved to be so successful that it even outperforms a narrowband complex QPSK system operating in a flat fading channel with $K_i = 9$ dB and $B_D = 100$ Hz. Thus, RAKE reception can be used successfully to obtain diversity gains in DS/SSMA communication systems employing filtered or unfiltered CSSs.

(c) The use of RAKE reception in a 10-user ABC sequence-based DS/SSMA system delivered weaker BER performances than a non-RAKE receiver-based system. For the DSB CE-LI-RU filtered GCL, QPH and ZC CSS families, however, RAKE reception delivered superior performances at even such high user loads. Therefore, one can conclude that the poor periodic auto-correlation and cross-correlation properties of ABC sequences [48] generate excessive self-noise in a standard RAKE receiver structure, which has been optimally configured to combine the different paths in the power delay profile of the multipath fading channel.

(d) As was to be expected, the MUI generated at high user loads influence the BER performance of the CSS-based wideband complex DS/SSMA communication systems negatively, resulting in persistent error floors at high E_b/N_0. It is interesting to note, however, that the degradation in performance due to MUI is more severe for the DS/SSMA systems employing filtered CSSs. Thus, one can conclude that the *Root-of-Unity* (RU) interpolation filtering techniques [7, 8] used to construct ABC and DSB CE-LI-RU filtered GCL CSSs, degrade the periodic cross-correlation characteristics of the parent ZC CSSs, resulting in higher MUI levels.

8. Conclusions from the simulated BER performance results for binary rate $R_c = 1/2$ NSC and rate $R_c = 2/3$ RSC codes, operating in varying mobile communication channel conditions (see *Section* 6.5.2):

(a) In AWGN channel conditions the binary rate $R_c = 1/2$ NSC and rate $R_c = 2/3$ RSC codes considered in this study performs comparably. However, due to its lower d_{free}, the NSC code lags slightly at low E_b/N_0. Thus, the classic belief that, in non-concatenated coding schemes the use of NSC codes is preferable over RSC codes due to their superior performance at low E_b/N_0 in AWGN conditions, did not hold in this study.

(b) From the flat and multipath fading simulation results it is apparent that the NSC code is better suited at combatting bursty errors. The RSC code's poor performance can be attributed to its recursive nature, a characteristic which makes RSC codes prone to error propagation when presented with correlated error bursts.

(c) As demonstrated by the multi-user multipath fading simulated BER performance results, the binary rate $R_c = 1/2$ NSC and rate $R_c = 2/3$ RSC codes proved to be the most effective in suppressing MUI for all of the codes considered in this study. Thus, from this observation one can conclude that even simple convolutional codes are more effective at suppressing the

errors caused by the MUI, present in DS/SSMA systems at high user loads, than powerful linear block codes.

(d) CSI-enhanced soft decision sliding window VA decoding of the NSC code in fading channel conditions showed BER performance improvements, ranging between 0.15 dB and 0.25 dB, over standard soft decision sliding window VA decoding. In the case of the RSC code, the observed improvements ranged between 0.1 dB and 0.2 dB. One can therefore conclude that the inclusion of fading amplitude CSI in the soft decision VA decoding of convolutional codes is not as effective as with the soft decision VA decoding of linear block codes.

9. Conclusions from the simulated BER performance results for VA decoded binary Hamming $(7, 4, 3)$ linear block codes, operating in varying mobile communication channel conditions (see *Section* 6.5.3.1):

   (a) From the AWGN, flat fading and multi-user multipath fading channel BER performance results presented in *Section* 6.5.3.1, one can conclude that the VA decoding of binary linear block codes, using BCJR trellis structures, deliver hard and soft decision BER performances matching those of classic ML decoding, based on brute force code book searches.

   (b) Flat and multipath fading channel BER performance results demonstrate that the inclusion of perfect fading amplitude CSI in the metric calculations, during the VA decoding of the binary Hamming $(7, 4, 3)$ linear block code, can improve soft decision ML decoding's BER performance by 0.2 dB to 0.4 dB, depending on the temporal and spectral characteristics of the fading channel. It is important to note the use of fading amplitude CSI is less effective for multipath fading channel conditions.

   (c) Overall, the binary Hamming $(7, 4, 3)$ linear block code considered in this study performed poorly, due to its low d_{min}. This is especially true for fading channel conditions, since it is not capable of correcting bursty errors.

10. Conclusions from the simulated BER performance results for VA decoded non-binary RS $(7, 5, 3)$ linear block codes, operating in varying mobile communication channel conditions (see *Section* 6.5.3.2):

    (a) Hard decision VA decoding of the non-binary RS $(7, 5, 3)$ linear block code, operating in AWGN, flat fading and multi-user multipath fading channel conditions, delivers BER performances equivalent to that obtained using the classic Berlekamp Massey syndrome decoding approach. One can therefore conclude that the VA is capable of performing optimal ML decoding of non-binary linear block codes.

    (b) The simulated BER performance results show that optimal soft decision ML decoding of non-binary codes, such as RS codes, is possible through the application of the VA to these codes' BCJR trellis structures. Asymptotic gains as high as 3 dB above hard decision decoding was achieved for the non-binary RS $(7, 5, 3)$ code, depending on the channel characteristics.

    (c) Simulated BER performance results for flat and multipath fading channels show that, as with the binary Hamming $(7, 4, 3)$ linear block code, the use of fading amplitude CSI during soft decision VA decoding of the non-binary RS $(7, 5, 3)$ code improves on standard soft decision decoding by as much as 0.4 dB. The factors that influence the gains achievable through the inclusion of fading amplitude CSI, is discussed in detail later in this subsection.

    (d) The non-binary RS $(7, 5, 3)$ linear block code proved to be more effective than the binary Hamming $(7, 4, 3)$ code at combatting the bursty errors produced by fading channel conditions. This was to be expected, since RS codes are burst error correcting codes.

(e) Unfortunately, non-binary linear block codes, such as RS codes, possess exceedingly complex BCJR trellis structures. For example, the simple RS $(7, 5, 3)$ code considered in this study has a BCJR trellis consisting of 8 layers of nodes, each layer containing 64 nodes with 8 branches emanating from each active node. Thus, one can argue that the gains achievable over classic non-binary linear block code decoding algorithms, such as the Berlekamp Massey algorithm, through soft decision VA decoding and the application of fading amplitude CSI, do not justify the increase in decoder complexity and implementation hardware/software requirements.

11. Conclusions from the simulated BER performance results obtained by using reduced complexity BCJR trellis structures during the VA decoding of binary cyclic $(5, 3, 2)$ linear block codes, operating in varying mobile communication channel conditions (see *Section* 6.5.4):

    (a) In AWGN channel conditions, the VA decoding of the binary cyclic $(5, 3, 2)$ linear block code, using the standard and reduced complexity BCJR trellis structures, delivered equivalent BER performances. Therefore, it is safe to assume that the trellis reduction algorithm presented in *Section* 4.3.2 is successful in obtaining less complex and easier implementable equivalent BCJR trellis structures for both binary and non-binary linear block codes.

    (b) From the flat fading channel simulations it was discovered that VA decoding of the binary cyclic $(5, 3, 2)$ code, using the reduced complexity BCJR trellis, exhibited an inferior performance to that obtained using the original BCJR trellis structure. However, this peculiarity can not be attributed to a deficiency in the reduced BCJR trellis structure, but rather to the fact that a non-systematic linear block code (which is a byproduct of the trellis reduction scheme) is slightly less able to minimise the bit error probability than a systematic equivalent. This is especially true for flat fading channels that generate bursty errors. Therefore, this phenomenon was negligible during the AWGN channel simulations and only took on measurable proportions during the flat fading channel simulations.

    (c) Results obtained during the flat fading channel simulations establish that fading amplitude CSI can easily be incorporated into the soft decision VA decoding of linear block codes that make use of reduced complexity BCJR trellis structures. For the binary cyclic $(5, 3, 2)$ linear block code, inclusion of fading amplitude CSI resulted in gains, ranging between 0.2 dB and 0.4 dB, over standard hard decision decoding for both the original and reduced BCJR trellis structures.

12. Conclusions from the simulated BER performance results for VA decoded interleaved binary Hamming $(7, 4, 3)$ and non-binary RS $(7, 5, 3)$ linear block codes, operating in varying fading channel conditions (see *Section* 6.5.5.1 and *Section* 6.5.5.2, respectively):

    (a) Performing channel interleaving proved to be beneficial to the BER performances of the VA decoded binary Hamming $(7, 4, 3)$ and non-binary RS $(7, 5, 3)$ linear block codes, operating in fading channel conditions. However, the improvements obtained were more drastic for the binary Hamming $(7, 4, 3)$ linear block code, since interleaving disperses error bursts, against which this code is ineffective.

    (b) In general, the BER performance improvements obtained by the addition of interleaving to coded narrowband communication systems, operating in flat fading channel conditions, increase as the maximum Doppler spread (i.e. fading rate) of the channel decreases. This can be explained by recalling that, for a fixed symbol rate, a decrease in maximum Doppler spread creates longer deep fades, resulting in lengthier error bursts. From this one can conclude that interleaving is best suited for slow fading channels.

    (c) Simulations performed with coded wideband complex DS/SSMA systems in multi-user multipath fading channel conditions revealed that interleaving is not only capable of improving

the performance of the channel codes, but also alleviate the harmful effects of MUI, incited by high user loads in the CDMA system. One can therefore conclude that the MUI generated in the RAKE receiver structure considered in this study is not IID for each received and demodulated code bit, resulting in bursty errors that can be diffused using interleaving.

13. Conclusions from the simulated BER performance results for VA decoded punctured binary rate $R_c = 1/2$ RSC codes and binary BCH $(15, 7, 5)$ linear block codes, operating in varying mobile communication channel conditions (see *Section* 6.5.6.1 and *Section* 6.5.6.2, respectively):

    (a) Although the punctured binary 4-state, rate $R_c = 1/2$ RSC code of *Section* 6.5.6.1 has the same overall code rate as the binary 8-state, rate $R_c = 2/3$ RSC code discussed in *Section* 6.5.2.2, it produces inferior AWGN and flat fading channel BER performances. It is important to note, however, that the rate $R_c = 2/3$ RSC consistently outperformed the rate $R_c = 1/2$ code by 0.8 dB for hard decision VA decoding and 1.2 dB for soft decision VA decoding under all channel conditions considered. The punctured rate $R_c = 1/2$ RSC code's poor BER performance, however, is not the consequence of the puncturing procedure. This can be attributed to the code's small d_{free}. One can therefore conclude that the puncturing of binary RSC codes enables a code designer to accomplish rate adaptation, without severe losses in code performance.

    (b) For all channel conditions considered, soft decision VA decoding of the punctured binary BCH $(15, 7, 5)$ code delivered BER performances comparable to that of the soft decision VA decoded binary Hamming $(7, 4, 3)$ code. However, hard decision VA decoding of the punctured BCH code proved to consistently deliver BER performances inferior to that obtained through the hard decision VA decoding of the Hamming code. Recognising that the BCH $(15, 7, 5)$ code is far more powerful than the Hamming $(7, 4, 3)$ code, one can conclude that puncturing significantly degrades the BER performance of VA decoded linear block codes, especially when hard decision decoding is employed.

14. Conclusions regarding the BER performance improvements obtained by employing fading amplitude CSI during the soft decision VA trellis decoding of convolutional and linear block codes, operating in varying fading channel conditions (see *Section* 6.5):

    (a) The inclusion of fading amplitude CSI during the soft decision VA decoding of convolutional and linear block codes produced coding gains over standard soft decision decoding, ranging from 0.1 dB to 0.4 dB, depending on the code and channel conditions. Thus, if CSI estimation hardware/software is available in a linear block coded communication system operating in fading channel conditions, the system's BER performance can be marginally improved, without a profound increase in system complexity. However, if a CSI estimator is not implemented in the system, the increased system complexity might not justify the BER performance improvements obtainable through soft decision VA decoding with fading amplitude CSI.

    (b) In flat fading channel conditions, the gains achievable during the soft decision VA decoding of linear block codes by including fading amplitude CSI during the metric calculations, increase as the Rician factor or the fading rate (i.e. maximum Doppler spread) of the channel increases. Thus, using fading amplitude CSI during VA decoding is most effective for fast, Rician flat fading channels.

    (c) Using fading amplitude CSI during soft decision VA decoding yields more impressive BER performance improvements for linear block codes than for binary convolutional codes. From the simulation results obtained for the linear block codes considered in this study, it is clear that code complexity and strength has no influence on the BER performance improvements obtained by incorporating fading amplitude CSI during VA decoding.

(d) Interleaving increases the BER performance improvements obtained by employing fading amplitude CSI during the soft decision VA decoding of linear block codes and binary convolutional codes. Conversely, performing puncturing impacts these gains negatively.

(e) The multi-user multipath fading channel BER performance results show that the CSS family used and CDMA user load has no influence on the gains achievable by incorporating fading amplitude CSI during the soft decision VA decoding of linear block and binary convolutional codes, employed in wideband RAKE receiver-based DS/SSMA communication systems.

(f) Using a reduced complexity BCJR trellis structure (see *Section* 4.3.2) during the soft decision VA decoding of a linear block code in fading channel conditions has no effect on the gains obtained by incorporating fading amplitude CSI in the metric calculations.

15. Conclusions relating to the temporal qualities, correlation properties, spectral characteristics and simulated BER performance results for the different CSS families considered in this study's DS/SSMA simulations (see *Chapter* 6 and *Appendix D*):

(a) The multi-user multipath fading channel simulation results clearly reveal the superior BER performances of the unfiltered QPH and ZC CSS families over the pre-filtered ABC and DSB CE-LI-RU filtered GCL CSS families. For a fixed sequence length of $M_{seq} = 63$ chips, ABC sequences delivered the poorest BER performances of all of the CSS families considered in this study. Although the RU interpolation filtering techniques used to generate ABC and DSB CE-LI-RU filtered GCL CSSs (see *Section* D.3.2) reduce the spectral requirements of DS/SSMA systems employing these CSSs, the BER performance results lead one to conclude that these filtering approaches detrimentally influence the periodic correlation characteristics of CSSs, resulting in excessive MUI when used in CDMA systems. This observation is most evident for DS/SSMA systems employing ABC sequences, where the BER performances of RAKE receiver-based systems lag that of non-RAKE systems at high user loads, due to the self-noise generated in the RAKE receiver structures.

(b) Although RU interpolation filtering has an unfavourable influence on the periodic correlation properties of CSSs, the resultant PSDs of DS/SSMA systems employing pre-filtered CSSs, such as ABC and DSB CE-LI-RU filtered GCL CSSs, exhibit desirable characteristics. This study corroborated the findings of [4], demonstrating that ABC and DSB CE-LI-RU filtered GCL CSSs exhibit PSDs with cutoff rates only obtainable through Nyquist roll-off factor $\varsigma = 0$ filtering. Furthermore, ABC sequences generate spectrally economic SSB signals. Thus, using pre-filtered CSSs in DS/SSMA communication systems not only simplifies the wideband transmitter structures by removing the need for chip shaping filters, but also minimises the co-channel and adjacent channel interference [42, 47] encountered in cellular mobile networks. One can therefore conclude that the use of pre-filtered CSSs in future wideband B3G and 4G cellular DS/SSMA systems, will greatly simplify cell planning.

(c) Notwithstanding the fact that the maximum number of users supported by a DS/SSMA system is limited by MUI, it is mainly a function of the number of unique sequences available to be assigned to users. In turn, the number of unique sequences is largely dictated by the sequence length M_{seq} of the spreading sequence family used. Due to their superior SSLDs, the use of ABC and DSB CE-LI-RU filtered GCL CSSs enable the communications engineer to select sequences that are longer in length than QPH and ZC CSSs, but occupy an equivalent transmission bandwidth. Furthermore, using longer spreading sequences not only increases the number of possible users in the CDMA system, but also improves the system's MUI levels, since the periodic correlation characteristics of spreading sequences improve as their lengths increase.

(d) The investigation into the influence of the CSS selection approach on the multi-user multipath fading channel performance of an uncoded RAKE receiver-based complex DS/SSMA system,

employing length $M_{seq} = 63$ ABC sequences, shows that CSSs can not be arbitrarily chosen from the available set of sequences, if an optimal multi-user BER performance is desired. From the simulation results one can conclude that the proposed CSS selection approach of *Section* 6.5.1.3.2 is an efficient method whereby sequences can be selected from a GCL CSS [9] family, such that the mutual periodic correlation characteristics of the chosen CSSs are optimal.

This study demonstrated the dexterity of the block-wise VA as an eloquent MLSE detection technique, which can be used to accomplish perfect hard or soft decision ML trellis decoding of any type of binary or non-binary linear block code. Hence, when applied to the BCJR trellis structures of linear block codes, the VA equips the communications engineer with a single generic linear block code decoding algorithm, eliminating the quintessential need to implement code-specific decoding algorithms, such as the Berlekamp Massey algorithm. The theoretical analyses, novel algorithms, extensive performance evaluation platforms and simulation results presented in this study, expedite further research and development of generic SISO trellis-based decoding algorithms, capable of efficiently and optimally decoding convolutional codes, linear block codes and concatenated codes, all of which will conceivably be included in adaptive channel coding schemes for future wireless narrowband and wideband mobile communication systems.

7.3 FUTURE RESEARCH

This study touched on a broad variety of fields within digital communications, ranging from channel modelling and channel coding, to the development of simulation platforms. As such, several avenues for future research were identified. Only those prospective research areas where meaningful results and applicability to current and future communication systems seem to be forthcoming, are listed below:

1. From *Section* 3.3.5, it is clear that channel estimation remains an extremely active research field. The use of CSI in ML and MAP decoding schemes in order to improve BER performances, has become mainstream in most new developments in channel coding. However, chasing *Shannon*'s channel capacity limit [1, 13, 62] will remain a purely academic exercise, without commercial applicability, as long as practical and implementable CSI estimation techniques are lacking.

2. Although the novel complex flat and multipath fading channel simulator models presented in *Section* 2.6.2.3 and *Section* 2.6.3.2, respectively, are capable of adequately reproducing the statistical nature of real life mobile fading channels, they fall short in two aspects: Firstly, after initialisation the flat fading channel simulator is only capable of creating a fixed maximum Doppler spread. This can be improved by employing adaptive Doppler spread spectral shaping filters, instead of the fixed IIR filter structure of *Section* 2.6.2.4.2. Secondly, the complex multipath fading channel simulator is currently only capable of producing stationary channel characteristics (see *Section* 2.4.1), due to the use of fixed path delays. This model can be improved to also support non-stationary channels by simply incorporating time-variant path delays.

3. A SOVA decoder [16, 61, 165, 166] that can be used as a SISO decoder [87, 91] module for linear block codes, is an attractive proposition. Such a decoder will become an invaluable building block in classic and iteratively decoded concatenated coding schemes employing linear block codes. The original SOVA algorithm, developed by *Hagenauer* [61], as well as derivatives thereof, are aimed at the decoding of convolutional codes. The author of this dissertation has since attempted to develop a block-wise SOVA that can operate on linear block codes' BCJR trellises. Unfortunately, only partial success has been achieved with a viable SOVA for systematic binary linear block codes.

4. The use of trellis decoded linear block codes as CCs (alongside current RSC and NSC CCs) in future iteratively decoded concatenated coding schemes, might result in elegant concatenated encoder structures that will not fall victim to the ever present trellis termination [167–169] dilemma. In a classic TC [89] encoder, using for argument's sake RSCs C_1 and C_2 as the respective CCs, the input data bits encoded by encoder C_1 are interleaved before they are processed by C_2. However, the data bits encoded by C_1 usually contain termination bits that will ensure trellis termination for its associated SISO trellis decoder [170]. Unfortunately, these termination bits are also interleaved, leaving the trellis of encoder C_2 unterminated. This leads to inefficient iterative decoding and is partially responsible for the characteristic floors [66, 68, 92] observed in the measured BER performance results of TCs. To combat this problem in classic concatenated coding schemes, constructed using convolutional codes as CCs, two options are available: Firstly, try to design [168, 171] the interleaver such that all CCs terminate in a known state. Secondly, use extremely long input messages, thereby minimising the effect of incorrect decoding at the termination bit positions. The first option limits the concatenated code designer's selection of possible interleaver structures, usually resulting in interleaver gains [19,88] inferior to those that could have been achieved using s-random interleavers (see *Section* C.3.3). The second option, although effective, limits the use of powerful iteratively decoded concatenated coding schemes to data sources which are not delay sensitive, i.e. data sources other than realtime voice or video. Recalling from *Section* 4.2 that the BCJR trellis of a linear block code always terminates in state $(0, n)$, implies that trellis termination will not be a concern for concatenated coding schemes using linear block codes as CCs. It also makes the use of iteratively decoded concatenated coding schemes for short frame transmission viable. However, linear block codes do not exhibit the recursive nature required [19, 88] by PCC schemes, making it safe to assume that linear block codes as CCs will most likely find application only in SCCs [27, 28, 30, 31] and HCCs [30, 33].

5. The trellis decoding of non-linear block codes is a research field that has remained largely untouched. Contributions that can be made to this field include the design of trellis construction algorithms, similar to the BCJR trellis generation algorithm for linear block codes (described in *Section* 4.2), as well as possible trellis reduction techniques.

6. *Section* 5.4.3 presented a realistic multi-user multipath simulation platform, based on the wideband complex DSSS/MA QPSK communication system of *Section* 5.3. This CDMA platform utilises the CSS families detailed in *Appendix D*. In this study, only VA decoded classic convolutional and linear block coding schemes were tested on this platform. This still leaves room for experimentation with concatenated coding schemes (classic and iteratively decoded), *Space Time Code*s (STC), *Multi-Level Code*s (MLC), LDPCs and many others on this B3G [45] platform.

7. *Turbo Product Codes* [172] consist of two linear block codes, which simultaneously encode the rows and columns of a two-dimensional block of information symbols. Decoding is accomplished by processing the row and column encoded symbols with separate iterative ML or MAP SISO decoder modules, which exchange a-priori information on the decoded information symbols during each iteration. These concatenated block codes, considered to be one step down from TCs on the evolutionary ladder of channel coding schemes, have become the most prevalent iteratively decoded concatenated coding scheme in commercial digital communication systems, due to their simplicity and TC-like potency. However, the iterative ML and MAP decoding approaches thus far proposed [172–174], still make use of brute force code book searches. As such, employing trellis decoding techniques for linear block codes might be an interesting proposition to investigate. Furthermore, the construction of multi-dimensional trellis structures that simultaneously represent two or more linear block code CCs in a block product code, is also an interesting untapped field for future research.

"For years radios had been operated by means of pressing buttons and turning dials; then as the technology became more sophisticated the controls were made touch-sensitive - you merely had to brush the panels with your fingers; now all you had to do was wave your hand in the general direction of the components and hope. It saved a lot of muscular expenditure of course, but meant that you had to sit infuriatingly still if you wanted to keep listening to the same programme." [1]

[1] *Source: "The Hitch Hiker's Guide to the Galaxy," by Douglas N. Adams, 1985*

APPENDIX A

OPTIMAL RECURSIVE SYSTEMATIC CONVOLUTIONAL CODES

A.1 APPENDIX OVERVIEW

THE most extensive set of the best rate $R_c = k/n$ RSC coders thus far, has been presented by *Benedetto, Garello* and *Montorsi* in [88]. Their search approach for the best codes was based on a minimal encoder description as a finite-state machine, derived from a group-theoretic approach to binary convolutional codes. This appendix summarises the encoder parameters of the optimal rate $R_c = 1/4$, $R_c = 1/3$, $R_c = 1/2$, $R_c = 2/4$, $R_c = 2/3$, $R_c = 3/4$ and $R_c = 4/5$ RSC codes obtained from their exhaustive searches. The minimum free distance d_{free} of each encoder is also given. For illustrative purposes, these configuration parameters are used to construct an optimal 8-state, rate $R_c = 2/3$ RSC code encoder.

A.2 TABLES OF OPTIMAL RSC CODE ENCODER PARAMETERS

Instead of using the classic approach of describing encoder structures by means of their generator polynomials or matrices, *Benedetto, Garello* and *Montorsi* [88] opted to describe their set of optimal RSC code encoders using the following parameters:

υ_a = Number of delay elements in the shift register associated with the a^{th} message word bit in the encoder input vector $\overline{d}_{m,i}$.

2^{υ} = Number of states in the code's trellis. The parameter $\upsilon = \sum_{a=0}^{k-1} \upsilon_a$ denotes the total number of delay elements used in the encoder.

$z(a,b)$ = Output generator polynomial, given in octal form. When converted to a binary sequence, it indicates the tap connections associated with the a^{th} shift register that contribute to the b^{th} non-systematic output bit of the encoder.

$h(a,b)$ = Feedback generator polynomial, given in octal form. When converted to a binary sequence, it indicates the tap connections associated with the a^{th} shift register that contribute to the input of the b^{th} shift register.

These parameters are used in *Table* A.1, *Table* A.2, *Table* A.3, *Table* A.4, *Table* A.5, *Table* A.6 and *Table* A.7 to define the structures of optimal rate $R_c = 1/4$, $R_c = 1/3$, $R_c = 1/2$, $R_c = 2/4$, $R_c = 2/3$, $R_c = 3/4$ and $R_c = 4/5$ RSC code encoders, respectively.

Table A.1: Encoder Descriptions of Optimal Rate $R_c = 1/4$ RSC Codes

2^v	v_i	**Output Generators** $z(0,b)$	**Feedback Generators** $h(0,b)$	d_{free}
2	1	$1_8, 3_8, 2_8$	3_8	6
4	2	$5_8, 7_8, 6_8$	7_8	10
8	3	$15_8, 17_8, 11_8$	13_8	12
16	4	$35_8, 37_8, 27_8$	23_8	14
32	5	$51_8, 45_8, 71_8$	67_8	15

Table A.2: Encoder Descriptions of Optimal Rate $R_c = 1/3$ RSC Codes

2^v	v_i	**Output Generators** $z(0,b)$	**Feedback Generators** $h(0,b)$	d_{free}
2	1	$3_8, 2_8$	3_8	5
4	2	$7_8, 5_8$	7_8	8
8	3	$15_8, 17_8$	13_8	10
16	4	$37_8, 33_8$	23_8	10
32	5	$51_8, 45_8$	67_8	11
64	6	$131_8, 101_8$	163_8	11

Table A.3: Encoder Descriptions of Optimal Rate $R_c = 1/2$ RSC Codes

2^v	v_i	**Output Generators** $z(0,b)$	**Feedback Generators** $h(0,b)$	d_{free}
2	1	2_8	3_8	3
4	2	5_8	7_8	5
8	3	17_8	13_8	6
16	4	37_8	23_8	6
32	5	17_8	67_8	8
64	6	115_8	147_8	9

Table A.4: Encoder Descriptions of Optimal Rate $R_c = 2/4$ RSC Codes

2^v	υ_i	**Output Generators**		**Feedback Generators**		d_{free}
		$z(0,b)$	$z(1,b)$	$h(0,b)$	$h(1,b)$	
2	$1,0$	$1_8, 2_8$	$1_8, 1_8$	$3_8, 0_8$	$1_8, 1_8$	4
4	$1,1$	$3_8, 3_8$	$3_8, 0_8$	$0_8, 3_8$	$3_8, 2_8$	5
8	$2,1$	$3_8, 5_8$	$3_8, 1_8$	$2_8, 5_8$	$3_8, 2_8$	5
16	$2,2$	$1_8, 3_8$	$5_8, 7_8$	$5_8, 4_8$	$2_8, 5_8$	6

Table A.5: Encoder Descriptions of Optimal Rate $R_c = 2/3$ RSC Codes

2^v	υ_i	**Output Generators**		**Feedback Generators**		d_{free}
		$z(0,b)$	$z(1,b)$	$h(0,b)$	$h(1,b)$	
2	$1,0$	2_8	0_8	$3_8, 0_8$	$1_8, 1_8$	2
4	$1,1$	0_8	3_8	$2_8, 3_8$	$3_8, 0_8$	3
8	$2,1$	7_8	1_8	$0_8, 5_8$	$3_8, 2_8$	4
16	$2,2$	5_8	3_8	$6_8, 3_8$	$5_8, 4_8$	5
32	$3,2$	15_8	7_8	$0_8, 13_8$	$7_8, 0_8$	6
64	$3,3$	1_8	11_8	$13_8, 12_8$	$16_8, 1_8$	6

Table A.6: Encoder Descriptions of Optimal Rate $R_c = 3/4$ RSC Codes

2^v	υ_i	**Output Generators**			**Feedback Generators**			d_{free}
		$z(0,b)$	$z(1,b)$	$z(2,b)$	$h(0,b)$	$h(1,b)$	$h(2,b)$	
2	$1,0,0$	2_8	0_8	0_8	$3_8, 0_8, 0_8$	$1_8, 0_8, 1_8$	$1_8, 1_8, 0_8$	2
4	$1,1,0$	2_8	1_8	1_8	$2_8, 1_8, 0_8$	$2_8, 3_8, 1_8$	$1_8, 0_8, 0_8$	3
8	$2,1,0$	7_8	3_8	1_8	$0_8, 5_8, 0_8$	$3_8, 0_8, 0_8$	$1_8, 1_8, 1_8$	4
16	$2,2,0$	7_8	5_8	1_8	$0_8, 7_8, 0_8$	$7_8, 0_8, 0_8$	$1_8, 1_8, 1_8$	4
32	$2,2,1$	1_8	6_8	3_8	$3_8, 0_8, 5_8$	$6_8, 0_8, 5_8$	$2_8, 3_8, 3_8$	5

Table A.7: Encoder Descriptions of Optimal Rate $R_c = 4/5$ RSC Codes

2^v	υ_i	**Output Generators**				**Feedback Generators**				d_{free}
		$z(0,b)$	$z(1,b)$	$z(2,b)$	$z(3,b)$	$h(0,b)$	$h(1,b)$	$h(2,b)$	$h(3,b)$	
2	1, 0, 0, 0	2_8	0_8	0_8	0_8	$3_8, 0_8, 0_8, 0_8$	$1_8, 0_8, 0_8, 1_8$	$1_8, 0_8, 1_8, 0_8$	$1_8, 1_8, 0_8, 0_8$	2
4	1, 1, 0, 0	2_8	1_8	1_8	0_8	$2_8, 1_8, 0_8, 0_8$	$2_8, 3_8, 0_8, 1_8$	$0_8, 1_8, 1_8, 0_8$	$1_8, 0_8, 0_8, 0_8$	2
8	1, 1, 1, 0	0_8	3_8	1_8	1_8	$2_8, 0_8, 3_8, 0_8$	$0_8, 1_8, 2_8, 0_8$	$2_8, 3_8, 1_8, 1_8$	$1_8, 0_8, 0_8, 0_8$	3

A.3 ENCODER CONSTRUCTION EXAMPLE

Fig. A.1 shows the generic structure of an 8-state, rate $R_c = 2/3$ RSC code. In this figure, $d_{m,i,0}$ and $d_{m,i,1}$ denote the i^{th} pair of input data bits within the m^{th} vector of input bits, whereas $\text{v}_{m,i,0}$ denotes the i^{th} single output parity bit within the m^{th} vector of output bits. Applying configuration parameters such as those specified in *Section* A.2, this generic encoder structure can be altered to obtain several distinctly different 8-state, rate $R_c = 2/3$ RSC code encoders. According to *Table* A.5 (code no. 3), the best rate $R_c = 2/3$ 8-state RSC code encoder is constructed by setting $z(1,1) = 7_8$, $z(2,1) = 1_8$, $h(1,1) = 0_8$, $h(2,1) = 3_8$, $h(1,2) = 5_8$ and $h(2,2) = 2_8$ in *Fig.* A.1. The resultant optimal RSC code encoder is shown in *Fig.* A.2.

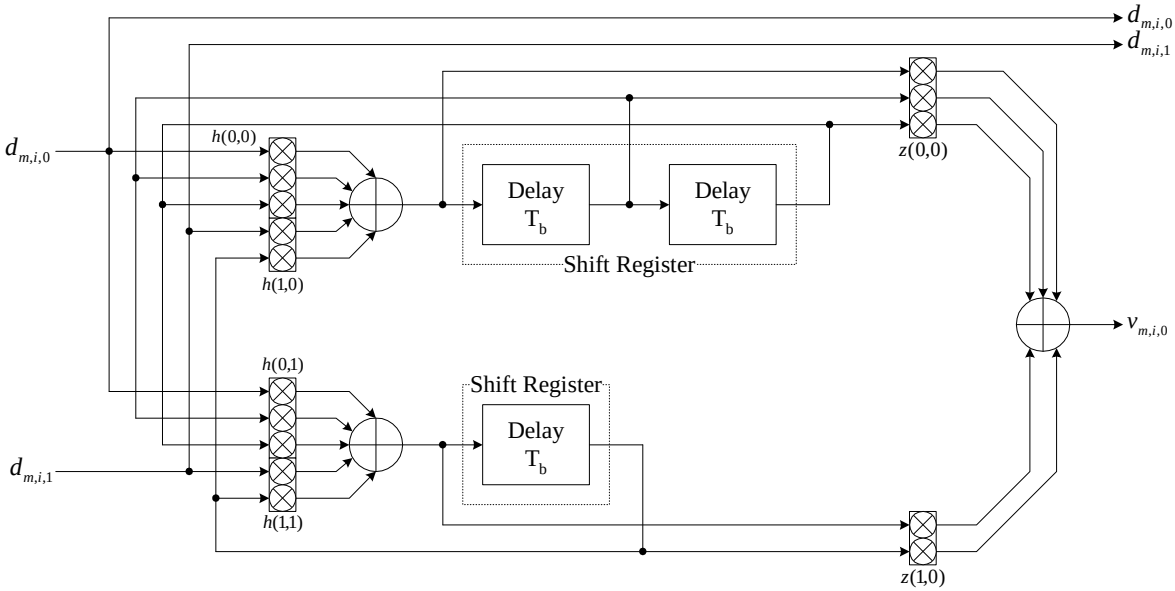

Figure A.1: General Structure of a 8-State, Rate $R_c = 2/3$ Minimal Linear Systematic Convolutional Code Encoder

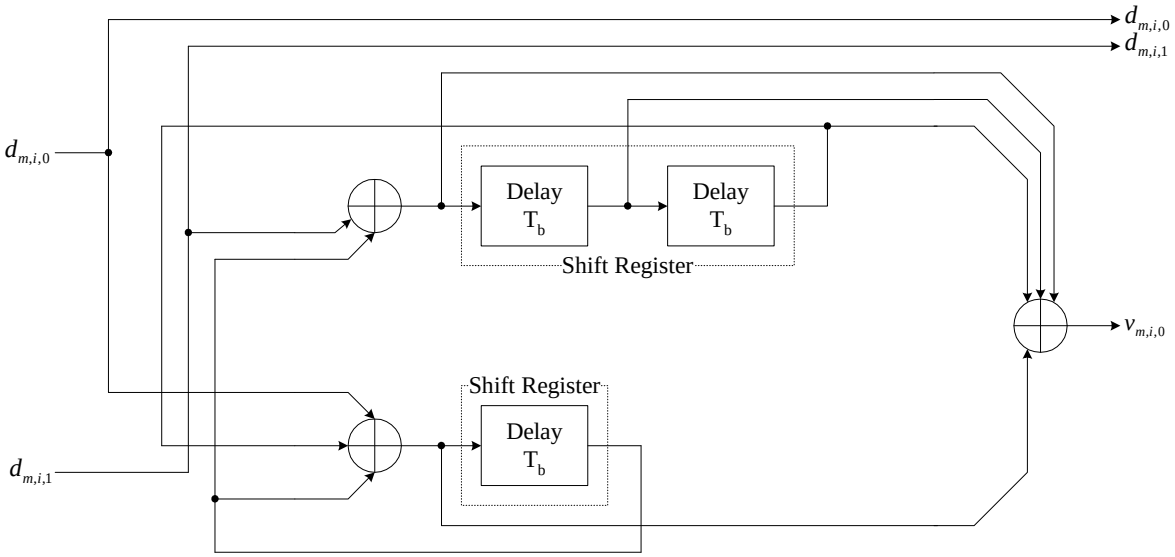

Figure A.2: Optimal 8-State, Rate $R_c = 2/3$ Minimal Linear Systematic Convolutional Code Encoder

APPENDIX B

BERLEKAMP-MASSEY DECODING OF REED-SOLOMON BLOCK CODES

B.1 APPENDIX OVERVIEW

THIS appendix presents a conceptual description of the *Berlekamp-Massey* decoding algorithm [74, 75], frequently employed in the syndrome decoding of classic BCH and RS block codes. Since it falls beyond the scope of this study, the classic *Berlekamp-Massey* algorithm is not described in detail. However, several valuable references that focus on variations of this decoding algorithm are cited for the interested reader.

B.2 THE BERLEKAMP-MASSEY ALGORITHM

The classic approach followed in the decoding of RS block codes entails hard decision syndrome decoding [94], which is described below (all mathematical operations are performed in $GF\left(2^{\xi}\right)$): Assume that $c_m(p) = c_{m,n-1}.p^{n-1} + c_{m,n-2}.p^{n-2} + ... + c_{m,0}$ is the code word polynomial generated by an (n, k, d_{min}) $GF\left(2^{\xi}\right)$ RS block code encoder at encoding instance m, given the message polynomial $d_m(p) = d_{m,k-1}.p^{k-1} + d_{m,k-2}.p^{k-2} + ... + d_{m,0}$. This code word is then transmitted through a non-ideal communication channel. Let $y_m(p) = y_{m,n-1}.p^{n-1} + y_{m,n-2}.p^{n-2} + ... + y_{m,0}$ represent the corrupted code word after hard decisions have been made on the received and demodulated code word symbols. The relationship between this polynomial and the original code word polynomial $c_m(p)$ is as follows [94]:

$$y_m(p) = c_m(p) + e_m(p) \tag{B.1}$$

where $e_m(p) = e_{m,n-1}.p^{n-1} + e_{m,n-2}.p^{n-2} + ... + e_{m,0}$, referred to as the *error polynomial*, describes the alterations made by the channel to the original code word during transmission.

From *Section* 3.2.2.3.3.1 it follows that the number of parity symbols present in each code word, generated by a $t_{correct}$-symbol error correcting RS block code, is $n - k = 2.t_{correct}$. Thus, $2.t_{correct}$ syndromes can be calculated for the received code word. The i^{th} syndrome, with $i = 1, 2, ..., 2.t_{correct}$, is calculated as follows [74, 75, 94, 175]:

$$\$_m^i = y\left(\varphi^i\right) = c_m\left(\varphi^i\right) + e_m\left(\varphi^i\right) = e_m\left(\varphi^i\right) \tag{B.2}$$

where φ is the primitive element of $GF\left(2^{\xi}\right)$. In *Eq.* (B.2) $c_m\left(\varphi^i\right) = 0$, because φ^i is a root of the block code's generator polynomial (see *Section* 3.2.2.3.3.2).

Assume that a number of $M_{correct}$, with $M_{correct} \leq t_{correct}$, correctable errors are present in $y_m(p)$, situated at positions $\chi_m^1, \chi_m^2, ..., \chi_m^{M_{correct}}$, where $0 \leq \chi_m^j < n$ for $j = 1, 2, ..., M_{correct}$. For each symbol in error, an *error locater* is defined [74, 75, 94, 175]:

$$\kappa_m^j = (\varphi)^{\chi_m^j} \qquad \text{for } j = 1, 2, ..., M_{correct} \tag{B.3}$$

Noting that only symbols received in error contribute to the syndrome values, it is possible to rewrite *Eq.* (B.2) in terms of the error locators:

$$\$_m^i = \sum_{j=1}^{M_{correct}} e_{m,\chi_m^j} . \left(\kappa_m^j\right)^i \tag{B.4}$$

The *error locator polynomial* polynomial $\Theta_m(p)$, which describes the error pattern present in $y_m(p)$, is defined as a polynomial whose inverse roots are the error locators [74, 75, 94, 175]:

$$\Theta_m(p) = \prod_{j=1}^{M_{correct}} \left(1 - \kappa_m^j . p\right) \tag{B.5}$$

The *Berlekamp-Massey* algorithm is an iterative algorithm that computes both the $2.t_{correct}$ syndromes and the error locator polynomial $\Theta_m(p)$. A detail description of this algorithm, which can be performed in both the time and frequency domains, falls beyond the scope of this study. The interested reader is referred to [74, 75, 175] and [176] for descriptions of the time and frequency domain versions of the *Berlekamp-Massey* algorithm, respectively.

In order to decode binary block codes, knowledge of the error positions in the received code words are sufficient information. However, with non-binary block codes, the error magnitudes must also be determined: Assume that the error locater polynomial $\Theta_m(p)$ for the received code word $y_m(p)$ has been successfully constructed. Using the error locator polynomial's coefficients and the $2.t_{correct}$ syndromes, an *error evaluator polynomial* $\nabla_m(p)$ is determined [175]:

$$\nabla_m(p) = \Theta_m(p) + \sum_{j=1}^{M_{correct}} \left[e_{m,\chi_m^j} . \kappa_m^j . p \prod_{\substack{i=1 \\ i \neq j}}^{M_{correct}} \left(1 - \kappa_m^i . p\right) \right] \tag{B.6}$$

An estimate of the magnitude of the error at position χ_m^j, with $j = 1, 2, ..., M_{correct}$, is then calculated as follows [175]:

$$\hat{e}_{m,\chi_m^j} = - \left(\frac{\kappa_m^j . \nabla_m(p)}{\frac{d\Theta(p)}{dp}} \right) \Bigg|_{p=1/\left(\kappa_m^j\right)} \tag{B.7}$$

Completing the hard decision syndrome decoding process involves constructing an estimate of the original code word polynomial, denoted by $\hat{c}_m(p)$. This is accomplished by subtracting $\hat{e}_{m,\chi_m^j}$ from position χ_m^j in $y_m(p)$, for $j = 1, 2, ..., M_{correct}$.

APPENDIX C

POPULAR BLOCK INTERLEAVERS

C.1 APPENDIX OVERVIEW

SEVERAL prevalent block interleaver structures, frequently encountered in iteratively and non-iteratively decoded concatenated coding schemes, are considered in this appendix. The implementable interleavers considered are divided into two categories: Deterministic and random interleavers. The deterministic interleavers presented include classic block interleavers, *Berrou-Glavieux* interleavers and JPL interleavers. PN generator interleavers, random number generator interleavers and s-random interleavers constitute the random interleavers of interest. The appendix is concluded with a short discussion on the concept of a probabilistic uniform interleaver, frequently encountered in the theoretical performance evaluations of concatenated codes.

C.2 DETERMINISTIC BLOCK INTERLEAVERS

A deterministic block interleaver has a mapping function $\Pi(i)$ that, for a given interleaver depth J and interleaver width F, always produces the same fundamental permutation. Several popular deterministic block interleaver mapping schemes are discussed in the following subsections.

C.2.1 CLASSIC BLOCK INTERLEAVERS

A classic block interleaver [87] consists in essence of a size $J \times F$ memory matrix. The first step in the interleaving process performed by this type of interleaver is to write the interleaver input symbols into this matrix in a row-wise fashion. The second and final step whereby the interleaver output symbols are obtained, is to write out the data stored in the memory matrix in a column-wise fashion. It is easy to see that the interleaver period of this type of interleaver is $N = J.F$.

C.2.2 BERROU-GLAVIEUX INTERLEAVERS

The depth and width of this type of interleaver are restricted to powers of two, i.e. $J = 2^a$ and $F = 2^b$, with a and b positive integer values. Firstly, a set of eight prime numbers are defined: $X(1) = 17$, $X(2) = 37$, $X(3) = 19$, $X(4) = 29$, $X(5) = 41$, $X(6) = 23$, $X(7) = 13$ and $X(8) = 7$. The interleaver mapping function is then defined as follows [87]:

$$\Pi(i) = \emptyset(i) + F.\mathcal{F}(i) \tag{C.1}$$

where:

$$\begin{aligned} \digamma_0 &= i \bmod F \\ \emptyset_0 &= (i - \digamma_0)/F \\ \beth &= (\digamma_0 + \emptyset_0) \bmod 8 \\ \digamma(i) &= (X(\beth + 1).(\emptyset_0 + 1) - 1) \bmod J \\ \emptyset(i) &= (F/2 + 1).(\digamma_0 + \emptyset_0) \bmod F \end{aligned} \tag{C.2}$$

for every $0 \leq i < J \cdot F = N$.

C.2.3 JPL INTERLEAVERS

With JPL interleavers, the interleaver depth J must be even. As with *Berrou-Glavieux* interleavers, eight prime values are defined: $X(1) = 31$, $X(2) = 37$, $X(3) = 43$, $X(4) = 47$, $X(5) = 53$, $X(6) = 59$, $X(7) = 61$ and $X(8) = 67$. For every $0 \leq i < J.F = N$, the JPL interleaver mapping function is defined as follows [87]:

$$\Pi(i) = 2.\digamma(i) + J.\emptyset(i) - \mho(i) + 1 \tag{C.3}$$

where:

$$\begin{aligned} \mho(i) &= i \bmod F \\ \emptyset_0 &= (i - \mho(i))/2 \bmod F \\ \digamma_0 &= ((i - \mho(i))/2 - \emptyset_0)/F \\ \digamma(i) &= (10.\digamma_0 + 1) \bmod J/2 \\ \beth &= \digamma(i) \bmod 8 \\ \emptyset(i) &= (X(\beth + 1).\emptyset_0 + 21.\mho(i)) \bmod F \end{aligned} \tag{C.4}$$

C.3 RANDOM BLOCK INTERLEAVERS

A random interleaver can be described as a block interleaver with a mapping function generated from a permutation, based on the outputs of a random noise source [87]. The basic idea behind the design of random block interleavers is to eliminate regular patterns in $G_\pi(D)$, resulting in extremely long interleaver periods. Some of the more popular random interleavers, frequently used in concatenated coding schemes, are discussed in the following subsections.

C.3.1 PN GENERATOR INTERLEAVERS

The generation of the mapping function of this type of interleaver makes use of PN generators. Assuming a maximal length-a PN generator is employed, the interleaver will have a period of $N = 2^a - 1$, since the period of the sequence generated by the PN generator is $2^a - 1$. It is obvious that the interleaver period N will always be an odd number. The interleaver mapping function is determined as follows [87]:

1. Set $i = 0$.
2. At time index i, $\Pi(i)$ is the decimal equivalent of the a-bit binary word stored in the PN generator's shift register.
3. If $i < 2^a - 1$, increment i and return to step (2).

C.3.2 RANDOM NUMBER GENERATOR INTERLEAVERS

Although similar to PN generator interleavers, this type of interleaver's period N need not be an odd number. Using any type of uniform number generator, a period N random number generator interleaver's mapping function is determined as follows [87]:

1. Generate N random numbers. Store these numbers in a length-N vector, denoted by $\overline{U} = \{U_0, U_1, ..., U_{N-1}\}$.
2. Reorder the elements contained in $\overline{U}$ to range from the smallest to the largest value. The result is stored a length-N vector, denoted by $\overline{V} = \{V_0, V_1, ..., V_{N-1}\}$
3. For every i, with $0 \leq i < N$, determine the index j such that $U_i = V_j$. The mapping function of the interleaver is then simply $\Pi(i) = j$.

C.3.3 s-RANDOM INTERLEAVERS

In [177] a simple method to generate a random period-N interleaver that includes a constraint on the spreading factor M_{spread} (see *Section* 3.2.3.2) is presented. The process whereby such an interleaver's mapping function is created, is as follows:

1. Store the numbers 0 to $N-1$ in a length-N vector, denoted by $\overline{U} = \{U_0, U_1, ..., U_{N-1}\}$.
2. Choose an integer value for the spread factor M_{spread}. For a given value of N, it is important to choose $M_{spread} < \sqrt{\frac{N}{2}}$ in order for the interleaver construction method to be successful.
3. Set counter $i = 0$. Repeat the following steps:
   (a) Randomly pick a number from the list of available numbers contained in $\overline{U}$. If the chosen number differs by more than $\pm M_{spread}$ when compared to the previous M_{spread} values stored in $\overline{V}$, store it as element V_i in the vector $\overline{V} = \{V_0, V_2, ..., V_{N-1}\}$ and mark it as unavailable for the next random selection from $\overline{U}$. Otherwise, repeat step (a).
   (b) Increment counter i.
   (c) Repeat (a) to (b) for $0 \leq i < N$.
4. For every i, with $0 \leq i < N$, determine the index j such that $U_i = V_j$. As with random number generator interleavers, the mapping function of the interleaver is then $\Pi(i) = j$.

C.4 UNIFORM INTERLEAVERS

A concept frequently encountered in the derivation of concatenated coding scheme BER performance bounds, is that of a uniform interleaver [100, 101]. A size N uniform interleaver is a probabilistic device that maps any given input word $\overline{\mu}_m^{in}$ of Hamming weight w into all distinct $\binom{N}{w}$ permutations of the input word, each permutation having a probability of occurrence of:

$$\text{Prob.}\left(w_H\left(\overline{\mu}_m^{in}\right) = w\right) = 1/\binom{N}{w} \tag{C.5}$$

APPENDIX D

COMPLEX SPREADING SEQUENCES

D.1 APPENDIX OVERVIEW

THE application of binary sequences in DS/SSMA systems has been exhaustively investigated since introduction of SS. Due to the availability of potentially large sets of sequences that exhibit comparable auto-correlation and improved cross-correlation properties when compared to binary sequences, interest has started to shift towards the use of non-binary and CSSs. There are numerous advantages in using CSSs in future 4G DS/SSMA systems, including the possibility to generate CE and SSB [4, 7, 10] transmitter output signals, etc. This appendix not only summarises some of the important performances measures utilised in the analysis of CSSs, but also gives concise overviews of the filtered and unfiltered CSS families considered in this study.

D.2 IMPORTANT PERFORMANCE MEASURES FOR COMPLEX SPREADING SEQUENCES

D.2.1 SEQUENCE LENGTH AND FAMILY SIZE

The length of a CSS, denoted by M_{seq}, is the number of chips in a single CSS. It is a cardinal factor in the determination of a DS/SSMA system's processing gain (see *Section* D.2.4). Furthermore, it also influences the correlation characteristics of a CSS (see *Section* D.2.2 and *Section* D.2.3), which in turn is the factor determining a DS/SSMA system's capacity.

Inseparably intertwined with the sequence length, is the family size M_{fam} of a CSS. Usually a longer sequence length implies that more sequences, i.e. a larger family, can be generated that exhibit acceptable correlation properties.

D.2.2 PERIODIC AUTO-CORRELATION

Two types of auto-correlation functions can be calculated for spreading sequences, namely periodic and aperiodic. In synchronous DS/SSMA systems, such as the systems considered in this study, the former is of greater importance. The periodic auto-correlation of a continuous length-M_{seq} CSS, $S(t)$, having chips of duration T_{chip} [s], is defined as follows [43, 47, 48]:

$$R_{S(t),S(t)}(\tau) = \int_0^{M_{seq}.T_{chip}} S(t)S^*\left((t+\tau) \bmod (M_{seq}.T_{chip})\right) dt \tag{D.1}$$

The periodic auto-correlation function gives an indication of the signal amplitude to be expected at the output of a coherent, perfectly synchronous correlator receiver [47]. As such, this function can also be used for synchronisation purposes in code tracking loops [43].

D.2.3 PERIODIC CROSS-CORRELATION

The periodic cross-correlation measures the periodic similarity between two different CSSs having a relative phase shift of τ seconds. It is defined as follows for the continuous length-M_{seq} CSSs $S_1(t)$ and $S_2(t)$, both consisting of M_{seq} chips of duration T_{chip} [s] [47, 48]:

$$R_{S_1(t),S_2(t)}(\tau) = \int_0^{M_{seq}.T_{chip}} S_1(t) S_2^* \left((t+\tau) \bmod (M_{seq}.T_{chip})\right) dt \tag{D.2}$$

The periodic cross-correlation characteristics of the sequences in a CSS family dictate the degradation in performance in a multi-user DS/SSMA system due to MUI. Lower periodic cross-correlation values (especially at $\tau = 0$ in synchronous systems) deliver less MUI, resulting in better BER performances. Also, false code-lock is less probable for sequences with lower periodic cross-correlation values, especially in the range $|\tau| \leq \frac{M_{seq}.T_{chip}}{4}$, centered on $\tau = 0$.

A very popular lower bound on the periodic cross-correlation for the length-M_{seq} sequences $S_1(t)$ and $S_2(t)$ from a family of size-M_{fam}, is the *Welsh*-bound, given by [48]:

$$\max\left\{R_{S_1(t),S_2(t)}(\tau)\right\} \geq M_{seq}\sqrt{\frac{M_{fam}-1}{M_{seq}.M_{fam}-1}} \tag{D.3}$$

Note that for $M_{seq} \to \infty$, the Welsh-bound simplifies to $\max\left\{R_{S_1(t),S_2(t)}(\tau)\right\} \approx \sqrt{M_{seq}}$.

D.2.4 SPREADING FACTOR AND PROCESSING GAIN

Assume a spreading sequence with a chip rate of f_{chip} is used to directly spread a symbol stream with a rate of f_s. The *Spreading Factor* (SF) for this scenario is defined as follows [43, 44]:

$$SF = \frac{f_{chip}}{f_s} \tag{D.4}$$

The PG (measured in [dB]) of a DS/SSMA system, which is directly related to its SF, is calculated as follows [43, 44]:

$$PG = 10\log_{10}(SF) = 10\log_{10}\left(\frac{f_{chip}}{f_s}\right) \tag{D.5}$$

The SF and PG are important measures that reflect the spreading diversity introduced by the DS/SSMA system in order to combat the detrimental effects of narrowband interferers or jamming signals [43, 44, 81].

D.2.5 BANDWIDTH EXPANSION FACTOR

When comparing DS/SSMA systems employing filtered (or chip-level pulse shaped) and unfiltered CSSs, parameters such as PG and SF are insufficient, since these measures do not reflect the spectral characteristics of the spreading sequences and/or chip-level pulse shaping filters employed. As such, a new parameter, referred to as the BEF of a DS/SSMA system needs to be defined. The BEF for a DS/SSMA system with a transmitter output signal bandwidth of B_{sig}^{pre} prior to spreading and B_{sig}^{post}

after spreading (and chip-level pulse shaping), is calculated as follows:

$$BEF = \left(\frac{B_{sig}^{post}}{B_{sig}^{pre}} \right) \tag{D.6}$$

As with the SF and PG, the immunity a DS/SSMA system obtains against a narrowband jamming signal by increasing its transmitter output signal's dimensionality [43, 44, 81] through spreading, is reflected by the BEF. However, the BEF also includes the effects of chip-level pulse shaping and other DS/SSMA transmitter filtering on the bandwidth diversity obtained through the spreading process. Furthermore, the spectral characteristics of the spreading sequences used in the DS/SSMA system are also incorporated in the BEF.

D.2.6 SPREADING SEQUENCE LENGTH DIVERSITY

Certain pre-filtered CSS families (or chip-level pulse shaped CSSs), such as the ABC (see *Section* D.3.2.2) and DSB CE-LI-RU filtered GCL CSSs (see *Section* D.3.2.1), are highly bandlimited. Using these CSSs in DS/SSMA communication systems are more bandwidth efficient than using unfiltered CSSs or binary sequences of an equivalent length. As such, employing pre-filtered CSSs, equivalent SFs, but lower BEFs will be obtained. Generally, commercial communication systems are restricted in terms of their transmission bandwidth requirements. Thus, DS/SSMA communication systems employing pre-filtered CSSs support the use of higher data rates and/or longer CSSs in order to deliver permissable BEFs, when compared to systems using unfiltered CSSs. For fixed data rates and BEFs, the SSLD obtained by using bandlimited spreading sequences, is defined as follows:

$$SSLD = \frac{SF}{BEF} \tag{D.7}$$

Thus, the length of the filtered CSSs, denoted by M_{seq}, can be increased SSLD-times in order for the DS/SSMA communication system to occupy the same transmission bandwidth as a DS/SSMA system using unfiltered CSSs of the same length. Moreover, a larger pre-filtered CSS family can be used, possibly supporting more CDMA users.

D.3 IMPORTANT COMPLEX SPREADING SEQUENCE FAMILIES

D.3.1 UNFILTERED SEQUENCES

D.3.1.1 ZADOFF-CHU SEQUENCES

ZC CSSs is a subclass of GCL CSSs [9], which is generated and characterised as follows: Let $\overline{S}_{ZC}^{q} = \left\{ S_{ZC}^{q}[0], S_{ZC}^{q}[1], ..., S_{ZC}^{q}[M_{seq}-1] \right\}$ represent the vector of chips of the q^{th} length-M_{seq} unfiltered continuous-time ZC sequence $S_{ZC}^{q}(t)$. With $j = \sqrt{-1}$, the i^{th} chip in this sequence is determined as follows [4, 5]:

$$S_{ZC}^{q}[i] = \begin{cases} \exp\left(j\frac{\pi.a.i^2}{M_{seq}} \right) & \text{if } M_{seq} \text{ is even} \\ \exp\left(j\frac{\pi.a.i(i+1)}{M_{seq}} \right) & \text{if } M_{seq} \text{ is odd} \end{cases} \tag{D.8}$$

where the sequence number a can only take on integer values relatively prime to M_{seq}. As such, the family size for length-M_{seq} ZC CSSs is calculated as follows:

$$M_{fam} = 1 + \sum_{a=2}^{M_{seq}-1} \begin{cases} 1 & \text{if } M_{seq} \bmod(a) \neq 0 \\ 0 & \text{if } M_{seq} \bmod(a) = 0 \end{cases} \tag{D.9}$$

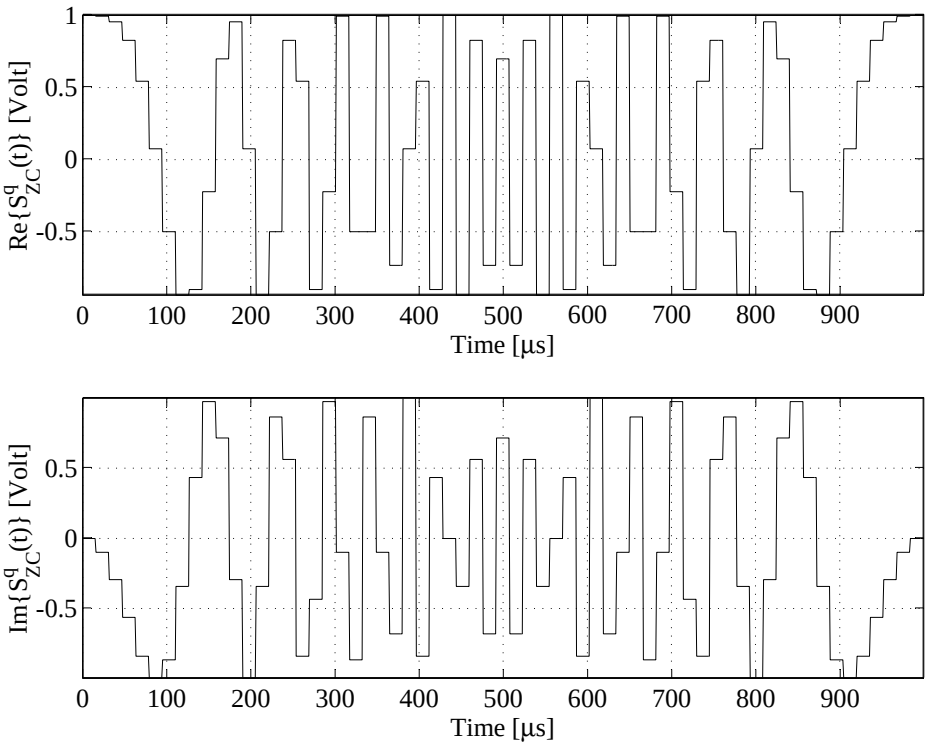

Figure D.1: Real and Imaginary Parts of a Length $M_{seq} = 63$ Unfiltered ZC CSS for $a = 1$, $f_{chip} = 63000$ Hz and 16 Samples per Chip

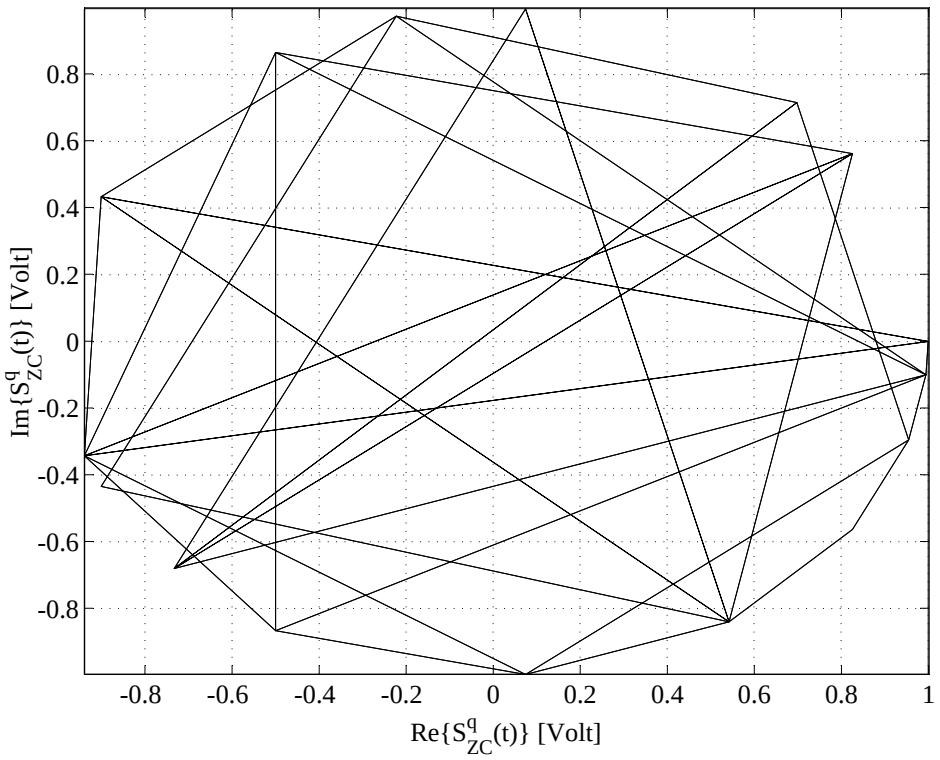

Figure D.2: Envelope of a Length $M_{seq} = 63$ Unfiltered ZC CSS for $a = 1$, $f_{chip} = 63000$ Hz and 16 Samples per Chip

Hence, the largest ZC CSS families are obtained when M_{seq} is an odd prime number. In such a case the family size is $M_{fam} = M_{seq} - 1$ [4]. *Fig.* D.1 shows the real and imaginary parts of the $a = 1$ length-63 ZC CSS with a chip rate of $f_{chip} = 63000$ Hz and 16 samples per chip. Also note that the complex envelope of the sequence, shown in *Fig.* D.2, is not constant.

D.3.1.2 QUADRIPHASE SEQUENCES

QPH sequences are closely related to binary sequences. A length-M_{seq} QPH sequence's chip vector $\overline{S}^q_{QPH} = \left\{S^q_{QPH}[0], S^q_{QPH}[1], ..., S^q_{QPH}[M_{seq}-1]\right\}$ is constructed using two length-M_{seq} binary sequences' chip vectors, denoted by $\overline{S}^q_A = \left\{S^q_A[0], S^q_A[1], ..., S^q_A[M_{seq}-1]\right\}$ and $\overline{S}^q_B = \left\{S^q_B[0], S^q_B[1], ..., S^q_B[M_{seq}-1]\right\}$, respectively. Calculation of the i^{th} chip of the QPH sequence is accomplished as follows [6]:

$$S^q_{QPH}[i] = \frac{1}{2\sqrt{2}}(1+j)S^q_A[i] + \frac{1}{2\sqrt{2}}(1-j)S^q_B[i] \tag{D.10}$$

It follows that each chip in the QPH sequence will have a value from the complex 4-symbol alphabet $\left\{\frac{1}{\sqrt{2}} + \frac{j}{\sqrt{2}}, \frac{1}{\sqrt{2}} - \frac{j}{\sqrt{2}}, -\frac{1}{\sqrt{2}} + \frac{j}{\sqrt{2}}, -\frac{1}{\sqrt{2}} - \frac{j}{\sqrt{2}}\right\}$, if the binary sequences' chip vectors $\overline{S}^q_A$ and $\overline{S}^q_B$ have chips from the antipodal alphabet $\{-1, +1\}$. For *Alltop*-type QPH sequences [4], the family size is given as $M_{fam} = M_{seq} - 1$, with the sequence length M_{seq} limited to prime values. Furthermore, using Gold binary sequences for $\overline{S}^q_A$ and $\overline{S}^q_B$ is a popular approach [48]. *Fig.* D.3 show the real and imaginary parts of user-q's length-63 QPH CSS with a chip rate of $f_{chip} = 63000$ Hz and 16 samples per chip. Since QPH sequences are binary in nature, it follows that their complex envelopes will not be constant. This characteristic is shown in *Fig.* D.4 for the QPH depicted in *Fig.* D.3.

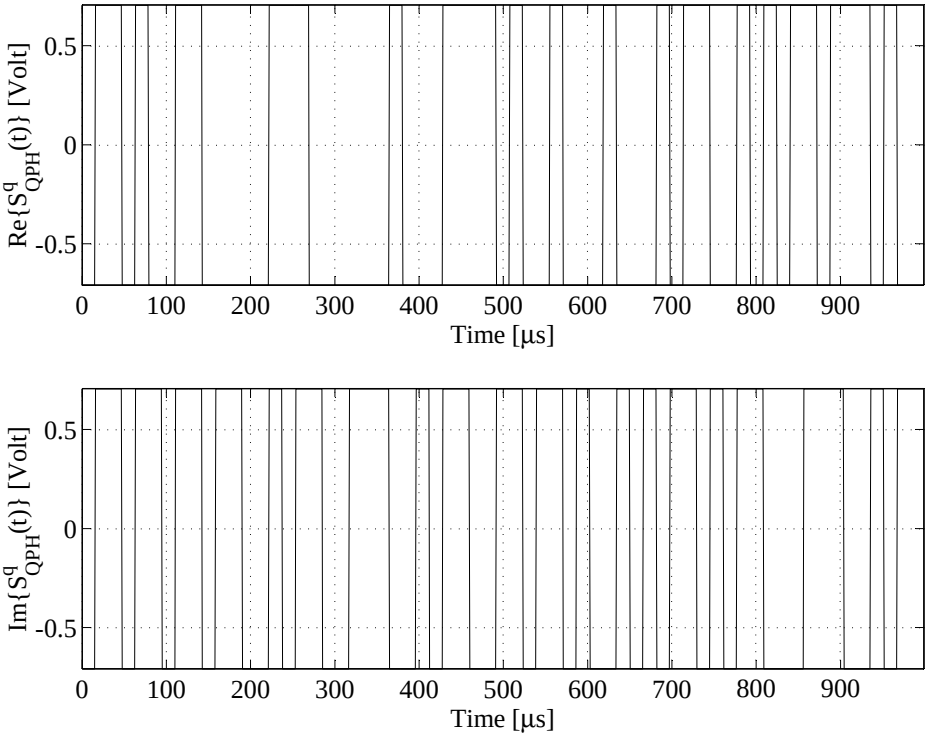

Figure D.3: Real and Imaginary Parts of a Length $M_{seq} = 63$ Unfiltered QPH CSS for $f_{chip} = 63000$ Hz and 16 Samples per Chip

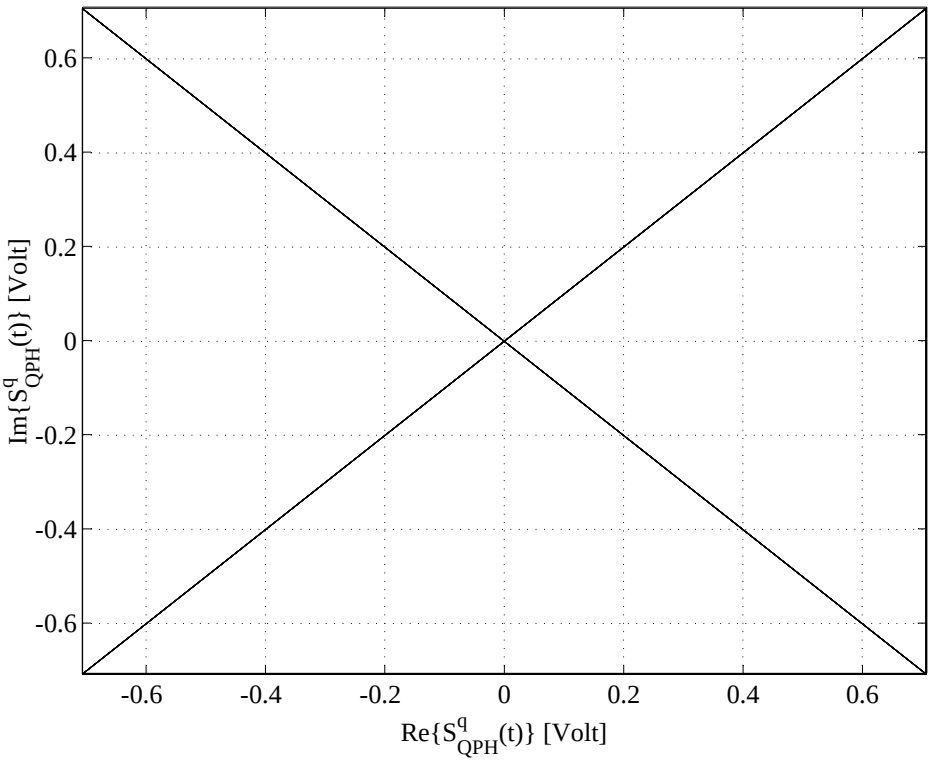

Figure D.4: Envelope of a Length $M_{seq} = 63$ Unfiltered QPH CSS for $f_{chip} = 63000$ Hz and 16 Samples per Chip

D.3.2 FILTERED SEQUENCES

D.3.2.1 DSB CE-LI-RU FILTERED GCL SEQUENCES

It has been shown that ZC sequences contain all the frequencies in the range $[0, M_{fam}/T_{chip})$ [Hz], with T_{chip} the duration of a chip [48]. Thus, the bandwidth of such sequences are a function of the family size. In order to bandlimit $S^q_{ZC}(t)$ and remove its dependency on the sequence index a, a $\mathrm{mod}(2\pi)$ phase constraint can be incorporated, resulting in a *Chu* sequence's chip vector denoted by $\overline{S}^q_{Chu} = \left\{S^q_{Chu}[0], S^q_{Chu}[1], ..., S^q_{Chu}[M_{seq}-1]\right\}$ [4,5]. The i^{th} chip of a *Chu* sequence is determined as follows:

$$S^q_{Chu}[i] = \begin{cases} \exp\left(j\frac{a.\pi.i^2}{M_{seq}}\right) \bmod (2\pi) & \text{if } M_{seq} \text{ is even} \\ \exp\left(j\frac{a.\pi.i.(i+1)}{M_{seq}}\right) \bmod (2\pi) & \text{if } M_{seq} \text{ is odd} \end{cases} \tag{D.11}$$

It has been shown [4] that the bandwidth of *Chu* sequences are $1/T_{chip}$ [Hz]. DSB CE-LI-RU filtered GCL sequences are obtained by filtering $S^q_{Chu}[i]$ with a *linearly interpolating root-of-unity filter* [7,8] in order to achieve the minimum Nyquist bandwidth of $1/(2.T_{chip})$ [Hz]. The family size of such sequences is also given by *Eq.* (D.9). *Fig.* D.5 gives the real and imaginary parts of user-q's length-63 DSB CE-LI-RU filtered GCL CSS with $a = 1$, a chip rate of $f_{chip} = 63000$ Hz and 16 samples per chip. *Fig.* D.6 shows the complex envelope of this sequence, depicting its constant nature. This characteristic alleviates and even eliminates the linearity constraint on power amplifiers used in DS/SSMA systems employing such sequences. Since the instantaneous power of the transmitter output signal will be constant, the communication system engineer no longer needs to be concerned with amplifier back-off. Thus, it will be possible to more efficiently utilise partially linear power amplifiers.

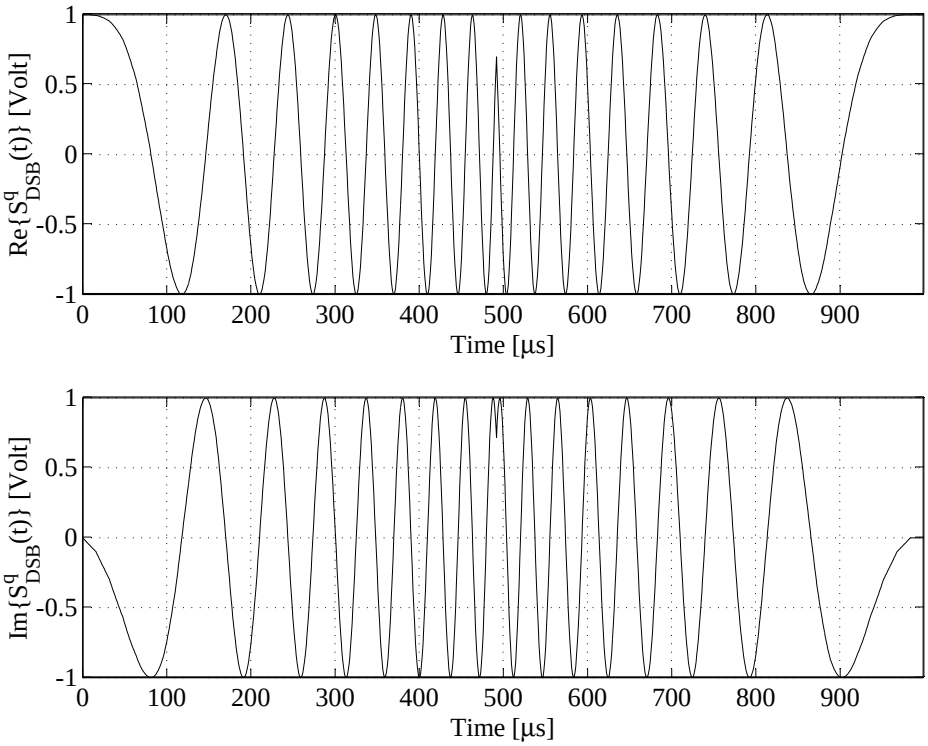

Figure D.5: Real and Imaginary Parts of a Length $M_{seq} = 63$ DSB CE-LI-RU filtered GCL CSS for $a = 1$, $f_{chip} = 63000$ Hz and 16 Samples per Chip

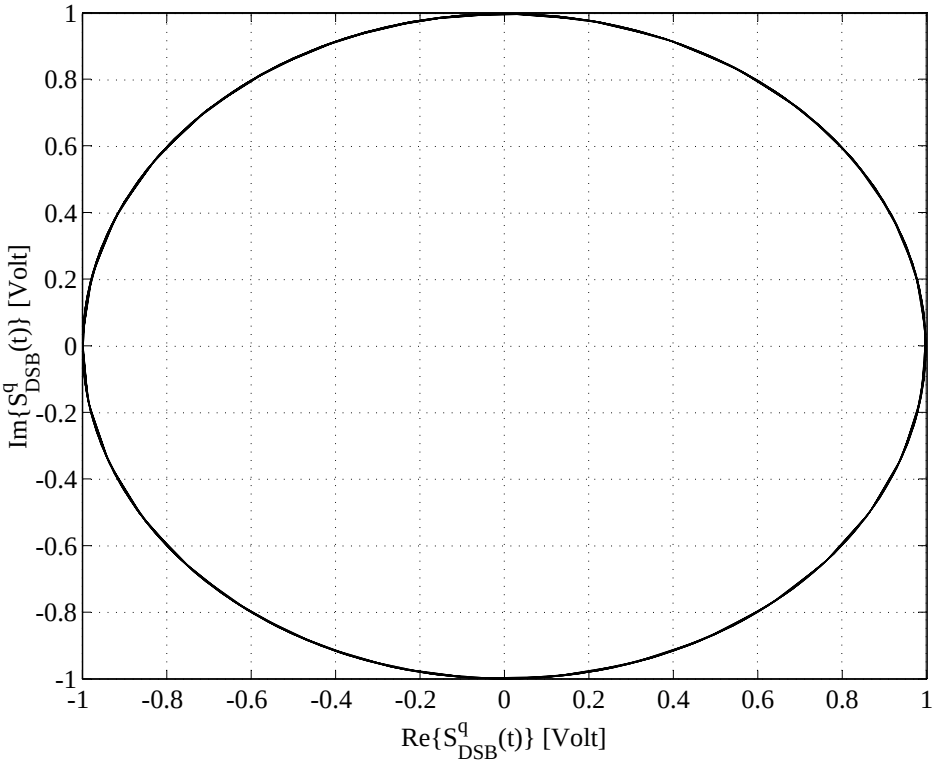

Figure D.6: Envelope of a Length $M_{seq} = 63$ DSB CE-LI-RU filtered GCL CSS for $a = 1$, $f_{chip} = 63000$ Hz and 16 Samples per Chip

D.3.2.2 ABC SEQUENCES

ABC sequences are generated by appropriately modifying the previously defined DSB CE-LI-RU filtered GCL sequences in order to produce an injective function, as described in [7, 10]. When used in balanced QPSK structures, ABC sequences [7, 10] exhibit analytical properties, i.e. a SSB DS/SSMA signal is obtained after modulation onto in-phase and quadrature carriers (see *Fig.* 6.16 in *Section* 6.4.3) [4]. As with ZC and DSB CE-LI-RU filtered GCL sequences, the family size of ABC sequences is determined using *Eq.* (D.9). *Fig.* D.7 depicts the real and imaginary parts of user-q's length-63 ABC sequence with $a = 1$, a chip rate of $f_{chip} = 63000$ Hz and 16 samples per chip. *Fig.* D.8 shows its constant complex envelope.

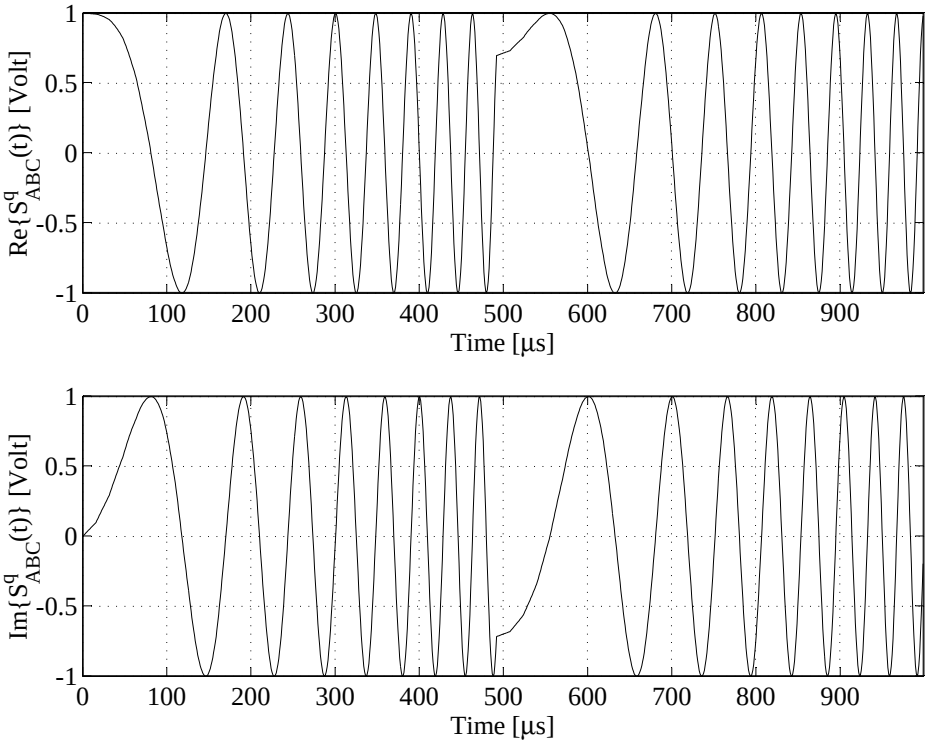

Figure D.7: Real and Imaginary Parts of a Length $M_{seq} = 63$ ABC Sequence for $a = 1$, $f_{chip} = 63000$ Hz and 16 Samples per Chip

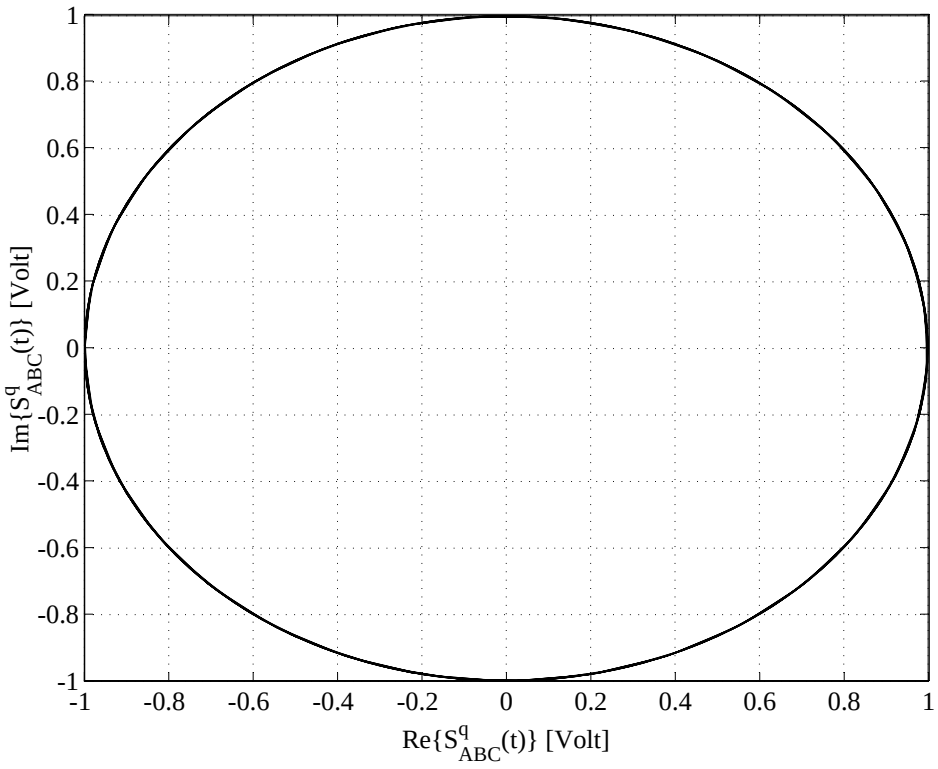

Figure D.8: Envelope of a Length $M_{seq} = 63$ ABC Sequence for $a = 1$, $f_{chip} = 63000$ Hz and 16 Samples per Chip

APPENDIX E

SIMULATION SOFTWARE INDEX

E.1 APPENDIX OVERVIEW

ACQUIRING the results presented in *Chapter* 6 required the development of an extensive set of simulation software tools, ranging from BER performance measurement platforms (see *Chapter* 5), to data analyses and plotting tools. C++ was chosen to implement the simulation platforms presented in *Chapter* 5, whereas Matlab was employed to create the necessary filter design and data analyses/plotting tools.

This appendix firstly presents the labelling conventions applied extensively in the filenames of the Matlab scripts/functions, C++ classes and compiled applications. Next follow detailed indexes, listing the filenames and short descriptions of the simulation software components developed during this study. All of the listed Matlab and C++ software modules are available on the CD-ROM accompanying this dissertation. Note that each of the simulation software tools presented here were created by the author without making use of any prior base code.

E.2 NAMING LABEL CONVENTIONS

The naming label conventions applied in the filenames of the Matlab m-files and compiled executables are given in *Table* E.1.

E.3 MATLAB FUNCTIONS AND SCRIPTS

Table E.2 and *Table* E.3 list the Matlab functions and scripts developed during the course of this study. Note that the Matlab functions and scripts were not employed in the actual performance evaluation of the VA decoded linear block codes under investigation, but rather for the creation of filters and pulse shapes, the processing and plotting of measured simulation results, etc. Although the results presented in *Chapter* 6 were obtained running these scripts and functions on a *Microsoft Windows* platform, they can be used on *Unix* or *Linux* platforms without any alterations.

Table E.1: Matlab Script and C++ Executable Filename Labelling Convention

Naming Label	**Options Available**	**Description**
CODENAME	half_rate_NSC / hr_NSC	4-state, rate $R_c = 1/2$ NSC code
	Hamming_7_4_Classic / Ham_7_4_cl	Hamming $(7, 4, 3)$, classic decoding
	Hamming_7_4_VA / Ham_7_4_cl_VA	Hamming $(7, 4, 3)$, VA decoding
	Interl_Hamming_7_4 / iHam_7_4	Interleaved Hamming $(7, 4, 3)$ code
	Interl_RS_7_5 / iRS_7_5	Interleaved RS $(7, 5, 3)$ code
	Original_5_3 / or_5_3	Cyclic $(5, 3, 2)$ code, original trellis
	Punct_BCH_15_7 / pBCH_15_7	Punctured BCH $(15, 7, 5)$ code
	Punct_half_rate_RSC / phr_RSC	Punctured, rate $R_c = 1/2$ RSC code
	Reduced_5_3 / or_red_5_3	Cyclic $(5, 3, 2)$ code, reduced trellis
	RS_7_5	RS $(7, 5, 3)$ block code
	two_thirds_rate_RSC / ttr_RSC	8-state, rate $R_c = 2/3$ RSC code
	uncoded / uc	Uncoded
SEQNAME	ABC	ABC sequences
	DSB	DSB CE-LI-RU GCL CSSs
	ZC	ZC CSSs
	QPH	QPH CSSs

Table E.2: Description of the Matlab Functions and Scripts - Part I

Matlab Function/Script	**Function/Script Description**
calc_pdf_1D.m	Calculate the 1-dimensional PDF of a set of samples
calc_pdf_2D.m	Calculate the 2-dimensional PDF of 2 sets of samples
create_elliptic_rx_filter.m	Create the numerator and denominator coefficients of an elliptic IIR lowpass filter, plot its amplitude response
create_nyquist_pulse_shape.m	Create a Nyquist pulse shape, plot the pulse shape
create_sqrt_nyquist_pulse_shape.m	Create a square-root Nyquist pulse shape, plot the pulse shape

Table E.3: Description of the Matlab Functions and Scripts - Part II

Matlab Function/Script	**Function/Script Description**
delay_spread.m	Configure the path delays for 10 unique users' multipath fading channels
doppler_filter.m	Create the numerator and denominator coefficients of a Doppler IIR lowpass filter, plot its amplitude response
plot_*CODENAME*_AWGN_ber.m	Plot the BER curves of a *CODENAME* code in AWGN channel conditions
plot_*CODENAME*_*SEQNAME*_ber.m	Plot the BER curves of a *CODENAME* code in multipath fading channel conditions for *SEQNAME* CSSs
plot_*CODENAME*_33Hz_FF_ber.m	Plot the BER curves of a *CODENAME* code in flat fading channel conditions with a 33 Hz Doppler spread
plot_*CODENAME*_100Hz_FF_ber.m	Plot the BER curves of a *CODENAME* code in flat fading channel conditions with a 100 Hz Doppler spread
plot_eye_diagram.m	Plot the eye diagrams of a pulse shaping or matched filter's output
plot_*SEQNAME*_envelope.m	Plot the complex envelope of a *SEQNAME* CSS
plot_*SEQNAME*_PSD.m	Plot the PSD of a *SEQNAME* CSS
plot_*SEQNAME*_time_signals.m	Plot the real and imaginary time signals of a *SEQNAME* CSS
power_delay_profile.m	Create an exponential decay power delay profile
process_sequence_family_files.m	Generation of the user CSS configuration files
random_interleaver.m	Create the interleaver mapping of a random interleaver
Rayleigh_PDF.m	Plot a theoretical Rayleigh PDF
Rician_PDF.m	Plot theoretical Rician PDFs
*SEQNAME*_generate	Generate and store a length-M_{seq} *SEQNAME* CSS family
systematic_cyclic_matrices.m	Convert an (n, k, d_{min}) linear block code's generator matrix to systematic form
classic_doppler_spectrum.m	Plot the classic Doppler spread PSD

E.4 C++ CLASSES

A large number of coding, modulation and channel simulator building blocks are required to construct the AWGN, flat fading and multipath fading channel performance platforms shown in *Fig.* 5.5, *Fig.* 5.8 and *Fig.* 5.9, respectively. The header and *.cpp* files of each C++ class that was created to realise the required performance evaluation platform building blocks are listed in *Table* E.4 and *Table* E.5, with their primary functions. Note that these files are *ANSI C* compliant, ensuring portability to *Microsoft Windows*, *Unix* or *Linux* platforms.

Table E.4: Description of the C++ Classes - Part I

C++ Class	Class Description
B_Trellis_Advanced.h B_Trellis_Advanced.cpp	BCJR trellis class for an (n, k, d_{min}) linear block code
B_Viterbi_Advanced.h B_Viterbi_Advanced.cpp	Block-wise VA decoder class that operates on a BCJR trellis
BC_with_Interleaver.h BC_with_Interleaver.cpp	(n, k, d_{min}) linear block code encoder and length-N interleaver combination class
BC_with_Puncturer.h BC_with_Puncturer.cpp	(n, k, d_{min}) linear block code encoder and puncturer combination class
Block_Coder.h Block_Coder.cpp	(n, k, d_{min}) linear block code encoder class
C_Trellis.h C_Trellis.cpp	Rate-n/k convolutional code trellis class
CC_with_Puncturer.h CC_with_Puncturer.cpp	Rate-n/k convolutional code encoder and puncturer combination class
Convolutional.cpp Convolutional.h	Rate-n/k convolutional code encoder class
De-interleaver_with_B_Viterbi.h De-interleaver_with_B_Viterbi.cpp	Length-N de-interleaver and block-wise VA block code decoder combination class
Delay_line.h Delay_line.cpp	General delay line class
De-puncturer_with_B_Viterbi.h De-puncturer_with_B_Viterbi.cpp	De-puncturer and block-wise VA block code decoder combination class
De-puncturer_with_SW_Viterbi.h De-puncturer_with_SW_Viterbi.cpp	De-puncturer and sliding window VA convolutional code decoder combination class

Table E.5: Description of the C++ Classes - Part II

C++ Class	Class Description
DSSS_QPSK_RAKE_Rx.h DSSS_QPSK_RAKE_Rx.cpp	Wideband classic and complex DS/SSMA QPSK RAKE receiver class
DSSS_QPSK_Tx.h DSSS_QPSK_Tx.cpp	Wideband classic and complex DS/SSMA QPSK transmitter class
FIR.h FIR.cpp	General FIR filter class
GF_Calculator.h GF_Calculator.cpp	Galois field mathematics calculator class
IIR.h IIR.cpp	General IIR filter class
Int_dump.h Int_dump.cpp	Integrate-and-dump circuit class
Interleaver.h Interleaver.cpp	General block interleaver class
Mapper.h Mapper.cpp	General input-to-output mapper class, used as a block code ML decoder
Multipath_Fading_Channel.h Multipath_Fading_Channel.cpp	Classic and complex multipath fading channel simulator class
Noise.h Noise.cpp	AWGN, uniform noise and Poisson noise generator class
PN_Gen.h PN_Gen.cpp	Length-N PN generator class
Puncturer.h Puncturer.cpp	Block or convolutional code puncturer class
QPSK_Rx.h QPSK_Rx.cpp	Narrowband classic and complex QPSK receiver class
QPSK_Tx.cpp QPSK_Tx.h	Narrowband classic and complex QPSK transmitter class
Rician_Channel.cpp Rician_Channel.h	Classic and complex *Clarke* flat fading channel simulator
SW_Viterbi_Conv.cpp SW_Viterbi_Conv.h	Sliding window VA convolutional code decoder class

E.5 COMPILED EXECUTABLES

Using the C++ classes listed in *Section* E.4, the compiled executable files, listed in *Table* E.6 and *Table* E.7, were created to obtain the simulation results presented in *Chapter* 6. The executables created to test the channel simulators, verify the operation of the narrowband and wideband communication systems, construct block and convolutional code trellises, and creating the mapping functions of random interleaver, were developed using *Borland C++ Builder* 6, since they contain *Microsoft Windows* graphic components, such as forms, buttons, dialog boxes, etc. As such, these executables are not portable to OS platforms other than *Microsoft Windows*.

A command line approach was used for the executables performing the actual BER performance evaluations. These executables were created using *Borland C++ Builder* 6, but compiled using *Intel*'s *ICC* and GNU's *G++* compilers for *Linux* platforms. The BER performance results presented in *Chapter* 6 were obtained in record breaking time by distributing the applications' computational load over the multiple workstations in the *University of Pretoria*'s *I-percube*, donated by *Intel*. The *I-percube* consists of 16 2.4 GHz *Pentium* 4 stations, each station running a *Mandrake Linux* operating system. The 16 stations are linked via *Fast Ethernet* connections. Process migration and message handling between the stations are managed transparently by means of *Open Mosix* for *Linux*.

Table E.6: Description of the Compiled Executables - Part I

Executable	**Description/Function**	**Portability**
BC_Trellis_Creator	Creation of an (n, k, d_{min}) linear block code's BCJR trellis	Windows
CC_Trellis_Creator	Creation of a rate-n/k convolutional code's trellis	Windows
Interleaver_Creator	Creation of a random or classic block interleaver	Windows
main_*CODENAME*_QPSK_AWGN	BER performance evaluation of a *CODENAME* code in AWGN channel conditions	Windows Linux DOS
main_*CODENAME*_QPSK_FF	BER performance evaluation of a *CODENAME* code in flat fading channel conditions	Windows Linux DOS
main_*CODENAME*_DSSSMA_QPSK_MPFC	BER performance evaluation of a *CODENAME* code in multipath fading channel conditions	Windows Linux DOS

Table E.7: Description of the Compiled Executables - Part II

Executable	**Description/Function**	**Portability**
Test_flat_fading_channel	Verify the operation of classic and complex flat fading channel simulators	Windows
Test_frequency_selective_fading_channel	Verify the operation of classic and complex multipath fading channel simulators	Windows
Test_narrowband_QPSK	Verify the operation of a narrowband classic or complex QPSK communication system	Windows
Wideband_Correlator	Verify the operation of a classic or complex DS/SSMA QPSK communication system employing a correlator RAKE receiver	Windows
Wideband_Matched_Filter	Verify the operation of a classic or complex DS/SSMA QPSK communication system employing a matched filter RAKE receiver	Windows

REFERENCES

[1] C. Shannon, "A Mathematical Theory of Communications," *Bell Systems Technical Journal*, vol. 27, October 1948.

[2] L. R. Bahl, J. Cocke, F. Jelinek, and J. Raviv, "Optimal Decoding of Linear Codes for Minimizing Symbol Error Rate," *IEEE Transactions on Information Theory*, pp. 284–287, March 1974.

[3] J. Wolf, "Efficient Maximum Likelihood Decoding of Linear Block Codes Using a Trellis," *IEEE Transactions on Information Theory*, vol. IT-24, pp. 76–80, January 1978.

[4] M. Jamil, L. P. Linde, J. E. Cilliers, and D. J. van Wyk, "Comparison of Complex Spreading Sequences Based on Filtering Methods and Mean Square Correlation Characteristics," *Transactions of the SAIEE*, vol. 89, no. 3, pp. 98–112, September 1998.

[5] R. L. Frank and S. A. Zadoff, "Phase Shift Pulse Codes with Good Periodic Correlation Properties," *IRE Transactions on Information Theory*, vol. IT-7, pp. 381–382, October 1962.

[6] S. M. Korne and D. V. Sarwate, "Quadriphase Sequences for Spread Spectrum Multiple Access Communication," *IEEE Transactions on Information Theory*, vol. IT-38, no. 3, pp. 1101–1113, May 1992.

[7] M. P. Lötter and L. P. Linde, "Constant Envelope Filtering of Complex Spreading Sequences," *IEE Electronics Letters*, vol. 31, no. 17, pp. 1406–1407, 17 August 1995.

[8] M. P. Lötter, "A Generalised Linear Root-of-Unity Interpolation Filter," in *Proc., IEEE COMSIG'95*, (University of Pretoria, Pretoria, South Africa), pp. 43–46, September 1995.

[9] B. M. Popović, "Generalized Chirp-like Polyphase Sequences with Optimum Correlation Properties," *IEEE Transactions on Information Theory*, vol. 38, July 1992.

[10] M. P. Lötter and L. P. Linde, "A Class of Bandlimited Complex Spreading Sequences with Analytic Properties," in *Proc., IEEE Int. Symp. on Spread Spectrum Techniques and Applications*, (Mainz, Germany), pp. 662–666, 22-25 September 1996.

[11] G. D. Forney, Jr., "Concatenated Codes." Cambridge, MA: MIT Press, 1966.

[12] G. Ungerboeck, "Channel Coding with Multilevel/Phase Signaling," *IEEE Transactions on Information Theory*, vol. IT-25, pp. 55–67, January 1982.

[13] C. Berrou, A. Glavieux, and P. Thitimajshima, "Near Shannon Limit Error-Correcting Coding and Decoding: Turbo Codes," in *Proc., IEEE Int. Conf. on Communications*, (Geneva, Switzerland), pp. 1064–1070, 23-26 May 1993.

[14] I. S. Reed and G. Solomon, "Polynomial Codes Over Certain Finite Fields," *SIAM Journal*, vol. 8, pp. 300–304, June 1960.

[15] S. Benedetto and G. Montorsi, "Unveiling Turbo Codes: Some Results on Parallel Concatenated Coding Schemes," *IEEE Transactions on Information Theory*, vol. 42, no. 2, pp. 409–429, March 1996.

[16] L. Papke and P. Robertson, "Improved Decoding With SOVA in a Parallel Concatenated (Turbo-Code) Scheme," in *Proc., IEEE Int. Conf. on Communications*, (Dallas, TX, USA), pp. 102–106, 23-27 June 1996.

[17] P. Robertson, "Illuminating the Structure of Code and Decoder of Parallel Concatenated Recursive Systematic (Turbo) Codes," in *Proc., IEEE GLOBECOM*, (San Francisco, CA, USA), pp. 1298–1303, 28 November - 2 December 1994.

[18] S. Benedetto, D. Divsalar, G. Montorsi, and F. Pollara, "Bandwidth Efficient Parallel Concatenated Coding Scheme," *IEE Electronics Letters*, vol. 31, no. 24, pp. 2067–2069, November 1995.

[19] S. Benedetto and G. Montorsi, "Design of Parallel Concatenated Convolutional Codes," *IEEE Transactions on Communications*, vol. 44, no. 5, pp. 591–600, May 1996.

[20] S. Benedetto, D. Divsalar, G. Montorsi, and F. Pollara, "Parallel Concatenated Trellis Coded Modulation," in *Proc., IEEE Int. Conf. on Communications*, (Dallas, TX, USA), pp. 974–978, 23-27 June 1996.

[21] S. Benedetto and G. Montorsi, "Performance of Continuous and Blockwise Decoded Turbo Codes," *IEEE Communications Letters*, vol. 1, no. 3, pp. 77–79, May 1997.

[22] J. Anderson, "Turbo Coding for Deep Space Applications," in *Proc., IEEE Int. Symp. on Inform. Theory*, (Whistler, British Columbia, Canada), p. 36, 17-22 September 1995.

[23] A. S. Barbulescu and S. S. Pietrobon, "Rate Compatible Turbo-Codes," *IEE Electronics Letters*, vol. 31, pp. 535–536, March 1995.

[24] C. Berrou and M. Jezequel, "Frame-Oriented Convolutional Turbo Codes," *IEE Electronics Letters*, vol. 32, no. 15, pp. 1362–1363, July 1996.

[25] S. Benedetto, G. Montorsi, D. Divsalar, and F. Pollara, "Algorithm for Continuous Decoding of Turbo-Codes," *IEE Electronics Letters*, vol. 32, no. 4, pp. 314–315, February 1996.

[26] W. J. Blackert and S. G. Wilson, "Turbo Trellis Coded Modulation," in *Proc., Conf. on Inform. Systems and Sciences*, (Princeton, NJ, USA), 20-22 March 1996.

[27] S. Benedetto, G. Montorsi, D. Divsalar, and F. Pollara, "Serial Concatenation of Interleaved Codes: Performance Analysis, Design and Iterative Decoding," TDA Progress Report 42-126, JPL, (Pasadena, CA, USA), August 1996.

[28] S. Benedetto and G. Montorsi, "Iterative Decoding of Serially Concatenated Convolutional Codes," *IEE Electronics Letters*, vol. 32, no. 13, pp. 1186–1187, June 1996.

[29] S. Benedetto and G. Montorsi, "Serial Concatenation of Block and Convolutional Codes," *IEE Electronics Letters*, vol. 32, no. 10, pp. 887–888, May 1996.

[30] D. Divsalar and F. Pollara, "Serial and Hybrid Concatenation Codes with Applications," in *Proc., Int. Symp. on Turbo Codes and Related Topics*, (Brest, France), pp. 80–87, 3-5 September 1997.

[31] P. K. Gray, *Serial Concatenated Trellis Coded Modulation*. PhD Thesis, The University of South Australia, March 1999.

[32] P. Adde, R. Pyndiah, and C. Berrou, "Performance of Hybrid Turbo Codes," *IEE Electronics Letters*, vol. 32, no. 24, pp. 2209–2210, November 1996.

[33] D. Divsalar and F. Pollara, "Hybrid Concatenated Codes and Iterative Decoding," TDA Progress Report 42-130, JPL, (Pasadena, CA, USA), August 1997.

[34] R. G. Gallager, "Low-Density Parity-Check Codes," *IRE Transactions on Information Theory*, vol. 8, no. 1, pp. 21–28, January 1962.

[35] M. Alouini and A. J. Goldsmith, "A Unified Approach for Calculating Error Rates of Linearly Modulated Signals over Generalized Fading Channels," *IEEE Transactions on Communications*, vol. 47, no. 9, pp. 1324–1334, September 1999.

[36] M. K. Simon and M. Alouini, "A Unified Approach to the Performance Analysis of Digital Communication over Generalized Fading Channels," in *Proceedings of the IEEE*, vol. 86, no. 9, September 1998.

[37] B. Sklar, "Rayleigh Fading Channels in Mobile Digital Communication Systems Part I: Characterization," *IEEE Communications Magazine*, pp. 90–100, July 1997.

[38] J. S. Swarts, "Aspects of Multipath Channel Characterization," Master's Thesis, Rand Academic University, November 1998.

[39] A. K. Salkintzis, "Implementation of a Digital Wide-Band Mobile Channel Simulator," *IEEE Transactions on Broadcasting*, vol. 45, no. 1, pp. 122–128, March 1999.

[40] L. E. Vogler and J. A. Hoffmeyer, "A Model for Wideband HF Propagation Channels," *Radio Science*, vol. 28, no. 6, pp. 1131–1142, November-December 1993.

[41] C. C. Watterson, J. R. Juroshek, and W. D. Bensema, "Experimental Confirmation of an HF Channel Model," *IEEE Transactions on Communication Technology*, vol. COM-18, no. 6, pp. 792–803, December 1970.

[42] T. S. Rappaport, *Wireless Communications: Principles and Practice*. Upper Saddle River, NJ, USA: Prentice Hall, First ed., 1996.

[43] R. L. Peterson, R. E. Ziemer, and D. E. Borth, *Introduction to Spread Spectrum Communications*. Upper Saddle River, NJ, USA: Prentice Hall, 1995.

[44] K. Feher, *Wireless Digital Communications - Modulation and Spread-Spectrum Applications*. Upper Saddle River, NJ, USA: Prentice-Hall, First ed., 1995.

[45] F. Adachi, M. Sawahashi, and H. Suda, "Wideband DS-CDMA for Next-Generation Mobile Communications Systems," *IEEE Communications Magazine*, pp. 56–69, September 1998.

[46] IS-95 Interim Standard: *'An Overview of the Application of Code Division Multiple Access (CDMA) to Digital Cellular Systems and Personal Cellular Networks'*, Qualcomm Inc., May 1992.

[47] J. G. Proakis, *Digital Communications*. New York, NY, USA: McGraw-Hill, Third ed., 1995.

[48] M. Jamil, "Comparative Study of Complex Spreading Sequences for CDMA Applications," Master's Thesis, University of Pretoria, May 1999.

[49] T. Li, M. Hatori, and N. Suehiro, "Analysis of Asynchronous Direct-Sequence Spread-Spectrum Multiple-Access Communications with Polyphase Sequences," in *Proc., IEEE GLOBECOM*, (Phoenix, AZ, USA), 4-8 November 1997.

[50] L. Staphorst, M. Jamil, and L. P. Linde, "Performance of a Synchronous Balanced QPSK CDMA System Using Complex Spreading Sequences in AWGN," in *Proc., IEEE AFRICON'99*, (Cape Town, South Africa), pp. 215–220, 28 September - 1 October 1999.

[51] L. Staphorst, M. Jamil, and L. P. Linde, "Performance Evaluation of a QPSK System Employing Complex Spreading Sequences in a Fading Environment," in *Proc., IEEE VTC'99-Fall*, (Asterdam, The Netherlands), pp. 2964–2967, 19-22 September 1999.

[52] W. H. Büttner, L. Staphorst, and L. P. Linde, "Trellis Decoding of Linear Block Codes," in *Proc., IEEE COMSIG'98*, (Cape Town, South Africa), pp. 171–174, 7-8 September 1998.

[53] L. Staphorst and L. P. Linde, "Performance Evaluation of Viterbi Decoded Binary and Non-binary Linear Block Codes in Flat Fading Channel Conditions," in *Proc., IEEE AFRICON 2002*, (George, South Africa), pp. 181–186, 2-4 October 2002.

[54] L. Staphorst and L. P. Linde, "On theViterbi Decoding of Linear Block Codes," *Transactions of the SAIEE*, vol. 94, no. 4, pp. 28–41, December 2003.

[55] L. Staphorst and L. P. Linde, "Performance Evaluation of Viterbi Decoded Reed-Solomon Block Codes in Additive White Gaussian Noise and Flat Fading Channel Conditions," in *Proc., IEEE WCNC'2002*, (Orlando, Florida, USA), 17-21 March 2002.

[56] D. Chase, "A Class of Algorithms for Decoding Block Codes with Channel Measurement Information," *IEEE Transactions on Information Theory*, vol. IT-18, pp. 170–181, July 1972.

[57] H. T. Moorthy, S. Lin, and T. Kasami, "Soft-Decision Decoding of Binary Linear Block Codes Based on an Iterative Search Algorithm," *IEEE Transactions on Information Theory*, vol. 34, pp. 1049–1053, 1988.

[58] S. Lin, T. Kasami, T. Fujiwara, and M. Fossorier, *Trellises and Trellis-Based Decoding Algorithms for Block Codes*. Boston, MA, USA: Kluwer Academic Publishers, First ed., 1998.

[59] R. J. McEliece, "On the BJCR Trellis for Linear Block Codes," *IEEE Transactions on Information Theory*, vol. 42, pp. 1072–1092, 1996.

[60] J. Hagenauer, "Viterbi Decoding of Convolutional Codes for Fading- and Burst- Channels," in *Proc., Int. Zurich Seminar on Digital Communications*, (Zurich, Switzerland), pp. G2.1–G2.7, 1980.

[61] J. Hagenauer and P. Hoeher, "A Viterbi Algorithm with Soft-Decision Outputs and its Applications," in *Proc., IEEE GLOBECOM*, (Dallas, TX, USA), pp. 47.1.1–47.1.7, 27-30 November 1989.

[62] H. Nickel, J. Hagenauer, and F. Burkert, "Approaching Shannon's Capacity Limit by 0.27 dB Using Simply Hamming Codes," *IEEE Communications Letters*, November 1997.

[63] S. Benedetto and G. Montorsi, "Average Performance of Parallel Concatenated Block Codes," *IEE Electronics Letters*, vol. 31, no. 3, pp. 156–157, February 1995.

[64] O. Aitsab and R. Pyndiah, "Performance of Reed-Solomon Block Turbo Code," in *Proc., IEEE GLOBECOM*, (London, UK), pp. 121–125, 18-22 November 1996.

[65] D. Divsalar and F. Pollara, "Turbo Codes for PCS Applications," in *Proc., IEEE Int. Conf. on Communications*, (Seatle, WA, USA), pp. 54–59, 18-22 June 1995.

[66] S. Benedetto and G. Montorsi, "Performance Evaluation of Parallel Concatenated Codes," in *Proc., IEEE GLOBECOM*, (Singapore, Malaysia), pp. 2273–2277, 13-17 November 1995.

[67] G. Battail, C. Berrou, and A. Glavieux, "Pseudo-Random Recursive Convolutional Coding for Near-Capacity Performance," in *Proc., IEEE Int. Conf. on Communications*, (Geneva, Switzerland), pp. 23–27, 23-26 May 1993.

[68] S. Benedetto and G. Montorsi, "Performance Evaluation of Turbo-Codes," *IEE Electronics Letters*, vol. 31, no. 3, pp. 163–165, February 1995.

[69] E. K. Hall, "Performance and Design of Turbo Codes on Rayleigh Fading Channels," Master's Thesis, University of Virginia, May 1996.

[70] G. E. Moore, "Cramming More Components onto Integrated Circuits," *Electronics*, vol. 38, no. 8, pp. 119 – 122, 19 April 1965.

[71] L. Staphorst, J. Schoeman, and L. P. Linde, "Performance Evaluation of a Joint Source/channel Coding Scheme for DS/SSMA Systems Utilizing Complex Spreading Sequences in Multipath Fading Channel Conditions," in *Proc., IEEE CCECE 2003*, (Montreal, Quebec, Canada), pp. 1679–1682, 4-7 May 2003.

[72] L. Staphorst and L. P. Linde, "Evaluating Viterbi Decoded Reed-Solomon Block Codes on a Complex Spreaded DS/SSMA CDMA System: Part I - Background and Communication System Models," in *Proc., IEEE AFRICON 2004*, (Gabarone, Botswana), pp. 329–334, 15-17 September 2004.

[73] L. Staphorst and L. P. Linde, "Evaluating Viterbi Decoded Reed-Solomon Block Codes on a Complex Spreaded DS/SSMA CDMA System: Part II - Channel Model, Evaluation Platform and Results," in *Proc., IEEE AFRICON 2004*, (Gabarone, Botswana), pp. 335–340, September 2004.

[74] J. L. Massey, "Step-by-Step Decoding of the BCH Codes," *IEEE Transactions on Information Theory*, vol. IT-11, pp. 580–585, October 1965.

[75] J. L. Massey, "Shift-Register Synthesis and BCH Decoding," *IEEE Transactions on Information Theory*, vol. IT-15, January 1969.

[76] R. H. Clarke, "A Statistical Theory of Mobile-Radio Reception," *Bell Systems Technical Journal*, vol. 47, pp. 957–1000, 1968.

[77] M. Lecours, M. Têtu, A. Chefaoui, J. Ahern, and A. Michaud, "Phase Measurements and Characterization of Mobile Radio Channels," *IEEE Transactions on Vehicular Technology*, vol. 45, no. 1, pp. 105–113, February 1996.

[78] G. Marsagalia and T. A. Bray, "A Convenient Method for Generating Normal Variables," *SIAM Rev.*, vol. 6, pp. 260–264, 1964.

[79] R. F. W. Coates, G. J. Janacek, and K. V. Lever, "Monte Carlo Simulation and Random Number Generation," *IEEE Journal on Selected Areas of Communication*, vol. 6, no. 1, pp. 58–66, January 1988.

[80] B. Wichmann and D. Hill, "Building a Random-Number Generator," *Byte Magazine*, pp. 127–128, March 1987.

[81] S. Haykin, *Communications Systems*. New York, NY, USA: John Wiley and Sons, Third ed., 1994.

[82] W. C. Jakes, Jr., *Microwave Mobile Communications*. IEEE Press, 1974.

[83] S. O. Rice, "Mathematical Analysis of Random Noise," *Bell Systems Technical Journal*, vol. 24, pp. 46–156, January 1945.

[84] S. O. Rice, "Statistical Properties of a Sine Wave Plus Random Noise," *Bell Systems Technical Journal*, vol. 27, pp. 109–157, January 1948.

[85] M. J. Gans, "A Power Spectral Theory of Propagation in the Mobile Radio Environment," *IEEE Transactions on Vehicular Technology*, vol. VT-21, pp. 27–38, February 1972.

[86] R. E. Ziemer, B. R. Vojcic, L. B. Milstein, and J. G. Proakis, "Effects of Carrier Tracking in RAKE Reception of Wide-Band DSSS in Rician Fading," *IEEE Transactions on Microwave Theory and Techniques*, vol. 47, no. 6, pp. 681–686, August 1999.

[87] C. Heegard and S. B. Wicker, *Turbo Coding*. Norwell, MA, USA: Kluwer Academic Publishers, First ed., 1999.

[88] S. Benedetto, R. Garello, and G. Montorsi, "A Search for Good Convolutional Codes to be Used in the Construction of Turbo Codes," *IEEE Transactions on Communications*, vol. 46, no. 9, pp. 1101–1105, September 1998.

[89] C. Berrou and A. Glavieux, "Near Optimum Error Correcting Coding and Decoding: Turbo Codes," *IEEE Transactions on Communications*, vol. 44, no. 10, pp. 1261–1271, October 1996.

[90] D. Divsalar and R. J. McEliece, "Effective Free Distance of Turbo Codes," *IEE Electronics Letters*, vol. 32, pp. 445–446, February 1996.

[91] B. Sklar, "A Primer on Turbo Code Concepts," *IEEE Communications Magazine*, pp. 94–102, December 1997.

[92] E. K. Hall and S. G. Wilson, "Design and Performance Analysis of Turbo Codes on Rayleigh Fading Channels," in *Proc., Conf. on Inform. Systems and Sciences*, (Princeton, NJ, USA), 20-22 March 1996.

[93] F. J. MacWilliams and N. J. A. Sloane, *The Theory of Error-Correcting Codes*, vol. 16. New York, NY, USA: North-Holland Mathematical Library, First ed., 1977.

[94] S. Lin and D. J. Costello, Jr., *Error Control Coding: Fundamentals and Applications*. Englewood Cliffs, NJ, USA: Prentice-Hall, First ed., 1983.

[95] R. W. Hamming, "Error Detecting and Error Correcting Codes," *Bell Systems Technical Journal*, vol. 29, pp. 147–160, 1950.

[96] A. Hocquenghem, "Codes Correcteurs d'Erreurs," *Chiffres*, vol. 2, pp. 147–156, 1959.

[97] R. C. Bose and D. K. Ray-Chaudhuri, "On a Class of Error Correcting Binary Group Codes," *Information and Control*, vol. 3, pp. 68–79, March 1960.

[98] R. C. Bose and D. K. Ray-Chaudhuri, "Further Results in Error Correcting Binary Group Codes," *Information and Control*, vol. 3, pp. 279–290, September 1960.

[99] W. W. Pieterson and E. J. Weldon, Jr., *Error-Correcting Codes*. MIT Press, Second ed., 1972.

[100] D. Divsalar and F. Pollara, "On the Design of Turbo Codes," TDA Progress Report 42-123, JPL, (Pasadena, CA, USA), November 1995.

[101] D. Divsalar, S. Dolinar, R. J. McEliece, and F. Pollara, "Transfer Function Bounds on the Performance of Turbo Codes," TDA Progress Report 42-122, JPL, (Pasadena, CA, USA), August 1995.

[102] J. B. Cain, G. C. Clark, Jr., and J. M. Geist, "Punctured Convolutional Codes of Rate (n-1)/n and Simplified Maximum Likelihood Decoding," *IEEE Transactions on Information Theory*, vol. IT-25, no. 1, pp. 97–100, January 1979.

[103] Y. Yasuda, K. Kashiki, and Y. Hirata, "High-Rate Punctured Convolutional Codes for Soft Decision Viterbi Decoding," *IEEE Transactions on Communications*, vol. COM-32, no. 3, pp. 315–319, March 1984.

[104] L. H. C. Lee, "New Rate-Compatible Punctured Convolutional Codes for Viterbi Decoding," *IEEE Transactions on Communications*, vol. 42, no. 12, pp. 3073–3079, December 1994.

[105] M. Öberg and P. H. Siegel, "The Effect of Puncturing in Turbo Encoders," in *Proc., Int. Symp. on Turbo Codes and Related Topics*, (Brest, France), pp. 184–187, 3-5 September 1997.

[106] G. D. Forney, Jr., "The Viterbi Algorithm," in *Proc. of the IEEE*, vol. 61, no. 3, pp. 268–277, March 1973.

[107] R. M. Fano, "A Heuristic Discussion of Probabilistic Coding," *IEEE Transactions on Information Theory*, vol. IT-9, pp. 64–74, April 1963.

[108] M. Jordan and R. Michols, "The Effects of Channel Characterization on Turbo Code Performance," in *Proc., IEEE MILCOM*, (McLean, VA, USA), pp. 17–21, 21-24 October 1996.

[109] D. Hatzinakos and C. Nikias, "Estimation of Multipath Channel Impulse Response in Frequency Selective Channels," *IEEE Journal on Selected Areas of Communication*, vol. S7, no. 1, pp. 12–19, January 1989.

[110] D. I. Laurenson and G. J. R. Povey, "Channel Modelling for a Predictive RAKE Receiver System," in *Proc., IEEE Int. Symp. on Personal, Indoor and Mobile Radio Communications (PIMRC)*, (The Hague, The Netherlands), pp. 715–719, 21-23 September 1994.

[111] M. Missiroli, Y. J. Guo, and S. K. Barton, "Near-Far Resistant Channel Estimation for CDMA Systems Using the Linear Decorrelating Detector," *IEEE Transactions on Communications*, vol. 48, no. 3, pp. 514–524, March 2000.

[112] M. Pätzold, *Mobile Fading Channels:Modelling, Analysis, and Simulation*. Chichester, West Sussex, UK: John Wiley and Sons, First ed., 2002.

[113] P. van Rooyen, "Using MEM to Describe CDMA Multiple Access Interference," *Transactions of the SAIEE*, vol. 89, no. 3, pp. 90–97, September 1998.

[114] S. Haykin, *Adaptive Filter Theory*. Englewood Cliffs, NJ, USA: Prentice-Hall, Second ed., 1991.

[115] E. Baccarelli and R. Cusani, "Recursive Kalman-Type Optimal Estimation and Detection of Hidden Markov Chains," *Signal Processing EURASIP*, vol. 51, no. 1, pp. 55–64, May 1996.

[116] J. K. Cavers, "An Analysis of Pilot Symbol Assisted Modulation for Rayleigh Fading Channels," *IEEE Transactions on Vehicular Technology*, vol. 40, no. 4, pp. 686–693, November 1991.

[117] A. N. D'Andrea, A. Diglio, and U. Mengali, "Symbol-Aided Channel Estimaton with Nonselective Rayleigh Fading Channels," *IEEE Transactions on Vehicular Technology*, vol. 44, no. 1, pp. 41–48, February 1995.

[118] X. Tang, M. Alouini, and A. J. Goldsmith, "Effect of Channel Estimation Error on M-QAM BER Performance in Rayleigh Fading," *IEEE Transactions on Communications*, vol. 47, no. 12, pp. 1856–1864, December 1999.

[119] K. M. Chugg and A. Polydoros, "MLSE for an Unknown Channel - Part II: Tracking Performance," *IEEE Transactions on Communications*, vol. 44, no. 8, pp. 949–958, August 1996.

[120] R. Raheli, A. Polydoros, and C. Tzou, "Per-Survivor Processing: A General Approach to MLSE in Uncertain Environments," *IEEE Transactions on Communications*, vol. 43, no. 2-4, pp. 354–364, February-April 1995.

[121] G. Auer, G. J. R. Povey, and D. I. Laurenson, "Per-Survivor Processing Applied to Decision Directed Channel Estimation for a Coherent Diversity Receiver," in *Proc., IEEE Int. Symp. on Spread Spectrum Techniques and Applications*, (Sun City, South Africa), pp. 580–584, 2-4 September 1998.

[122] N. Seshadri, "Joint Data and Channel Estimation Using Blind Trellis Search Techniques," *IEEE Transactions on Communications*, vol. 42, no. 2/3/4, pp. 1000–1011, February-April 1994.

[123] M. J. Omidi, P. G. Gulak, and S. Pasupathy, "Parallel Structures for Joint Channel Estimation and Data Detection over Fading Channels," *IEEE Journal on Selected Areas of Communication*, vol. 16, no. 9, pp. 1616–1629, December 1998.

[124] D. K. Borah and B. D. Hart, "Frequency-Selective Fading Channel Estimation with a Polynomial Time-Varying Channel Model," *IEEE Transactions on Communications*, vol. 47, no. 6, pp. 862–873, June 1999.

[125] E. Baccarelli and R. Cusani, "Combined Channel Estimation and Data Detection Using Soft Statistics for Frequency-Selective Fast-Fading Digital Links," *IEEE Transactions on Communications*, vol. 46, no. 4, pp. 424–427, April 1998.

[126] C. Tellambura, Y. J. Guo, and S. K. Barton, "Channel Estimation Using Aperiodic Binary Sequences," *IEEE Communications Letters*, vol. 2, no. 5, pp. 140–142, May 1998.

[127] J. K. Tugnait and U. Gummadavelli, "Blind Equalization and Channel Estimation with Partial Response Input Signals," *IEEE Transactions on Communications*, vol. 45, no. 9, pp. 1025–1031, September 1997.

[128] A. Müller and J. M. H. Elmirghani, "Blind Channel Estimation and Echo Cancellation Using Chaotic Coded Signals," *IEEE Communications Letters*, vol. 3, no. 3, pp. 72–74, March 1999.

[129] Z. Ding, "Characteristics of Band-Limited Channels Unidentifiable from Second-Order Cyclostationary Statistics," *IEEE Signal Processing Letters*, vol. 3, no. 5, pp. 150–152, May 1996.

[130] D. Boss, K. Kammeyer, and T. Petermann, "Is Blind Channel Estimation Feasible in Mobile Communication Systems? A Study Based on GSM," *IEEE Journal on Selected Areas of Communication*, vol. 16, no. 8, pp. 1479–1492, October 1998.

[131] G. Xu, H. Liu, L. Tong, and T. Kailath, "A Least-Squares Approach to Blind Channel Identification," *IEEE Transactions on Signal Processing*, vol. 43, no. 12, pp. 2982–2993, December 1995.

[132] J. Delmas, H. Gazzah, A. P. Liavas, and P. A. Regalia, "Statistical Analysis of Some Second-Order Methods for Blind Channel Identification/Equalization with Respect to Channel Undermodeling," *IEEE Transactions on Signal Processing*, vol. 48, no. 7, pp. 1984–1998, July 2000.

[133] E. S. A. Chevreuil, P. Loubaton, and G. B. Giannakis, "Blind Channel Identification and Equalization Using Periodic Modulation Precoders: Performance Analysis," *IEEE Transactions on Signal Processing*, vol. 48, no. 6, pp. 1570–1586, June 2000.

[134] X. Li and H. Fan, "Linear Prediction Methods for Blind Fractionally Spaced Equalization," *IEEE Transactions on Signal Processing*, vol. 48, no. 6, pp. 1667–1675, June 2000.

[135] T. Nagayasu, H. Kubo, K. Murakami, and T. Fujino, "A Soft-Output Viterbi Equalizer Employing Expanded Memory Length in a Trellis," *IEEE Transactions on Communications*, vol. E80-B, no. 2, pp. 381–385, February 1997.

[136] D. Hatzinakos and C. L. Nikias, "Blind Equalization Using a Tricepstrum-Based Algorithm," *IEEE Transactions on Communications*, vol. 39, no. 5, pp. 669–682, May 1991.

[137] A. J. Weiss and B. Friedlander, "Channel Estimation for DS-CDMA Downlink with Aperiodic Spreading Codes," *IEEE Transactions on Communications*, vol. 47, no. 10, pp. 1561–1569, October 1999.

[138] E. Aktas and U. Mitra, "Complexity reduction in subspace-based blind channel identification for ds/cdma systems," *IEEE Transactions on Communications*, vol. 48, no. 8, pp. 1392–1404, August 2000.

[139] M. Benthin and K. D. Kammeyer, "Influence of Channel Estimation on the Performance of a Coherent DS-CDMA System," *IEEE Transactions on Vehicular Technology*, vol. 46, no. 2, pp. 262–268, May 1997.

[140] M. Stojanovic and Z. Zvonar, "Performance of multiuser detection with adaptive channel estimation," *IEEE Transactions on Communications*, vol. 47, no. 8, pp. 1129–1132, August 1999.

[141] M. Honary, *Trellis Decoding of Block Codes*. Boston, MA, USA: Kluwer Academic Publishers, First ed., 1998.

[142] D. J. Muder, "Minimal Trellises for Block Codes," *IEEE Transactions on Information Theory*, vol. 34, pp. 1049–1053, 1988.

[143] S. Dolinar, L. Ekroot, A. Kiely, W. Lin, and R. J. McEliece, "The Permutation Trellis Complexity of Linear Block Codes," in *Proc., 32nd Allerton Conference on Communication, Control and Computing*, (Monticello, IL, USA), pp. 60–74, 28-30 September 1994.

[144] X. Wang and S. B. Wicker, "Soft Trellis Decoders for Some BCH Codes," in *Proc., International Symposium on Information Theory and its Applications*, (Victoria, BC, Canada), pp. 700–703, 17-20 September 1996.

[145] G. D. Forney, Jr., "Dimension/Length Profiles and Trellis Complexity of Linear Block Codes," *IEEE Transactions on Information Theory*, vol. IT-40, pp. 1741–1752, 1994.

[146] G. D. Forney, Jr., "Dimension/Length Profiles and Trellis Complexity of Lattices," *IEEE Transactions on Information Theory*, vol. IT-40, pp. 1753–1772, 1994.

[147] A. Lafourcade-Jumenbo and A. Vardy, "Lower Bounds on Trellis Complexity of Block Codes," *IEEE Transactions on Information Theory*, vol. IT-41, pp. 1938–1954, 1995.

[148] G. C. Clark, Jr. and J. C. Bibb, *Error-Correction Coding for Digital Communications*. New York, NY, USA: Plenum Press, 1981.

[149] F. R. Kschischang and G. B. Horn, "A Heuristic for Ordering a Linear Block Code to Minimize Trellis State Complexity," in *Proc., 32nd Allerton Conference on Communication, Control and Computing*, (Monticello, IL, USA), pp. 75–84, 28-30 September 1994.

[150] T. Kasami, T. Takata, T. Fujiwara, and S. Lin, "On the Optimum Bit Orders with Respect to the State Complexity of Trellis Diagrams for Binary Linear Codes," *IEEE Transactions on Information Theory*, vol. IT-39, pp. 242–245, 1993.

[151] D. Divsalar and F. Pollara, "Turbo Trellis Coded Modulation with Iterative Decoding for Mobile Satellite Communications," *International Journal of Satellite Communications*, 1997.

[152] E. Biglieri, "Coding and Modulation for the Fading Channels." Presented at ISSSTA'98, Tutorial 4, 2-4 September 1998.

[153] F. Gagnon and D. Haccoun, "Bounds of the Error Performance of Coding for Nonindependent Rician-fading Channels," *IEEE Transactions on Communications*, vol. 40, no. 2, pp. 351–360, February 1992.

[154] N. Sheikholeslami and P. Kabal, "A Family of Nyquist Filters Based on Generalized Raised-Cosine Spectra," in *Proc.*, 19^{th} *Biennial Symp. Communications*, (Kingston, Ontario, Canada), pp. 131–135, 31 May - 3 June 1998.

[155] F. Marx, , and L. P. Linde, "A Combined Coherent Carrier Recovery and Decision-Directed Delay-Lock-Loop Scheme for DS/SSMA Communication Systems Employing Complex Spreading Sequences," *Transactions of the SAIEE*, vol. 89, no. 3, pp. 131–139, September 1998.

[156] G. L. Turin, "The Effects of Multipath and Fading on the Performance of Direct-Sequence CDMA Systems," *IEEE Journal on Selected Areas of Communication*, vol. 2, no. 4, pp. 597–603, July 1984.

[157] R. Price and P. E. Green, Jr., "A Communication Technique for Multipath Channels," in *Proc., IRE*, vol. 46, pp. 555–570, March 1958.

[158] G. J. R. Povey, P. M. Grant, and R. D. Pringle, "A Decision-Directed Spread Spectrum RAKE Receiver for Fast-Fading Mobile Channels," *IEEE Transactions on Vehicular Technology*, vol. 45, no. 3, pp. 491–502, August 1996.

[159] S. Benedetto and E. Biglieri, *Principles of Digital Transmission with Wireless Applications*. New York, NY, USA: Plenum Press, First ed., 1998.

[160] J. Bingham, *The Theory and Practice of MODEM Design*. New York, NY, USA: John Wiley and Sons, 1988.

[161] B. D. O. Anderson and J. B. Moore, *Optimal Filtering*. Englewood Cliffs, NJ, USA: Prentice-Hall, Second ed., 1979.

[162] L. Staphorst and L. P. Linde, "On the Optimal Selection of ABC Sequences for MUI Minimization." Submitted to the IEEE Communications Letters, July 2005.

[163] M. P. C. Fossorier, S. Lin, and D. Rhee, "Bit-Error Probability for Maximum-Likelihood Decoding of Linear Block Codes and Related Soft-Decision Decoding Methods," *IEEE Transactions on Information Theory*, vol. 44, no. 7, pp. 3083–3090, November 1998.

[164] G. D. Forney, Jr., "Burst-Correcting Codes for the Classic Bursty Channel," *IEEE Transactions on Communications*, vol. COM-19, no. 5, pp. 772–781, October 1971.

[165] J. Hagenauer and L. Papke, "Decoding Turbo Codes with the Soft-Output Viterbi Algorithm (SOVA)," in *Proc., IEEE Int. Symp. on Inform. Theory*, (Trondheim, Norway), p. 164, 27 June - 1 July 1994.

[166] J. Hagenauer, P. Robertson, and L. Papke, "Iterative (Turbo) Decoding of Systematic Convolutional Codes with the MAP and SOVA Algorithms," in *Proc., ITG Conference on Source and Channel Coding*, (München, Germany), pp. 21–29, 26-28 October 1994.

[167] A. S. Barbulescu and S. S. Pietrobon, "Terminating the Trellis of Turbo-Codes in the Same State," *IEE Electronics Letters*, vol. 31, pp. 22–23, January 1995.

[168] W. J. Blackert, E. K. Hall, and S. G. Wilson, "Turbo Code Termination and Interleaver Conditions," *IEE Electronics Letters*, vol. 31, pp. 2082–2084, November 1995.

[169] O. Joerssen and H. Meyr, "Terminating the Trellis of Turbo-Codes," *IEE Electronics Letters*, vol. 30, pp. 1285–1286, August 1994.

[170] R. J. McEliece, E. R. Rodemich, and J. Cheng, "The Turbo Decision Algorithm." presented at *33rd Allerton Conf. on Communication, Control and Computing*, 4-6 October 1995.

[171] F. Daneshgaran and M. Mondin, "Design of Interleavers for Turbo Codes Based on a Cost Function," in *Proc., Int. Symp. on Turbo Codes and Related Topics*, (Brest, France), pp. 255–258, 3-5 September 1997.

[172] R. Pyndiah, A. Glavieux, A. Picart, and S. Jacq, "Near Optimum Decoding of Product Codes," in *Proc., IEEE Int. Conf. on Communications*, (New Orleans, LA, USA), pp. 339–343, 1-5 May 1994.

[173] R. Pyndiah, P. Combelles, and P. Adde, "A Very Low Complexity Block Turbo Decoder for Product Codes," in *Proc., IEEE GLOBECOM*, (London, UK), pp. 101–105, 18-22 November 1996.

[174] J. Lodge, R. Young, P. Hoeher, and J. Hagenauer, "Separable MAP Filters for the Decoding of Product and Concatenated Codes," in *Proc., IEEE Int. Conf. on Communications*, (Geneva, Switzerland), pp. 1740–1745, 23-26 May 1993.

[175] G. D. Forney, Jr., "On Decoding BCH Codes," *IEEE Transactions on Information Theory*, vol. IT-11, pp. 549–557, October 1965.

[176] R. E. Blahut, *Theory and Practise of Error Control Codes*. Reading, MA, USA: Addison-Wesley, First ed., 1983.

[177] S. Dolinar and D. Divsalar, "Weight Distributions for Turbo Codes Using Random and Non-Random Permutations," TDA Progress Report 42-121, JPL, (Pasadena, CA, USA), August 1995.